JET MIXING ENHANCEMENT BY HIGH AMPLITUDE PULSE-FLUIDIC ACTUATION

A Thesis
Presented to
The Academic Faculty

by

Paul Wickersham

In Partial Fulfillment
of the Requirements for the Degree
Doctor of Philosophy in the
School of Mechanical Engineering

Georgia Institute of Technology
December 2007

JET MIXING ENHANCEMENT BY HIGH AMPLITUDE PULSE-FLUIDIC ACTUATION

Approved by:

Dr. David Parekh, Advisor
School of Mechanical Engineering
Georgia Institute of Technology

Dr. Jeff Jagoda
School of Aerospace Engineering
Georgia Institute of Technology

Dr. Ari Glezer
School of Mechanical Engineering
Georgia Institute of Technology

Dr. Richard Gaeta
School of Aerospace Engineering
Georgia Institute of Technology

Dr. Samuel Shelton
School of Mechanical Engineering
Georgia Institute of Technology

Date Approved: May 29, 2007

To my Parents,
And to my Jacqueline

ACKNOWLEDGEMENTS

It is only right to first thank the members of my committee for taking the time to thoughtfully read through this monster of a thesis and to offer me their feedback on it and the work described inside. Since most of the people reading this section will not venture much beyond the next few pages I feel it is only right to first give those who actually will their due.

I cannot give enough thanks to my advisor, Dr. David Parekh, who has stood by me in the best and worst of times. His professional guidance and personal concern has been invaluable to me. This work springs from his work on pulse fluidic mixing enhancement at McDonnell-Douglas and later at Georgia Tech. Rick Gaeta was in many ways a co-advisor to me. I enjoyed our many discussions which ranged from the physical mechanisms of jet mixing to how awesome the pizza is in New York. I have taken classes taught by Jeff Jagoda, Ari Glezer, and Sam Shelton. Dr. Jagoda is probably the most approachable engineering professor I have ever met. Dr. Glezer always challenged me to go beyond just the surface in my explanations. Dr. Shelton's practical approach to teaching thermal systems was refreshing in a highly theoretical institution like Georgia Tech. I will especially remember his catchy sayings like: "any number is better than no number at all" and "trying to explain entropy is just an exercise in intellectual…"

There are more individuals at GTRI who have played a role in this work and my development than I could possibly recall. Cal Jameson designed the rotary actuators for

the jet engine. Terrell Brown and Jimmy Ross machined many of the parts. Mark Entrekin let me constantly bug him about machining techniques since I always wanted to make things myself, and even taught me how to weld. Grover Richardson helped me build many of the electronics and taught me the value of *being* a character.

A number of the GTRI Co-ops have a piece in this work by helping with the setup or data acquisition: Barry Hellman, Mike Huang, Rebecca Douglas, Ben Murdock, and Rob Combier. Thanks to all of the frisbee and volleyball regulars for making lunchtime up at Cobb all the more fun: Glen Hopkins, Juan Santamaria, Joe Hurst, Bill Guzak, Scott Munro, Charles, and even Ricky Ivey when he kept his cool. Cheri Weisman organized many fun volleyball games. Other GTRI research engineers provided valuable discussions and sometimes just some much needed laughter including Kevin Massey, Warren (DOG!) Lee, and Shayne Kondor. Rob Funk taught me the basics of data acquisition when I knew nothing. Krish Ahuja let me use his flow visualization lab to do the small scale mixing experiments on two separate occasions, and allowed me to stay longer than planned both times even though he had paying projects in line to use it.

I have been blessed with fantastic friends and roommates who have greatly enriched my life. Great friends like Pearl Fung and David Tamburello helped make the early days of graduate school more fun. I always seemed to draw the lucky straw with fantastic roommates like Samuel Guinet, Carl Hannah, Berk Taftali, and “Berkeley” Brent Nelson who taught me that people from California really are pretty nuts, but a lot of fun too. I’m very grateful for the friends I have met from around the world including Sebastien Nasse,

Caroline Metry, Elcin Kentel, Meltem Adelmar, Loubna Abdelloui, Benji Declety, Cherry Ovasith, Tae Choi, Gelsy Torres, and Onyi Irrechukwu, some of whom got to travel to Florida with me to meet my family. And if I didn't mention my good friend and roommate "My name is Ash-*raf*" Awad, well that just wouldn't be right. On the American front there was Donavon Gerty, Will & Diane Hughes, Jimmy & Angelyn Hill, and Seth & Jill Kelly. And who would have guessed that the guy living next door to me in the Graduate Living Center, Jonathan Waddell would become a closer friend after we moved out? In fact the whole Waddell family has a special place in my heart.

My parents, Mark and Pat Wickersham, were my biggest influence and my rock of encouragement. They taught me the importance of working hard, believing in myself, and most importantly of loving God by loving people. My mother always listened and taught me by example how to treat other people. My father constantly encouraged me to work hard so that I could find a job I enjoy, and taught me that being a man and having compassion can go hand in hand. I am especially grateful to them for my solid foundation in Jesus Christ.

Most of all I would like to thank Jacqueline, my best friend and the love of my life, who I met in the middle of this grand endeavor, and who has waited for me to finish much longer than I ever wanted her to. I know that she sacrificed some of her dreams to see me accomplish this. The support I have received from her and her family (Greg and Susan "school comes first" Beauvais, and Josh and Christine Armstrong) has been essential to the completion of this work.

TABLE OF CONTENTS

LIST OF FIGURES

NOMENCLATURE

Roman Symbols

A	amplitude
C_d	discharge coefficient
d	penetrating jet diameter
D	main jet nozzle diameter
D_e	equivalent diameter for non-circular nozzles
D_i	inner diameter
D_o	outer diameter
f	frequency
f_n	natural frequency, most amplified frequency, preferred frequency of a jet
J	jet to crossflow momentum flux ratio
l	length, typically for a nozzle slot
m	azimuthal mode number for a jet
Ma	Mach number
Mag	velocity magnitude
P	pressure
Q	volume flow rate
r	square root of the momentum flux ratio or the effective velocity ratio
Re	Reynolds number based on diameter unless otherwise specified
Re_D	Reynolds number based on jet diameter
Re_Θ	Reynolds number based on momentum thickness

St	Strouhal number
St_D	Strouhal number based on jet diameter
St_Θ	Strouhal number based on momentum thickness
t	time
T	temperature
T*	dimensionless temperature
U(t)	instantaneous velocity in the axial direction
U	time averaged axial velocity
U_{CL}	centerline velocity
U_{exit}	axial velocity at the jet nozzle exit
U*	velocity reduction ratio
w	width, typically for a nozzle slot, also used for an annulus
x	streamwise coordinate
y	horizontal coordinate
z	vertical coordinate
%MFR	percent mass flow ratio
%TI	percent turbulence intensity

Greek Symbols

δ	boundary layer thickness
ρ	density
Θ	momentum thickness
Φ	pulsing phase between multiple actuators

Acronyms

ACE	Active Core Exhaust control
CCD	Charge Coupled Device
CVP	Counter-rotating Vortex Pair
ES	Evolution Strategy
GA	Genetic Algorithm
JICF	Jet In Crossflow
LHS	Left Hand Side
PIV	Particle Image Velocimetry
PID	Proportional Integral Derivative
PLIF	Planar Laser Induced Fluorescence
POD	Proper Orthogonal Decomposition
RHS	Right Hand Side
SRMR	Square Root of the Momentum Ratio
STOL	Short Take-Off and Landing

SUMMARY

Turbulent mixing enhancement has received a great deal of attention in the fluid mechanics community in the last few decades. Generally speaking, mixing enhancement involves the increased dispersion of the fluid that makes up a flow. For a jet this means increased entrainment of surrounding fluid and more rapid spreading over the unforced case. There are many applications where mixing enhancement is desirable and among aerospace technologies one of the most obvious choices is jet engines. Benefits of implementing mixing enhancement on a jet engine include: improved combustion efficiency, reduced noise, and reduced plume temperature. The last of these benefits is the focus of the current work.

The current work focuses on mixing enhancement of an axisymmetric jet via high amplitude fluidic pulses applied at the nozzle exit. The work consists of small scale "clean jet" experiments, small scale micro-turbine engine experiments, and full scale laboratory simulated core exhaust experiments using actuators designed to fit within the engine nacelle of a full scale aircraft.

The small scale clean jet experiments show that mixing enhancement compared to the unforced case is likely due to a combination of mechanisms. The first mechanism is the growth of shear layer instabilities, similar to what occurs with an acoustically excited jet except that in this case the forcing is highly nonlinear. The result of the instability is a frequency "bucket" with an optimal forcing frequency. The second mechanism is the generation of counter rotating vortex pairs similar to those generated by mechanical tabs.

In this case the penetration depth determines the extent to which this mechanism acts. This mechanism is therefore more important as the pulsing amplitude is increased. Finally, for a jet that is being forced in the antisymmetric mode the alternate back and forth vectoring of the jet in the near field coupled with the other mixing mechanisms plays a small role as well. However, since actuator to jet momentum ratios are on the order of 1%, the effect is minimal. The key mixing parameters were found to be the actuator to jet momentum ratio (amplitude) and the pulsing frequency, where the optimal frequency depends on the amplitude. The importance of phase, offset, duty cycle, and geometric configuration were also explored.

The experiments on the jet engine and full scale simulated core nozzle demonstrated that pulse fluidic mixing enhancement was effective on realistic flows. The same parameters that were important for the cleaner small scale experiments were found to be important for the more realistic cases as well. This suggests that the same mixing mechanisms are at work. Additional work was done to optimize, in real time, mixing on the small jet engine using an evolution strategy.

CHAPTER 1

INTRODUCTION AND BACKGROUND

Turbulent mixing enhancement has received a great deal of attention in the fluid mechanics community in the last few decades. Generally speaking, mixing enhancement involves the increased dispersion of the fluid that makes up a flow. For a jet this means increased entrainment of surrounding fluid and more rapid spreading over the unforced case. There are many applications where mixing enhancement is desirable and among aerospace technologies one of the most obvious choices is jet engines. Benefits of implementing mixing enhancement on a jet engine include: improved combustion efficiency, reduced noise, and reduced plume temperature resulting in lower heat signature and thermal loading on parts. The last of these benefits is the focus of the current work.

Techniques for implementing jet mixing enhancement are typically classified as either active or passive. Examples of passive techniques include non-circular nozzles and mechanical tabs mounted at the nozzle exit. Most of the early studies on active enhancement used acoustic actuators because they are highly controllable and well suited to laboratory scale experiments with clean jets. Unfortunately these actuators often do not work well with the higher Reynolds number turbulent flows typically encountered in industry since the turbulent fluctuations overwhelm the small amplitude perturbations. In more recent years some researchers have begun to study pulse-fluidic actuators, which

have shown great promise in delivering effective mixing enhancement for full scale realistic jet flows.

The current work focuses on mixing enhancement of an axisymmetric circular jet via high amplitude fluidic pulses applied normal to the main jet at the nozzle exit. The work consists of small scale "clean jet" experiments, small scale micro-turbine engine experiments, and full scale laboratory simulated core exhaust experiments using actuators designed to fit within the engine nacelle of a production aircraft. The objectives of the small scale experiments were to discover the critical pulse-fluidic jet mixing parameters and to understand the physical mechanisms. The other experiments demonstrate the effectiveness of pulse-fluidic jet mixing on more realistic flows and compare the results with the more fundamental small scale results. Additional work was done to optimize, in real time, mixing on a micro-turbine using an evolution strategy.

Background

Early History of Excited Jets

Sensitive Flames

The discovery of acoustically excited laminar jets is attributed to John Leconte. In 1858 he was attending a party and noticed that some of the gas flames lighting the room appeared to dance in harmony with the music being played. This phenomenon, which became known as "sensitive flames", was first studied in 1867 by Tyndall at Leconte's suggestion. Tyndall created a number of different flame tubes with different sized orifices out of drawn glass and excited the flames acoustically with tuning forks. He

discovered that, in addition to flames, jets of unlit gases could also be excited when they were brought to the verge of turbulence and sound was applied at much lower frequencies than for the flames. Tyndall concluded that the effect of sound on the jets was to cause them to transition to turbulent as if the driving pressure of the jet was slightly increased.[24]

In 1932, G.B. Brown examined the matter further. In particular, he paid close attention to the instabilities that resulted when the sensitive flames were excited by sound. He observed that the effect of the sound was to produce undulations in the jet column. The wave length of the undulations varied with the sound frequency and the jet velocity. Further downstream the undulations produced a series of alternating vortices which started on the side facing the source and then alternated sides with a frequency equal to that of the sound. He also observed that the vortices grew as they traveled downstream and that they grew fastest when the jet was just about to become turbulent.[24, 25]

Theoretical Modeling

In 1879, Lord Rayleigh created a theoretical model of a circular jet and discovered that an axisymmetric disturbance results in instability.[113] In 1933, Schlichting developed a model for a 2-D high Reynolds number laminar jet and assumed it could be modeled using the boundary layer approximation. In reality a high Reynolds number laminar jet can not exist because the instabilities result in turbulence formation. Nevertheless, his analysis provided some useful results. For example, the widely cited principle that the momentum of a jet is constant with respect to downstream distance, but the mass flow

continually increases is derived from Schlichting's laminar jet model. Additionally, the model was later modified and applied to turbulent jet flows.[128]

The Role of Coherent Structures in Jet Mixing

Many early studies on jets focused on the mixing layer. When it was found that the spectra of the measured fluctuations in this region have a broadband character it was concluded that the fluctuations are random and can only be addressed statistically. But by the 1960's some researchers began to suspect that there may be some sort of order underlying the randomness. In 1971 Lau et al came up with a simple model to explain observed velocity and phase relationships in the mixing layer. The model suggested a regular array of vortices spaced at about 1.25 nozzle diameters which were convecting downstream in the jet shear layer at a velocity of about 0.6 times the jet exit velocity.[103]

Reasoning that any underlying structures in the mixing layer would affect other regions of the jet, they made detailed hotwire and microphone measurements in the potential core and entrainment regions. They calculated the correlation coefficients of simultaneous measurement fluctuations at pairs of points with variable spacing using an analogue correlator. An analysis of the correlation results showed that their model was essentially correct. The broadband appearance of the mixing layer spectra was explained in terms of a semi-regular array of vortices that deviated in passage frequency in a manner such that any spectral peaks would be smeared out. They argued that instead of containing clearly defined peaks the broadband spectra should be "generally disposed about the

fundamental frequency and show a hint of a peak there". This was verified by the fact that varying the jet velocity resulted in a corresponding shift of the broadband mound. [103]

As early as 1967 Vlasov and Ginevsky in the USSR studied the effect of acoustic excitation of turbulent jets.[60] They discovered that lower frequency excitation enhanced turbulent mixing and frequencies an order of magnitude higher suppressed mixing. In the West the work of Crow and Champagne is considered seminal to the current barrage of studies. In 1971 they used flow visualization methods to study jets with Reynolds numbers ranging from 10^2 to 10^5. They noticed that as the jet velocity was increased so that the jet transitioned to turbulent, a series of large scale vortex puffs formed downstream with an average Strouhal number (dimensionless frequency) of about 0.3. They noted that this frequency did not vary with the Reynolds number of the jet. Furthermore, they discovered that axisymmetric acoustic excitation of the jet at a Strouhal number (based on the jet exit diameter) of 0.3 resulted in the largest amplification of the vortex puffs as they moved downstream.[41] The orderly structures described by Crow and Champagne became commonly known as 'coherent structures'.

In 1974 Winant and Browand observed that vortices in a mixing layer with moderate Reynolds numbers (ranging from 45 at the origin to 850 downstream) begin to roll around each other and eventually merge as they travel downstream. The result is a new series of vortices with twice the spacing of the originals. This process of merging occurs repeatedly and is the primary mechanism by which the vortices grow.[176] In the same year

Brown and Roshko showed, using flow visualization methods, that this vortex pairing mechanism also occurs in higher Reynolds number turbulent shear layers.[26]

In 1980, Zaman & Hussain reported that two different acoustic excitation conditions in a round jet were observed to result in pairing of rolled up vortex rings. The first condition is for a Strouhal number based on the initial shear layer momentum thickness (St_Θ) equal to about 0.012. This was called the "shear layer mode". In this case, the thin vortex rings near the exit pair up when the initial boundary layer is laminar, irrespective of the Strouhal number based on the jet diameter (St_D). This Strouhal number is slightly lower than the most unstable frequency predicted by spatial stability theory ($St_\Theta = 0.017$). The second condition that results in vortex pairing is for St_D of about 0.85 and is called the "jet column mode". In this case, thicker vortex rings pair up near $x/D \approx 1.75$, irrespective of St_Θ or whether the boundary layer is laminar or turbulent. These thicker rings result in the large coherent structures that travel downstream and do not appear to be a result of the smaller rings that form initially. For laminar exit boundary layers where $Re_D < 5x10^4$, pairing occurs regularly in space and time. As Re_D is increased, the pairing becomes less stable or intermittent. $St_D = 0.3$ is still the "preferred mode" in terms of the average centerline velocity, but not in terms of fluctuation.[179]

In 1982, Ho and Huang showed the effect of varying amplitude on the development and growth of vortices in the mixing layer. At low amplitudes, vortices form and pair as usual. At higher excitation levels and forcing at a subharmonic of the most amplified frequency a “collective interaction” occurs where several vortices coalesce into a single

large structure. At higher amplitudes still, the mixing layer directly forms a single large vortex, bypassing the pairing and collective interaction stages.[73]

In 1981 Hussain and Clark tested the idea that coherent structures are fundamental to jets and that the primary growth mechanism is vortex pairing for high Reynolds number jets (Re = 360,000) by performing a flow visualization study. They discovered that "most of the time the mixing layer is in a state of disorganized 3-D motion, consisting of relatively smaller scale random and diffuse turbulent motions." Occasionally, distinct organized large-scale structures formed within the disorganized flow, but when they did they were torn apart rather quickly. The 'survival distance' was typically on the order of the size of the structure itself. Furthermore, the tearing up of these structures was seen to be just as significant as their pairing. When pairing did occur, it usually involved torn pieces of the coherent structures, not the structures in their entirety. They concluded that while coherent structures are inherent to all turbulent shear flows, their characteristics at high Reynolds numbers can not be inferred from lower Reynolds number observations. As the Reynolds number increases, so does the complexity.[79] The debate over the "uniqueness, ubiquity, and importance of coherent structures" continues to this day.[53]

In 1986 Lepicovsky et al found that vortices can be induced in very high Reynolds number jets. They studied acoustic axial forcing on heated and unheated jets (up to 800 K) at very high velocities which resulted in an orderly arrangement of vortex structures for jets with Reynolds numbers from 350,000 to 1,300,000 and Mach numbers from 0.3 to 0.8.[106] In 1989 Jin and Hussain studied the large scale vortical motions in the fully

developed region of an unforced jet with Re = 69,000 using a novel detection scheme to detect and sample the vortical structures. They concluded that axisymmetric, helical, and double helical structures existed. Among them the helical structures were the most dominant and the most important in terms of the spreading of the jet.[84]

Preferred Modes and Stability

Throughout the 20th century, much progress was made in the area of linear stability theory. The ultimate goal of linear stability theory is to determine whether a given flow pattern is stable, and under what conditions it maintains or loses its stability. A classic example of a hydrodynamic instability is the Kelvin-Helmholtz instability which occurs when a perturbation is introduced between two inviscid flows with uniform velocity profiles. The Kelvin-Helmholtz instability shows that the roll up of vortices in an ideal inviscid shear layer occurs with a regular frequency. In an axisymmetric circular jet, the initial annular vortex rings that form near the jet exit resemble a Kelvin-Helmholtz instability. As these vortex structures move downstream, they grow rapidly and become more chaotic. Thus, non-linear effects become more important.[128]

In 1971, Michalke found that that the phase velocity of the coherent structures measured by Crow and Champagne agreed with that derived from stability theory when the turbulent mean velocity profile was used in the stability calculation. Numerous studies on jet turbulence have verified that the coherent structures are a result of the instability of the turbulent shear layer.[113] Linear stability theory correctly predicts the most amplified

frequency f_n which only dominates near the jet exit. At greater distances the subharmonic $f_n/2$ becomes dominant. [128]

The most amplified frequency, or preferred mode, is the frequency at which large scale vortex structures tend to form in an unforced jet. Crow and Champagne found that this occurred at $St_D = 0.3$ for their jet, but variations from 0.24 to 0.64 are given in the literature. The consensus is that the spread is due to differences in initial conditions. In 1987, Peterson and Samet showed that the preferred mode depends on the region of interest. They argued that beyond the potential core, helical disturbances are more strongly amplified than axisymmetric ones.[146] Cohen and Wygnanski concluded that increasing the shear layer thickness limits the number of unstable modes. By the end of the potential core the only unstable mode left is the helical mode.[38]

It is well known that higher initial turbulence results in a faster velocity decay of an unforced turbulent jet. Raman et al. showed the importance of initial turbulence level on mixing efficiency. They produced jets with varying turbulence levels and found that with increasing initial turbulence level the effect of acoustic excitation on mixing diminished.[140]

A good example of how the growth rate of a shear layer depends heavily on its initial conditions is the bifurcating and blooming jets produced by W.C. Reynolds in the 1980's. These jets are produced using an appropriate combination of axial and circumferential acoustic excitations.[143] A bifurcating jet forks off into two separate jets downstream of

the exit with a certain spreading angle. A blooming jet splits into many jets and resembles a bouquet of flowers. Research by Parekh on bifurcating jets concluded that the jet spreading angle increases with both excitation amplitudes. The excitation level needed to create the bifurcation increases with Reynolds number, but the corresponding excitation Strouhal number is invariant. A vortex filament code was written to simulate the large scale features of the bifurcating jets. The simulation showed that inviscid vortex interactions determine how the jet develops, and that the spreading angle increases with axial forcing frequency. [131]

Proper Orthogonal Decomposition (POD)

In recent years proper orthogonal decomposition has become a very attractive method for analyzing and modeling turbulent flows. In general terms, POD is a statistical method which aims to create low-dimensional approximate descriptions for multidimensional systems. The POD provides a basis for the modal decomposition of a system of functions, usually data obtained from experiments or numerical simulations. The basis functions retrieved are called proper orthogonal modes. POD provides an efficient way of representing the essential characteristics of a multidimensional system to the desired precision by using the relevant set of modes, thus reducing the order of the system. [85, 153] By analogy, the POD can be described as a lower dimensional best fit to a higher dimensional system where the eigenfunctions define the basis.

The Proper Orthogonal Decomposition was first introduced in the field of fluid mechanics by Lumley, and is now frequently applied to turbulent flows.[108] It is optimal

in terms of the kinetic energy contained in the successive modes. In stationary quasi-parallel turbulent flows (e.g. jets, mixing layers and boundary layers) the main objectives are to identify and analyze the properties of coherent structures embedded in the turbulence and to construct low dimensional models which exhibit most of the coherent properties of the flow.[16] The eigenfunctions, or modes, are calculated from the cross correlation tensor of the velocity fluctuations in the flow, and are then used as basis functions to represent the flow. The structure is represented by an ordered set of orthogonal eigenfunctions that are defined by the maximization of their normalized mean square projection on the velocity vector.[108] At this point, the modes are projected onto real-time experimental (or numerical) data. Alternatively, the Navier Stokes equations can be projected onto the eigenmodes to derive a set of linear ordinary differential equations to predict flow behavior.[30]

For experimental studies, POD typically requires simultaneous measurement at a large number of points through time (i.e. high spatial and temporal resolution are both needed). In the past, this was typically done with very large rakes of hotwires. The recent introduction of kilohertz frame rate particle image velocimetry, called dynamic PIV (DPIV), has for the first time allowed experimentalists to resolve the spatial and temporal details of turbulence with resolution similar to that of numerical simulation.[171] This new measurement method is well suited to POD analysis.

According to a POD analysis performed by Citriniti on an unforced high Reynolds number axisymmetric jet, the azimuthal modes m = 0, 3, 4, 5, and 6 are the most

important in the dynamics of the large scale structures in the axisymmetric shear layer at x/D = 3. The higher modes 3, 5 and 6 are associated with the formation of streamwise vortex pairs which advect fluid into and out of the potential core, similar to the action of side jets. It is hypothesized that previous success in mixing enhancement by multiple-mode excitation is due to the increased energy placed in these modes. Thus, the fact that they contain a substantial portion of the kinetic energy in the layer suggests that they are important to the layer dynamics and specifically entrainment and growth. An interesting feature is the lack of energy in the m = 1 (helical) mode.[37] This is likely due to the choice of measurement location.

The Application of Different Methods of Mixing Enhancement

In past decades a number of different active and passive methods for enhancing jet mixing were studied. Some of the passive methods included tabs mounted on the jet nozzle exit, fluted nozzles, and other non-circular shaped nozzles.[4, 5, 13] Among the active methods studied were acoustic actuators, fluidic actuators, blowing, synthetic jets, and hybrid actuators.[35, 45, 56, 91, 132, 137, 139, 148, 158] With advances in computing technology, it has become feasible to perform numerical simulation on both natural and excited jets under various actuation configurations.[66, 102, 109, 125]

Tabs and Blowing

Ahuja and Brown studied the effect of mechanical tabs protruding normally into the flow for round and rectangular jets. The major findings were that the addition of tabs result significant mixing enhancement by the production of counter rotating streamwise vortices

that result in added entrainment of ambient air. This occurred for both subsonic and supersonic flows. Jet noise increased for subsonic flows and decreased for supersonic flows. Rectangular jets were found to mix better than circular jets, and the addition of tabs to these increased mixing even more. The optimal tab configuration was found to be two tabs on opposing sides of the jet.[4, 5]

More recently, these devices have been studied by Behrouzi et al. They found that blowing, which they call "fluid tabs", results in similar mixing enhancement to mechanical tabs. The fluidic tabs produce the same streamwise vortices of mechanical tabs, and have the advantage that they can be turned on and off when desired.[13, 14] Davis also studied the effect of blowing radially inward on mixing enhancement of a circular jet. He concluded that there are two regimes of control. In the first regime the low amplitude control jets are swept away in the shear layer and significant velocity reduction can be achieved without distorting the jet significantly. In the second regime higher amplitudes are applied and the control jets penetrate the potential core. The main jet is strongly distorted from a circular cross section and mixing is less sensitive to blowing velocities.[44]

Synthetic Jets

In the last decade several researchers have used synthetic jets to implement jet mixing.[45, 158] Synthetic jets suck in and blow out equal amounts of ambient fluid resulting in zero net mass flow and a positive net momentum flux. There are a number of ways to create synthetic jets, using a piston and cylinder for example, but piezoelectric disks mounted

on thin flexible metal plates which serve as a diaphragm in a small plenum is currently the most common design since it results in a robust and compact actuator.

In theory synthetic jets can be produced at any desired amplitude. In practice they are usually low amplitude combination fluidic/acoustic actuators. Current piezo driven actuators are typically run at vary high frequencies (kHz), which results in a train of vortices that can ultimately be used for flow control. An advantage of using such high frequencies is that the usual energy cascade mechanism is partly bypassed and the small scale turbulent fluctuations are more directly excited.[175] To produce lower frequency excitations, the higher frequency "carrier wave" is amplitude modulated at a lower frequency. A detailed review of synthetic jets and their flow control applications can be found in Glezer and Amitay.[62]

Wiltse and Glezer studied subsonic and supersonic high aspect ratio rectangular jets excited with synthetic jets actuators and discovered that very large increases in the spreading angle could be obtained.[132] Davis and Glezer used synthetic jet actuators to excite a coaxial jet and measured mixing using hotwire anemometry and PLIF. High frequency excitation resulted in increased turbulence intensity in the near field and increased turbulence dissipation. Amplitude modulation (effective lower frequency excitation) resulted in the formation of large-scale vortical structures and greatly enhanced mixing.[45]

In recent years Tamburello and Amitay have studied the effect of a single synthetic jet actuator on a circular jet using PIV.[158] Their jet was run at two different velocities with Re = 6,600 and 26,500, and the actuator was driven at 1000 Hz. They specified amplitude in terms of momentum coefficient which was set to either 0.02 or 0.16. The actuator exit was located upstream of the jet exit, and the positioning affected the direction in which the jet vectored. Actuation resulted in the formation of vortex structures which enhanced mixing and vectored the jet. Increased amplitude had an increased effect. They also found that the lower Reynolds number jet was more responsive to actuation than the higher Reynolds number jet.

High Amplitude Fluidic Actuators

For many years, acoustic drivers (speakers) were the actuator of choice for exciting jets because they are readily available and highly controllable over a wide range of frequencies. This makes them ideally suited for studying the dynamics of flows in the laboratory where fundamental understanding often takes priority over practical implementation. Unfortunately, acoustic actuators are not very effective at exciting larger scale, higher Reynolds number flows since the turbulent fluctuations overwhelm the relatively low amplitude applied perturbations. Most practical flows are larger scale, higher Reynolds number flows. They therefore require actuators capable of producing higher amplitude perturbations in order to have any significant impact on the flow. Motivated by a desire to see jet mixing enhancement applied to more realistic flows, several researchers in the 1990's began to study of jet mixing enhancement using high amplitude fluidic actuators. [56, 137]

Raman used a pair of fluidic oscillator nozzles to excite a rectangular jet in the antisymmetric (flapping) mode. Actuation frequency was performed at a $St_D = 0.15$, the subharmonic of the preferred frequency of Crow and Champagne ($St_D = 0.3$).[41] The subharmonic was chosen because it excites the flapping mode, which is dominant farther downstream than the axisymmetric mode. A mass addition of 12% of the main flow (4% momentum addition) resulted in a 35% reduction of the potential core length, a 60% increase in normalized mass flux, and about a 10% drop in centerline velocity at $x/D_e = 10$ (where D_e is the equivalent diameter).[137]

Studies in 1996 by Parekh et al on pulse-fluidic jet mixing enhancement showed that mixing depends strongly on both frequency and amplitude. They found that when increasing the amplitude of forcing, mixing saturated at around a 2% mass flow ratio. Fluidic pulses applied at the exit of a circular jet at 1% mass flow ratio and $St_D = 0.2$ resulted in more than a 50% reduction in centerline velocity at $x/D = 10$.[132] Based on this work, in the late 1990's a full scale test of jet mixing enhancement via fluidic pulsing was performed on a JT8D missile engine. The test resulted in a reduction in centerline temperature of about 50% at $x/D = 10$.[91] Ibrahim et al had success using unsteady microjets as actuators to enhance the mixing of a sonic main jet. They excited the jet at $St = 0.16$ in both the axisymmetric and flapping modes and measured the centerline velocity decay and performed cross traverses. They found that mixing was enhanced for both cases, but more so for the flapping case.[82]

Behrouzi and McGuirk studied the effect of fluidic pulses on mixing in a water tunnel and high speed air flow facility. They compared solid tabs, blowing, and pulsing and found that low amplitude pulsing and solid tabs perform comparably. Additionally, they found that pulse fluidic actuation appears to be effective for both subsonic and supersonic flow.[14, 15]

Direct numerical simulation of a jet excited by fluidic pulses performed by Freund and Moin showed that the jet responds closer to the nozzle when forced at $St_D = 0.4$, but forcing at $St_D = 0.2$ is more effective at spreading the jet downstream.[56] Numerical simulation performed by Chenault et al suggests that pulse fluidic mixing enhancement is effective for both static and forward flight conditions.[35] These conclusions are further validated by the numerical simulations of Smith et al.[152]

Faivre and Poinsot used blowing and pulsing flow to add swirl upstream of the exit of a circular jet, and observed the effects using Schlieren and PLIF. They found that the addition of swirl resulted in enhanced mixing with ambient fluid which they measured in terms of the spread angle of the jet. They also injected different gases (air, air-helium, and CO_2) to create the swirl and discovered that the resulting spread angle did not collapse on the mass flow ratio, but instead on the momentum flux ratio J. The spread angle increases linearly with J.[51]

Jet In Crossflow (JICF)

The jet in crossflow has been studied for many years because it is frequently encountered in industry. Common occurrences include fuel injection into a premixing burner, dilution air injection into combustor liners, and discharge of chimney exhaust into the atmosphere.[50] JICF studies are relevant to the current work because the interaction between the pulse-fluidic jet and the main jet is similar to the interaction between a jet and crossflow. In both cases a smaller scale flow penetrates the shear layer of a much larger scale flow. It would not be a surprise to find that the two cases have some dimensionless parameters in common. It should be noted, however, that there are some key differences between the two cases. In the case of the JICF mixing only takes place between the jet and the crossflow, while in the current work mixing takes place between the pulsing jet, the main jet, and entrained ambient fluid. The goal of the JICF is to disperse and mix the smaller scale penetrating jet with the crossflow, while the primary goal of the current work is to enhance the mixing of the larger scale main jet with ambient fluid. Efficient mixing of the smaller scale pulsing jet with the main jet is also desirable, but not the primary concern.

A JICF shares some characteristics with viscous flow around a bluff body. When the injected fluid is impacted by the free stream viscous layers develop in the contact region due to the friction between the two flow fields.[81] The jet centerline initially has an essentially linear trajectory as it moves through the boundary layer, and begins to bend more and more as it moves through the free stream. Researchers have identified four different vortical structures in the JICF, which include: horseshoe vortices which form

upstream of the jet exit and wrap around the jet column, jet shear layer vortices which form at the interface between the jet and the cross flow, wake vortices which form on the downstream side of the jet and persist far downstream, and the counter-rotating vortex pair (CVP) which is formed is formed by the folding and rollup of the jet shear layer after the jet has been turned in the direction of the cross flow. The CVP is the dominant structure in the farfield region of the penetrating jet.[151]

The most important parameter that governs the flow field of the JICF is the momentum flux ratio, J.[74] This is the ratio of the smaller scale penetrating jet to the larger scale free stream crossflow momentum per unit area. The square root of this ratio, r, determines the extent of penetration into the free stream crossflow and is sometimes referred to as the *effective velocity ratio* since it reduces to the velocity ratio for flows of equal density. [75, 105, 151] Mathematically, the two ratios are defined as follows:

$$J = \frac{\rho_j V_j^2}{\rho_\infty V_\infty^2} \tag{1}$$

$$r = \sqrt{\frac{\rho_j V_j^2}{\rho_\infty V_\infty^2}} \tag{2}$$

The subscript j refers to the penetrating jet and ∞ refers to the free stream crossflow.

A majority of the studies conducted on the JICF focus on a steady circular jet blowing normal to the crossflow. Some studies have examined the effect of different nozzle

shapes, configuration geometries, and blowing angles. When the nozzle shape is varied, the area is typically held constant so that jets with identical mass flow rates can be compared. Nozzle shape is found to have a significant effect on penetration. Velocity ratios studied typically range from about r = 5 and up, but some studies include lower ratios. Effective velocity ratios of r = 5 and lower are though to be in a different flow regime than higher values because of wall effects.[151] According to Davitian the nature of the penetrating jet instability differs significantly for r < 3.5 compared to jets with higher velocity ratios.[46]

Different length scales are used by researchers for different regions of the jet. The most common scales are: d, rd, and r^2d (where d is the diameter of the penetrating jet). Smith and Mungal used d-scaling for jet structures, rd-scaling for the initial trajectories, and r^2d-scaling in the farfield. Scaling with rd has been shown to collapse the initial trajectories for a limited range of r. Ensemble averaged concentration profiles of jets of different r show that the physical dimensions of the jet scale well with rd.[151]

None of the previously mentioned parameters result in a complete collapse of the penetration trajectory. It is therefore likely that the initial conditions of the jet and boundary layer play an important role in penetration. In recent years more sophisticated scaling parameters have been developed which collapse the data better. One example requires calculation of the local boundary layer thickness, δ, and integration of the penetrating jet exit velocity profile. The collapse is not perfect, but it is much better over a wide range of effective velocity ratios and trajectory distances.[81, 151]

Su and Mungal made simultaneous PLIF and PIV measurements of a JICF with r = 5.7 for both a flush mounted jet and a pipe protruding into the crossflow. Penetration was similar for both cases indicating that geometry is not as important as exit conditions. The center streamline obtained from PIV measurements was a fairly good indicator of the scalar centerline obtained from PLIF measurements.[156]

In more recent years studies have been done on pulsing jets in crossflows, referred to as fully modulated jets in the literature.[50, 70, 86] Studies by Johari et al performed on pulsing jets in crossflow reveal that short injection times result in vortex ring structures that penetrate deep into the crossflow and mix rapidly compared to steady jets with the same velocity ratio. Long injection times result in axially elongated turbulent puffs that resemble steady jets and penetrate only slightly further than steady jets of the same velocity ratio. Penetration distance of the shorter pulses was as much as 5 times that of the steady blowing case when measured 50 jet diameters downstream of the exit. For a fixed injection time increasing the duty cycle (i.e. by increasing the frequency) resulted in decreased penetration for frequencies up to 5 Hz (the limit of the study). The authors concluded that this was due to the fact that it decreased the spacing between successive pulses. Thus adjacent pulses in close proximity tend to retard penetration. The velocity ratios studied were r = 5 and 10.[86]

Eroglu and Breidenthal also studied pulsing jets in crossflow. They observed that the pulsing jet creates vortex loops with strength and spacing determined by the pulsing

frequency and the velocity ratio r. By sweeping the pulsing frequency for a given r, they were able to find the optimal vortex loop spacing and strength resulting in maximum penetration while concurrently enhancing the mixing. They also modulate pulsing at 20% of jet's flow rate (i.e. they added offset to the pulse) and found that penetration and mixing were better than the steady blowing case but worse than the fully pulsed case. In general, they found that low frequency pulsing worked best since the spacing of the vortex rings play an important role in the penetration depth.[50]

Optimization of Mixing Enhancement

Several studies have been done on the optimization of turbulent jet mixing using stochastic methods.[71, 98, 99, 172] Koumoutsakos et al showed that an evolution strategy applied to a direct numerical simulation could successfully optimize the forcing parameters of a low Reynolds number turbulent jet, resulting in the Blooming jet similar to that created by Reynolds et al. The algorithm converged on a Strouhal number around 0.2, which is very close to the optimal value found in previous experiments.[132] In addition, an evolution strategy applied to a vortex simulation was able to 'discover' a flow state not previously observed, a bifurcating jet with a secondary bifurcation resulting in much greater spreading angles.[99]

The advantages of stochastic methods over more traditional gradient methods are that they are able to search complicated multidimensional 'surfaces' without giving up (i.e. converging to the nearest solution) too easily.[98, 99] Thus, they are well suited for applications with multiple parameters, complex parameter spaces, and noisy

environments. In some instances they have been able to find parameter combinations that result in optimal (or semi-optimal) configurations that were previously unidentified. This illustrates of the utility of this optimization strategy both in optimizing flow development without *a priori* knowledge about the flow and in discovering new phenomenon that might easily be missed even by systematic searches through the parameter space.[172] The major disadvantage of stochastic methods is that they are slower to converge, sometimes significantly so, than their gradient method counterparts.

Scope of Current Work

To date, there has not been a comprehensive parametric study of jet mixing enhancement by pulsed-fluidic actuation. Hence, although it has been established that this is a viable technology for mixing enhancement of realistic jet flows, designing a specific system would still require a significant amount of trial and error. The high nonlinearity of the interaction between the main jet and fluidic pulses suggests that a completely different physical phenomenon drives mixing enhancement compared to the more thoroughly studied acoustically excited jet case. It is therefore the intention of the current study to advance the state of the art of jet mixing via pulsed fluidic excitation by determining what the critical scaled parameters are, and by understanding the relevant physical mechanisms that make these parameters important.

CHAPTER 2

SMALL SCALE JET - EXPERIMENTAL SETUP AND EQUIPMENT

Chapter Overview

This chapter describes the overall experimental setup and the major pieces of equipment used in the experiments on a small scale 4" diameter clean jet. Experiments were performed in the Flow Visualization Laboratory of the Cobb County facility of the Georgia Tech Research Institute (GTRI). Testing took place in two phases. In the first phase of testing mixing performance was characterized for a number of different conditions and geometric configurations in order to sort out what the key mixing parameters were. During this phase the primary mixing enhancement metric was downstream velocity reduction ten diameters from the nozzle exit. In the second phase of testing detailed PIV and hotwire measurements were made of the interaction region and the downstream flow field in order to better understand the physics of the mixing process. Additional parametric characterization was performed to confirm consistency with phase I tests and, in some cases, to extend them.

Experimental Setup Objectives

The overall objectives of the setup were:

1. To create a low-turbulence, clean, axisymmetric, circular jet in the laboratory with a near top-hat nozzle velocity profile. It was to be small enough to maintain reasonable flow rates and use available flow conditioning equipment, but large enough to simplify pulse actuator integration, provide an appropriate pulsing frequency (i.e.

Strouhal) range, and a sufficiently high Reynolds number within the incompressible flow regime.

2. To design and build fluidic actuators that were capable of delivering a high quality, high-amplitude, fluidic pulse to the jet at the nozzle exit. A high quality pulse is one that resembles a square wave with respect to time as closely as possible, with little or no DC offset, and a 50% duty cycle. The actuators were to have variable geometric configurations where the nozzle size, actuator position (pulsing angle), and number of actuators could be varied. One of the possible configurations was to be a scaled down version of a full scale jet (Chapter 4) with a similar jet to actuator area ratio.
3. To have control of the following pulsing parameters: amplitude (i.e. velocity), frequency, phase between actuators, duty cycle, and DC offset.
4. To accurately measure all appropriate physical quantities in order to know the state of the system and the effect of the different pulsing parameters on mixing.
5. To automate data acquisition and processing routines using a personal computer for measurement and control, and by writing computer algorithms to batch process acquired data.

Overall Setup

Figure 2.1 is a schematic showing the overall small scale jet mixing setup used for both phases of experiments. The main jet was created with a 4" (0.1016 m) diameter nozzle bolted to an 18" (0.457 m) diameter cylindrical plenum with internal flow conditioning. The plenum sat atop a table that was approximately centered in the back of the room. Figure 2.2 is a close-up schematic of the equipment on the table. The room is frequently

used to make noise measurements and thus was lined with sound absorbing foam. The plenum was also covered with foam on the outside. For the first phase of testing a 2" I.D. compressed air line supplied the plenum with pressure. Control of the plenum pressure, and therefore jet velocity, was achieved using a pressure regulator and a gate valve in series.

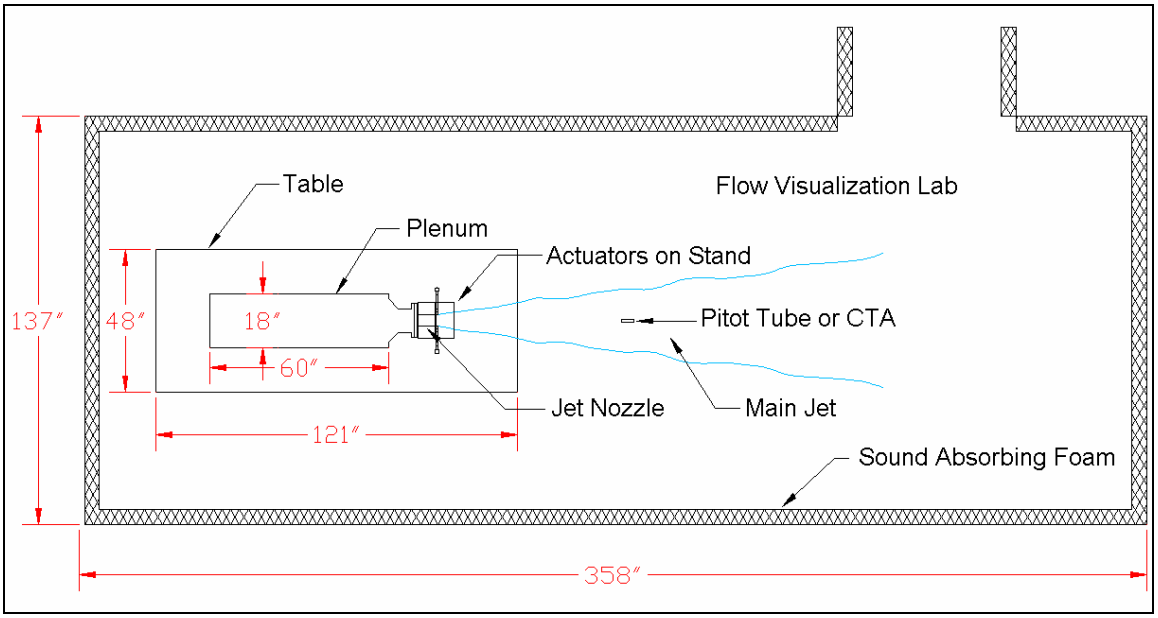

Figure 2.1: Schematic of Small Scale Jet Setup In the GTRI Flow Visualization Lab

For the second phase of testing, which involved PIV and hotwire measurements, the setup was modified so that a centrifugal blower supplied the plenum. In this case jet velocity control was achieved by blocking the blower inlet by varying amounts. The fluidic actuators were mounted at the jet nozzle exit on a custom built stand that allowed the circumferential position and pulsing angle to be varied. Small solenoid valves were used to drive the actuators. The actuators were supplied with 100-PSI filtered shop air and mass flow was measured with a venturi flowmeter. The jet exit and flow field velocities were measured using a pitot tube, a portable anemometer, a research

anemometer (hotwire and hotfilm), and PIV. Data acquisition and control was performed using a personal computer with National Instruments data acquisition cards and LabView software.

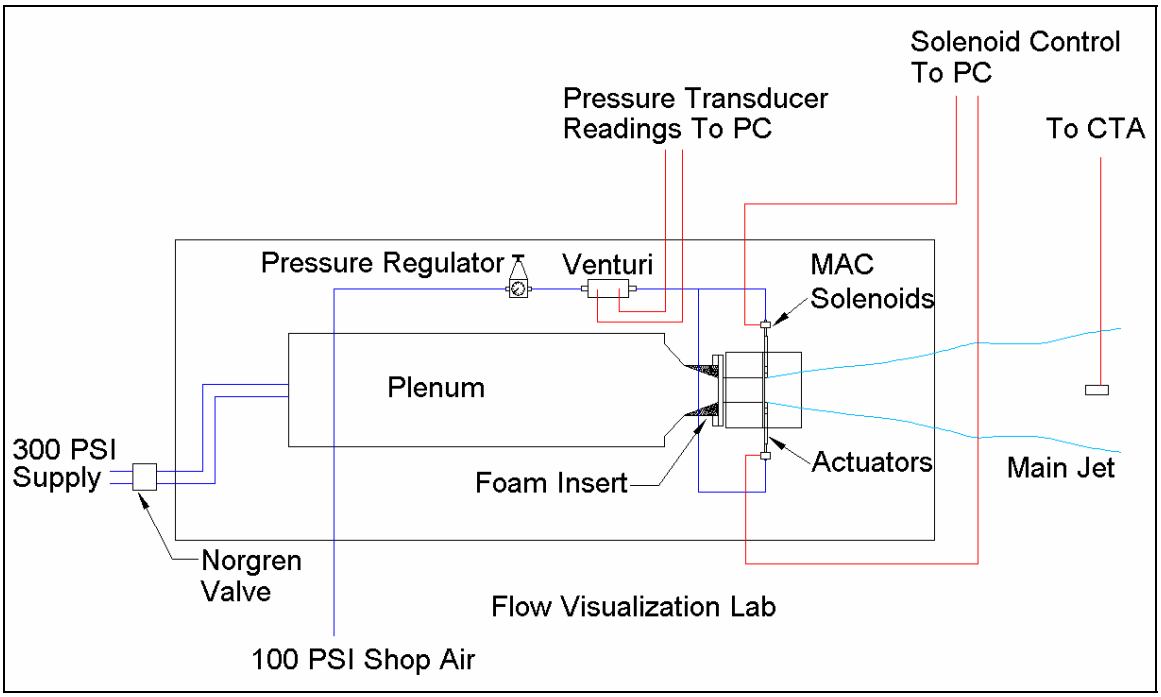

Figure 2.2: Close-up Schematic of Small Scale Jet Setup Showing Relevant Components for Phase I Experiments, For Phase II the Compressed Air Line was Replaced with a Blower

The Jet Plenum and Nozzle

A cylindrical steel plenum 18" (0.457 m) in diameter by 60" (1.52 m) long was used to create the jet. It necked down to 8" diameter flanged sections at both the inlet and outlet. The plenum contains flow straightening and conditioning components (honeycomb, screens, etc) which help to produce uniform internal flow. Preliminary velocity profiles taken at the jet nozzle exit revealed that the jet was nowhere near the desired top-hat profile and highly asymmetric because the plenum converged to only 8" in diameter at the nozzle bolt on plate. To improve this, a Styrofoam reducing insert was constructed

and inserted into the 8” diameter plenum exit to gradually reduce the cross section down to 4” (figure 2.3). The jet nozzle thus consisted of the converging foam insert inside the plenum and truncated with a 5” long, 4” diameter pipe that was bolted onto the steel plate at the plenum exit. Auto body filler (Bondo) was used to fill gaps in the transitional joints and smooth the flow path.

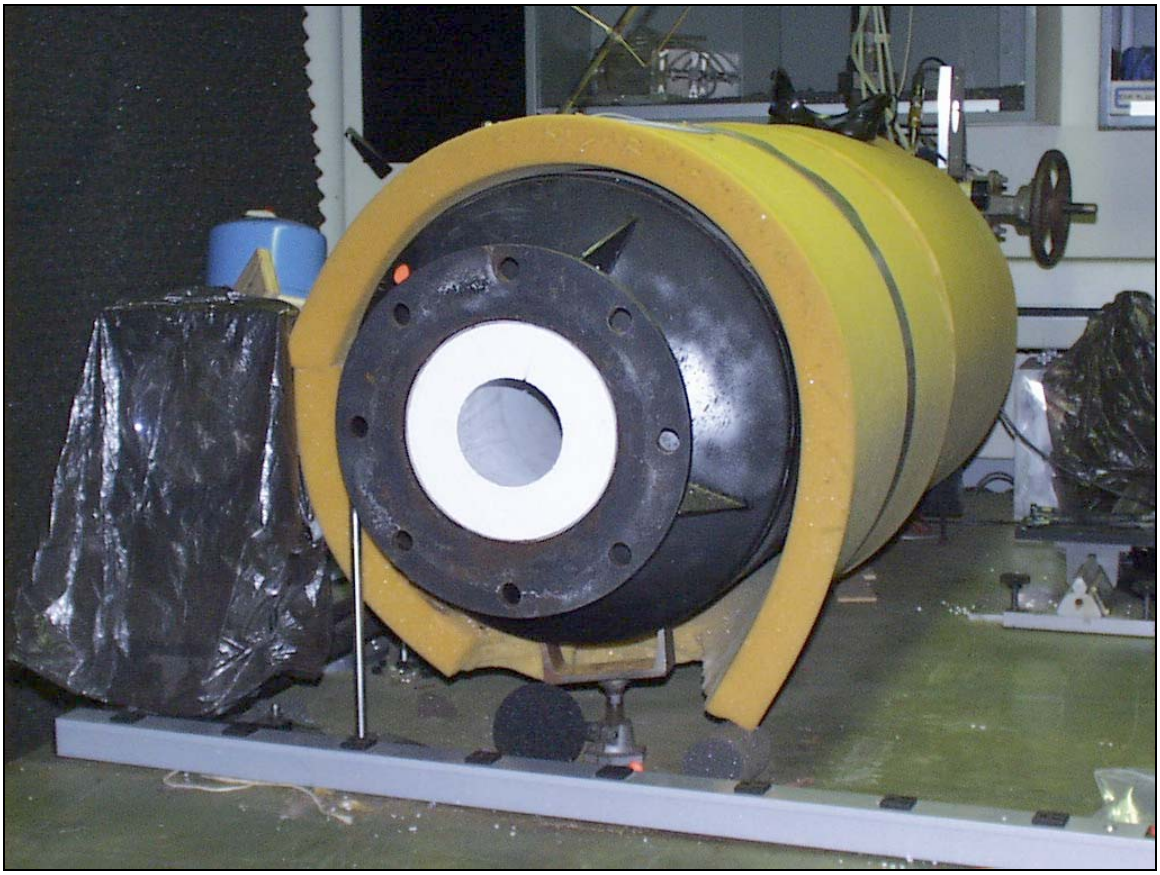

Figure 2.3: Picture of Plenum with Converging Foam Insert

The Main Jet Velocity Control Hardware

During the first phase of experiments, a 2” I.D. 150-PSI compressed air line supplied the plenum with pressure. Control of the jet exit velocity was achieved by adjusting the plenum pressure using a Norgren R18 Pilot Operated pressure regulator in series with a

Pacific K1G50R gate valve. Figure 2.4 is a picture of the Norgren regulator with the pilot valve mounted on top. The Pacific gate valve can be seen behind the plenum in figure 2.3. With this setup jet velocities ranging from 10 m/s to 50 m/s were achieved, resulting in Reynolds numbers between 71,000 and 355,000. Below 10 m/s, control of the velocity was difficult.

Figure 2.4: Picture of Norgren Main and Pilot Regulator Used to Control the Jet Velocity during the First Phase of Experimentation

During the second phase of testing, the rear bolt on plate was removed from the plenum, and a Lockwood Model 1AX centrifugal blower was adapted to fit the inlet. The blower setup provided better velocity control than the compressed air setup (especially at velocities below 10 m/s) at the expense of a more limited velocity range. It also facilitated seeding of the jet for PIV. Jet velocity was controlled by blocking the blower inlet with a flat wooden plate. The plate was clamped to the inlet to assure it didn't move. With this setup, the jet velocity could be set with high accuracy anywhere between 3 to 20 m/s (Reynolds numbers from 21,300 to 142,000).

The Main Jet Velocity Measurement Hardware

During the first phase of experiments, the jet exit velocity and temperature were measured with a United Sensor PAD-T-8-K-KL combination pitot static and temperature probe (figure 2.5) which was mounted on a stand that could be placed at the nozzle exit. During the second phase of experiments the jet exit velocity was measured with a Dantec research anemometer Model 90C10 (figure 2.6) and a 55P11 hotwire probe, which was also mounted on a removable stand. Once the velocity was set, the exit probe was removed to eliminate all flow obstructions for downstream velocity measurements. Jet exit velocity was measured at both the beginning and end of every run. To make sure the jet velocity didn't fluctuate too much during a run, the static pressure of the plenum was monitored using a Druck PDCR 810 transducer (with a range of 0 – 5 PSIG) connected to a Druck DPI 420 digital pressure indicator.

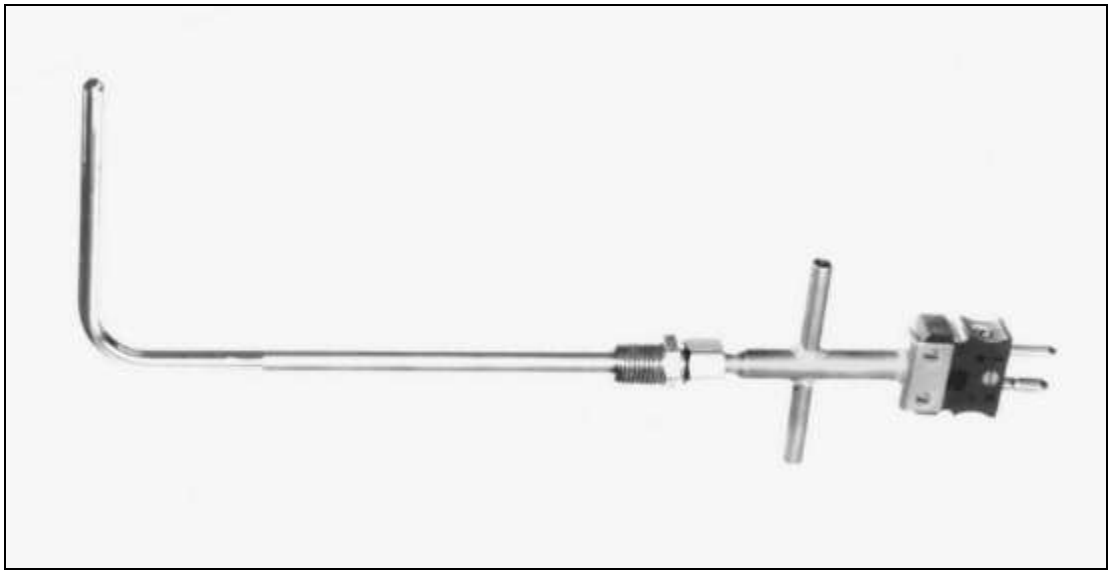

Figure 2.5: United Sensor Combination Pitot-Static Temperature Probe used to measure Jet Exit and Downstream Velocity during Phase I Experiments

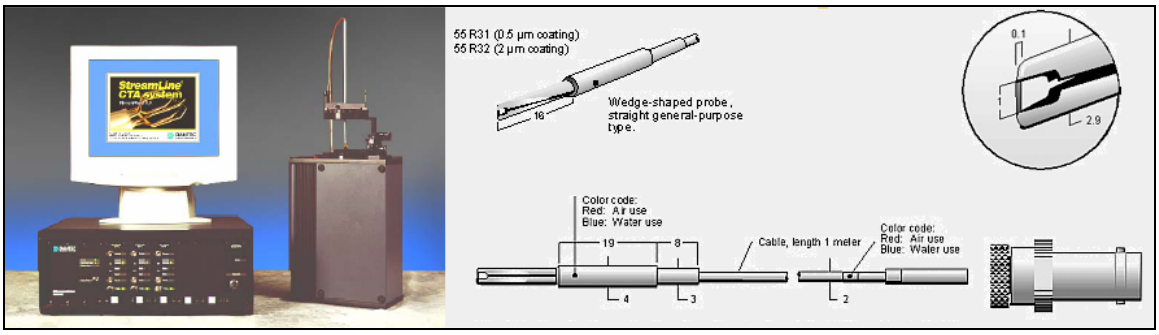

Figure 2.6: Picture of Dantec 90C10 Research CTA and 55R31 Hot Film Probe

The velocity downstream of the nozzle exit was measured using five different instruments, depending on the type of testing that took place. During the initial days of phase I experiments, where the goal was to identify the critical mixing parameters, a TSI Model 8460-23E-V portable anemometer was used to measure centerline velocity at 10 diameters downstream on the centerline. Many of the initial frequency and amplitude sweeps for 2 and 4 actuator cases at multiple jet velocities were measured with this instrument. This device provided valuable information about overall trends, but it required frequent recalibration and accuracy was not as good as desired. It was replaced with a United Sensor pitot probe (identical to the one used to measure exit velocity) for later and more critical phase I experiments. These included experiments demonstrating the collapse of mixing on momentum ratio, offset experiments, duty cycle experiments, and other miscellaneous experiments, some of which were repeats of the initial experiments where measurements were made with the portable anemometer. Finally, most of the phase I traverses were performed with the Dantec research anemometer and a type 55R31 hot film probe.

The total pressure port of the pitot tube was connected to the high pressure side of an Omega model PX653-10D5V pressure transducer, figure 2.7. This is a differential

transducer with an amplified output, ambient temperature compensation, and a pressure range of zero to ten inches of water (about 0.36 PSI). The other side of the differential transducer was left open to the atmosphere. The transducer was powered with a 12-volt Yuasa motorcycle battery. Battery power was chosen to reduce measurement noise caused by power supply fluctuations and resulted in more accurate pressure readings, especially at lower pressures. The transducer was calibrated with a Meriam Model 34FB2TM micromanometer, accurate to 0.002 inches of water. Corrections were made for density and gravity using standard methods.

Figure 2.7: Picture of Omega PX653 Pressure Transducer Used to Make Total Pressure Measurements of the Jet

For the phase II experiments, where the goal was to better understand the physics of pulse fluidic jet mixing, velocity was measured in two different ways. The first was with the Dantec research anemometer and a 55P11 hot wire probe. It was used to take detailed measurements of the flow field including planar, axial, and cross traverses of the jet under unforced and various forced conditions. The hotwire was calibrated with a Dantec Streamline 90H02 calibrator. This device is able to produce a clean jet within a velocity

range of 0.02 – 300 m/s at very low turbulence (T.I. < 0.2%) and with high accuracy (< ±0.5%). The measurement accuracy of the hotwire probes was checked daily against the calibrator at two different velocities, and probes were recalibrated when they were off by more than 0.1 m/s (which was usually about every other day).

The second method used for measuring velocity was with a PIV system from Integrated Design Tools (IDT). It consisted of a SharpVision 1000 Series Digital camera with a Nikon AF Nikor 28 – 105 mm lens, a National Instruments PCI-6602 32-bit counter timer card, and an IDT laser timing controller. The laser used was a New Wave LaserPulse Nd:YAG laser with a Minilase-III/15 Hz power supply/laser controller. The laser sheet was created using a -24.5 cylindrical lens and a 1000 mm spherical lens, both made by TSI. The optics were mounted on a TSI model 1098782 LaserPulse articulating laser arm. The arm contained a series of internal mirrors that allowed the laser beam to be contained until the light sheet was created with the optics which were mounted at the end of the arm. These optics were attached to a Manfrotto 3-axis camera mount which was bolted to a slide sitting on a 1-meter long optical rail that ran parallel to the centerline of the jet.

Figure 2.8 is a schematic showing the basic PIV setup. For a majority of experiments the jet was seeded and the actuators were not. The two actuators were typically mounted on the top and bottom side of the jet as shown in the figure, although a few experiments involved rotating the actuators 45° and 90° in order to get some off-plane results. The digital camera was mounted on a 3-axis traverse and attached to a Manfrotto camera

mount. The laser optics on the optical rail could be moved with the camera to keep the waist of the laser in the region of interest. Figure 2.9 shows the eleven image sections for which data was acquired. Good images were acquired from the jet nozzle exit to 5 diameters downstream. Beyond that, the thickness of the fog resulted in poorer image quality. All of the components hit by the laser sheet (including the inside of the jet nozzle, the actuators, etc.) were painted flat black to reduce glare and improve image quality. Instrument control, image acquisition, and processing were performed with IDT provision software on a duel Xeon Dell PC.

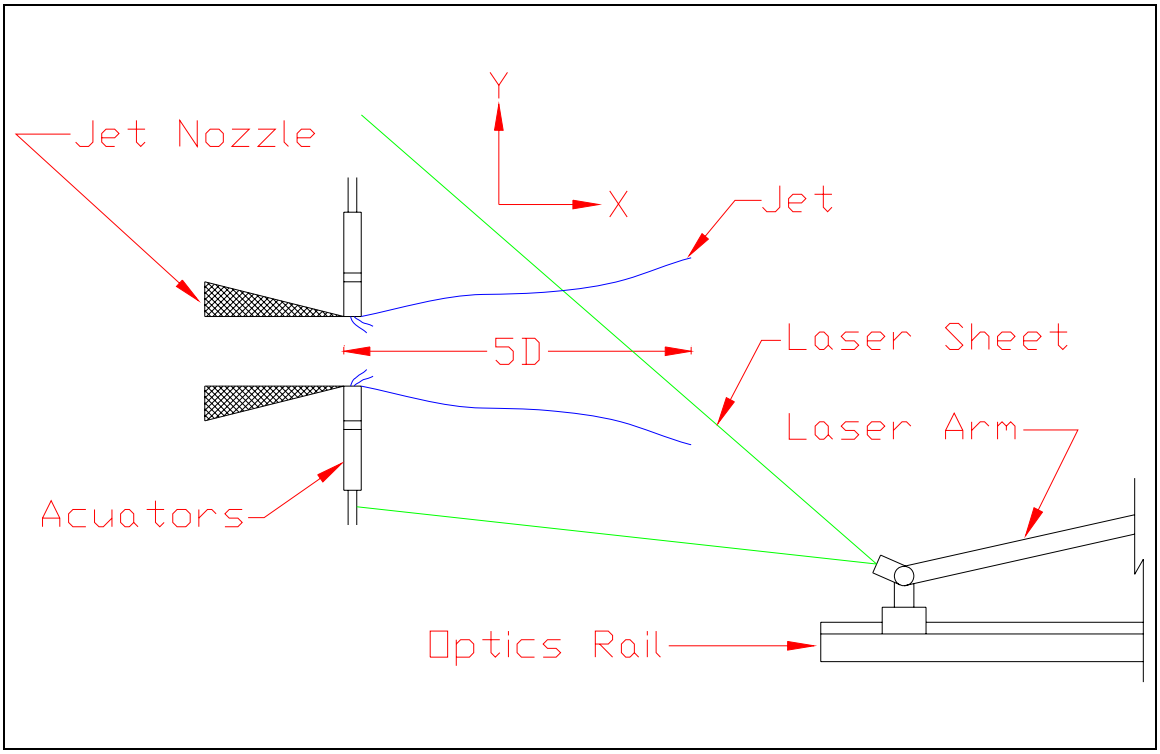

Figure 2.8: PIV Setup Schematic

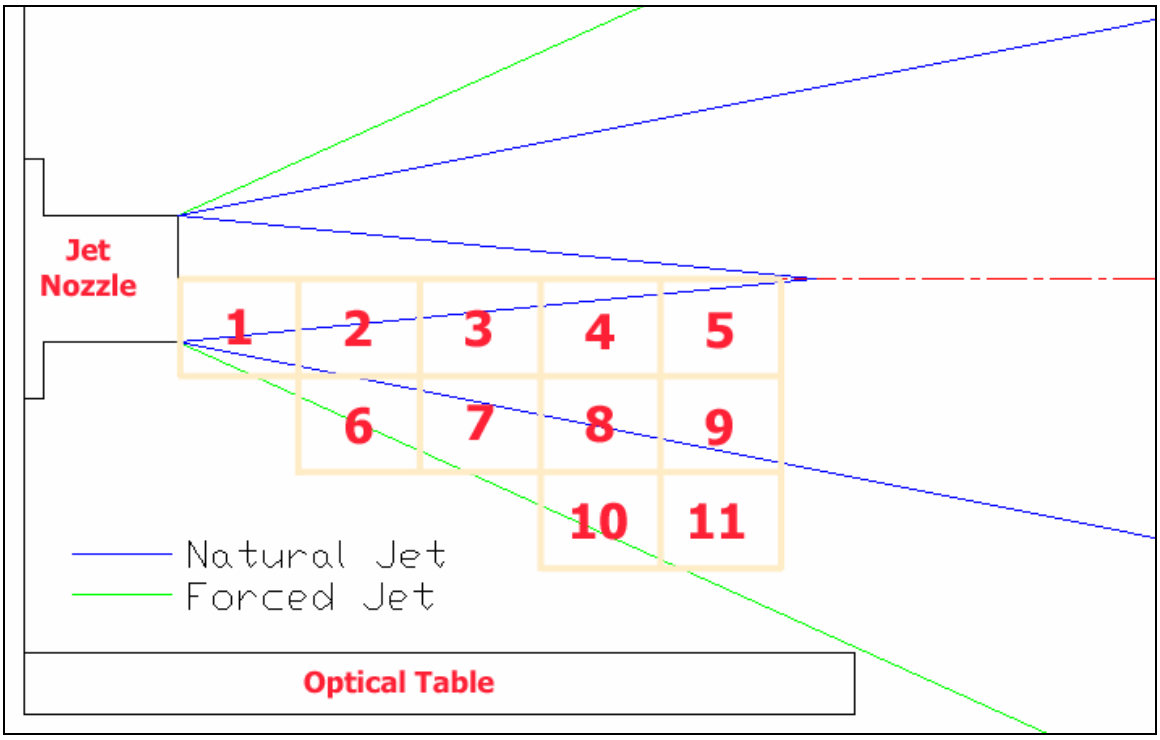

Figure 2.9: Schematic of the PIV Image Planes

The Fluidic Actuators

The small scale pulse-fluidic actuators were designed and built by GTRI. Figure 2.10 is a collage of pictures showing an actuator from different angles and its constituent components. The actuators were built in two sizes so that either two large actuators or four small actuators could be used to excite the jet. The fluidic actuator nozzles were positioned at the jet exit plane around the circumference of the jet nozzle. Each pulse was delivered 1/8" downstream of the nozzle exit and spaced away from the edge of the jet 1/8" in the radial direction (see figure 2.12).

As seen in figure 2.10, each actuator consisted of three parts: a pipe adapter, a diffuser, and a nozzle. The pipe adapter was a 1.5" long tube and had a threaded inlet where a solenoid was screwed on. The exit of the pipe adapter had a square flange that bolted to

the inlet of the diffuser. The inner diameter of the pipe was 0.27", resulting in an area of 0.0573 in^2. The diffuser exit was tapered to match the square diffuser inlet, which was 0.375" on each side (or 0.1406 in^2). The large diffuser diverged to a rectangular exit of 2.36" by 0.375" (0.885 in^2), and the small diffuser to 1.115" by 0.375" (0.418 in^2). Finally, the nozzle was bolted to the diffuser exit. The large actuator had four available nozzles to choose from, and the small actuator had two nozzles to choose from. The large nozzle exit slots measured 1.7" long by 0.020", 0.040", 0.080", or 0.200" wide. The small nozzle exit slots were 0.795" inches long and either 0.020" or 0.080" wide.

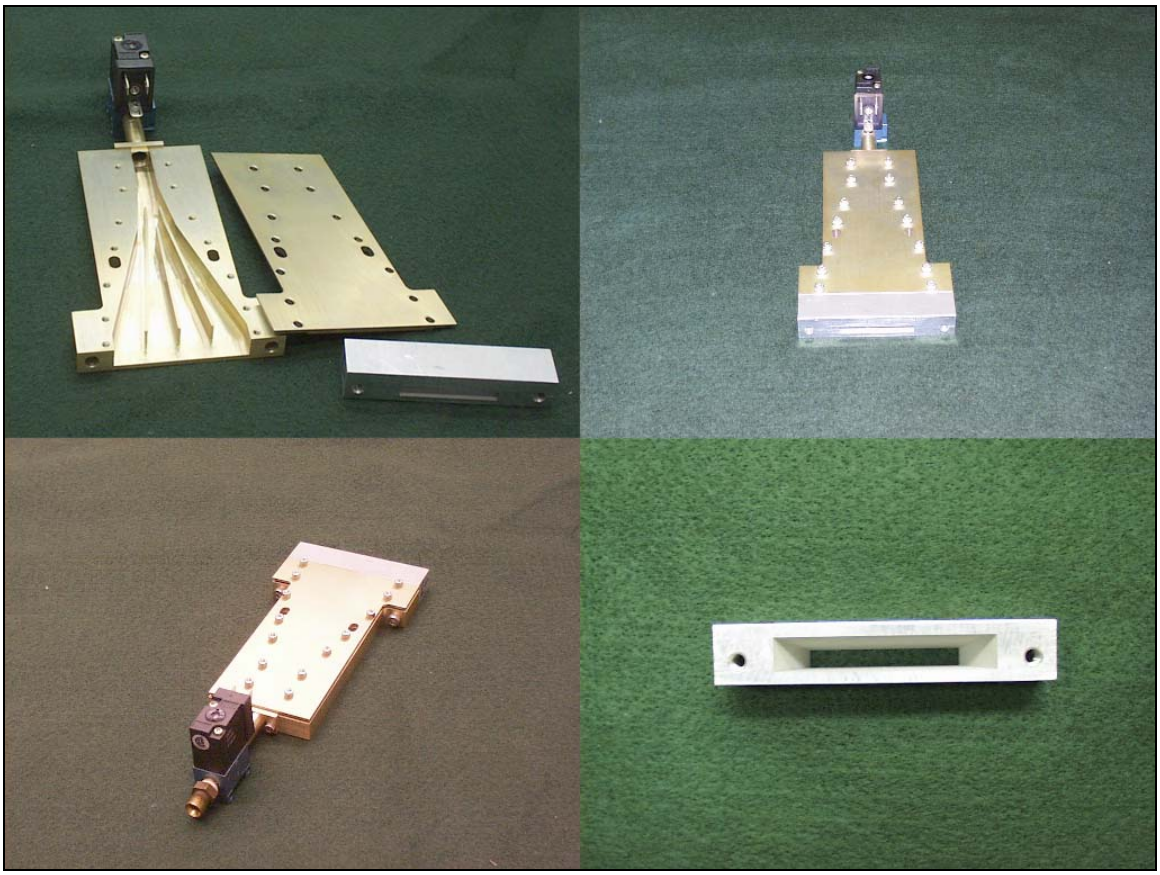

Figure 2.10: Pictures of the Small Scale Jet Actuators and Components

The actuators were mounted on a custom built stand that allowed their position around the circumference of the jet to be varied in increments of 5º. The stand had a large hole in the center that was slightly larger than the outer diameter of the jet nozzle allowing the actuators to be placed near the jet nozzle exit. Figure 2.11 is a picture of the stand with a single actuator attached to it. Figures 2.12 and 2.13 show the different actuator circumferential configurations that were tested. Figure 2.12 is a close up picture that compares the 2-actuator and 4-actuator configurations used during phase I experiments. The 1/8" offset of the actuator exit slots from the jet in the downstream and radial directions is clearly visible. The actuators used in the 4-actuator case are smaller than those used in the 2-actuator case. This was done in order to keep the sum of the actuator nozzle exit areas about the same for the two cases. Figure 2.13 shows the two configurations for the 4-actuator case: 90° and 50° pulsing angles.

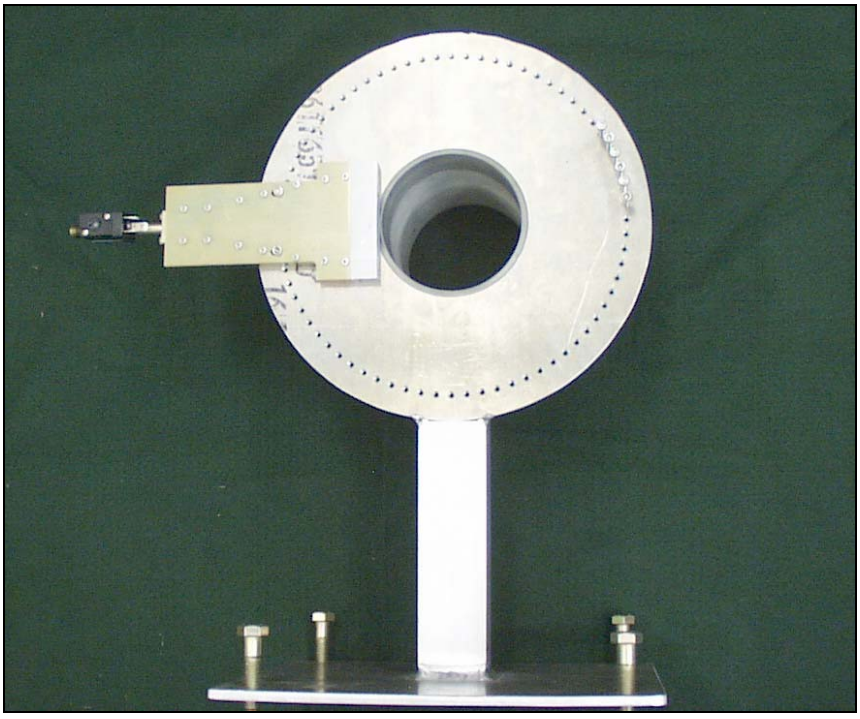

Figure 2.11: The Actuator Stand with a Single Actuator Mounted to it

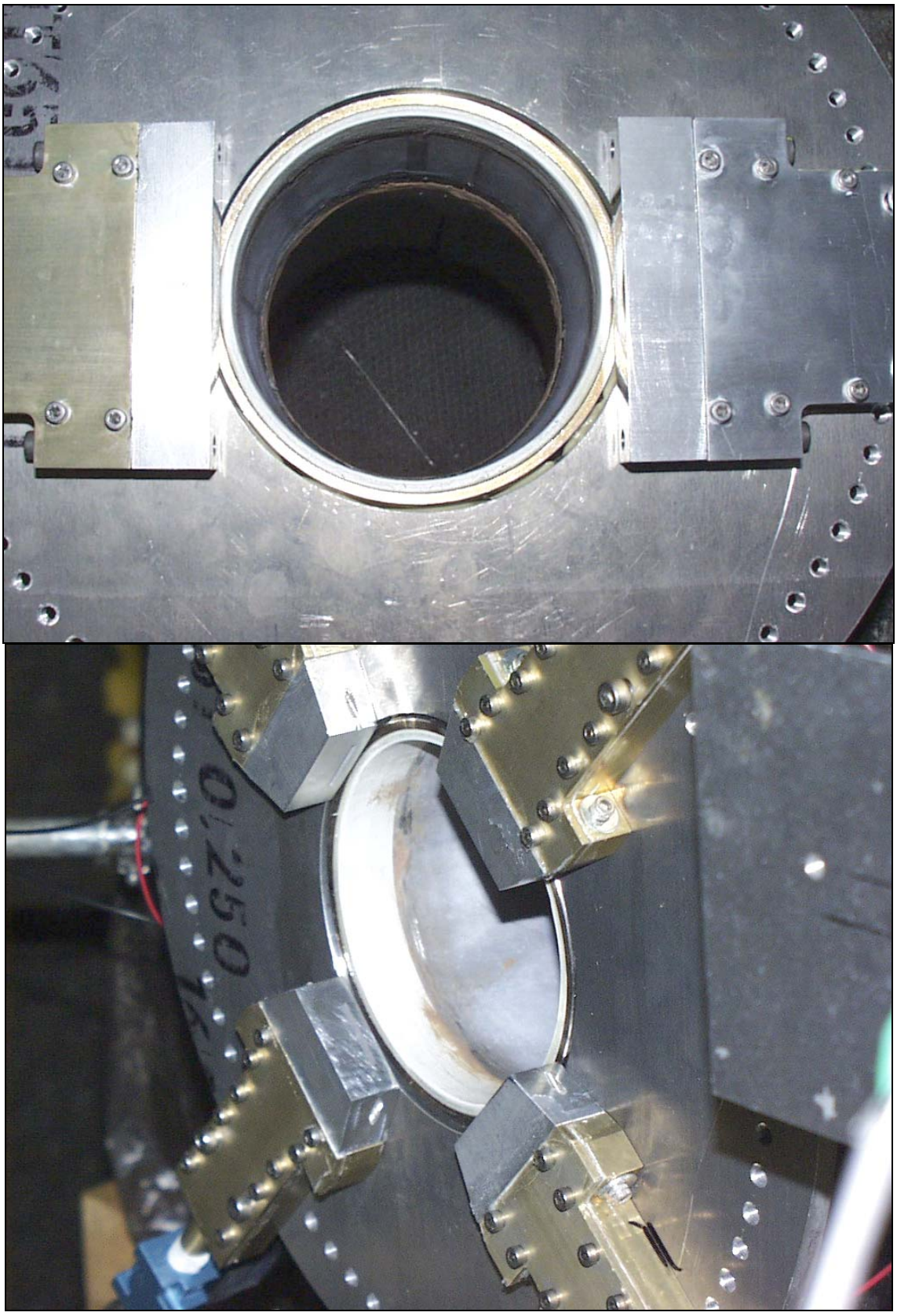

Figure 2.12: Phase I Configurations, 2-actuators and 4-actuators

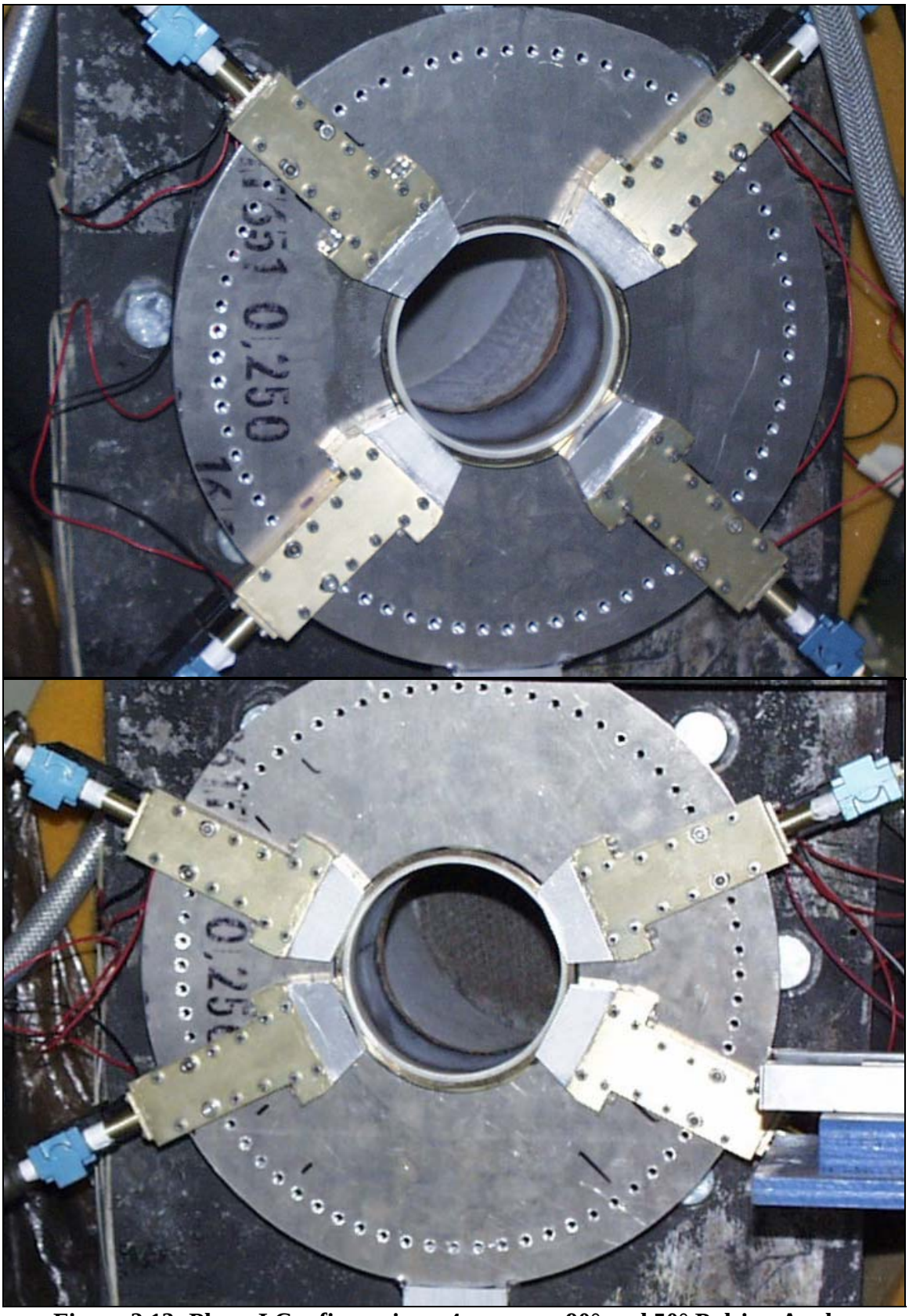

Figure 2.13: Phase I Configurations, 4-actuator 90° and 50° Pulsing Angles

Actuator Control and Measurement Hardware

Figure 2.14 is a picture of the control and measurement hardware used for the actuators. The mass flow rate through the actuators was measured with a Flow-Dyne model VSH1201-APM venturi flow meter. This venturi has an inner diameter of 0.5" and a throat diameter of 0.08". The pressure ports of the venturi were hooked up to Endevco model 8510C-100 piezoresistive pressure transducers. These transducers have a high frequency response that allows the accurate measurement of unsteady pressure. The transducers require 10 volts and were powered by two 6-volt batteries wired in series along with a 1000-Ohm potentiometer acting as a voltage divider. A Coilhose Pneumatics model 8804 pressure regulator with a 160-PSI mechanical pressure gage was used to control the mass flow rate. Pulsing was performed using MAC model 35A-AAA-DDAJ-1JB solenoid valves. The frequency range of the solenoids was 0 to 100 Hz, but pulse quality began to decay after about 50 Hz. The solenoids were powered by a Leader model LPS-152 power supply, and controlled with the PC via two Antex Electronics ODC-01 solid-state relays.

In order to perform DC offset testing, the original setup was modified to produce pulses with a known DC offset. This was done by adding a parallel flow path to each actuator which bypassed the solenoids. Additionally, two needle valves were added; one to the bypass air to control the offset flow and one upstream of the actuators to balance the flow path resistance and force flow down the bypass path. Figure 2.15 is a schematic of the modified setup used to create the DC offset. With this setup, offset of the pulse could be

varied from 0% (i.e. no offset) up to approximately 65% where the %offset is defined as the bottom of the total pressure waveform divided by the top.

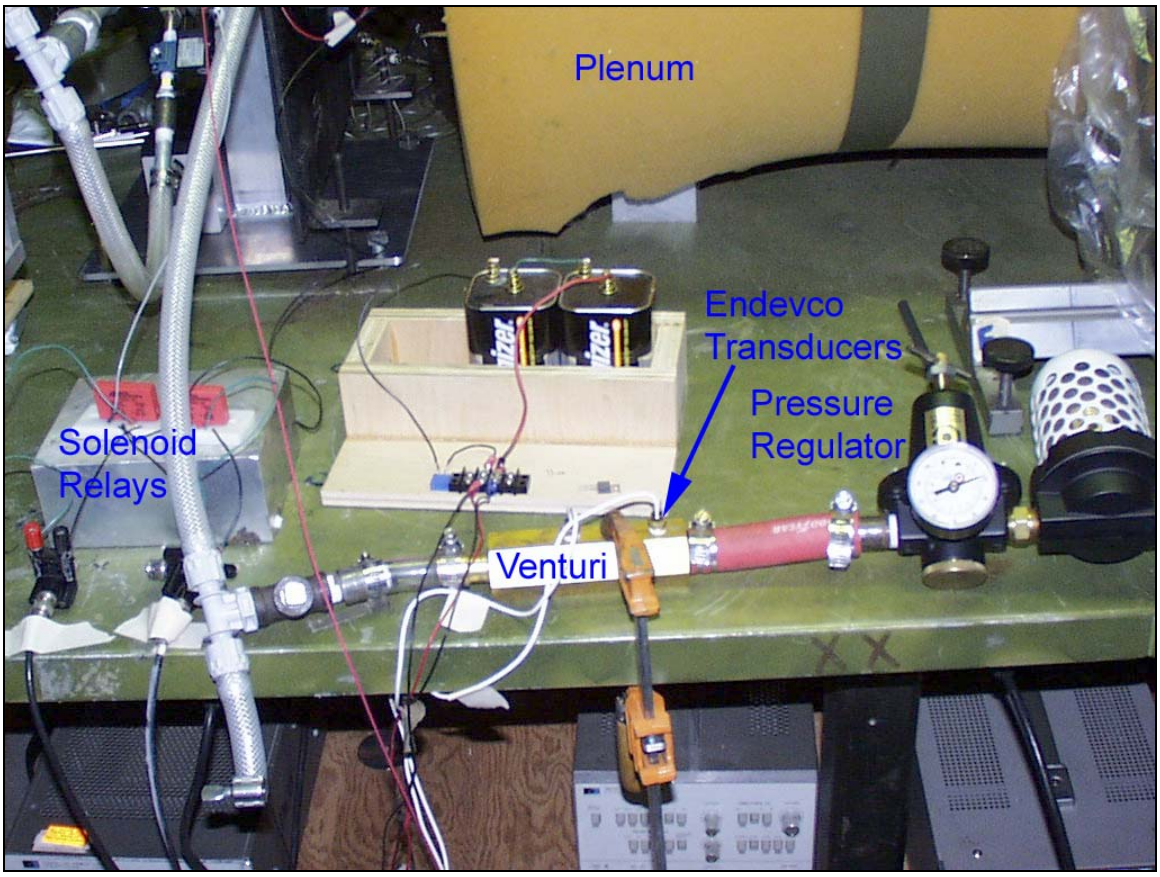

Figure 2.14: Picture of the Actuator Control and Measurement Hardware

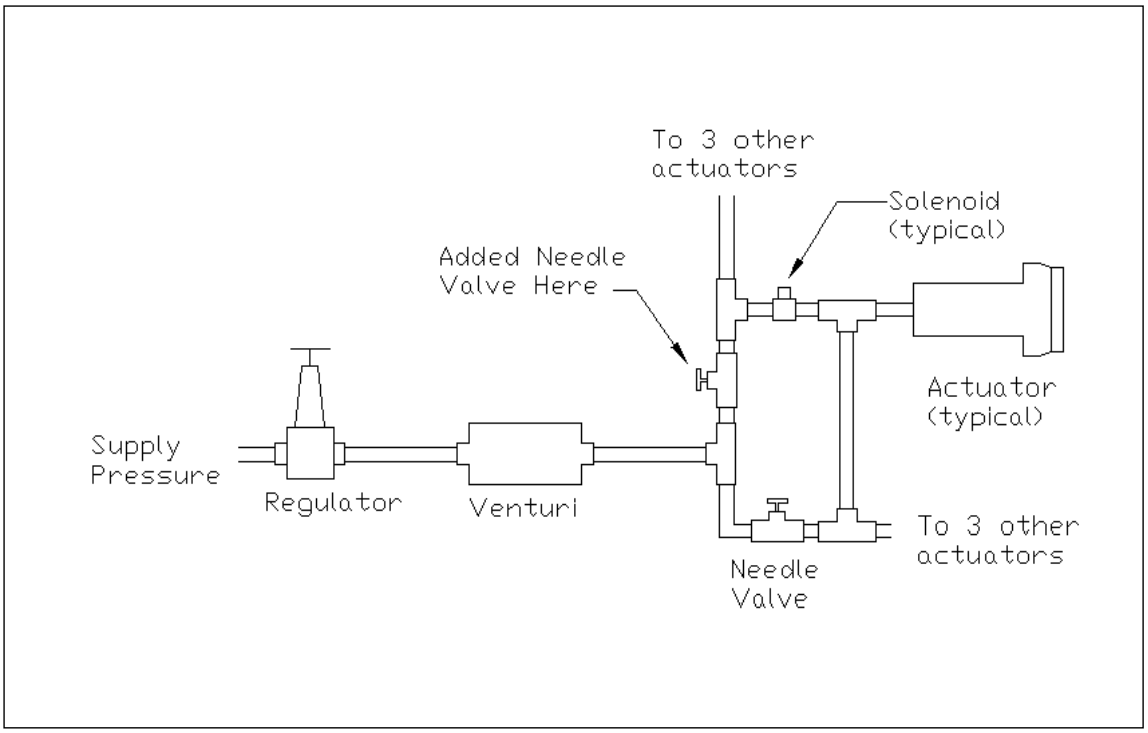

Figure 2.15: Schematic Showing Hardware Modifications Needed to Vary DC Offset

Seeding Hardware

There were two different types of flow seeding implemented for PIV: seeding of the jet and seeding of one of the actuators. The jet was seeded with smoke generated with a Rosco Model 1700 fog machine. The fogging fluid used was Rosco Clear Fog Fluid (polyethylene glycol). To seed the jet, the output of the fog machine was directed into the inlet of the blower. Actuator seeding was much more complicated and tenuous. To seed the actuator, unheated fogging compound was inserted into a small reservoir just upstream of the actuator solenoid. As air ran over the reservoir, it picked up some of the compound which then got atomized as it accelerated through the small orifice inside the solenoid. This produced brief moments of good seeding (usually several seconds long) but only worked within a limited pressure range.

Traversing Hardware

The velocity probes and PIV camera were mounted on multi axis traverses affixed to an optical table that was aligned with the jet. Figure 2.16 shows the traversing setup used for phase II hotwire measurements. The traverses were controlled by a Velmex VXM traverse controller connected to a PC. The hotwire probe could be moved throughout the flow field with a high level of accuracy. The top picture in the figure shows the configuration of the jet and two large actuators, the optical table, the 3-axis traverse, the hotwire probe setup, and the second hotwire probe on a movable stand used to measure the jet exit velocity (left hand side of the picture). The bottom picture is a close up of the hotwire probe traversing in the jet shear layer near the exit. Note that the actuators are mounted vertically for the phase II experiments, compared to horizontally for phase I experiments.

Data Acquisition and Control Hardware

Data acquisition and control was performed with a PC using National Instruments PCI-MIO-16E-1 and PCI-6035E multipurpose input/output DAQ cards. Each card had 8 differential analog input channels, built in multiplexing, on board software programmable amplification, 2 analog output channels, and timing outputs. All of the instruments and controllers were wired into a National Instruments SCB-68 shielded I/O connector box. This device facilitates wiring by providing screw terminals for easy connections. The terminal blocks are located in a shielded enclosure that helps reduce noise caused by electromagnetic induction. It also has an onboard temperature sensor for thermocouple cold-junction compensation.

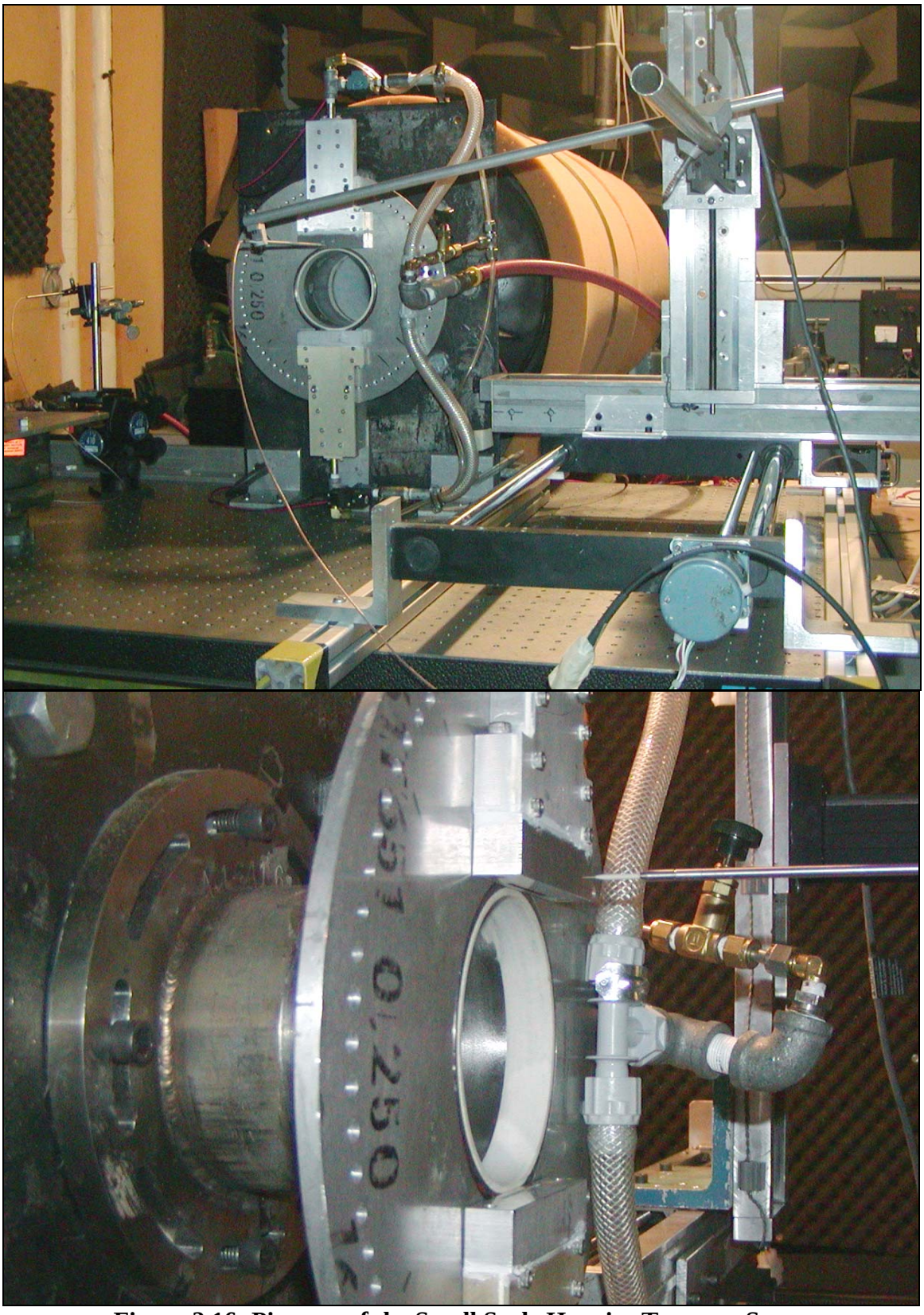

Figure 2.16: Pictures of the Small Scale Hotwire Traverse Setup

Software

The operating system used on the PC was Microsoft Windows 2000. National Instruments LabView was used for data acquisition and instrument control. The data acquisition and control algorithms were written in “G”, the graphical programming language native to LabView. PIV control and processing was performed with IDT Provision XS. Data processing algorithms were written in G, ANSI C, Matlab, Visual Basic, and both Tecplot and DOS Macros. Post processing was performed with Microsoft Excel, Mathworks MatLab, and Amtec Tecplot.

CHAPTER 3

SMALL SCALE JET – ANALYSIS RESULTS AND DISCUSSION

Chapter Overview

This chapter describes the results for mixing enhancement experiments performed on the small scale jet. Experiments were done in two phases. The goal for the first phase was to sort out the key mixing parameters. The primary mixing enhancement metric was downstream velocity reduction ten diameters from the nozzle exit. The goal for the second phase was to gain a better understanding of the physics of mixing enhancement via pulse fluidic actuation. During this phase detailed PIV and hotwire measurements were taken in the jet-actuator interaction region and the downstream flow field with a focus on the optimal cases for both in-phase and out-of-phase pulsing. Additional mixing parameter experiments were performed to confirm that results from the two phases of testing were consistent.

Nearly identical setups were used for the two phases of experiments on the small scale jet. The same facility and equipment were used to create the jet and fluidic pulses. There were only two major differences between the setups: 1) the actuators for the 2-actuator configuration were mounted vertically instead of horizontally, and 2) the air supply used to create the main jet was changed from compressed air to a blower. Other small differences may have existed because the setup was disassembled after phase I and reassembled for phase II, but it is not likely that they were significant. Several of the

phase I experiments were repeated during phase II to verify consistency. Chapter 2 contains a detailed description of the setup for both phases.

The current chapter begins with characterization of the unforced jet. Characterization was done during both phases, but more detailed measurements were made during phase II with the hotwire and PIV. The characterization experiments primarily consisted of various traverses measuring instantaneous velocity from which mean velocity, turbulence level, and spectral characteristics were calculated. The next major section in the chapter concerns characterization of the pulse fluidic actuators. It contains velocity traverses, centerline pulse waveforms, and other actuator performance characteristics. This is followed by the results of the parameter discovery experiments where the effect of pulsing frequency, amplitude, duty cycle, offset, and the number and arrangement of actuators was explored. Then the results from the detailed hotwire and PIV measurements are presented. The chapter concludes with a summary.

Characterization of the Unforced Jet

Phase I Setup

The coordinate axes for the small scale jet were defined as shown in Figure 3.1. The axes originated at the jet exit center point. The x-axis ran downstream along the centerline, the y-axis ran in the horizontal direction, and the z-axis ran in the vertical direction. The horizontal and vertical exit velocity and turbulence intensity profiles for the main jet are shown in figures 3.2 through 3.5 with nominal velocities ranging from 5 m/s to 50 m/s. The position coordinates have been normalized by the jet diameter and the velocities by

the maximum velocity measured during the traverse. A relatively clean plug flow exists for all of the cases with fairly low turbulence intensities (< 3%). The turbulence intensity in the potential core for the 10 m/s case was slightly higher than it was for the higher velocity cases, but close enough (3% vs. 2.5%) to assume similarity. The velocity profiles show that there was somewhat of a boundary layer at the jet exit due to the 4" diameter pipe that served as the end of the nozzle. The average momentum thickness was 0.8 mm for the velocities tested. The flow falls somewhere in between an ideal top hat profile jet and fully developed pipe flow. The Reynolds number range was from 35,500 to 355,000 meaning the jet was essentially inviscid and fully turbulent. The Mach number range was from 0.0145 to 0.145, well within the incompressible regime.

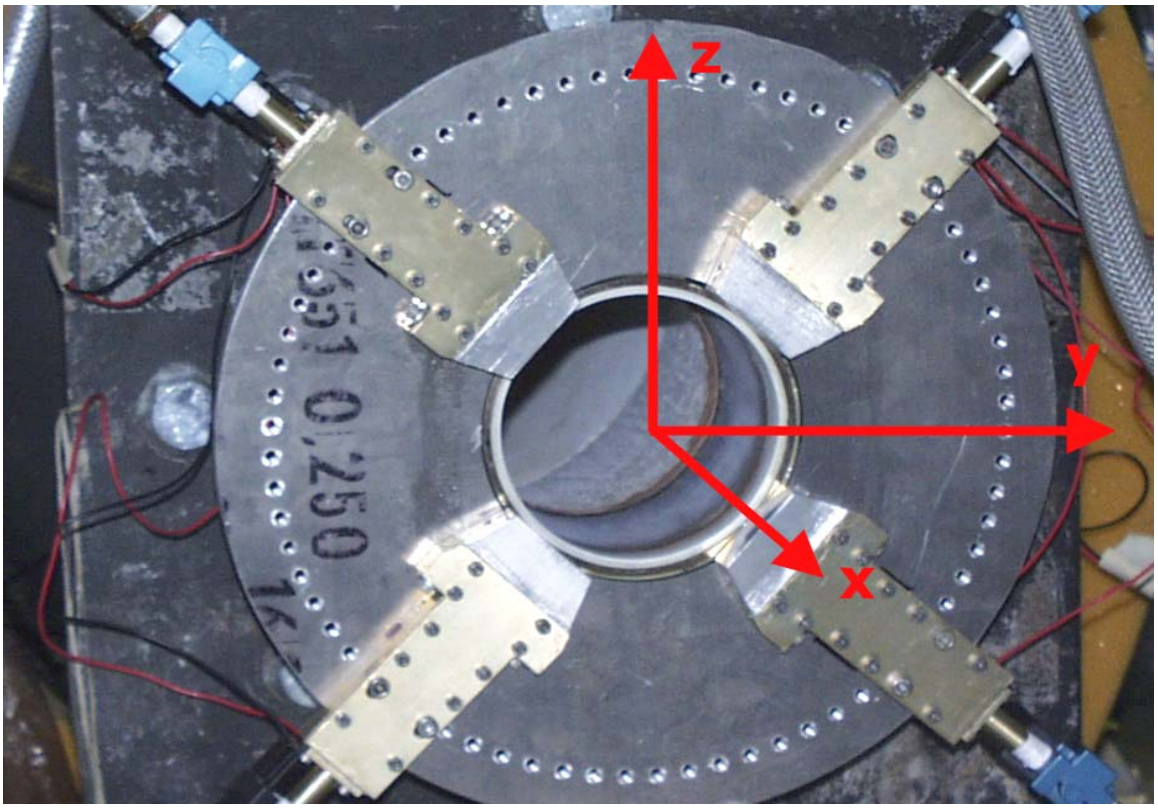

Figure 3.1: Picture Showing How the Coordinate Axes were Defined for the Small Scale Jet; the x-axis Runs Down the Centerline, the y-axis Runs Horizontal, and the z-axis Runs Vertical

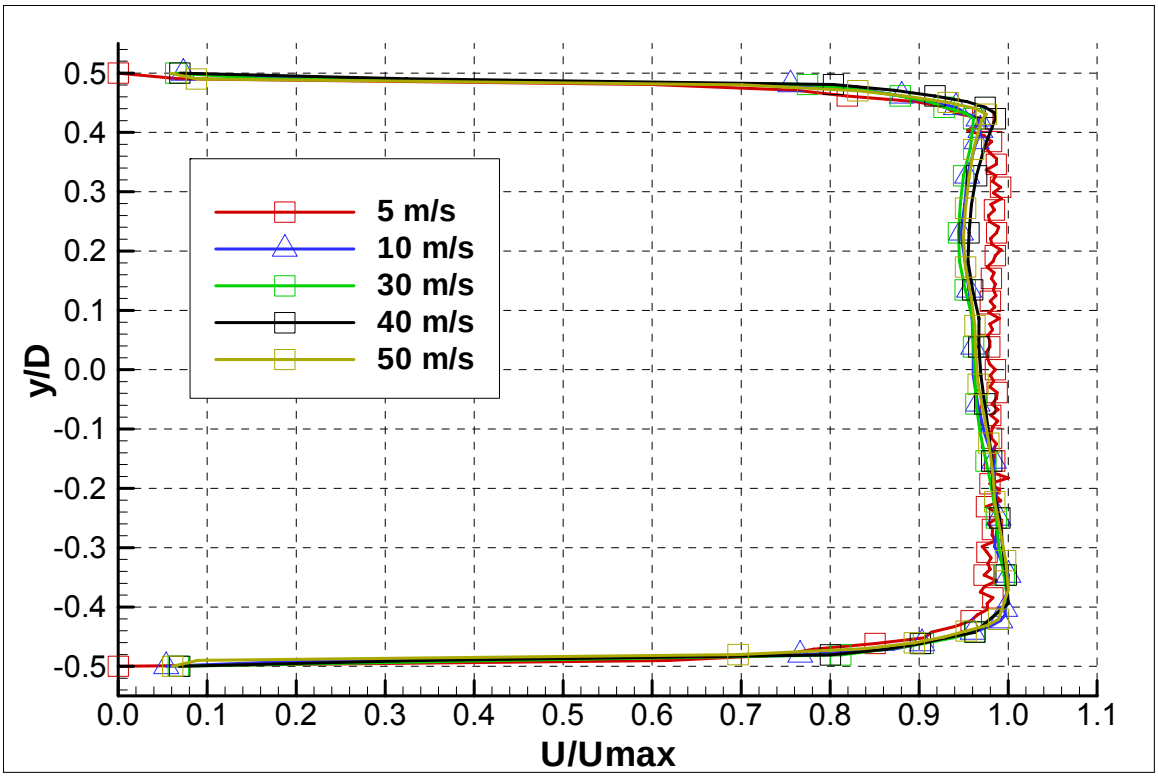

Figure 3.2: Horizontal Velocity Traverses of the Small Scale Jet, Re = 35,500 (5 m/s) to 355,000 (50 m/s), Phase I Setup

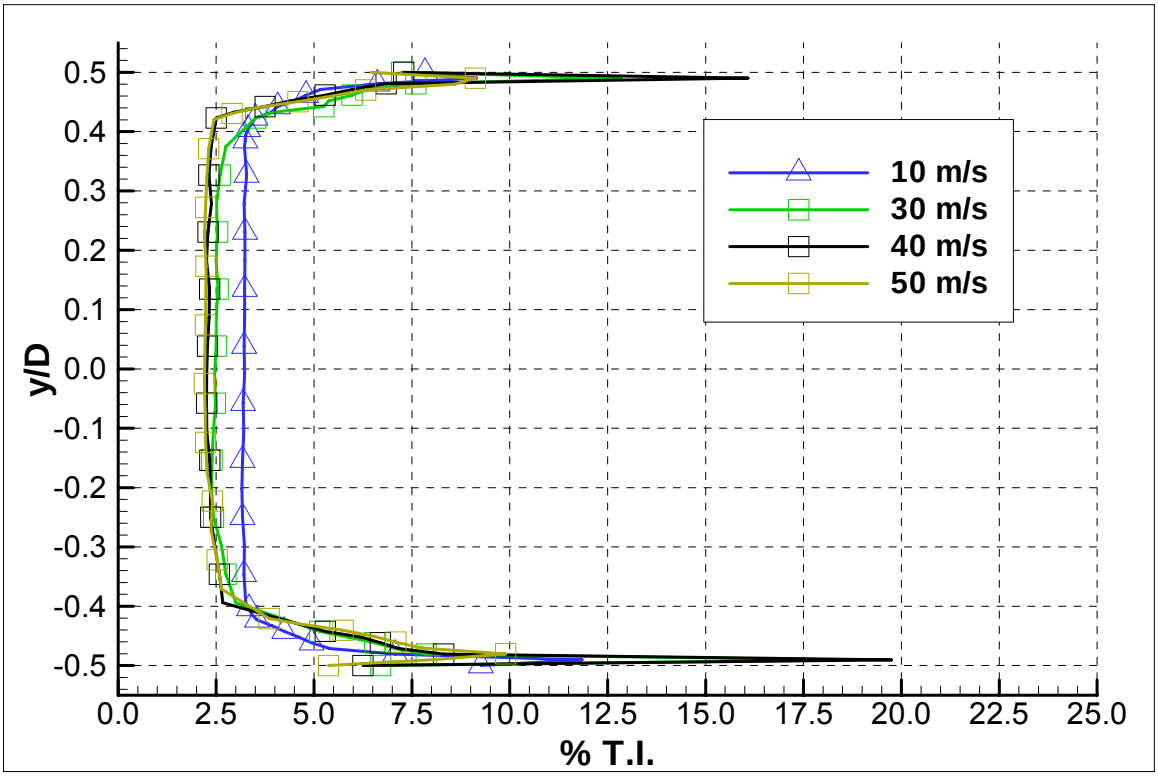

Figure 3.3: Corresponding Horizontal Turbulence Intensity Traverses

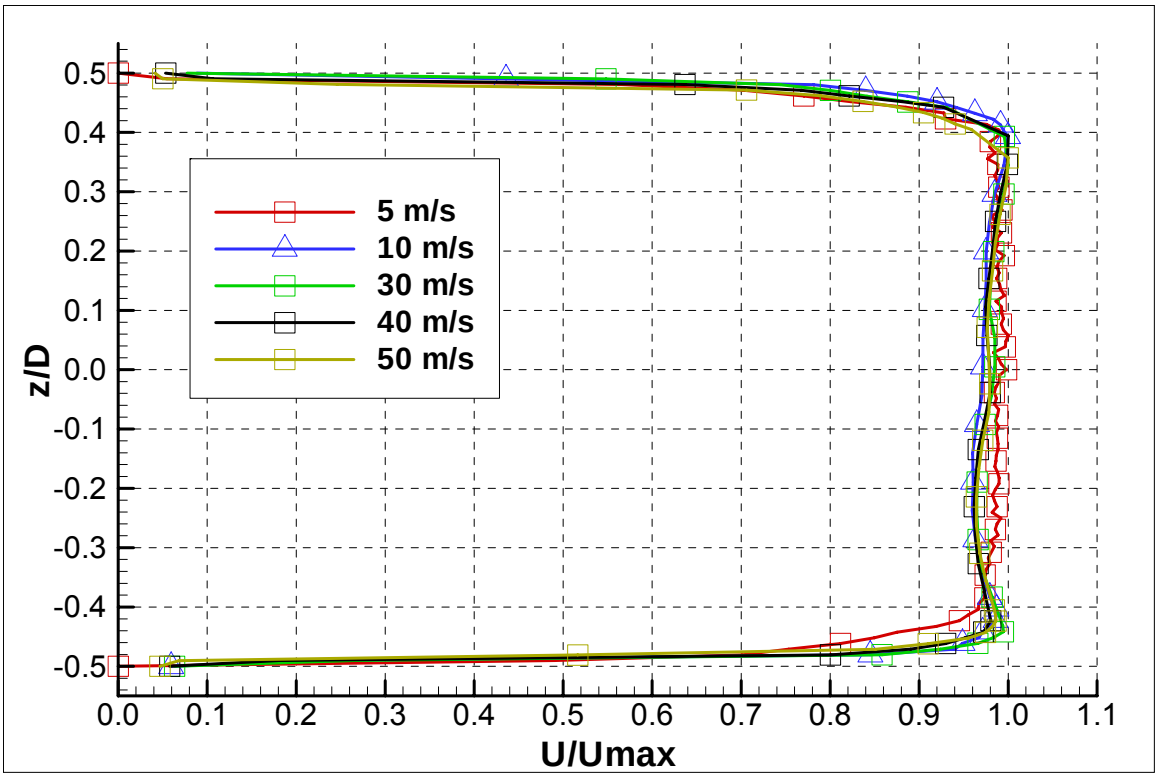

Figure 3.4: Vertical Velocity Traverses of the Small Scale Jet, Re = 35,500 (5 m/s) to 355,000 (50 m/s), Phase I Setup

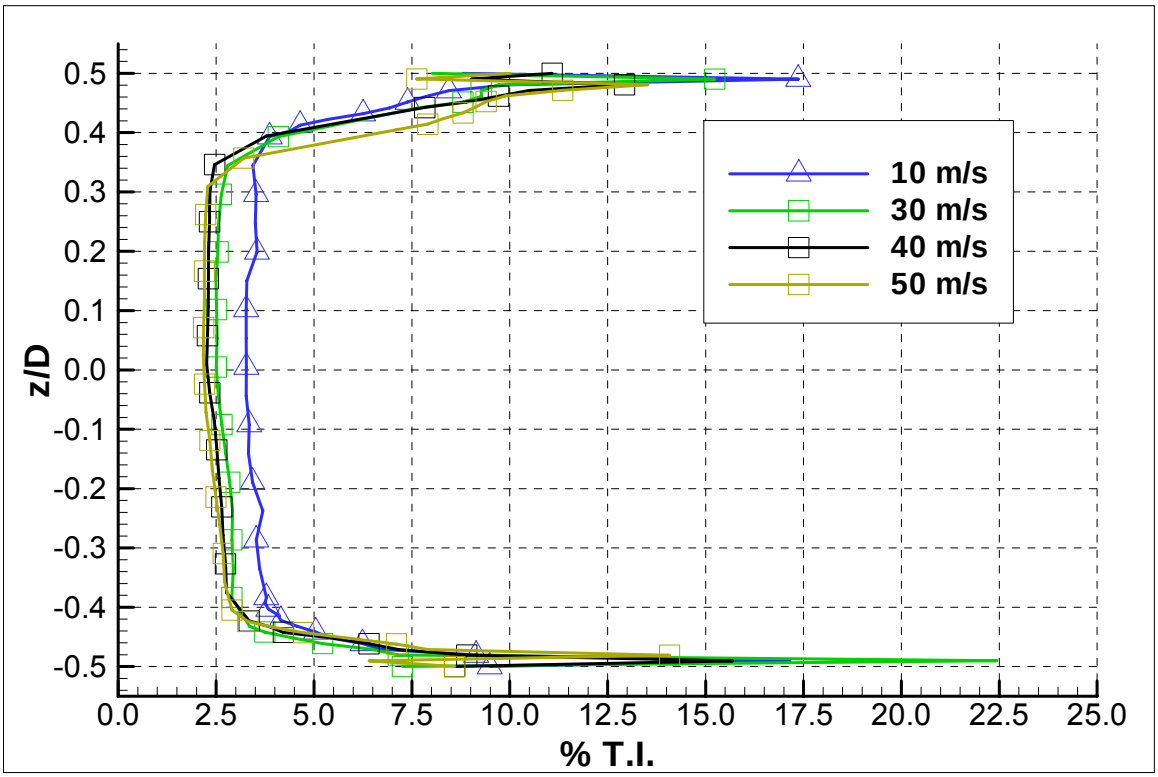

Figure 3.5: Corresponding Vertical Turbulence Intensity Traverses

Figures 3.6 and 3.7 show the horizontal and vertical velocity profiles for the unforced jet out to x/D = 4. Spreading takes place as it should and symmetry between the y and z directions is good. Figure 3.8 shows the centerline velocity decay for the unforced jet out to almost 20 diameters. The data points shown are the averages from several different traverses with the exit velocity ranging from 5 to 50 m/s. The data was fit with the equation shown in the figure and compared against the empirical fit of VanGlahn.[167] Figure 3.9 shows the centerline turbulence intensity, which has been averaged and fit in the same way. The curves are typical for clean turbulent jets.

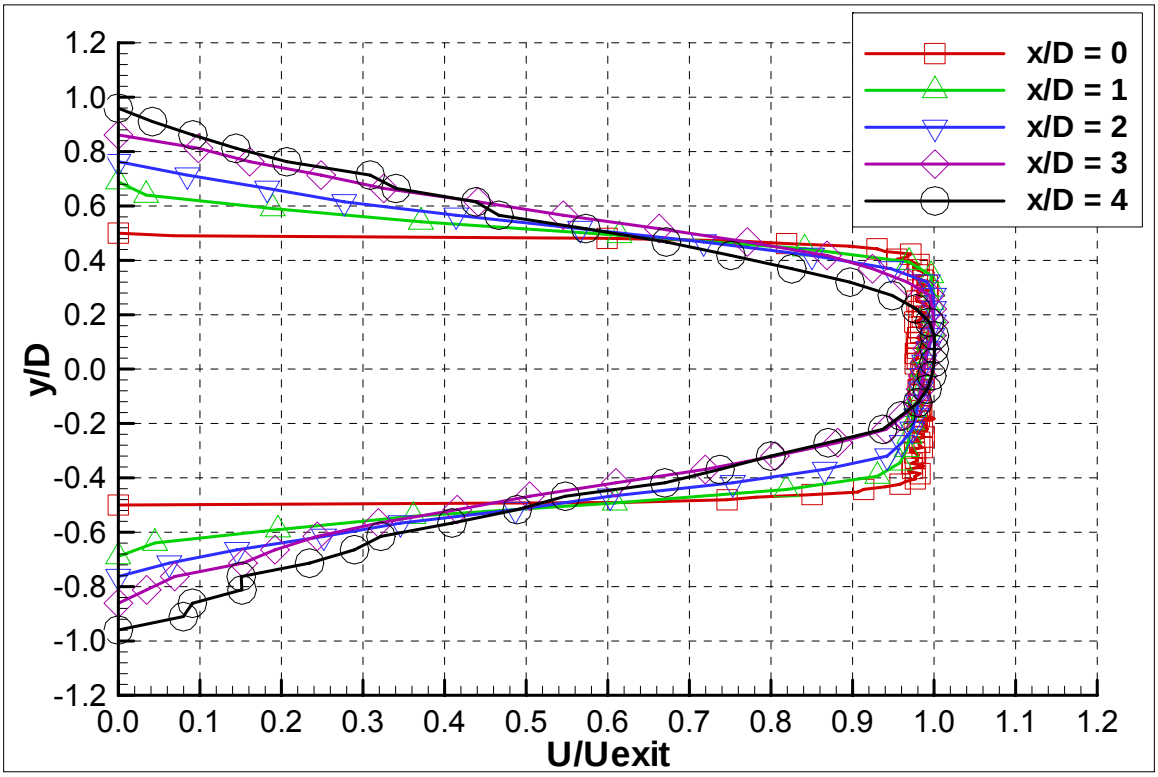

Figure 3.6: Horizontal Mean Velocity Traverses for the Small Scale Jet at Multiple Downstream Locations, U_{exit} = 10 m/s, Phase I Setup

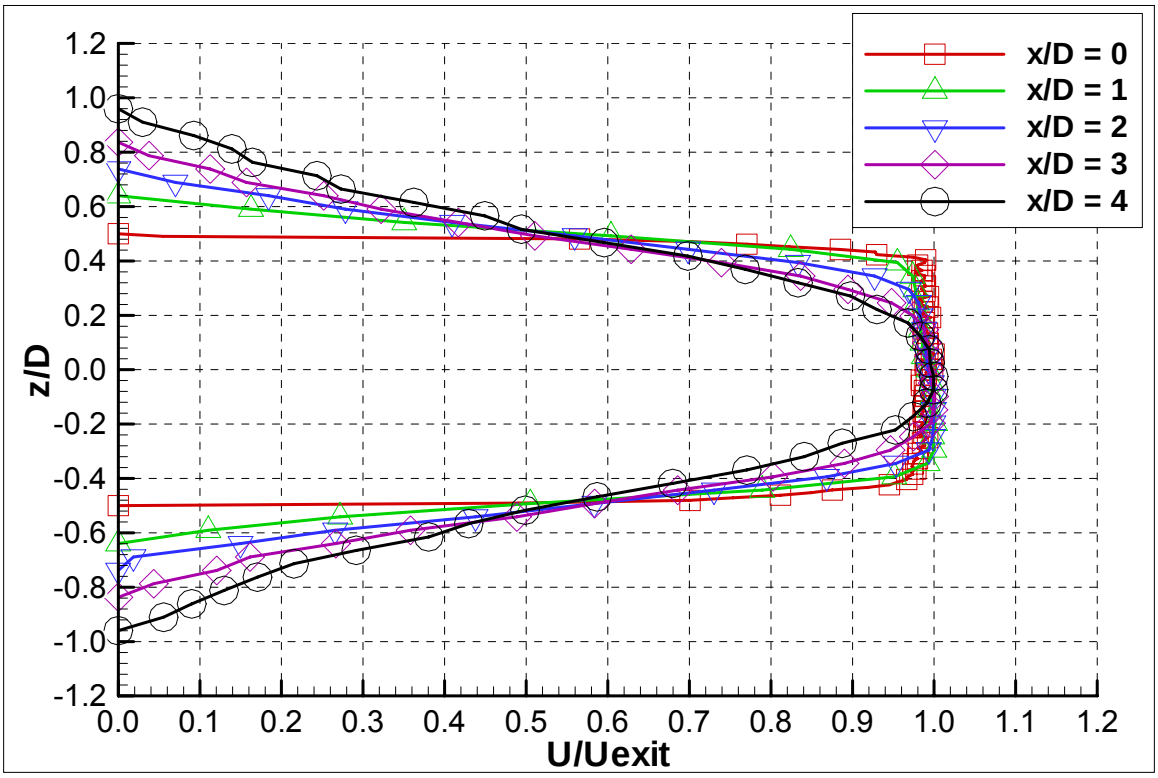

Figure 3.7: Vertical Mean Velocity Traverses for the Small Scale Jet at Multiple Downstream Locations, U_{exit} = 10 m/s, Phase I Setup

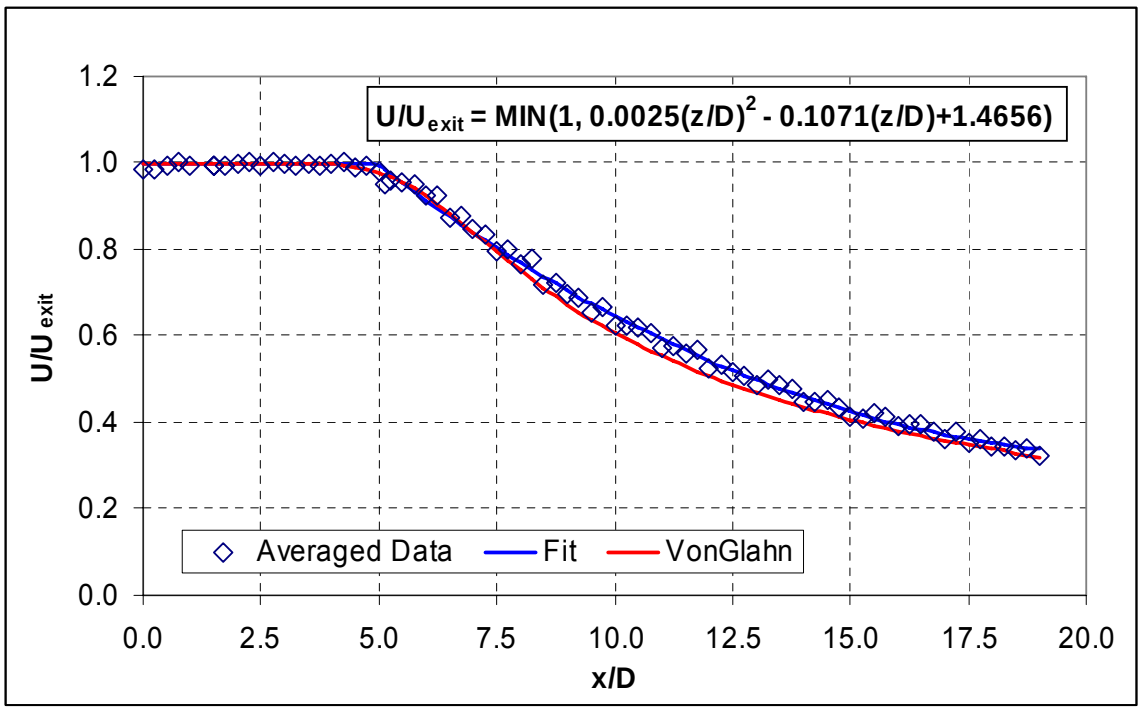

Figure 3.8: Centerline Velocity Decay for the Unforced Small Scale Jet, Data is the Average of Five Runs with Reynolds Numbers Ranging from 35,500 (5 m/s) to 355,000 (50 m/s), Phase I Setup

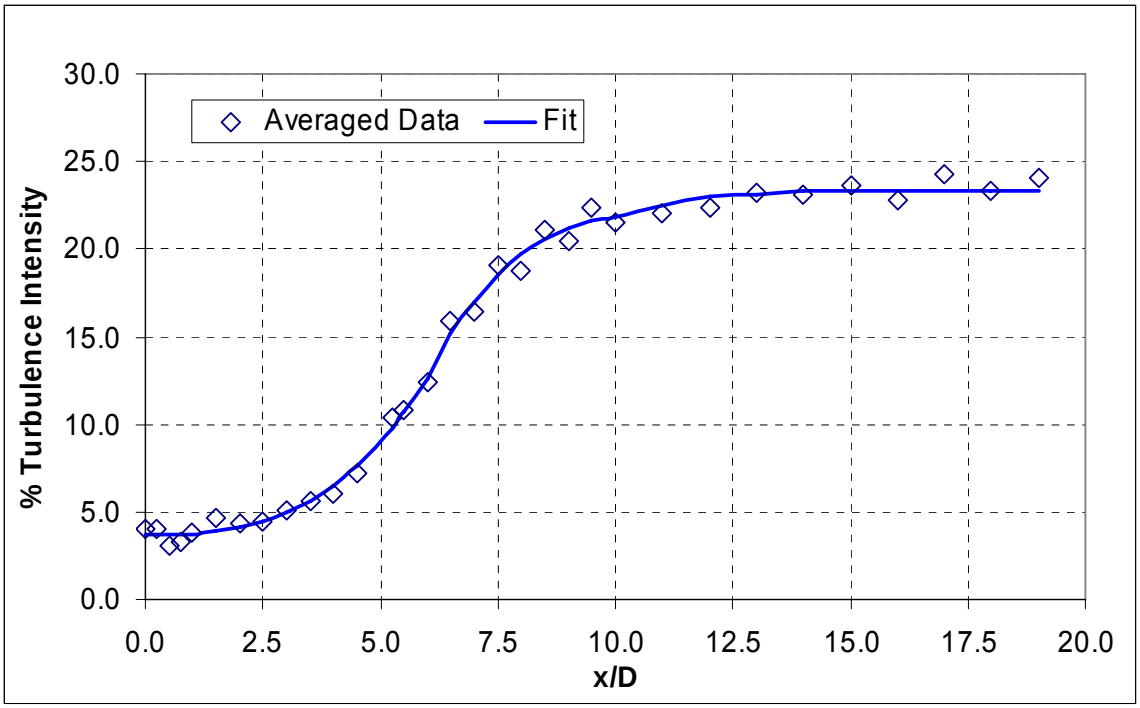

Figure 3.9: Centerline Turbulence Intensity for the Unforced Small Scale Jet, Data is the Average of Five Runs with Reynolds Numbers Ranging from 35,500 (5 m/s) to 355,000 (50 m/s), Phase I Setup

Phase II Setup

Figure 3.10 shows that exit velocity profiles for a 5 m/s jet taken during phase I and II compare favorably with each other. The slight differences are likely due to the fact that the setup was taken down and then re-erected at a later time. Figure 3.11 shows that the turbulence intensity measured for the phase II jet was about 2% to 2.5% lower than for the phase I jet in the potential core at the exit. There were two reasons for this. The first is that measurements for phase I were made with a hot film probe vs. a hot wire probe for phase II. The second reason is that there was some low frequency pressure fluctuation in the compressed air supply that wasn't present in the blower. Thus, the phase II jet can be seen as a slightly "cleaner" version of the phase I jet.

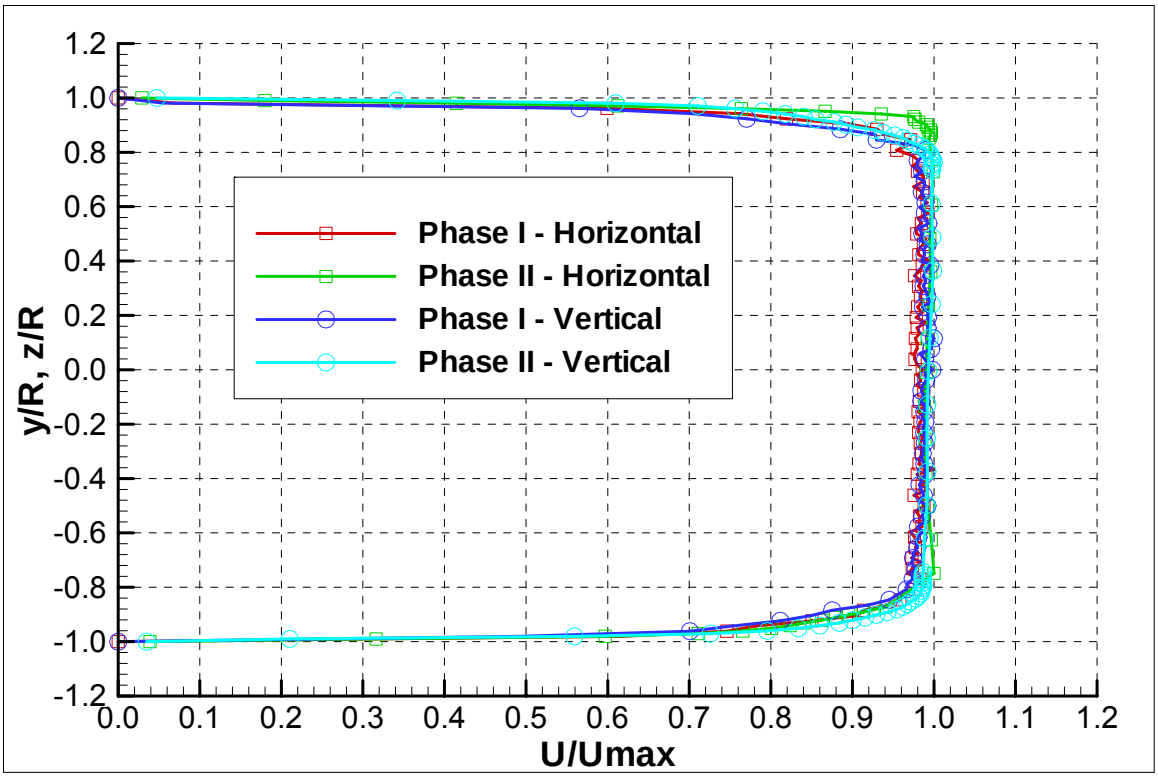

Figure 3.10: Comparison of Vertical and Horizontal Jet Exit Velocity Profiles between Phase I and Phase II Jets, U_{exit} = 5 m/s

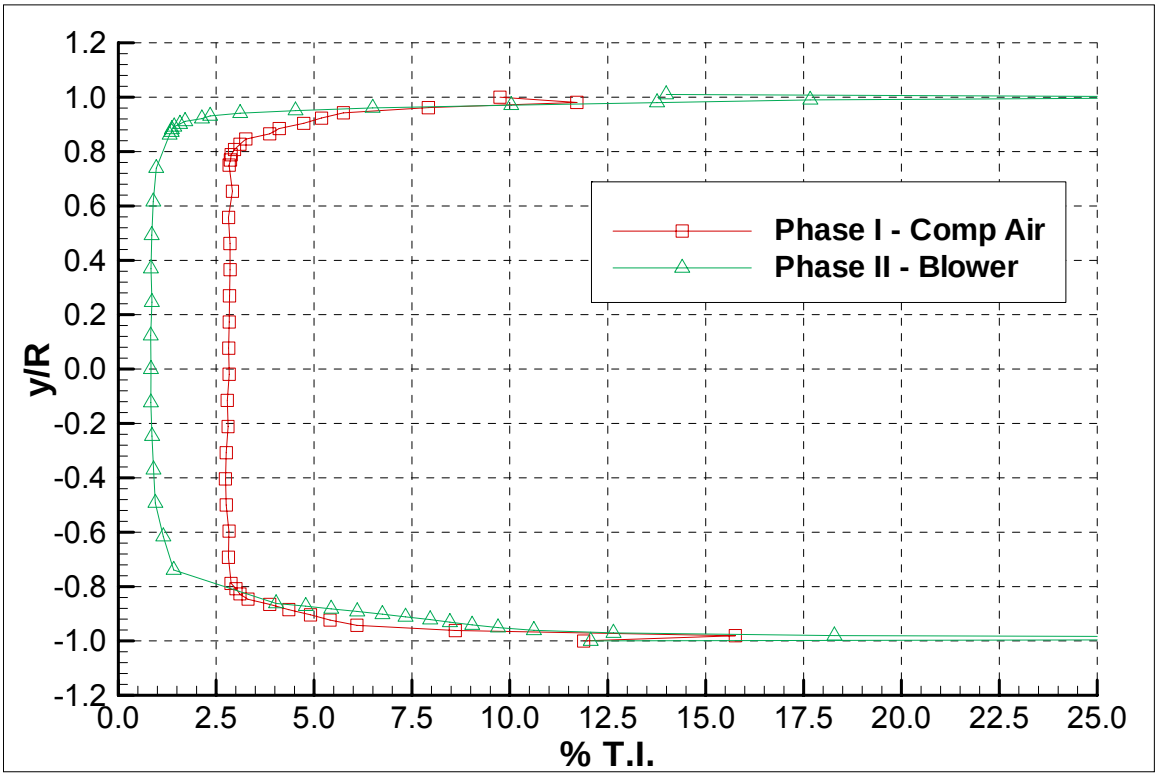

Figure 3.11: Comparison of Horizontal Turbulence Intensity Profiles between Phase I and II Jets, U_{exit} = 10 m/s

A comparison of the decay in the average centerline velocity for the phase I and II setups is shown in figure 3.12, with the corresponding turbulence intensity curves shown in figure 3.13. Once again the velocity curves compare well. There is a bit of an offset between the turbulence intensity curves, especially near the jet exit. Moving downstream and away from the exit the offset between the curves almost disappears.

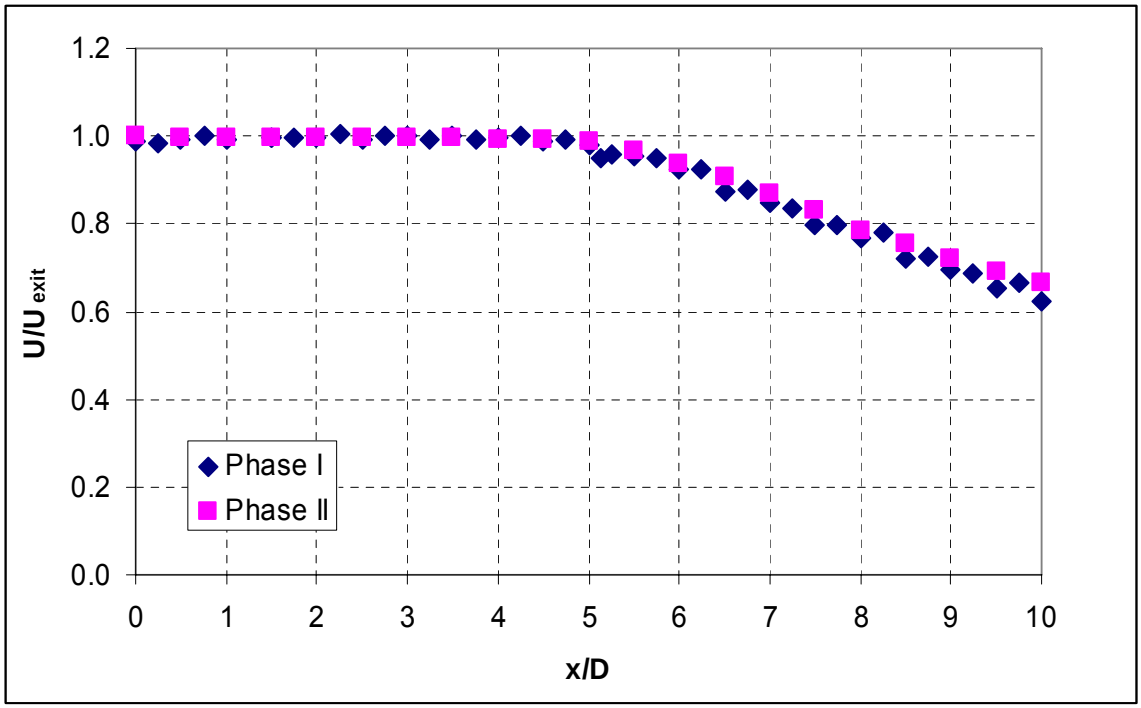

Figure 3.12: Comparison of Centerline Velocity Decay for Phase I and II, U_{exit} = 10 m/s

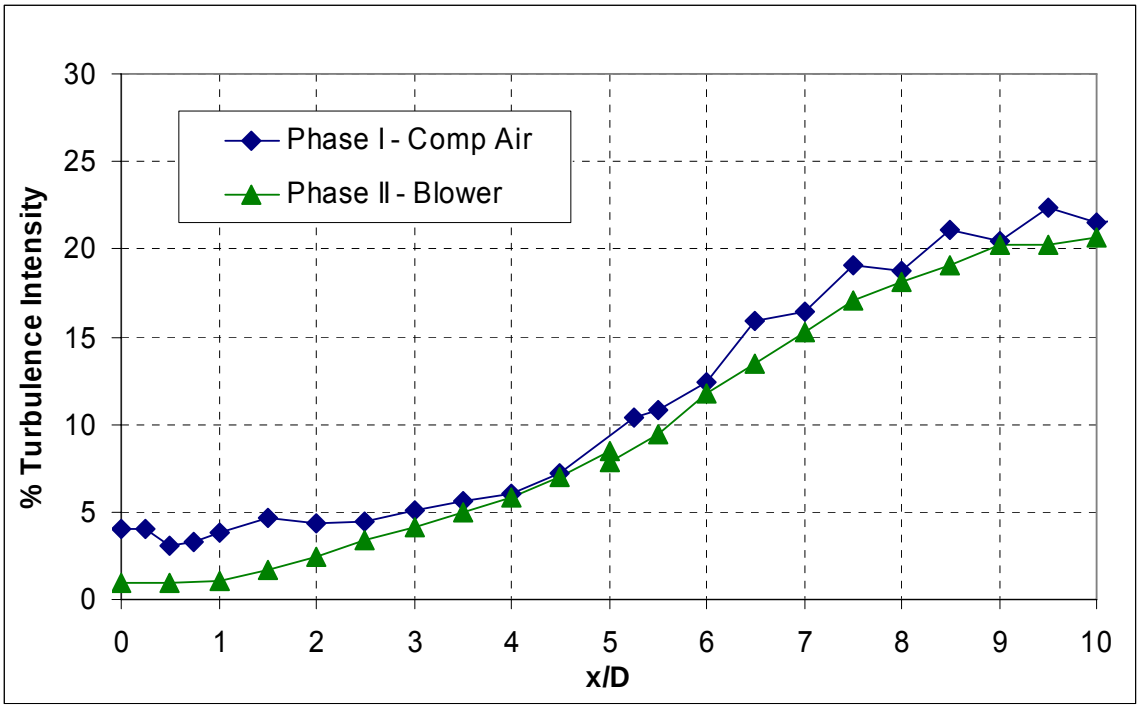

Figure 3.13: Comparison of Centerline Turbulence Intensity for Phase I and II, U_{exit} = 10 m/s

Figures 3.14 through 3.17 show the vertical and horizontal average velocity and turbulence intensity profiles for the phase II jet from the exit to five diameters downstream, the end of the potential core. The curves behave as expected with good symmetry between the y and z directions. Since there is no preferred spreading direction forcing in the vertical direction should be equivalent to forcing in the horizontal direction. The curves shown are actually slices of more detailed planar traverses of the jet performed with the hotwire.

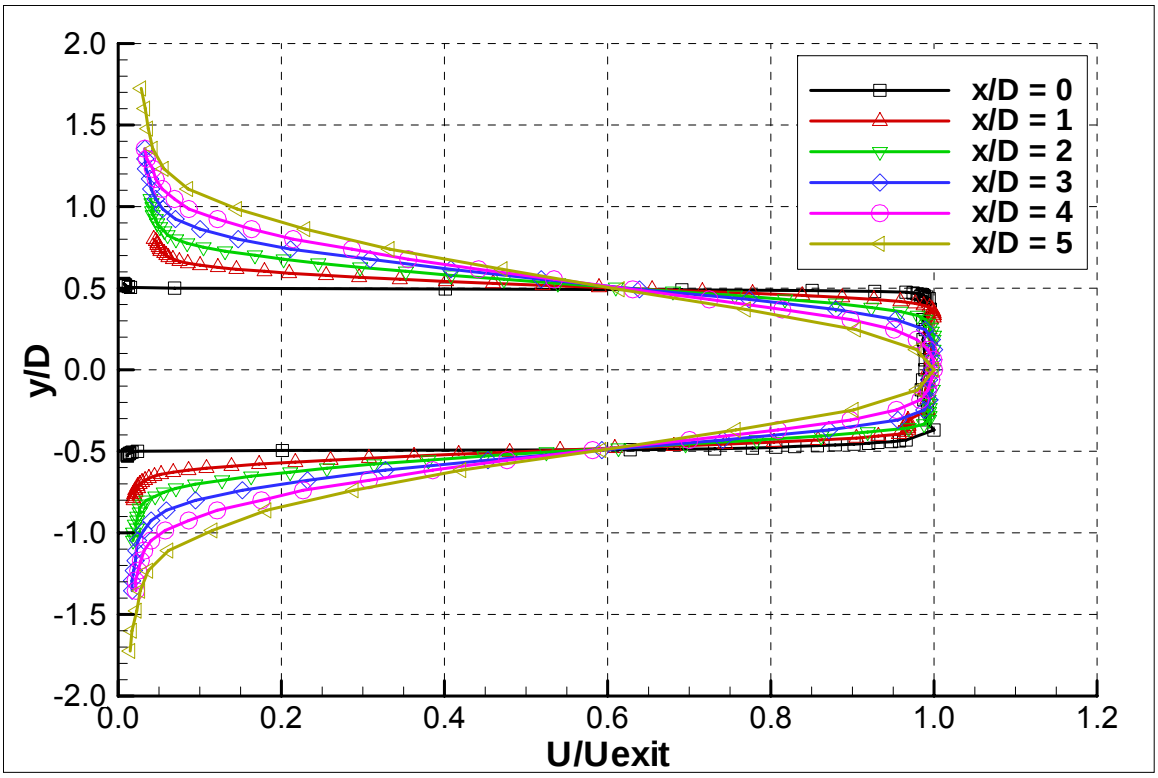

Figure 3.14: Horizontal Velocity Traverses for the Small Scale Jet at Multiple Downstream Locations, U_{exit} = 10 m/s, Phase II Setup

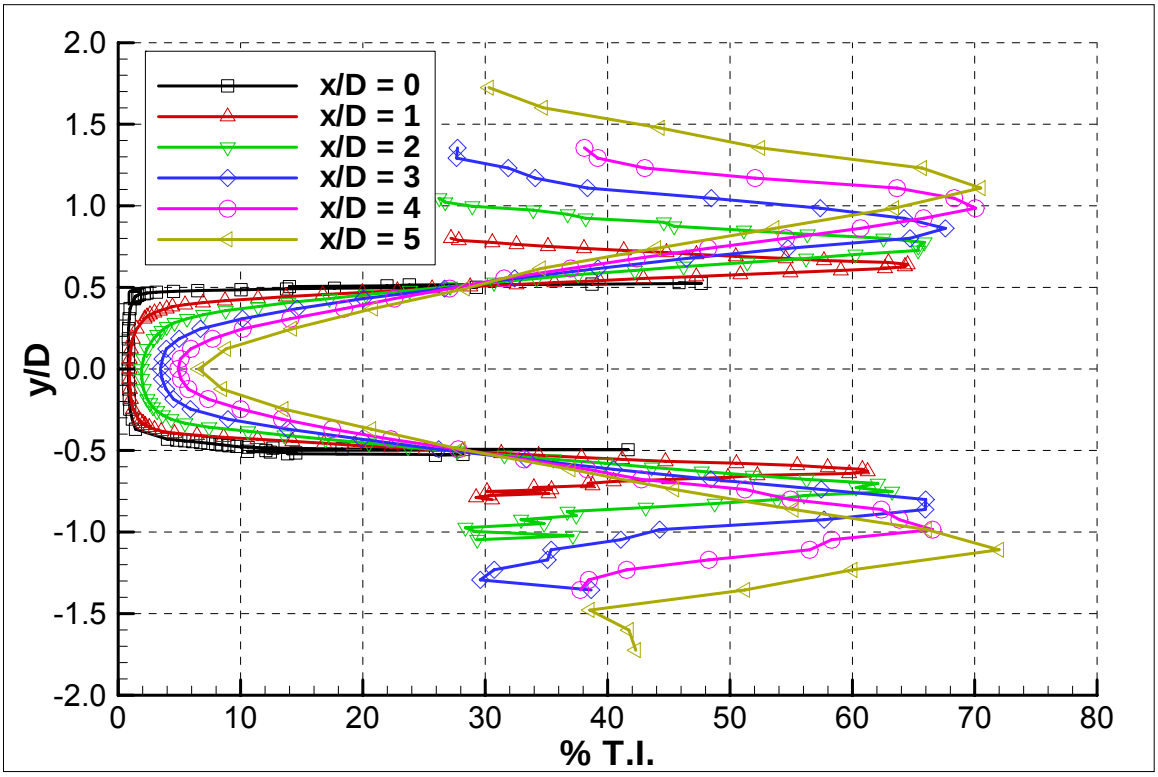

Figure 3.15: Corresponding Horizontal Turbulence Intensity Traverses

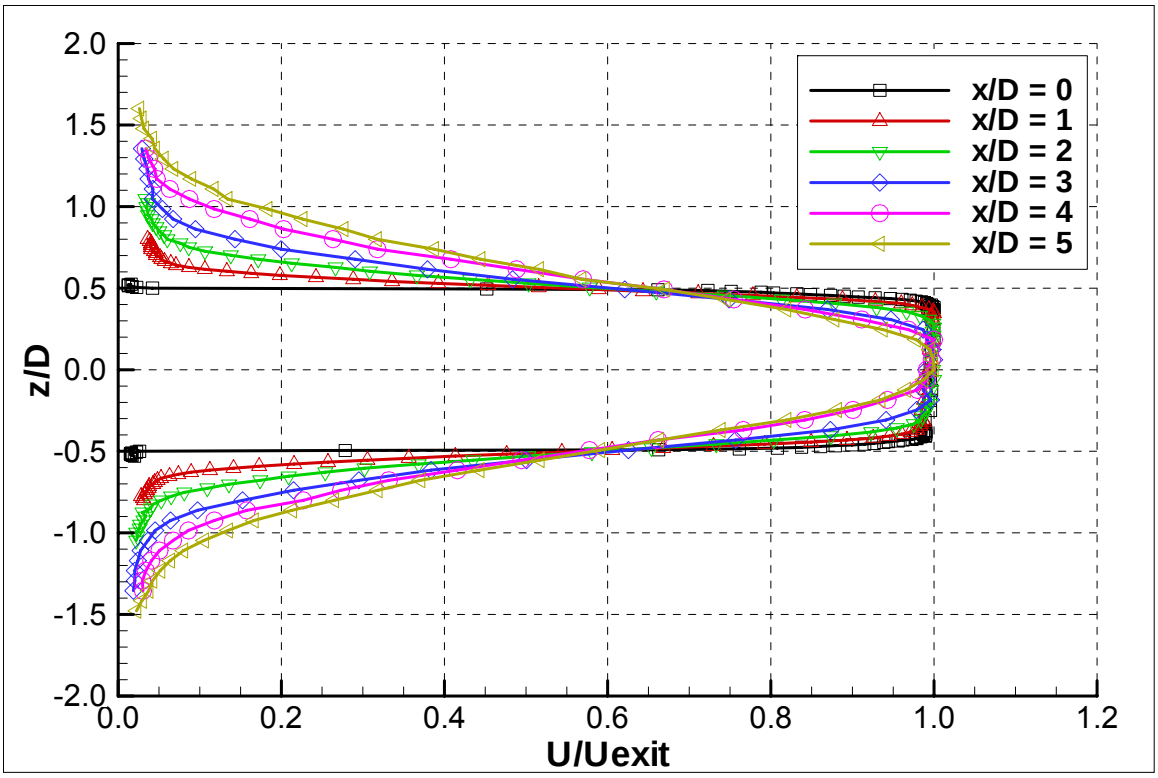

Figure 3.16: Vertical Velocity Traverses for the Small Scale Jet at Multiple Downstream Locations, U_{exit} = 10 m/s, Phase II Setup

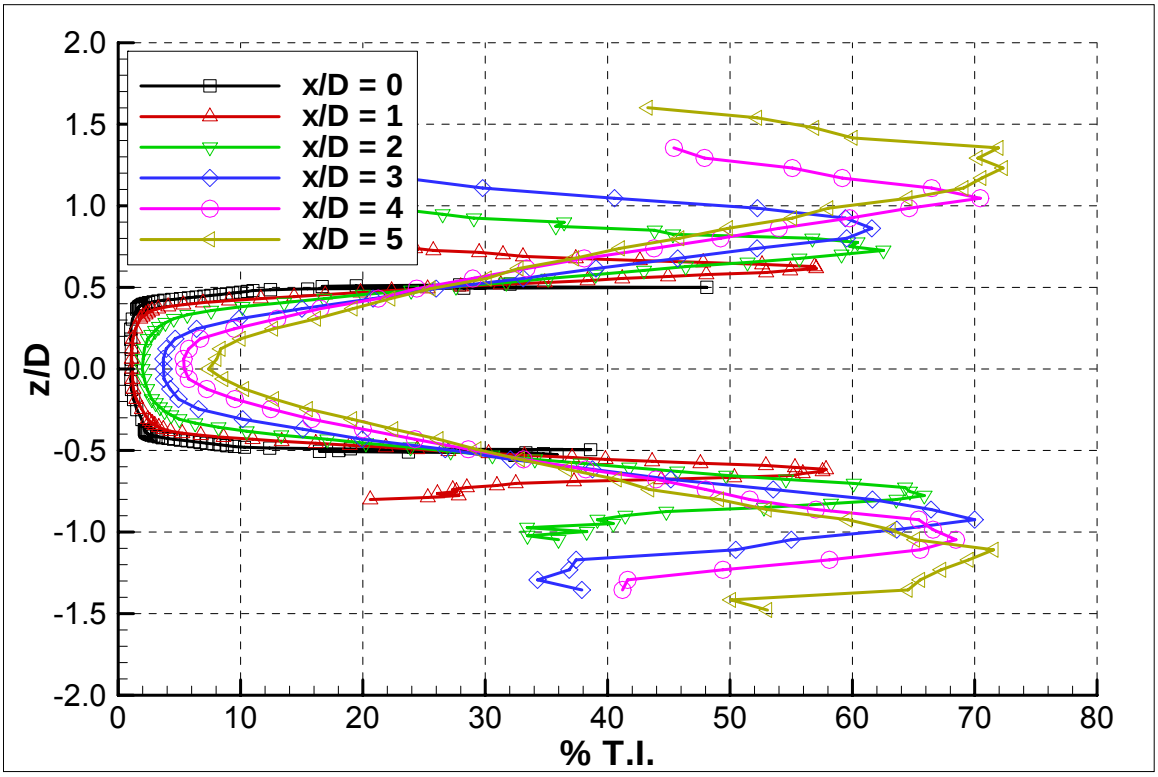

Figure 3.17: Corresponding Vertical Turbulence Intensity Traverses

Figures 3.18 and 3.19 are contour plots of the mean velocity and turbulence intensity of the unforced jet in the xz-plane created from the hotwire traverse data. Figure 3.20 is the same as 3.18, except the contour plot was created from PIV measurements. The two contour plots compare well with each other. The velocity field obtained from the PIV measurements was used to calculate the momentum thickness as a function of downstream distance. Figure 3.21 is the plot of the calculated momentum thickness versus downstream distance. The linear fit to the data is useful because the PIV measurements near the frame edges tend to get skewed. The image frames were overlapped somewhat to smooth out this effect, but the skewing effect is clear where the frame edges were not overlapped (at 0D and 5D, the edges of frames 1 and 5 from figure 2.9).

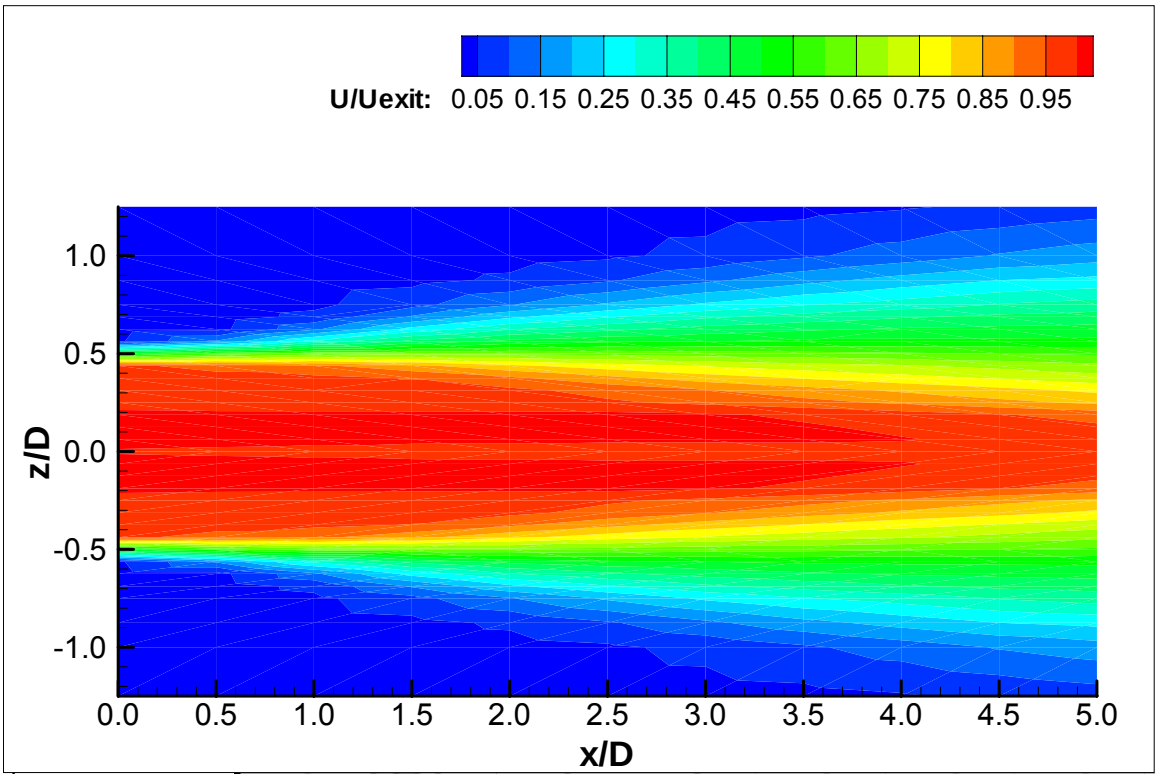

Figure 3.18: Contour Plot of Unforced Jet Velocity from Hotwire Traverses, U_{exit} = 10 m/s, Phase II Setup

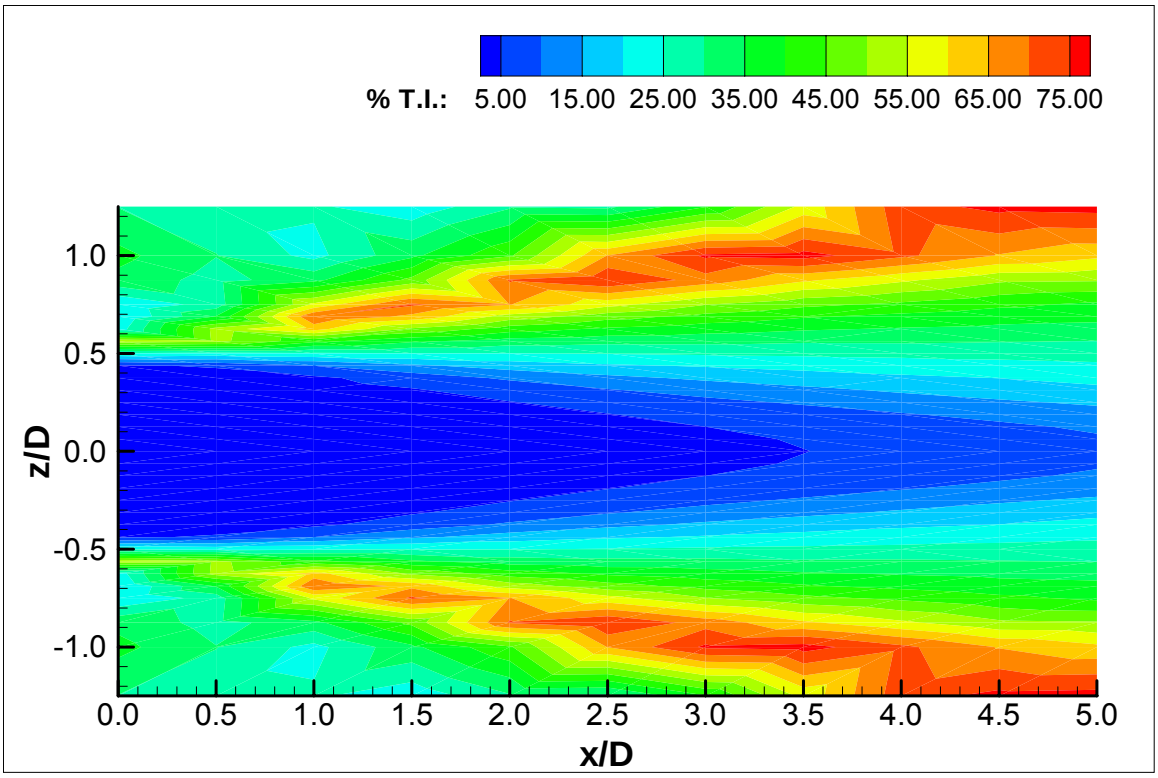

Figure 3.19: Contour Plot of Unforced Jet Turbulence Intensity from Hotwire Traverses, U_{exit} = 10 m/s, Phase II Setup

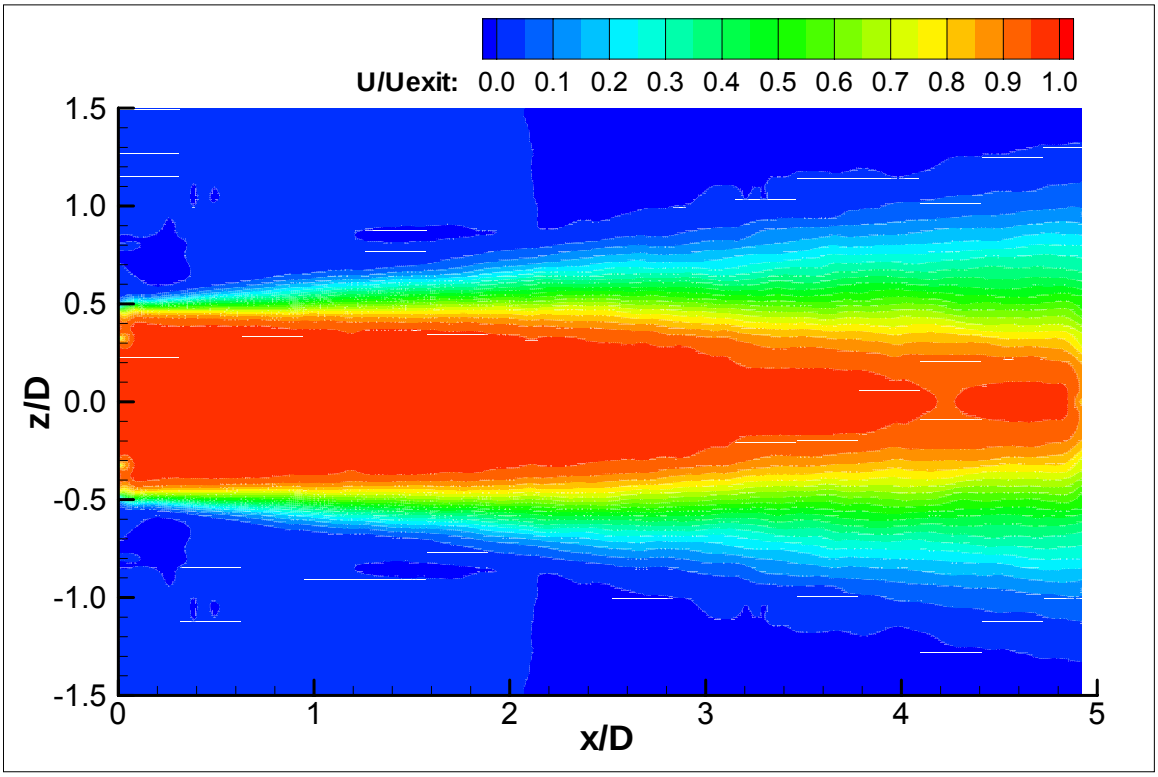

Figure 3.20: Contour Plot of Unforced Jet Velocity from PIV, U_{exit} = 10 m/s, Phase II Setup

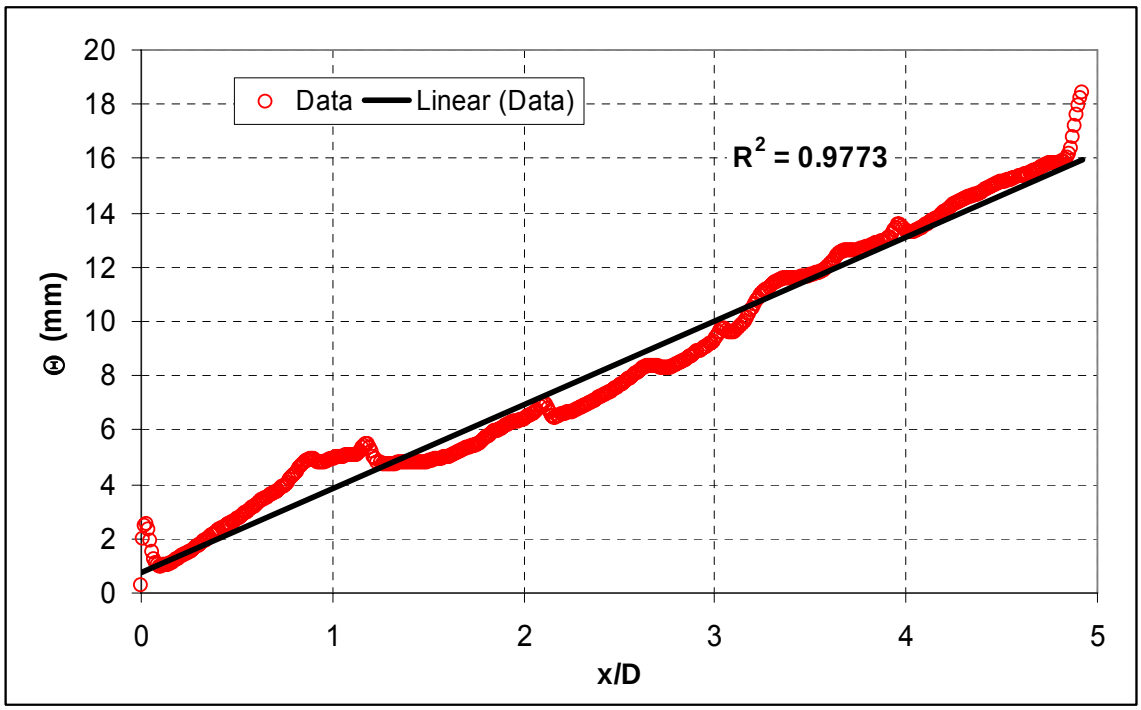

Figure 3.21: Momentum Thickness of the Unforced Jet as a Function of Downstream Distance, Calculated from PIV Measurements, U_{exit} = 10 m/s

Figures 3.22 and 3.23 are examples of the spectral characteristics calculated for the unforced jet. In these examples, the Fourier transform was calculated from velocity measurements made with the hotwire at the jet exit and five diameters downstream on the centerline. The specific type of Fourier transform used was the power spectral density, which was implemented using the Welch method. The power spectral density was chosen because it results in spectrum amplitudes that (ideally) do not vary with sampling frequency and sampling time. This allows for easy comparison of data sets sampled at different rates. The two figures contain the same data. Figure 3.22 was rescaled as figure 3.23 to make it easier to see what was happening in the lower frequency ranges.

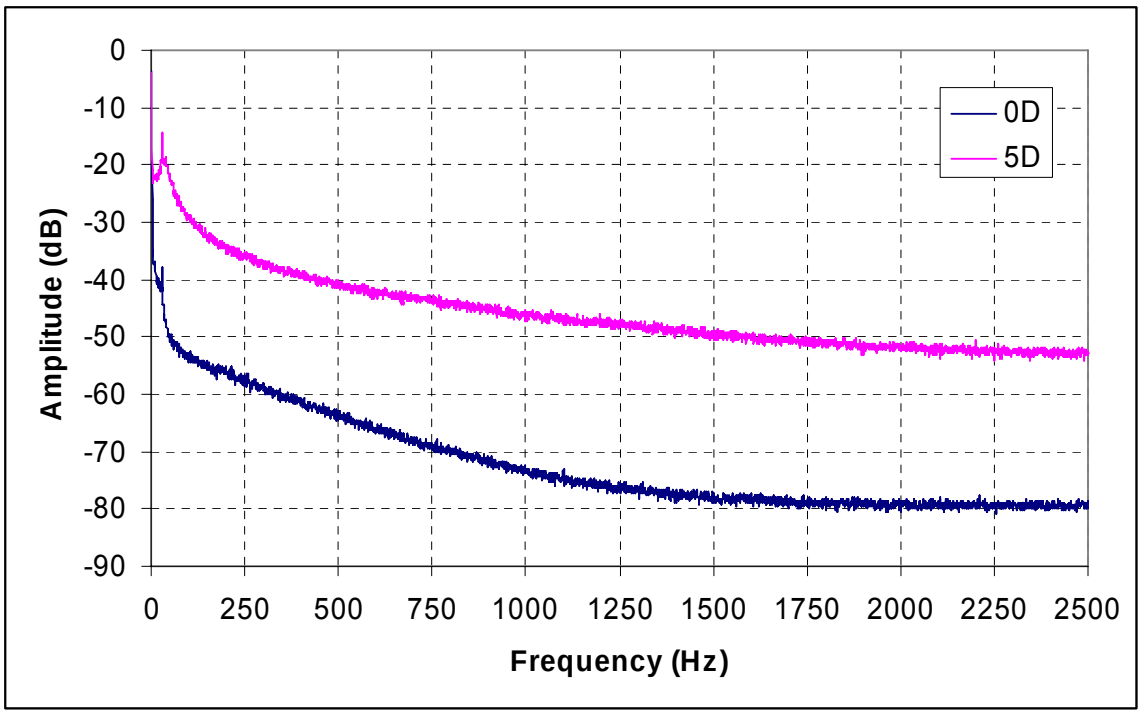

Figure 3.22: Power Spectral Density of Unforced Jet at the Exit and at 5D on the Centerline, Calculated from Hotwire Velocity Measurements, U_{exit} = 10 m/s

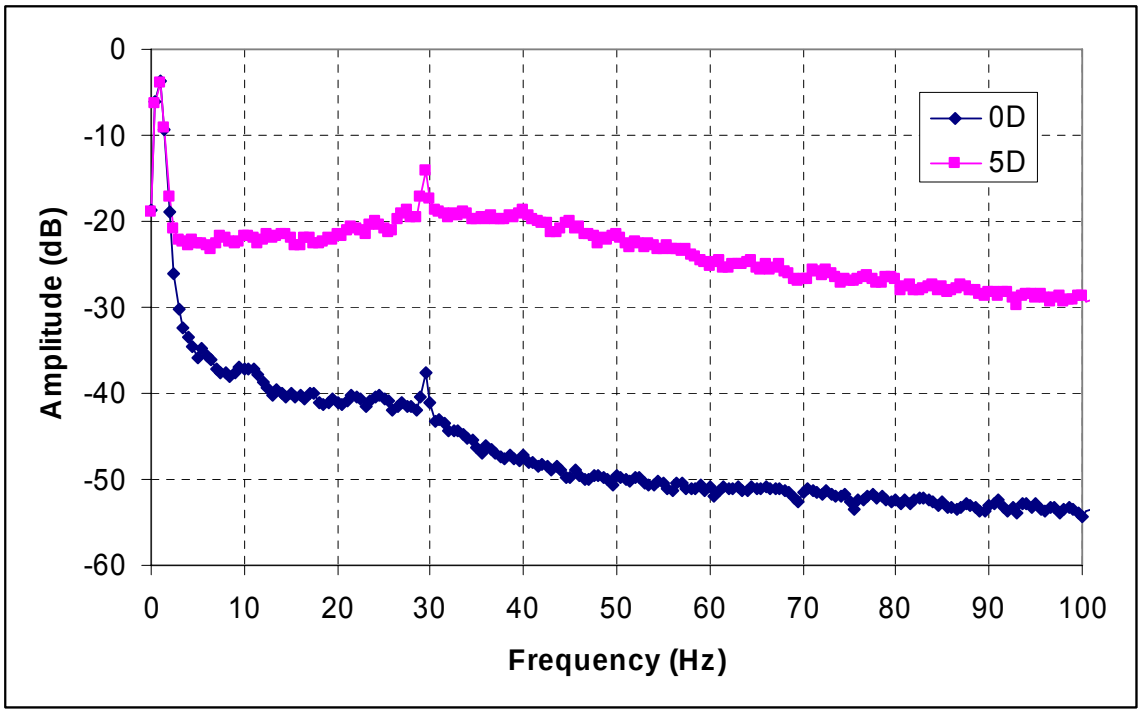

Figure 3.23: Power Spectral Density of Unforced Jet at the Exit and at 5D on the Centerline, Calculated from Hotwire Velocity Measurements, U_{exit} = 10 m/s (Plot is a Rescaled Version of Figure 3.22)

The spectrum is typical for that of a turbulent jet. The turbulent energy is well distributed among the frequencies and generally decreases with increasing frequency. When the probe was moved downstream to a more turbulent region (the end of the potential core) the energy in all of all frequencies increased. There is a lump in the spectrum in the low frequency region and a small peak in the spectrum near 30 Hz which corresponds to a natural frequency of the blower. The two are not related because changing the blower speed while keeping the jet velocity constant by blocking the inlet more shifted the frequency of the small peak but not the lump. Note that when moving from 0D to 5D the lump grows more than the rest of the broadband frequencies meaning those frequencies are amplified more.

Characterization of the Actuators

The pulse fluidic actuators used to excite the jet were characterized by hotwire measurements for steady and pulsing flow. Velocity traverses were performed on all of the actuators for steady blowing and pulse waveforms were obtained at the exit centerlines for a range of frequencies and amplitudes. There were two large actuators with four different nozzle sizes and four small actuators with two different nozzle sizes resulting in a total of 6 combinations. The actuators were specified by their number and nozzle size. For example, 2-act-0.08” specifies two large actuators with 0.08” nozzles, while 4-act-0.02” specifies four smaller actuators with 0.02” nozzles. A small sample of the actuator characterization results is presented here which is typical of the results as a whole.

Figures 3.24 and 3.25 are examples of pulse waveforms measured with the hotwire for the 2-act-0.08” case. Measurements were taken in the geometric center of the actuator nozzles at the exit. In this particular instance the two actuators were arranged on the top and bottom side of the jet nozzle, hence the labels “top” and “bottom”. The results demonstrate that at multiple frequencies and amplitudes the two actuators perform comparably. This assures that symmetric actuation is taking place. The waveforms also show that there is some “ringing” due to oscillations in the solenoid. As the pulsing frequency is increased, the ringing has a more noticeable effect on the pulse shape since the solenoid has less time to stabilize. The actuation amplitude was set with a pressure regulator and measured as the mass flow rate with a venturi flow meter (see Chapter 2 for details). The wave in figure 3.25 has approximately twice the amplitude of the one in figure 3.24. Note that this results in doubling of the average wave top from about 6 m/s to 12 m/s (if one imagines a line representing the average wave top replacing the oscillations for the 50 Hz case).

The actuator waveform measurements were cycle averaged (i.e. multiple cycles were averaged together to show what an average pulsing cycle looks like) and normalized by the cycle period. Figure 3.26 shows how the waveforms compare with each other for multiple frequencies at a single amplitude. The waveforms shown are for the 2-act-0.08” case. The waveforms compare well with each other. They have similar duty cycles, wave tops, and wave bottoms (or offset). As the frequency is increased, it is clear that the solenoid ringing distorts the waves away from an ideal square wave.

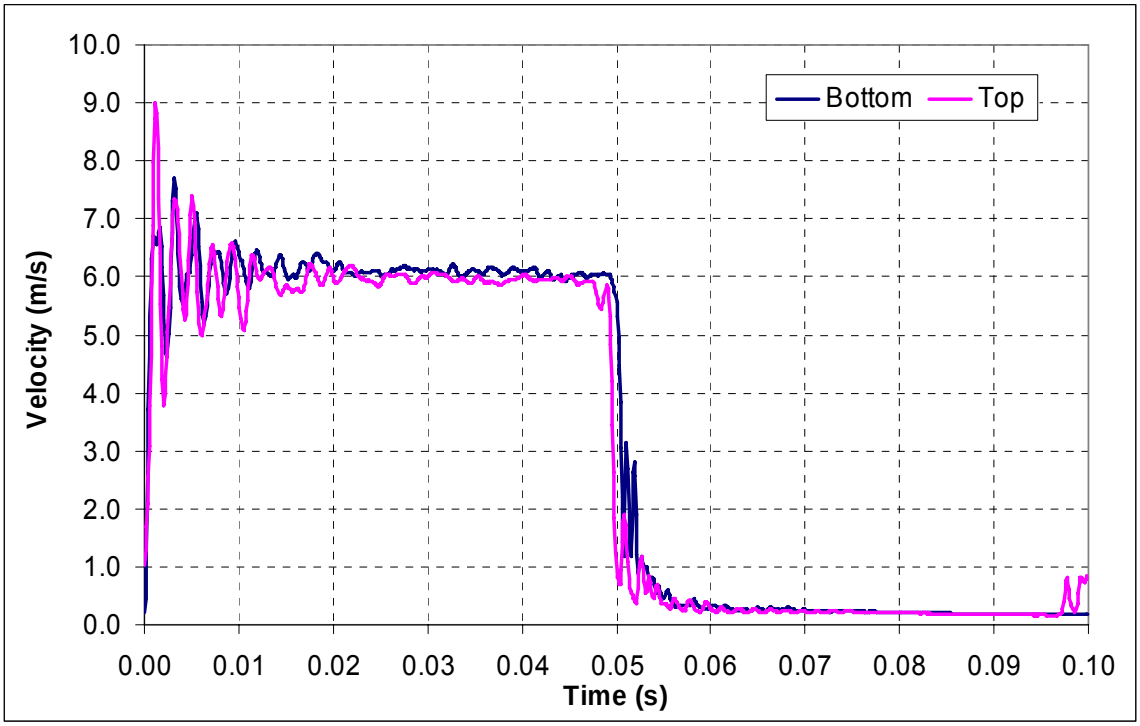

Figure 3.24: Comparison of Pulse Waveforms Obtained from Two Different Actuators with 0.08" Nozzles, f = 10 Hz, A = 0.001 lb_m/s (0.5% MFR for a 10 m/s jet)

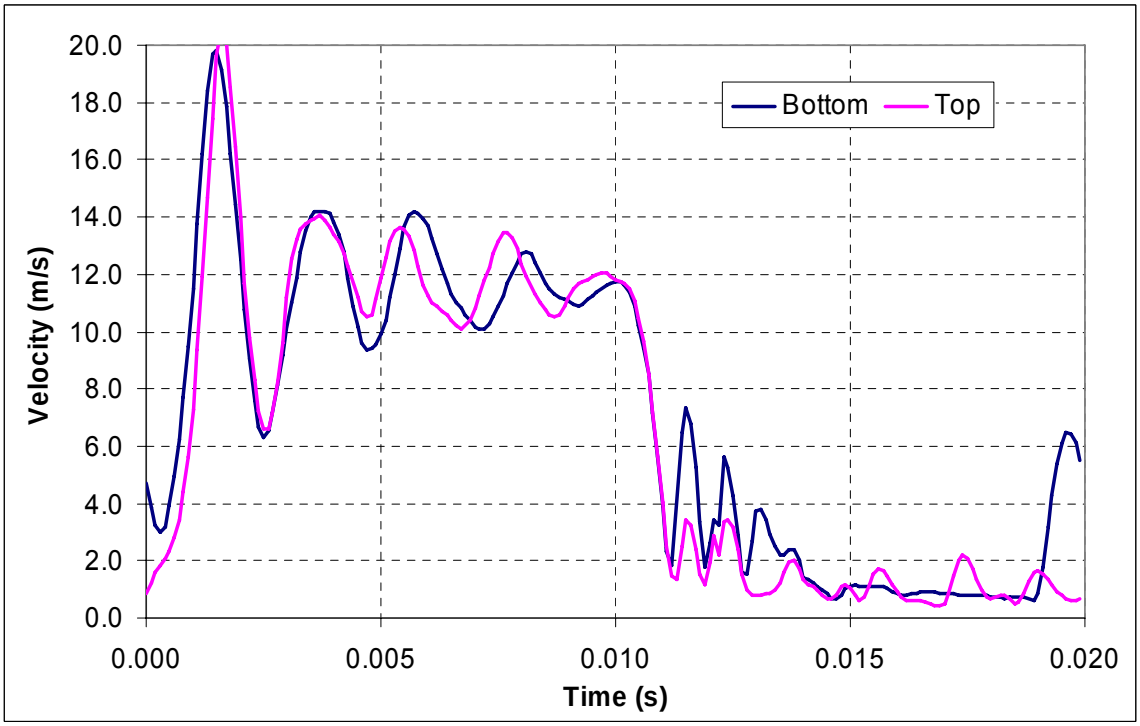

Figure 3.25: Comparison of Pulse Waveforms Obtained from Two Different Actuators with 0.08" Nozzles, f = 50 Hz, A = 0.002 lb_m/s (1.0% MFR for a 10 m/s jet)

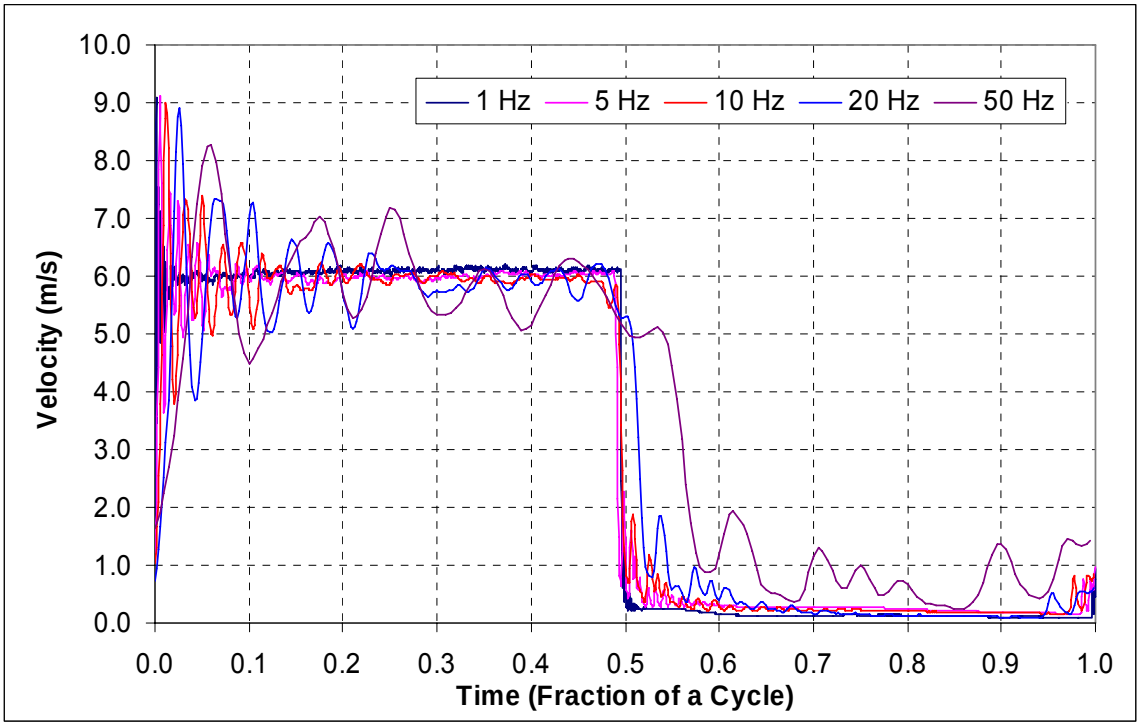

Figure 3.26: Comparison of Cycle Averaged Actuator Pulse Waveforms at Multiple Frequencies, Top Actuator, A = 0.001 lb_m/s (0.5% MFR for a 10 m/s Jet)

Figure 3.27 compares three 10 Hz waveforms at multiple amplitudes for the 2-act-0.08" case. Here the amplitude is specified in terms of percent mass flow ratio (%MFR) based on a jet with an exit velocity of 10 m/s. These are equivalent to mass flow rates of 0.0005 lb_m/s (0.25%), 0.002 lb_m/s (1%), and 0.004 lb_m/s (2%). As the amplitude is increased, the solenoid ringing increases as well. Note that for the pulse with the highest amplitude the rising edge of the velocity waveform jumps up to its peak in two steps. Thus the deviation of the waveform from an ideal square wave was somewhat dependent on amplitude, but still much more strongly dependent on frequency.

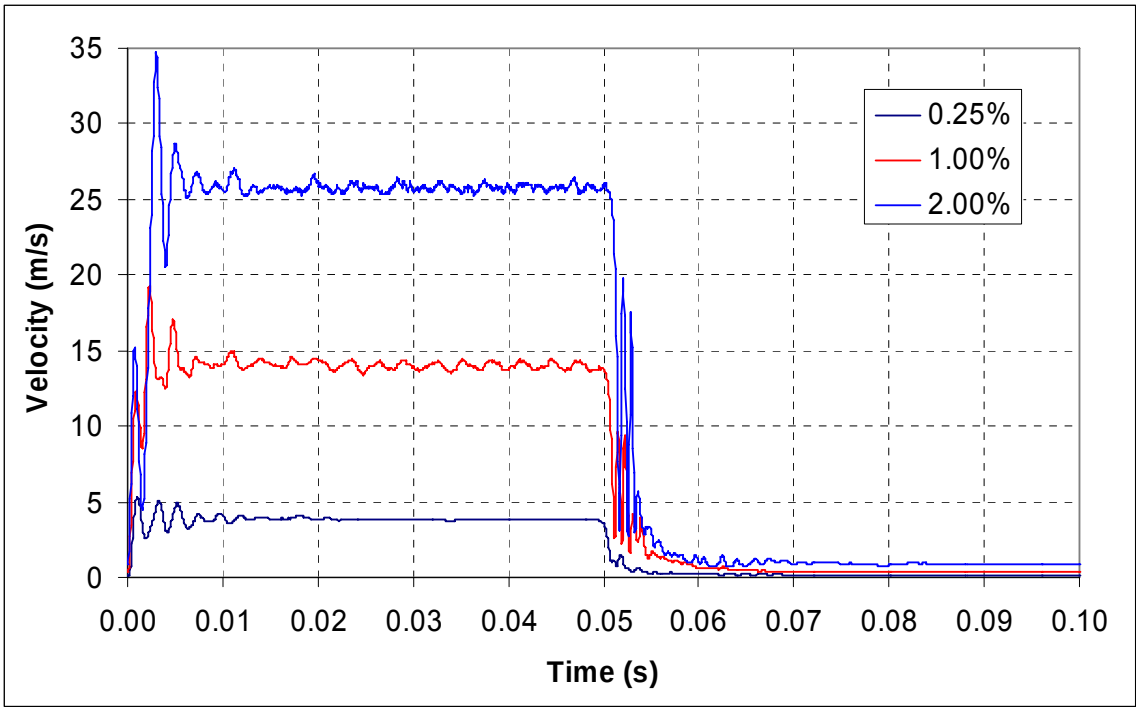

Figure 3.27: Comparison of Actuator Pulses at Different Amplitudes, Large Actuators with 0.08" Nozzles, f = 10 Hz, Amplitude is %MFR for a 10 m/s Jet

Figures 3.28 and 3.29 show the long and short axis traverses for steady flow through the large actuators with 0.08" nozzles. The velocity is scaled by the centerline exit velocity and the position is scaled by the slot dimension in the direction being traversed. The profiles from the two actuators (top and bottom) line up nicely indicating uniformity between them. This also helps to confirm that the pulsing was symmetric.

At low frequencies (< 20 Hz), the fluidic pulse duty cycle was virtually the same as the signal duty cycle used to control the switching of the solenoids. As the frequency was increased, the signal duty cycle had to be adjusted to keep the fluidic duty cycle close to 50%. This worked well for frequencies up to about 50 Hz, but beyond that the fluidic duty cycle became somewhat inconsistent between actuators. For example, while one actuator may have pulsed with a 50% duty cycle, the other may have pulsed with a 40%

duty cycle. Additionally, pulse quality became rather poor at higher frequencies. Figure 3.30 is an example of a pulse waveform obtained for the 2-act-0.008" case where the frequency was set to 90 Hz. Note that the offset has increased, the duty cycle is too small, and the ringing of the solenoid significantly affects the shape of the wave. These inconsistencies led to changes in the mixing performance and asymmetric forcing conditions.

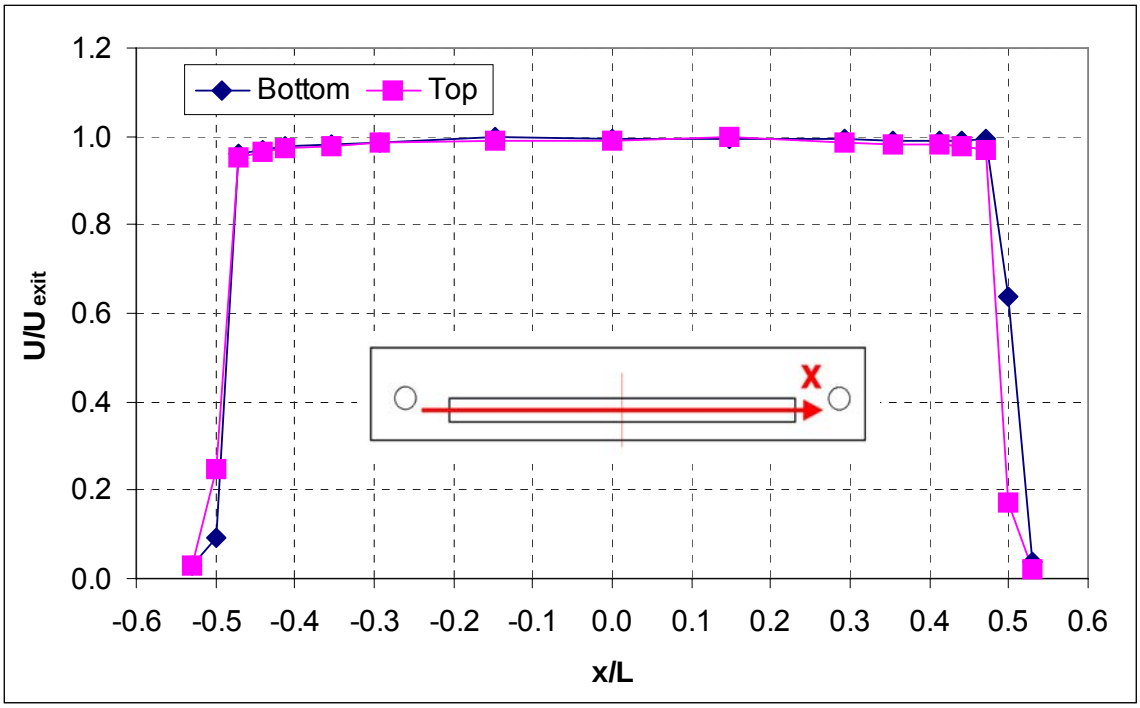

Figure 3.28: Long Axis Traverse of the Small Scale Jet Actuators with 0.08" Nozzles

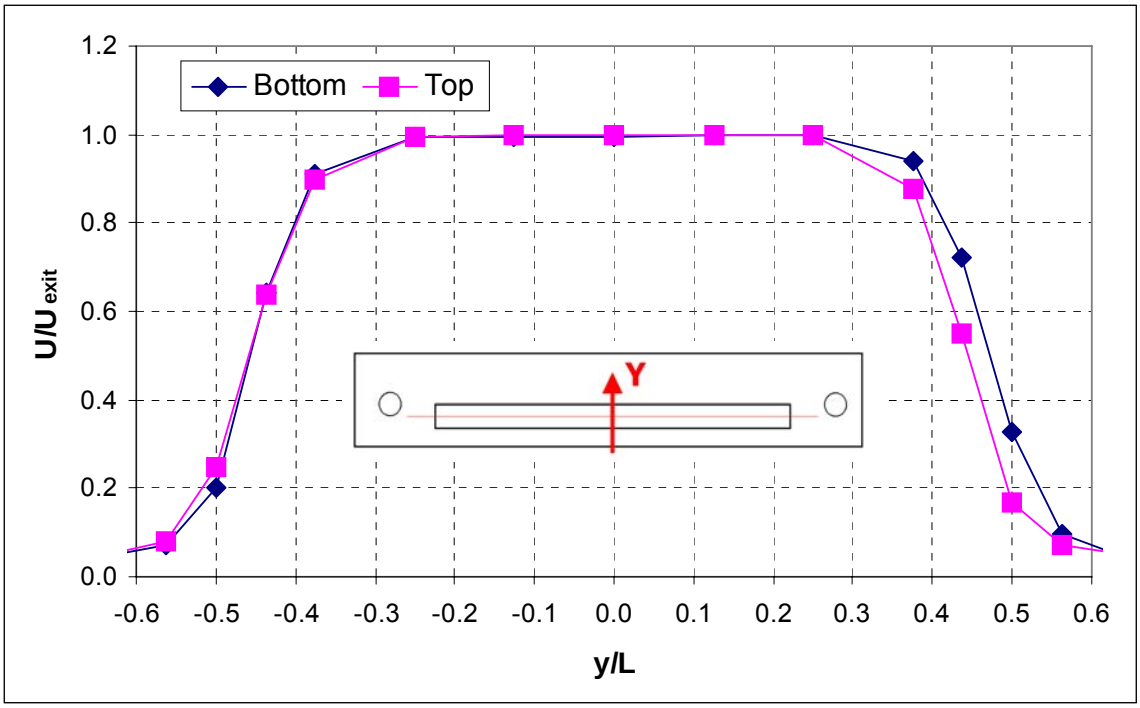

Figure 3.29: Short Axis Traverse of the Small Scale Jet Actuators with 0.08" Nozzles

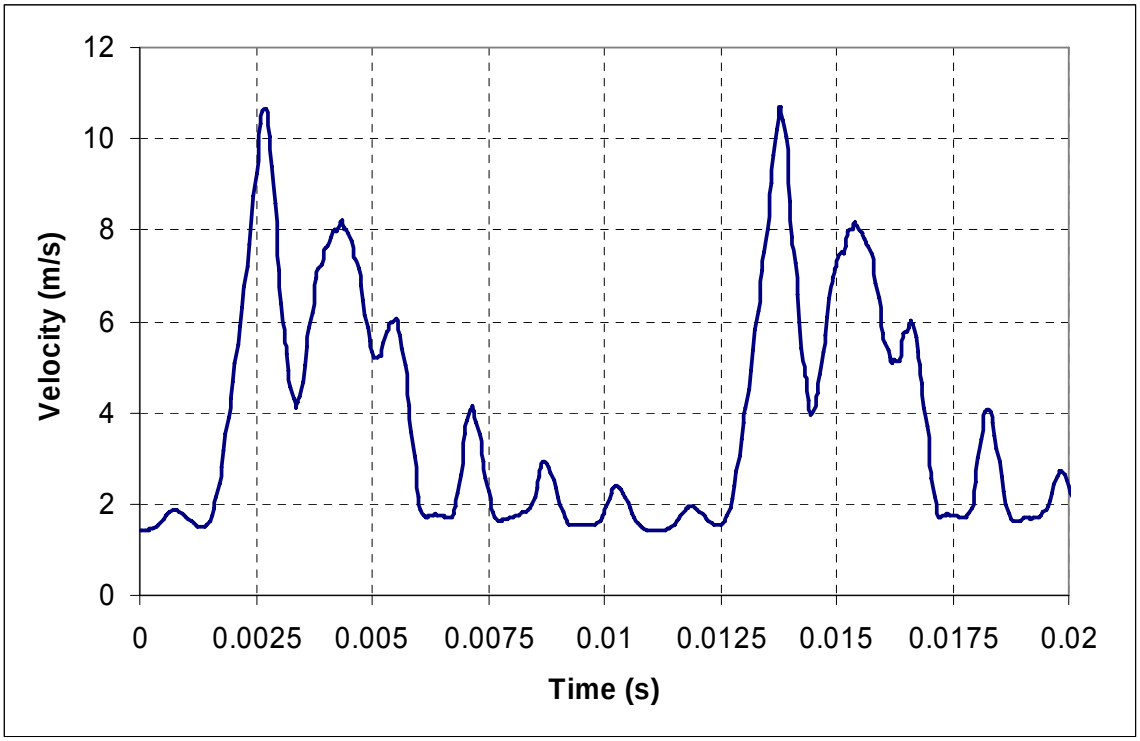

Figure 3.30: Example of a High Frequency Pulse Waveform of Poor Quality, f = 90 Hz

During jet mixing enhancement experiments, actuator amplitude was measured with a venturi flow meter, which assumes that the flow is steady. In most cases out-of-phase (antisymmetric) forcing was implemented, which resulted in only slightly pulsatile flow through the venturi. In some cases in-phase (axisymmetric) forcing was implemented which resulted in more pulsatile flow through the venturi and, hence, greater measurement error. This error is investigated in detail in Appendix C. The two most important results from the appendix are: 1) the error is generally low for out-of-phase pulsing, and 2) it is slightly higher, but still reasonable, for in-phase pulsing at frequencies near the optimum. Additionally, it was found that mass flow rate measured with the venturi correlated well with, and thus was an excellent indicator of, wave top velocity for high quality square wave pulses (i.e. below 50 Hz).

Jet Mixing Enhancement: Discovery of Key Parameters

The purpose of the Phase I experiments was to discover the parameters that were most important to jet mixing enhancement via pulse fluidic actuation and to characterize their effect. In order to accomplish this, the jet was run under a wide variety of configurations. Mixing enhancement was measured in terms of the velocity reduction compared to the unforced case at x/D = 10 on the centerline. It has been previously shown for heated flows that velocity correlates with temperature.[167] Thus, the measurement of velocity at a point can be a simple and effective way to measure mixing enhancement, and has been used by previous researchers for this purpose.[132, 137] For the current study, the mixing metric U* was defined as the average velocity for the unforced jet measured at 10D divided by the average velocity for the forced jet at 10D:

$$U^* = \frac{\overline{U}_{10D,unforced}}{\overline{U}_{10D,\,forced}} \tag{1}$$

Generally speaking, the lower this value the more effective the mixing. However, there were some exceptions to this. For example, when forcing antisymmetrically at very low frequencies and very high amplitudes extremely low values of U* (close to zero) were measured. This was because the pulses were completely pushing the jet back and forth across the centerline. This artificial mixing is clearly distinguished from real mixing in the data. The overall goal was to find the combination of parameters that minimized U* and to characterize their importance individually. Because a large number of parameters were varied, the combination of parameters tested was extremely large resulting in a massive amount of data. Therefore only the data deemed most relevant is reported and representative results and summaries are used extensively.

The Effect of Pulsing Frequency and Amplitude

Early on it became clear that mixing depends on both pulsing frequency and amplitude. This is demonstrated in figure 3.31, which gives mixing effectiveness curves as a function of both frequency and amplitude for 2-sided forcing in the antisymmetric mode. The dimensionless frequency used here is the Strouhal number and is defined as the pulsing frequency times the jet diameter divided by the exit velocity:

$$St = \frac{fD}{U_{exit}} \tag{2}$$

The amplitude shown is the ratio of the mass flow of the jet to the actuator which is defined as:

$$MFR = \frac{\dot{m}_{act}}{\dot{m}_{jet}} \tag{3}$$

Here, as in most cases, the mass flow ratio was expressed as a percentage. This parameter was a convenient way to express the amplitude since the jet mass flow rate was know from its exit velocity and the mass flow rate through the actuators was measured with the venturi. It was initially hoped that mixing for a given frequency would scale on this parameter. This was not the case as demonstrated in figure 3.32, which gives the mixing curves for amplitude sweeps with the same actuator configuration and all four nozzle sizes. Here the Strouhal number was set to 0.1, equivalent to 10 Hz for the 10 m/s jet. The curves clearly do not collapse, but they all follow a similar trend in that they initially fall rapidly, flatten out, and rise again slightly. The curve for the 0.02" nozzle, which extends further than any of the other sizes, shows an additional decrease in U*. The similarity of the curves suggests that there might be a common parameter to collapse the data. Amplitude sweeps for other actuator configurations show the same basic trend. The mixing curves, along with figure 3.31, show why a Strouhal number of 0.1 was chosen. It is the optimal pulsing frequency at the point where mixing as a function of amplitude saturates.

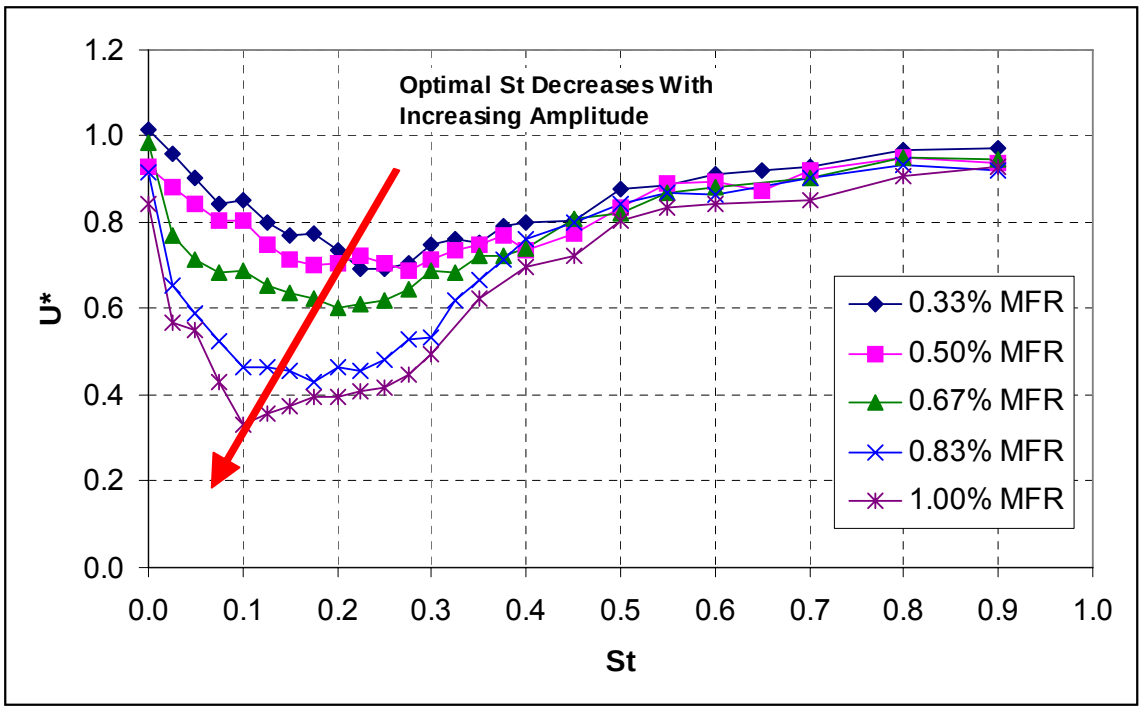

Figure 3.31: Jet Mixing Enhancement Curves for Frequency & Amplitude Sweeps, 2 Actuators, 0.08" Nozzles, 180° Phase, x/D = 10, U_{exit} = 10 m/s

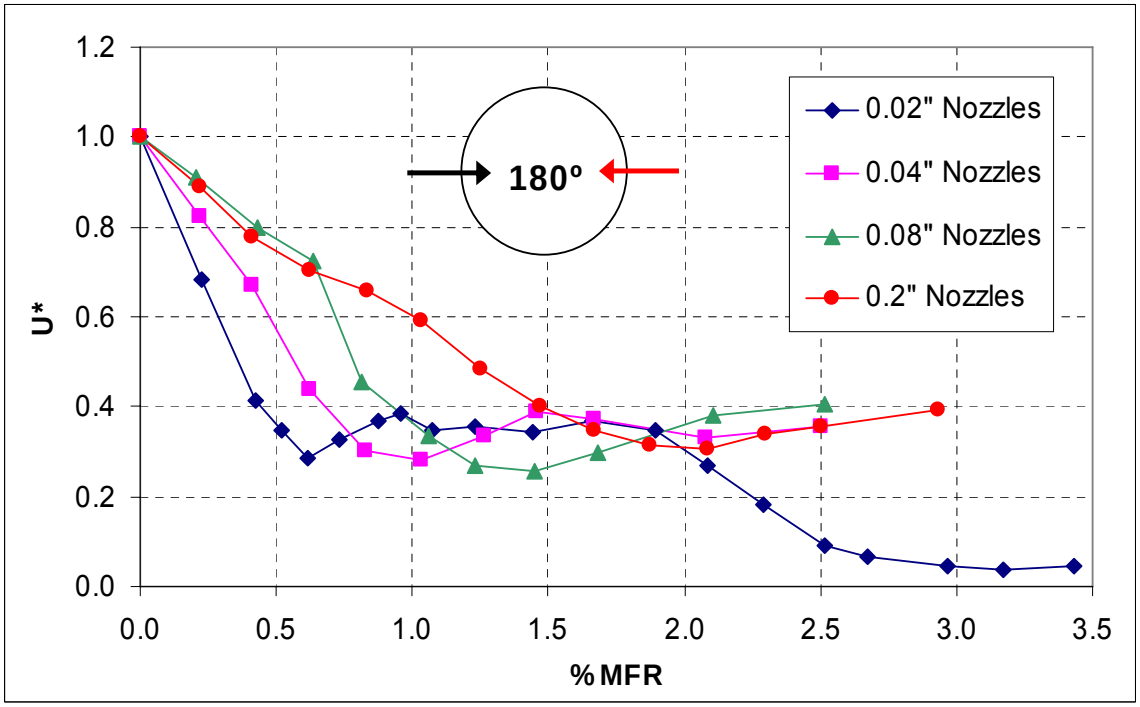

Figure 3.32: Jet Mixing Enhancement Curves for Amplitude Sweeps, St = 0.1, 2-Actuators, Multiple Nozzle Sizes, 180° Phase, x/D = 10, U_{exit} = 10 m/s

Collapse on Momentum Ratio

If the flow injected into the jet is considered analogous to a jet-in-crossflow, another parameter emerges that could be important to jet mixing. The problem of penetration of a jet into crossflow has been studied extensively, and it has been found that penetration distance scales with the square root of the momentum ratio. If it is assumed that the density of the injection and main jet are equal and the velocity profile at the actuator exit is uniform, the square root of the momentum ratio for the different actuator nozzles becomes:

$$SRMR = \sqrt{\frac{\left(\rho V^2 A\right)_{act}}{\left(\rho V^2 A\right)_{jet}}} = \sqrt{\frac{\dot{m}_{act} U_{act}}{\dot{m}_{jet} U_{jet}}} = \frac{\dot{m}_{act}}{\dot{m}_{jet}} \sqrt{\frac{A_{jet}}{A_{act}}} = \%MFR \times 0.01 \times \sqrt{AR} \qquad (4)$$

where AR = the area ratio of the jet exit to the actuator slot exit

Thus the square root of the momentum ratio (SRMR) can easily be calculated given the measured mass flow rate and the area ratio for the nozzle being used. Figure 3.33 shows that the same amplitude sweep data shown in figure 3.32 collapses when scaled using the SRMR. This is probably the most important discovery of the phase I experiments. From this point forward the SRMR became the primary actuator amplitude metric.

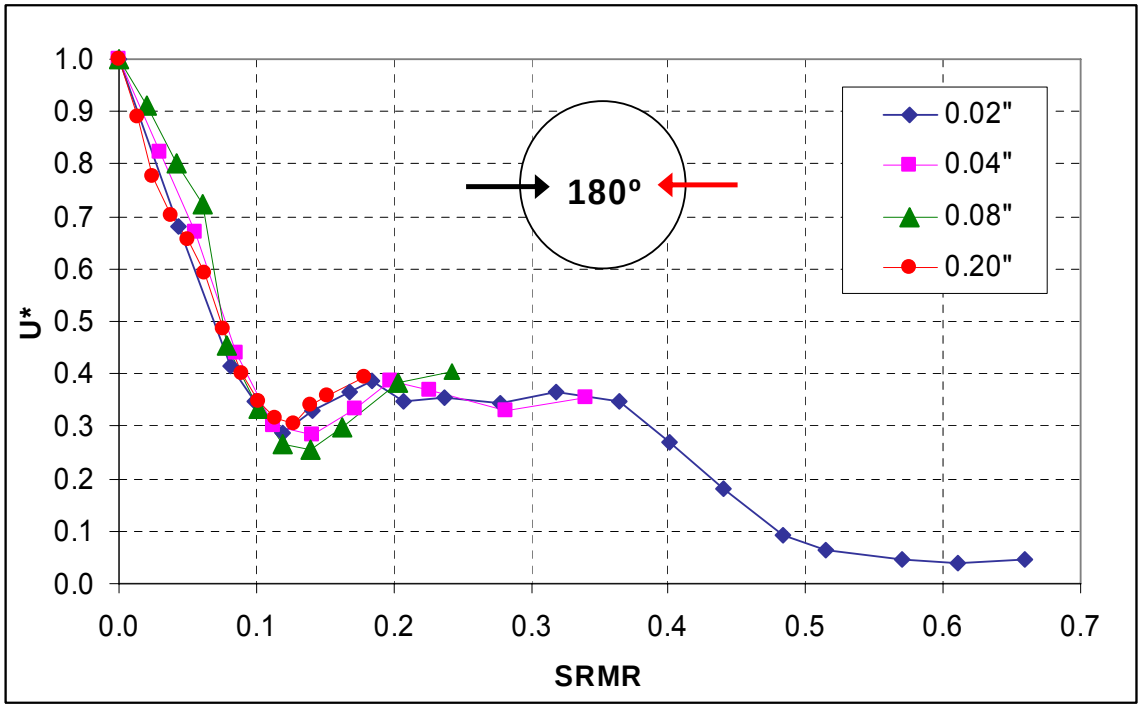

Figure 3.33: Jet Mixing Enhancement Curves Scaling on the Square Root of the Momentum Ratio, St = 0.1, 2-Actuators, Multiple Nozzle Sizes, 180° Phase, x/D = 10, U_{exit} = 10 m/s

A large number of experiments were performed for each of the actuator configurations. For the 2-actuator case this included frequency and amplitude sweeps with exit velocities ranging from 3 m/s to 50 m/s. The resulting Reynolds number range was 21,300 to 355,000. The data from these runs was compiled for St = 0.1 since this was the optimal case when pulsing antisymetrically at saturation level amplitudes. A piecewise curve fit was performed on the data and is shown in figure 3.34. Similar collapses occur for other Strouhal numbers as well.

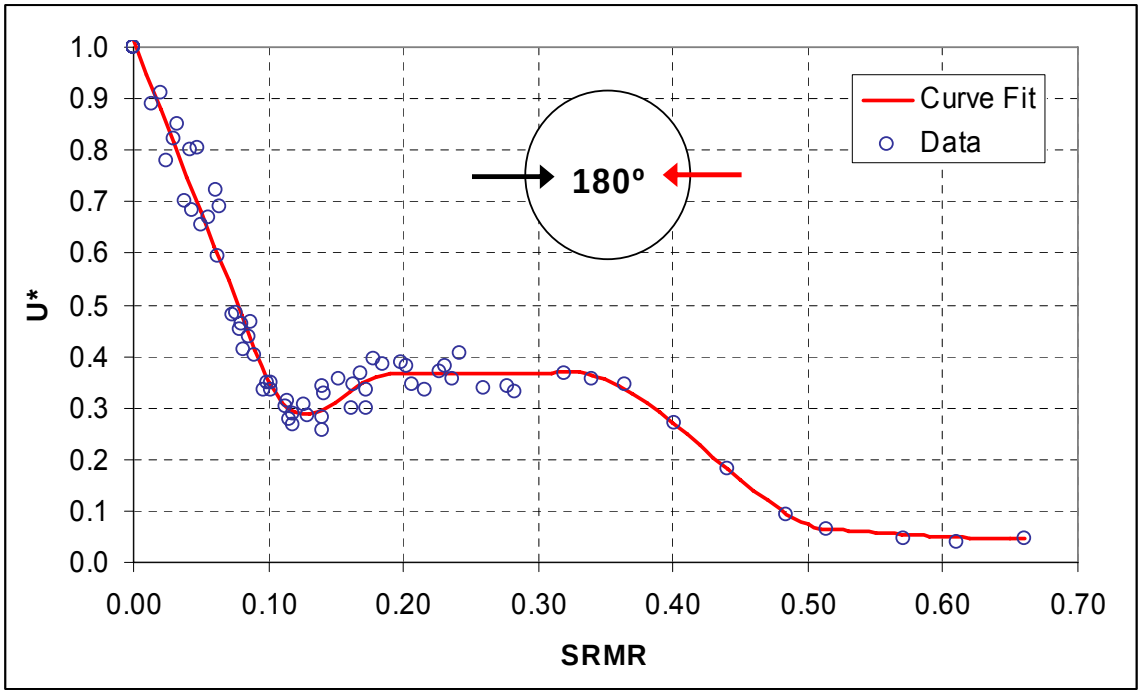

Figure 3.34: Curve Fit to all of the Data Compiled for 2-Actuators, St = 0.1, Multiple Nozzle Sizes, 180° Phase, x/D = 10, U_{exit} = 3 m/s to 50 m/s (Re_D = 21,300 to 355,000)

Frequency Sweeps

Frequency sweeps performed with different nozzle sizes can now be compared against each other in terms of their respective momentum ratios. Frequency sweeps for different nozzle sizes and the same SRMR collapse just like the amplitude sweeps (not shown). Figure 3.35 is graph of frequency sweeps at a number of different amplitudes for 2-actuator antisymmetric forcing. The initial increase in amplitude results in a sharp drop in U* across the lower frequencies (St < 0.4). As before, the optimal Strouhal number decreases with increasing amplitude, converging near 0.1. Saturation occurs at a SRMR of about 0.1, indicated by the fact that a notable increase in amplitude has relatively little effect on the mixing curve. As the amplitude is increased further, the curves deviate from the previous trend and U* actually begins to rise near St = 0.1 while continuing to fall or

remaining stationary elsewhere. A new *false optimum* appears close to 0 Hz where the curve for the highest amplitude drops down almost to U* = 0.1. The false optimum is due to the fact that, at low frequencies and high amplitudes, the jet is flopping between two states where it is being vectored away from the centerline. Note the indication on the graph where 50 Hz pulsing occurs. Even though Strouhal sweep data is available above this level, the trend can not be completely trusted because of the reduction of pulse quality, especially at high forcing amplitudes.

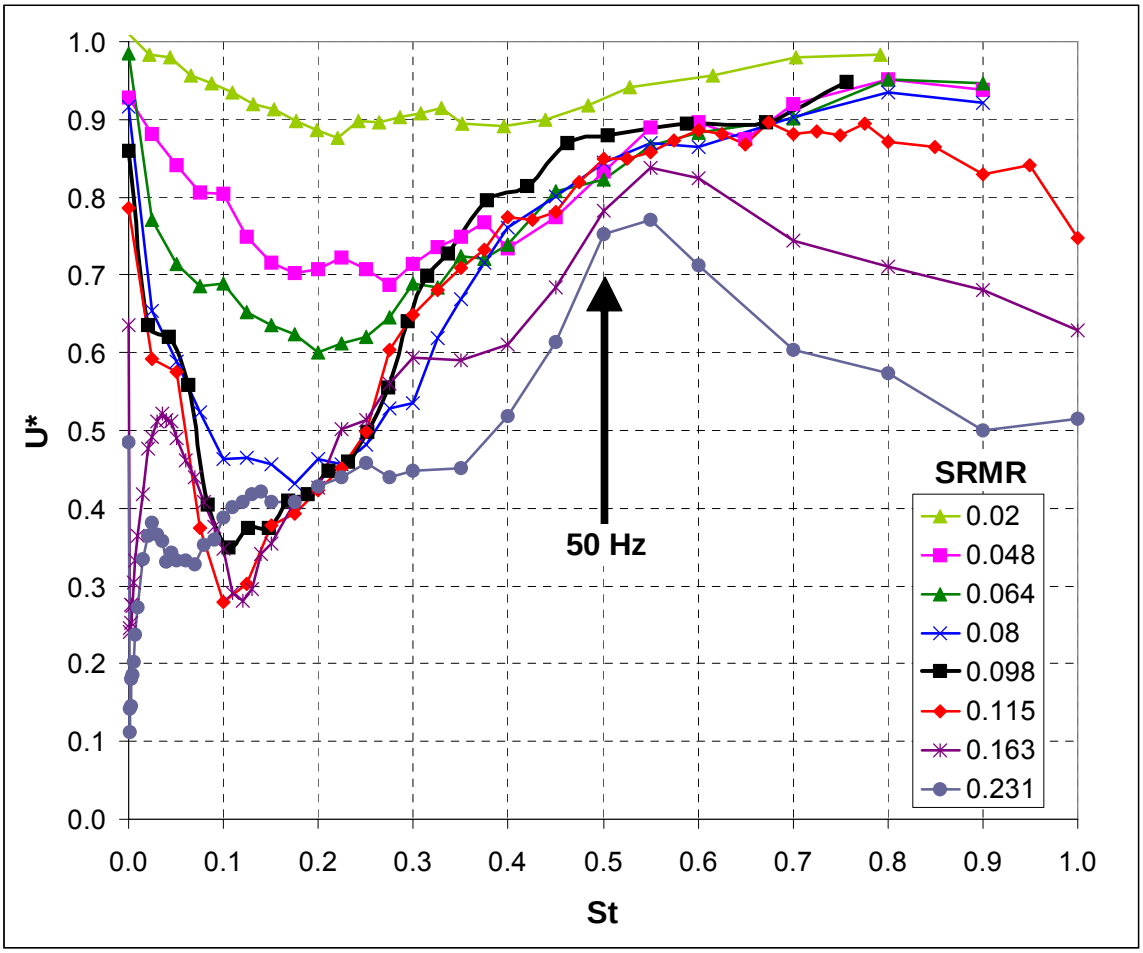

Figure 3.35: Jet Mixing Curves for Frequency Sweeps at Multiple Amplitudes, 2-Actuators, Multiple Nozzle Sizes, 180° Phase, x/D = 10, U_{exit} = 10 m/s

The Effect of Higher Frequency Pulses

The effect of higher frequencies was examined by decreasing the jet exit velocity in order to increase the Strouhal range. Frequency sweeps were performed on slower jets with exit velocities of 3 m/s and 5 m/s while keeping the pulsing amplitude constant at a nominal SRMR of 0.1. The resulting curves are compared to those obtained at higher velocities, shown in figure 3.36.

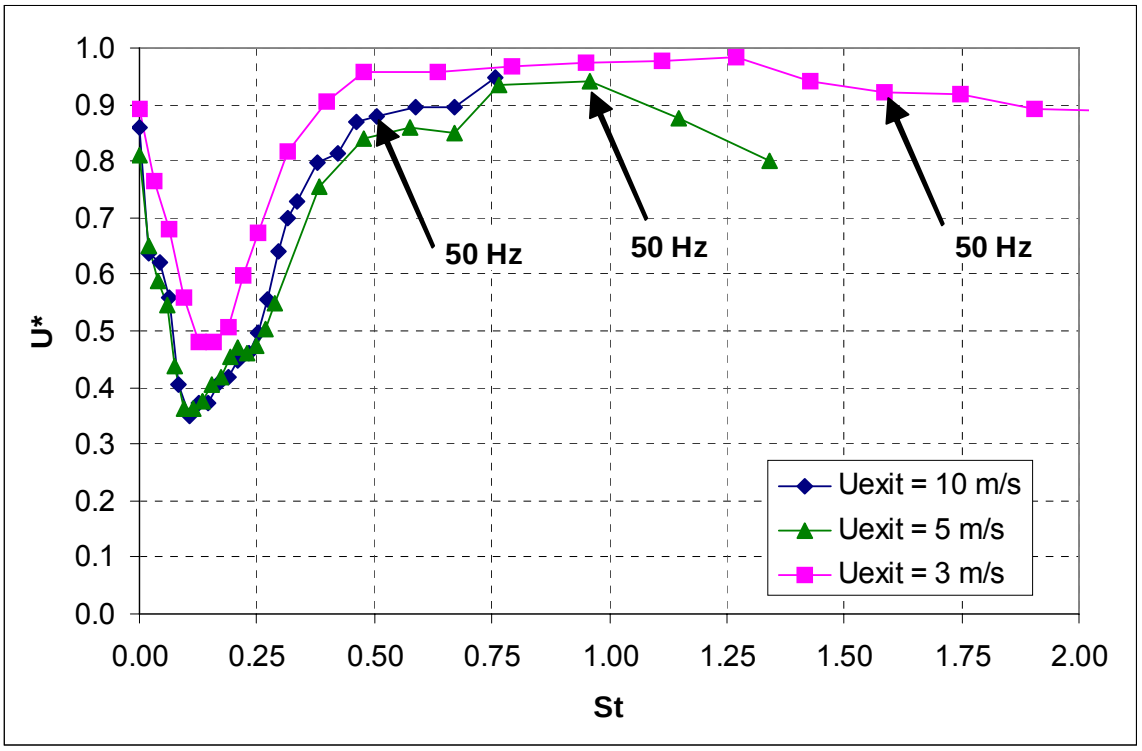

Figure 3.36: Comparison of Frequency Sweeps with a Constant Amplitude for Three Different Jet Exit Velocities, 2-Actuators, 0.08" Nozzles, 180º Phase, Nominal SRMR = 0.1, x/D = 10

The curves for the 5 m/s and 10 m/s jets follow each other closely, while the curve for the 3 m/s jet is slightly offset above them. It is possible that the offset is due to the lower Reynolds number, but a more likely explanation is that the amplitude could not be set as

precisely for that velocity since the mass flow measurement error is higher in the lower amplitude ranges. This has more to do with the types of transducers used than anything else. More detail on this can be found in Appendix C. The key characteristic is that U* stays relatively flat for Strouhal numbers well above one at saturation level amplitudes. The location where 50 Hz pulsing occurs is indicated in the figure for each curve. This is in a loose sense the "cut off" of where high quality pulses end. Thus, the slight dip in the 5 m/s curve above St = 1.0 is more likely an artifact of poor pulse quality rather than mixing enhancement. It is not known whether the downward dips in the mixing curves for very high levels of forcing are real (as in Figure 3.35), but it is thought that they are not because they did not occur for similar levels of forcing during the full scale jet mixing experiments (see Chapter 5).

The Effect of the Number of Actuators and Circumferential Location

There were three major configurations for the small scale jet as shown in figures 2.12 and 2.13 from chapter 2:

1) 2-Actuators, 180º Apart
2) 4-Actuators, 90º Apart
3) 4-Actuators, 50º Apart

The usual frequency and amplitude sweeps were performed at multiple jet exit velocities for the 4-actuator configurations just as in the 2-actuator configuration. There were only two nozzle sizes for the 4-actuator setup. The exit slots were approximately half the length of those used for the larger 2-actuator configuration and either 0.02" or 0.08"

wide. Figure 3.37 shows that the optimal Strouhal number decreases with increasing pulsing amplitude for one of the 4-actuator configurations, just as in the 2-actuator configuration.

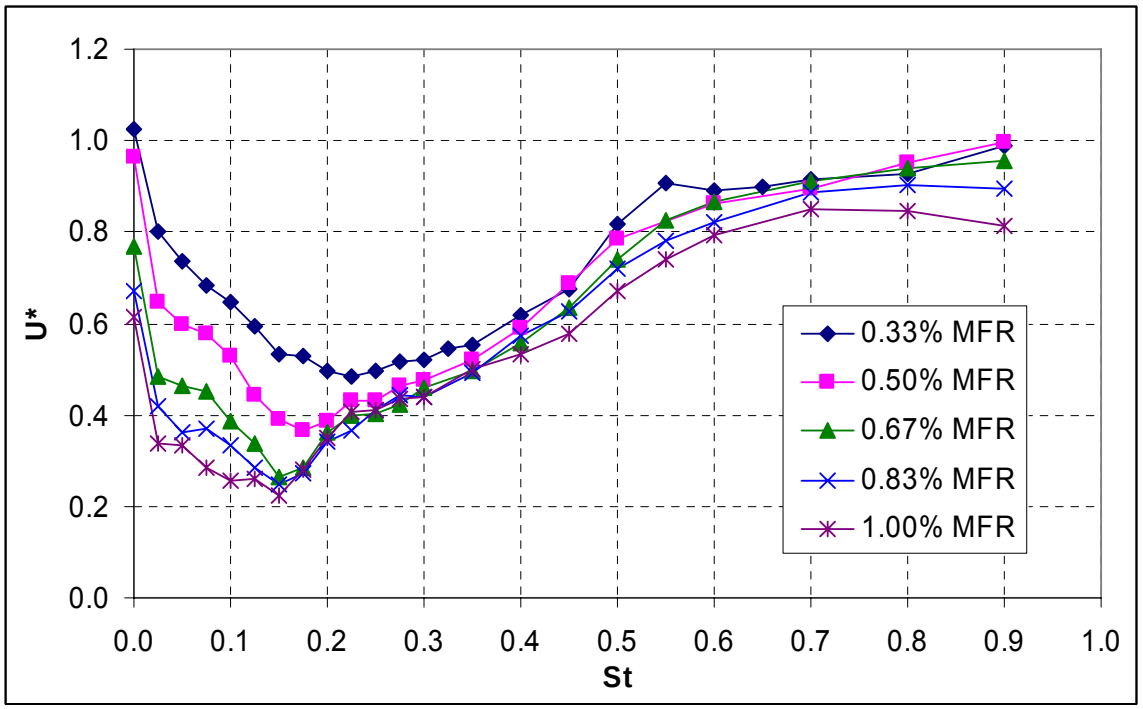

Figure 3.37: Mixing Enhancement Curves for Frequency & Amplitude Sweeps, 4-Actuators, 0.02" Nozzles, 90º Angle, 180º Phase, x/D = 10, U_{exit} = 10 m/s

The overall trends for the 4-actuator cases were basically the same as those for the 2-actuator cases, although the curves differed depending on the configuration. This is demonstrated in figure 3.38 which compares the frequency sweeps for a single amplitude between the three configurations. Here the SRMR is equal to 0.26, which is well beyond the saturation value of 0.1 demonstrated previously. The curves are for the most part similar, except that the 4-actuator curves seem to show slightly better mixing in the St = 0.05 to 0.2 frequency range. Whether the mixing is actually better is debatable. The amplitude is so high that a certain amount of vectoring may be taking place.

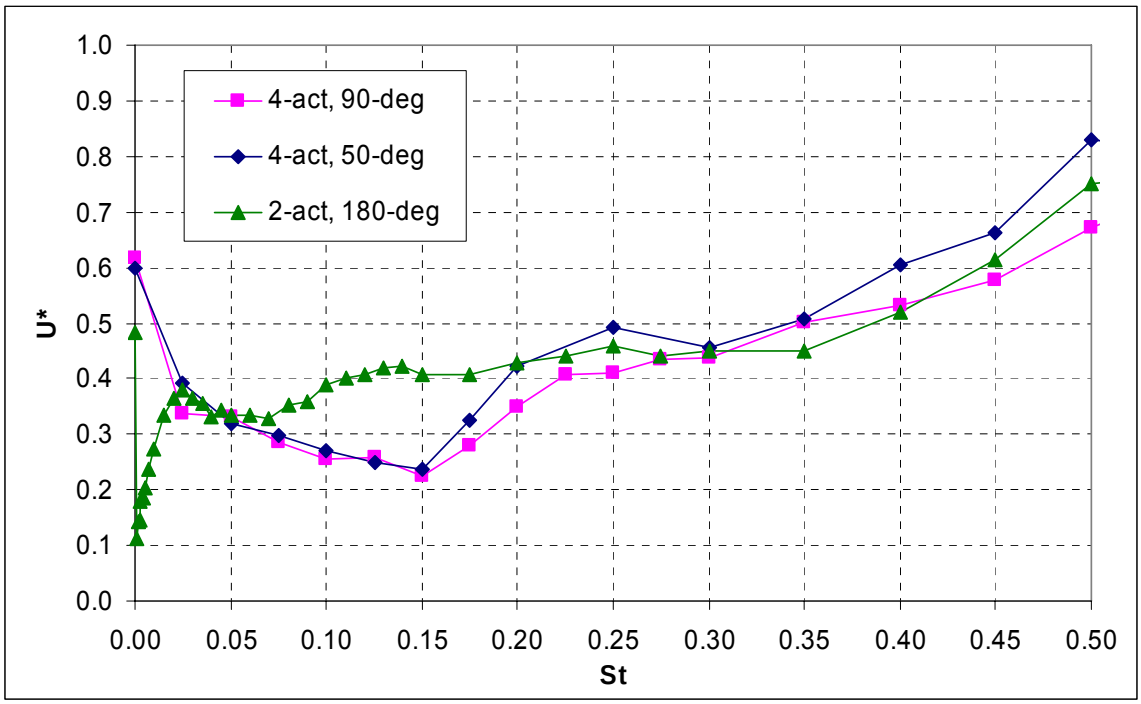

Figure 3.38: Comparison of Frequency Sweeps for the 3 Major Actuator Configurations, 0.02" Nozzles, 180º Phase, x/D = 10, U_{exit} = 10 m/s, SRMR = 0.26

Figure 3.39 makes the same frequency sweep comparison between configurations at a lower amplitude. The SRMR is 0.12, just above the 2-actuator saturation level. This time the 4-act-50º case looks almost identical to the 2-act case while the curve for the 4-act-90º case is unique. Mixing does not drop as sharply with frequency for the latter case, and the optimal frequency is located at a Strouhal number of 0.17 compared to 0.1 for the other two cases. So it appears that for lower amplitude pulsing the 4-act-50º configuration acts like the 2-act-180º case, and for higher amplitudes it acts like the 4-act-90º case.

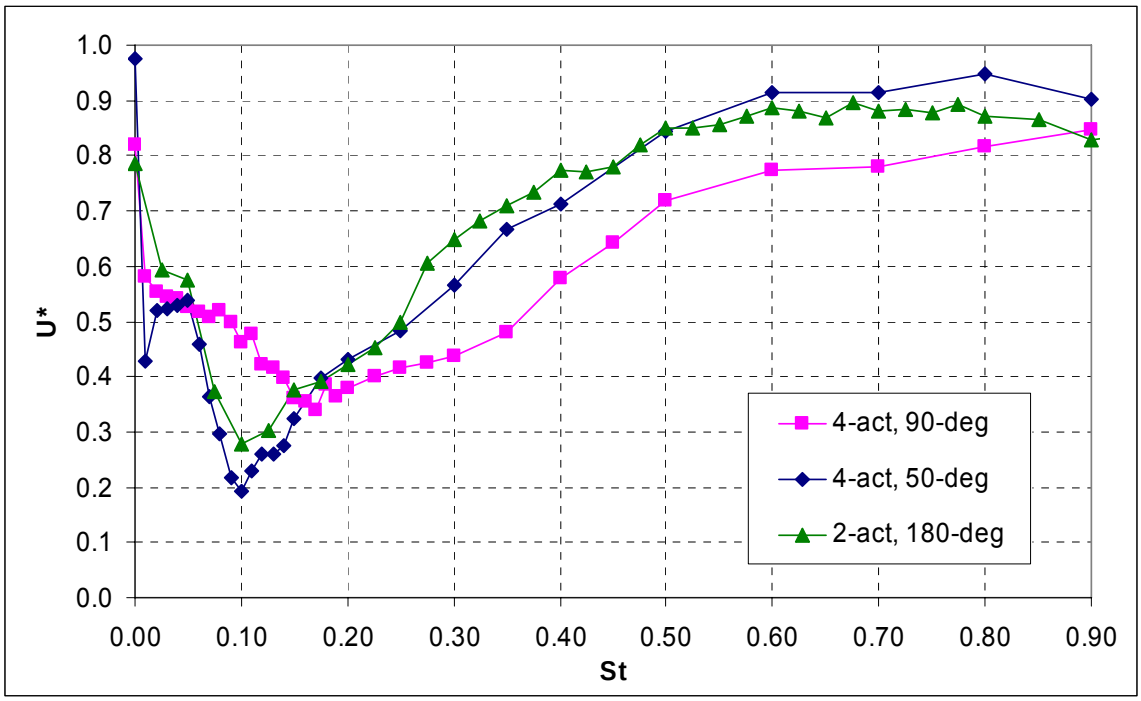

Figure 3.39: Comparison of Frequency Sweeps for the 3 Major Actuator Configurations, 0.08" Nozzles, 180º Phase, x/D = 10, U_{exit} = 10 m/s, SRMR = 0.12

Figures 3.40 and 3.41 show the momentum ratio collapses from compiled data and their resulting curve fits for the 4-act-50º and 4-act-90º cases respectively. The Strouhal number is 0.1 and once again the data spans different amplitudes created by varying the actuator mass flow rate, nozzle size, and jet exit velocity. The curves are analogous to the curve for the 2-act case (figure 3.34), and the three cases are compared in figure 3.42. It is interesting to watch the progression of the curves from the 2-act case to the 4-act-90º case. Initially, all of the curves appear to fall at the same rate, but the 4-act-90º curve begins to peel off at an amplitude (SRMR) of about 0.04 and is clearly distinct from the others at 0.1. The 4-act-50º curve follows the 2-act-180º curve to its saturation point and continues to drop further, saturating at about SRMR = 0.15. It continues to follow the 2-act-180º trend but remains offset from it. Above amplitudes of 0.2 it tends to act more like the 4-act-90º curve.

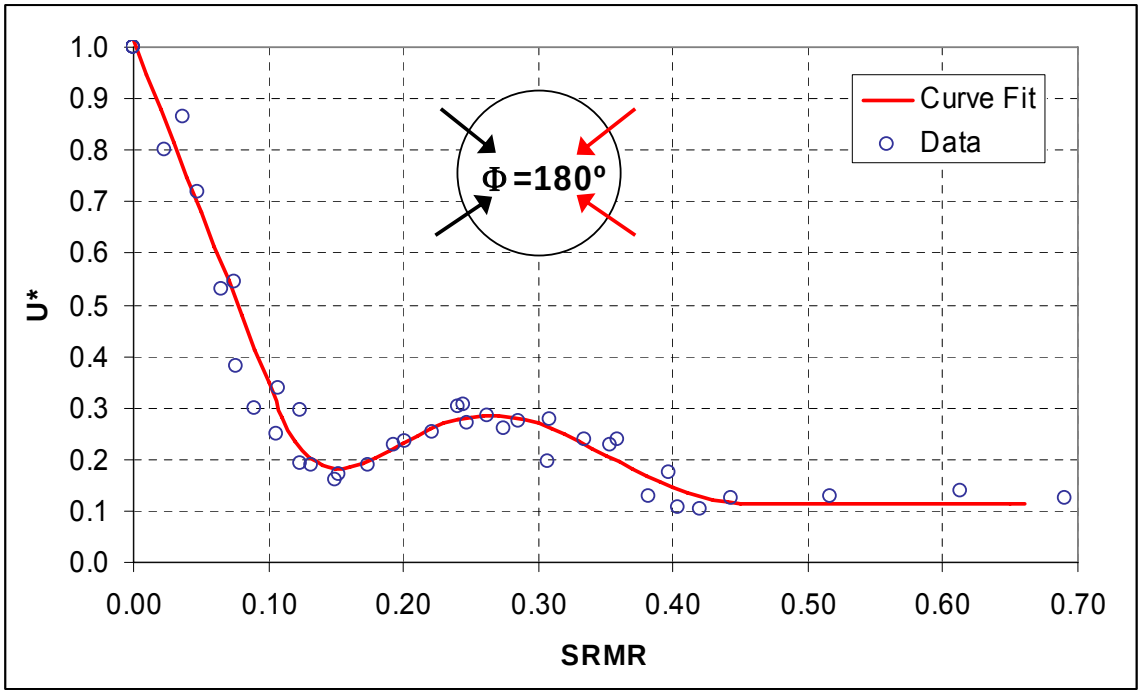

Figure 3.40: Curve Fit to All of the Data Compiled for 4-Actuators 50º Angle, St = 0.1, Multiple Nozzle Sizes, 180º Phase, x/D = 10, U_{exit} = 10 m/s to 30 m/s

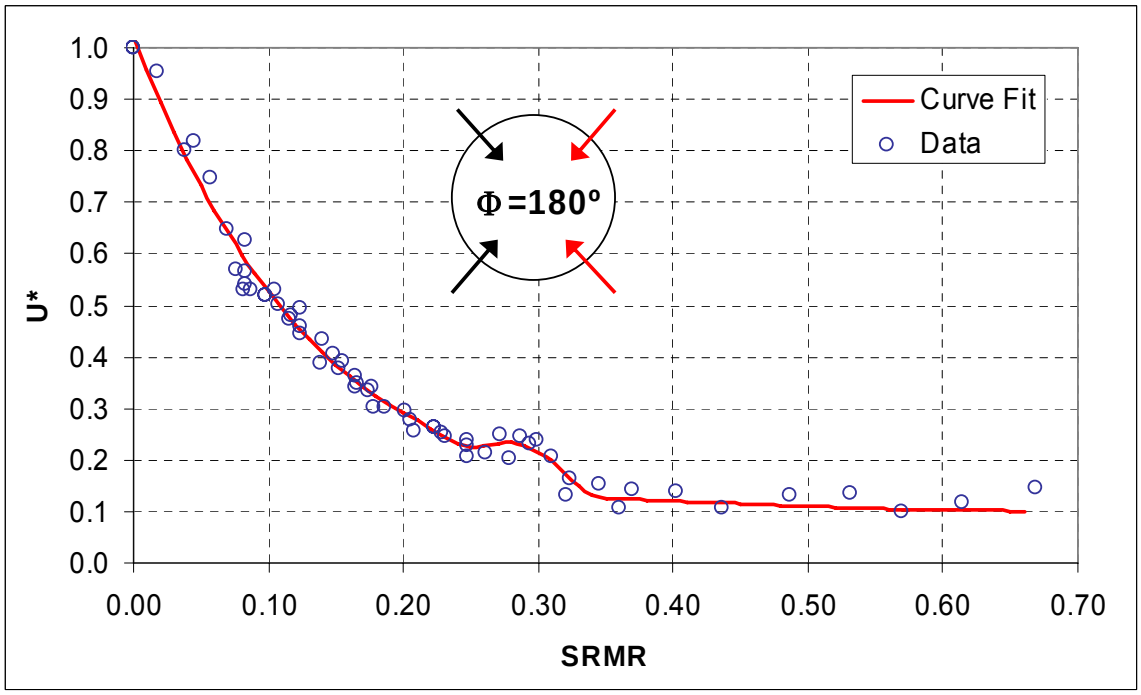

Figure 3.41: Curve Fit to All of the Data Compiled for 4-Actuators 90º Angle, St = 0.1, Multiple Nozzle Sizes, 180º Phase, x/D = 10, U_{exit} = 10 m/s to 50 m/s

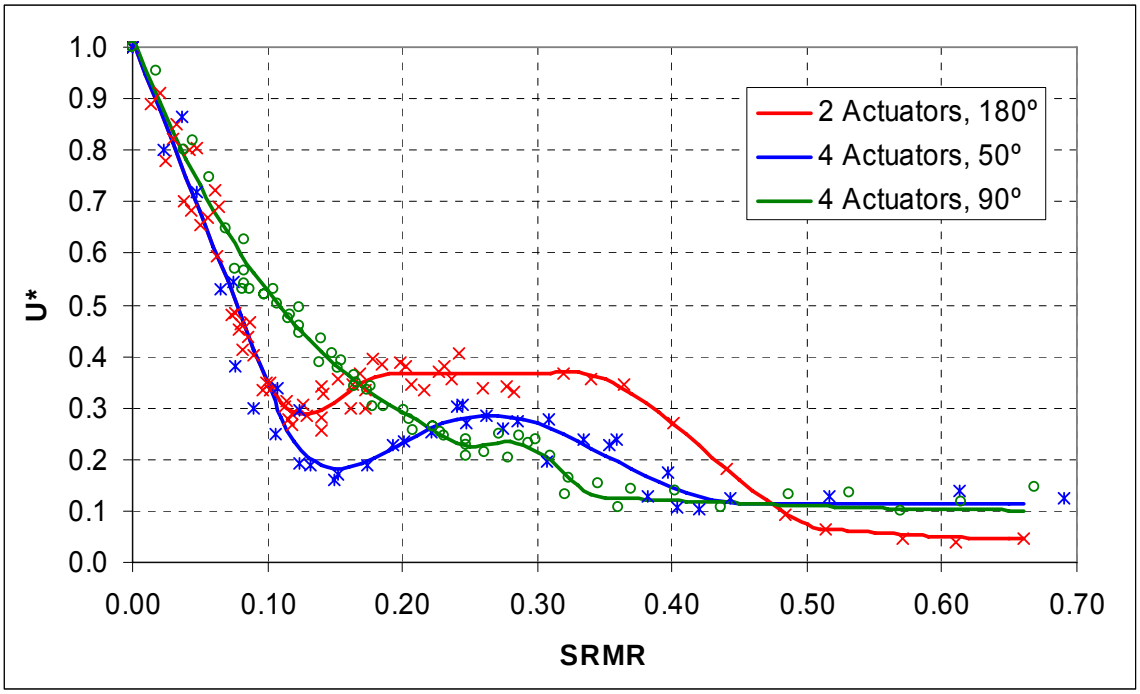

Figure 3.42: Comparison of the Three Curve Fits to SRMR Collapse for the Three Major Actuator Configurations

The primary reason for the divergence of the 4-act-90º curve from the others is that the optimal Strouhal number has shifted from 0.1 to 0.15. This was seen earlier in figure 3.37. In the 4-act-50º case, the optimal Strouhal number was 0.1, just like the 2-act-180º case. Hence the geometry of the setup (the number of actuators and their circumferential location) has a slight to moderate affect on mixing enhancement, and it is likely due to the complex 3D flow field that results from the interaction of adjacent streamwise vortices generated by the pulses. Similar levels of mixing are achievable for all of the cases, but the configuration does appear to affect the optimal Strouhal number or, alternatively, where saturation occurs.

The Effect of Reynolds Number

Figure 3.36 showed that frequency sweeps for jet exit velocities of 5 m/s and 10 m/s resulted in very similar mixing curves. These velocities correspond to Reynolds numbers of 35,500 and 71,000 respectively. For some experiments, the jet exit velocity was set as high as 50 m/s. This had the effect of greatly limiting the Strouhal number range, but allowed the comparison of mixing curves over a wider range of Reynolds numbers. For the most part, the curves showed comparable results. Sometimes the curves diverged at higher frequencies where the pulse quality was degraded, so frequencies above 50 Hz were not compared. Figure 3.43 is an example of a good Reynolds number collapse for the 4-act-90º configuration. Here the exit velocity was varied from 10 m/s to 50 m/s resulting in Reynolds numbers from 71,000 to 355,000. The amplitude for all of the cases was SRMR = 0.165. Even higher Reynolds numbers were achieved during full scale testing (Chapter 5).

The Effect of Pulsing Phase

Early experiments and a review of the literature indicated that antisymmetric pulsing results in better mixing enhancement than axisymmetric pulsing. Hence a majority of the experiments, and all of those presented thus far, were for 180º phase pulsing. Figure 3.44 shows the mixing curves for frequency and amplitude sweeps for the 0º phase case. Note that optimal pulsing frequency decreases with increasing amplitude, as before. At higher amplitudes the curves are flatter which makes it difficult to specify exactly where the optimal frequency occurs. For SRMR = 0.1 the dip in the curve appears to be centered

about St = 0.15. This was confirmed by a taking the derivative of a curve fit to this region.

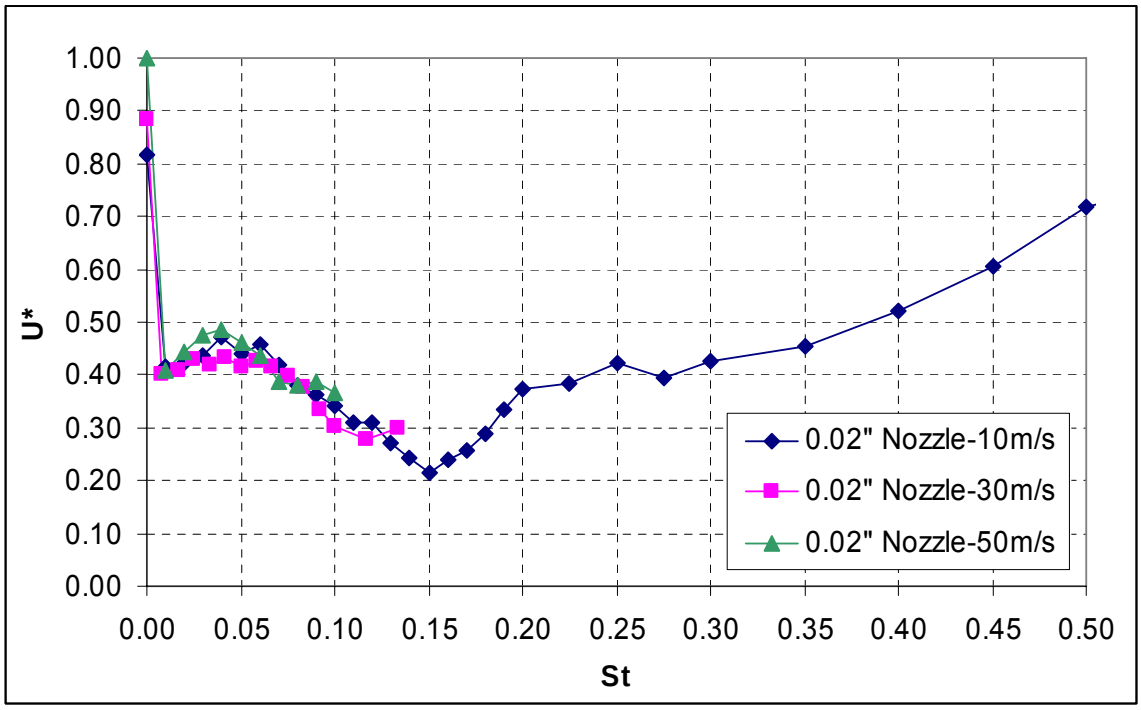

Figure 3.43: Mixing Curves at for Multiple Reynolds Numbers, The Curves Shown Are For 4-Actuators, 90º Pulsing Angle, 0.02" Nozzles, 180º Phase, x/D = 10, Reynolds Numbers from 71,000 (10 m/s) to 355,000 (50 m/s), SRMR = 0.165

Note that all of the curves in figure 3.44 kink upward at St = 0.35 (corresponding to 40 Hz). The kinks are caused by error in the mass flow measurement around that frequency due to a system resonance (see Appendix C for more detail). Thus the true mixing curves do not have the kinks in them. The data points near this frequency were not worth revising since the trend is clear and the resonance was not near St = 0.1, the optimal frequency for SRMR = 0.1. Note that 50 Hz corresponds to a Strouhal number of 0.44. Above this value the exact nature of the curves is typically questionable because of

poorer pulse quality. However, runs with a lower velocity jet (not shown) confirmed that U* continues to rise with a slope similar to the one in the figure.

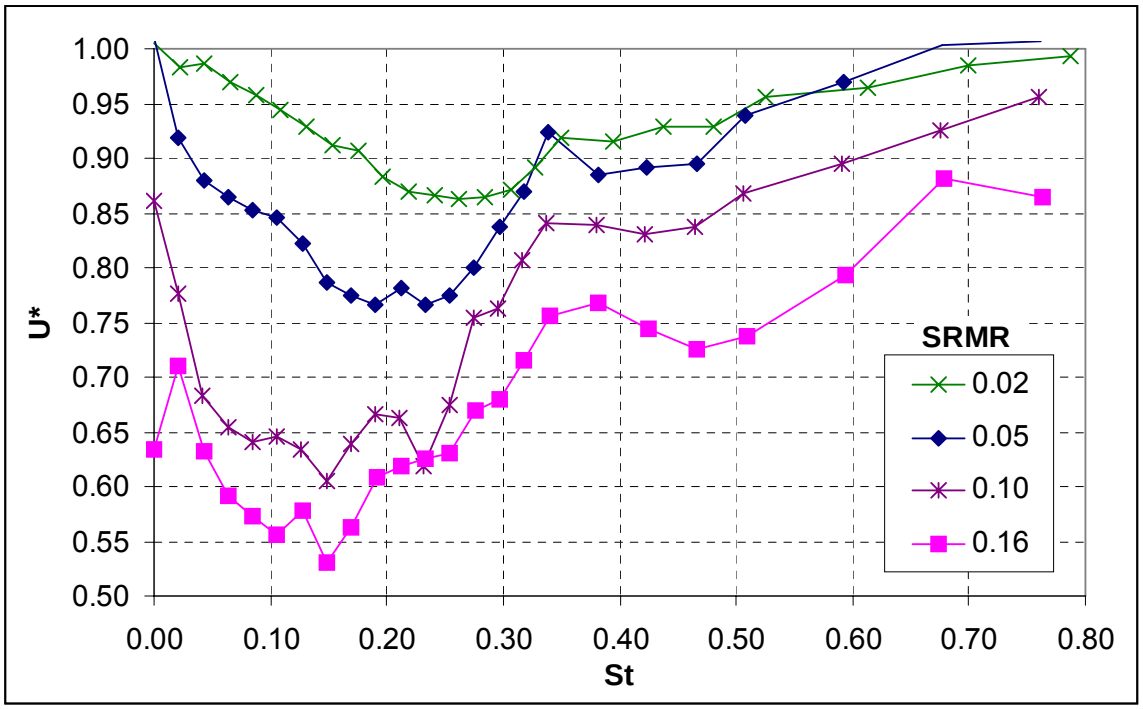

Figure 3.44: Mixing Enhancement Curves for Frequency & Amplitude Sweeps, 2-Actuators, 0.08" Nozzles, 0º Phase, x/D = 10, U_{exit} = 12 m/s

Figure 3.45 compares frequency sweeps for the 0º and 180º phase cases at a single amplitude (SRMR = 0.1). Out-of-phase pulsing clearly results in better mixing over all frequencies and has a more distinct optimum. The two curves are alike in that they fall and rise together, suggesting that they share a common phenomenon. Figure 3.46 compares the amplitude sweeps between the same two cases for a St = 0.1. As before, saturation occurs near SRMR = 0.125 for the 180º phase case. The curve for the 0º phase case is less steep than for 180º. Beyond a SRMR of 0.2 mixing has still not saturated and continues to improve with increasing amplitude.

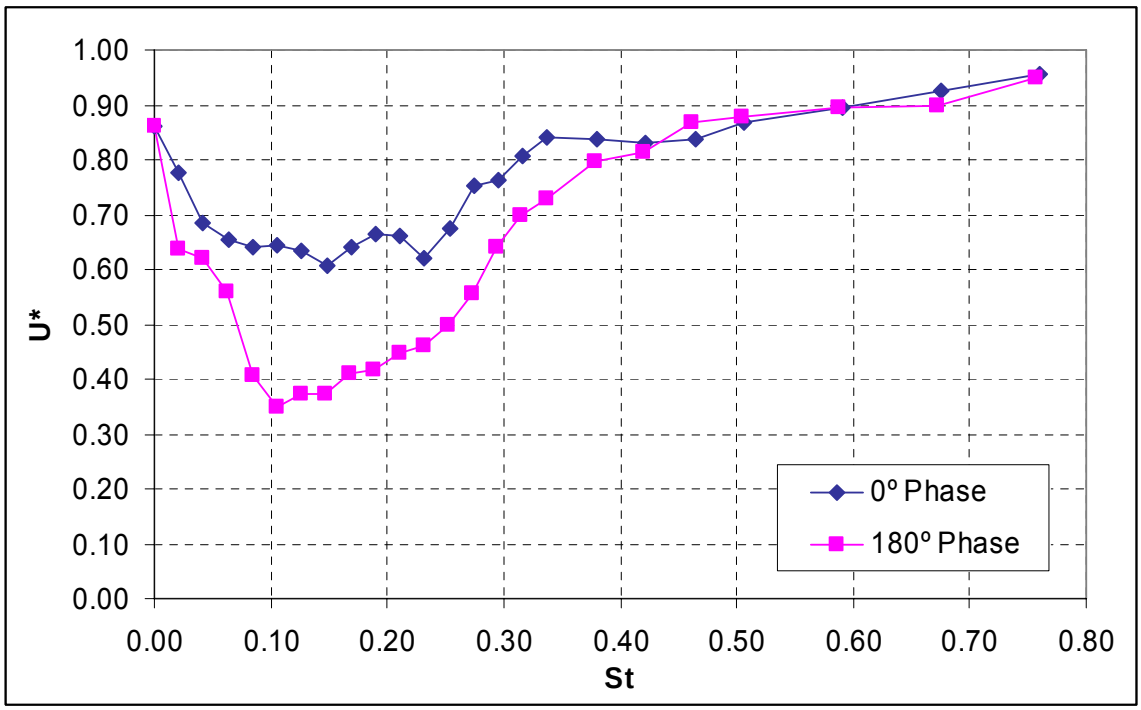

Figure 3.45: Comparison of Frequency Sweeps for 0º and 180º Phase Pulsing, SRMR = 0.1, 2-Actuators, 0.08" Nozzles, x/D = 10, U_{exit} = 12 m/s

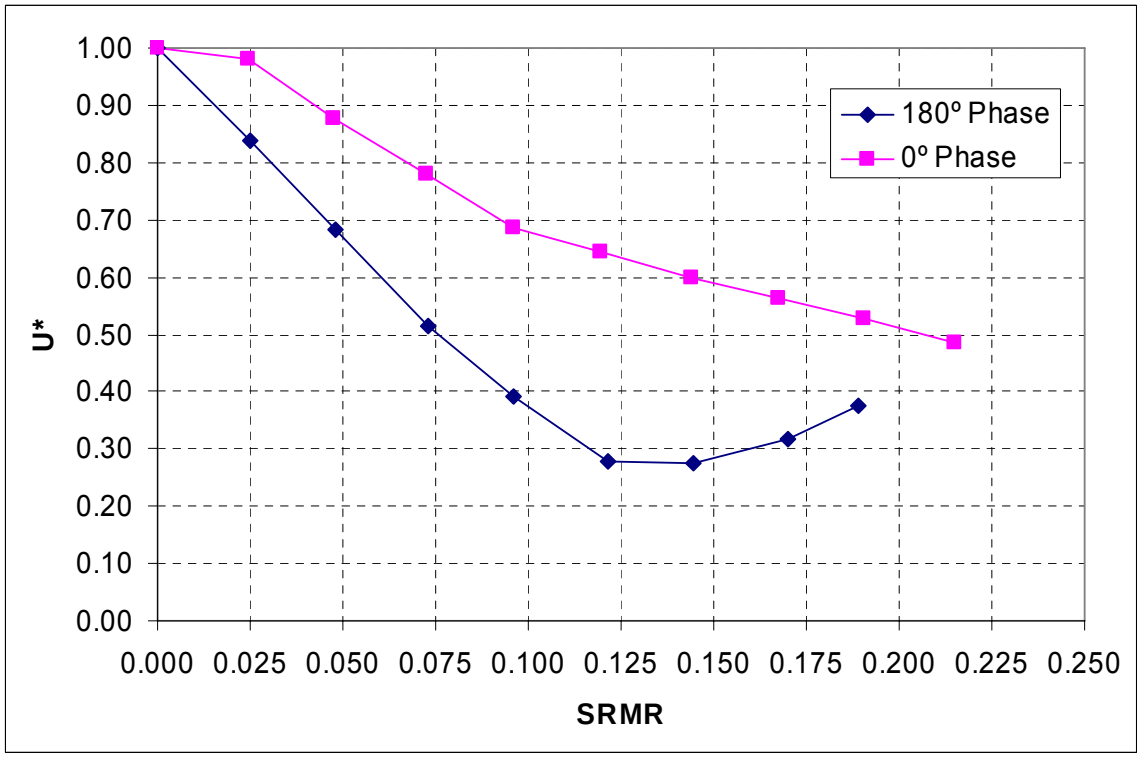

Figure 3.46: Comparison of Amplitude Sweeps for 0º and 180º Phase Pulsing, St = 0.1, 2-Actuators, 0.08" Nozzles, x/D = 10, U_{exit} = 12 m/s

The Effect of Pulse Duty Cycle

Experiments were performed to characterize the effect of varying the fluidic pulse duty cycle on mixing enhancement. All tests were performed on the 4-actuator, 90º angle, 0.02" nozzle configuration. The duty cycle was varied from about 10% up to 100% (blowing) for three pulsing frequencies at three amplitudes. The results for 10 Hz pulsing are shown in figures 3.47 and 3.48 for 0º and 180º phase pulsing respectively.

For 0º phase pulsing, the curves are basically flat, although the curve for the lowest amplitude pulsing has a slightly positive slope. This indicates that reducing the duty cycle had little to no impact on mixing for the amplitudes tested. For 180º phase pulsing, decreasing the duty cycle had a slightly positive effect on mixing for amplitudes below saturation (SRMR = 0.125). However, decreasing it too much had a negative effect. At higher amplitudes, a duty cycle near 50% appears to be the most effective. In all cases, increasing the duty cycle has a negative impact on mixing. Similar results were obtained for 15 Hz and 40 Hz pulsing (not shown). Thus, it is only advantageous to decrease the duty cycle when the pulse amplitude is below saturation for 180º phase actuation, and the duty cycle shouldn't be decreased too much. The increased mixing is almost certainly linked to the increased momentum due to the shorter but higher velocity pulse.

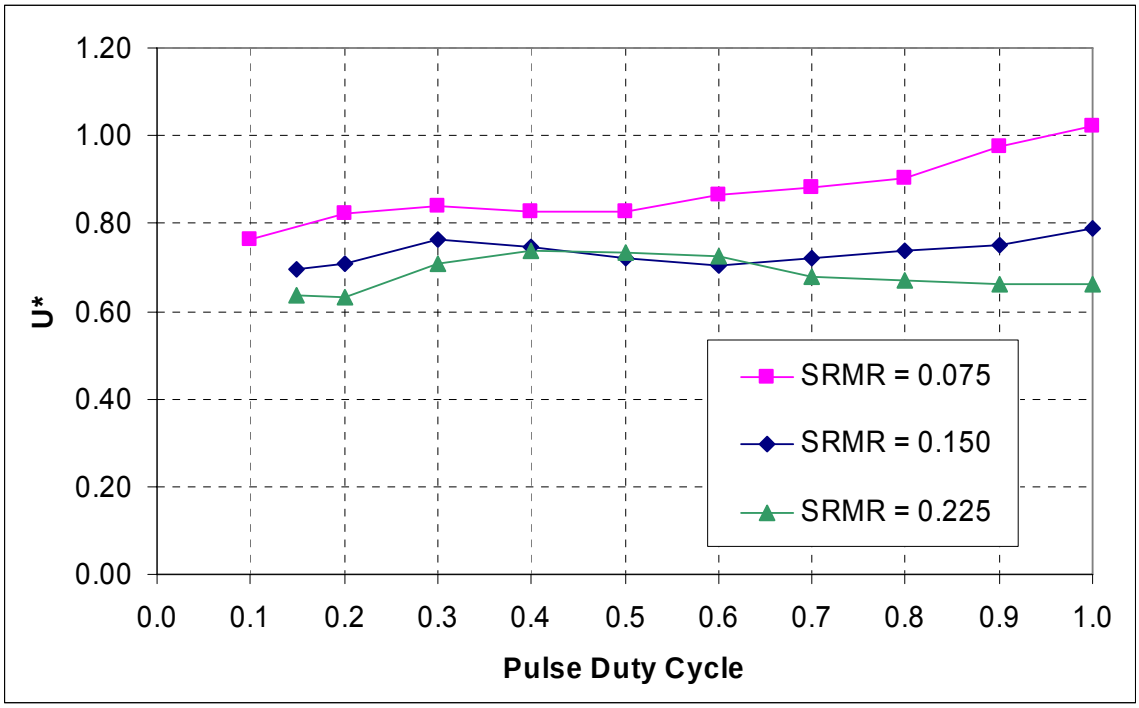

Figure 3.47: Mixing Enhancement vs. Pulse Duty Cycle for 0º Phase Pulsing, St = 0.1, 4-Actuators, 0.02" Nozzles, 90º Angle, x/D = 10, U_{exit} = 10 m/s

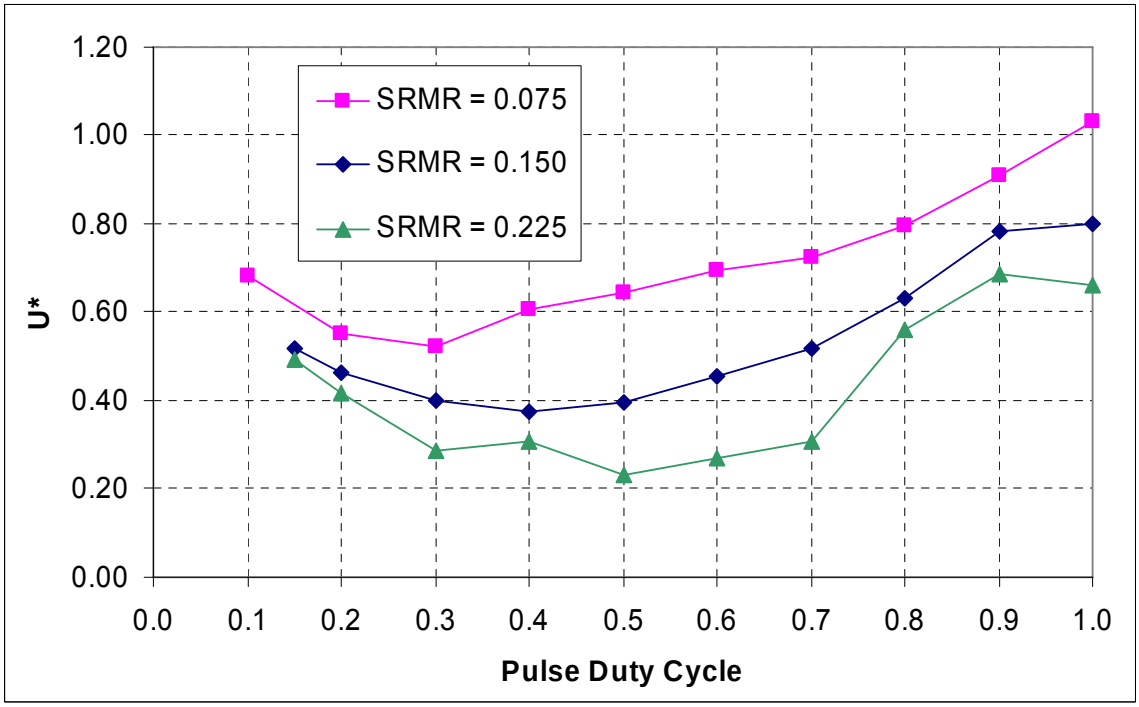

Figure 3.48: Mixing Enhancement vs. Pulse Duty Cycle for 180º Phase Pulsing, St = 0.1, 4-Actuators, 0.02" Nozzles, 90º Angle, x/D = 10, U_{exit} = 10 m/s

The Effect of Pulse Offset

The setup was modified as explained in chapter 2 to allow experiments to be conducted which deliberately added a known amount of DC offset to the pulse. Once again testing was performed on 4-actuator, 90º angle, 0.02" nozzle configuration. The DC offset could be varied from 0% (i.e. no offset) up to approximately 65%. A 100% offset was achieved by simply leaving the solenoid open and blowing air through the actuator. The offset level was measured using small total pressure probes and unsteady pressure transducers. Percent offset was thus defined as the ratio of the bottom of the total pressure waveform divided by the top. Since total pressure is proportional to the square of the velocity when the static pressure is atmospheric, it is also proportional to the momentum flux.

Three different combinations of frequency and amplitude were tested and the results are shown in figure 3.49. Two things are of particular importance. First, from the results it is clear that the offset has a negative impact on mixing. Second, as seen in the figure, there is a roughly linear relationship between % offset and increase in velocity compared to the unforced case. Since the amplitude was set based on mass flow measurement, increasing the offset has the effect of lowering the wave top for a constant mass flow rate. Figure 3.50 shows the effect of varying % offset on mixing that results when the pulse wave top was held constant by increasing the mass flow rate every time the offset was adjusted. Again, there is a negative effect on mixing. This is compared against the previous data from figure 3.49 where the MFR was held constant for the same Strouhal number and initial amplitude. The two curves show similar effects until 50% offset is

reached. At that point the higher amplitude (constant wave top, varying MFR) case levels off and no longer results in reduced mixing.

The Effect of Blowing

The effect of steady blowing through all of the actuators was tested on the 4-actuator, 90º angle, 0.02" nozzle configuration. Figure 3.51 shows the effect of different blowing amplitudes on mixing. There is initially no noticeable effect until a threshold is reached (SRMR ≈ 0.15), after which mixing enhancement becomes a function of blowing amplitude.

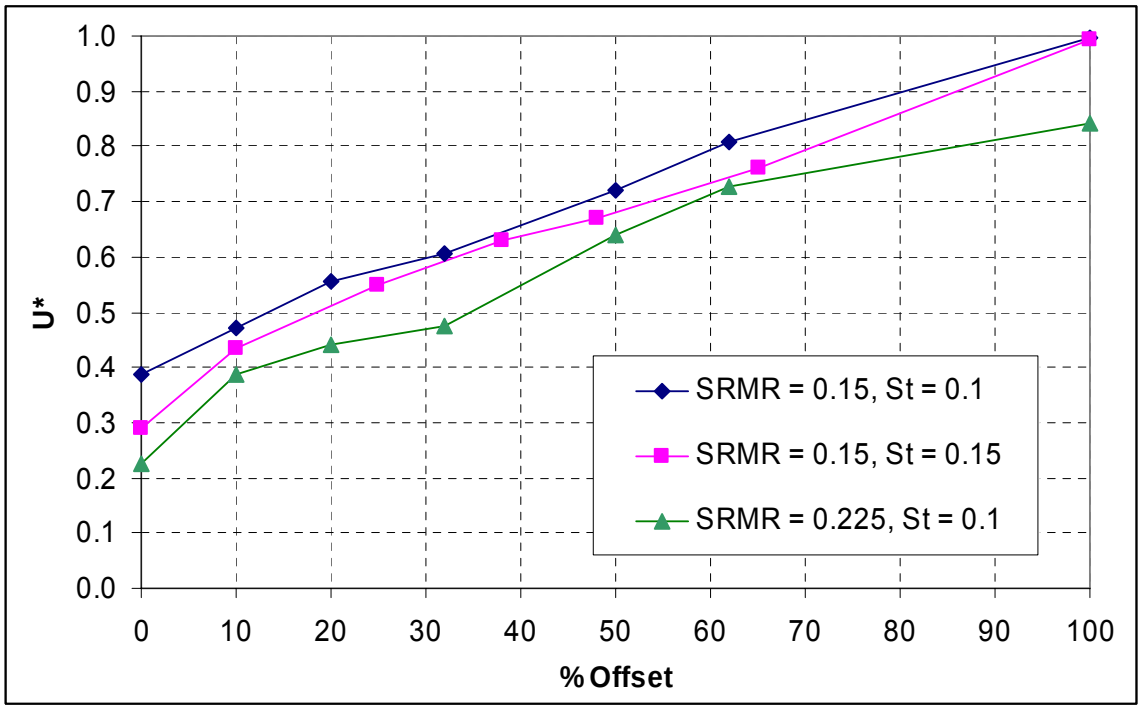

Figure 3.49: Mixing Enhancement vs. % Offset for 180º Phase Pulsing where the MFR of the Pulse was Held Constant, 4-Actuators, 0.02" Nozzles, 90º Angle, x/D = 10, U_{exit} = 10 m/s

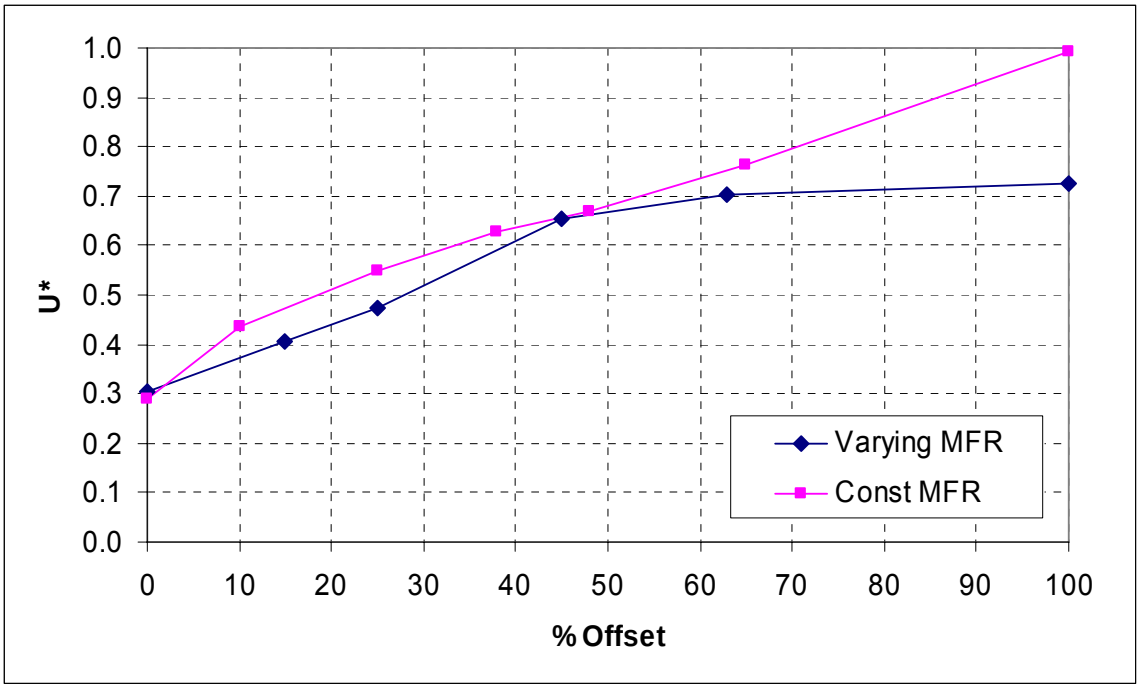

Figure 3.50: Mixing Enhancement vs. % Offset for 180º Phase Pulsing where the MFR was Increased to Keep the Wave Top Constant, St = 0.15, 4-Actuators, 0.02" Nozzles, 90º Angle, x/D = 10, U_{exit} = 10 m/s

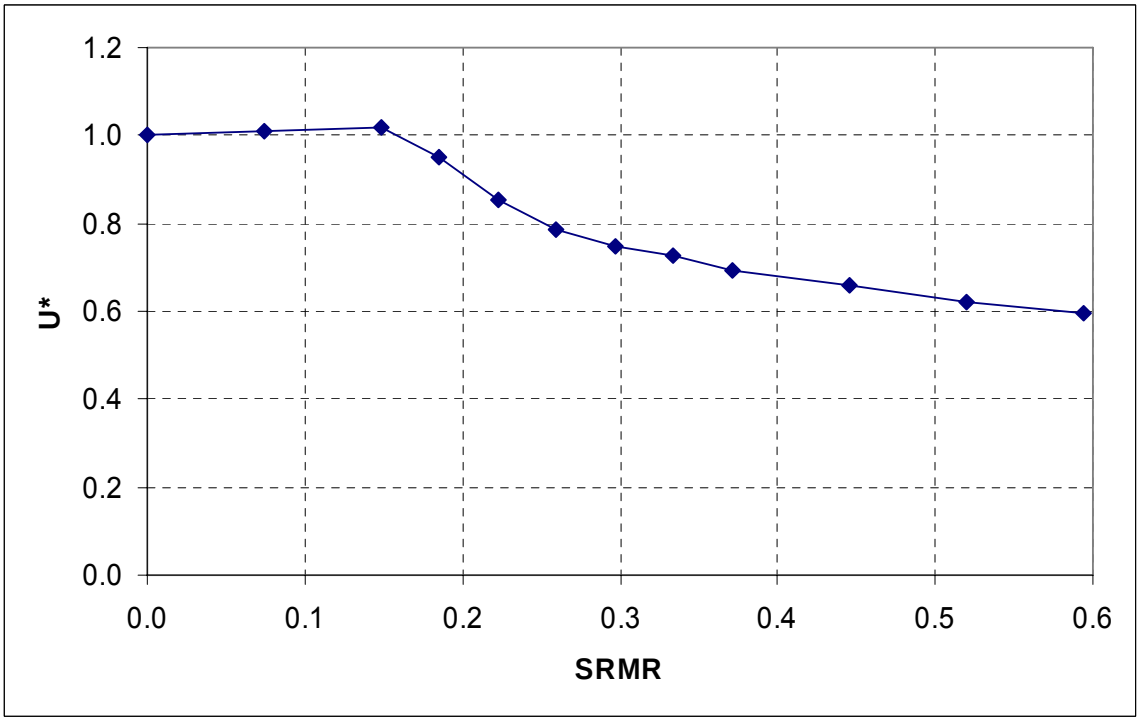

Figure 3.51: Mixing Enhancement vs. Amplitude for Steady Blowing, 4-Actuators, 0.02" Nozzles, 90º Angle, x/D = 10, U_{exit} = 10 m/s

Detailed Characterization of the Optimal Forcing Cases – Hotwire Results

Before making the detailed measurements necessary to study the physical mechanisms of jet mixing enhancement, it was necessary to choose and actuator configuration and define a set of baseline mixing parameters. The 2-actuator, 0.08" nozzle configuration was chosen since it was the simplest case and resulted in pulse velocities that were on the same order as the jet velocity. The actuators were mounted on the top and bottom of the jet to facilitate PIV measurements. An amplitude of SRMR = 0.1 (which happens to correspond to 1% MFR for this nozzle) was chosen since it is close to the saturation amplitude for this configuration. Both antisymmetric and axisymmetric forcing were studied, and the pulsing frequencies were set to the optimal values for each case: St = 0.1 for 180º phase pulsing, and St = 0.15 for 0º phase pulsing. The exit velocity of the jet was typically 10 m/s or 12 m/s.

Centerline Traverses

Figure 3.52 compares the centerline velocity decay curves for the 0º-phase and 180º-phase cases against the unforced jet. Both of the curves begin to break downward after 1.5D, but the curve 180º-phase case decays more rapidly initially. It then levels off after 3D and begins to decay again after 5D. The 0º-phase curve shows a more consistent decay. At 10D there is a significant difference between the three curves. The 180º-phase curve shows the greatest mixing, followed by the 0º-phase curve, and then the natural jet. At this point they all appear to have roughly the same slope, but this is not expected to last much beyond 10D since one would expect the jet velocity to asymptotically approach zero.

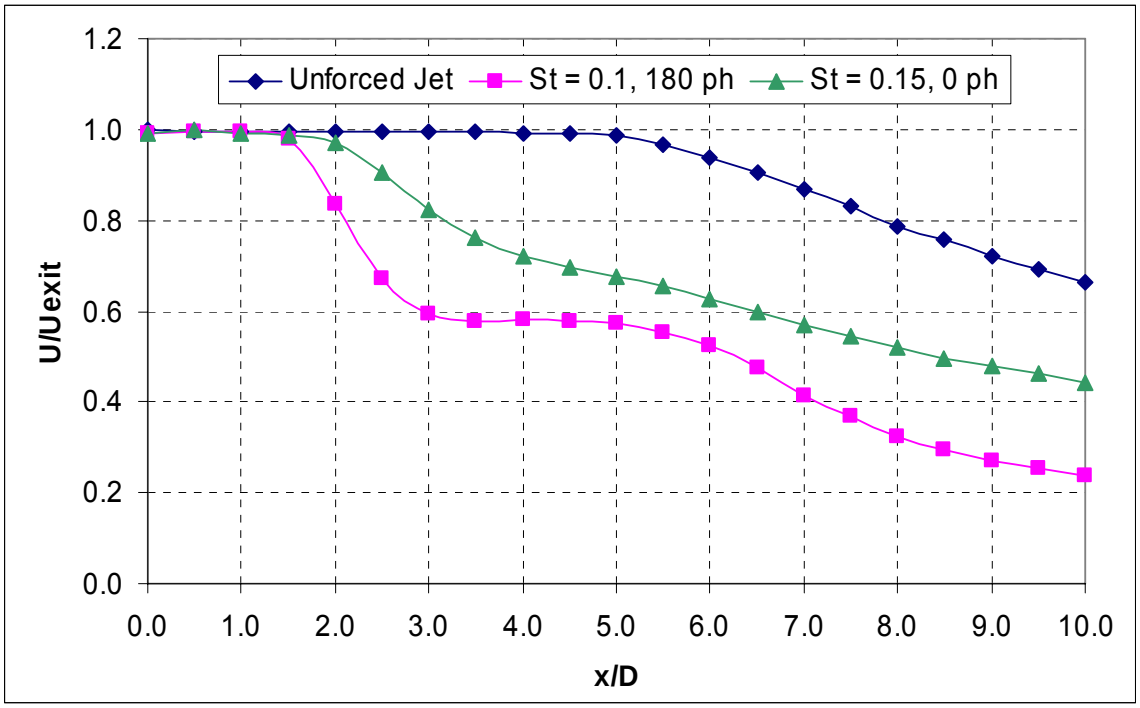

Figure 3.52: Comparison of Centerline Velocity Decays, 2 Actuators, 0,08" Nozzles, SRMR = 0.1, U_{exit} = 12 m/s

Figure 3.53 shows the corresponding turbulence intensity curves for the three cases. The curve for the natural jet follows the expected trend of slow and steady growth until it begins to level off at 20% around 10D. The 0º-phase curve climbs quickly and levels off at 25% by 3D. Once again the 180º-phase curve has a more complicated shape. It climbs quickly initially, dips down a bit around 4.5D, and then climbs again to level off at about 40% near 8.5D. The 0º-phase and 180º-phase curves stay in close proximity initially, suggesting that they share a common physical mechanism.

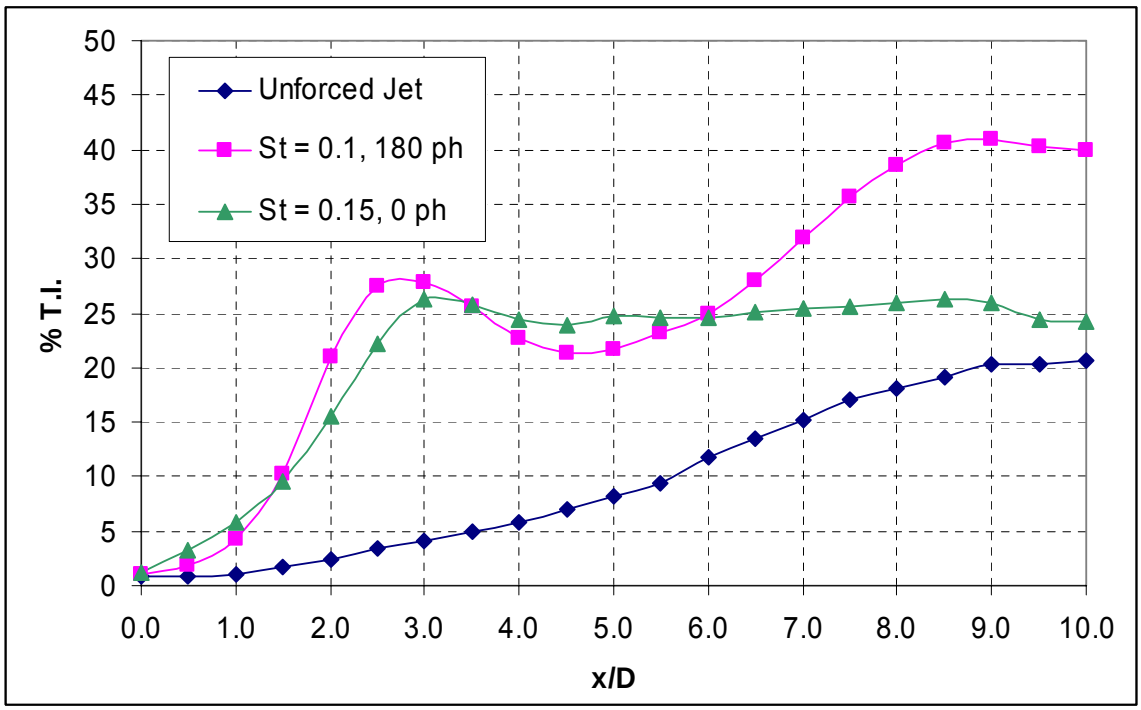

Figure 3.53: Comparison of Centerline Turbulence Intensities, 2 Actuators, 0,08" Nozzles, SRMR = 0.1, U_{exit} = 12 m/s

Simple Averaged Contours

Figures 3.54 and 3.55 are contour plots that compare the average velocity and turbulence intensity fields for the three cases out to 5D. Each point on the contour is a simple average of hotwire data sampled at 5 kHz for 200 seconds. The contours are only loosely representative of mixing enhancement since averaging tends to smear flapping motions as lower velocity measurements. It is therefore not possible to distinguish between actual and apparent mixing based on the average velocity reduction alone. Nevertheless, the graphs have some value in that they show the extent to which the pulses affect the flow. Figure 3.54 shows that 180º-phase pulsing has a much more significant impact on the flow field than 0º-phase pulsing.

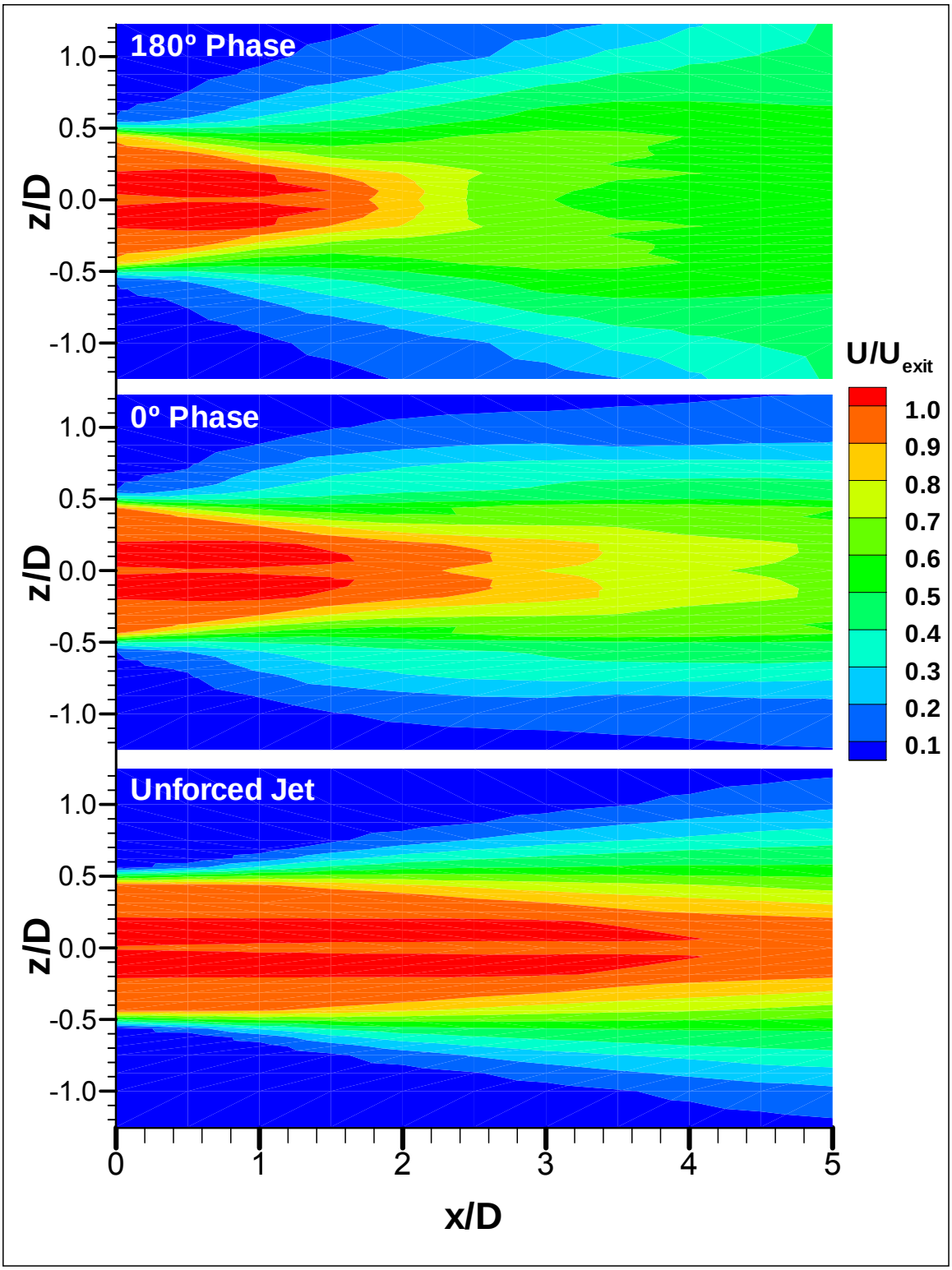

Figure 3.54: Comparison of Simple Averaged Velocity Fields from Hotwire Measurements, 2 Actuators, 0.08" Nozzles, SRMR = 0.1, U_{exit} = 12 m/s

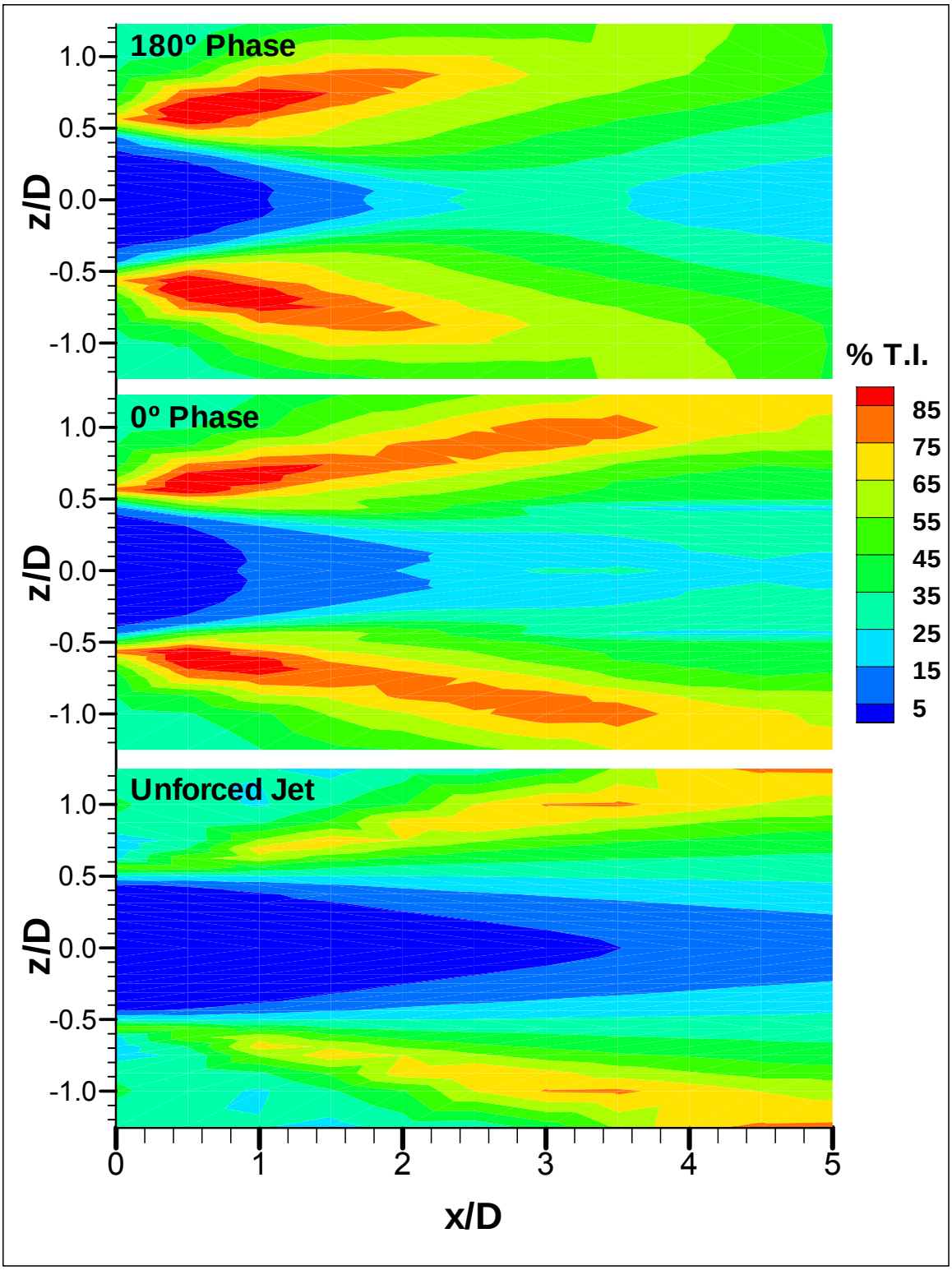

Figure 3.55: Comparison of Turbulence Intensity Fields from Hotwire Measurements, 2 Actuators, 0.08" Nozzles, SRMR = 0.1, U_{exit} = 12 m/s

What is true for average velocity measurements is true for turbulence intensity as well. An increase in turbulence intensity is not necessarily an indicator that the actual turbulence level has risen. Periodic oscillation induces artificial increases in turbulence intensity by increasing large scale fluctuations in the flow. However, these large scale fluctuations do ultimately result in increased turbulent fluctuation as the energy cascades down to smaller scales. Figure 3.55 shows that the extent of the effect of forcing on the flow is even larger than one might gather from Figure 3.54 alone. Significant increases in fluctuations are evident throughout the entire flow field.

Phase Averaged Contours

Phase averaged contours are one step closer to showing how mixing is actually taking place. By using the actuator driving signal as the time clock, the velocity field for a specific phase during a pulse cycle can be computed. The rising edge of the signal serves as the end time for one cycle and time zero for the next. If it is assumed that the fluctuations about the phase averaged value are not very large for the particular phase of interest, then the phase average is a good representation of how the velocity in the flow field changes in time.

Figure 3.56 shows a phase averaged contour plot for 0º-phase pulsing. The velocity magnitude measured by the hotwire has been scaled by the jet exit velocity. Recalling that 5D is typically the end of the potential core, it is clear that velocity reduction due to mixing has occurred. Figures 3.57a and 3.57b show a series of phase averaged contours

in phase increments of 60º. The color scale used is the same as that for figure 3.56. Figures 3.58a and 3.58b show the same thing for 180º-phase pulsing.

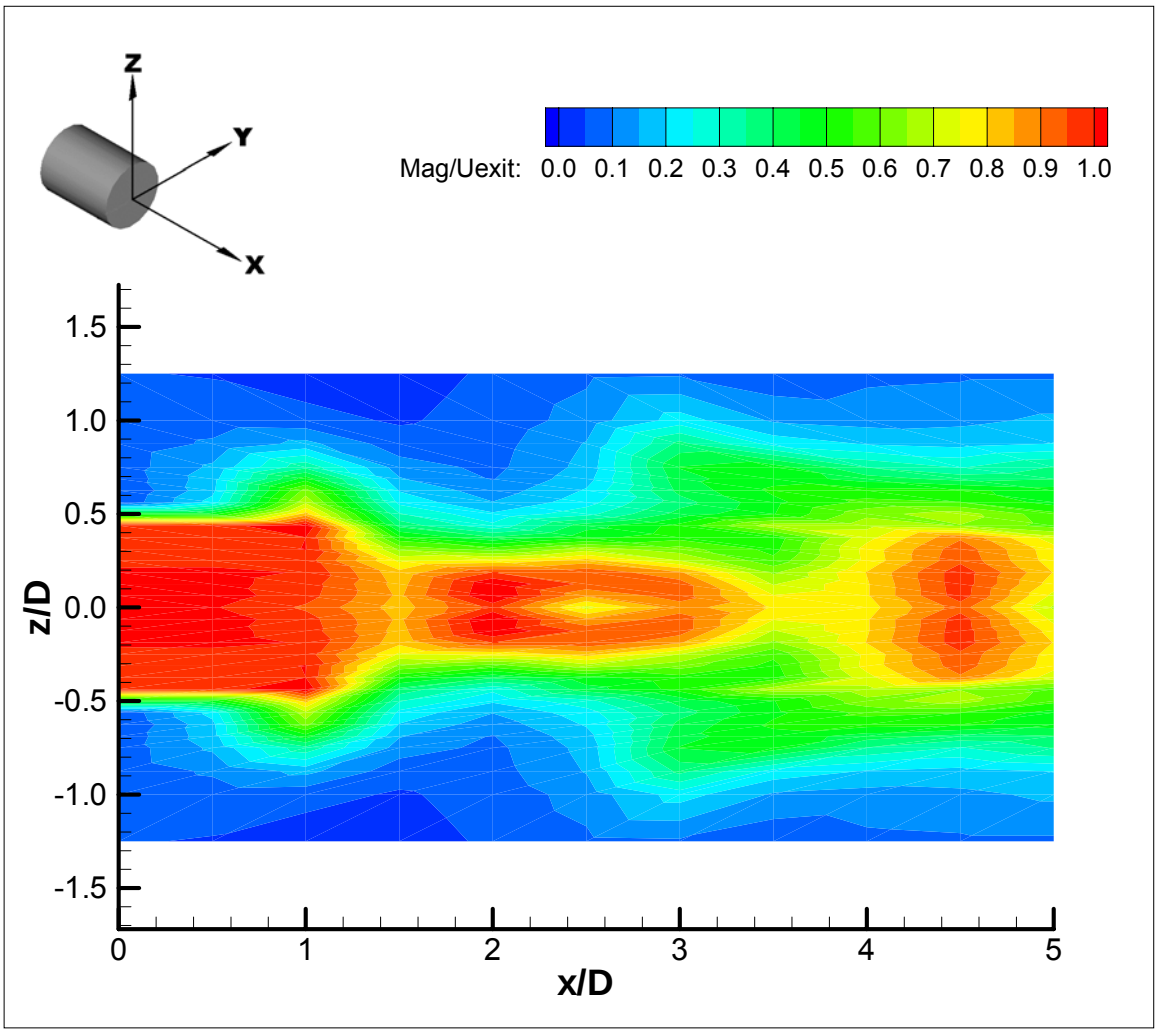

Figure 3.56: Phase Averaged Velocity from Hotwire Measurements for 0º-Phase Pulsing, 2 Actuators, 0.08" Nozzles, SRMR = 0.1, U_{exit} = 12 m/s (The Same Color Scale is used in Subsequent Plots)

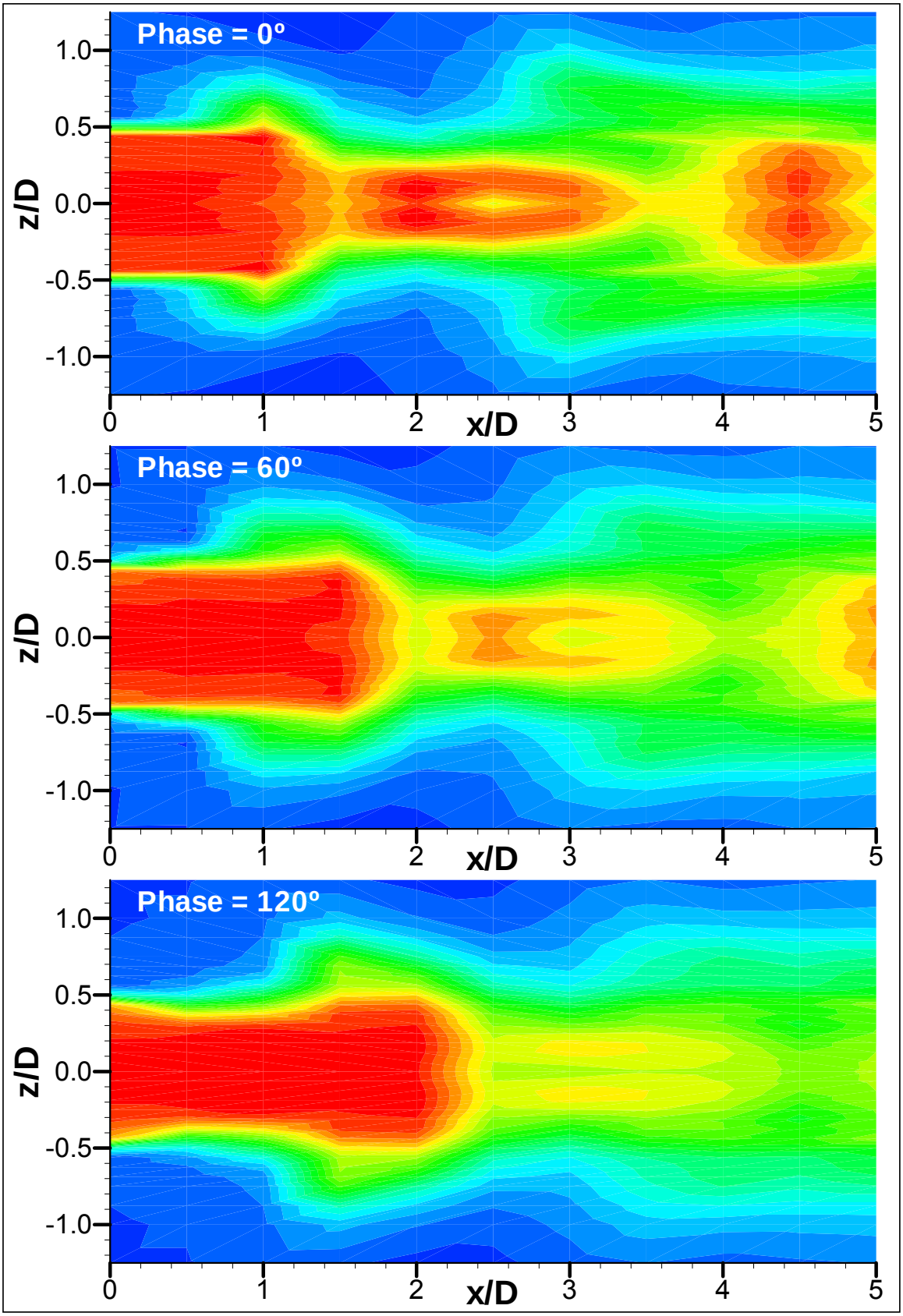

Figure 3.57a: Phase Averaged Velocity from Hotwire for 0°-phase Pulsing

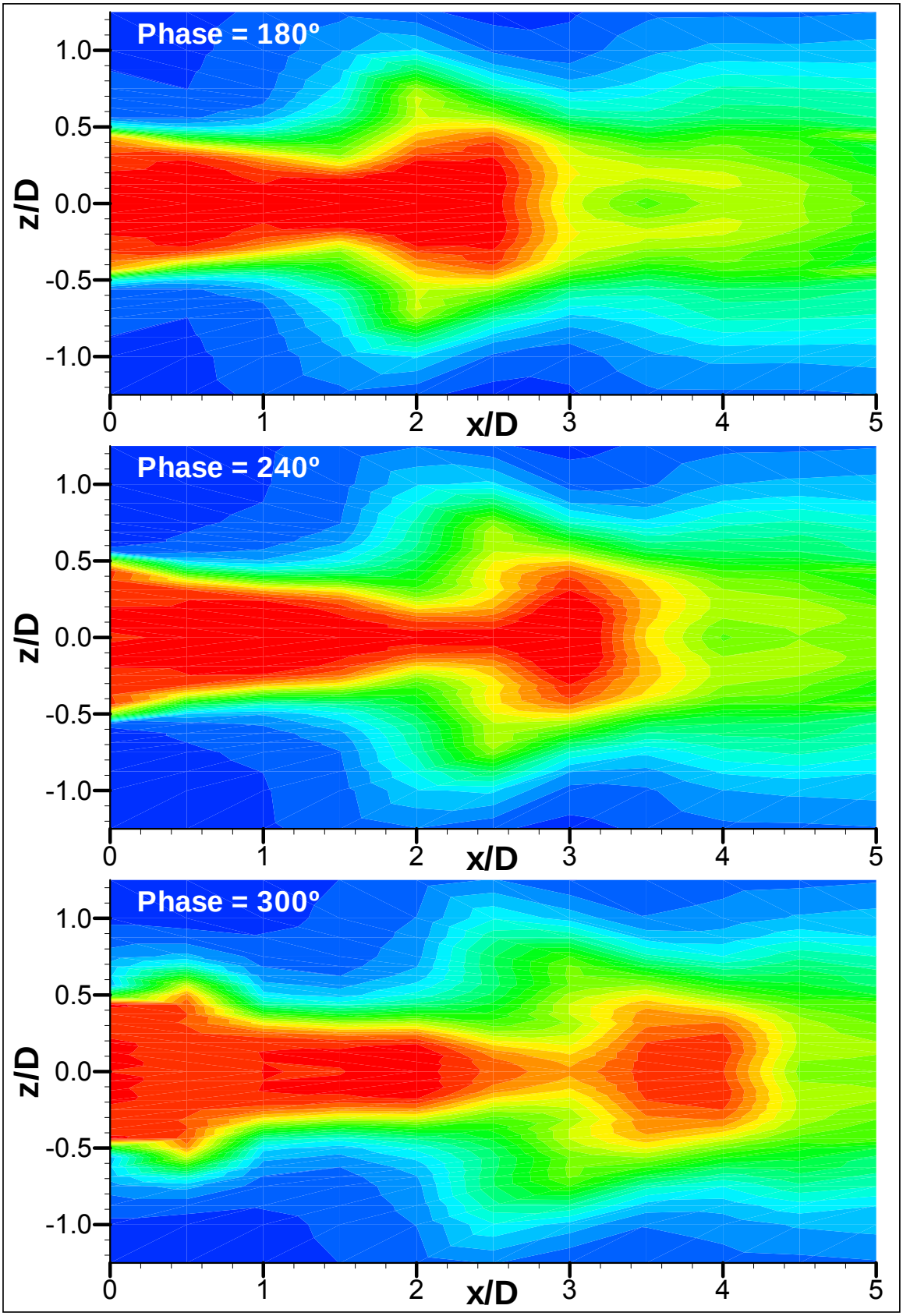

Figure 3.57b: Phase Averaged Velocity from Hotwire for 0°-phase Pulsing

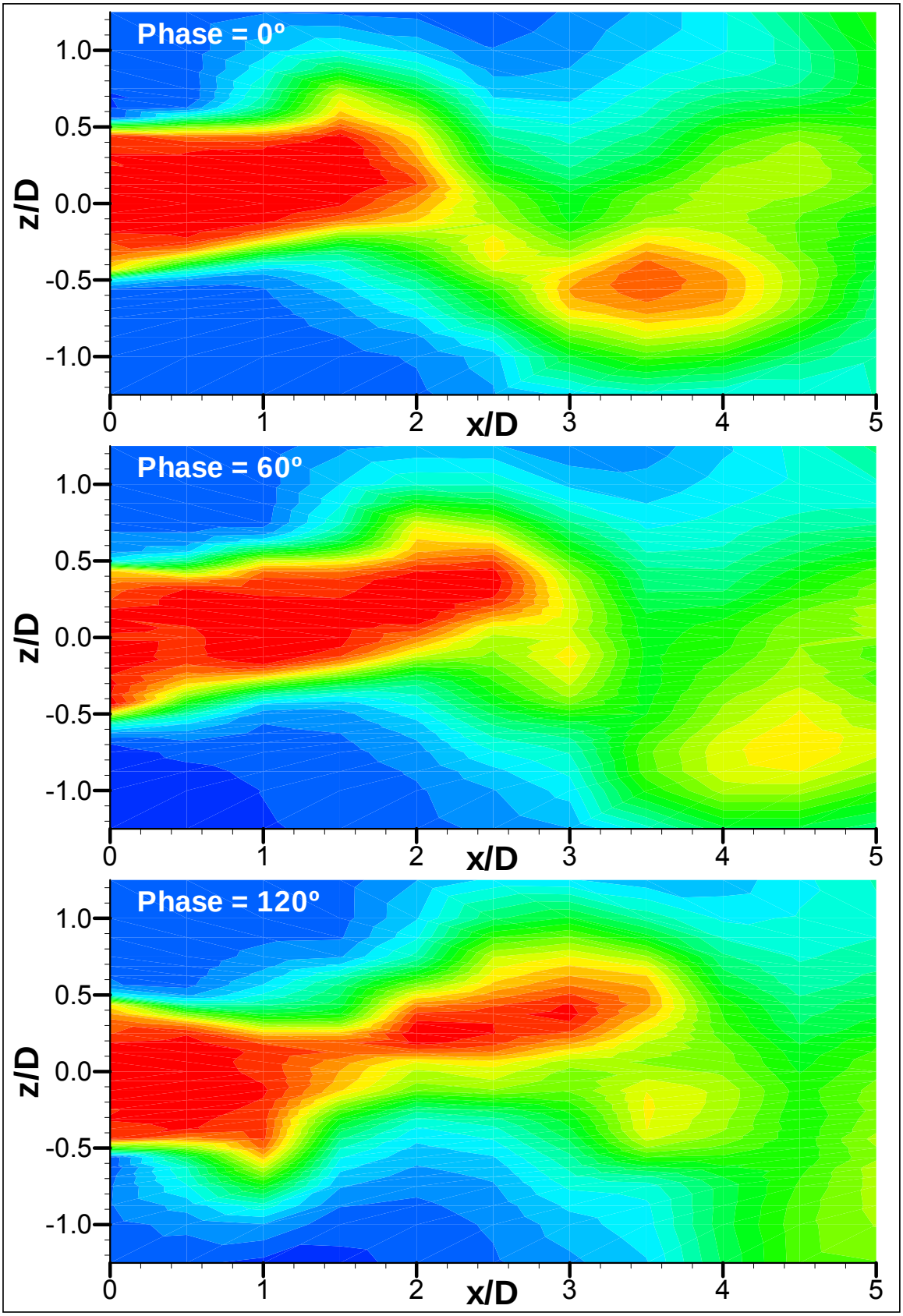

Figure 3.58a: Phase Averaged Velocity from Hotwire for 180°-phase Pulsing

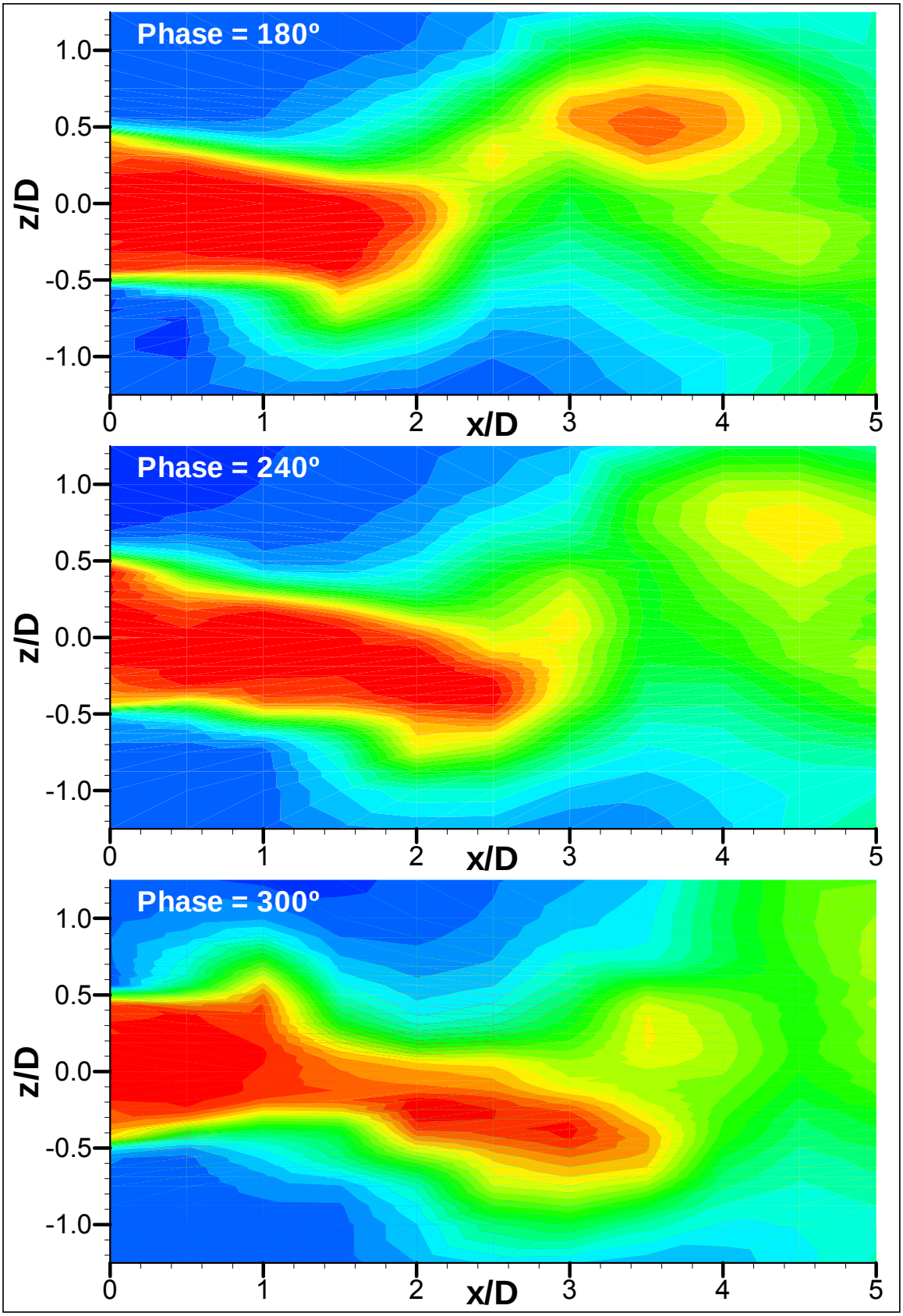

Figure 3.58b: Phase Averaged Velocity from Hotwire for 180°-phase Pulsing

Two things stand out in the contour plots. First, it is clear that for the 180º-phase case the jet is flapping back and forth resulting in apparent mixing (i.e. jet flopping) around x/D ≈ 2 to 3. Second, as the flow moves downstream the maximum phase averaged velocity drops significantly, especially in the 180º-phase case. The evidence for this is the red "blob" that appears to break off and move downstream, quickly turning yellow. This should be compared to the natural jet where a significant red zone persists past x/D = 5. This behavior indicates that mixing is taking place on both large and small scales. For 0º-phase pulsing the time step between images is 0.011 seconds. For 180º-phase pulsing the time step between images is 0.0167 seconds.

In order to get a handle on how much the instantaneous velocity deviated from the phase averaged values, phased RMS values were calculated. The phased RMS is simply the RMS fluctuation (or standard deviation) of the velocity at a particular point for a given phase. It is somewhat desirable to have a *low* phased RMS since this indicates that the phase averaged velocity is a good representation of the actual fluctuating velocity. Of course an extremely low value would mean that the phase average is almost an exact representation of the flow, and this is not desirable (or realistic) since it would indicate that the flow is not very turbulent. The top plot in figure 3.59 shows an example contour plot of phased RMS for the 0º-phase pulsing case. The bottom plot in the figure is the usual RMS Velocity field. Both plots use the same color scale to make comparison between them easier. Note that the fluctuation levels for the phase averaged jet are lower throughout the flow field than for the simple averaged jet, but not too close to zero. The color scale in this figure is used for all subsequent phased RMS contours. Figures 3.60

and 3.61 show the phase averaged RMS fluctuations of the flow for the 0º-phase and 180º-phase pulsing cases in phase increments of 60º. The RMS fluctuations about the phase average are about 10% of the exit velocity throughout much of the flow field.

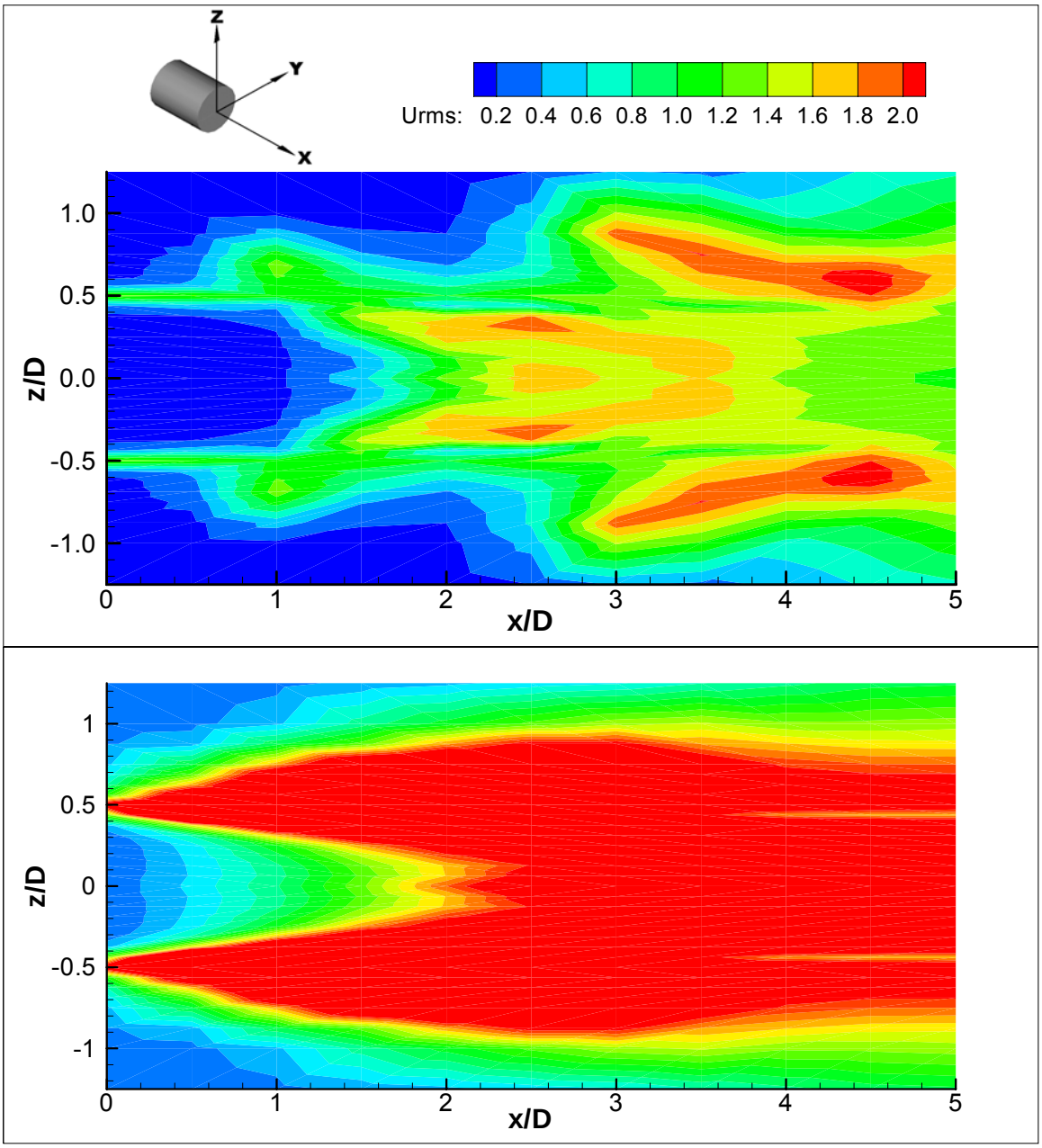

Figure 3.59: Phased RMS Fluctuation of the Velocity from Hotwire Measurements (top) compared to the usual RMS Velocity (bottom) for the 0º-Phase Jet, 2 Actuators, 0.08" Nozzles, SRMR = 0.1, U_{exit} = 12 m/s (The Same Color Scale is used in Subsequent Plots)

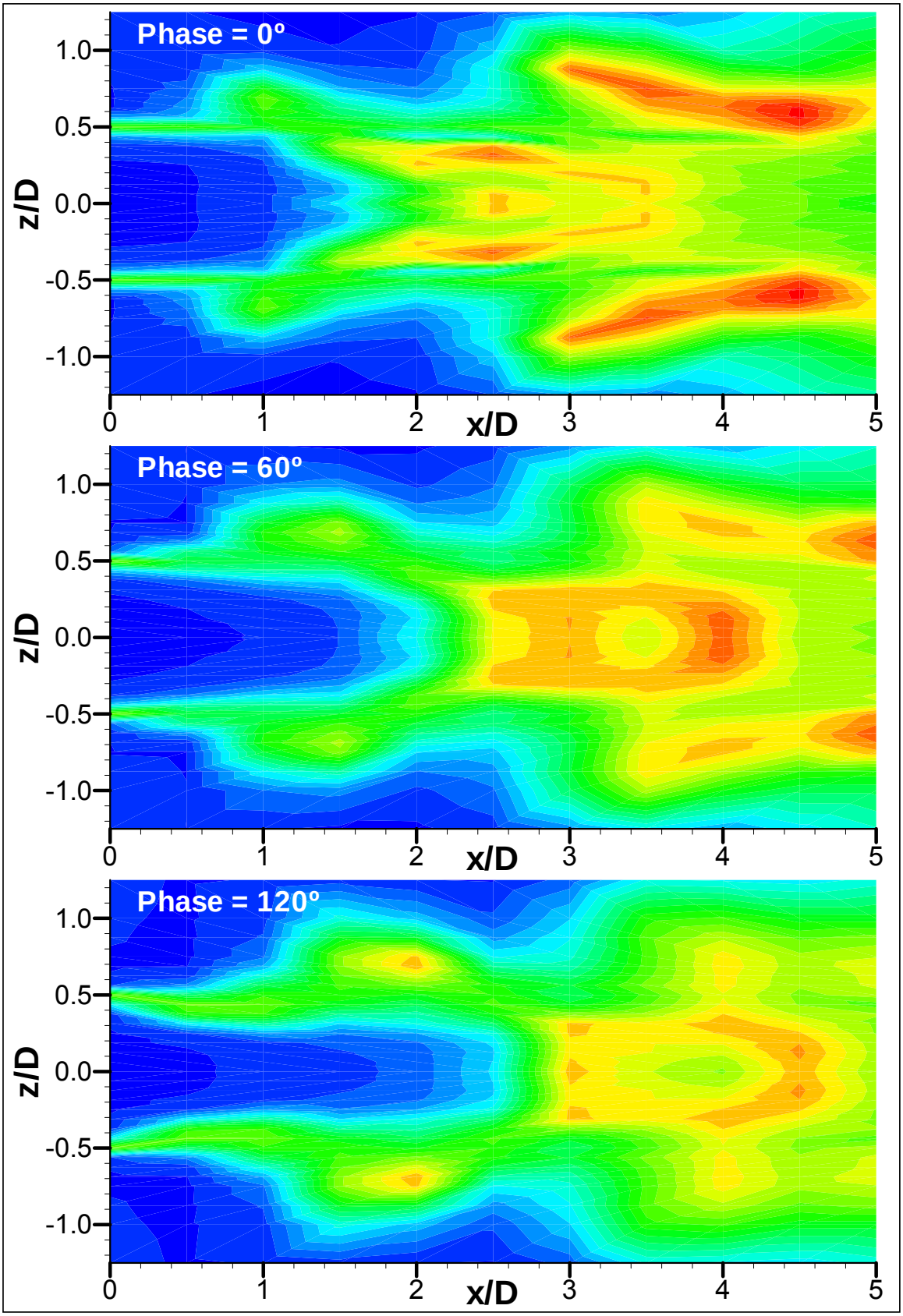

Figure 3.60a: Phased RMS Fluctuation of the Velocity for 0°-phase Pulsing

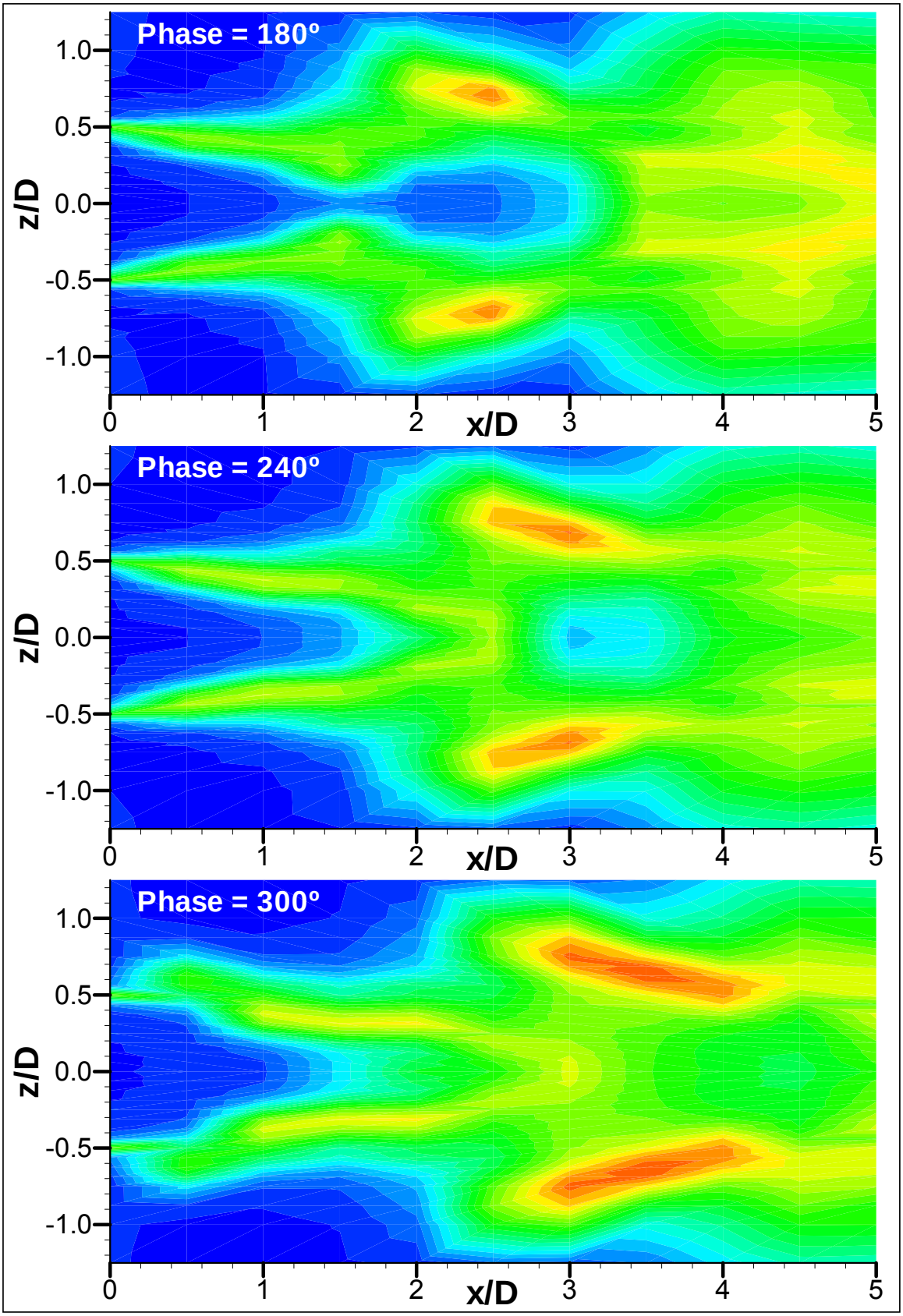

Figure 3.60b: Phased RMS Fluctuation of the Velocity for 0°-phase Pulsing

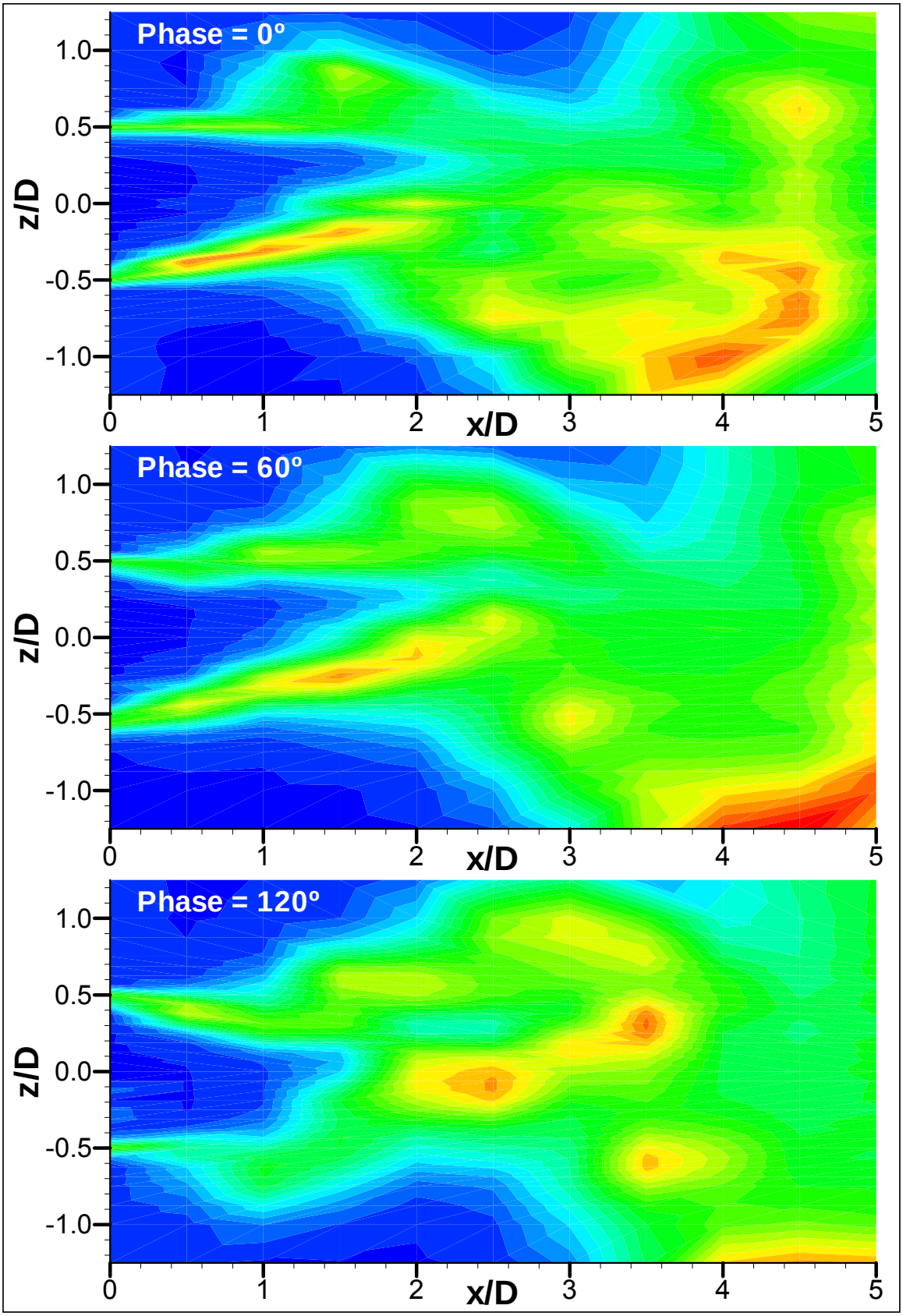

Figure 3.61a: Phased RMS Fluctuation of the Velocity for 180°-phase Pulsing

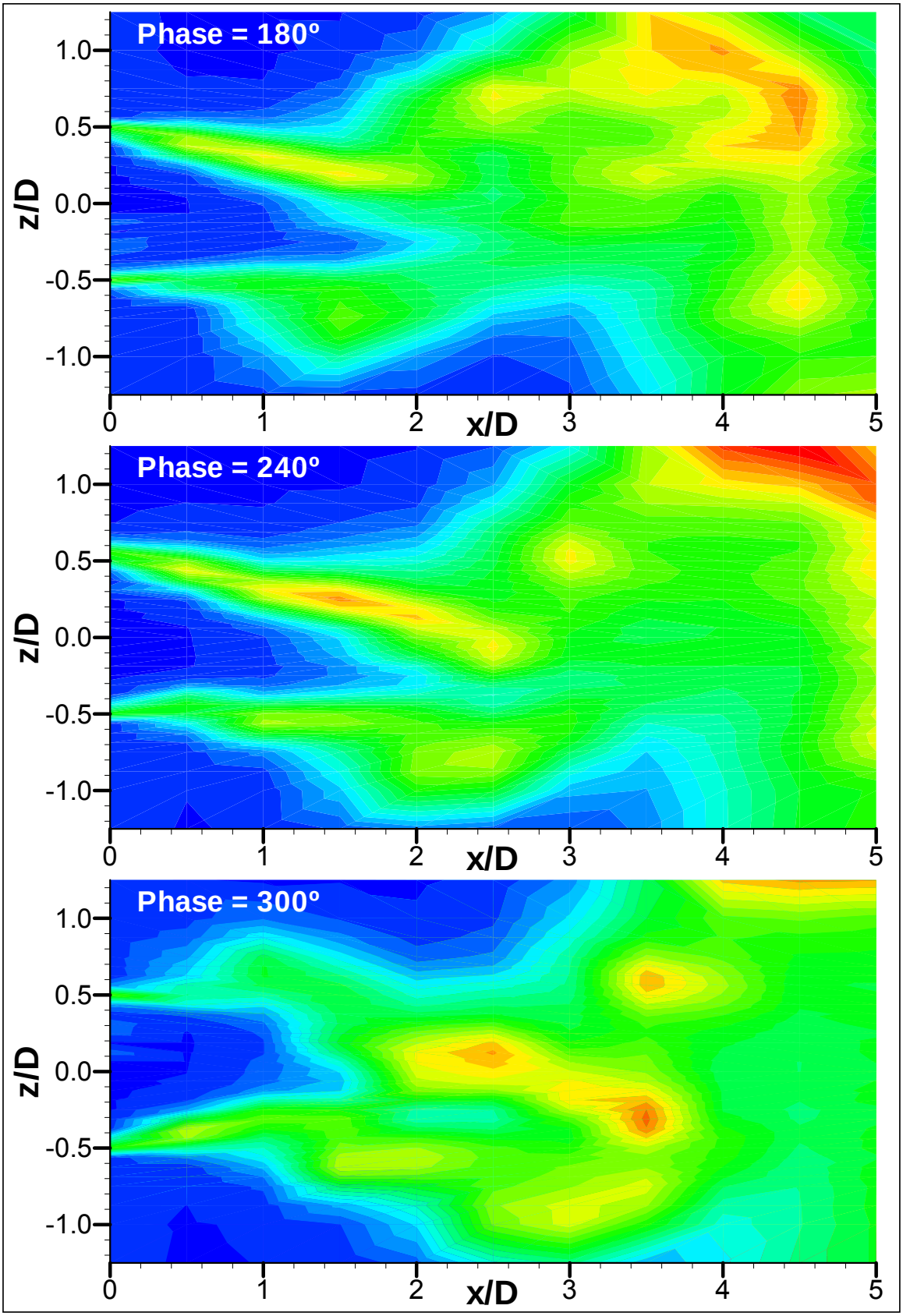

Figure 3.61b: Phased RMS Fluctuation of the Velocity for 180°-phase Pulsing

The Results of Axial and Cross Traverses

Axial Traverse Down the Centerline

Figure 3.52 showed the velocity decay for an axial traverse down the centerline (y/D = z/D = 0) from the jet exit to x/D = 10. Figure 3.62 gives the spectral content at five distinct points along the same traverse for the three baseline cases. Once again power spectral density Fourier transforms were used. Each point in space was sampled at 5 kHz for 200 seconds resulting in one million samples per point. The data was low pass filtered at 1 Hz and run through a Hanning window prior to the Fourier transform. Each spectrum was the result of 100 RMS averages. The velocity spectrum gives more information than the average or RMS values because it indicates how the turbulent energy is distributed.

The spectra in Figure 3.62 are stacked together to make it easy to see the progression moving down the centerline axis. The three cases are almost identical at the jet exit except for spikes at the forcing frequencies and harmonics. The Strouhal number for the axisymmetric case is 0.15 (corresponding to 15 Hz), and for the flapping case it is 0.1 (10 Hz). Moving to x/D = 2.5 the two forced cases show higher amplitudes everywhere except near 0 Hz. This makes sense because the higher average velocity (i.e. DC offset) of the unforced jet gives it a higher value at low frequencies, and the large fluctuation levels induced by the pulses for the forced jets results in higher amplitudes across the rest of the spectrum. Moving downstream, as the energy in the induced fluctuations becomes more distributed throughout the flow, the peaks decline and the forced curves move closer to the unforced curve. The trend continues and by x/D = 10 there is no longer any

evidence of forcing in the spectrum. At this point the curves appear in the same order as their corresponding average velocities with the unforced case on top, followed by the 0º-phase case, and finally the 180º-phase case.

Axial Traverse Down the Lipline

Next up is the spectral record from a traverse down the jet lipline (z = 0.5D), figure 3.63. The spectra have slightly different characteristics than those for the centerline since they start in the shear layer instead of the potential core. Once again the spectra are virtually the same at the exit, except for the spikes at the pulsing harmonics. The spikes are much larger than they were for the centerline case since measurements are being made very close to the actuator exits. By x/D = 7.5 the spikes for the 0º-phase case have disappeared, and by x/D = 10 they are gone for the 180º-phase case as well. Also note that at x/D = 10 the spectra for the 0º and 180º-phase cases are very similar.

Vertical Traverse at 10D

To check whether peaks were present in other regions, a vertical traverse was performed at 10D. Figures 3.64a and 3.64b show the spectra at z/D = 0, 1, 2, and 3 for the three cases. The full frequency range of 0 to 2500 Hz is shown. At z/D = 0 the curves appear in their usual order, as before. At z/D = 1, which is the point where the mean velocity is about equal for all three cases, the spectral curves for the forced cases are about equal to each other and higher than the unforced curve. This suggests that the turbulent energy is well dispersed for the forced cases.

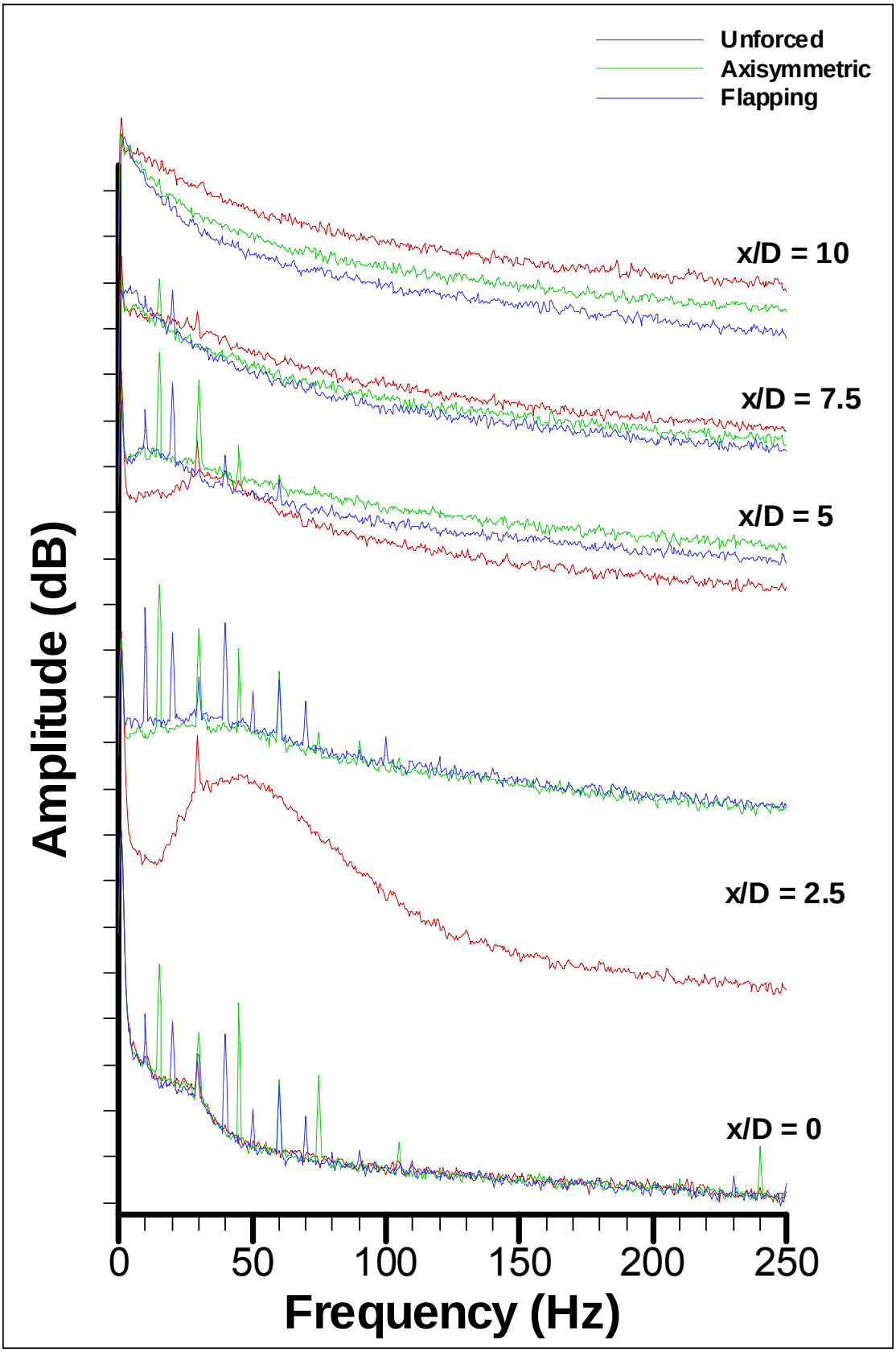

Figure 3.62: Centerline Fourier Transforms for the Three Configurations

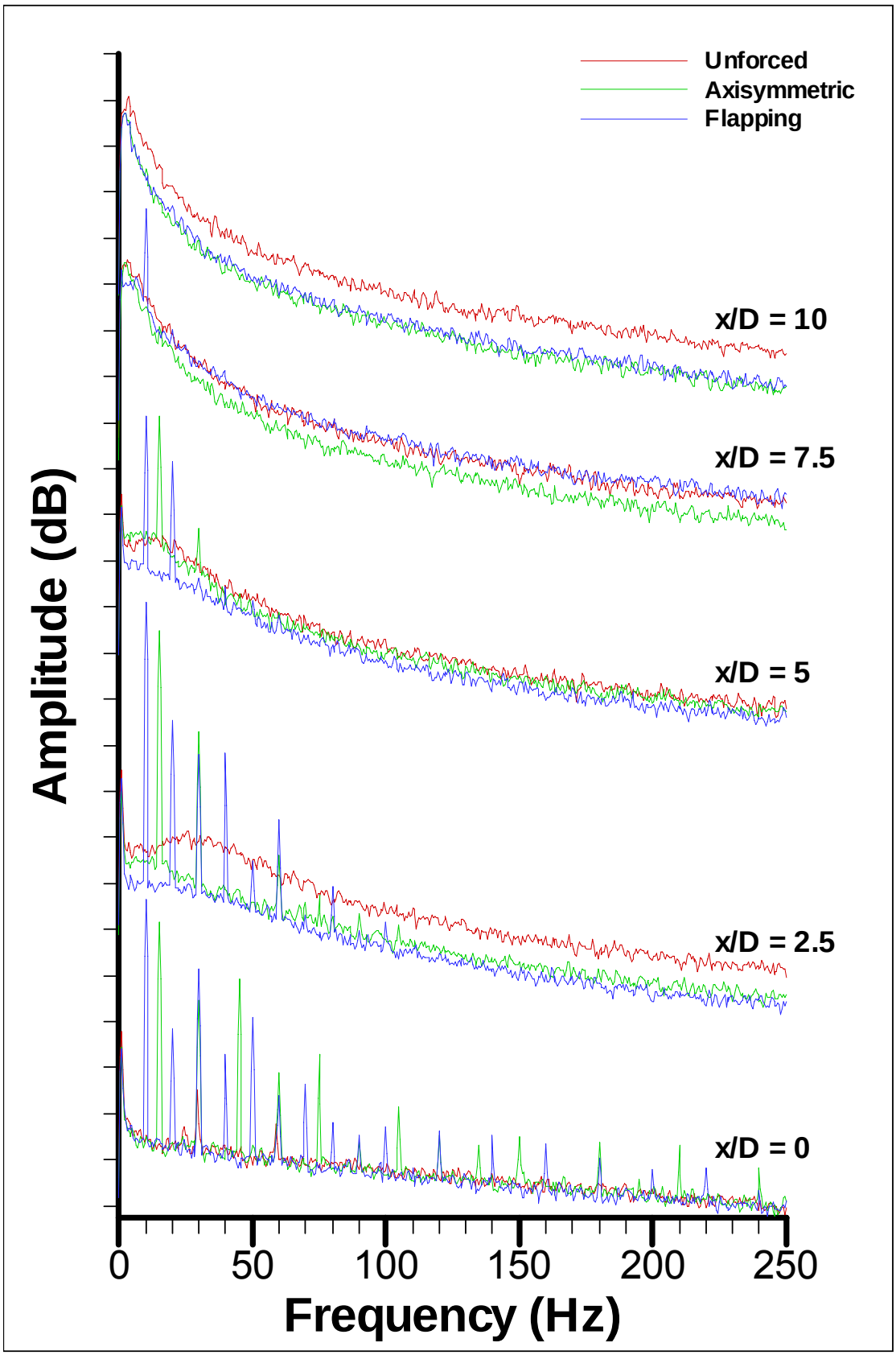

Figure 3.63: Lipline (z/D = 0.5) Fourier Transforms for the Three Configurations

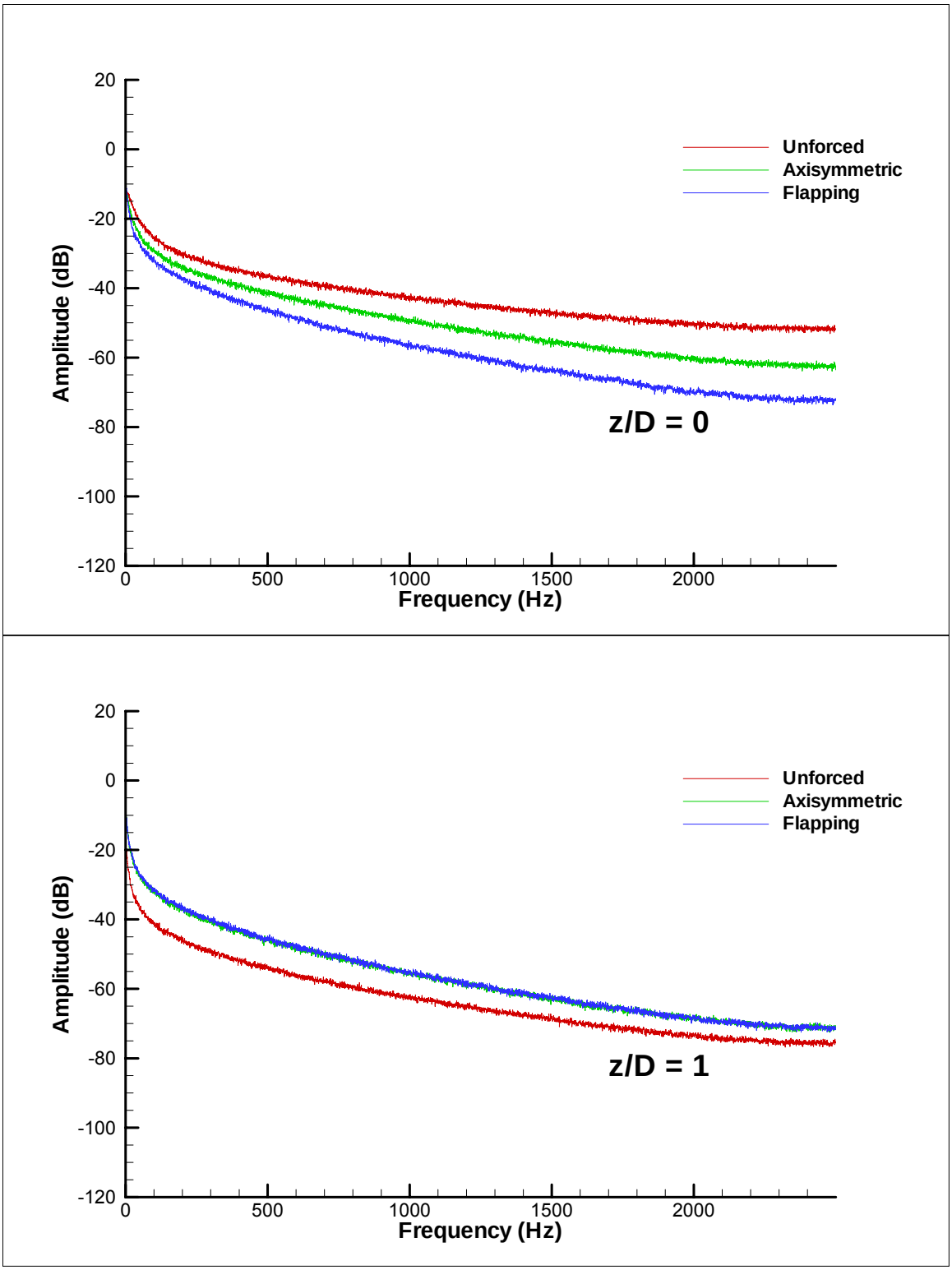

Figure 3.64a: Fourier Transforms for the Three Cases Along the z-axis at x/D = 10

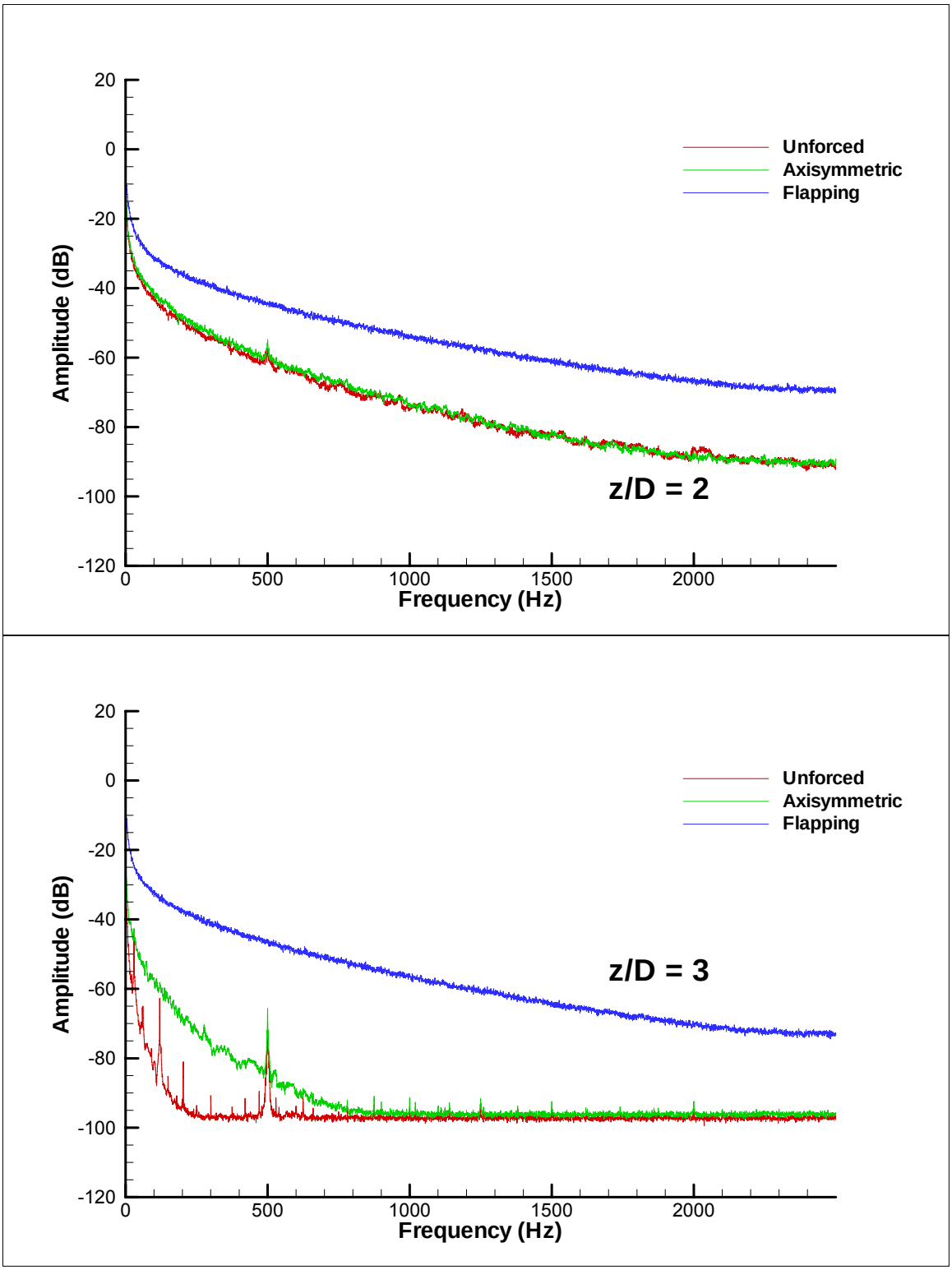

Figure 3.64b: Fourier Transforms for the Three Cases Along the z-axis at x/D = 10

Note that figure 3.69 shows the corresponding velocity profiles for the vertical traverse. It is clear that the unforced jet has decayed significantly at this point. At z/D = 2 the unforced and axisymmetric cases are similarly decayed, but the curve for the flapping mode case is still high and continues to be so even at z/D = 3. This all correlates well with the velocity profiles of Figure 3.69. Note that no spikes were found in any of the spectral curves. This suggests that mixing on both large and small scales has, in fact, taken place.

Velocity and Turbulence Intensity Profiles

Figures 3.65 through 3.72 give the velocity profiles and turbulence intensity curves at 7.5D and 10D for both the vertical and horizontal directions. The curves show the spread of the jets further downstream than the earlier contour data which only extended out to x/D = 5. At 7.5D the 0º-phase and 180º-phase jets have primarily spread in different orthogonal directions. The 0º-phase jet has spread in the y-direction and the 180º-phase jet has spread in the z-direction (the direction of forcing). By 10D the 0º-phase jet has balanced out and appears to be more symmetric, though it may be undergoing an axis switch. The 180º-phase jet is still largely asymmetric.

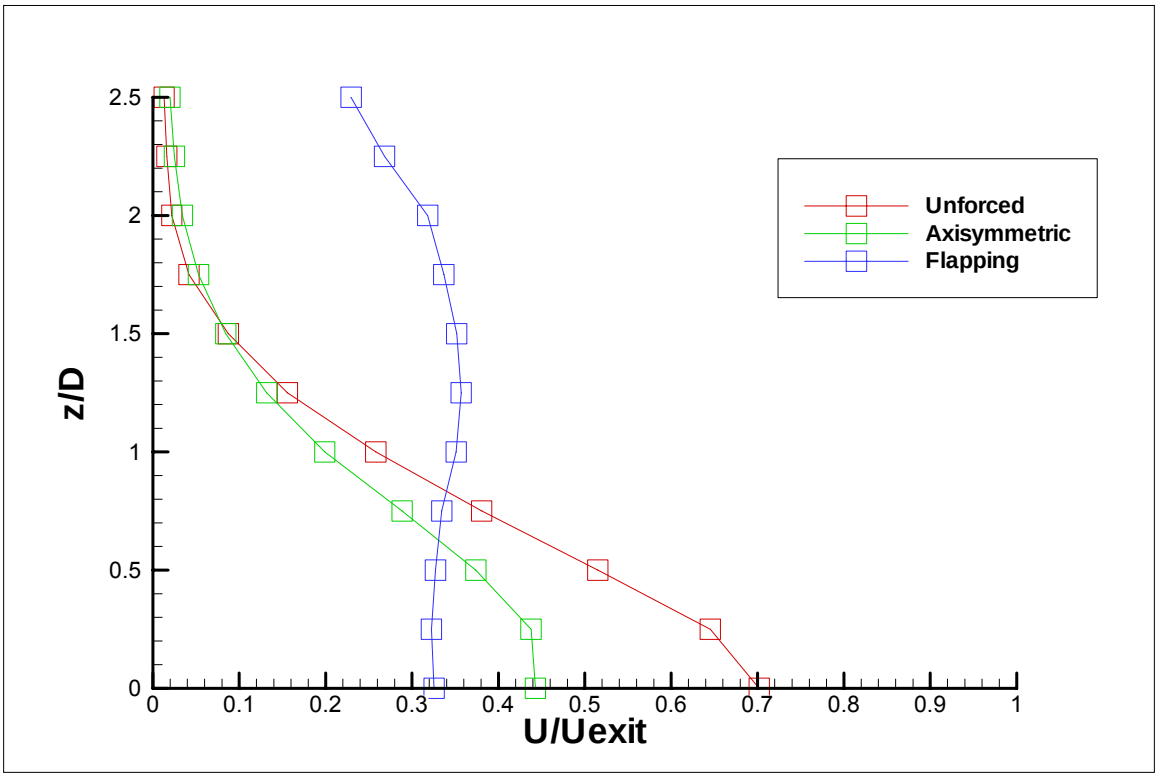

Figure 3.65: Mean Velocity Profiles in the z-direction (Top Half of the Jet) at x/D = 7.5 for the Three Cases

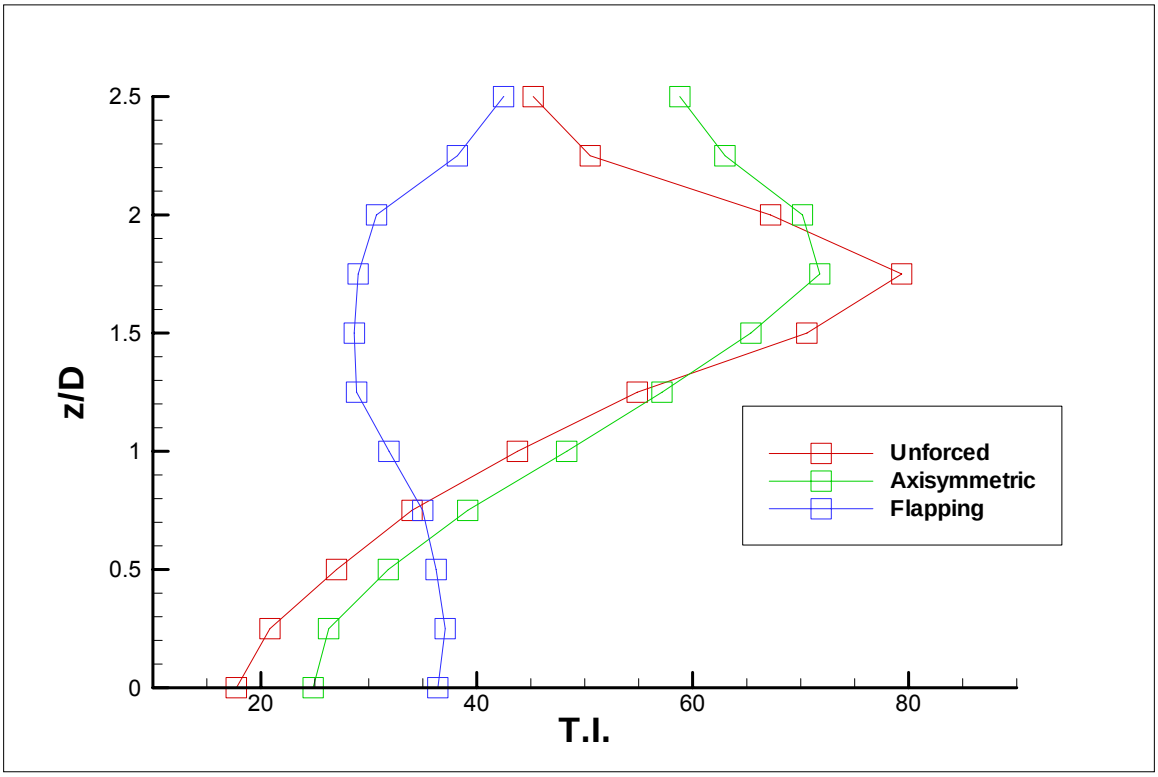

Figure 3.66: Mean Turbulence Intensity Profiles in the z-direction (Top Half of the Jet) at x/D = 7.5 for the Three Cases

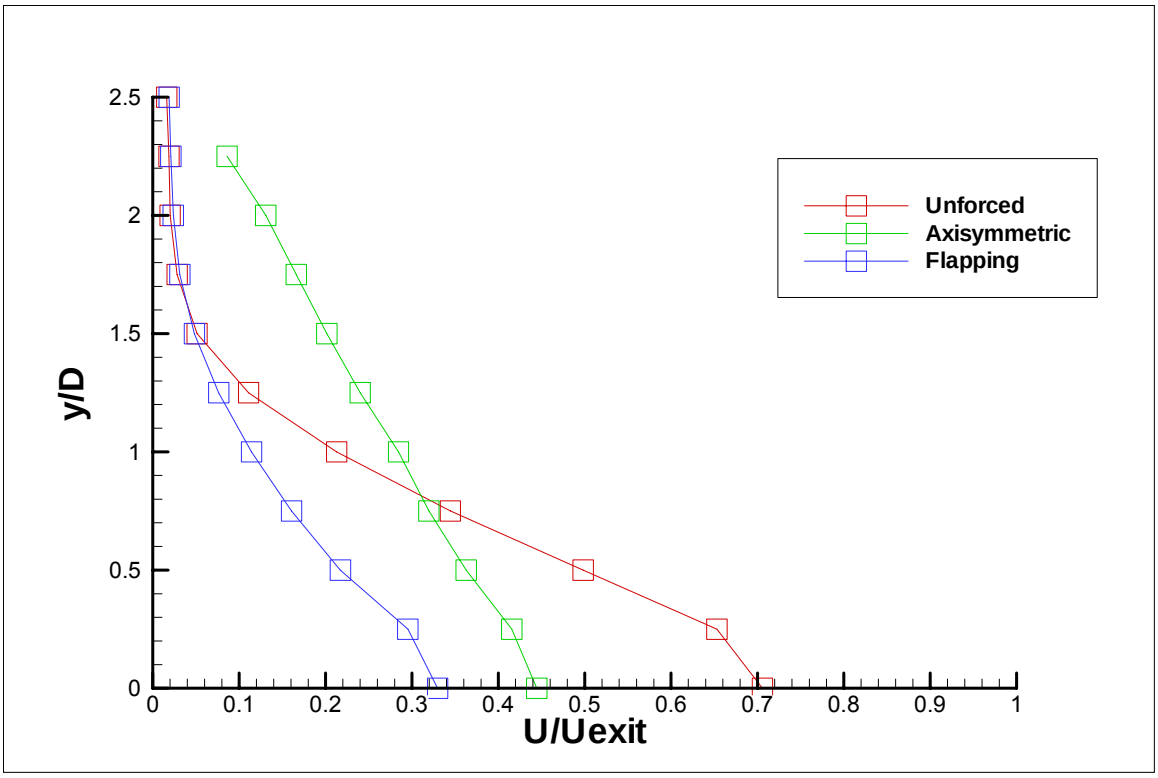

Figure 3.67: Mean Velocity Profiles in the y-direction (Right Half of the Jet) at x/D = 7.5 for the Three Cases

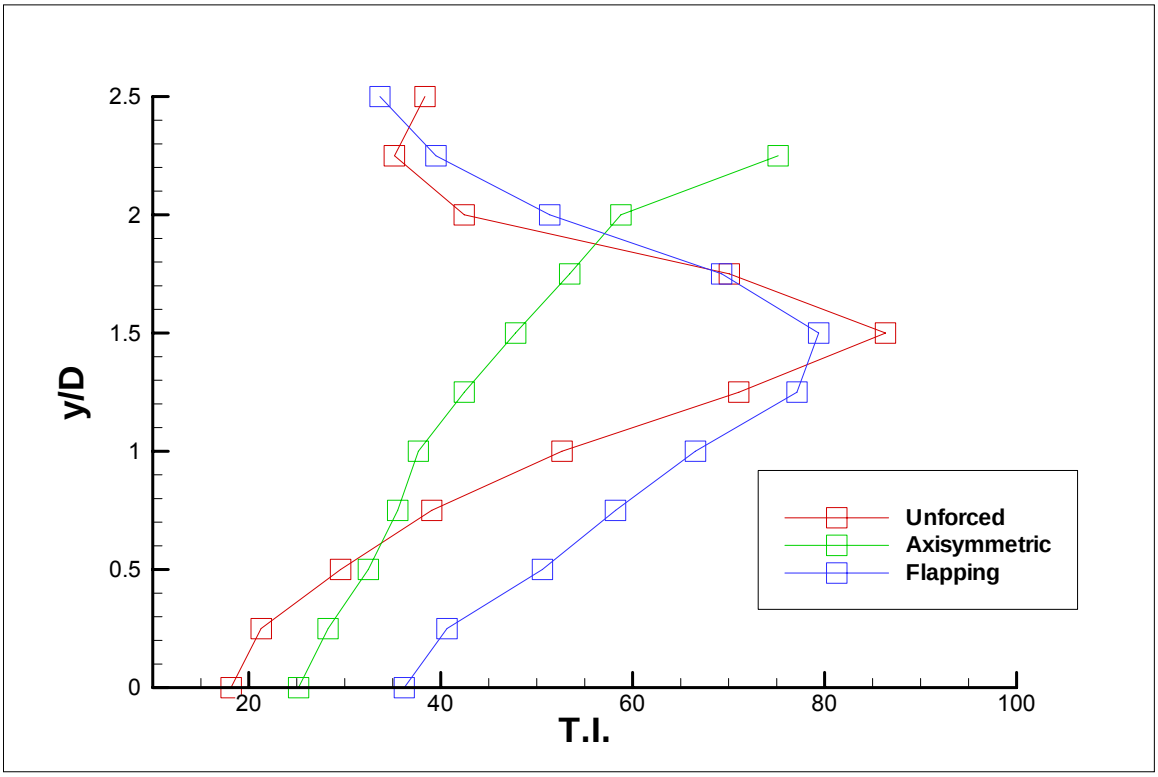

Figure 3.68: Mean Turbulence Intensity Profiles in the y-direction (Right Half of the Jet) at x/D = 7.5 for the Three Cases

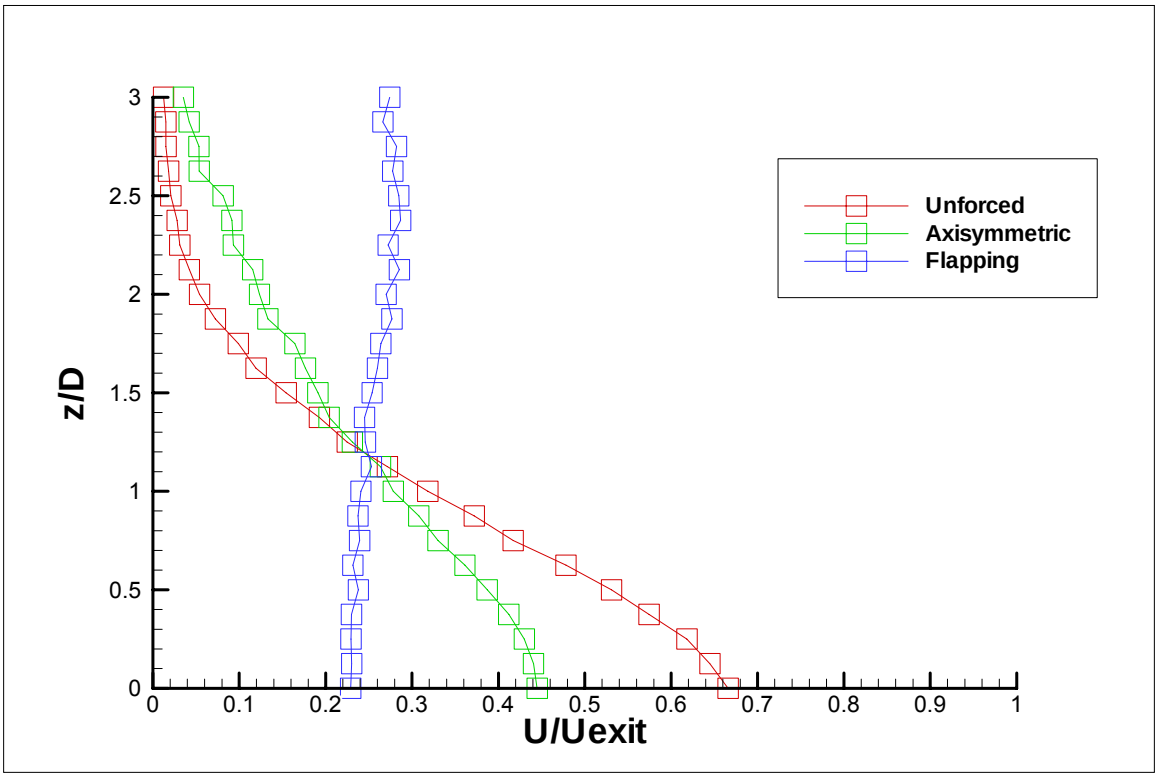

Figure 3.69: Mean Velocity Profiles in the z-direction (Top Half of the Jet) at x/D = 10 for the Three Cases

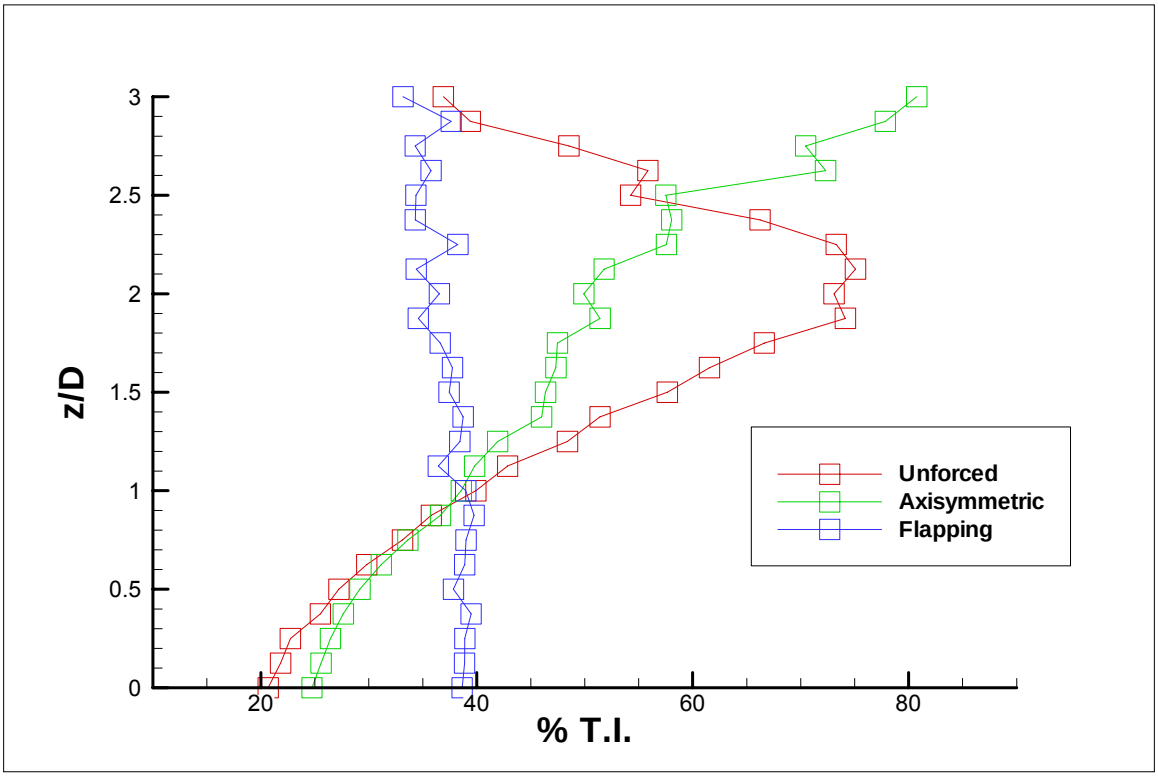

Figure 3.70: Mean Turbulence Intensity Profiles in the z-direction (Top Half of the Jet) at x/D = 10 for the Three Cases

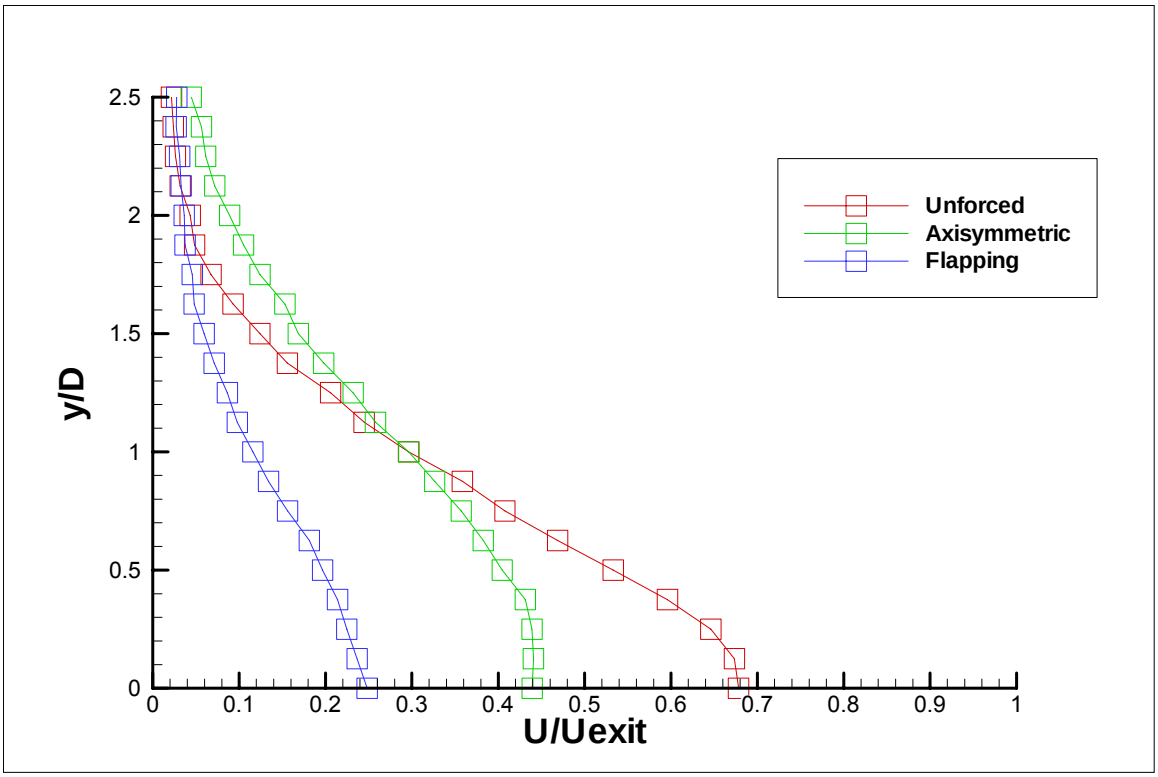

Figure 3.71: Mean Velocity Profiles in the y-direction (Right Half of the Jet) at x/D = 10 for the Three Cases

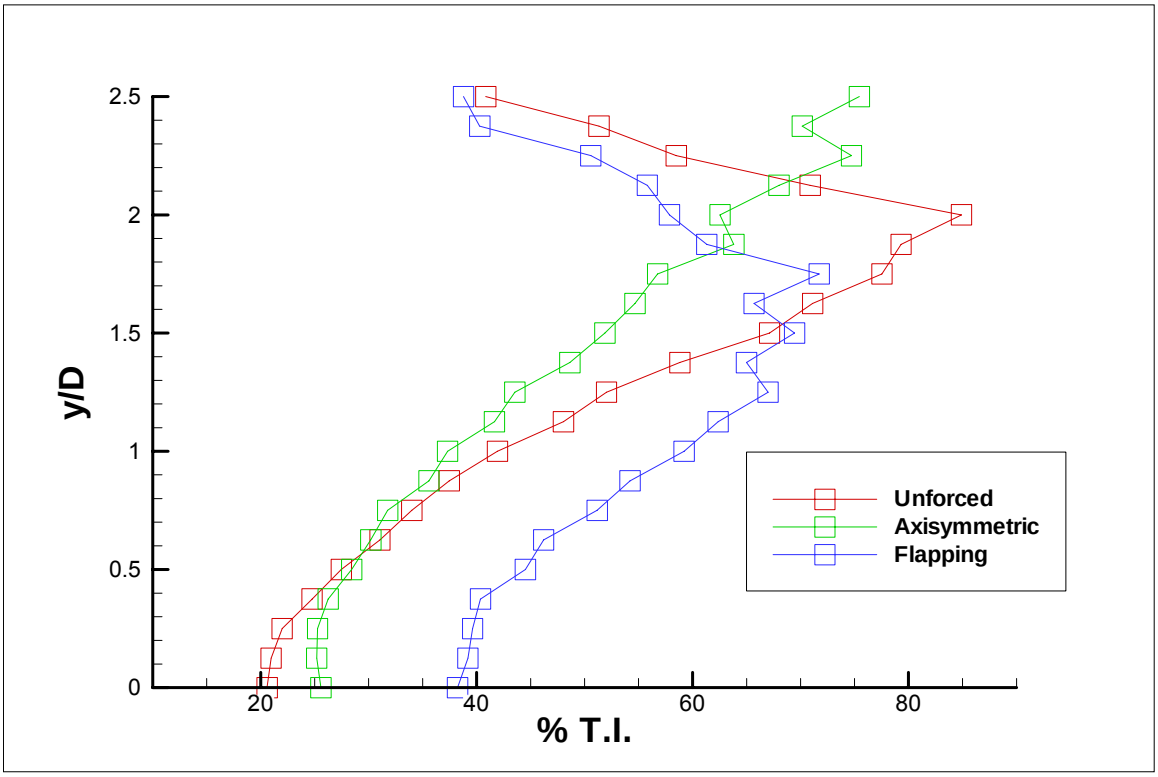

Figure 3.72: Mean Turbulence Intensity Profiles in the y-direction (Right Half of the Jet) at x/D = 10 for the Three Cases

Phase Averaged vs. Instantaneous Data

It is interesting to compare the phase averaged velocities in the flow to instantaneous velocities occurring at the same phase time. Figures 3.73 through 3.77 make such comparisons for velocities measured on the centerline from 0D to 5D for the three baseline cases. The locations correspond to the same points spectral information was given for in figure 3.62. Close to the nozzle where the spectra showed large peaks for the forced cases, the instantaneous data roughly follows the phase averaged data. However, as one moves away from the nozzle the phase averaged velocity flattens to a line and instantaneous data shows less correlation with it. Also note that, in terms of fluctuation, there is no distinguishable difference between the instantaneous data for the forced and unforced cases at 10D. The same trend occurs for instantaneous and phase averaged velocity comparisons made along a lipline traverse (not shown). Note that the inclusion of a "phase average" for the unforced case is a bit of a stretch. It was calculated by picking an arbitrary frequency, in this case 10 Hz. As expected, the result is a flat line. The calculation was only made so that similar comparisons could be made with the forced cases.

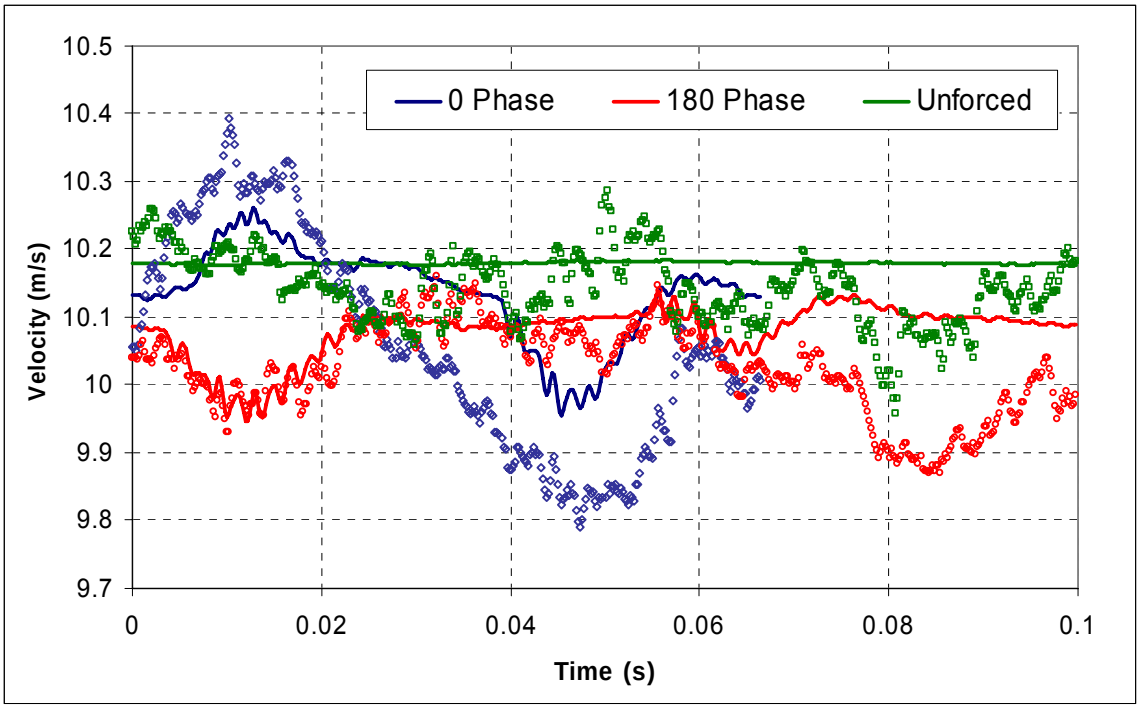

Figure 3.73: Comparison of Phase Averaged Velocity to Instantaneous Velocity on the Centerline, z/D = 0 (Averaged-Solid, Instantaneous-Symbols)

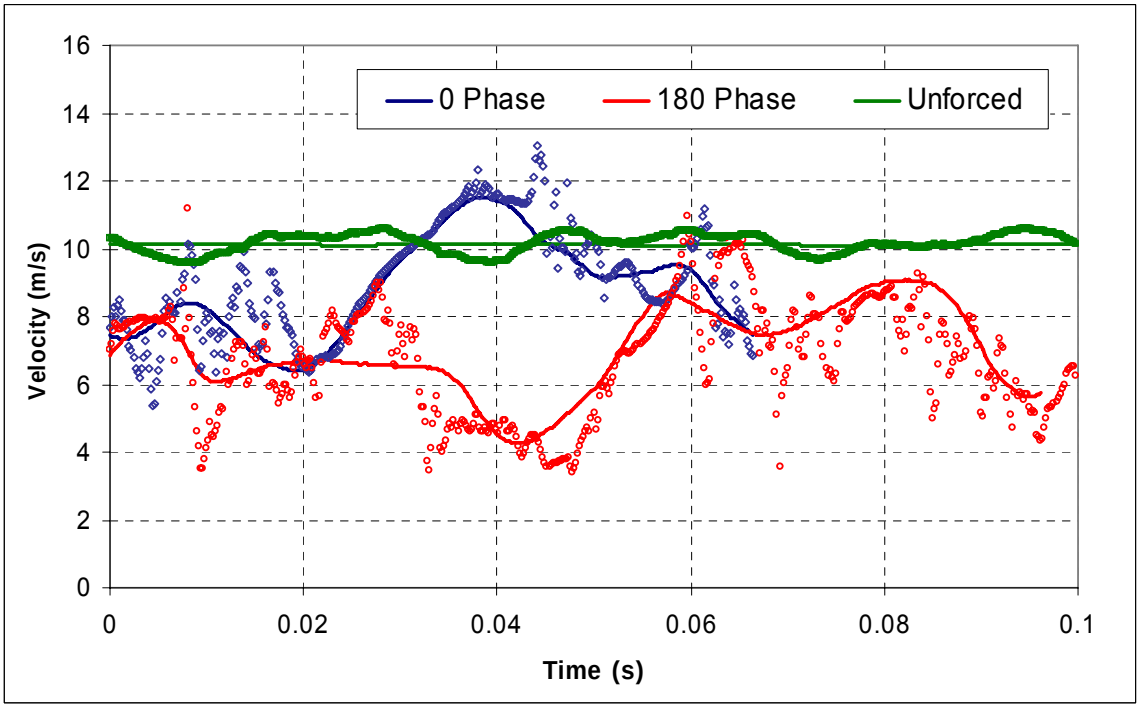

Figure 3.74: Comparison of Phase Averaged Velocity to Instantaneous Velocity on the Centerline, z/D = 2.5

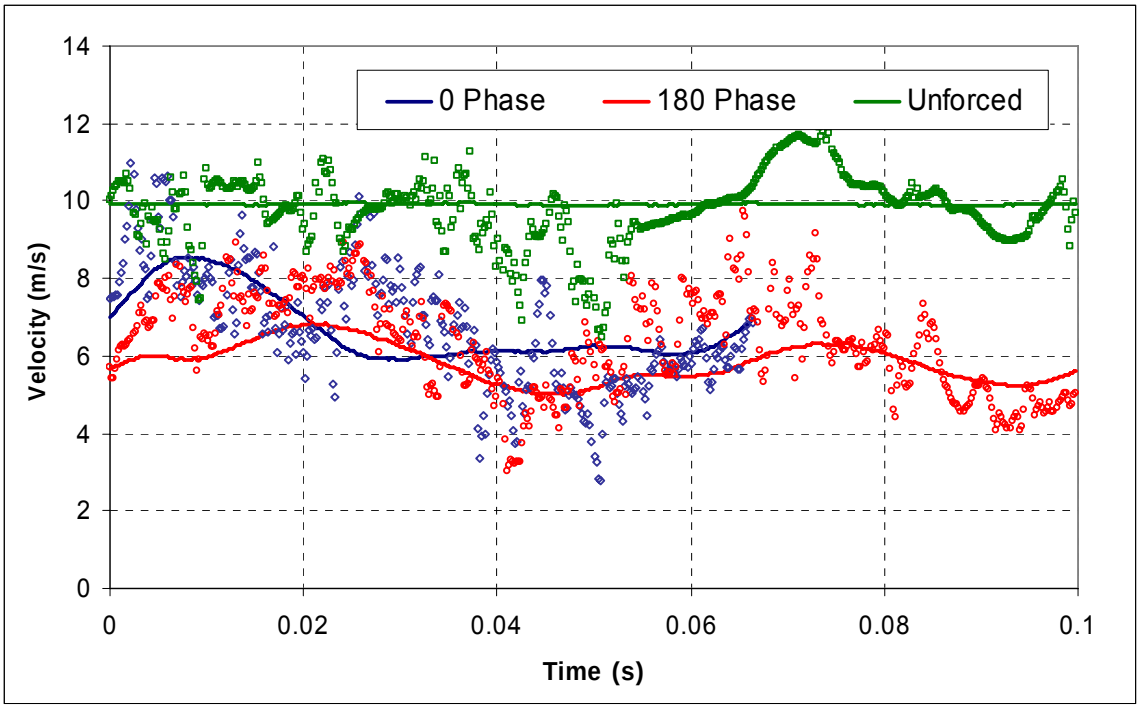

Figure 3.75: Comparison of Phase Averaged Velocity to Instantaneous Velocity on the Centerline, z/D = 5

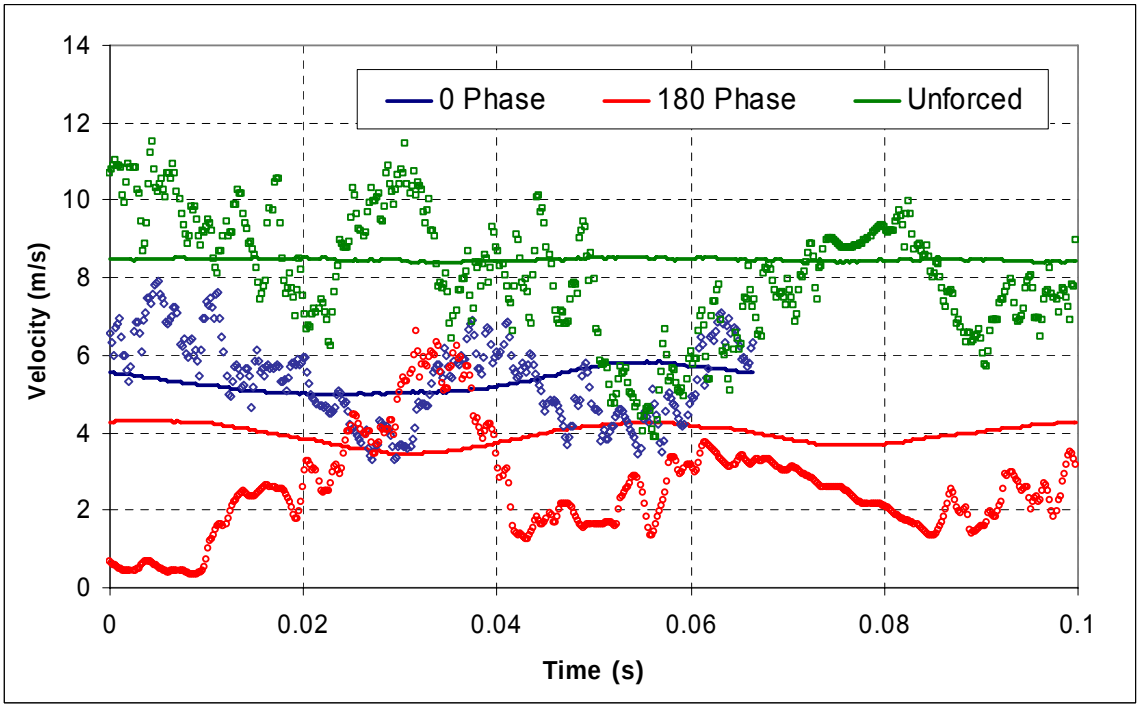

Figure 3.76: Comparison of Phase Averaged Velocity to Instantaneous Velocity on the Centerline, z/D = 7.5

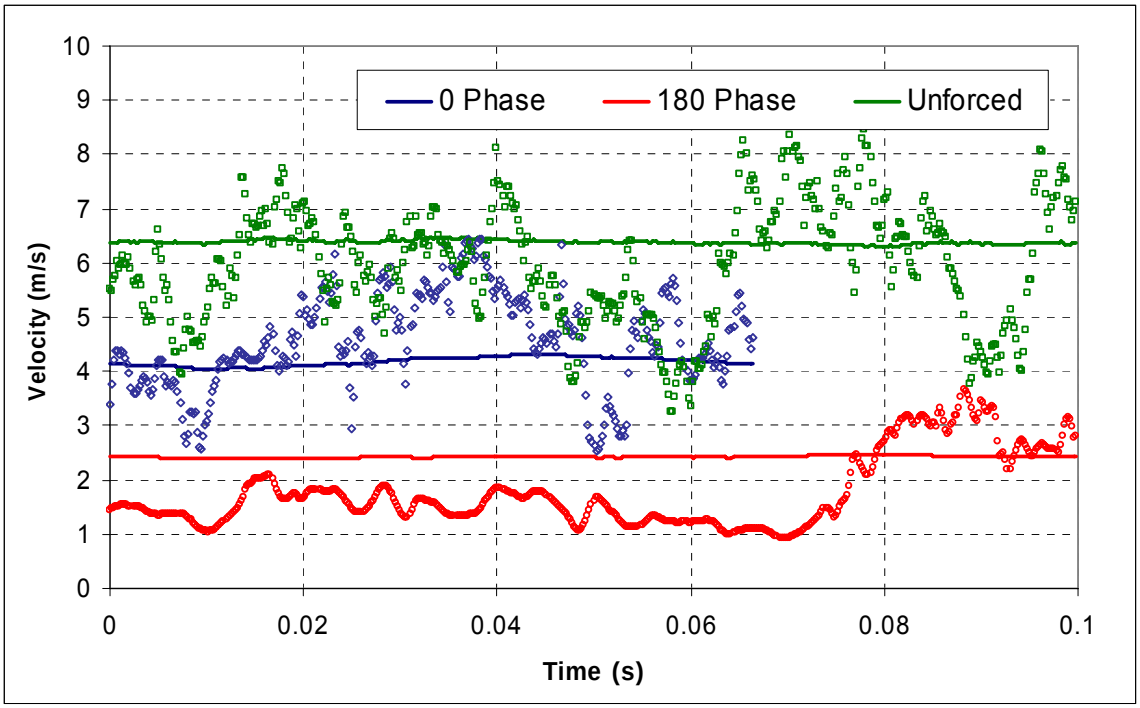

Figure 3.77: Comparison of Phase Averaged Velocity to Instantaneous Velocity on the Centerline, z/D = 10

2D Planar Traverses from Phase I

During the phase I experiments, a number of 2D planar traverses were performed at x/D = 10 for different actuator configurations. They are presented here, after the phase II hotwire results, so that they would appear nearer to the linear traverse results. Note that during phase I, pulsing took place from side to side, not top to bottom as in phase II. Measurements of the average velocity were made for one minute per point with a pitot probe and a very accurate pressure transducer. Figure 3.78 summarizes the results for nine different cases. The unforced jet is compared with jets forced at both 0º and 180º-phase, with 2 or 4 actuators, and at two different Strouhal numbers. The forcing amplitude was SRMR = 0.75, somewhat short of saturation.

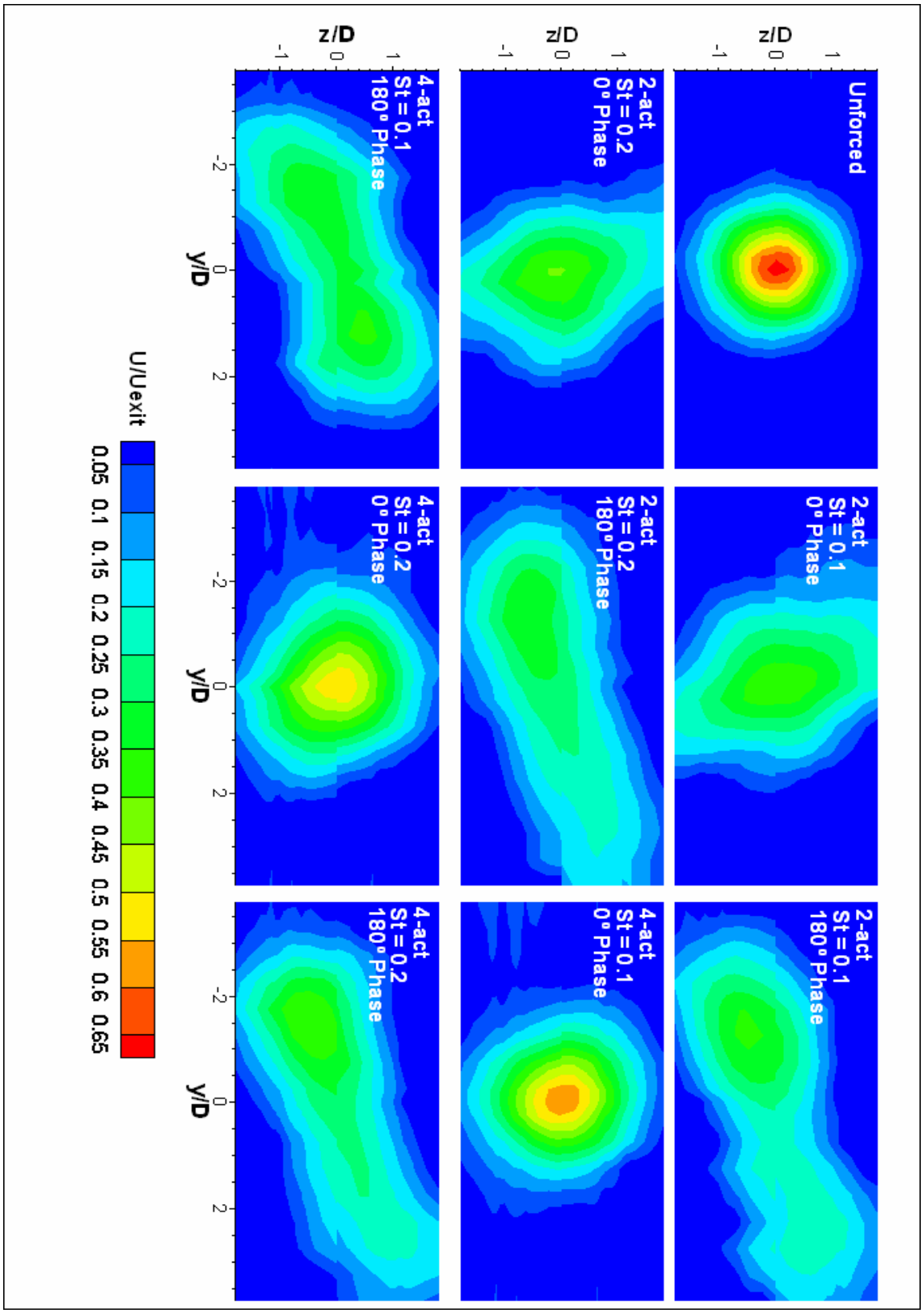

Figure 3.78: Mean Velocity Contours at x/D = 10, U_{exit} = 30 m/s, SRMR = 0.75 (Note that Pulsing acts along y-axis or side to side in plot)

Detailed Characterization of the Optimal Forcing Cases - PIV Results

Two different seeding methods were used for the PIV experiments: seeding of the bottom actuator and seeding of the main jet. The two methods were implemented separately resulting in pictures with distinct regions of the flow field tagged with particles. As before, three different cases were compared against each other: the unforced jet, the jet forced at 0º-phase, and the jet forced at 180º-phase. Unless otherwise specified, baseline conditions were used. This consisted of a jet exit velocity equal to 10 m/s, an amplitude of SRMR = 0.1, and Strouhal numbers of 0.15 and 0.1 for the 0º and 180º-phase cases respectively. A majority of the PIV measurements were taken in eleven different overlapping regions (figure 2.9) which were ultimately combined to produce average and phase averaged plots with a range of 0D to 5D in the streamwise x-direction and ±1.75D in the y, z, or 45º plane direction. A few measurements were only taken in a single region, the jet actuator interaction region (region 1 from figure 2.9). The primary plane of measurement was the xz-plane with the actuators mounted on the top and bottom side of the jet exit. A few measurements were made where the actuators were rotated 45º and 90º to obtain measurements in other planes as well. The baseline actuator nozzle was the 0.08" nozzle, but for a few experiments the 0.04" nozzle was used.

Flow Visualization

Many of the PIV images were useful for flow visualization. It was often easy to see the coherent structures that formed in the flow either naturally or due to actuation. Figures 3.79 through 3.98 are sample images pulled from the PIV database which show the interaction of the jet and actuator pulses under a variety of conditions. Figures 3.79

through 3.88 are images where only the actuator has been seeded, while 3.89 through 3.98 are images where the jet has been seeded.

Actuator Seeded Images

The actuator seeded images show the extent of penetration of the pulses into the jet, the basic paths that they follow, and the rapidity with which they mix with the jet. The three dimensional flow field is very complex due to the high aspect ratio of the actuator nozzle. Nevertheless, it is still possible to get a sense of what is happening from a 2D slice. The fluid from the pulses that is tagged by the fog particles collects into structures that start out as shear layer vortices (figure 3.81) near the actuator exit and resemble cloud-like clumps further downstream (figures 3.86 and 3.87). The particles first move inward toward the center of the jet, and then outward across the lipline (figure 3.88) indicating the presence of a large scale vortex structure in the untagged flow. Small scale vortex structures are induced in the shear layer (figure 3.85).

Jet Seeded Images

By seeding only the jet, it was possible to distinguish between various regions of the flow in the near field. The heavily seeded jet fluid was white, mixing regions were grey, and unmixed ambient fluid was dark. The jet seeded images show the contrast between the forced and unforced cases. For the unforced case (figure 3.89), small scale turbulent structures form in the shear layer downstream of the jet nozzle exit and grow as they move downstream. Comparing multiple images, it appears that the structures are somewhat random in terms of their shape and spacing. For excited flow, two different

scales of coherent structures form. Large scale vortical structures are induced in the near field along with the smaller scale vortical structures which appear scattered about the near field. The large structures appear to be about an order of magnitude larger in size than the small structures, and occur at regular intervals with similar shapes (figure 3.90). The images also demonstrate that mixing of the actuator fluid with the jet fluid occurs rapidly since the tagged particles in the actuator seeded pictures overlap with the tagged particles in the jet seeded pictures. The overlap region shows up as lighter seeding in the jet seeded pictures.

The large scale structures appear to be roughly the same size for the 0º and 180º-phase cases (figure 3.90 vs. 3.92). However, for the 180º-phase case there is an additional increase in entrainment due to the flapping of the jet which occurs just downstream of the initial vortex formation (figures 3.93 through 3.95). For a higher frequency pulsing case all of this can be seen in one frame (figure 3.96). Note that the near field vortical structures for the higher frequency pulses are not as large as those for the optimal frequencies. Similar structures form for the 0.08" and 0.04" nozzles with the pulsing frequency and SRMR (figure 3.98). Pictures of the flow when the actuators have been rotated 90º do not show the large scale vortical structures (figure 3.97). Additionally, they suggest that the jet is not spreading nearly as fast in that direction.

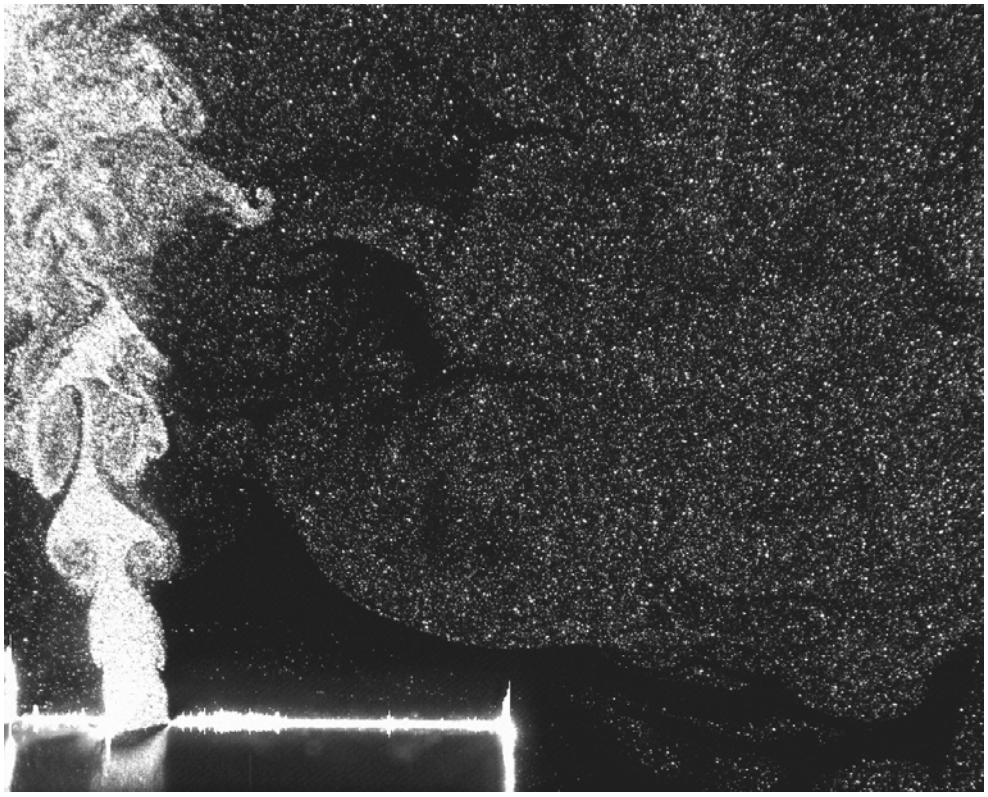

Figure 3.79: PIV Image – Steady Blowing From Actuator, No Jet

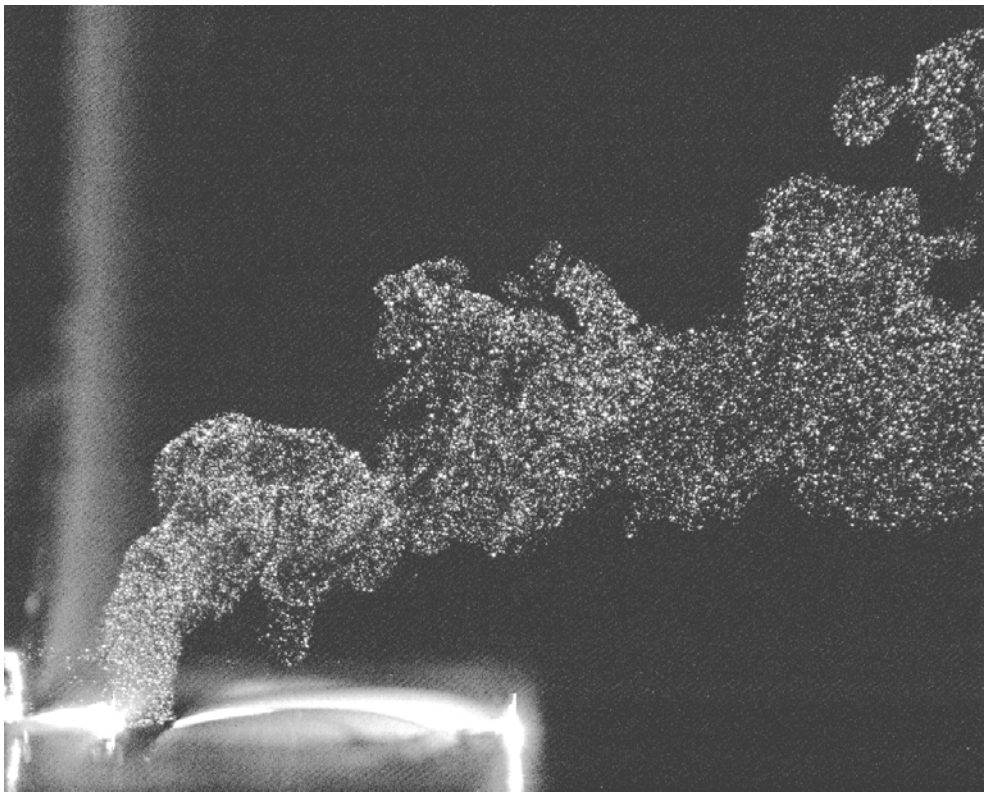

Figure 3.80: PIV Image – Steady Blowing from Actuator, U_{jet} = 10 m/s

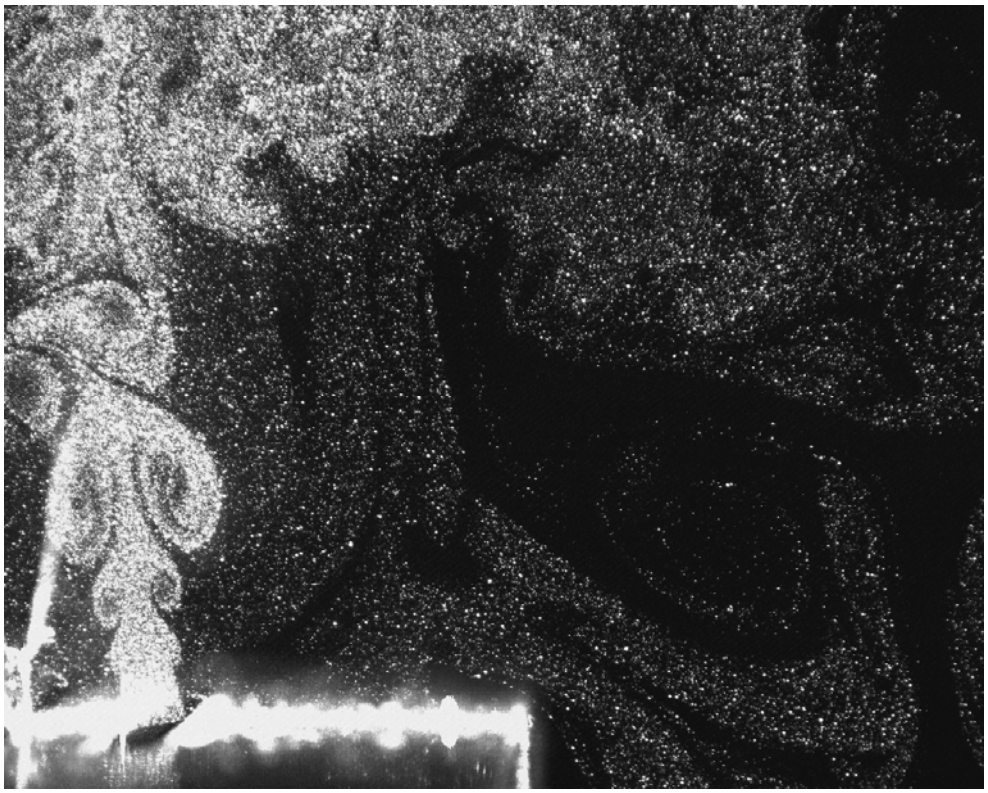

Figure 3.81: PIV Image – Pulsing at 10 Hz, No Jet

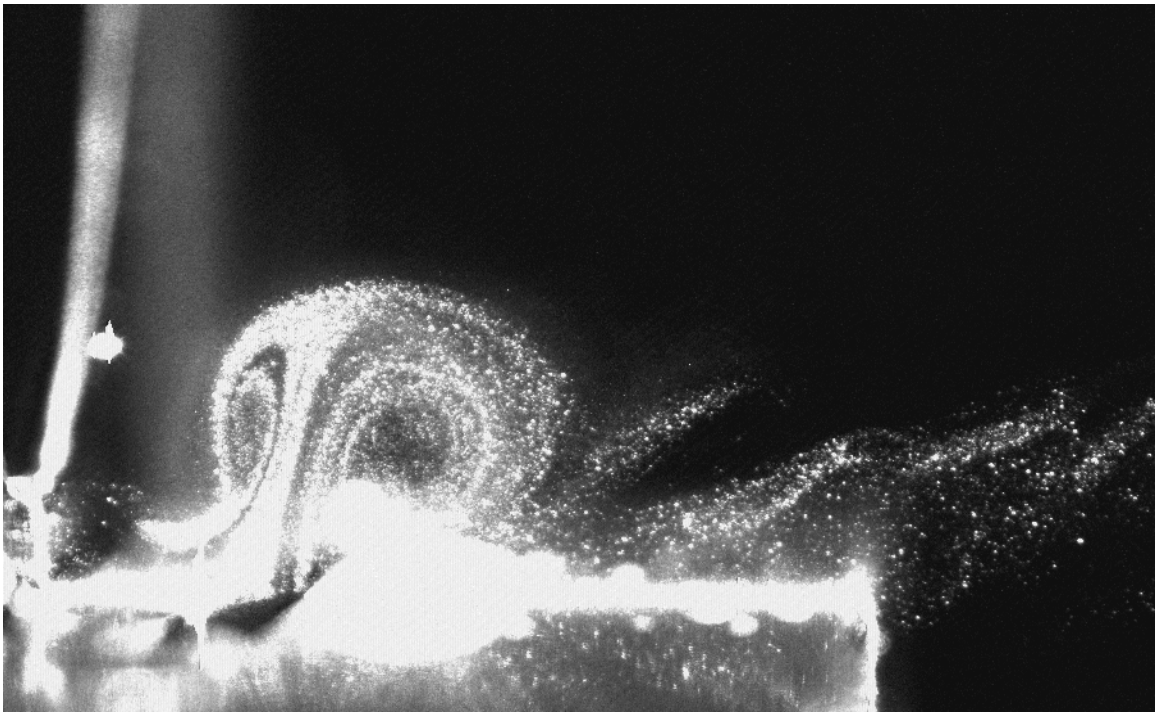

Figure 3.82: PIV Image – Pulsing at 10 Hz, U_{jet} = 10 m/s, Beginning of Pulsing Cycle

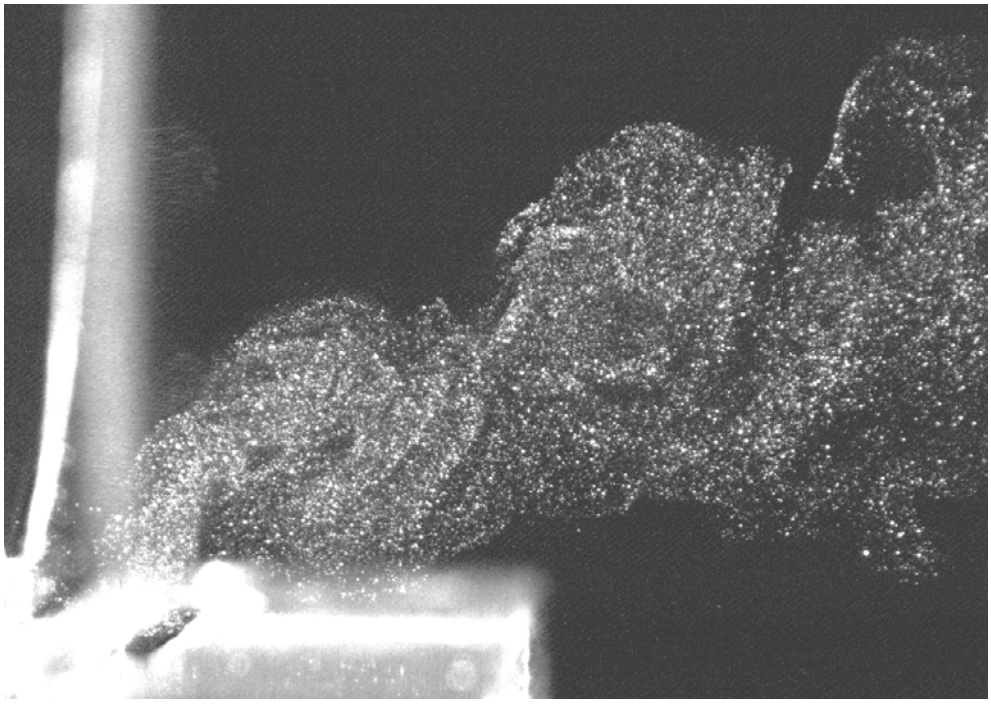

Figure 3.83: PIV Image – Pulsing at 10 Hz, U_{jet} = 10 m/s, Middle of Pulsing Cycle

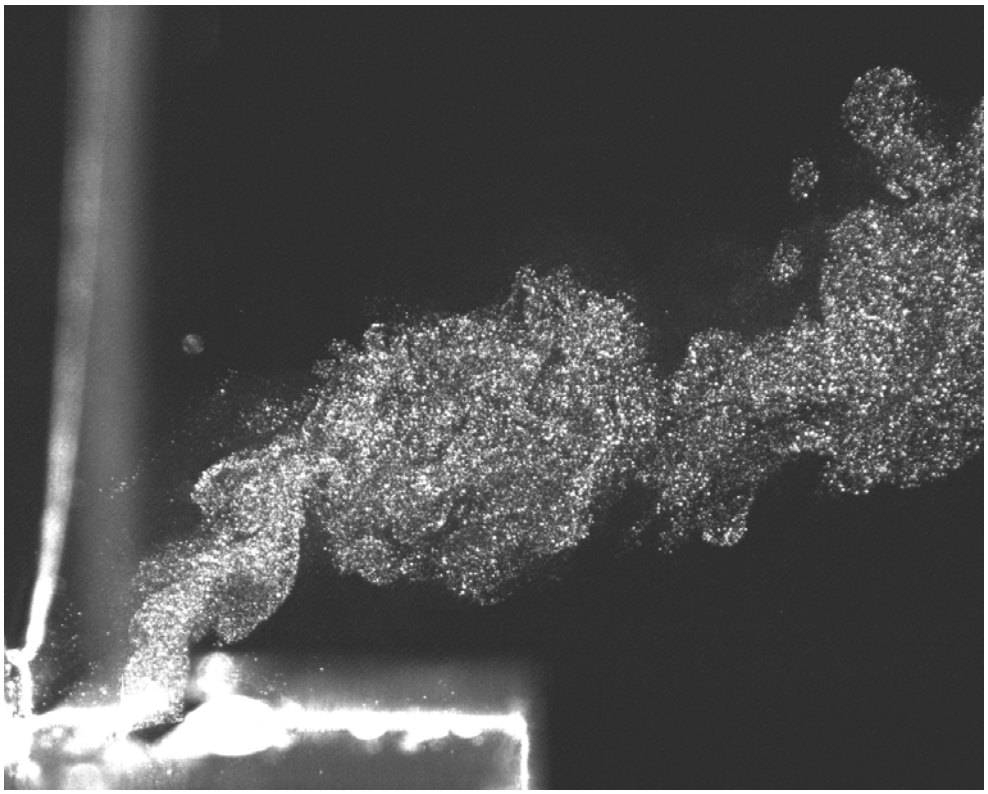

Figure 3.84: PIV Image – Pulsing at 10 Hz, U_{jet} = 10 m/s, End of Pulsing Cycle

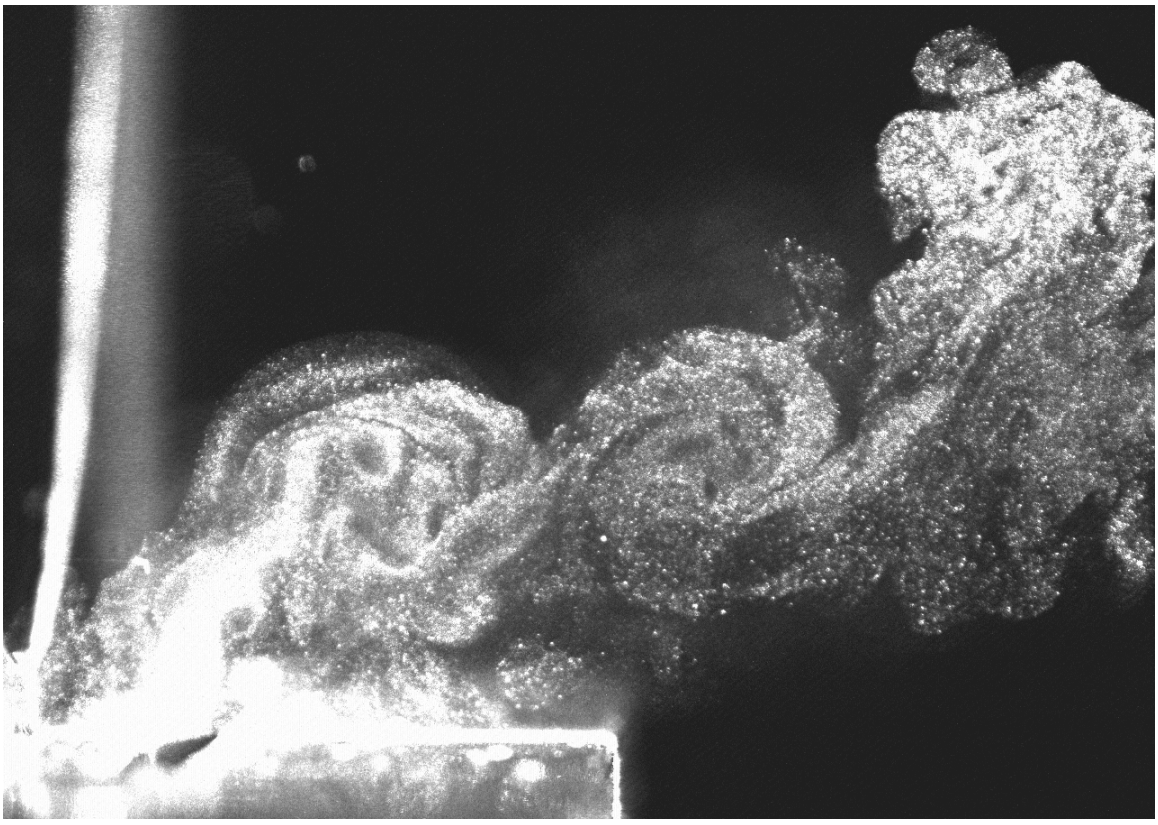

Figure 3.85: PIV Image – Pulsing at 30 Hz, U_{jet} = 10 m/s, End of Pulsing Cycle

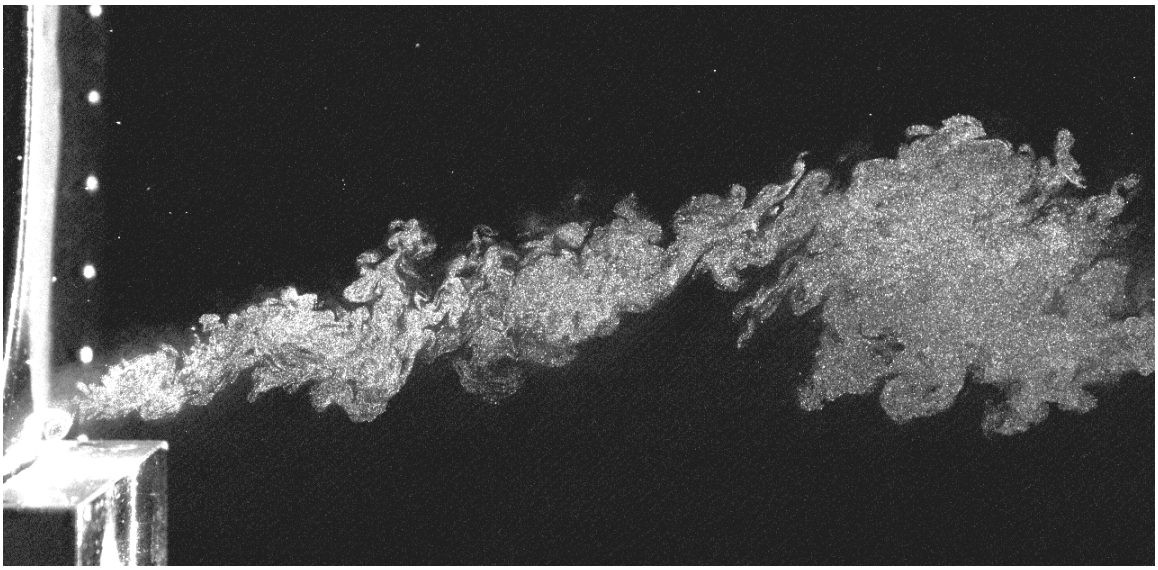

Figure 3.86: PIV Image – Pulsing at 10 Hz, U_{jet} = 10 m/s, Wider View, End of Pulsing Cycle

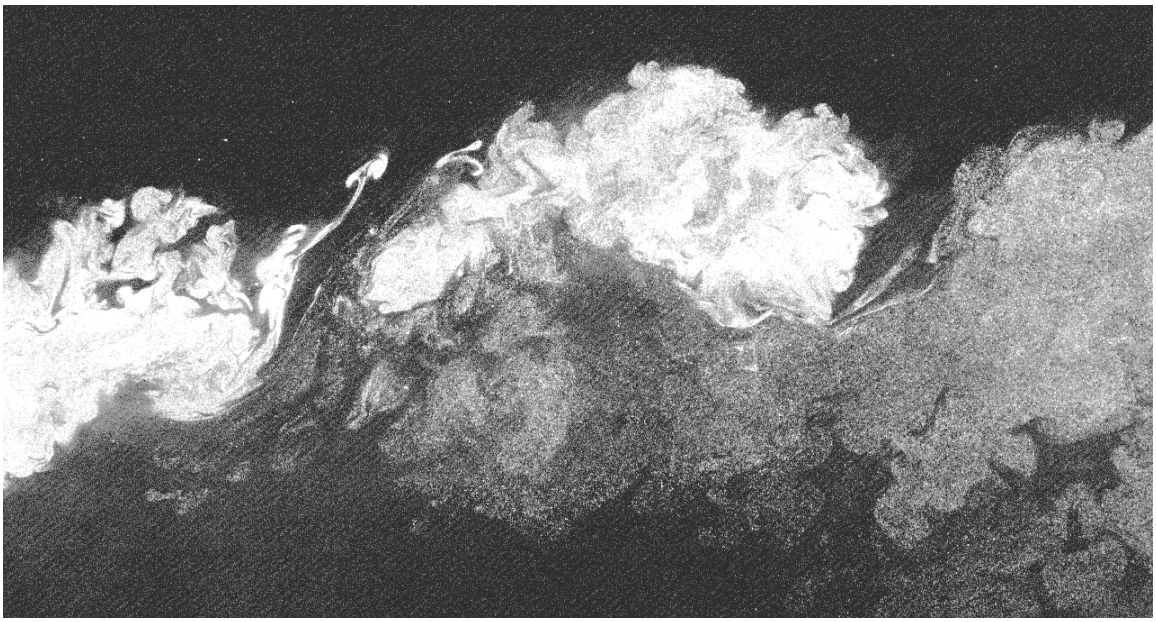

Figure 3.87: PIV Image – Pulsing at 10 Hz, U_{jet} = 10 m/s, End of Pulsing Cycle, Further Downstream

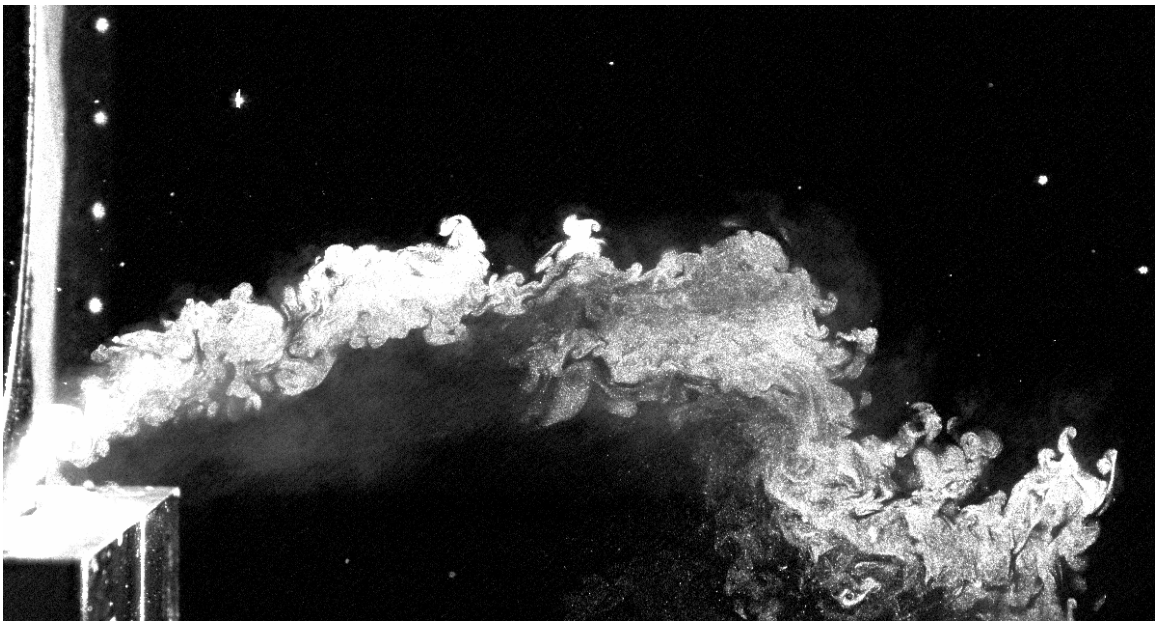

Figure 3.88: PIV Image – Pulsing at 30 Hz, U_{jet} = 10 m/s, End of Pulsing Cycle, Wider View

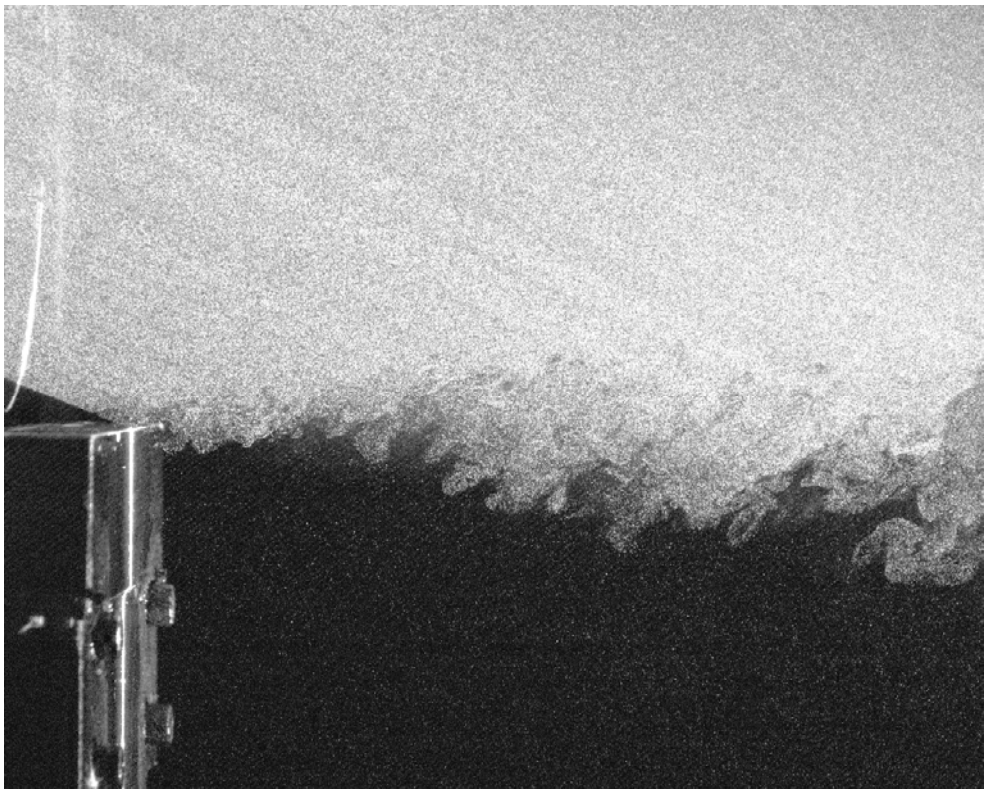

Figure 3.89: PIV Image – Natural Jet

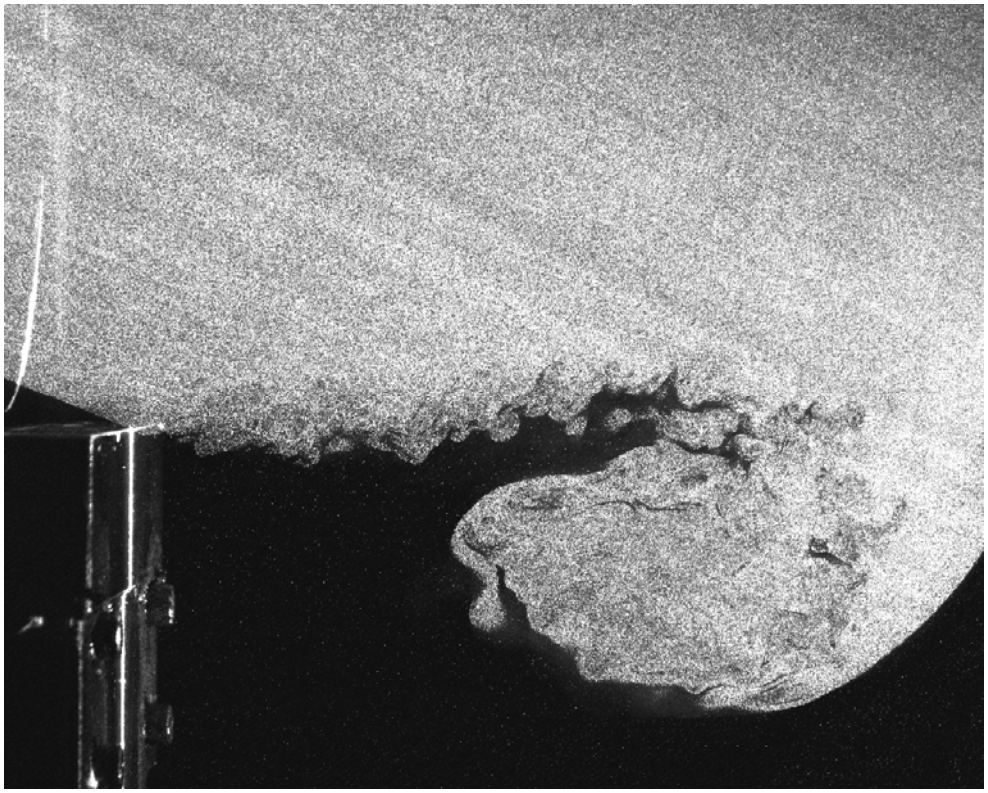

Figure 3.90: PIV Image – 0º Phase Pulsing, Baseline Conditions

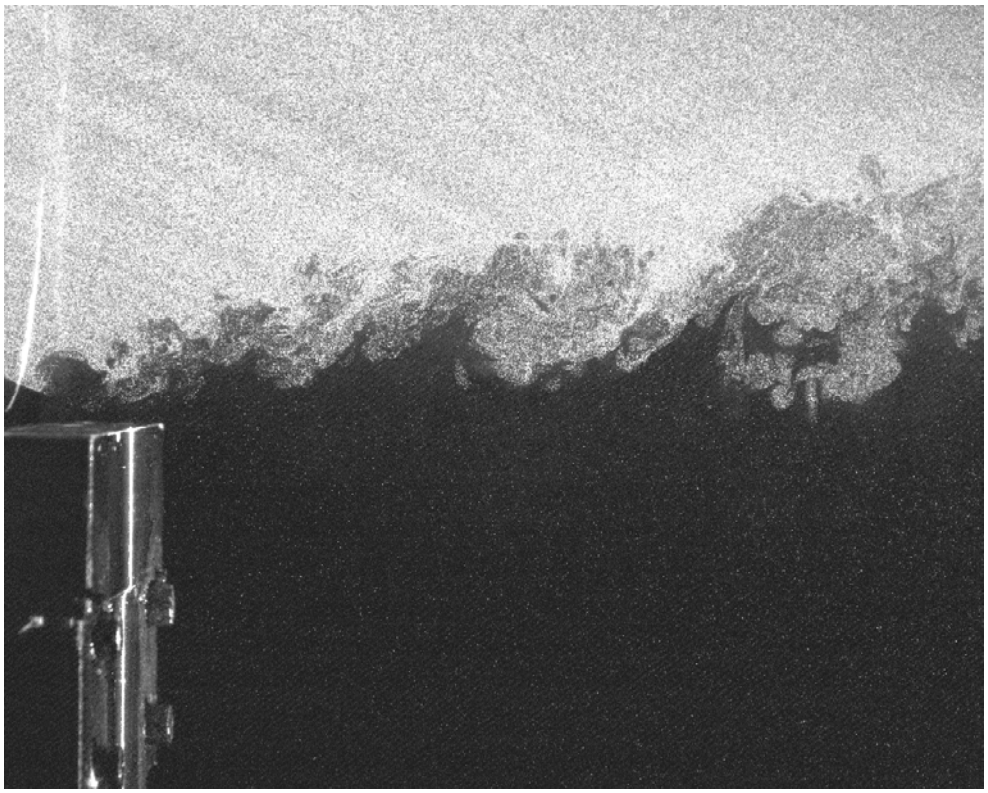

Figure 3.91: PIV Image – Blowing, Ujet = 10 m/s

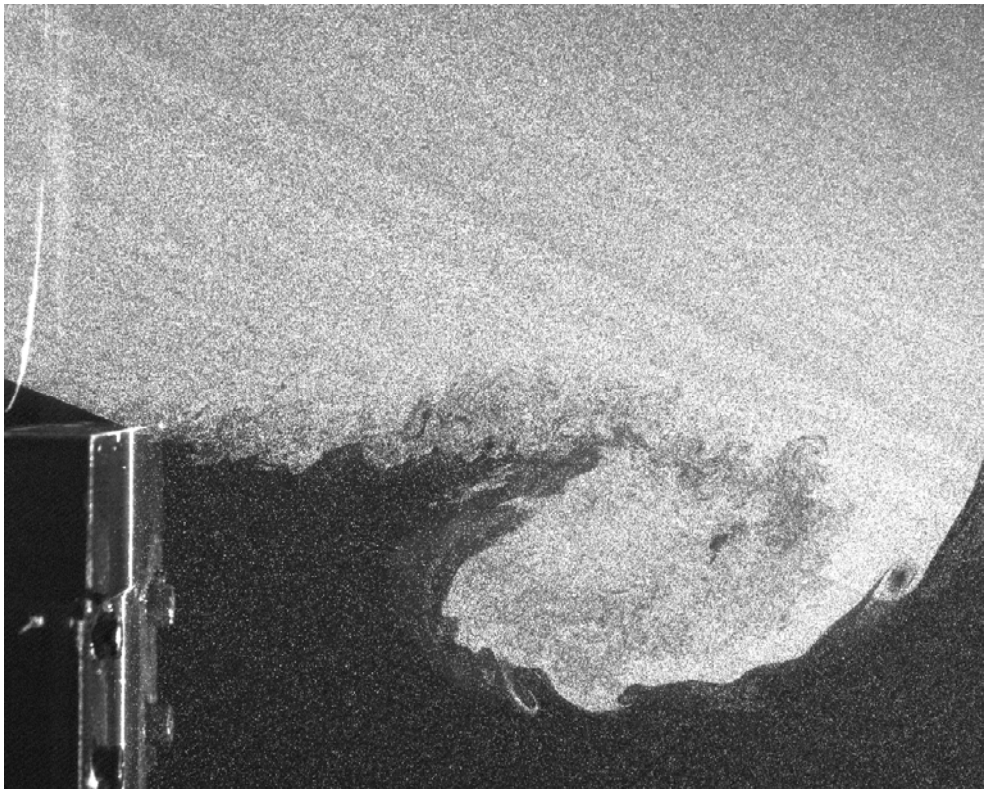

Figure 3.92: PIV Image – 180º Phase Pulsing, Baseline Conditions

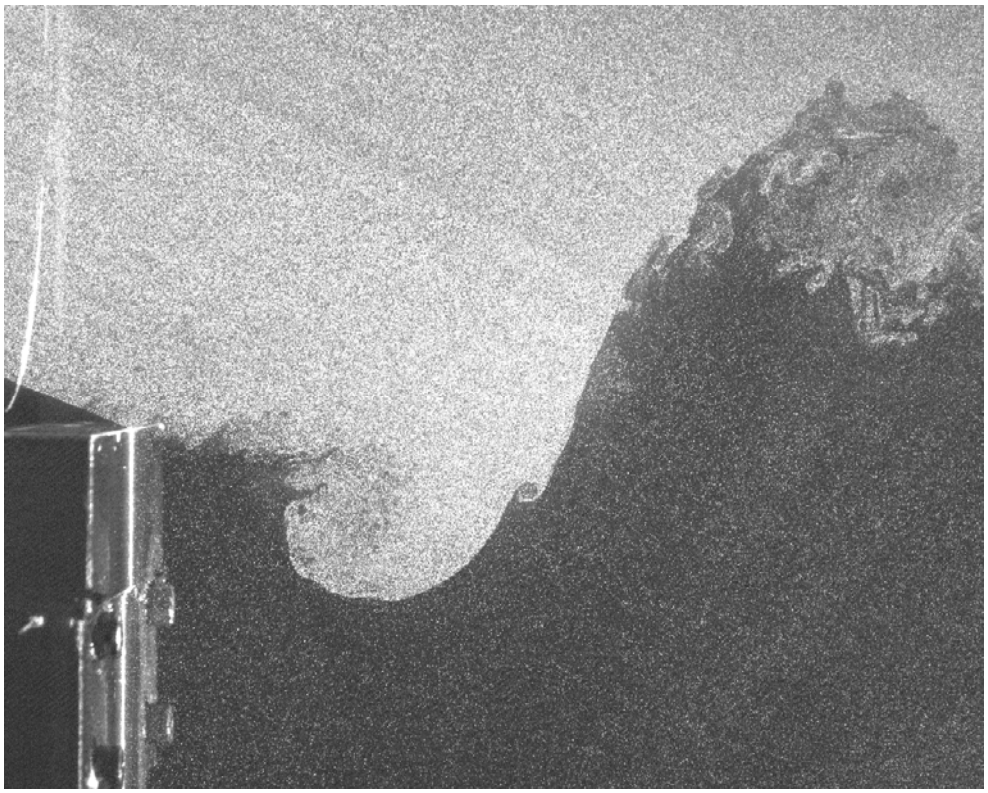

Figure 3.93: PIV Image – 180º Phase Pulsing, Flapping Down

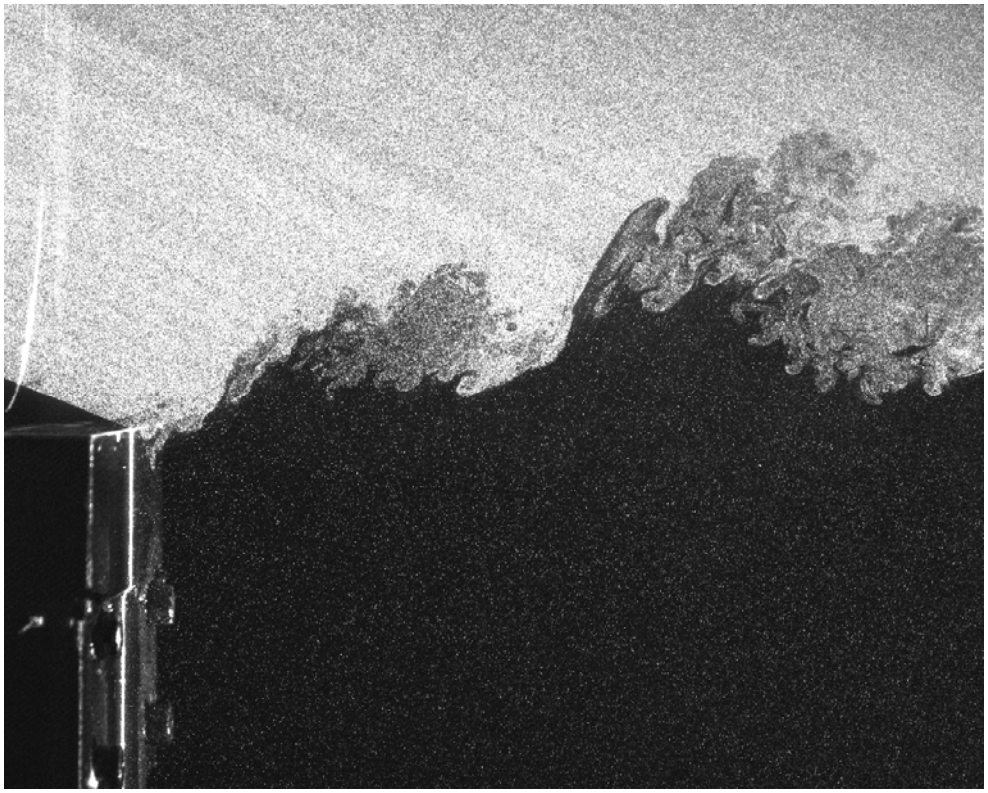

Figure 3.94: PIV Image – 180º Phase Pulsing, Flapping Up

Figure 3.95: PIV Image – 180º Phase Pulsing, Entrainment One Frame Downstream

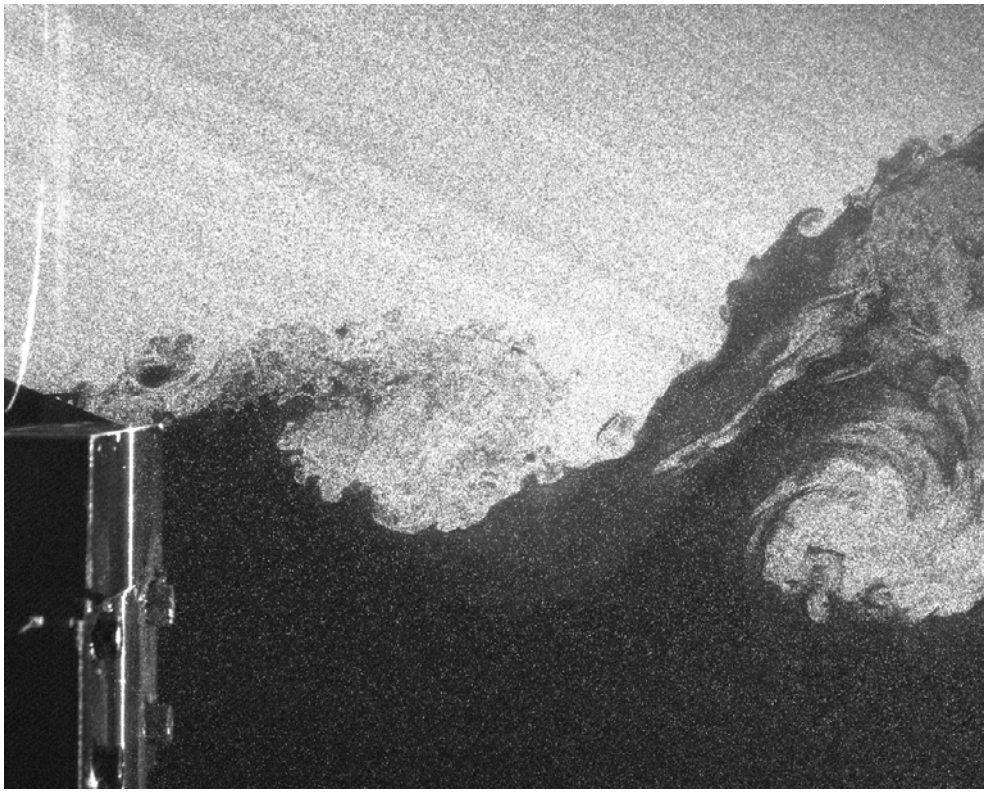

Figure 3.96: PIV Image – 180º Phase Pulsing, 50 Hz

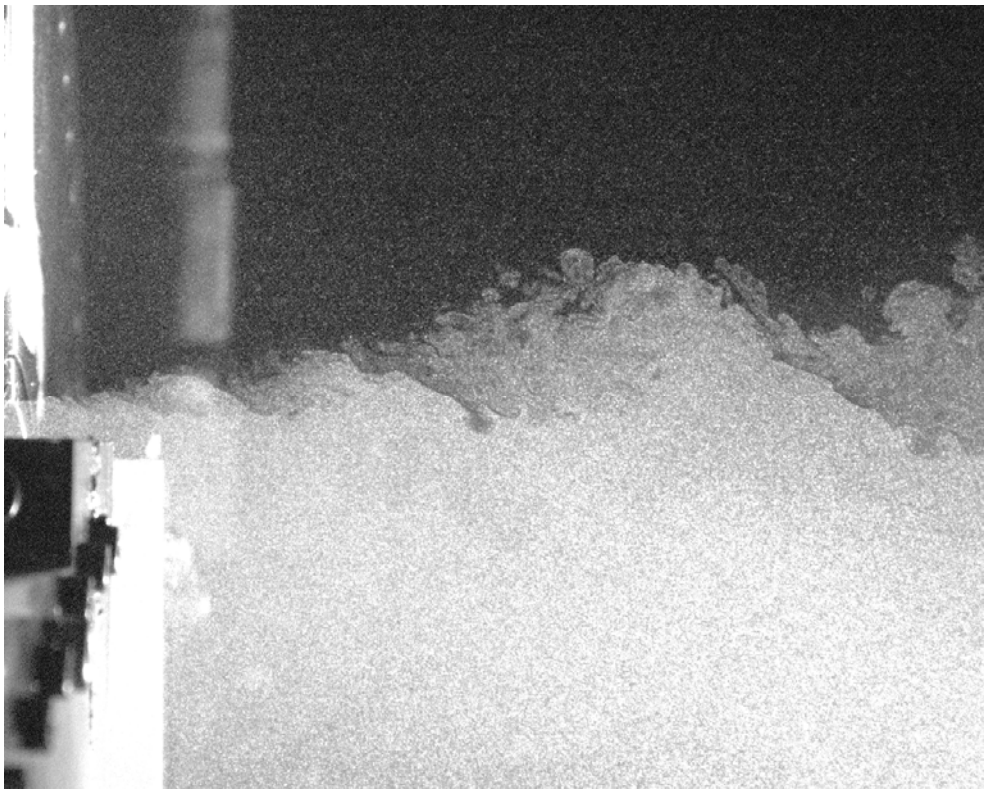

Figure 3.97: PIV Image – 180º Phase Pulsing, Measurement Plane Rotated 90º (i.e. Topview)

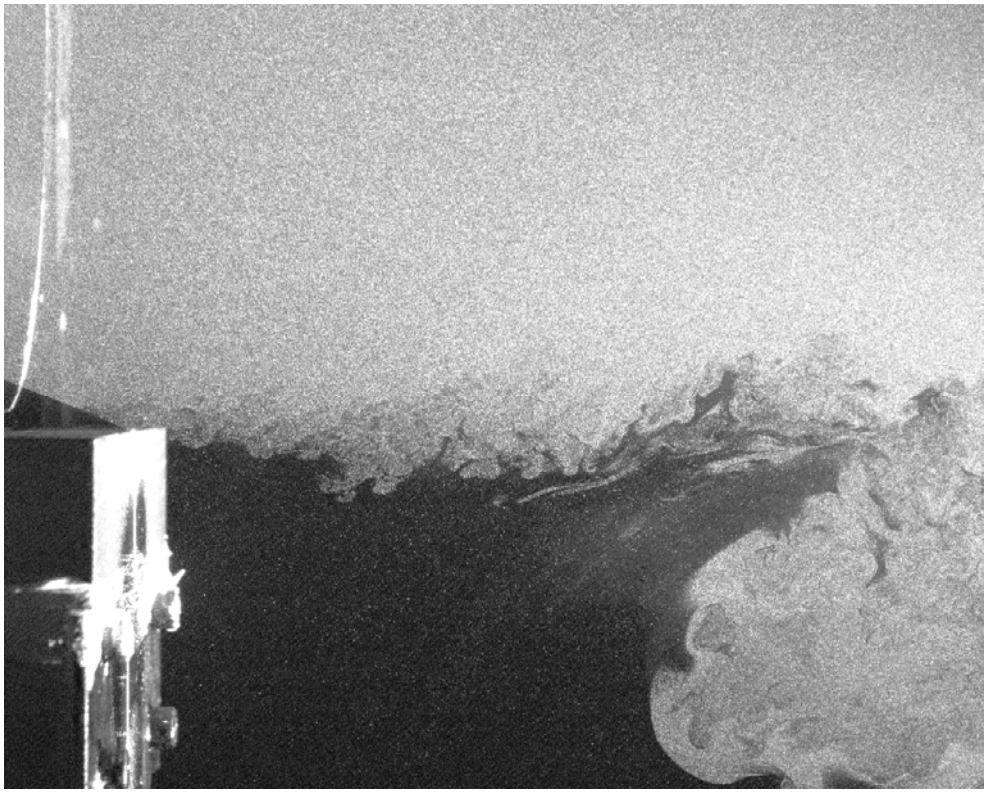

Figure 3.98: PIV Image – 180º Phase Pulsing, 0.04" Nozzles, Same SRMR

Phase Averaged Results

The data from PIV images taken in different regions of the flow field were phase averaged and combined to produce the overall phase averaged flow. Two hundred image pairs were used to produce each phase average. Inverse distance interpolation and data smoothing was used to smooth the overlapping regions. The results confirm the measurements taken with the hotwire and provide more spatial detail of the flow field. The PIV measurements give better spatial resolution than the hotwire measurements (since the hotwire traverse was somewhat coarse in the x-direction) and provide two velocity components in the plane of measurement.

The Natural Jet

Figure 3.99 compares the phase averaged velocity field for the natural jet to an instantaneous velocity field. The ambient air was tagged with fog particles by filling the room before running the experiments. This made it possible to capture the flow vectors in the ambient region as well as the jet. The ambient vectors are not clearly distinguishable in the figure since they are an order of magnitude smaller than the vectors in the main jet flow field. Their existence was confirmed by zooming in on the region (not shown). The streamlines show that they are present and give a sense of their general direction.

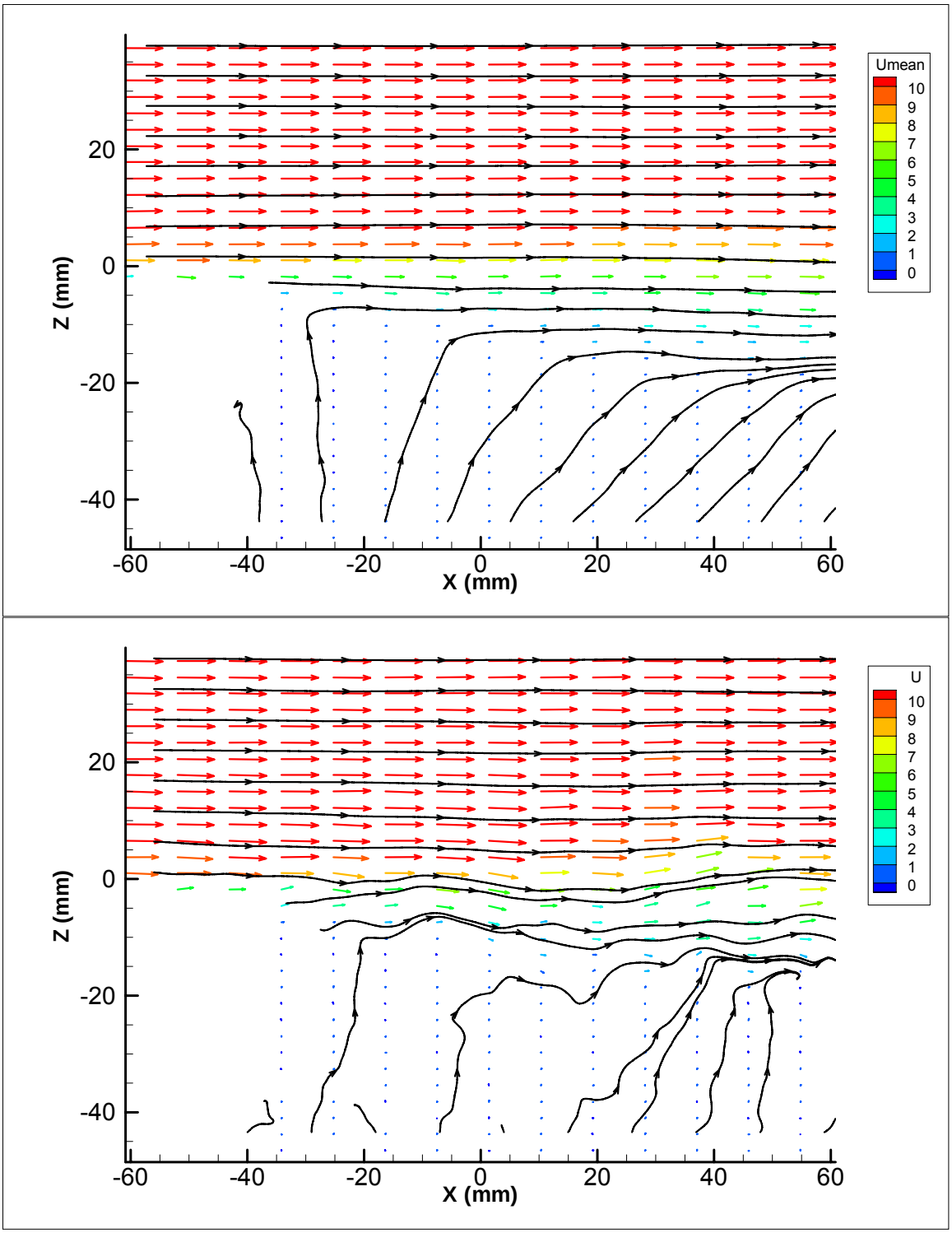

Figure 3.99: Comparison of Average (Top) and Instantaneous (Bottom) Velocity Field Plots for the Natural Jet, U_{exit} = 10m/s

Figure 3.100 shows the phase averaged velocity vector plot for the natural jet. Here the phase averaged date from all eleven regions has been combined, and symmetry of the top and bottom is assumed. Constant velocity contour lines were added to give a sense of the spread of the jet. Note the lack of vortices in the plot. This is expected since large coherent structures do not appear with a regular frequency in the flow. Smaller structures were apparent from the PIV images and instantaneous vector fields, but they were of irregular spacing and shapes. The color contour plot for the natural jet velocity magnitude was previously shown as figure 3.20.

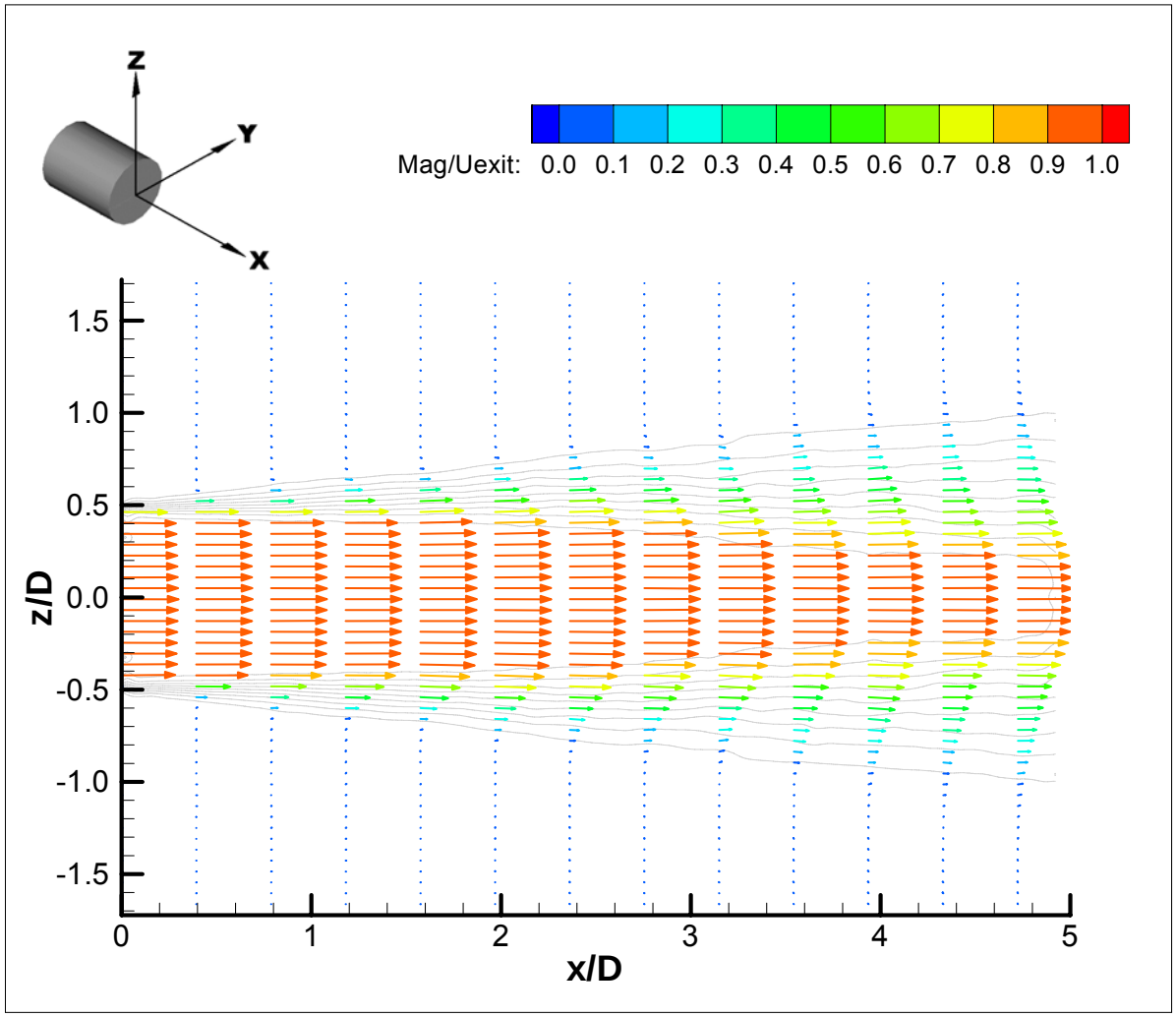

Figure 3.100: Averaged Velocity Vectors for the Natural Jet, U_{exit} = 10m/s

Baseline 0º-phase Forced Jet

Figure 3.101 shows two phase averaged velocity vector plots for the 0º-phase pulsing case at two different phase times. The first plot shows the flow field soon after pulsing has stopped, and the second plot shows the velocity field well into the pulsing cycle. Note the two vortex pairs on the top and bottom sides of the jet around x/D = 0.5 and 3 in the top plot. The vortex clearly grows and moves away from the centerline as it travels downstream, ejecting large amounts of the main flow into the ambient fluid and entraining large quantities of ambient fluid. The vortex is generated just downstream of the actuator after the pulse is turned off. Thus, it isn't just penetration during the on cycle of the pulse that is important, but also the "depenetration" that takes place during the off cycle. That is why pulse offset is such an important mixing parameter. During the phase I tests, increasing the offset of the pulse while keeping the wave top constant resulted in decreased mixing compared to the zero offset case. It is likely that the reason for this is that it resulted in the generation of a smaller vortex since the actuator did not switch completely off. Figure 3.102 is a contour plot of the velocity magnitude for the same case. This plot gives a better idea of the gradients in the flow, but the vortex information is lost.

Baseline 180º-phase Forced Jet

Figure 3.103 shows four velocity vector plots for the 180º-phase optimal pulsing case. Here, too, there are vortical structures, but they are staggered on opposite sides of the flapping jet. The vortices are the same size as those for the 0º-phase case indicating that both the size and positioning of the structures are important to mixing enhancement.

Figure 3.104 is a contour plot of the velocity magnitude. It shows significant mixing enhancement improvements over the equivalent plot for the 0º-phase pulsing case, figure 3.102.

Figure 3.105 is a comparison of the instantaneous and phase averaged vector plots for PIV data taken in section 5 (see figure 2.9). This section corresponds to the flow from x/D = 4 to 5 on the bottom half of the jet. The comparison shows visually that the phase averaged velocity field is a good representation of the instantaneous velocity field. Phased RMS plots confirmed this for the entire flow field (not shown). The phased RMS plots calculated from the PIV data were very similar to those calculated from the hotwire data (figures 3.59 through 3.61).

The Effect of Higher Frequencies

Figure 3.106 examines the effect that increasing the pulsing frequency above the optimum has on mixing enhancement. The optimal frequency case (St = 0.1) clearly penetrates farther into the jet and results in more spreading than the non-optimal case (St = 0.5). Examination of the vector plots (not shown) reveals that both cases produce a vortex downstream of the actuator on the off cycle, but the vortices for optimal frequency case persist farther downstream.

The Effect of Higher Amplitudes

Figure 3.107 shows the result of increasing the pulsing amplitude from just below the saturation level to just above it (SRMR increased from 0.096 to 0.144). The flow fields

are noticeably different in the near field, but by x/D = 5 they appear to be similar. A slice from the contour plot in the y-direction at x/D = 4.8 (figure 3.108) shows that the profiles for the velocity magnitude are in fact very similar. At this particular location, the curve for the lower amplitude forcing (SRMR = 0.096) is slightly lower than the curve for the higher amplitude.

Rotated Planes

The velocity field in the xy-plane was measured by rotating the actuators 90º. This gave a "top view" of actuation, compared to the usual "side view". Results were also obtained for a 45º rotation, but are not shown here. Figures 3.109 and 3.110 show the top view phase averaged PIV results for the 0º and 180º-phase cases respectively. Note that the velocity at the jet exit was not measured since the actuators were blocking the flow. In both cases the jet seems to fork into two distinct branches of higher velocity flow on each side of the centerline in the neighborhood of x/D = 2. This bifurcation suggests that the center of the jet has been penetrated by the pulse and is similar to the flow pattern obtained for a jet with mechanical tabs in which a counter rotating vortex pair has been formed. The bifurcation was confirmed by hotwire measurements, and is thus not a result of bias in the PIV measurements due to the lack of seeding from the actuators. It is uncertain exactly how far the two branches of high velocity fluid extend since measurements were not made in enough phase increments. However, it is clear that the flow evens out rather quickly. As previously reported, by x/D = 10 turbulence intensity and spectral measurements suggested that the flow is well mixed at all locations.

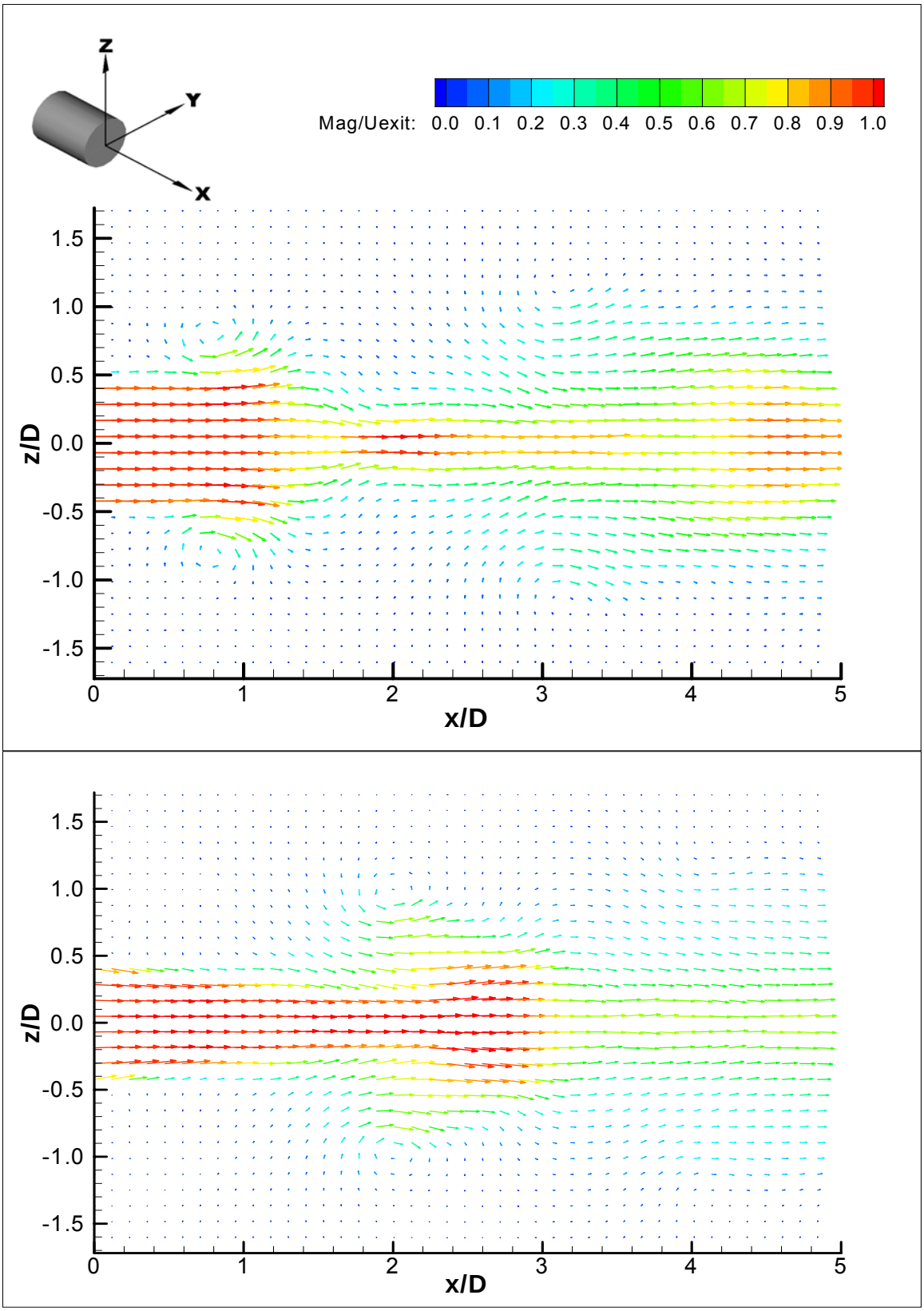

Figure 3.101: Vector Plots for 0-Phase Forcing, U_{exit} = 10 m/s, 0.08" Actuators, St = 0.15, SRMR = 0.096

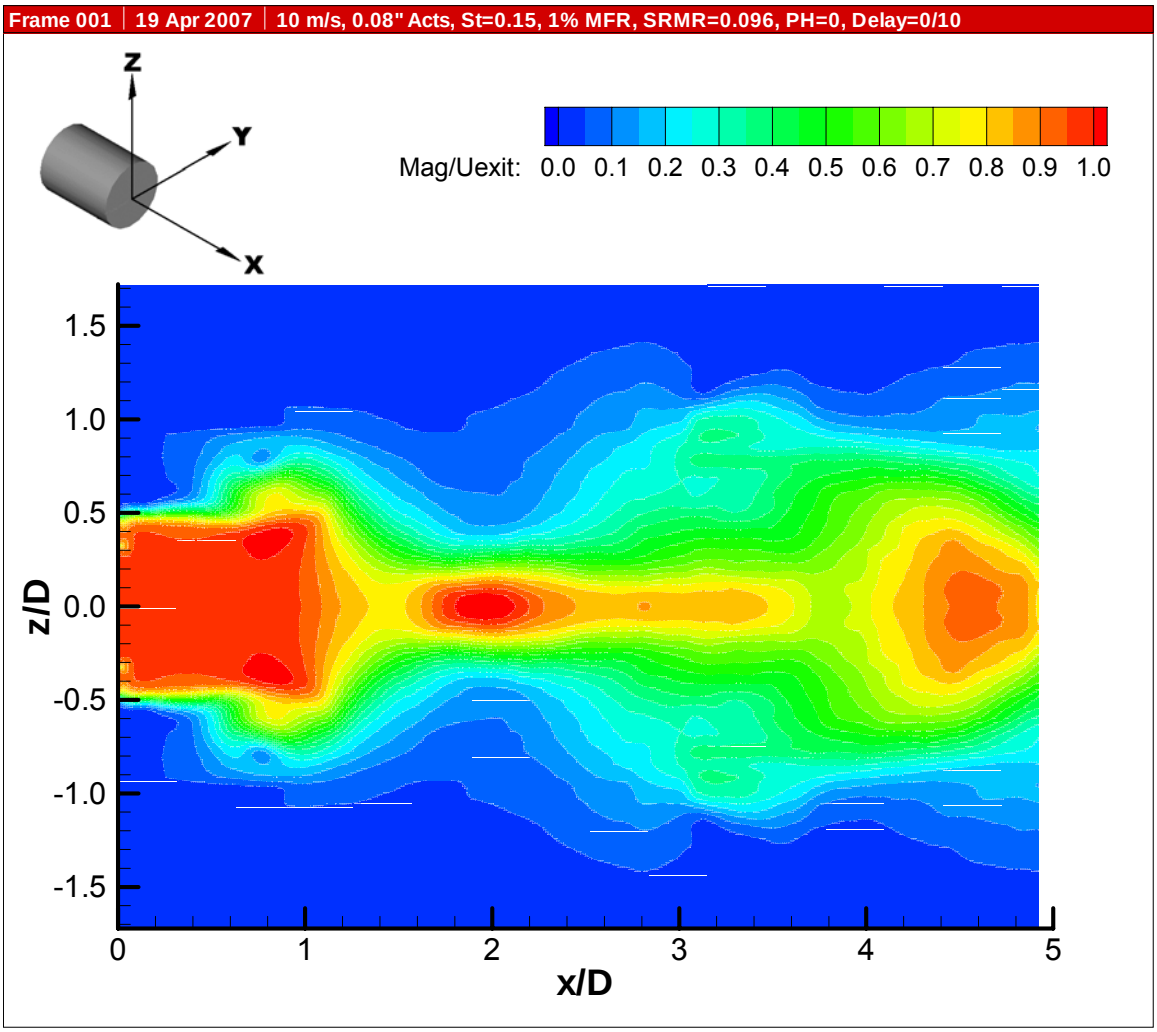

Figure 3.102: Contour Plot for 0-Phase Forcing, U_{exit} = 10 m/s, 0.08" Actuators, St = 0.15, SRMR = 0.096

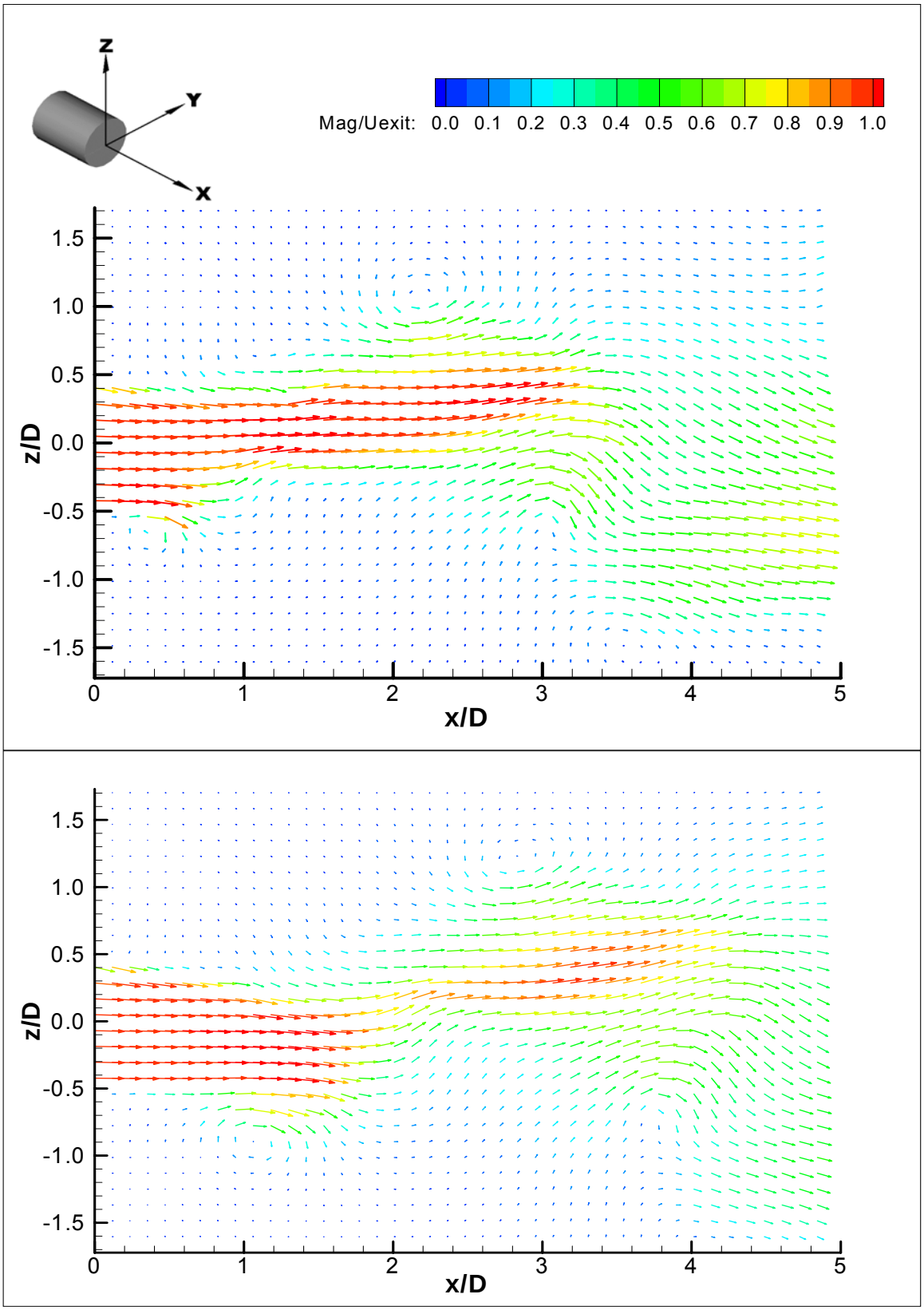

Figure 3.103a: Vector Plots for 180-Phase Forcing, U_{exit} = 10 m/s, 0.08" Actuators, St = 0.1, SRMR = 0.096

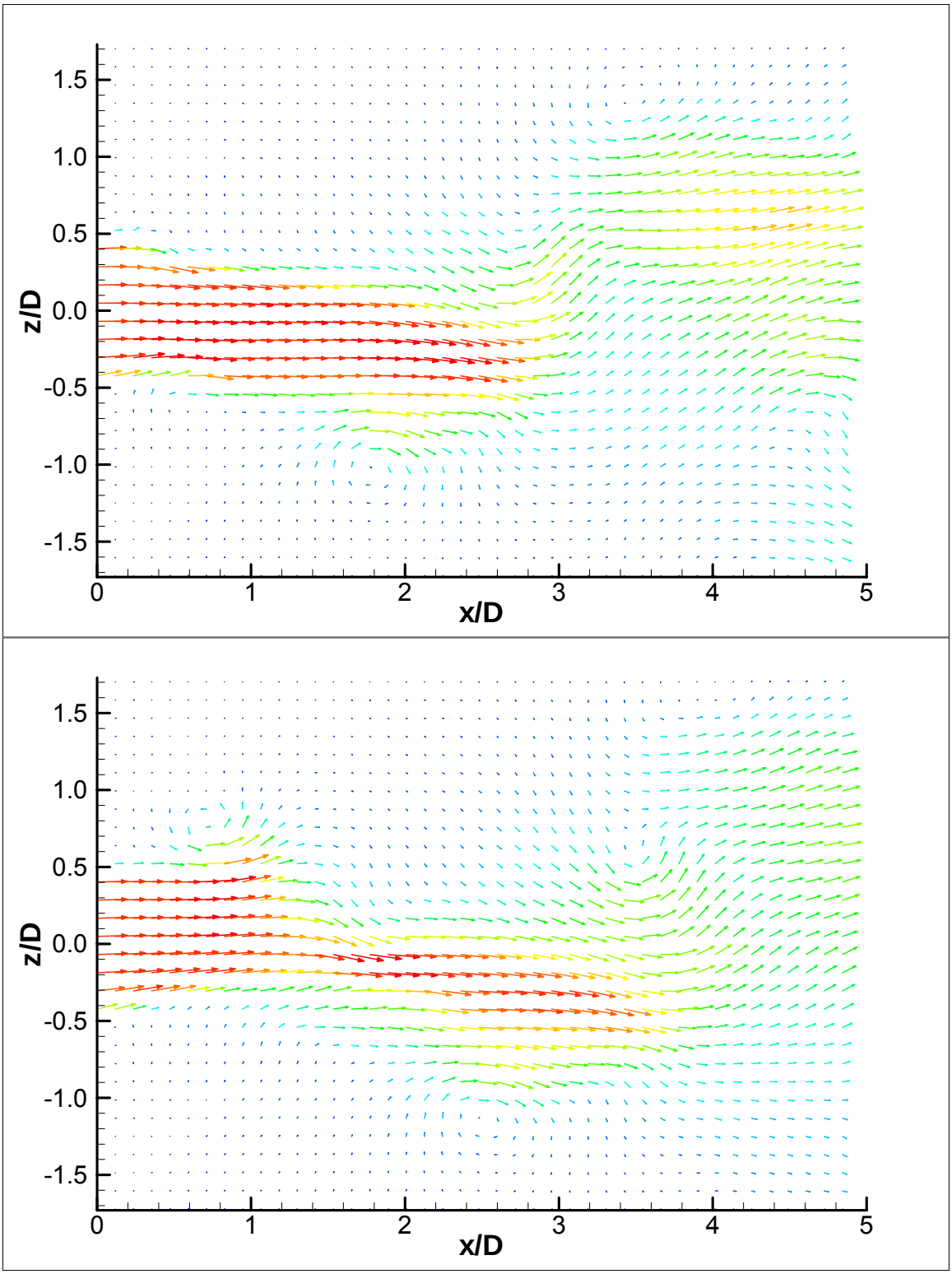

Figure 3.103b: Vector Plots for 180-Phase Forcing, U_{exit} = 10 m/s, 0.08" Actuators, St = 0.1, SRMR = 0.096

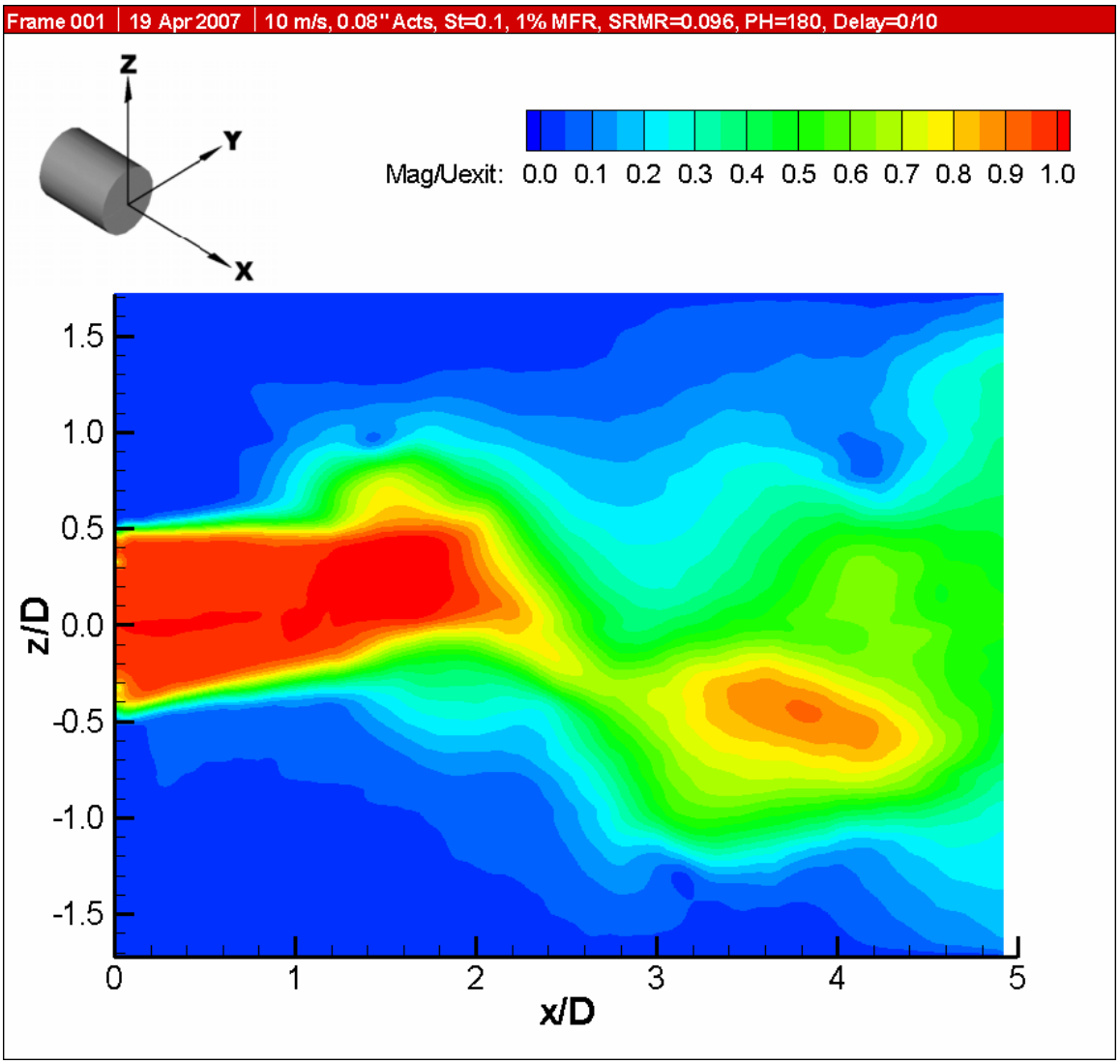

Figure 3.104: Contour Plot for 180-Phase Forcing, U_{exit} = 10 m/s, 0.08" Actuators, St = 0.1, SRMR = 0.096

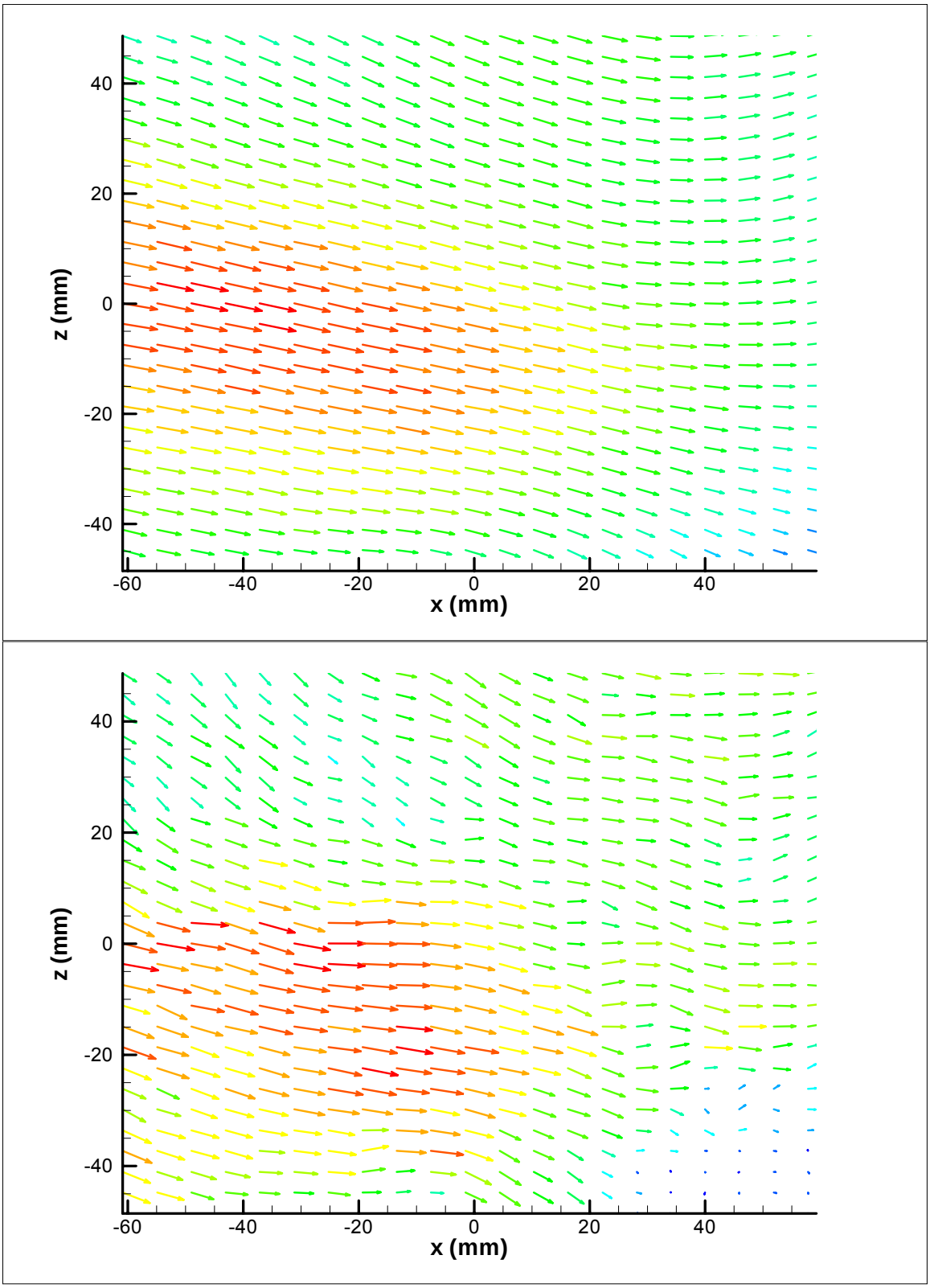

Figure 3.105: Comparison of Instantaneous (bottom) and Phase Averaged (top) Vector Plots at x/D = 4 to 5 for 180-Phase Forcing, U_{exit} = 10 m/s, 0.08" Actuators, St = 0.1, SRMR = 0.096

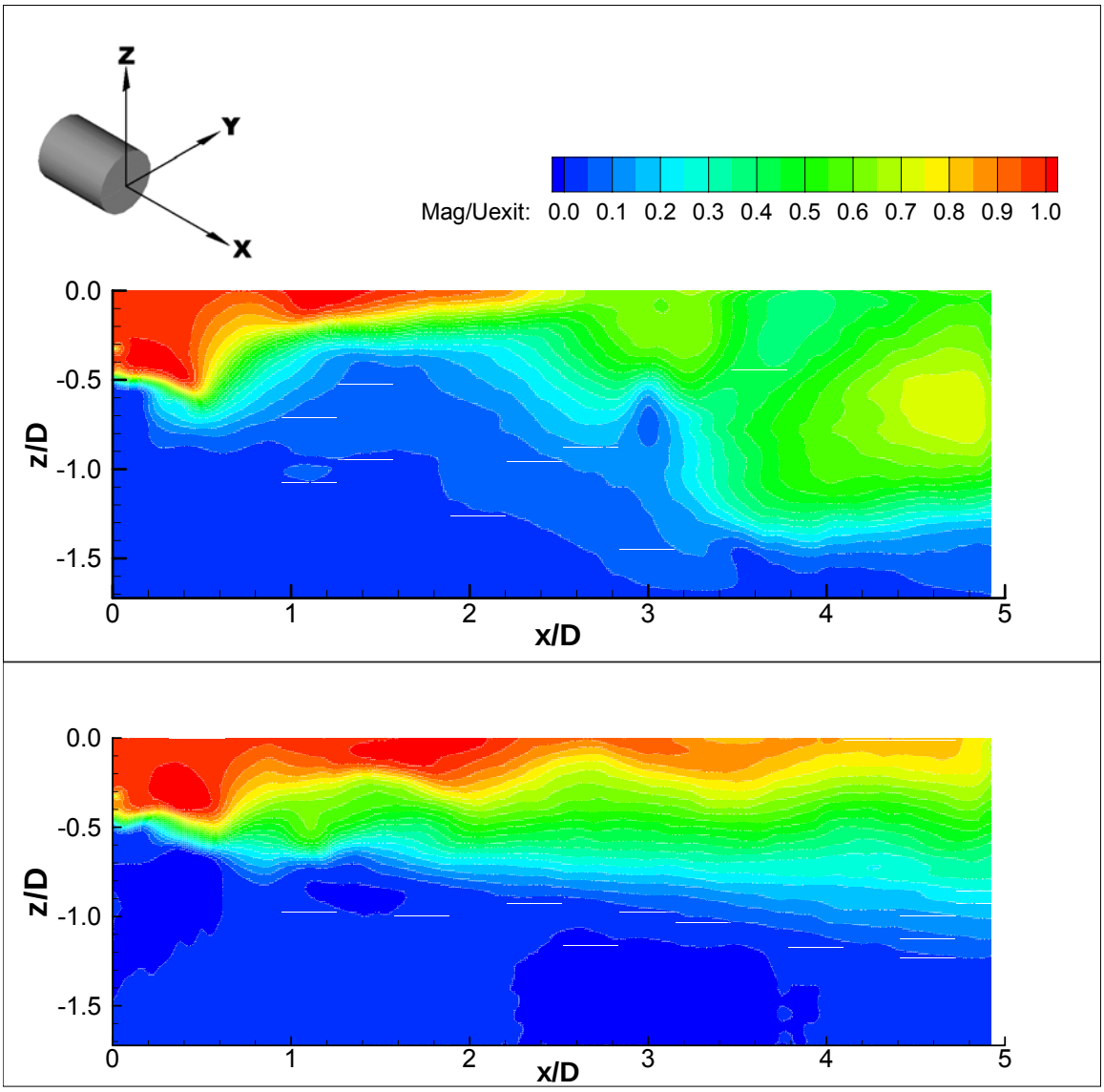

Figure 3.106: Effect of Higher Frequency Pulsing, St = 0.1 (top) vs. St = 0.5 (bottom) for 180-Phase Forcing, U_{exit} = 10 m/s, 0.08" Actuators, SRMR = 0.096

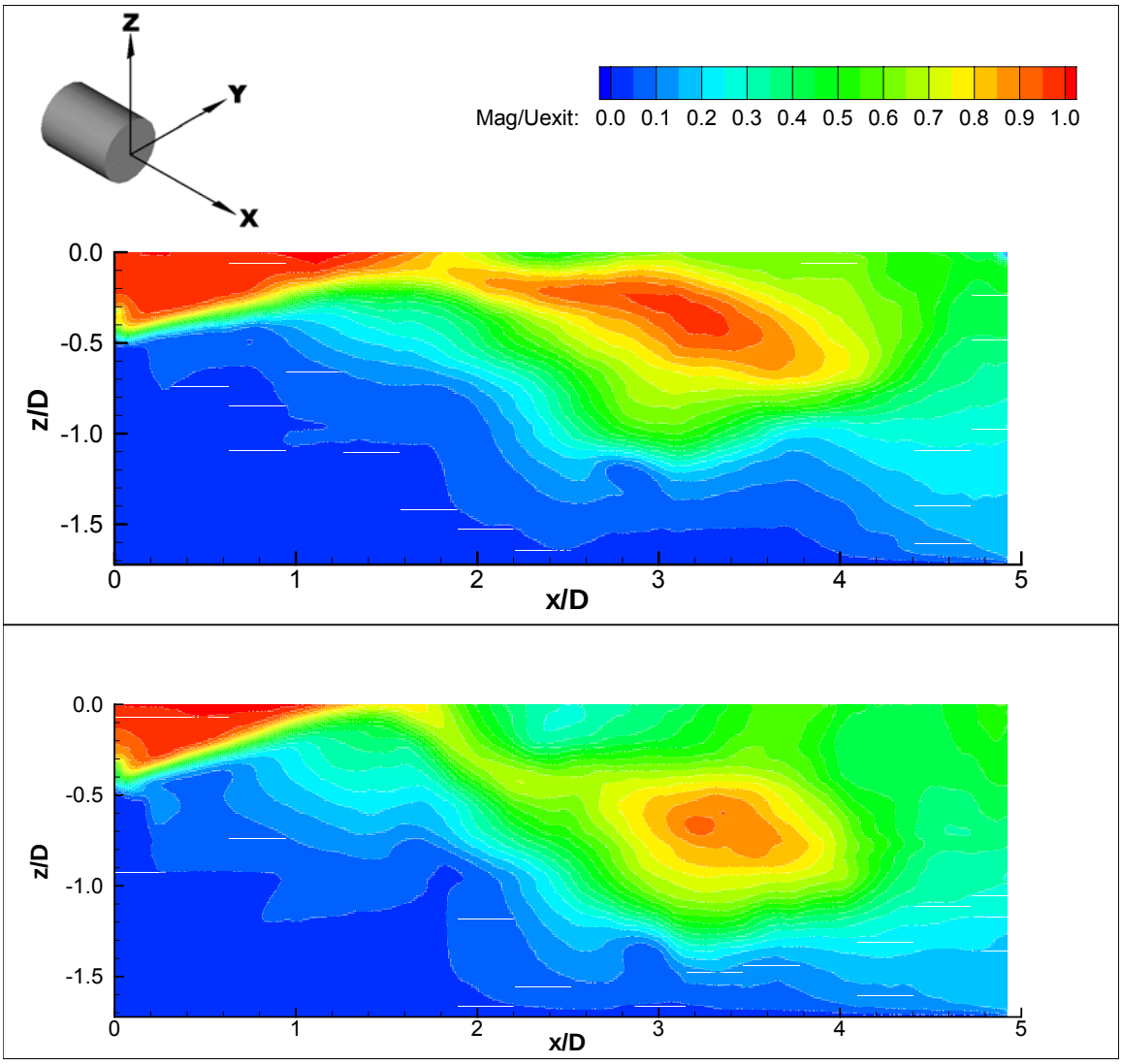

Figure 3.107: Effect of Higher Amplitude Pulsing, SRMR = 0.096 (top) vs. SRMR = 0.144 (bottom) for 180-Phase Forcing, U_{exit} = 10 m/s, 0.08" Actuators, St = 0.1

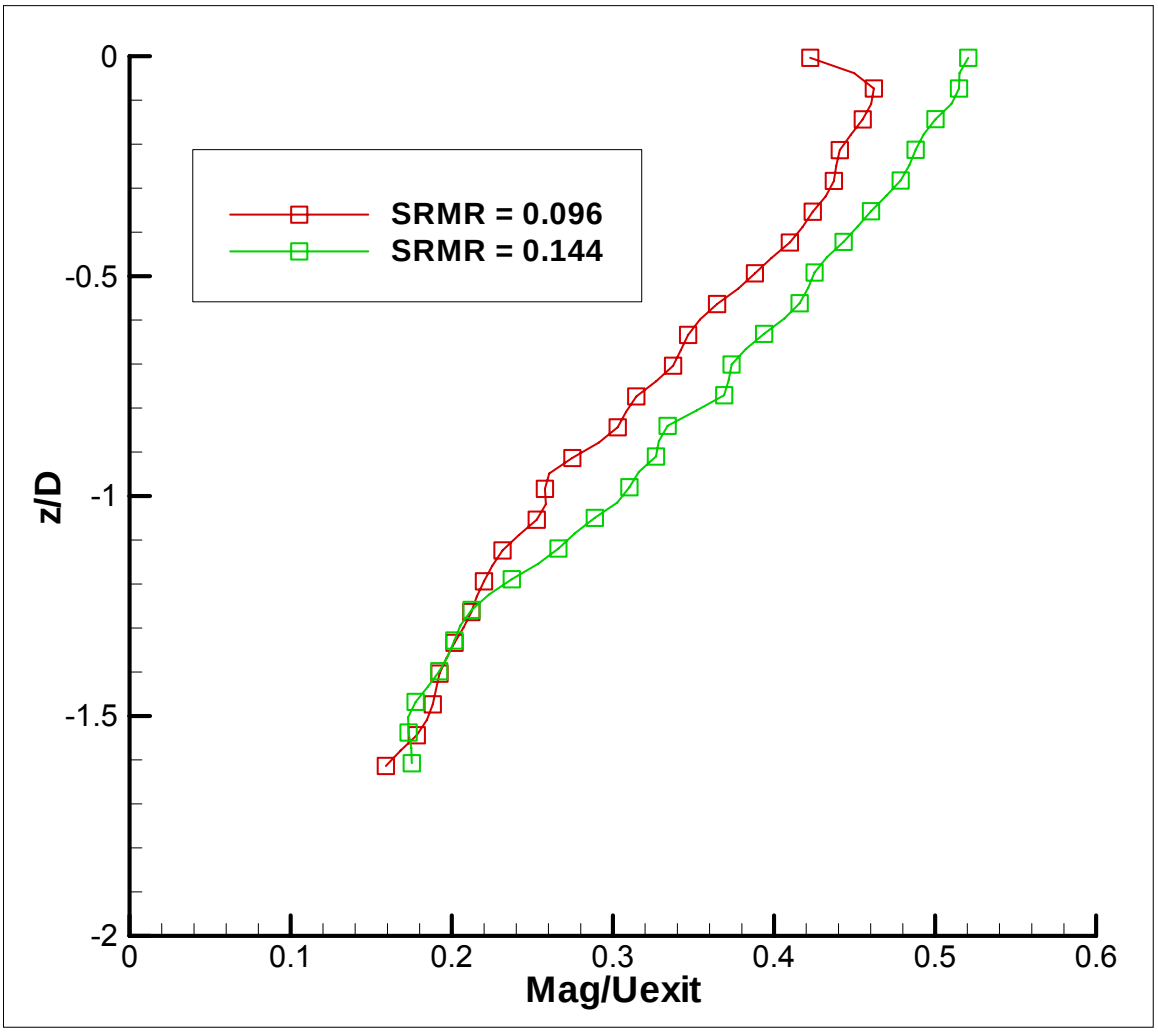

Figure 3.108: Comparison of Vertical Velocity Profiles for two Amplitudes, Curves are Slices of the Velocity Magnitude from Figure 3.107 at x/D = 4.8 for the Lower Half of the Jet, 180-Phase Forcing, U_{exit} = 10 m/s, 0.08" Actuators, St = 0.1

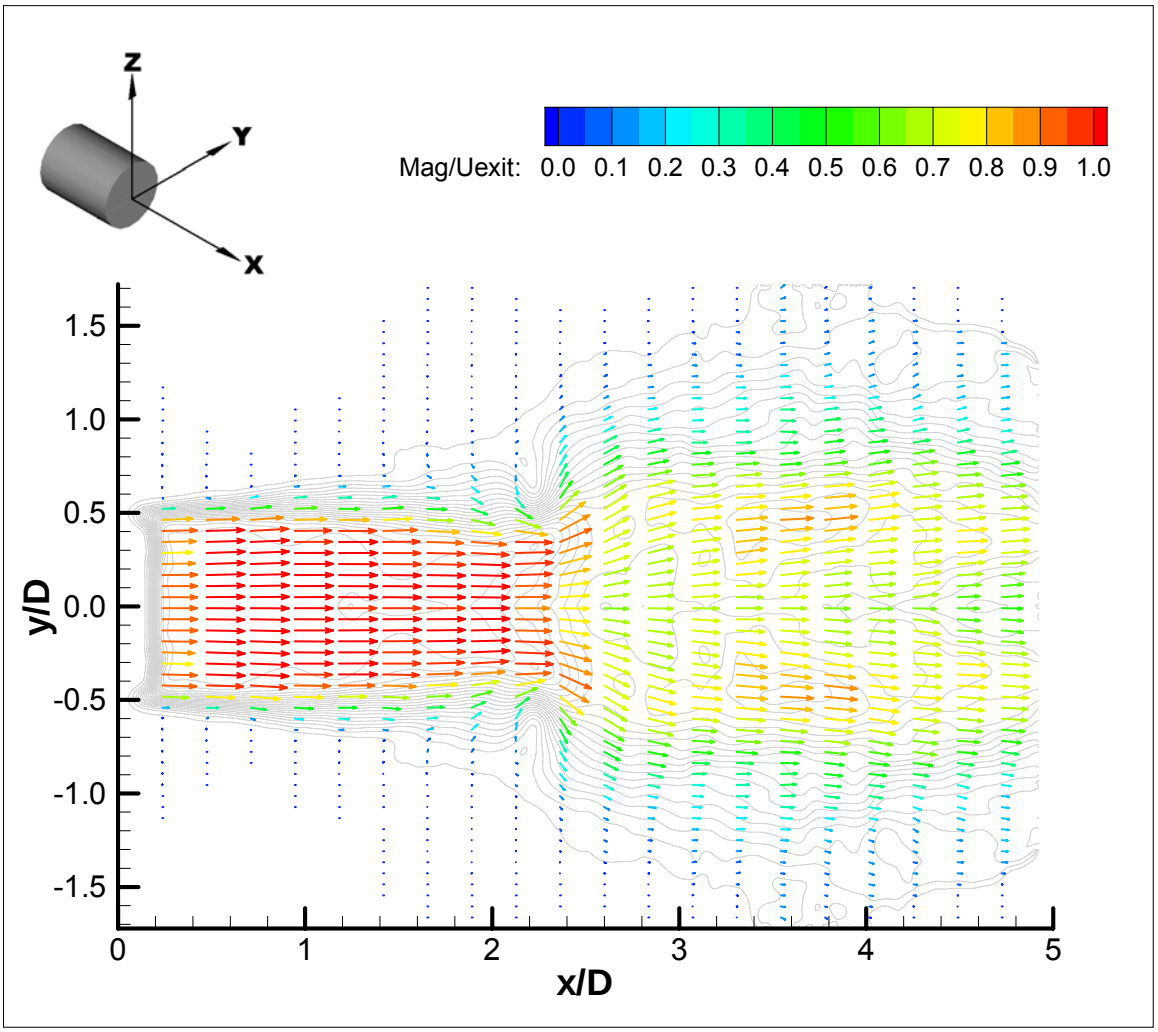

Figure 3.109: Top View Phase Averaged Velocity Vectors for 0º-phase Pulsing, U_{exit} = 10 m/s, 0.08" Actuators, St = 0.1

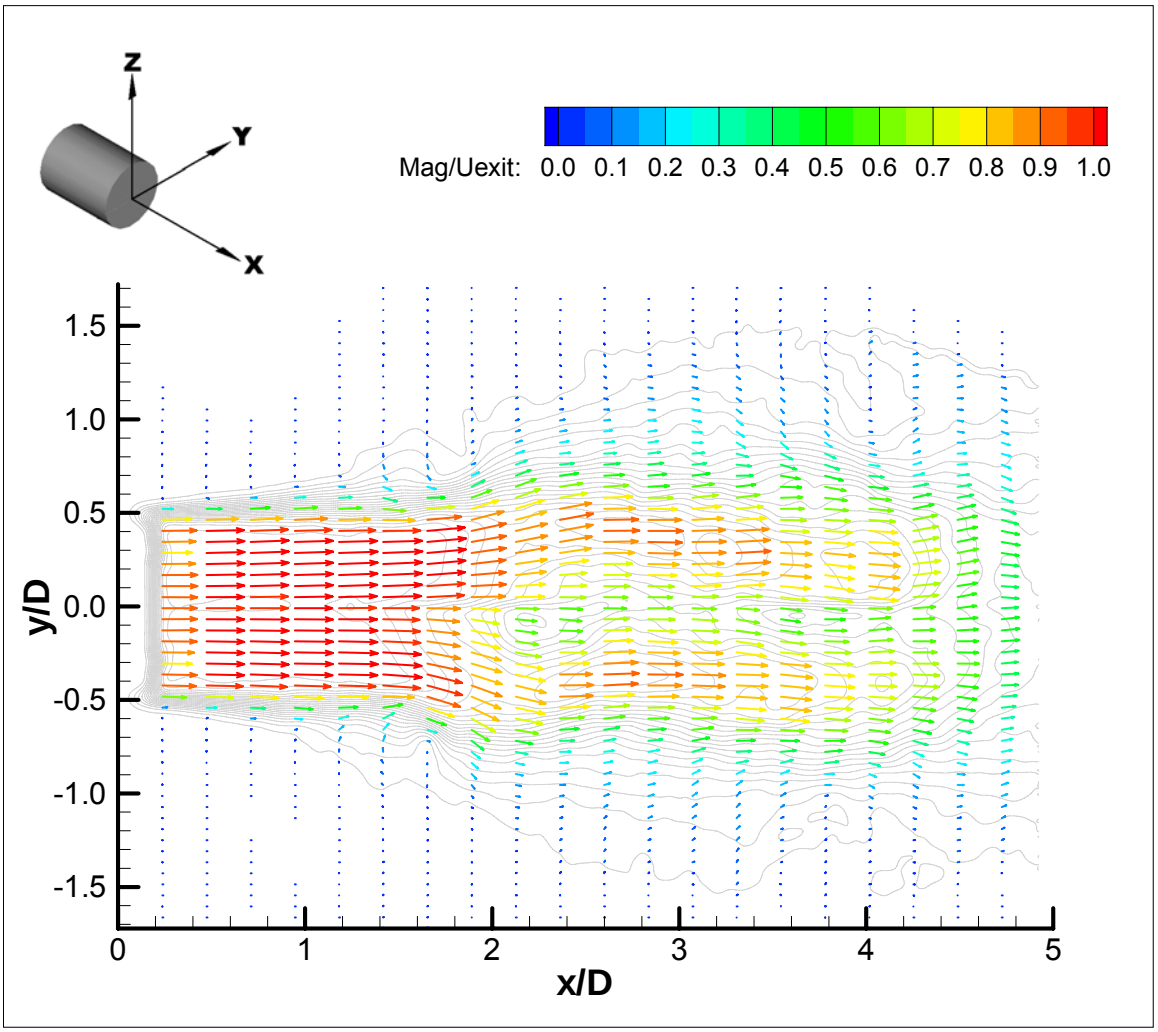

Figure 3.110: Top View Phase Averaged Velocity Vectors for 180º-phase Pulsing, U_{exit} = 10 m/s, 0.08" Actuators, St = 0.1

It is also clear from figure 3.109 that the 0º-phase jet initially spreads more in the y-direction than the z-direction. On the other hand, the 180º-phase jet spreads at a similar rate to the natural jet in the y-direction and rapidly in the z-direction. Cross traverses downstream revealed that by x/D = 10 the 0º-phase jet has almost become axisymmetric again, while the 180 phase jet is still very asymmetric.

Different Nozzles Sizes with Equal Momentum Ratios

The importance of momentum ratio was demonstrated by comparing the velocity fields produced by two different actuator nozzle sizes at similar momentum ratios. The 180º-phase baseline case, which used 0.08" nozzles, was compared against three separate cases with 0.04" nozzles, each at a slightly different amplitude. The following list summarizes the configurations that were compared:

- Baseline: 0.08" Nozzle, St = 0.1, SRMR = 0.0961 (1% MFR)
- Case 1: Lower SRMR, 0.04" Nozzle, St = 0.1, SRMR = 0.0829 (0.61% MFR)
- Case 2: Equal SRMR, 0.04" Nozzle, St = 0.1, SRMR = 0.0965 (0.71% MFR)
- Case 3: Higher SRMR, 0.04" Nozzle, St = 0.1, SRMR = 0.1101 (0.81% MFR)

The contour plot of velocity magnitude for the baseline case was previously given in figure 3.104. The contour plots for the three comparison cases are not shown, since they are similar to the baseline case. Instead, a *difference plot* was generated for each case in order to compare it with the baseline. To create a difference plot the velocity magnitude at each point in the flow field for each case was subtracted from the corresponding velocity magnitudes for the baseline case. The difference plot indicates the amount that each case diverges from the baseline. Since the color blue represents the lowest values, a blue plot signifies that there is little difference between the test case and the baseline. The three difference plots are shown in figure 3.111. The nominal cases are: slightly lower, equal, and slightly higher.

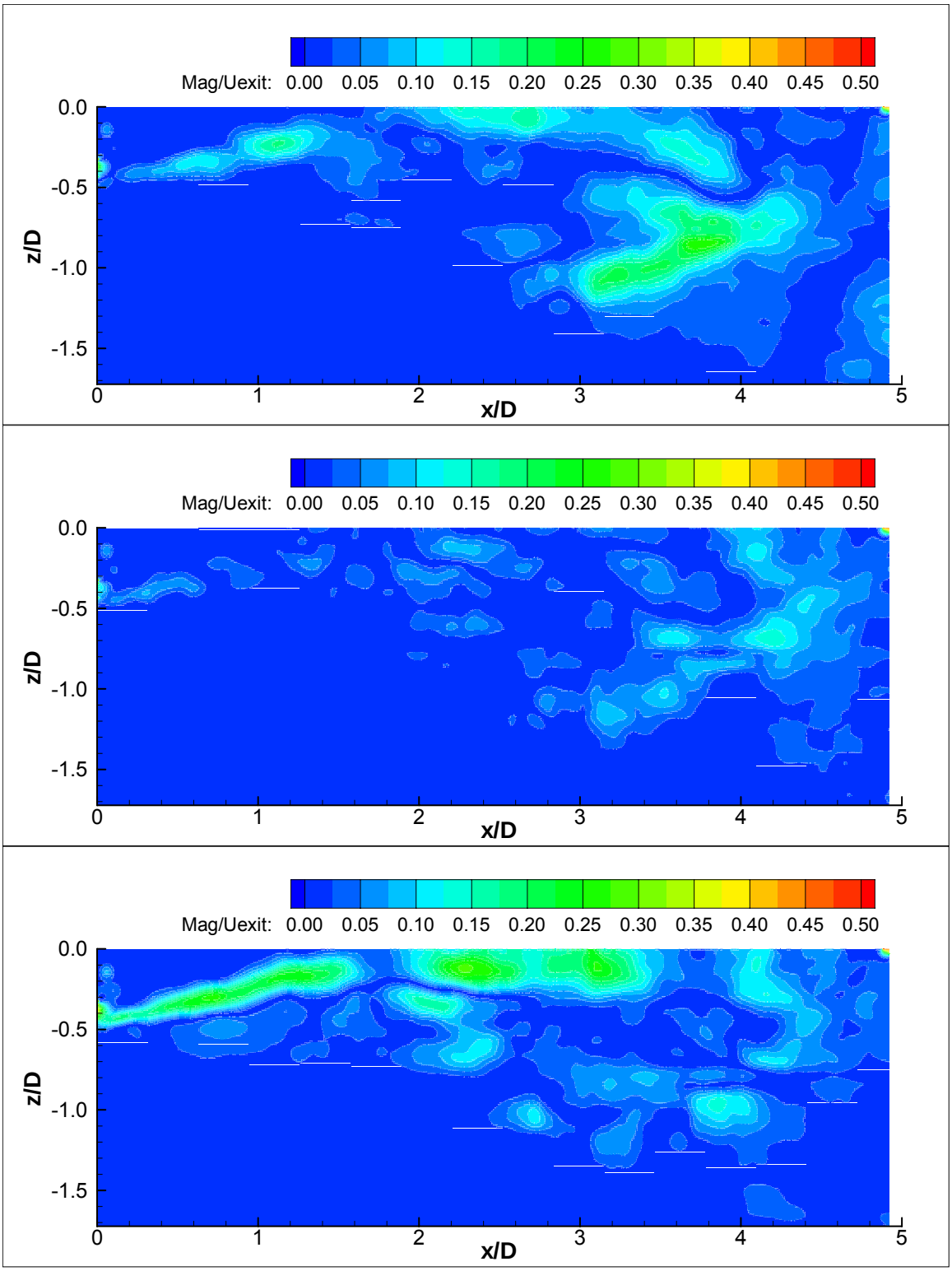

Figure 3.111: Difference Plots for Baseline 0.08" Actuators compared to 0.04" Actuators with Momentum Ratios that were: Slightly Lower (top), Equal (middle), and Slightly Higher (bottom); 180º-phase Pulsing, U_{exit} = 10 m/s, St = 0.1

The center plot clearly has the least difference with the baseline case. The key result is that different actuator nozzle sizes with the same momentum ratio have virtually identical effects on the flow field and therefore mixing enhancement as well.

Momentum Thickness Comparison

The flow field data from the PIV measurements was integrated to calculate the momentum thickness of the jet for each of the three baseline cases and also for blowing. For the forced cases, the momentum thickness was a function of both the downstream distance and the cycle phase. The results are shown in figure 3.112 and cycle averaged values are given for the forced cases. The plot shows that there is a clear difference between the natural jet and blowing cases vs. the pulsed cases. The deviation takes place almost immediately downstream of the actuation region and by x/D = 5 it is quite pronounced. The 0 and 180º-phase cases are very similar until x/D = 2, at which point the thickness for the 180º-phase case grows more sharply. Figure 3.113 shows how the phase averaged momentum thicknesses for the 180º-phase case compare to the momentum thickness averaged over the whole cycle.

Penetration Depth

The penetration depth of the pulse was calculated as the location where velocity in the z-direction, W, was maximum. The penetration depth was first calculated from actuator seeded PIV images in the jet/actuator interaction zone which extends from the jet nozzle exit down to about 0.25D (or 25 mm). Figure 3.114 shows the results at different time

increments starting soon after the actuator began pulsing (~0 ms) up to 13.3 ms. Note that the penetration reaches a maximum somewhere between 6 and 8 ms. This was true for all pulsing frequencies. Therefore, in this region there is no difference for all pulsing frequencies below about 125 Hz (the inverse of 8 ms).

Since mixing was clearly a function of frequency, it was necessary to examine the penetration depth for a larger field. A good way to do this is to examine contour plots of W, the velocity in the vertical direction. These plots are shown for Strouhal numbers of 0.1, 0.3, and 0.5 in figure 3.115. A good deal of information can be gathered from these plots. First, they show how the extent of penetration downstream varies with pulsing frequency. They give insight into why the higher frequencies do not penetrate as far. In addition to having a lower total impulse due to a shorter pulsing time, the lower frequency pulses appear to be drawn toward the vortices that form just downstream of the actuator on the pulse off cycle. The vortices correspond to the pair red and blue fluid blobs indicating upward and downward flow, and the centers are located at x/D = 2.5, 0.9, and 0.4 for the St = 0.1, 0.3, and 0.5 cases respectively. The location of the vortices was verified by comparing these contour plots to the corresponding vector plots (not shown). It is clear from the bottom two figures that the vortex works against the pulse by pulling it in, whereas for the St = 0.1 case the vortex has traveled too far downstream to have any effect on the pulse penetration.

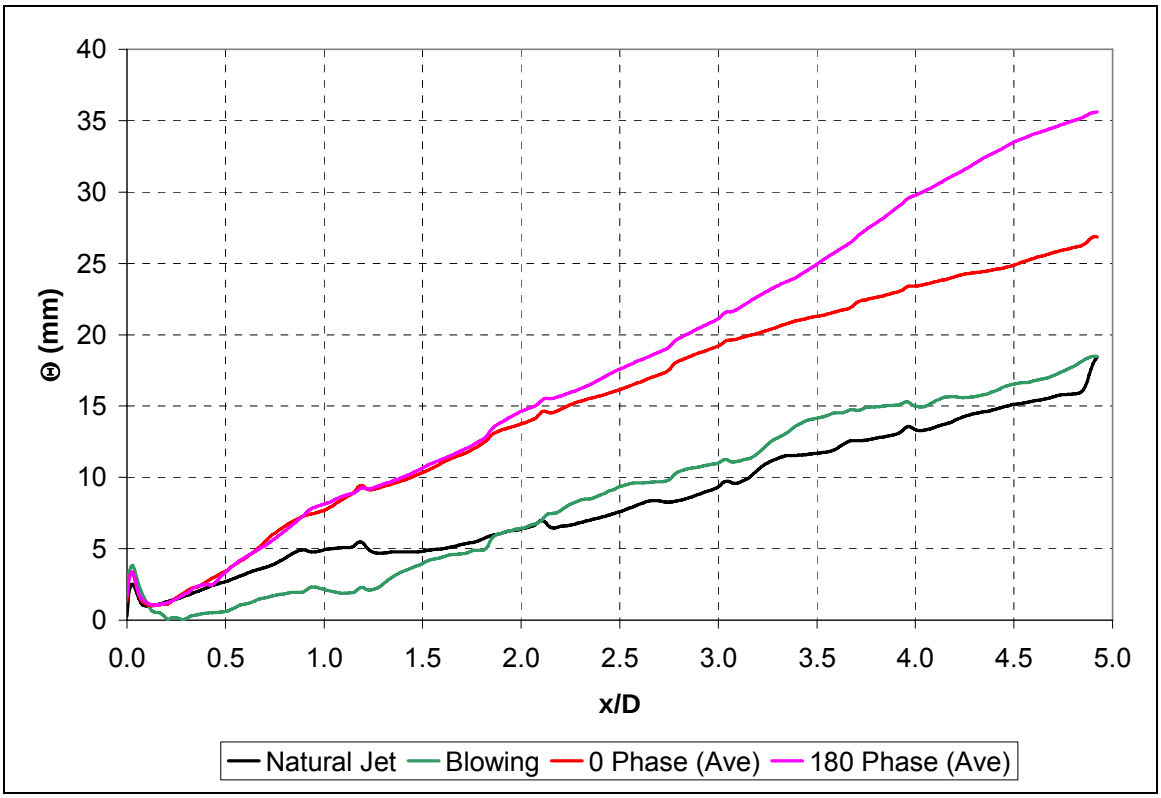

Figure 3.112: Momentum Thicknesses of the Natural and Forced Jet, U_{exit}=10 m/s, 0.08" Acts, SRMR=0.096, Optimal Pulsing Frequencies

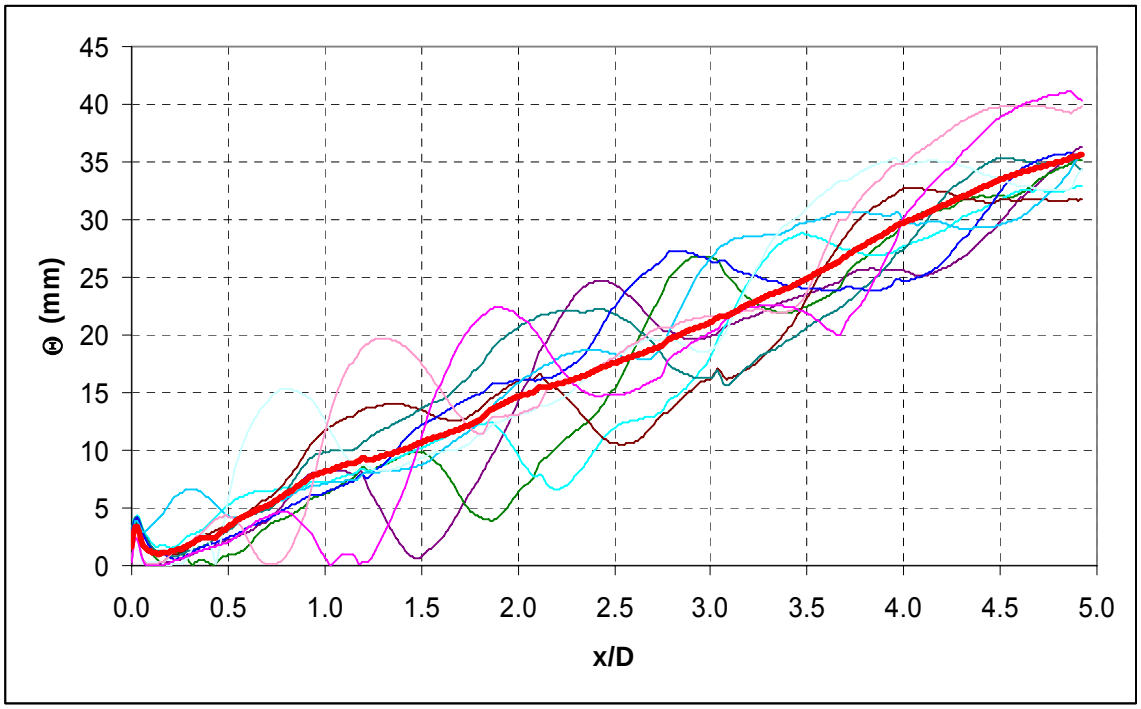

Figure 3.113: Example of the Variation of Instantaneous Momentum Thickness (Average in Red), 0.08" Acts, 180°-Phase Pulsing, St = 0.1, SRMR = 0.096, U_{exit} = 10 m/s

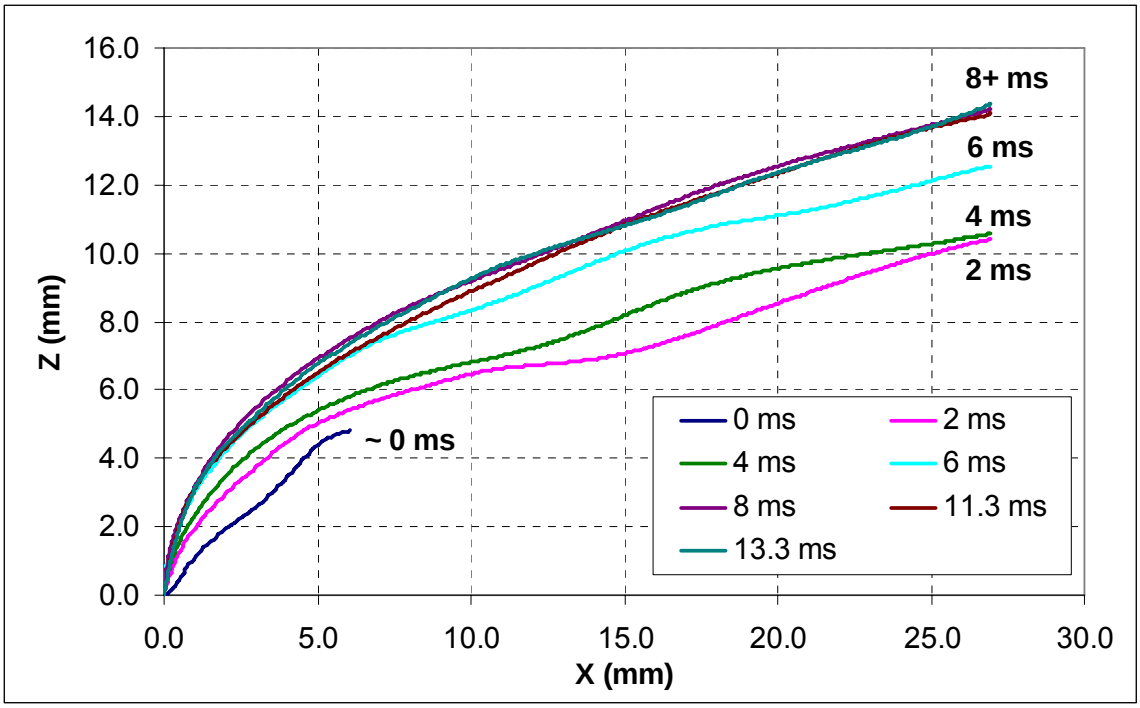

Figure 3.114: Penetration Depth in the Near Field as a Function of Time, 0.08" Acts, 180°-Phase Pulsing, SRMR = 0.096, U_{exit} = 10 m/s

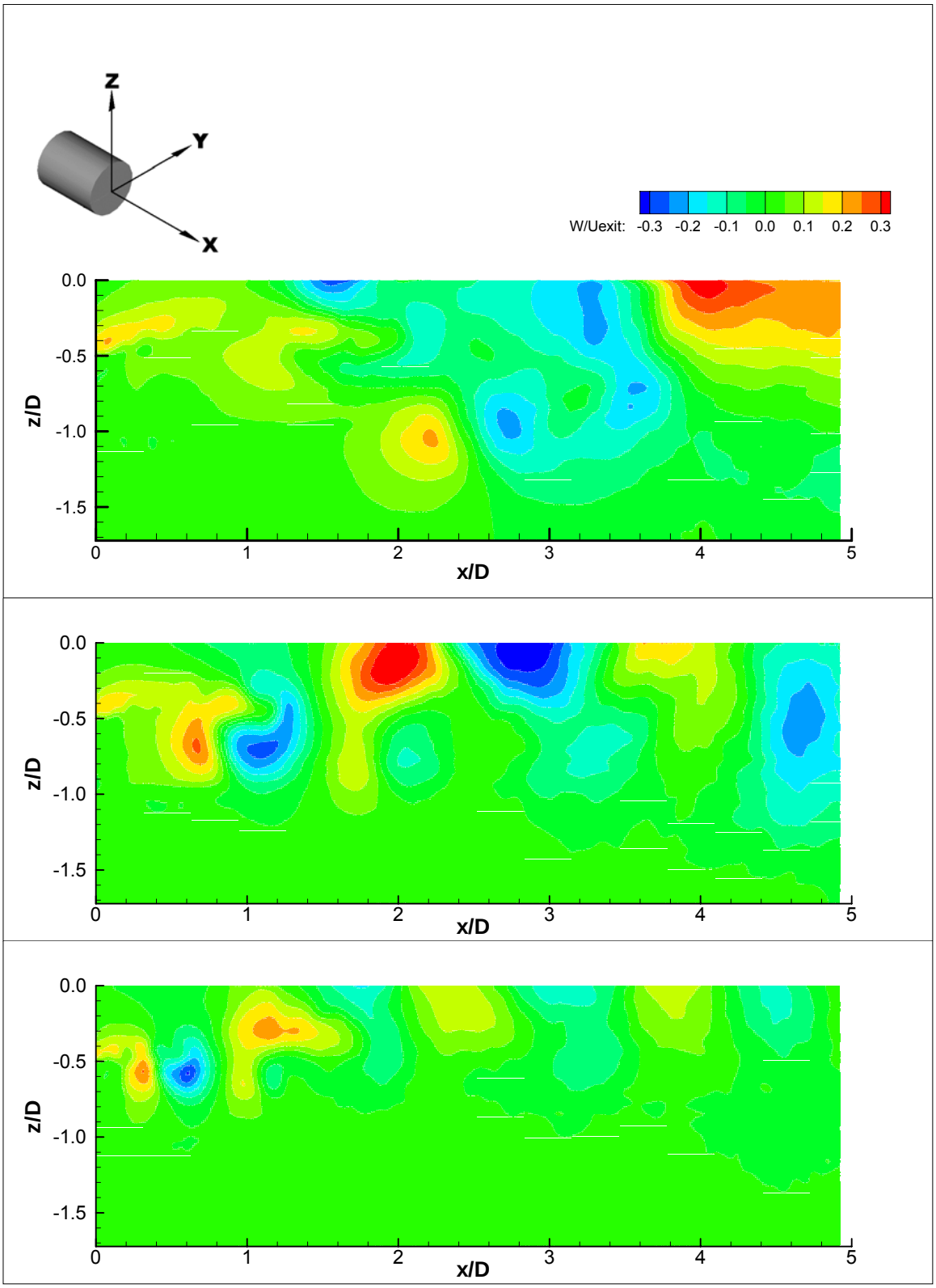

Figure 3.115: Contours of W, Velocity in the z-Direction for St = 0.1 (top), St = 0.3 (middle), and St = 0.5 (bottom), , 0.08" Acts, 180°-Phase Pulsing, SRMR = 0.096, U_{exit} = 10 m/s

The plots also show the decay rate of the strength of the vortices. First, it must be assumed that the magnitude of W correlates with the vorticity, which is in fact the case. In the two higher frequency cases, the vortices should be in close proximity to each other, and in the middle contour plot it is clear that there is some strength left in the vortex around x/D = 1.9. However, it is nowhere near as strong as the vortex at x/D = 2.5 in the top contour plot. The key conclusion is that the vortex for the St = 0.1 case persists further downstream.

Figure 3.116 shows the evolution of the phase averaged W-components of velocity in the xz-plane at different points in time. The plots read left to right and top to bottom going forward in time. They show the formation of the vortices on the off cycle, their progression, and death around x/D = 4. They also show the initiation of z-momentum into the flow, its penetration, and rapid growth as it moves through the center of the jet. The growth may be partly due to the induction of velocity into the core by a counter rotating vortex pair formed as a result of the penetration.

Vorticity Fields

Figure 3.117 shows the phase averaged vector and vorticity fields in the interaction region near the jet exit for the St = 0.1 and 0.3 cases. Once again the effect of the vortex on the pulse for the higher frequency case is to draw it in. Comparing the two plots, it appears that the vorticity for the St = 0.1 case is slightly stronger overall than for the St = 0.3 case, but the difference is not large. Cases for even higher frequencies (not shown) also result in vorticity of comparable strength. Vorticity for instantaneous velocity fields

(as opposed to phase averaged as shown here) did not suggest anything to the contrary either. Thus the downstream persistence of the vortex appears to be the major difference between the optimal frequency and higher frequency cases.

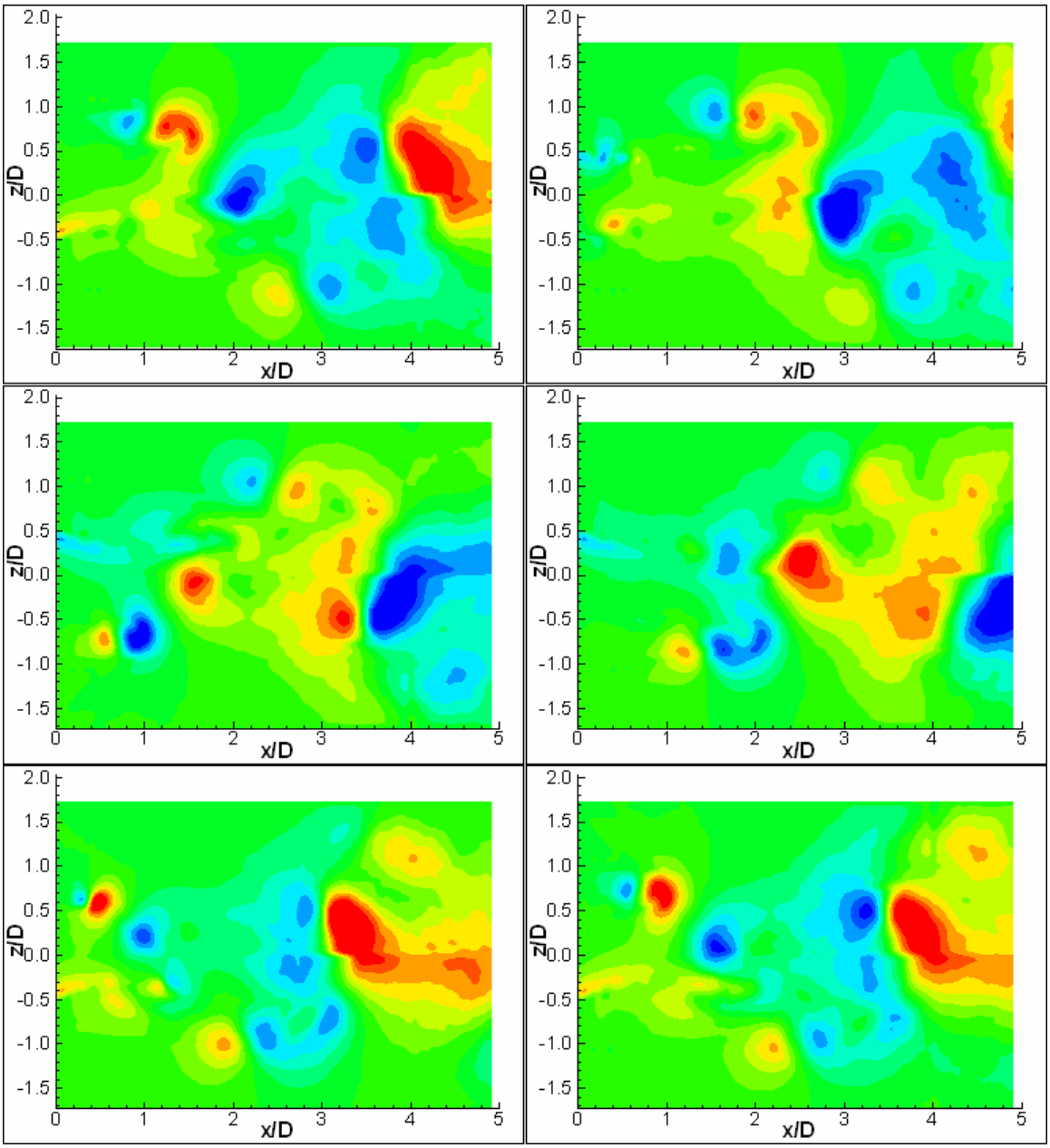

Figure 3.116: Contours of W, Velocity in the z-Direction at Different Time Steps for St = 0.1, 0.08" Acts, 180°-Phase Pulsing, SRMR = 0.096, U_{exit} = 10 m/s (Same Color Scale As Previous Figure)

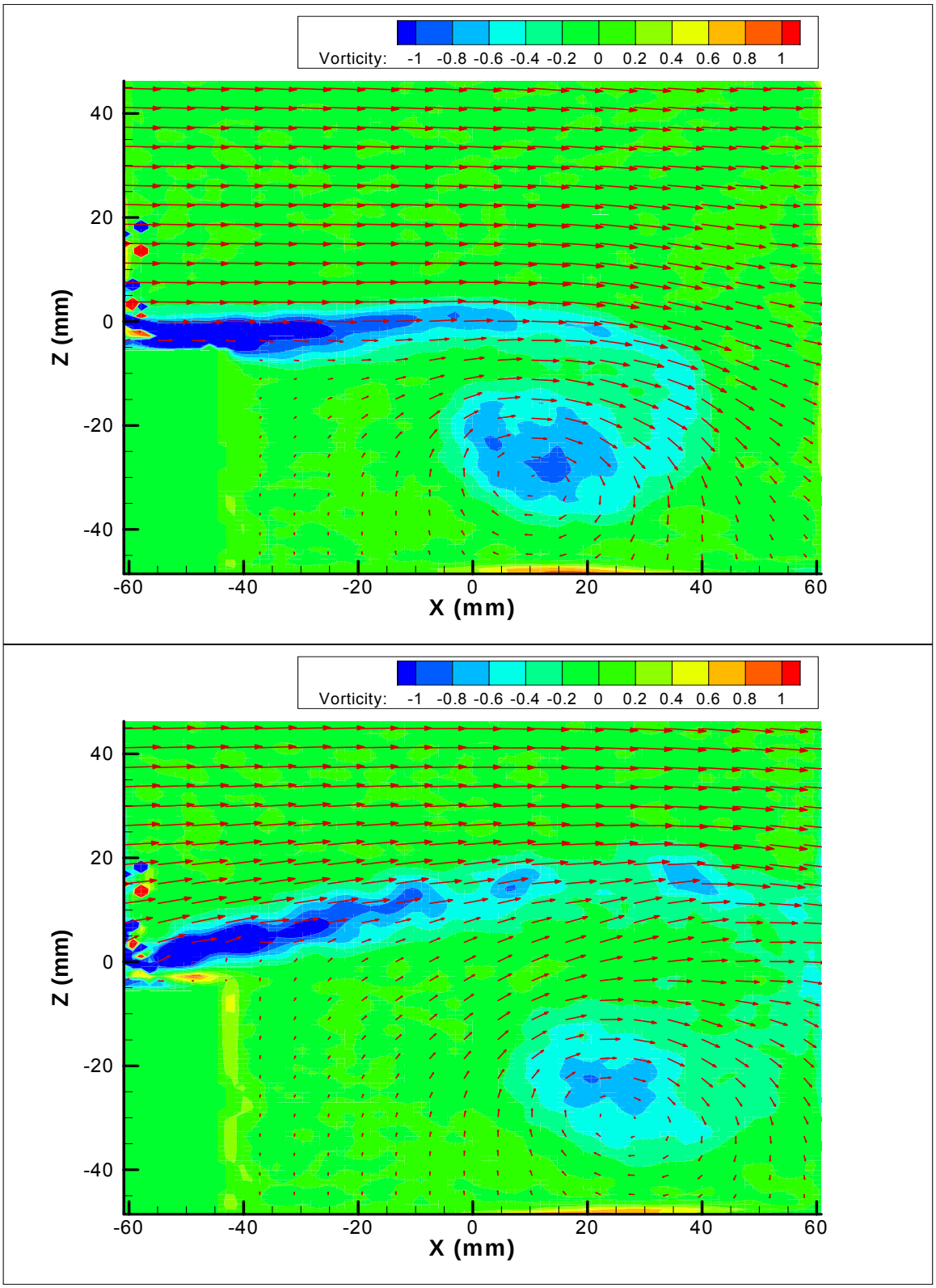

Figure 3.117: Phase Averaged Vector and Vorticity Plots for St = 0.1 (top) and St = 0.3 (bottom) near the Jet Exit, 0.08" Acts, 180°-Phase, SRMR = 0.096, U_{exit} = 10 m/s

Summary

The small scale phase I experiments have shown that the following parameters affect mixing enhancement of a circular turbulent jet forced with fluidic pulses:

1. Frequency – Mixing was strongly affected by frequency, and the optimal frequency depended on the amplitude, phase, and configuration. An important discovery was that optimal frequency always decreased with increasing amplitude. The optimal frequency for low amplitude excitation was generally in the neighborhood of St = 0.3, and for saturation level amplitudes it was around 0.1 to 0.15 depending on the configuration.
2. Amplitude – Mixing was strongly affected by amplitude as well. For all of the configurations tested, the amplitude at which mixing saturated depended directly on the pulsing frequency. It was found that it is generally desirable to pulse at the optimal frequency which, in turn, depends on the configuration. At a given pulsing frequency mixing was found to scale on the momentum ratio (or square root of the momentum ratio). This was probably the most important discovery of the small scale phase I experiments.
3. Phase – The pulsing phase had a moderate affect on mixing. Forcing the jet in the flapping mode resulted in better mixing than forcing it axisymmetrically. Also, the optimal frequency depended somewhat on the pulsing phase.
4. Configuration (number and location of actuators) – The number and location of the actuators shifted the optimal pulsing frequency somewhat. However, the most important result regarding this parameter was that similar levels of mixing were

achievable for all of the setups tested. The four actuator configurations appeared to be slightly better than the two actuator configuration.

5. Offset – Offset was found to always have a strongly negative effect on mixing. Increasing the offset by as little as %10 reduced mixing enhancement substantially.
6. Duty Cycle – Decreasing the duty cycle below 50% when the pulsing amplitude was below saturation improved mixing some, but decreasing it too much had a negative effect. Increasing the duty cycle above 50% always resulted in poorer mixing.

The phase II experiments and analysis showed many of the details of mixing enhancement. The PIV pictures show that pulsing creates large scale vortical structures which grow as they move downstream and entrain large amounts of ambient fluid. Tagged fluid from the jet and actuator are ejected into and swirled with the ambient fluid via these structures. A number of smaller scale vortical structures are also generated in the shear layer. This picture of mixing is contrasted with the case for the natural jet, where smaller scale structures form with much less of a defined shape and less regularity.

Phase averaged velocity measurements add to the above picture. They show that the large scale vortical structures are formed on the off cycle of the pulse. Thus the complete turning off of the pulse is believed to be just as important as the penetration. The large scale vortices move away from the jet in the radial direction as they travel downstream. The antisymetrically forced jet is clearly flapping in the near field, while the

axisymmetric jet is squeezed and released. Significant velocity reduction occurs for both cases by x/D = 5. Non optimal pulsing frequencies do not result in the same amount of penetration as optimal frequencies. Phased RMS calculations verify that the phase averaged values are a good representation of the instantaneous values.

Spectral Analysis, velocity profiles, and turbulence intensity profiles in the flow field at x/D = 10 show that the initial large scale structures no longer dominate the flow. There are no noticeable frequencies by 10D, suggesting that the flapping or squeezing motions that take place in the near field have essentially vanished. Velocity reduction at x/D = 10 is thus a good indicator of mixing.

The momentum ratio of the pulse to the jet is confirmed as a key parameter. When two different actuator nozzles were pulsed at different velocities but the same momentum, they resulted in almost identical flow fields.

Pulsing has the effect of increasing the thickness of the shear layer significantly compared to the natural jet and blowing cases. The momentum thickness was a function of both time and location. The increase in the thickness was closely tied to the presence of the shear layer vortex. For the optimal frequency, the shear layer thickened more than for the non-optimal cases.

Penetration was found to be the same for all frequencies below about 125 Hz in the region near the jet exit. The closer the pulsing frequency was to the optimum, the greater

the penetration that occurred downstream. For the higher frequencies, the penetrating jet appeared to be drawn towards the vortex formed during the last off cycle. Thus the spacing of the vortices was critical to penetration depth. The vortices for the optimal case persisted further downstream than the higher frequency cases. As the fluid with z-momentum moved through the center of the jet, it picked up additional momentum in that direction indicating that an influx of flow due to the generation of a counter rotating vortex pair may be present.

Vorticity contour plots near the jet exit also demonstrated how the shear layer vortex tended to draw in the fluidic pulse. It was not clear whether the optimal forcing case created a stronger vortex than the other cases, but if so the difference was not great in that region.

CHAPTER 4

FULL SCALE JET - EXPERIMENTAL SETUP AND EQUIPMENT

Chapter Overview

The experimental setup described in this chapter was built for the Active Core Exhaust (ACE) control project for the Air Force Research Lab.[35, 91] The overall goal of the ACE project was to develop a pulse fluidic injection system to enhance mixing of the turbofan core exhaust for a production aircraft. In pursuing this objective, a prototype pulse fluidic mixing system was developed and tested. A major objective of the program relevant to this thesis was to evaluate the effectiveness of the prototype on a full scale jet.

Overall Description

In conjunction with the Active Core Exhaust (ACE) control project, full scale jet mixing of the turbofan core nozzle was simulated in the laboratory using a 31-inch (0.79 meter) diameter aluminum duct acting as the nozzle exit. The setup is shown in figure 4.1. The simulated core flow was produced using two 200-hp industrial centrifugal blowers. In order to get the unusually large mass flow needed to simulate the core flow of the engine, an ejector-collector system was used. The jet exit velocity was set to 116 ft/s (35.4 m/s) resulting in a mass flow rate of approximately 42 lb_m/s (19 kg/s) and a Reynolds number based on diameter of about 1.65×10^6. This simulates the core flow for the engine at the idle reverse case (i.e. the *lowest* engine throttle setting with the core thrust reverser engaged).

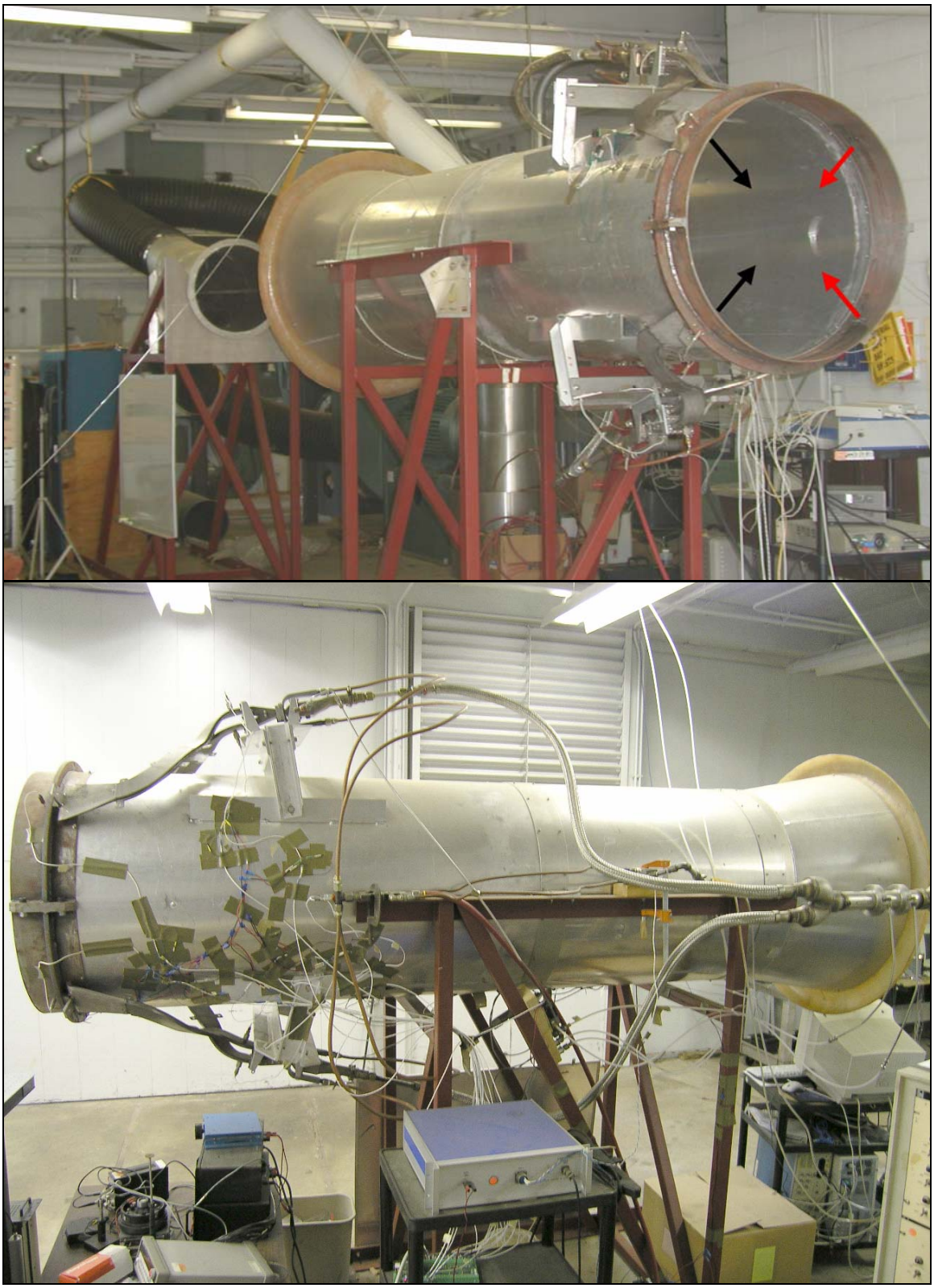

Figure 4.1: Overall Setup of Full Scale Jet at GTRI Laboratory.

Mixing was implemented using two pulsed fluidic diverter valves developed by Honeywell. The pulses were delivered just upstream of the jet exit by high aspect ratio distribution ducts designed by Boeing to fit within the engine nacelle. The geometric angle between each of the pulses was 90º, and the forcing mode was antisymmetric, or 180º out of phase left side to right side. Figure 4.2 is a 3D model of the design concept for the fluidic pulsing system mounted on the engine core nozzle.

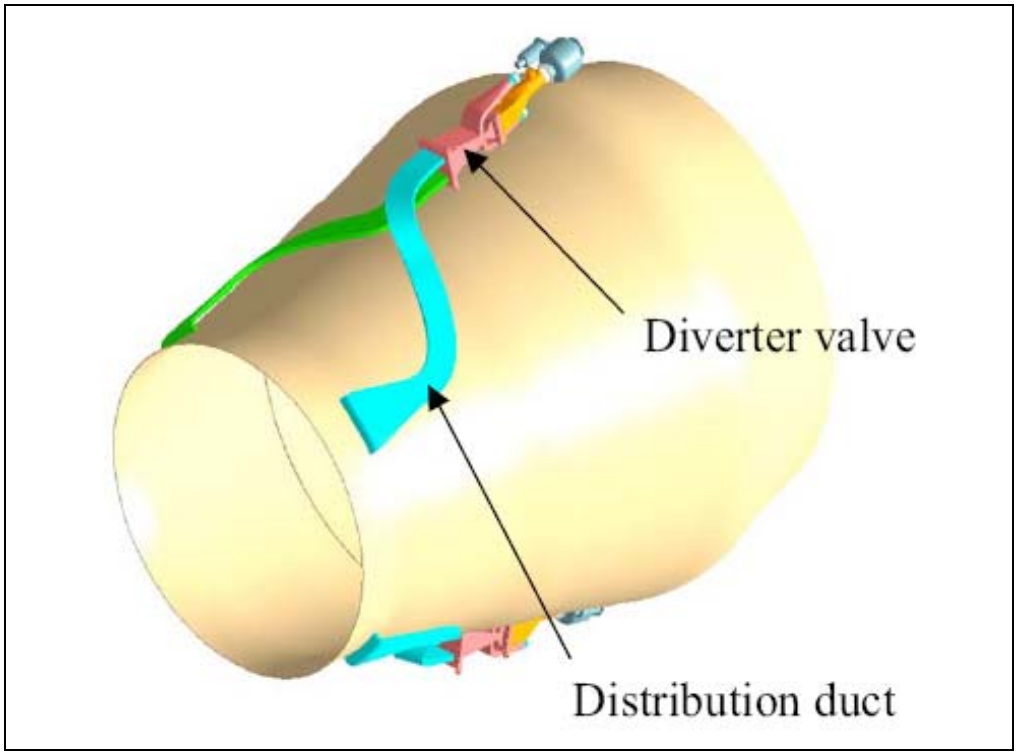

Figure 4.2: 3D Model of the Full Scale Pulse Fluidic Mixing System to Fit Under Engine Nacelle

Experimental Setup

Facility

The setup described in this chapter was located in the Building 2 Annex of the ATAS Laboratory of GTRI. Figure 4.3 is a schematic of the setup and building drawn to scale. The block building has dimensions 28 meters long by 7.3 meters wide by 4 meters high. It provided adequate protection from crossflows (which the jet would have been exposed to if located outdoors) at the expense of some confinement. The building has two sets of standard size double doors and two large sliding doors which open to give two 4 meter wide by 3 meter tall openings to the outside. The doors were opened during testing to reduce the amount of recirculation in the building. Figure 4.4 shows pictures of the facility with a test in progress.

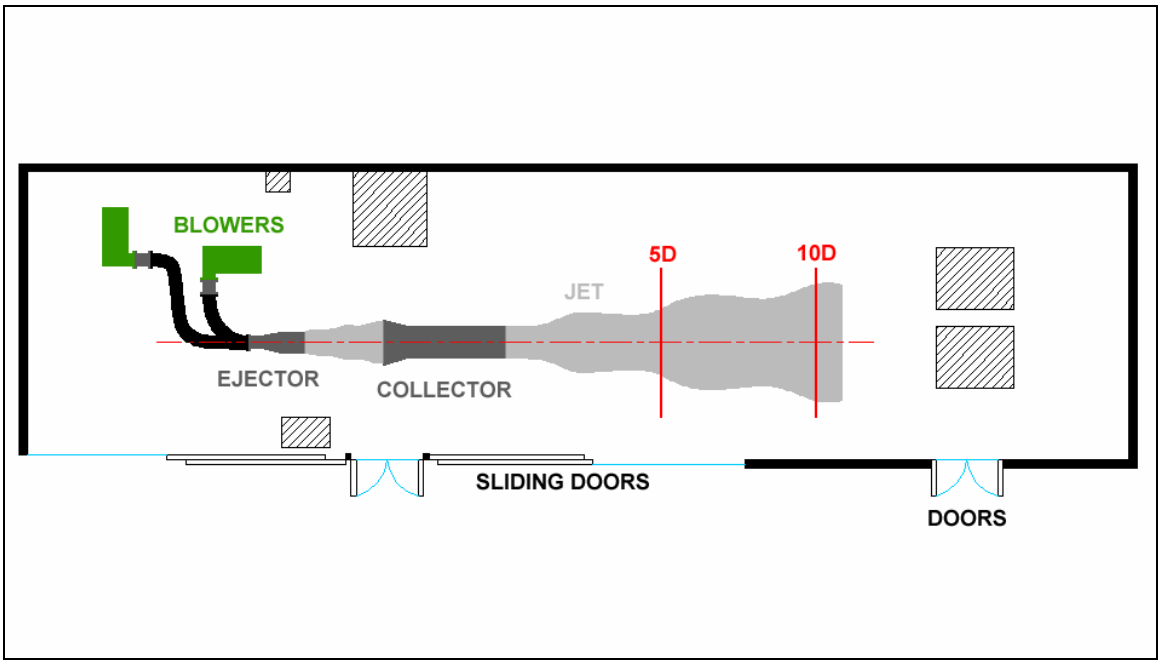

Figure 4.3: Scale Drawing/Schematic of the Building 2 Annex and Full Scale Setup

Figure 4.4: Pictures of the GTRI Facility, Traversing Mechanism, and Pitot Probe

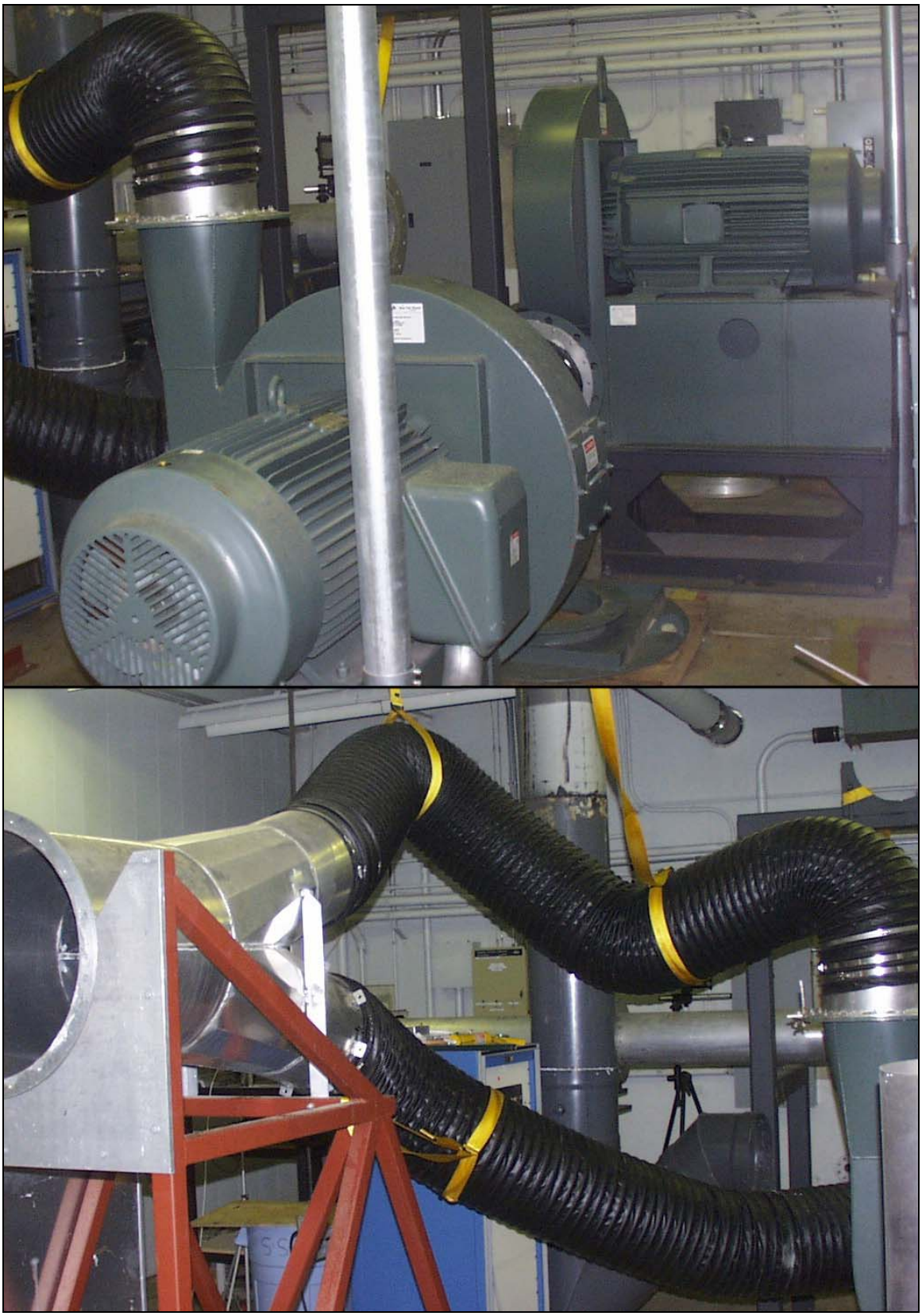

Figure 4.5: Pictures of the Centrifugal Blowers, Flex Ducts, and Y-connector/Ejector Used To Create the Full Scale Jet

Jet Ejector & Collector

The main flow for the jet was produced by two 200-hp New York Blower PRO 613-404643 industrial centrifugal blowers operating in parallel. The outlets of the two blowers were directed through 12-inch diameter nylon flex ducts which were tied together using a custom built Y-conduit into a 20-inch diameter aluminum ejector. These components are shown in figure 4.5. The ejector fed a 45-inch diameter collector located 79 inches downstream which converged to a 31-inch aluminum duct approximately 8 feet long that acted as the jet nozzle. The setup of all of these components can be seen in figures 4.1 and 4.3. There was virtually no spillage around the collector and the velocity of the exhausting plume from the collector duct was controlled with the variable speed motor on the blowers. The simulated core nozzle was situated in the building such that one side of the jet had a hard wall at 14 feet from the jet centerline and a wall with a large door opening at 10 feet on the other side. A hard floor was 6 feet below the jet centerline and a hard ceiling was 7 feet above the centerline. This arrangement is shown in figure 4.6.

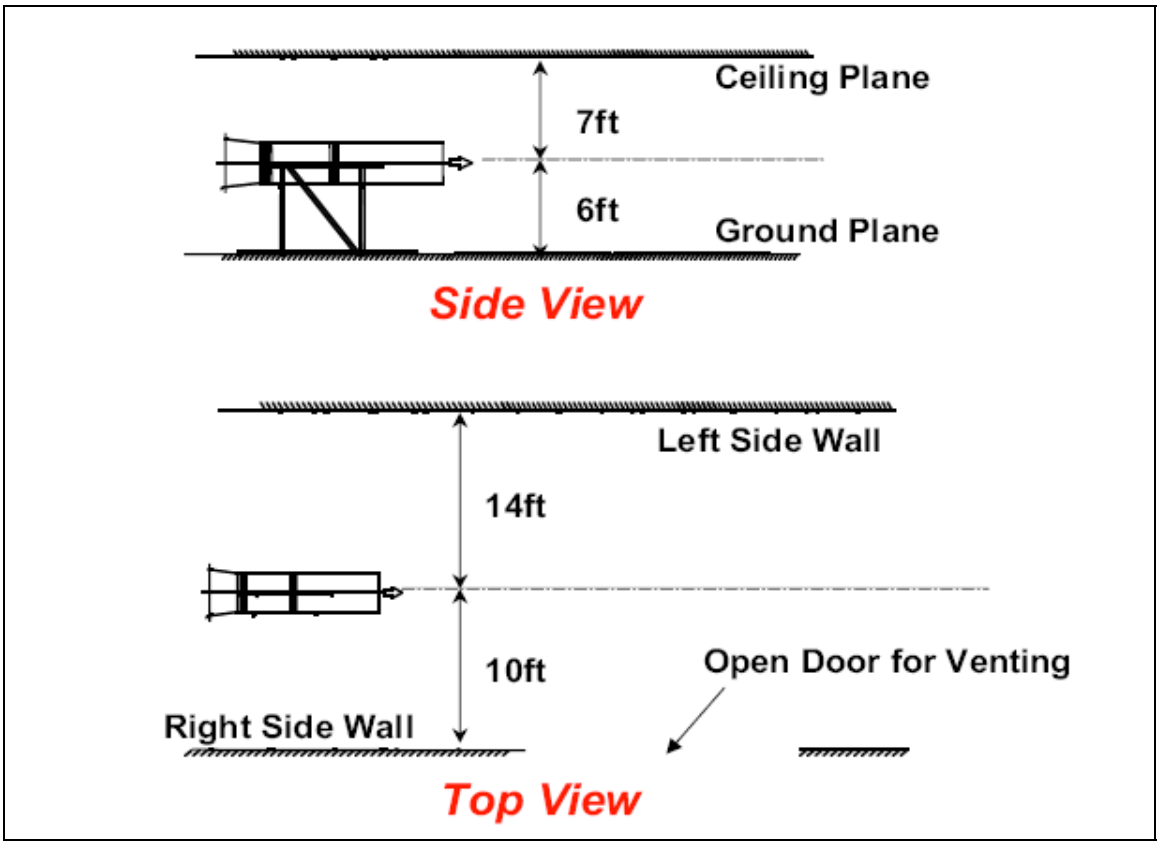

Figure 4.6: Full Scale Jet Collector Positioning in the ATAS Building 2 Annex

Fluidic Actuators

Actuation pulses were generated with two fluidic diverter valves developed by Honeywell. These diverter valves (shown in figure 4.7) are fluidic oscillators with no moving parts. The main flow for the diverter valves came from a 300-PSI air source controlled by a Valtek Mark II computer controlled valve (figure 4.8). Prior to reaching the diverter valves, the flow passed through a propane combustion chamber (figure 4.9). It could thus be either heated (to simulate on wing conditions) or unheated. It then passed through a 4-inch insulated stainless steel pipe and passed through a Flow-Dyne VP021000-SMPT 1-inch diameter venturi flow meter (figure 4.10) before splitting into two flexible stainless steel hoses that connected to the diverter valves. The diverter

valves were bolted to an aluminum frame that was welded to the collector. An actuator mounting ring was constructed out of steel and attached to the exit of the collector (figure 4.11). The ring had four exit slots cut into it, each of which measured 5.5" by 0.155" and spanned a 16º arc. The slots delivered pulses to the flow 6" upstream of the nozzle exit (figure 4.12). The high aspect ratio ducts designed by Boeing to fit within the engine nacelle were bolted to the diverter valve on one end and attached to the mounting ring on the other end, terminating with the exit slots (see figures 4.1, 4.2, 4.11, & 4.13).

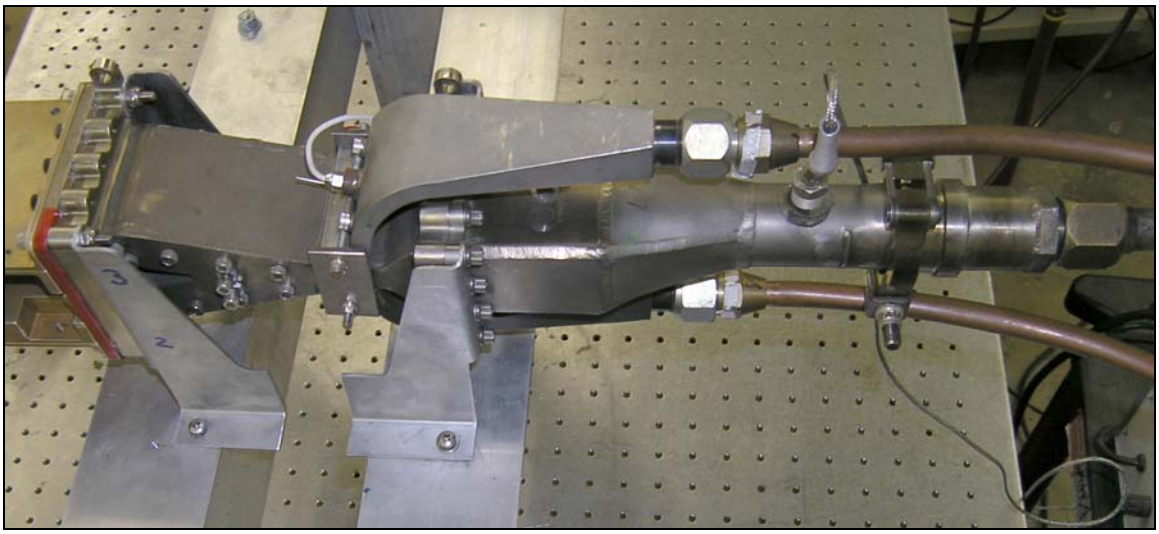

Figure 4.7: Picture of the Honeywell Diverter Valve

Figure 4.8: Picture of the Valtek Mark II Computer Controlled Valve Used to Control Actuator Flow

Figure 4.9: Propane Combustion Chamber Used to Heat Actuator Flow

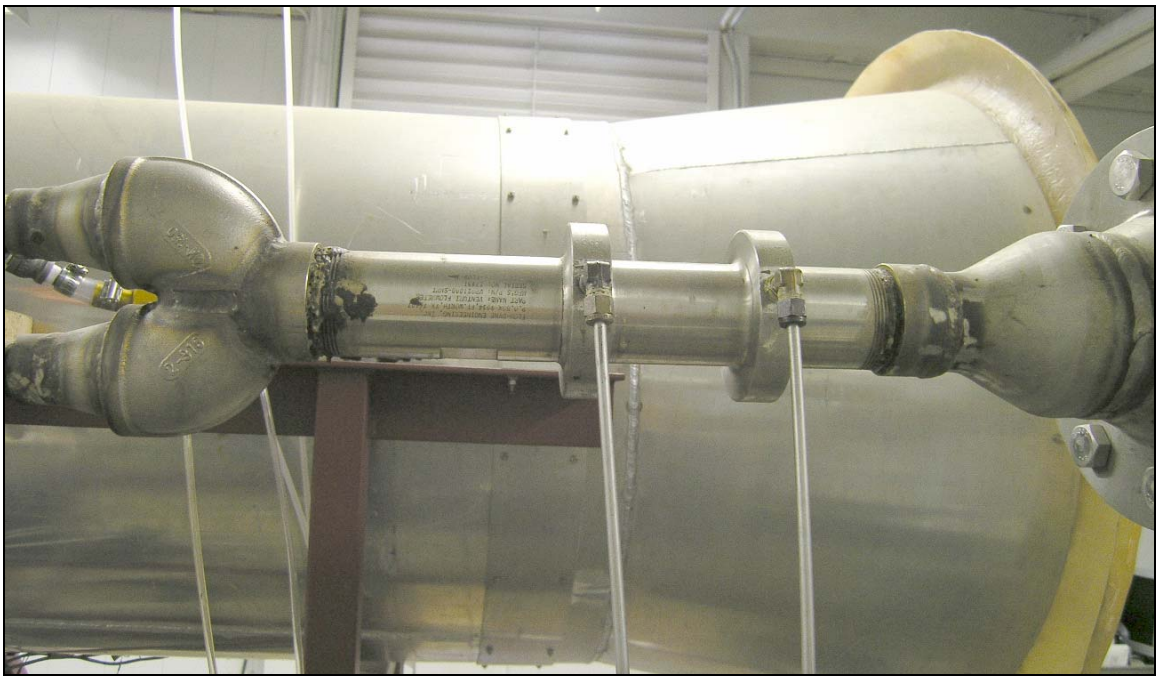

Figure 4.10: Picture of the 1-inch Venturi Flow Meter Used to Measure Actuator Mass Flow Rate

Figure 4.11: Picture of Actuator Mounting Ring at Jet Exit with Bottom Diverter Valve Attached

Figure 4.12: Close up of one of the Actuation Slots in the Mounting Ring Showing Location of Total Pressure Tube

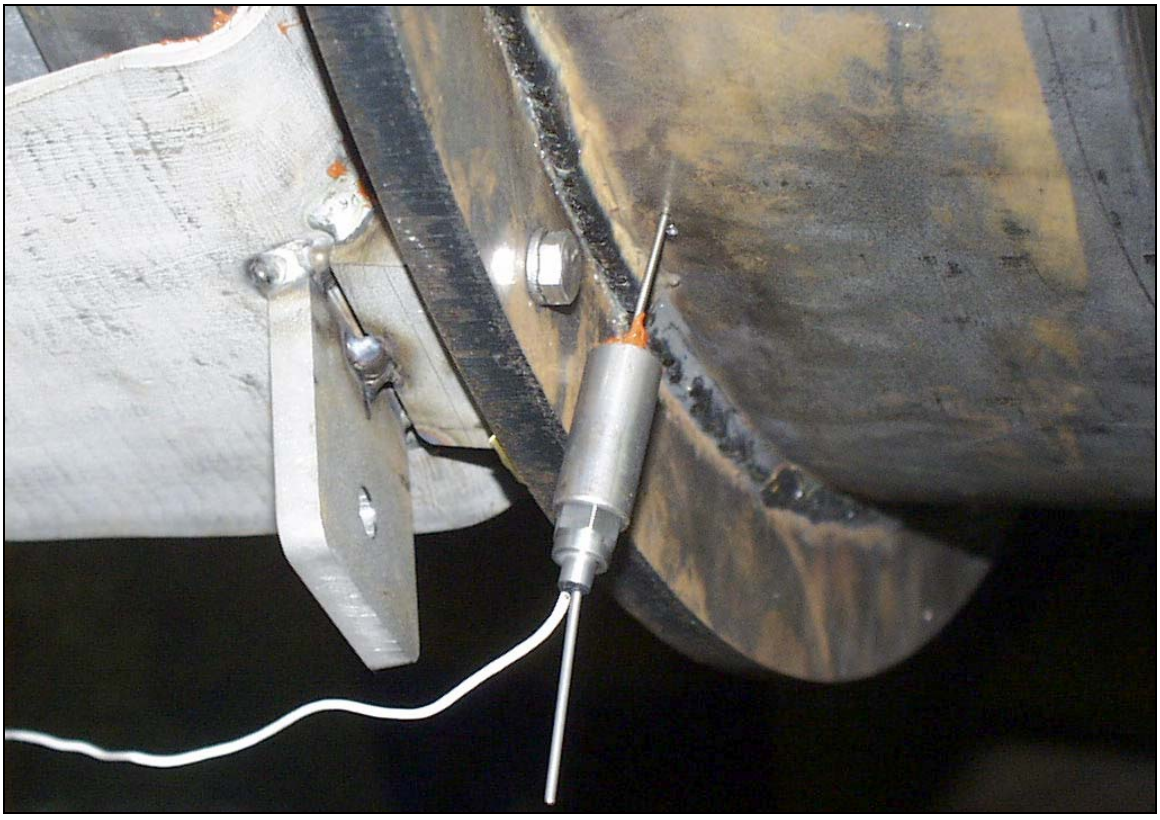

Figure 4.13: Close up of one of the Pulse Delivery Ducts Attached to Mounting Ring and the Start of the Total Pressure Probe

Instrumentation

Unsteady static and total pressure measurements were made at numerous locations along the actuator flow path for pulse characterization and diagnosis using transducers manufactured by Endevco and Kulite. This included unsteady total pressure measured at all of the slot exits. Most of the steady pressure measurements were made with a Pressure Systems Netscanner 98RK multiport rack mount system (figure 4.14). The upstream pressure for the venturi flowmeter was measured with an Omega PX302 pressure transducer, and the ΔP across the venturi was measured with a Validyne P305D differential pressure transducer. The total temperature of the flow was measured in the bottom diverter valve inlet using a type-T, plug type thermocouple. Based on flow symmetry, it was assumed that the temperature was the same for the top diverter valve inlet as well.

Point velocity measurements were made at the nozzle exit and various locations in the jet flow field using the large pitot static probe seen traversing in figure 4.4. The total pressure was read with a 0-10" W.C. pressure module in the Netscanner rack mount. The total temperature of the jet (which was typically about 20°F higher than ambient due to compression by the blowers) was measured using a type K thermocouple attached to the pitot probe. These instruments were moved through the flow field on a 22 foot long traverse which was clamped to a series of brackets bolted into the concrete floor. The brackets were placed such that they aligned with the jet centerline, as well as perpendicular to it at 5 and 10 diameters downstream. This setup allowed for the centerline and cross traverses at 5 and 10 diameters as shown in the schematic, figure 4.3.

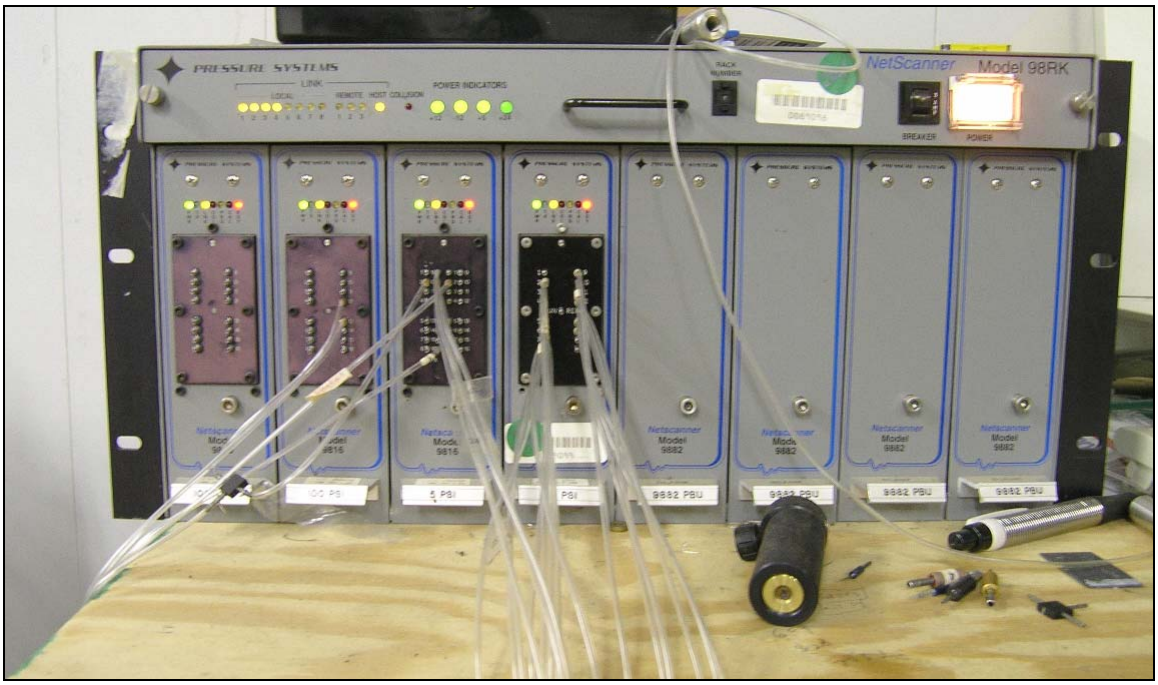

Figure 4.14: Picture of the Pressure Systems Inc NetScanner 98RK

Data Acquisition

Because there was an abundance of transducer measurements, they were tied into a National Instruments AMUX 64-T multiplexer (except for steady pressures measured with the Netscanner rack mount). The multiplexer allowed up to 32 differential analog input connections. To get the cleanest signals possible, shielded wire and differential inputs were used, and all transducers were powered with a 12-volt battery. Excitation voltage for the unsteady transducers was dropped to the required 10 volts via a potentiometer added in series. The multiplexer was connected to a National Instruments PCI-6035E 16-bit multifunction data acquisition board in a PC. The board has a TTL output that was used to control the pulsing frequency.

The Netscanner rack mount measures pressure autonomously and sends the results in the desired engineering units to a PC over a network using the TCP protocol. It samples at a

rate of 100 measurements per second with an accuracy of 0.05% Full Scale. Total pressure measurements made in the flow field had sampling times of one minute.

National Instruments LabView software was used for all data acquisition, reduction, and instrument control. Custom programs were written in 'G', the graphical language native to LabView for automated data acquisition and processing.

CHAPTER 5

FULL SCALE JET - ANALYSIS RESULTS AND DISCUSSION

Overall Description

Full scale testing was performed under the Active Core Exhaust (ACE) Control program for the Air Force Research Lab (AFRL). ACE is a fully integrated, non-intrusive pulsed injection system which destabilizes the core-exhaust plume resulting in enhanced mixing of the plume and the surrounding air.[35, 91] The ACE system hardware was designed to fit within an engine nacelle and mix the turbofan core exhaust for a production aircraft. The ACE hardware consists of two actuators and four pulsing slots spaced 90° apart from each other around the circumference of the jet. The slots operate in pairs pulsing 180° out of phase left to right. A prototype of the ACE design (figure 5.1) was tested in full scale with a simulated core exhaust nozzle at the engine idle reverse operating point. Using realistic compressor bleed temperatures and a cold core exhaust flow, the mixing performance of the ACE hardware was assessed on a 31" circular jet with an exit velocity of 35.4 m/s (116 ft/s) and a Reynolds number based on diameter of 1.65×10^6.

The tests and measurements performed on the full scale jet involved characterization of the pulse fluidic actuators, characterization of the natural jet, and evaluation of mixing performance under different configurations. The results from these experiments were compared with those obtained with the small scale jet for similar geometries, pulsing phase, slot to jet area ratios, and momentum ratios. The key results are presented here and agree very well with those obtained for small scale jet testing.

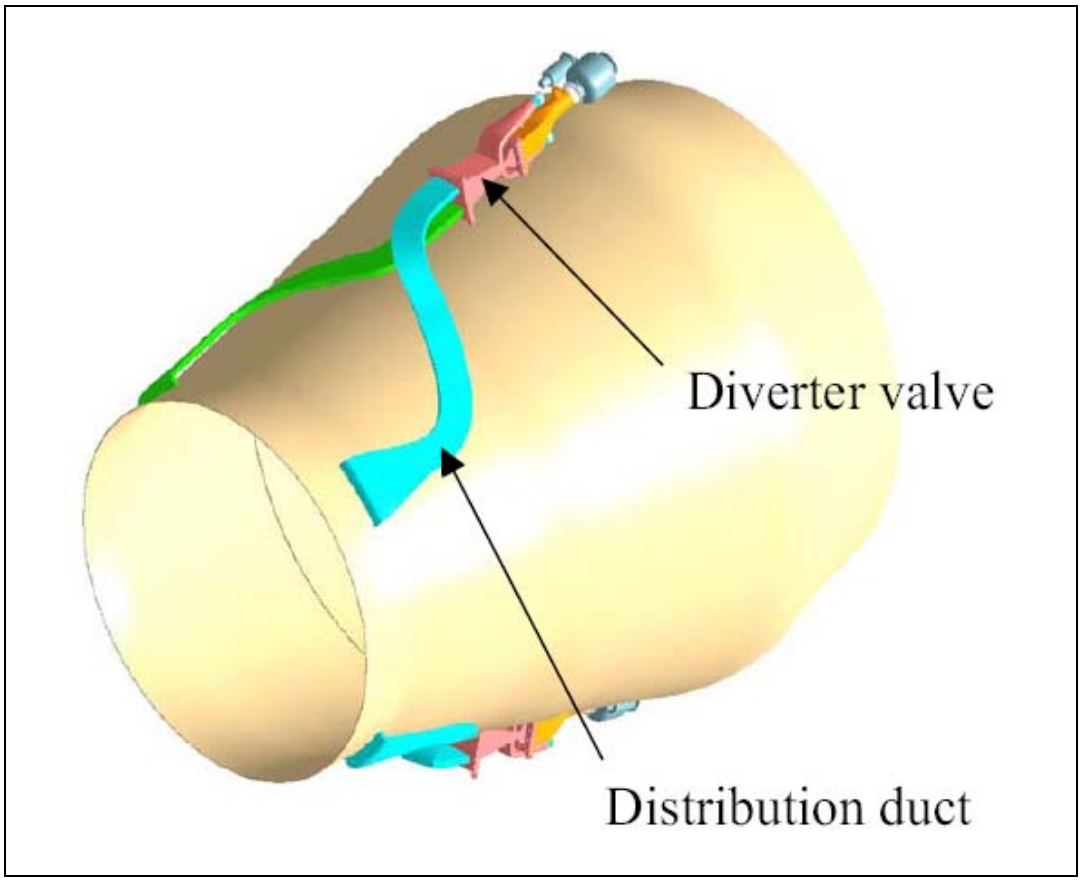

Figure 5.1: Schematic of the Prototype ACE Hardware

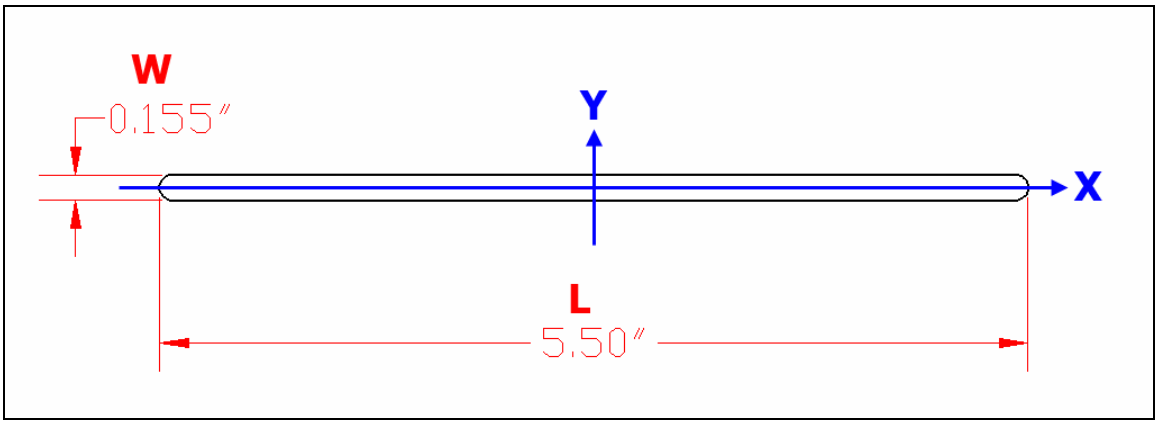

Figure 5.2: Coordinate System for the Actuator Pulsing Slots

Characterization of the Actuators

Velocity traverses were performed on the actuator slots along both the long and short axis (figure 5.2) at various distances from the slot exits for the blowing condition. The slot numbering scheme is shown in figure 5.3. Note that slots 1 and 2 fire together and slots 3 and 4 fire together. Figures 5.4 and 5.5 show the resulting profiles obtained from the traverses performed close to the slot exits for all four slots. They correspond to the long and short axes respectively. The profiles are roughly similar, the differences being due to manufacturing tolerances and installation effects. Numerical integration performed on the profiles estimates the average discharge coefficient for all of the slots at 0.716 with less than 5% deviation between the different slots. Short axis profiles taken downstream of the slot exits revealed that for all of the slots there was a slight upstream skew to the pulses. The centers of the downstream pulses were estimated by taking the derivatives of curve fits to the data. A line was then drawn from the geometric center of the slot to the corresponding downstream pulse center in order to estimate the skew angles. The skew angles were estimated at 1.1°, 8.9°, 16.5°, and 7.8° for slots 1 through 4 respectively. As an example, figure 5.6 shows the short axis profiles at two separate distances from the exit for slot #3.

Unsteady total pressure, static pressure, and temperature were measured at various points along the flow path for the pulse producing and delivering hardware as specified in chapter 4. This was done to evaluate the various system components under a span of operating conditions and design modifications. These characteristics are outside the scope of the current work and are not included in this chapter. It is sufficient to mention

that the actuation hardware design was modified to reduce pressure losses and deliver high quality pulses over a large a range of frequencies and amplitudes. Mixing results presented in this chapter are for the optimized design.

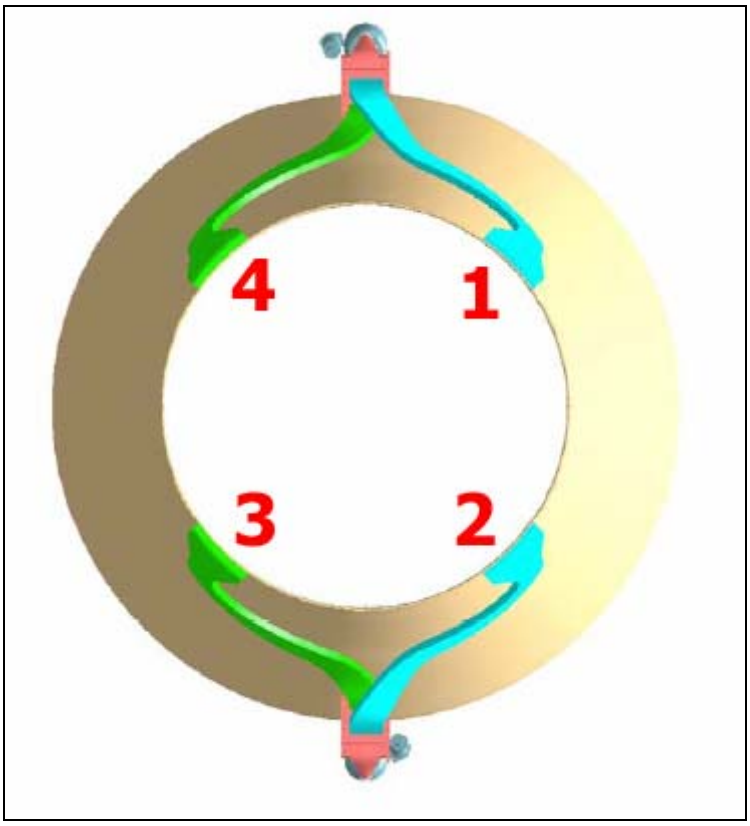

Figure 5.3: Slot Numbering Scheme

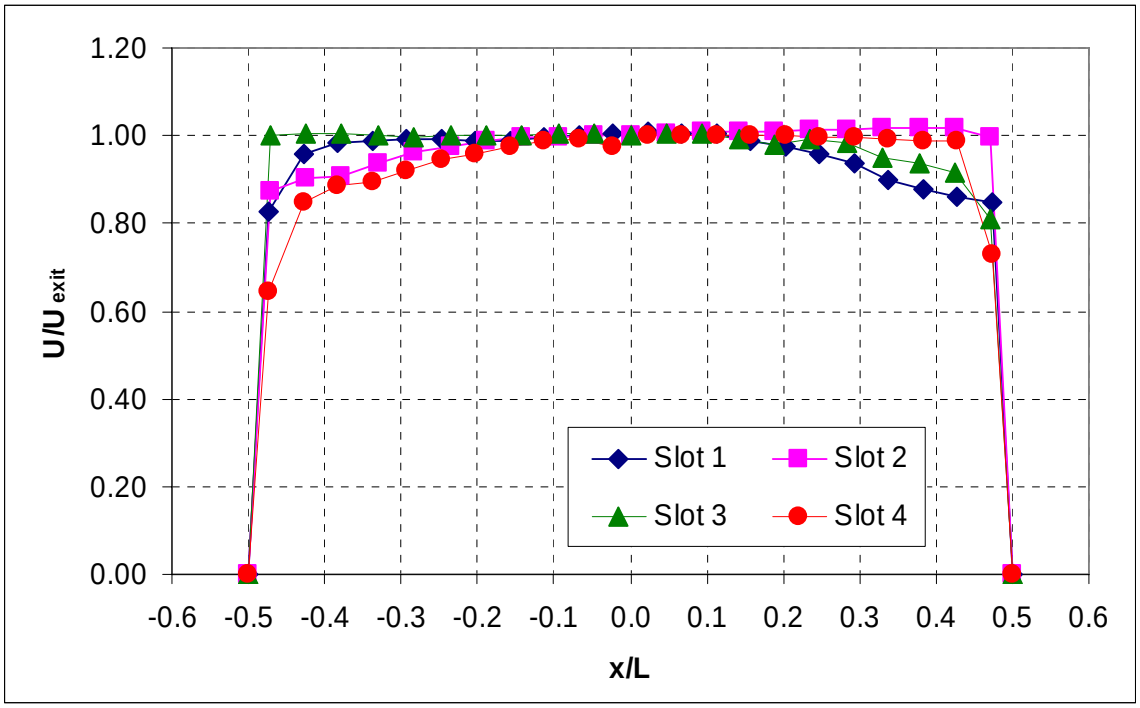

Figure 5.4: Velocity Profiles Across the LONG Axis of the Slot Exit for Steady flow

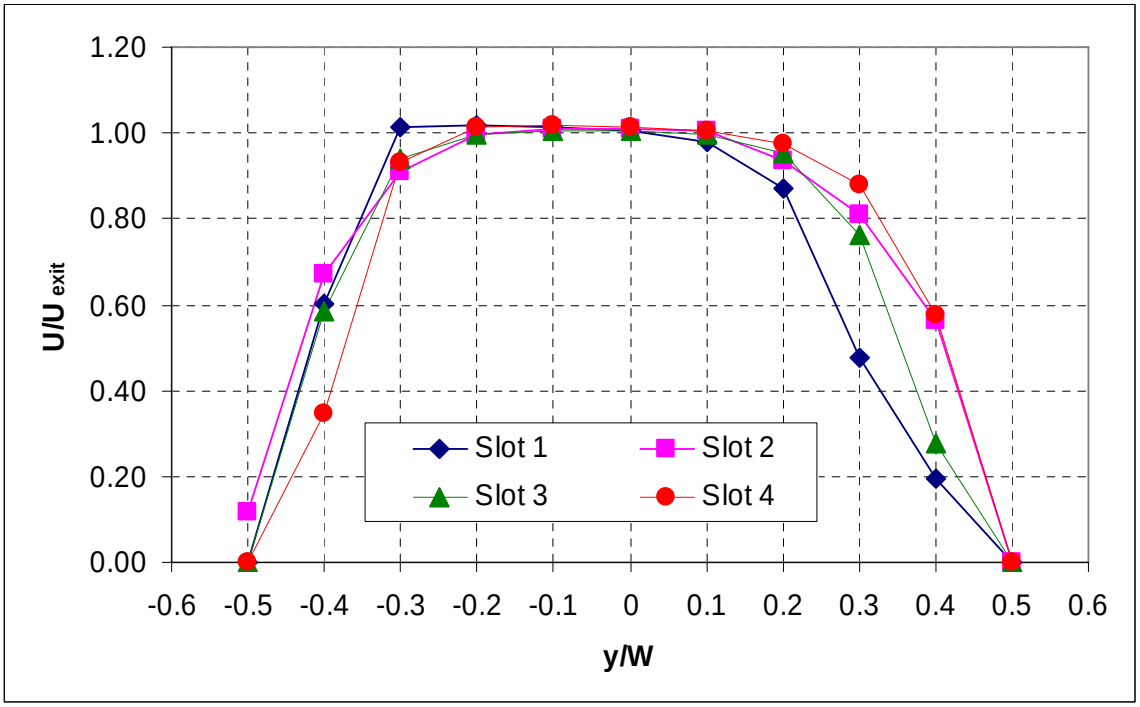

Figure 5.5: Velocity Profiles Across the SHORT Axis of the Slot Exit for Steady flow

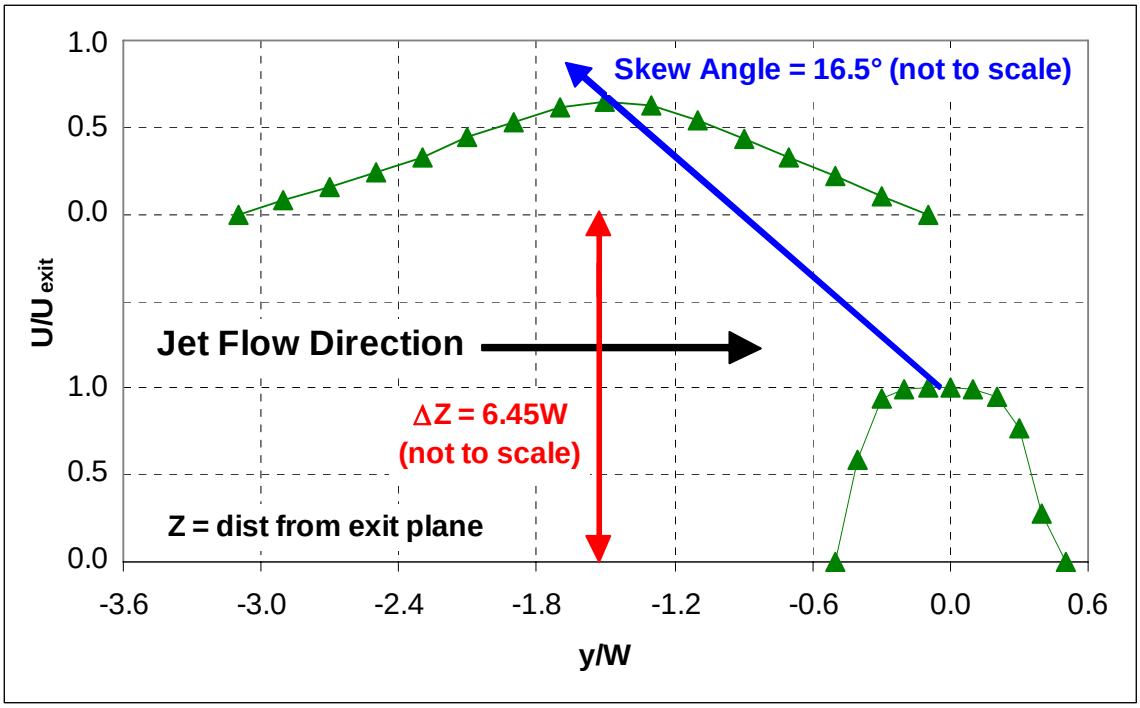

Figure 5.6: Velocity Profiles at Two Locations Across the SHORT Axis for Actuator Slot #3

Total pressure measurements were made simultaneously at all four slot exits for pulses across a range of amplitudes and frequencies and converted to velocity. Figures 5.7 and 5.8 are example time histories of velocity at the slot exits for 10 Hz and 80 Hz, respectively. These correspond to Strouhal numbers of 0.22 and 1.72 respectively for a 116 ft/s jet. The pulse quality was found to be very good (i.e. close to that of a square wave, low DC offset, and about 50% duty cycle) for frequencies ranging from 1 Hz to 200 Hz and amplitudes of SRMR > 0.2. Pulse quality is poor at very low amplitudes because below a minimum supply pressure threshold the fluidic oscillator has difficulty switching. At very high amplitudes the pulses are of high quality, but the pulsing system begins to self resonate at a specific frequency and thus control of the frequency is lost.

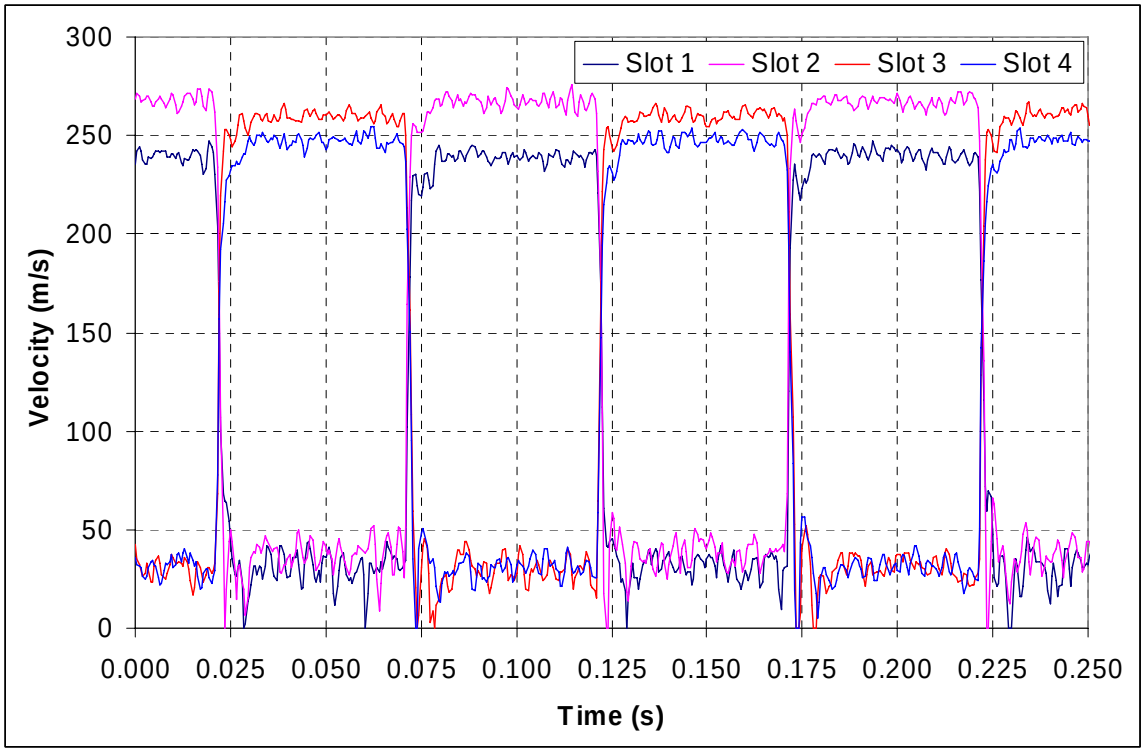

Figure 5.7: Actuator Pulse Velocity Time Histories for All 4 Slots, f = 10 Hz

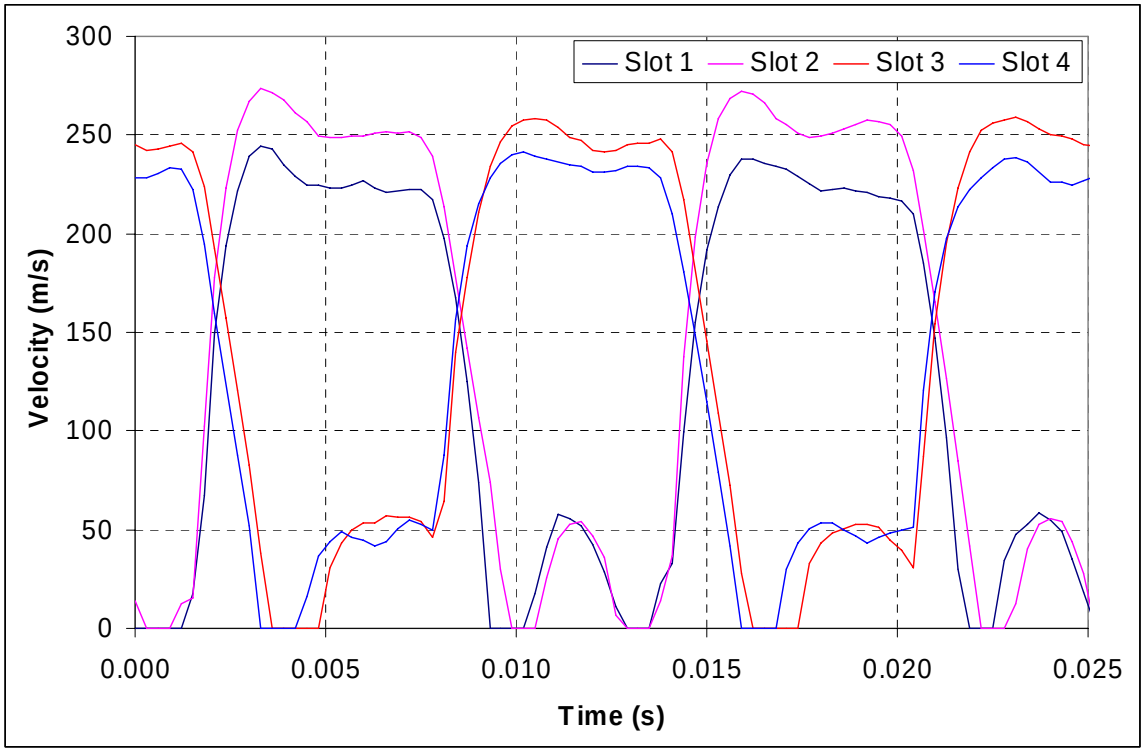

Figure 5.8: Actuator Pulse Velocity Time Histories for All 4 Slots, f = 80 Hz

Characterization of the Unforced Jet

The unforced jet velocity was characterized with centerline and cross traverses and compared to the small scale jet. Figure 5.9 shows the jet nozzle coordinate system that was used. Note that the y and z axes are swapped with respect to the convention used for the small scale jet. The centerline traverse, figure 5.10, shows that the potential core for the full scale jet ends approximately 2 diameters early compared to the small scale jet and the results of VonGlahn.[167] This is due to the high initial turbulence level.[140] Since a pitot probe was used to take all of the velocity measurements, turbulence intensity is not available. However, the turbulence is expected to be very high at the exit since:

1) the Reynolds number was very high (about 1.65×10^6)
2) there was no flow conditioning
3) the ejector was located well upstream of the collector (see figures 4.1 and 4.3)

The significance of #3 is that even if the jet issuing from the ejector had a low turbulence intensity (which is unlikely) it still had plenty of distance to develop turbulence before entering the collector. Additionally, the author is able to attest to the fact that very large velocity fluctuations could be felt when standing in the flow near the exit, as it was difficult to maintain one's balance in such a situation.

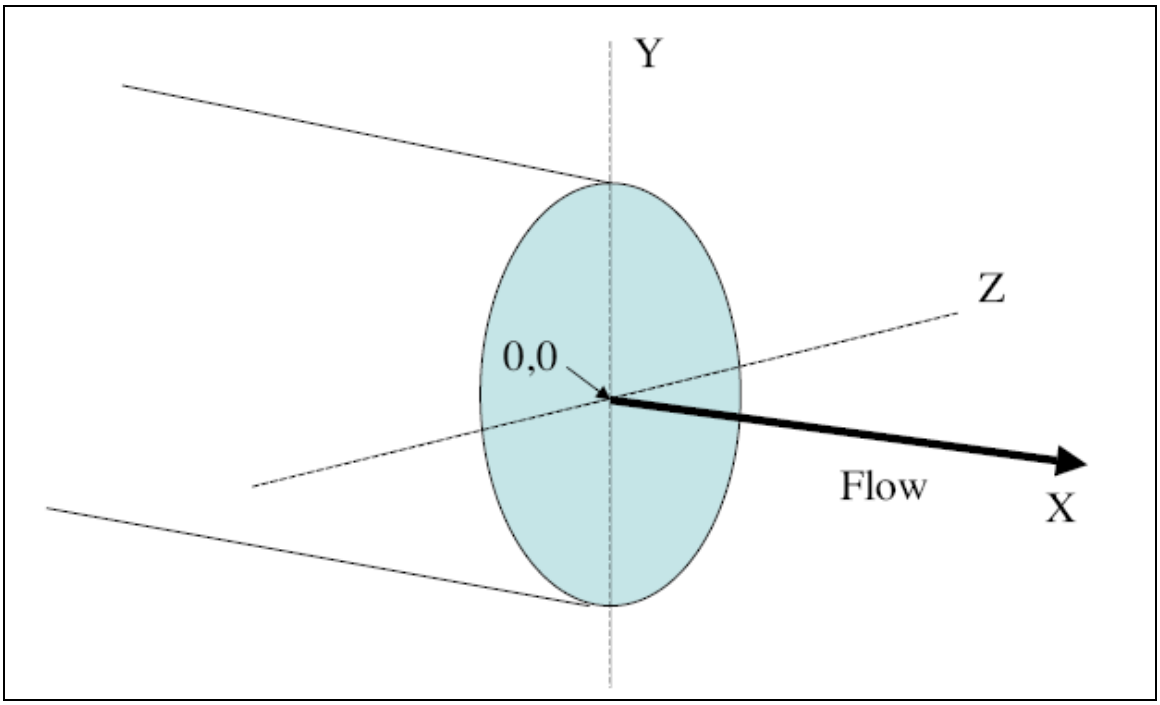

Figure 5.9: Jet Nozzle Coordinate System

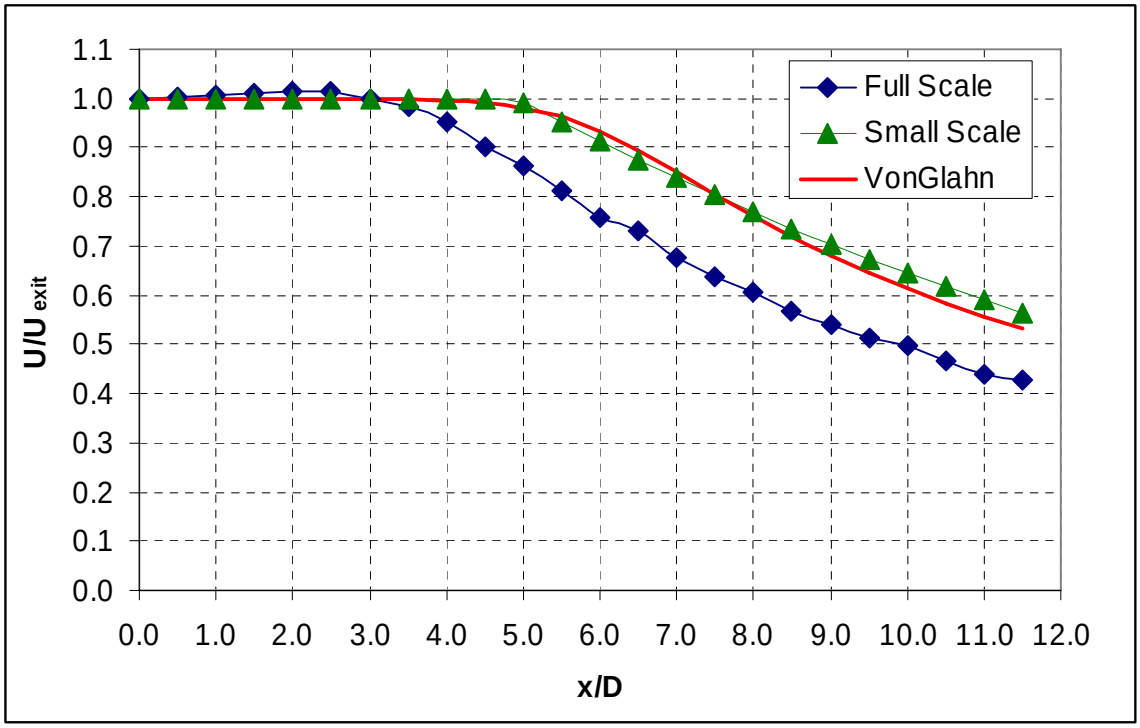

Figure 5.10: Centerline Velocity Decay for the Unforced Full Scale Jet Compared to that for the Small Scale Jet

Due to the nature of the setup, the full scale jet was somewhere in between the ideal near top-hat profile jet and a fully developed turbulent pipe flow. Figure 5.11 compares the dimensionless horizontal velocity profile of the full scale jet with that for the small scale jet. There is clearly more asymmetry in the full scale profile, but the boundary layer at the exit actually appears to be thinner than for the small scale case. This is likely due to the high level of turbulence which keeps momentum well distributed throughout the developing profile and hinders boundary layer development.

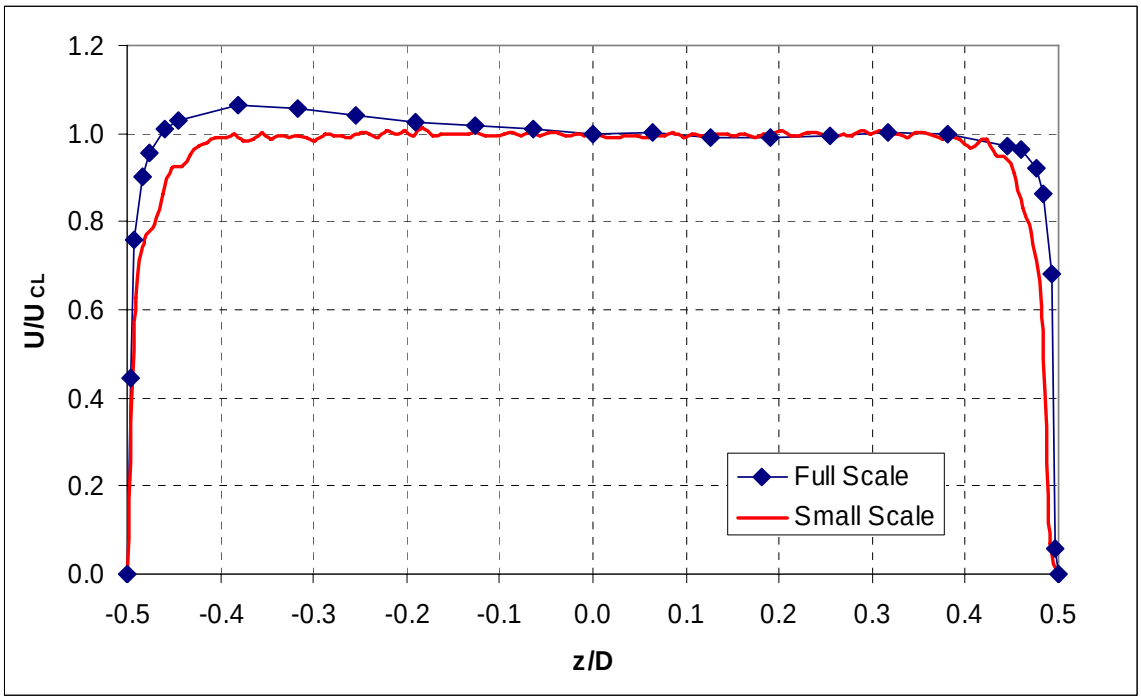

Figure 5.11: Comparison of Dimensionless Horizontal Velocity Traverses at the Jet Exit, Full Scale vs. Small Scale

Figure 5.12 compares the dimensional vertical (y-coordinate) and horizontal (z-coordinate) exit velocity profiles for the full scale jet. The jet is particularly asymmetric in the vertical direction since this is the plane in which the flows from the two centrifugal blowers are merged using a Y-shaped connector to form the ejector (figure 4.5). Figures

5.13 and 5.14 show the dimensional velocity profiles for the jet at the exit, at five diameters, and at ten diameters downstream. Despite the constriction of the room and the bends in the flow path (figure 4.3), the downstream symmetry is not bad.

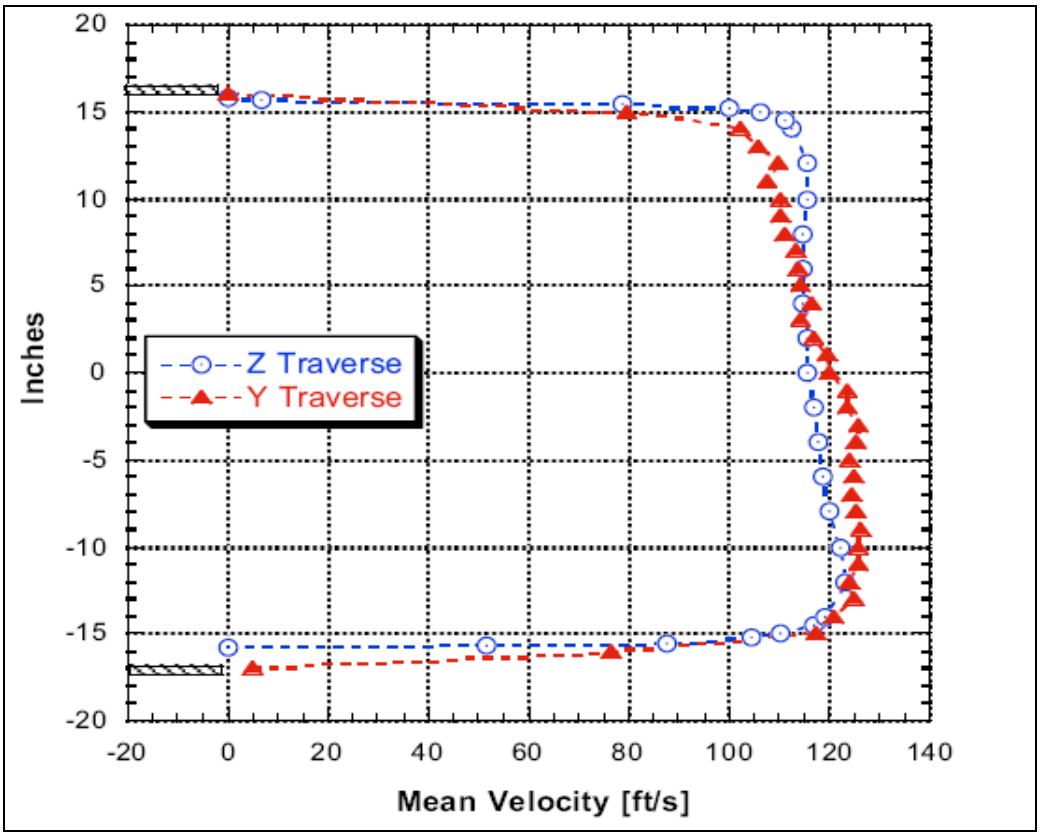

Figure 5.12: Vertical and Horizontal Unforced Nozzle Exit Velocity Profiles

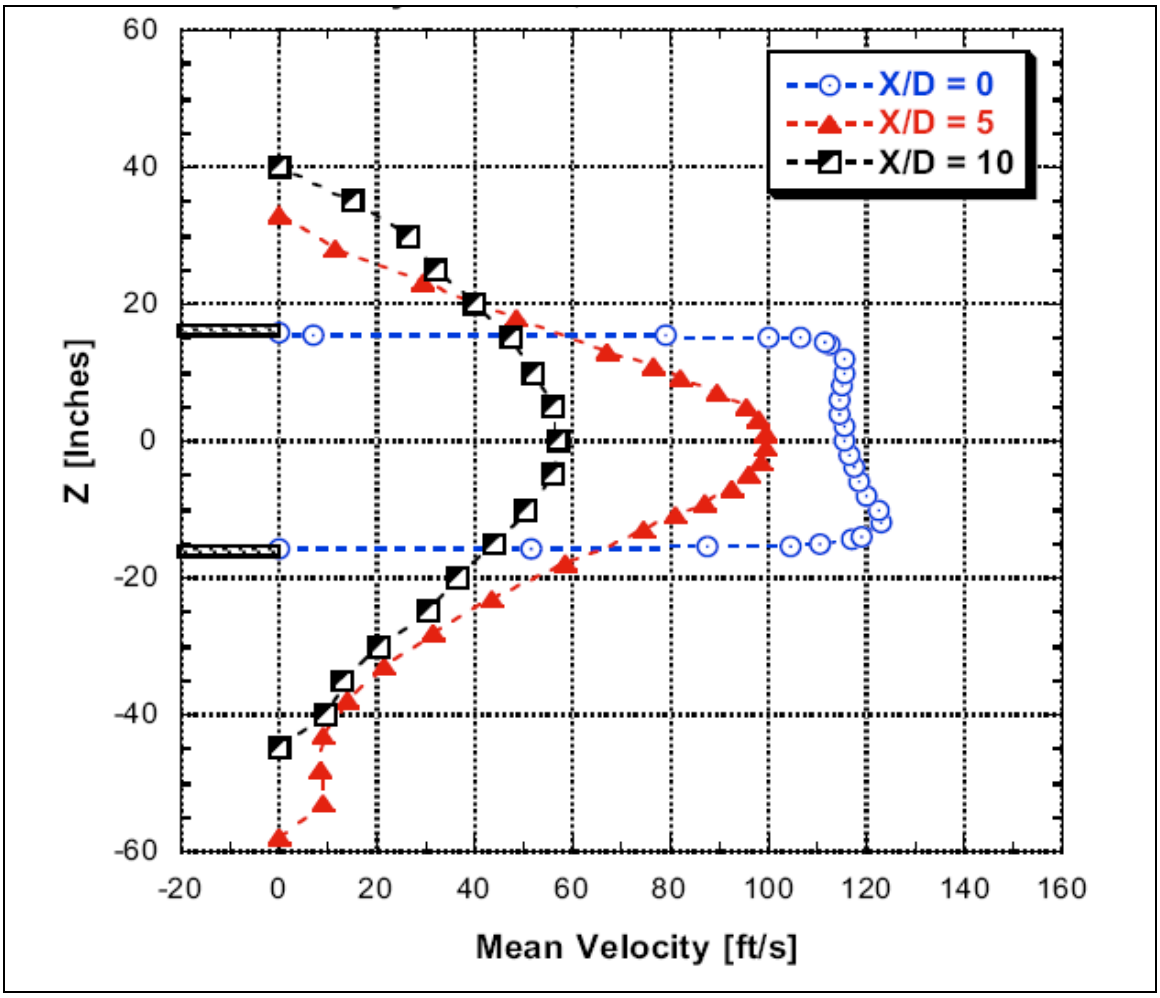

Figure 5.13: Unforced Jet Horizontal Traverses at x/D = 0, 5, and 10.

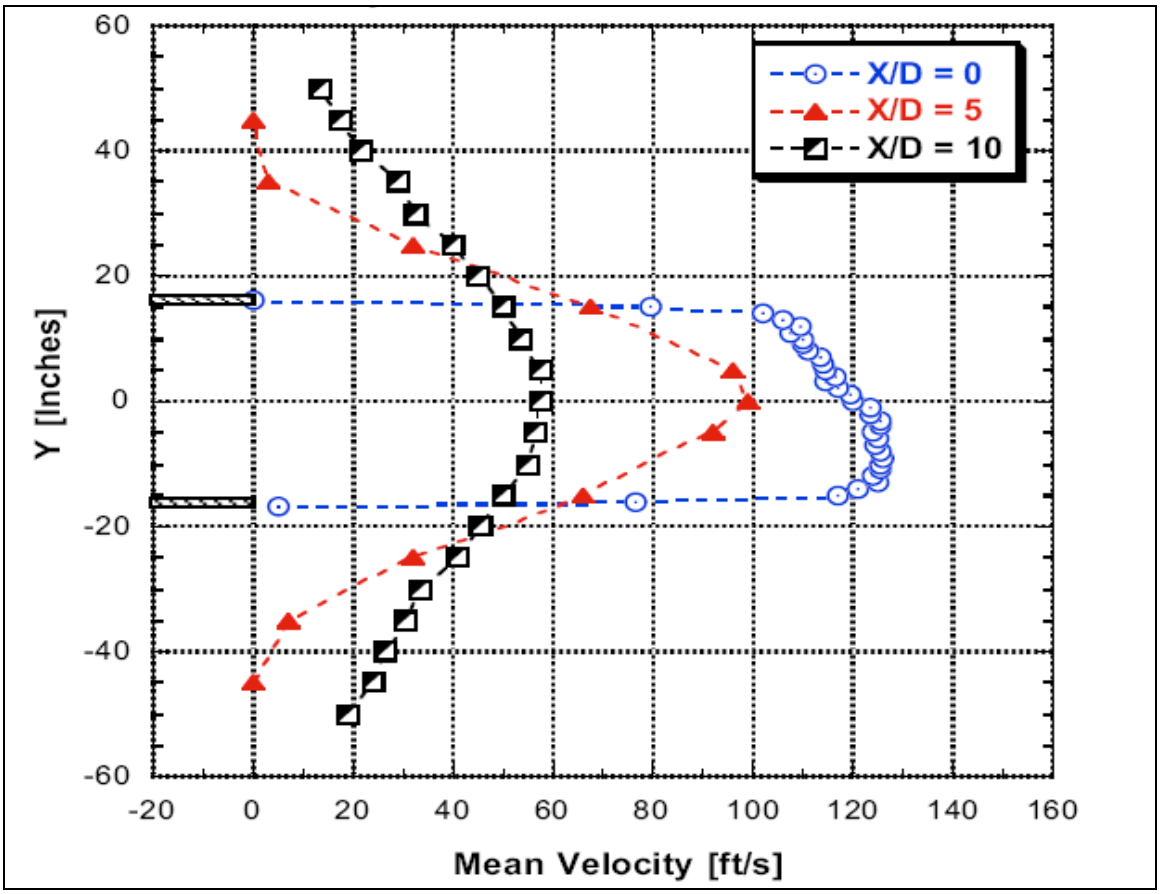

Figure 5.14: Unforced Jet Vertical Traverses at x/D = 0, 5, and 10.

Jet Mixing Results

Jet mixing results were obtained for four different types of experiments. Frequency sweeps were performed at three different pulsing air temperatures and a near ambient temperature jet. An amplitude sweep was performed at the optimal pulsing frequency corresponding to an expected amplitude level (SRMR = 0.25, or about 1.25% MFR for cold flow). A centerline velocity traverse was performed under the same condition. Finally, velocity cross traverses were performed at the jet exit, at 5 diameters downstream, and at 10 diameters downstream for the same condition. All of the results are compared to similar ones obtained with the small scale jet.

Frequency Sweeps

Jet mixing enhancement was evaluated primarily in terms of average centerline velocity reduction at 10 diameters downstream, although some measurements were also taken at 5 diameters downstream. Velocity measurements were made with a pitot static probe attached to a steady pressure transducer as described in the previous chapter. Mixing was characterized for a range of frequencies and amplitudes. Dimensionless frequency spanned from a Strouhal number of 0 to about 2, and amplitudes ranged from a momentum ratio square root of 0.27 to about 0.4. Mass flow ratios were typically on the order of about 1.3% to 1.5%. The actuators were run with either heated (250°F and 500°F) or unheated flow. Heated flow simulated realistic compressor bleed temperatures from an engine. This was done in order to verify that the equipment would operate under these conditions, and that mixing performance would be unaffected. This turned out to be beneficial to the current work since it resulted in flows with a variety of momentum ratios, even though the mass flow rates were about the same.

Figure 5.15 shows downstream velocity reduction versus Strouhal number at x/D = 10 for a number of different momentum ratios and compares them to small scale results obtained under similar conditions. It is obvious from the curves that mixing is almost saturated, even for the lowest amplitude (SRMR = 0.27) because further increase of the pulsing amplitude has only a marginal effect on mixing. The curves are clearly offset from the small scale case, which shows greater velocity reduction at a lower amplitude. This is expected since the unforced full scale jet is already in a somewhat mixed state revealed by its shift in virtual origin as previously explained (figure 5.10). The optimal

Strouhal numbers are very close as well. Figure 5.16 is the same as figure 5.15, except it is zoomed in near the optimal frequencies. It shows that there is a slight shift downward in optimal frequency as the amplitude is increased for the sweeps, which was not obvious from the previous figure. For the lowest amplitude the optimal Strouhal is about 0.14, while for the highest it is close to 0.11. This trend where the optimal Strouhal number decreases with increasing forcing amplitude was initially discovered during the small scale experiments.

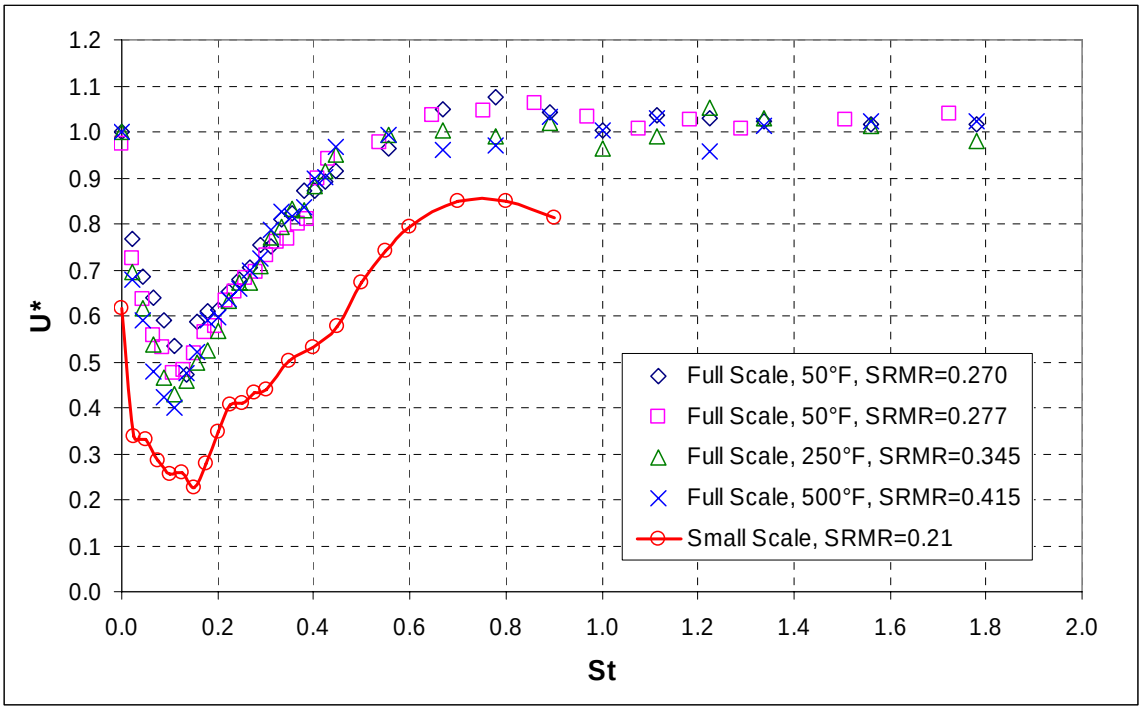

Figure 5.15: Jet Mixing Enhancement as a Function of Non-Dimensional Frequency for the Full Scale Jet at Multiple Pulsing Temperatures and Momentum Ratios, x/D=10

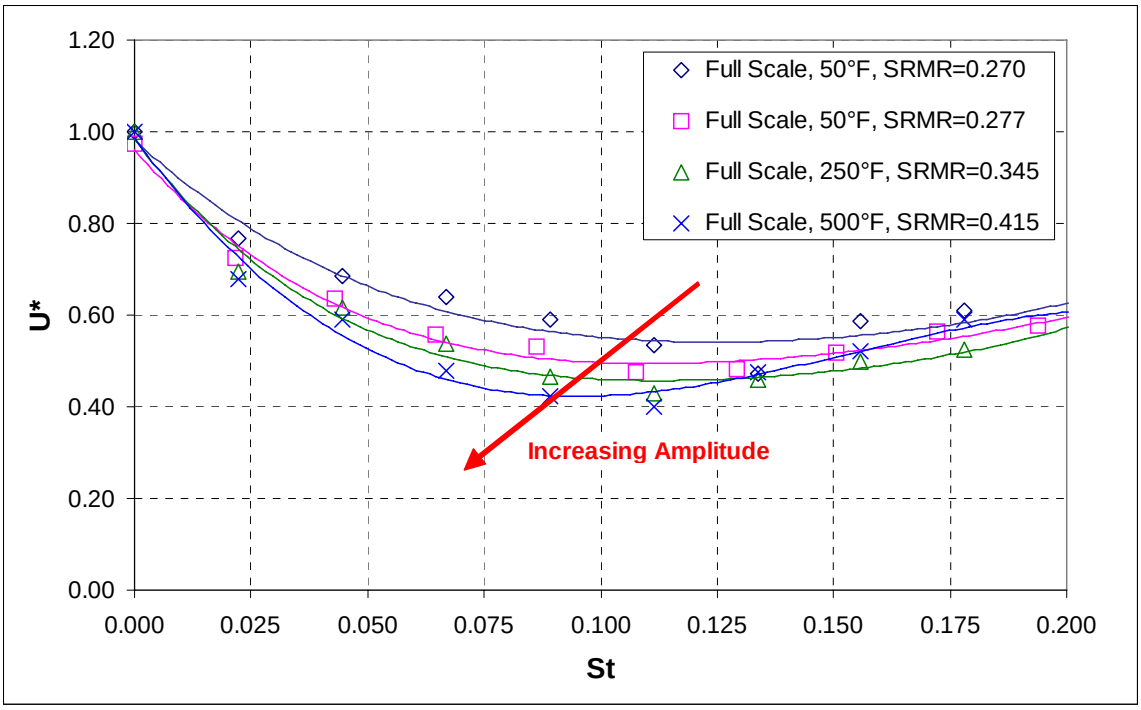

Figure 5.16: Expanded View of Figure 5.15 near Optimal Strouhal Numbers

It is interesting to note that the mixing curves do not dip back down again for high values of Strouhal number unlike some of the higher amplitude frequency sweeps with the small scale jet. The full scale results are likely a better representation of mixing behavior since the pulse quality is much better at high frequencies. The pulse quality from the actuators used in the small scale experiments was degraded at higher frequencies, and the cutoff was specified as 50 Hz. The full scale results follow the same trend as the very low jet exit velocity tests (U_{exit} = 3 m/s) performed on the small scale jet with two opposing actuators. At such a low exit velocity the Strouhal range was stretched about three times over the usual 10 m/s exit velocity case. A comparison of these results is made in figure 5.17. The near collapse of the curves is coincidental since the momentum ratios are very different, which is supported by the fact that the optimal Strouhal numbers are not

aligned. The key feature is that the curves are flat at high Strouhal numbers for high amplitude forcing with good quality square waves.

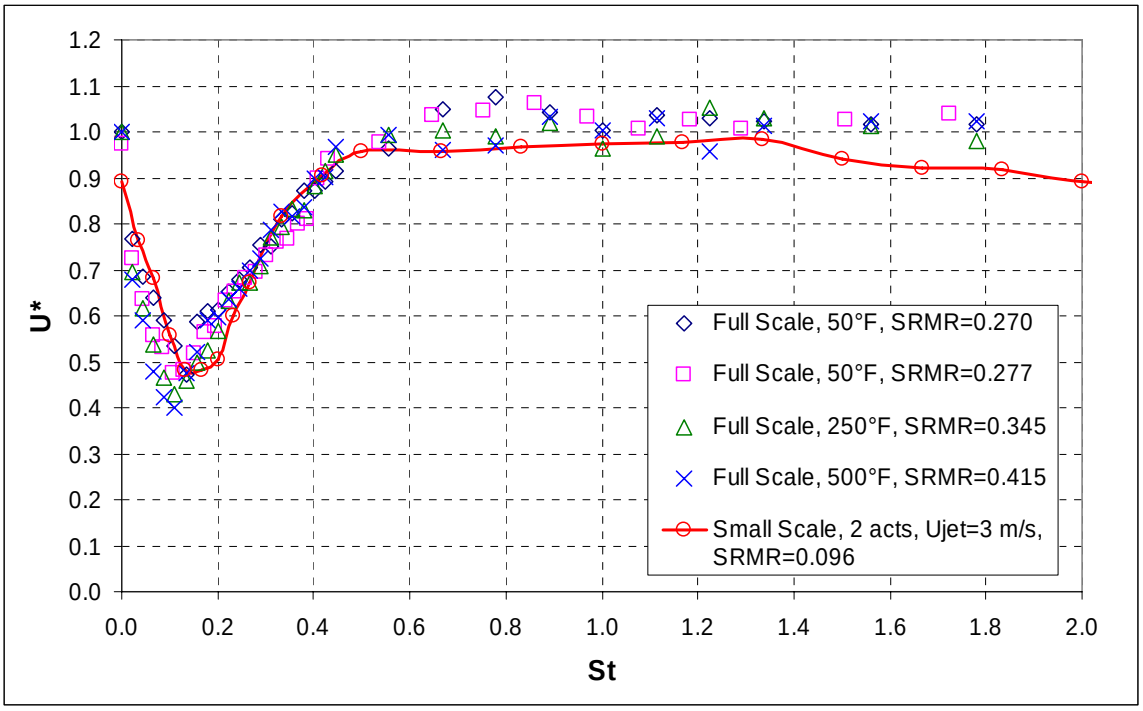

Figure 5.17: Comparison of Full Scale Frequency Sweeps to Small Scale 2-Actuator Case with Very Low Jet Exit Velocity

Figure 5.18 shows that centerline velocity reduction at five diameters is similar to that at ten diameters for the same forcing amplitude. Once again a trend discovered during the small scale experiments is followed; the optimal frequency decreases with increasing downstream location.

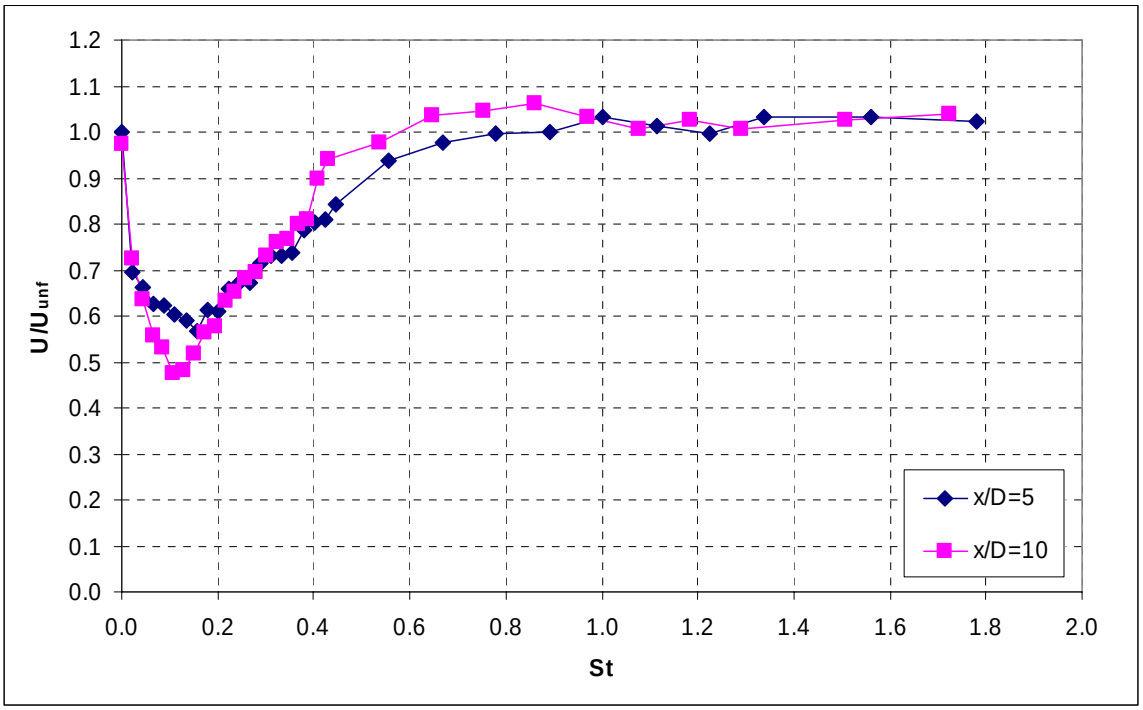

Figure 5.18: Jet Mixing Enhancement as a Function of Strouhal Number at Two Downstream Locations, Pulsing Air Temp = 50°F, SRMR = 0.277

Amplitude Sweeps

Figure 5.19 shows the result of performing an amplitude sweep on the full scale jet at a Strouhal number of 0.135, which is near the optimal frequency for most of the amplitudes tested. The results are once again compared to the small scale. The curve shown for the small scale data is a result of a curve fit on the collapsed data from both the 0.02" and 0.08" wide actuator nozzles. As expected, there is an offset between the small scale and full scale curves, but there is an additional difference in the first couple of nonzero points. Looking at the pulse time histories one observes that at low amplitudes the full scale actuators produce poor quality pulses (figure 5.20). As the SRMR approaches about 0.2, the quality improves and the mixing curves take on the same basic character as the small scale curves. It is interesting to note that both curves seem to bottom out (i.e. reach saturation) at about the same momentum ratio.

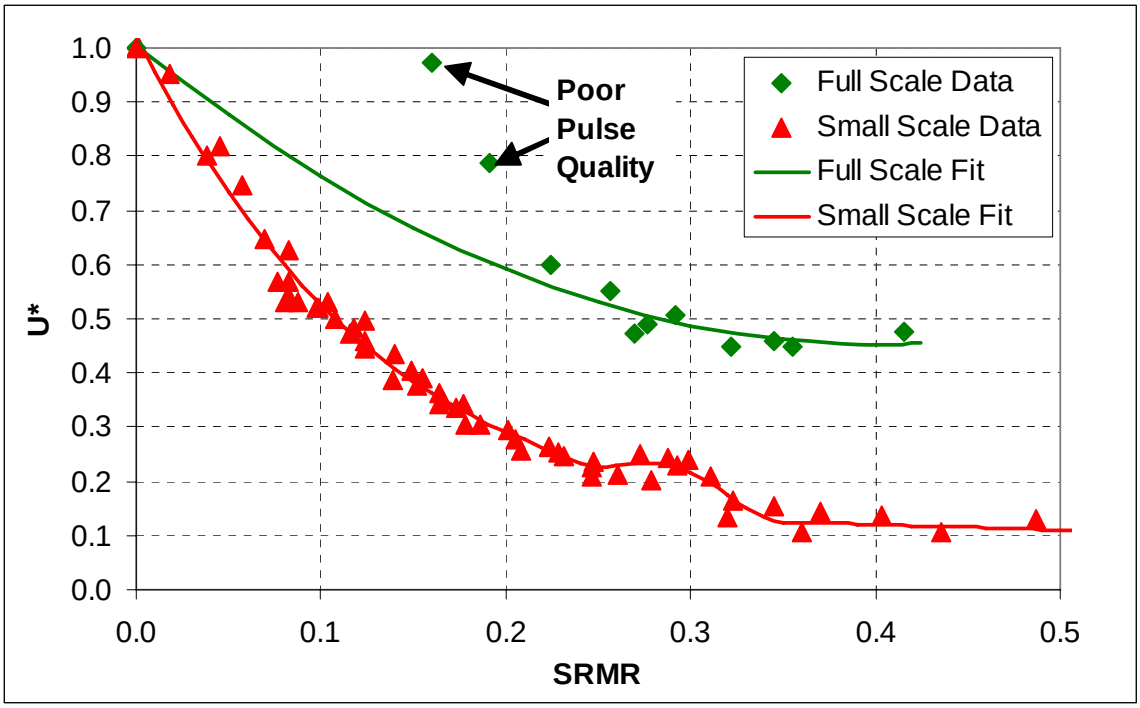

Figure 5.19: Jet Mixing Enhancement as a Function of Momentum Ratio at x/D = 10, Full Scale Jet (St = 0.134) Compared to Small Scale Jet (St = 0.10)

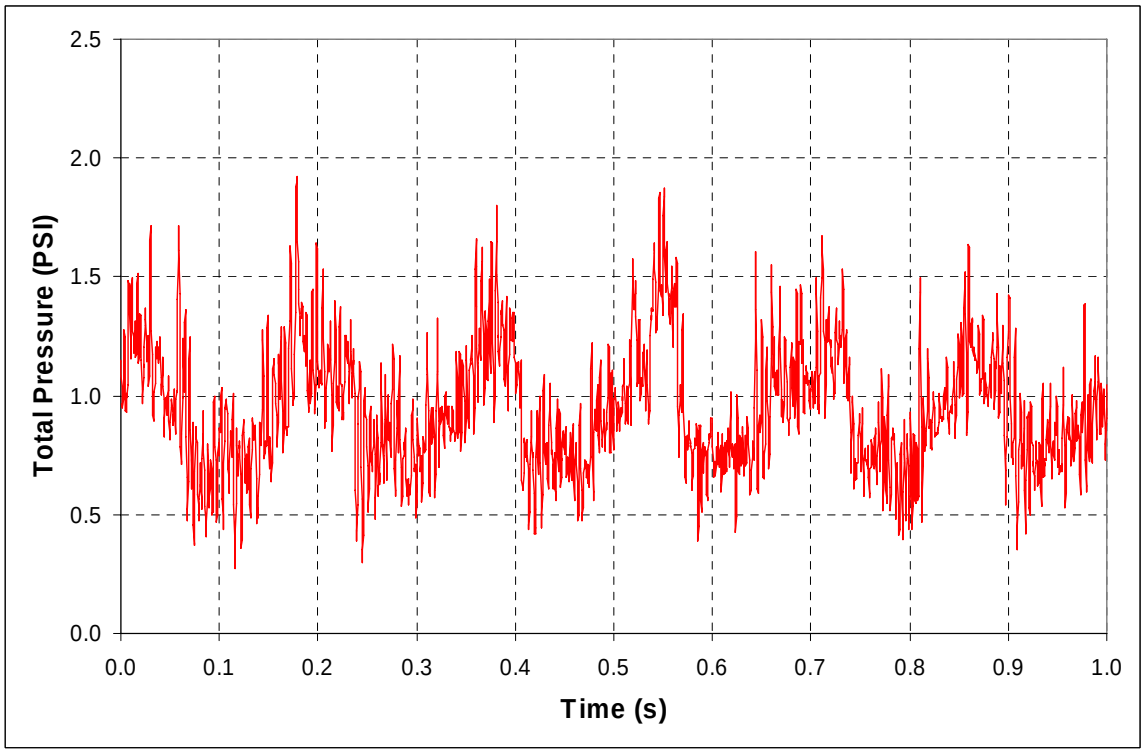

Figure 5.20: Example of a Poor Quality Pulse for Date from Figure 5.19

Since only one slot width was tested in the full scale, a comparison of slot widths versus momentum ratio could not be made. However, the comparison with the small scale results showed that the overall trends between the two systems were similar. The offset between the two curves may be due to a combination of factors, and it is difficult to establish the exact effect of each. Some of the factors include:

1. There were significant differences in the main jet flow quality, especially turbulence level.
2. Building space restrictions led to constriction of the jet and recirculation zones.
3. There are differences in actuator location: slightly upstream of the nozzle exit for the full scale jet and slightly downstream for the small scale.

Number 1 is believed to be the primary reason for the differences and is backed up by the literature.[140]

Centerline Traverses

Centerline mean velocity traverses, figure 5.21, were performed on the full scale jet and compared to a similar small scale case. In this particular instance the SRMR is 0.28 (mass flow ratio is 1.38%) for the full scale jet and the Strouhal number is 0.11. Note that the centerline mean velocity at the jet exit is slightly higher in the forced case due to the "pinching" of the jet plume within the nozzle. This results in a squeezing of the flow area and higher velocity. This increase in exit velocity did not occur with the small scale jet because excitation was external to the main jet nozzle (just downstream of the exit). Again, there is an offset between the two results, but this time the full scale decay curve

has a slightly different character than the small scale decay curve. This difference is believed to be due to two things: the difference in momentum ratios (there was not a small scale centerline traverse with the same momentum ratio to compare it against), and the difference in initial turbulence level. It is not surprising that the curve for the full scale forced jet is higher than the one for the small scale forced jet since one would expect a high initial turbulence level jet to saturate earlier than a low turbulence clean one.

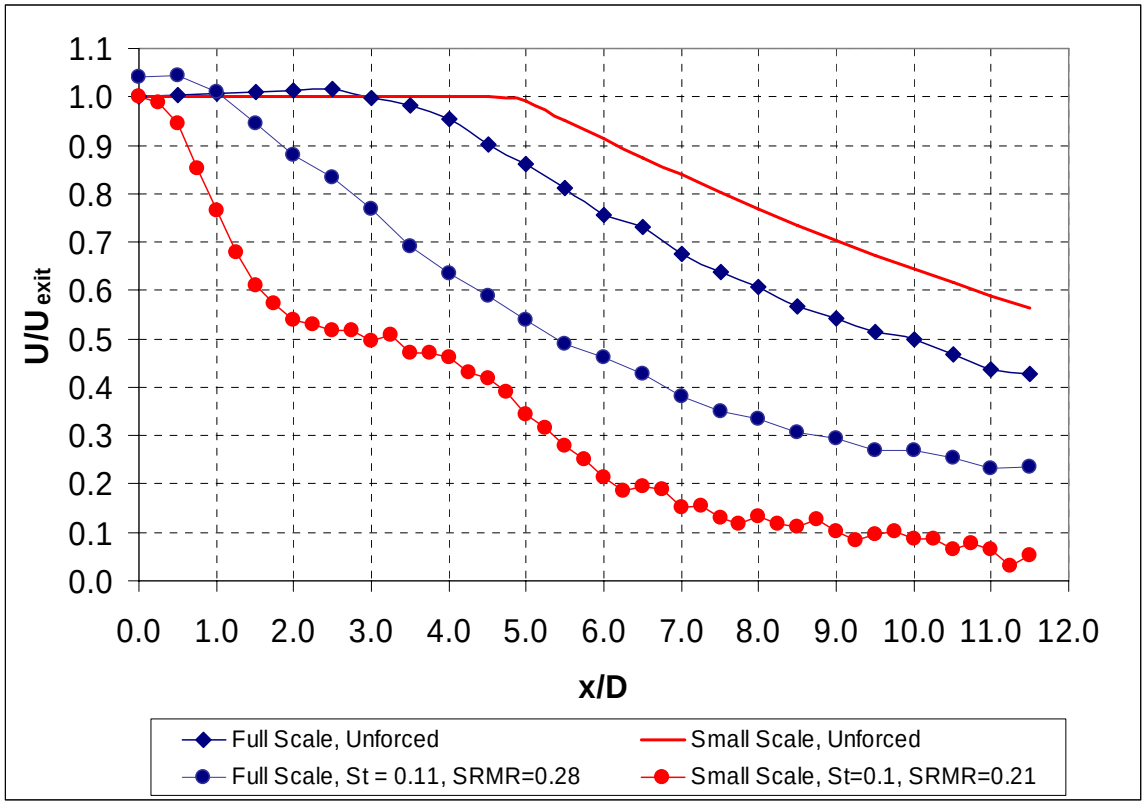

Figure 5.21: Mean Centerline Velocity Traverses For Forced and Unforced Jets, Comparison of Full Scale and Small Scale

Diagonal Traverse

A traverse of the main jet exit with a total pressure probe was made along a diagonal that intersected two of the slot exhaust locations. Combined with data taken in the horizontal and vertical axis, Figure 5.22 shows the resulting velocity profiles. The effect of the injected momentum is evidenced by the velocity deficits shown in the diagonal traverse data. This is indicative of the separation near the wall that is caused by the injected mass flow and is the reason the centerline velocity at the exit is slightly higher than the unforced case.

Summary

The results from the full scale tests were compared with the results of similar small scale tests. Both setups employed 4 actuators situated 90° apart pulsing in pairs antisymmetrically. The biggest difference between the two geometries was that full scale actuation took place slightly upstream of the nozzle exit, while small scale actuation took place slightly downstream of the nozzle exit. The ratios of jet exit area to pulsing slot area were also very similar: 880 for the full scale, and 785 for the small scale. Finally, similar momentum ratios were used wherever possible. The small scale jet rig had significantly less inherent turbulence, and was less confined by the room it was in. Despite the differences in the setups, it is clear that the full scale system exhibits very similar characteristics to the more controlled and cleaner small scale system. Some examples of this are:

1. The optimal Strouhal numbers were the same.
2. Saturation occurred at the same amplitude (SRMR).

3. The optimal Strouhal number decreased with increasing pulsing amplitude.
4. The mixing curves had the same shapes. Offsets between the curves were due to initial turbulence level.

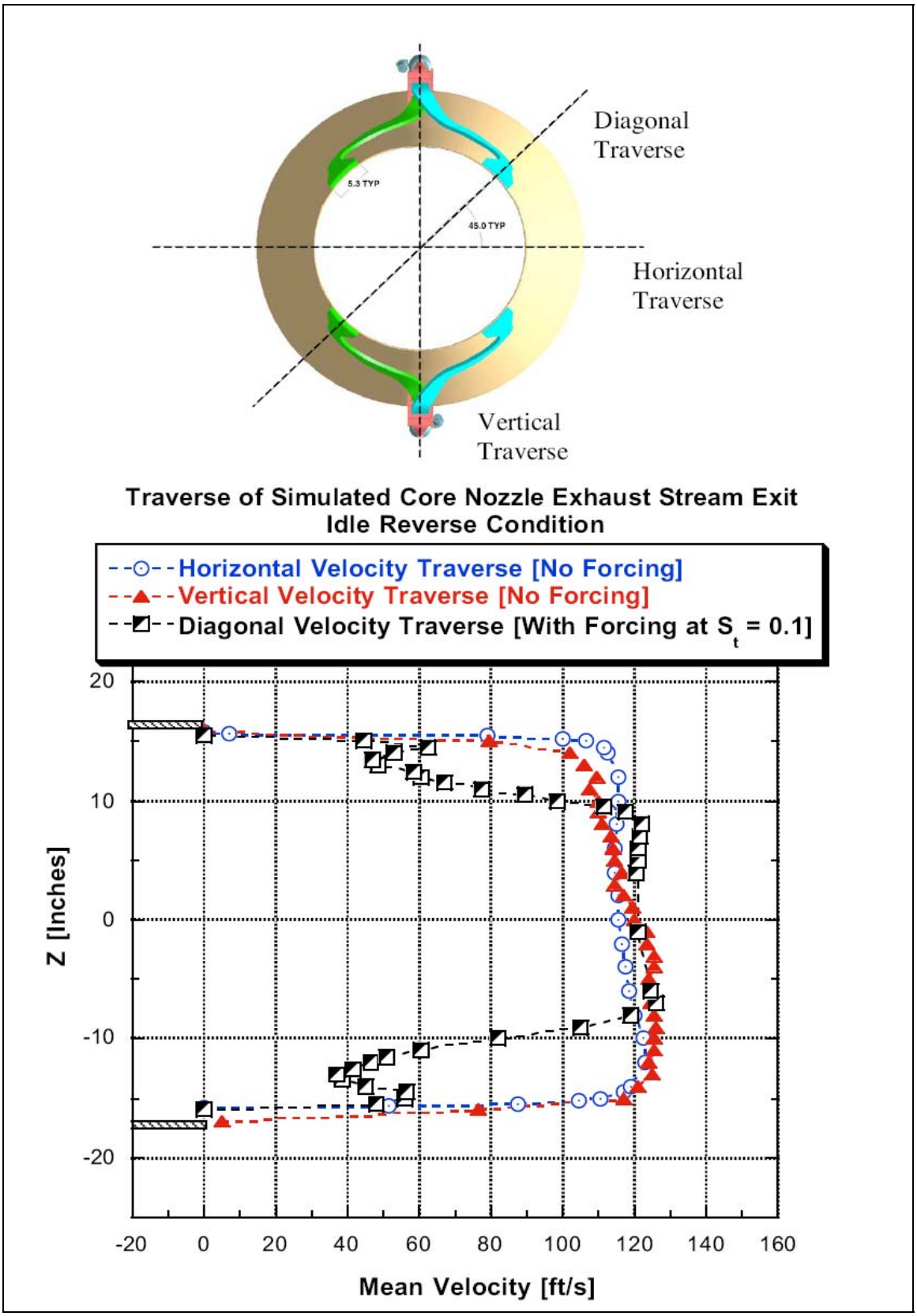

Figure 5.22: Full Scale Jet Exit Velocity Traverses

CHAPTER 6

JET ENGINE – EXPERIMENTAL SETUP AND EQUIPMENT

Chapter Overview

This chapter describes the overall experimental setup and the major pieces of equipment used in experiments on the small jet engine. Figure 6.1 shows how the chapter is organized.

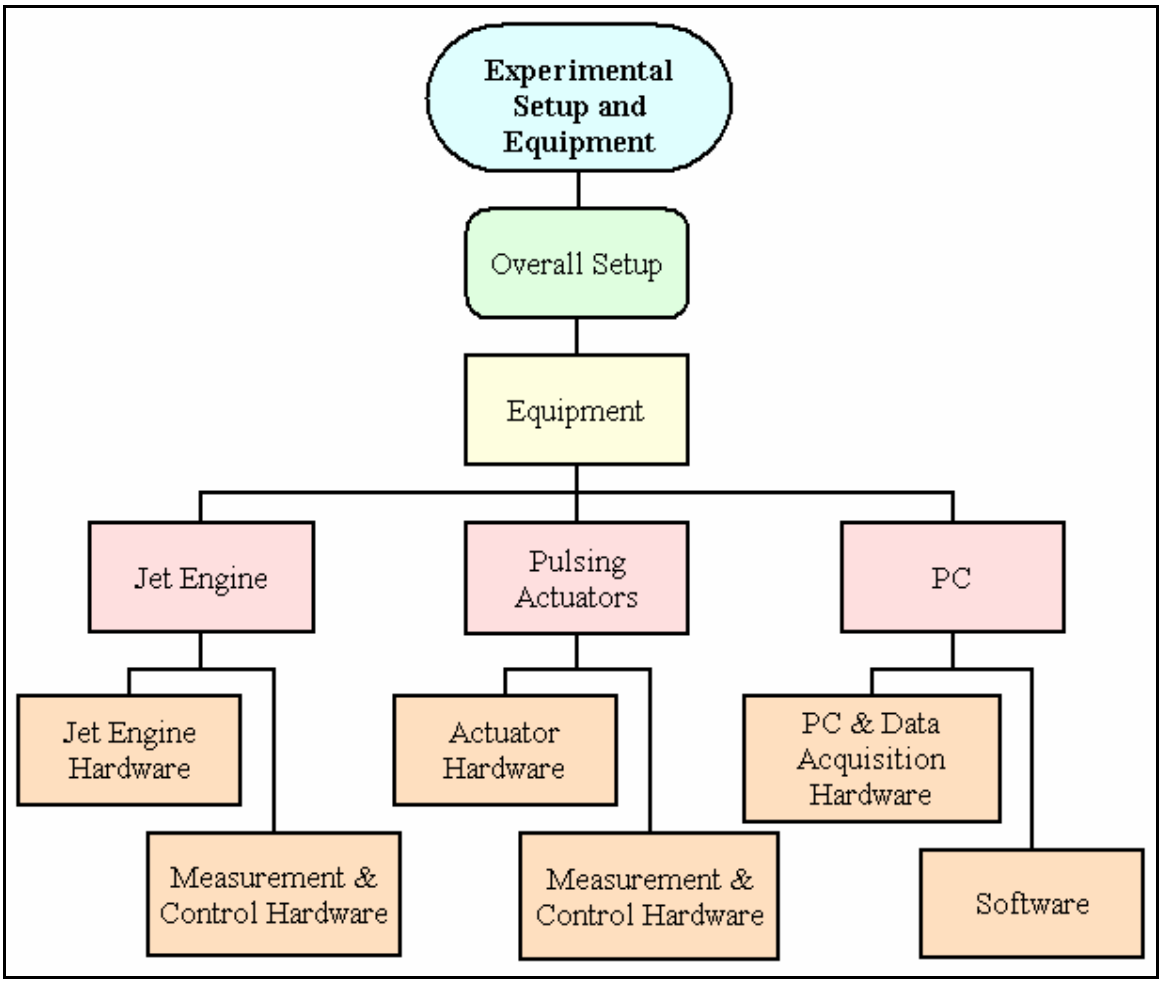

Figure 6.1: Organizational Chart Showing Organization of Chapter

Overall Setup Objectives

The overall objectives of the jet engine experiments were:

1. To verify the effectiveness of pulse fluidic mixing on a realistic (non-laboratory) flow.
2. To analyze mixing under various conditions and compare to small scale results.
3. To perform real time optimization of mixing enhancement on the flow.

Overall Description

A small hobby class jet engine was mounted on a test stand and two high speed pulse fluidic actuators were mounted at the nozzle exit such that they pulsed directly into the jet exhaust, normal to the flow. The plume created by the engine was heated (to about 600°C), annular, and swirling. The actuators were positioned on either side of the jet and were capable of producing fluidic pulses which were roughly sinusoidal in amplitude with respect to time. Pulsing frequency could be varied from essentially 0 Hz up to nearly 1600 Hz and from low to very high amplitudes. Both single-sided and two-sided actuation was implemented. During the first phase of testing the two actuators were operated independently, each with its own motor. During the second phase of testing, the actuators were mechanically phase locked with a timing belt and controlled by a single motor. For two-sided actuation, pulsing was either axisymmetric, antisymmetric, or with random phase. Mass flow through the actuators was measured with a venturi flowmeter. Jet nozzle exit temperature and velocity were measured with a thermocouple and total pressure tube. Point measurements in the flow field were taken with either a combination thermocouple pitot probe or an ‘air probe’ type thermocouple. A personal computer with

a general purpose data acquisition card was used for measurement, control, and automation. Experiments were performed in the building two annex of the Georgia Tech Research Institute Aerospace Lab, Cobb County facility. It is essentially a very large garage with a large sliding door. This setup allowed plume gasses to exhaust to the atmosphere while still shielding the flow field from large crosswinds. Figure 4.4 is a picture of the facility.

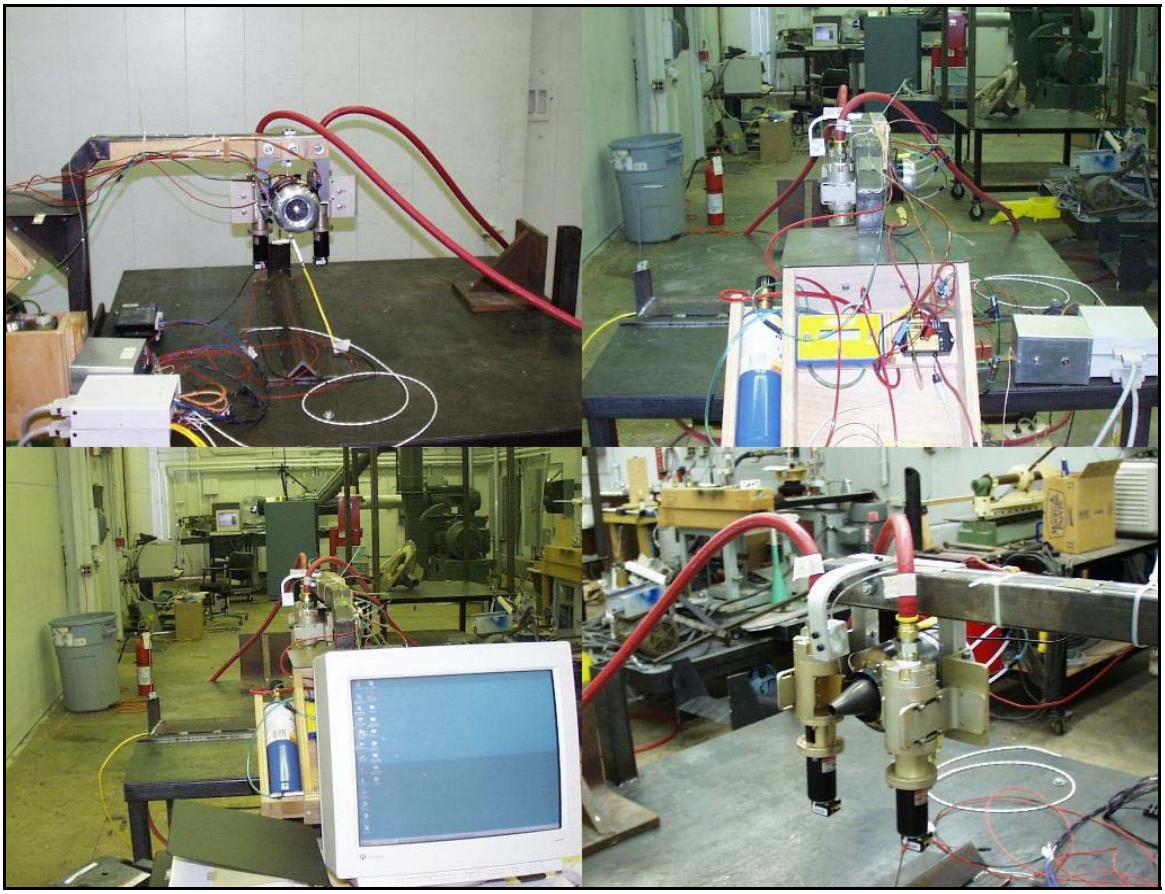

Figure 6.2: Collage of Pictures Showing Overall Setup of Jet Engine Experiments

Overall Setup

Figure 6.2 is a collage of photographs showing the overall jet mixing setup. A test stand was built to hold the jet engine. This test stand was a heavy, mobile, steel table made of 2" square steel tubing and 1/8" thick steel plates welded together. The jet engine was mounted on an arm over the center of the table, and was electrically isolated from the arm. The engine control unit (ECU), needed for startup and throttle control, was mounted in a custom built wooden control box on the side of the table. The pulsing actuators were also mounted on the arm with their nozzles right at the jet exit. Two servo motor controllers, which ultimately control the pulsing frequency of the rotary actuators, were on top of the table near the wooden control box. In the figure, there is an 'air probe' thermocouple on the table at a location of 4 outer diameters downstream. A personal computer with two National Instruments data acquisition and control cards running LabView software was used for data acquisition, control and automation of experiments.

The pulsing actuators were connected to a compressed air source via high pressure red hose made by Goodyear. Actuator mass flow rate control was achieved using a Moore electropneumatic actuator and pneumatic amplifying relays. Mass flow for each actuator was measured using Flow-Dyne venturi flow meters. The jet engine was started up using compressed air from a portable air compressor (to assure that the air was clean) and propane from a small portable tank mounted next to the ECU. Two valves control the flow of compressed air and propane, and an ignition switch ignites a glow plug to start the engine. The valves and ignition switch are located on the control panel next to the ECU. Once the engine is started, the ECU automatically switches over to kerosene fuel.

The kerosene fuel tank is mounted to the table under the ECU in a custom built wooden box.

Figure 6.3 is a technical schematic which shows the complete setup and all of the various major sub-components, including the electrical, pneumatic, and fuel lines. The mechanical drawings of the actuators are available in Appendix B.

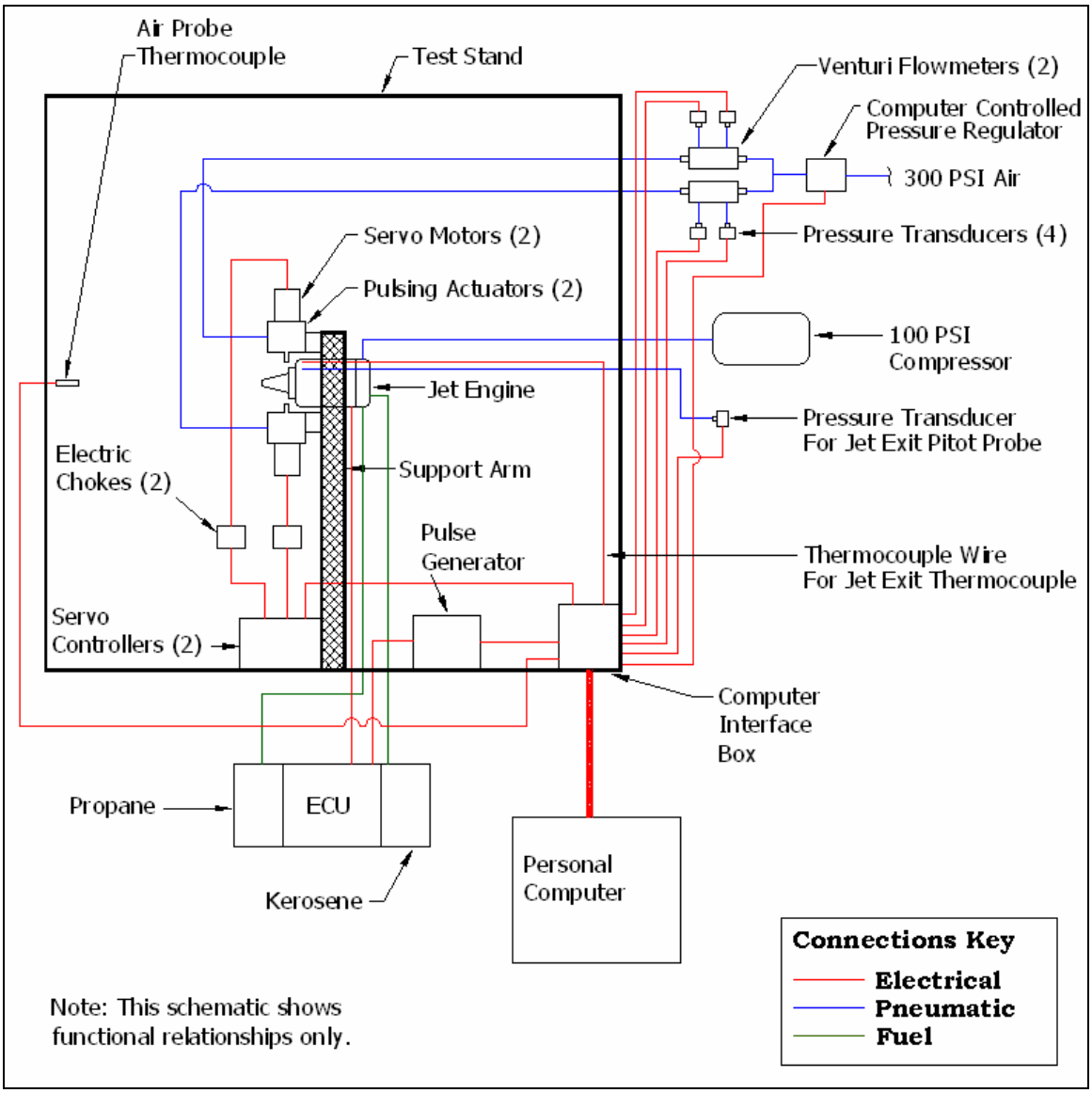

Figure 6.3 Technical Schematic of the Overall Setup for Jet Engine Experiments

The Jet Engine

The miniature jet engine used in the experiments was a RAM 750 manufactured by R.A. Microjets. It has a single-stage centrifugal compressor and a single-stage axial turbine. It is capable of producing approximately 90 Newtons (20 lbs.) of thrust and high subsonic exhaust flows at temperatures over 700˚C. Figure 6.4 is a collection of three photographs of the jet engine. The polypropylene tubes running through the inlet cover supply compressed air, propane, kerosene, and lubricant to the jet. The hole on top of the jet engine casing is where the ignition glow plug is screwed in.

The jet nozzle outer exit diameter is 66 mm (2.6 in.) and the inner diameter (i.e. the centerbody maximum diameter) is 43 mm (1.7 in.) at the exit. Figure 6.5 is a schematic of the jet nozzle exit which includes dimensions and a calculation of the exit area, which is shaded in blue. As shown in the figure, the resulting annular exit area of 1,880 square millimeters (2.9 square inches) is obtained when the blockage by the three struts supporting the centerbody is taken into account.

As mentioned earlier, the jet engine had to be electrically isolated from the test stand support arm. This was accomplished by sheathing the engine support bracket mounting bolts with shrink-wrap and by inserting thin wooden slabs between the bracket and support arm, and between the bracket and the mounting bolt heads as seen in Figure 6.6. It was necessary to do this because the body of the jet engine was tied to the glow plug's negative power terminal (ground). Had the jet not been electrically isolated, the table

would have served as an alternate return path for the power supply during startup, resulting in various electrical problems.

Figure 6.4: Photographs of the RAM 750 Jet Engine

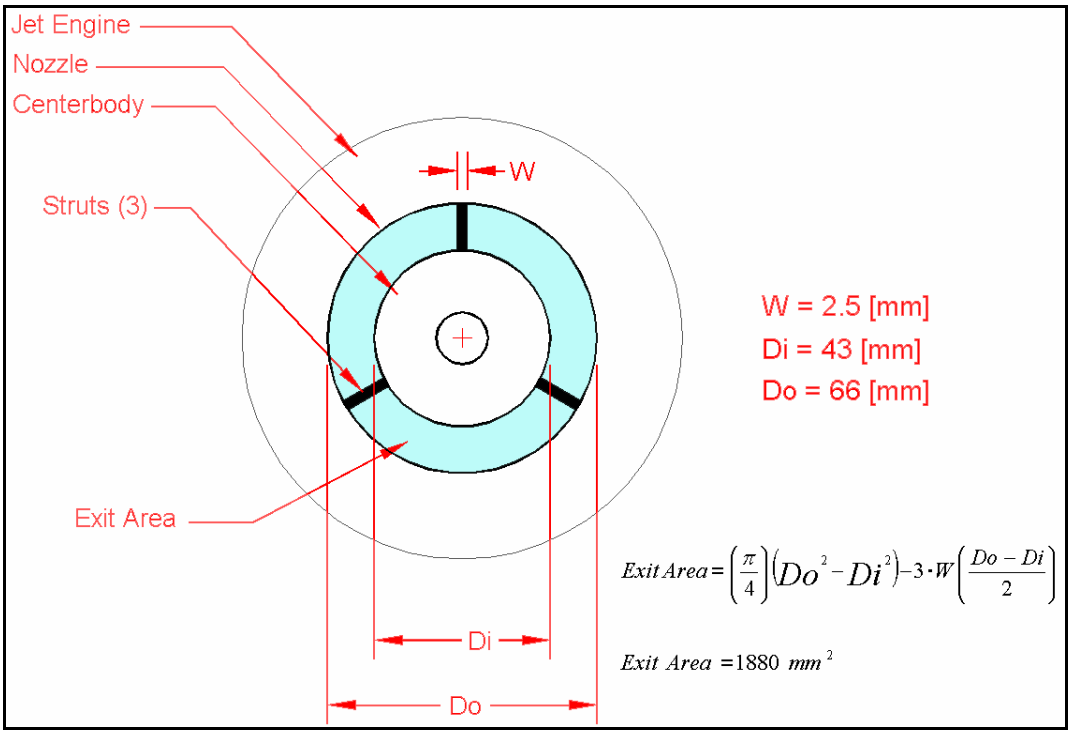

Figure 6.5: Exit Area Calculation Diagram

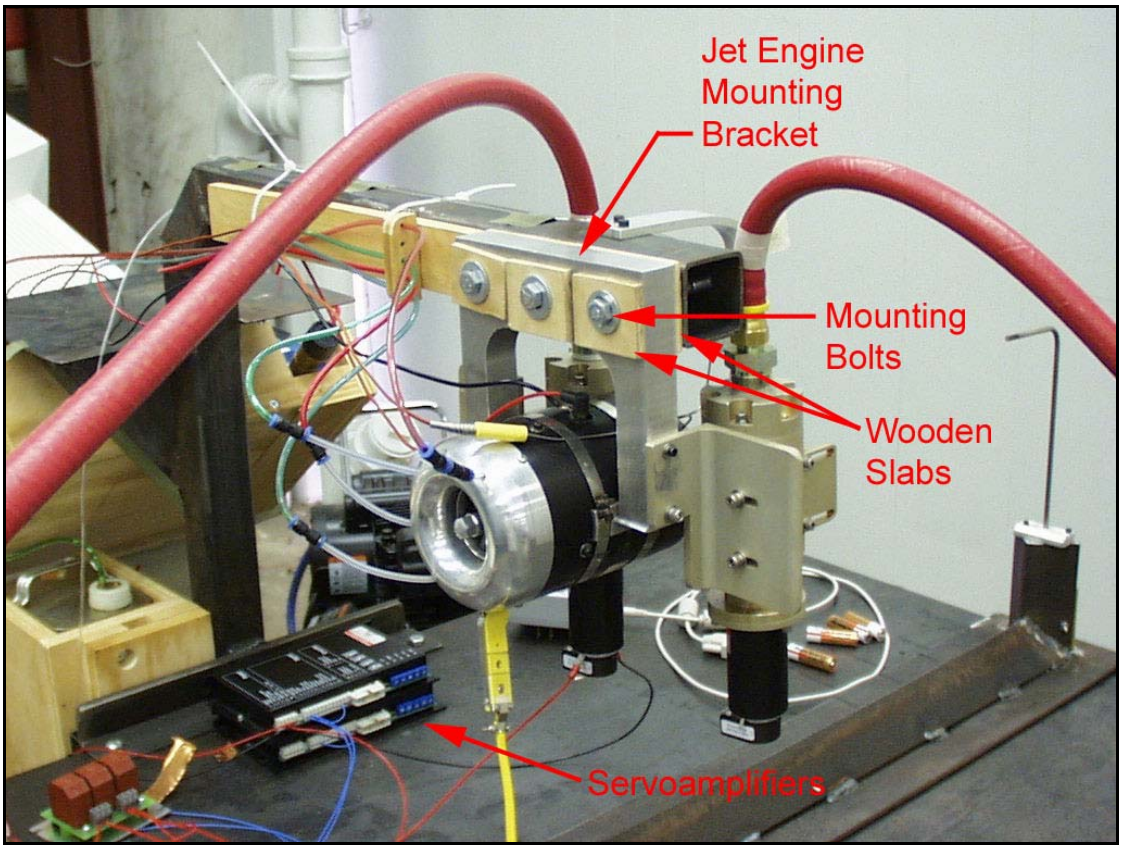

Figure 6.6: Photograph Showing Mounting and Electrical Isolation of Jet Engine

Jet Engine Control Hardware

The RAM 750 comes with an electronic control unit (ECU) as shown in figure 6.7. The ECU performs the following four major functions:

1. It aids in starting the jet engine.
2. It constantly monitors the combustion pressure and exhaust temperature and kills the engine if they exceed certain values.
3. It regulates the throttle according to user input.
4. It shuts down the jet engine.

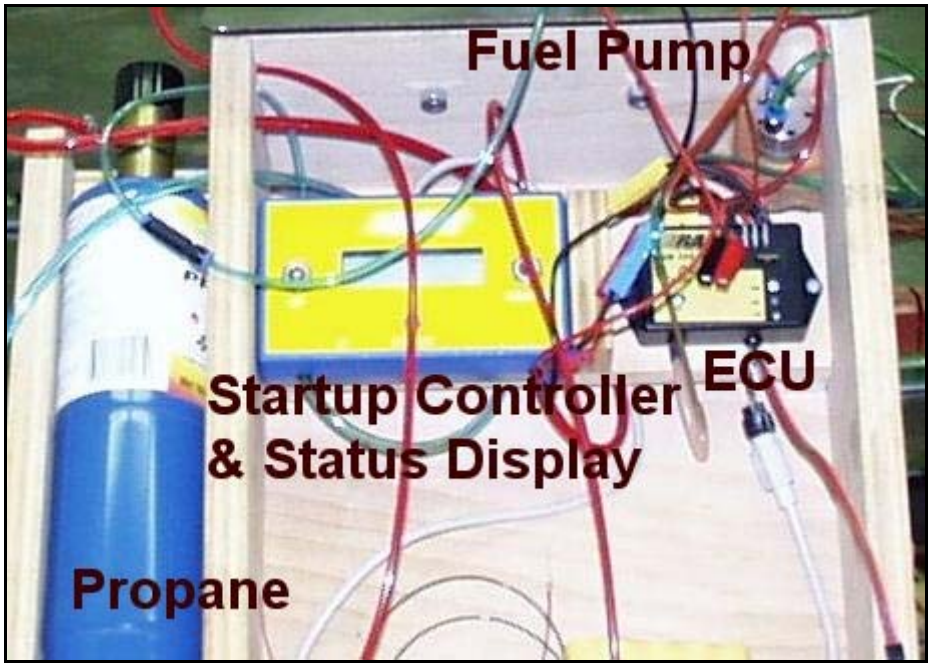

Figure 6.7: The Engine Control Unit (ECU) and Control Center

The jet engine is started manually by directly injecting propane and compressed air into the combustion chamber and igniting the mixture with a glow plug. The glow plug has a small platinum coated filament that must be pulled out of its sheath before it is installed in order for combustion to occur. The valves controlling the propane and air, as well as

the ignition switch, are located on the startup controller (see figure 6.7). After running on propane for approximately 5 seconds, the ECU automatically starts the fuel pump and supplies kerosene to the combustion chamber. At this point the user must turn off the propane. The ECU adjusts the throttle by linearly varying the speed of the fuel pump in accordance with the throttle setting.

The ECU has two electrical inputs: a power input, and a signal input. Because the engine was designed for a radio-controlled hobby aircraft, the power input normally comes from a 6-volt battery pack, and the signal input normally comes from a radio receiver. In this case, a Lambda model LLS-5008 power supply provided the 6V power input and a custom built controllable pulse generator provided the signal input. The power input supplies voltage to the glow plug for ignition and also to the engine's fuel pump. The voltage supplied to the fuel pump is regulated by the ECU and is proportional to the throttle setting. The signal input is a 46 Hz, 5 Volt square wave, and the pulse width controls the throttle level. In order to implement computer control of the throttle, a custom 46 Hz square wave pulse generator was constructed. This device (figure 6.8) receives a 0 to 5 volt analog output signal from the PC and adjusts the pulse width proportionally.

Initially, only pulse width throttle control was used. This was sufficient for preliminary experiments. But eventually, higher accuracy became desirable and greater control of the throttle was needed for two reasons. First, the resolution of the ECU throttle controller was too coarse. The desired jet velocity was often somewhere between two obtainable

velocities. Second, the ECU did not hold the velocity sufficiently steady throughout the course of a run. There were two main reasons for this. First, as the jet engine consumed fuel, the pressure in the fuel line due to decreasing liquid height in the fuel tank resulted in a downward drift in jet velocity throughout a run. Second, it was discovered that the throttle depended somewhat on the actuator servomotor speed because of electromagnetic radiation. As the servomotor speed was increased, the throttle decreased.

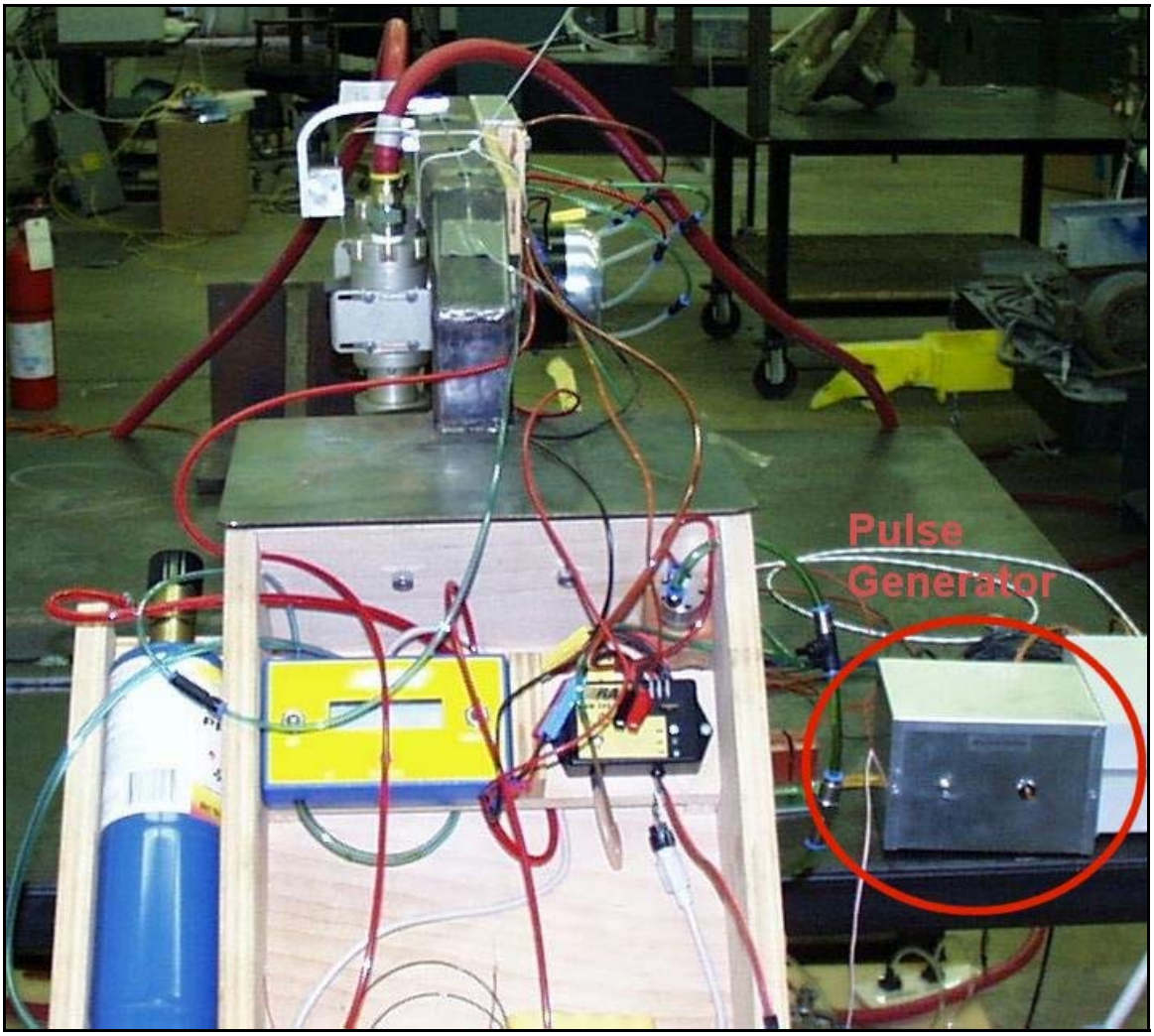

Figure 6.8: The Custom Square Wave Pulse Generator

Tighter control over the throttle was gained using a Lambda LLS5008 controllable power supply to provide the power input to the ECU. Instead of supplying the ECU with a constant 6 volts, the power input was allowed to vary between 5 and 7 volts. This was used in conjunction with the usual pulse width throttle control. The throttle level could be set 'in the ballpark' with pulse width control and fine-tuned using power supply control. The Lambda power supply was controlled by an analog output from the PC. A PID control algorithm was written to continually adjust the power supply as needed to maintain the desired jet velocity. Figure 6.9 is a schematic that shows the original throttle control setup, and the modifications made to improve it.

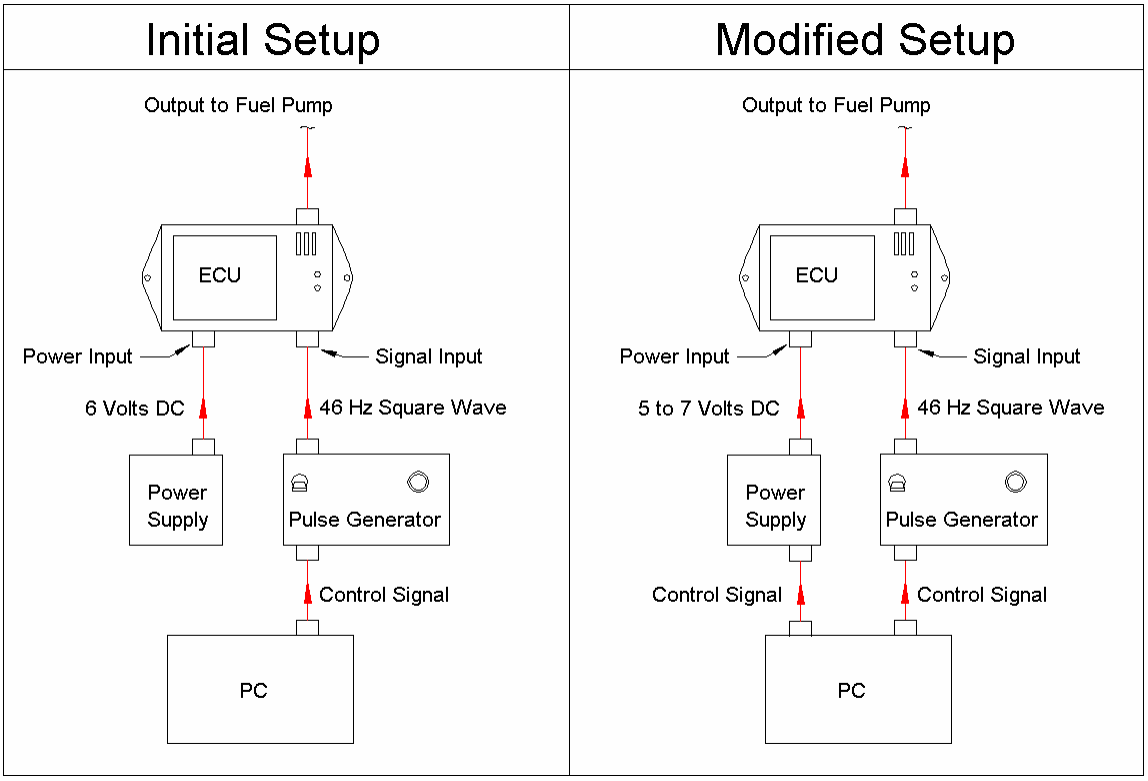

Figure 6.9: Schematic Showing Original and Modified Control System Setup

Jet Engine Measurement Hardware

The jet exit velocity was measured with a 0.065” O.D. (0.03” I.D.) total pressure tube mounted at the nozzle exit. This tube was connected to one side of a SenSym ASCX01DN pressure transducer, figure 6.10. This is a differential transducer with an amplified output (0 to 5 volts). It has ambient temperature compensation, and a pressure range of zero to one pounds per square inch (PSI). The other side of the differential transducer was left open to the atmosphere.

Figure 6.10: SenSym Pressure Transducer

Jet exit temperature was measured with a 0.04” diameter shielded Omega type K probe thermocouple. This probe was originally mounted against the body of the jet engine and protruded into the flow through a small hole in the jet nozzle (see figure 6.14). At first this presented no problems, but eventually the thermocouple had to be taken off of the jet and mounted next to the dynamic pressure tube so that it wasn’t in contact with the body of the jet engine (see figure 6.15). The body is apparently tied to the negative side of the power supply, and it was discovered that the power circuit was using the thermocouple shield as a return path, resulting in various electrical problems. It is not known why this

problem didn't appear initially, but it could have been due to a layer of oxidation on the probe that eventually wore through, and thus closed the circuit. Disconnecting the shield also solved the problem, but resulted in larger measurement noise. Downstream centerline temperature was measured with an Omega type K 'air probe' thermocouple (figure 6.11). This probe has an exposed junction element that is recessed into a drilled sheath tip. This gives it a fast response time, protection from accidental breakage, and partial radiation shielding.

Figure 6.11: Air Probe Used to Measure Downstream Temperature

The Pulsing Actuators

The actuators for this project were designed and built in-house. Detail and assembly drawings are in Appendix B. Figure 6.12 is a combination picture/schematic of a pulsing actuator, with all of its major components labeled. Figure 6.13 is a picture of a disassembled actuator with labels of the parts. The actuators function much like a siren. Compressed air enters an actuator from the top and moves into a cylindrical plenum in the rotor housing. Inside the housing is a cylindrical rotor with 12 slots. It is connected to a high power servomotor directly below it. The motor spins the rotor at a given angular speed, and when one of the slots aligns with the actuator nozzle a burst of air exits the actuator. Thus, the pulsing frequency is set by controlling the angular speed of the rotor. The amplitude of the pulse is set by controlling the mass flow rate.

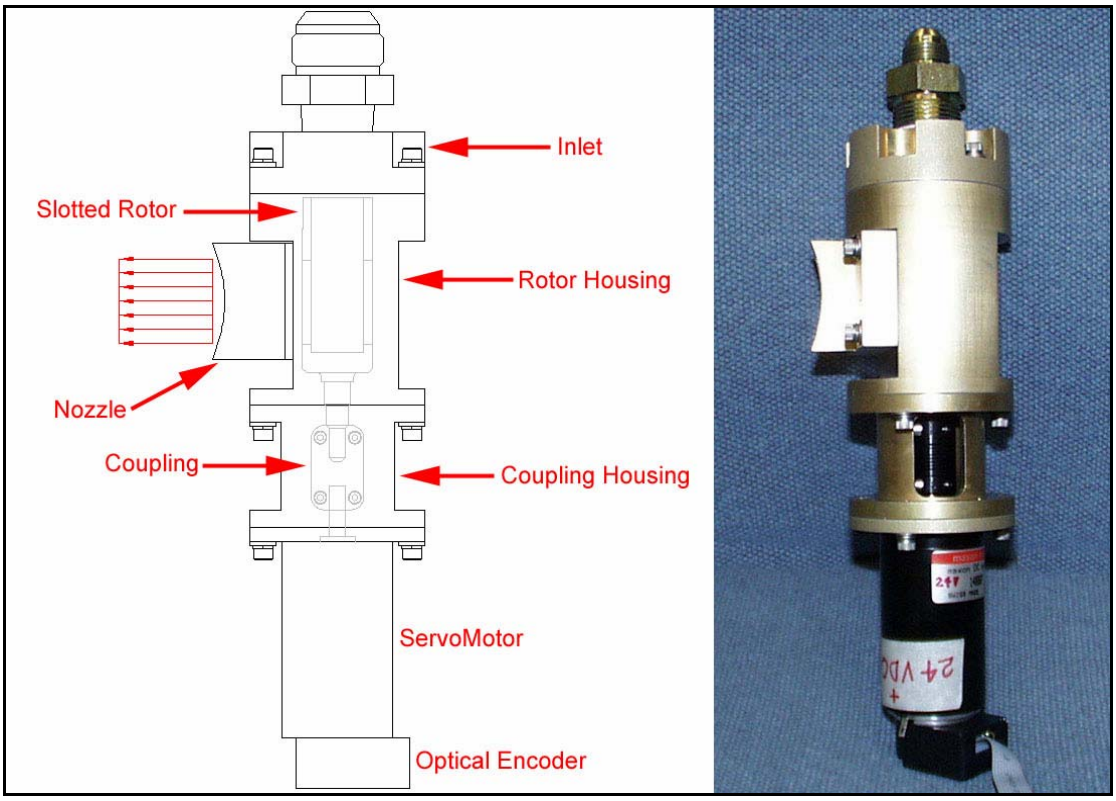

Figure 6.12: Schematic and Picture of a Pulsing Actuator

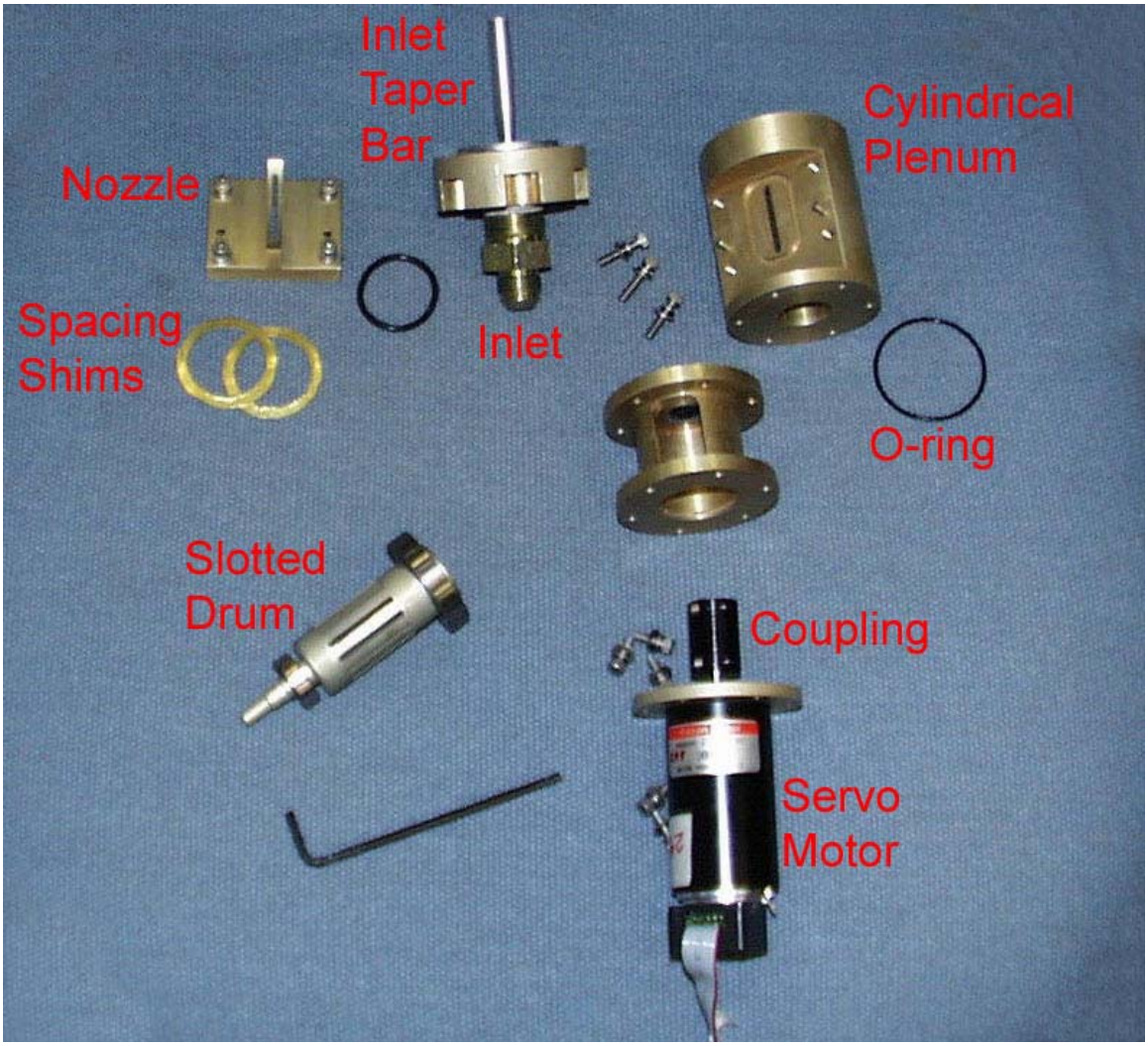

Figure 6.13: Disassembled Actuator

The fluidic actuator nozzles were positioned at the jet engine nozzle exit plane on opposing sides of the jet engine as seen in Figure 6.14. In this picture, the exit thermocouple is still attached to the jet engine. Figure 6.15 is a wider-angle picture of the setup taken at a different angle. Note the new position of the exit thermocouple, as it has been moved off of the jet engine for reasons discussed previously.

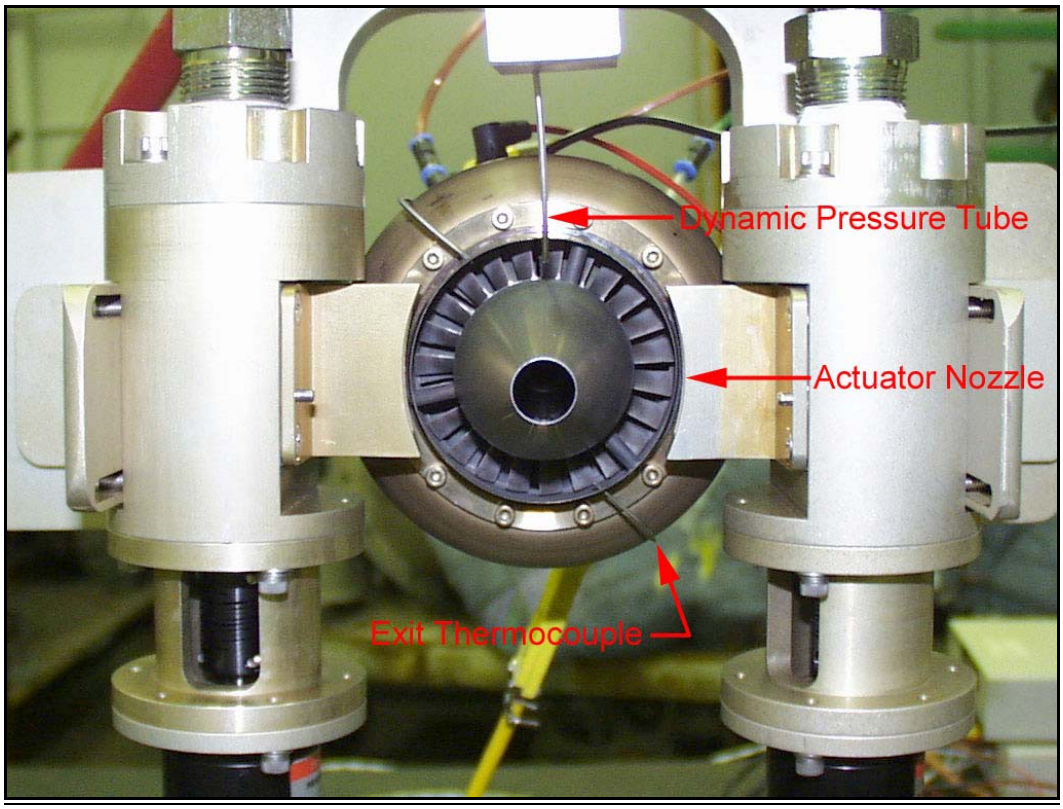

Figure 6.14: Close-up of Actuators at Jet Exit

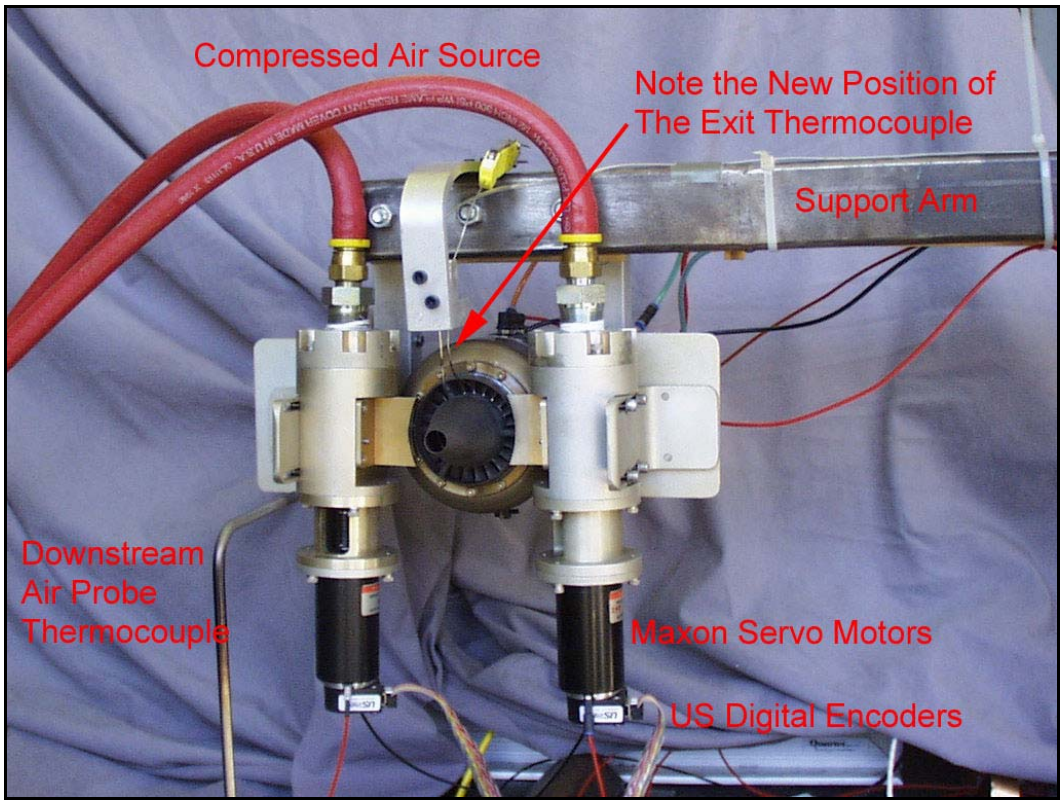

Figure 6.15: Jet Exit Setup

As compressed air moves through the actuator, inertial forces resulting from its high velocity forces most of the flow to the bottom side of the nozzle resulting in a non-symmetric velocity profile (figure 6.16). To remedy this problem and obtain symmetric velocity profiles from the actuators, a slot orifice plate made of PET (polyethylene terephthalate) cut from a 2-liter bottle was inserted between the nozzle and the rotor housing (figure 6.17). The slotted orifice, which is trapezoidal in shape, partially blocks the flow through the lower half of the nozzle but allows the flow through the upper half to pass unrestricted. The result is a more symmetric velocity profile (see the Results section, Chapter 7, for profile measurements).

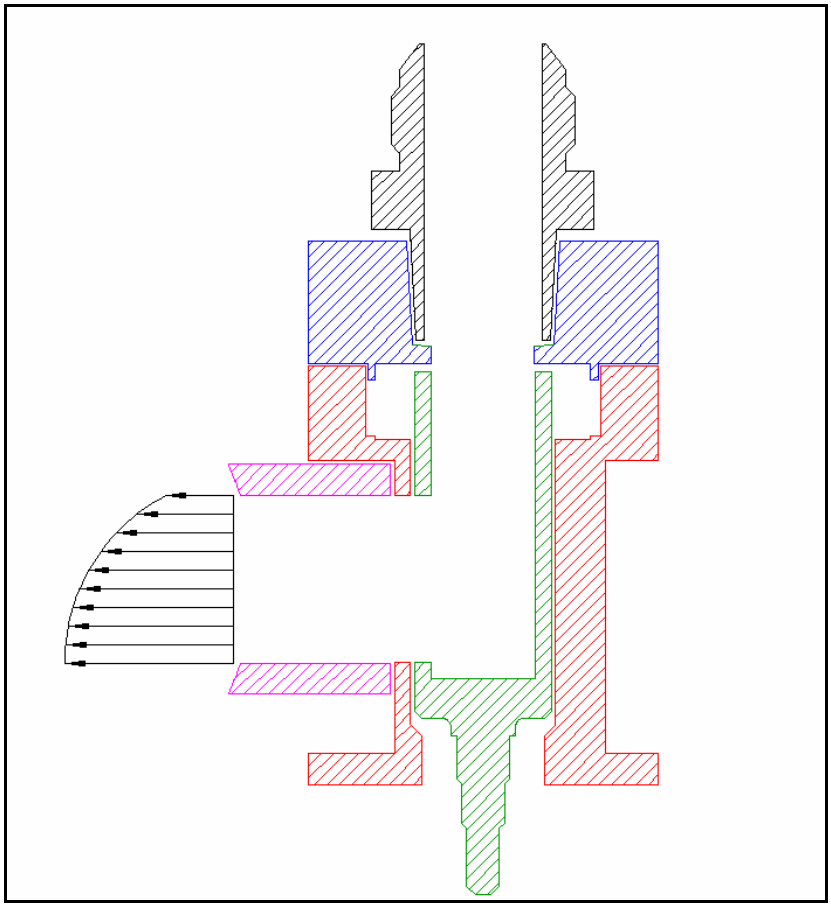

Figure 6.16: Schematic Showing Non-Symmetric Flow From Unmodified Actuator Nozzle

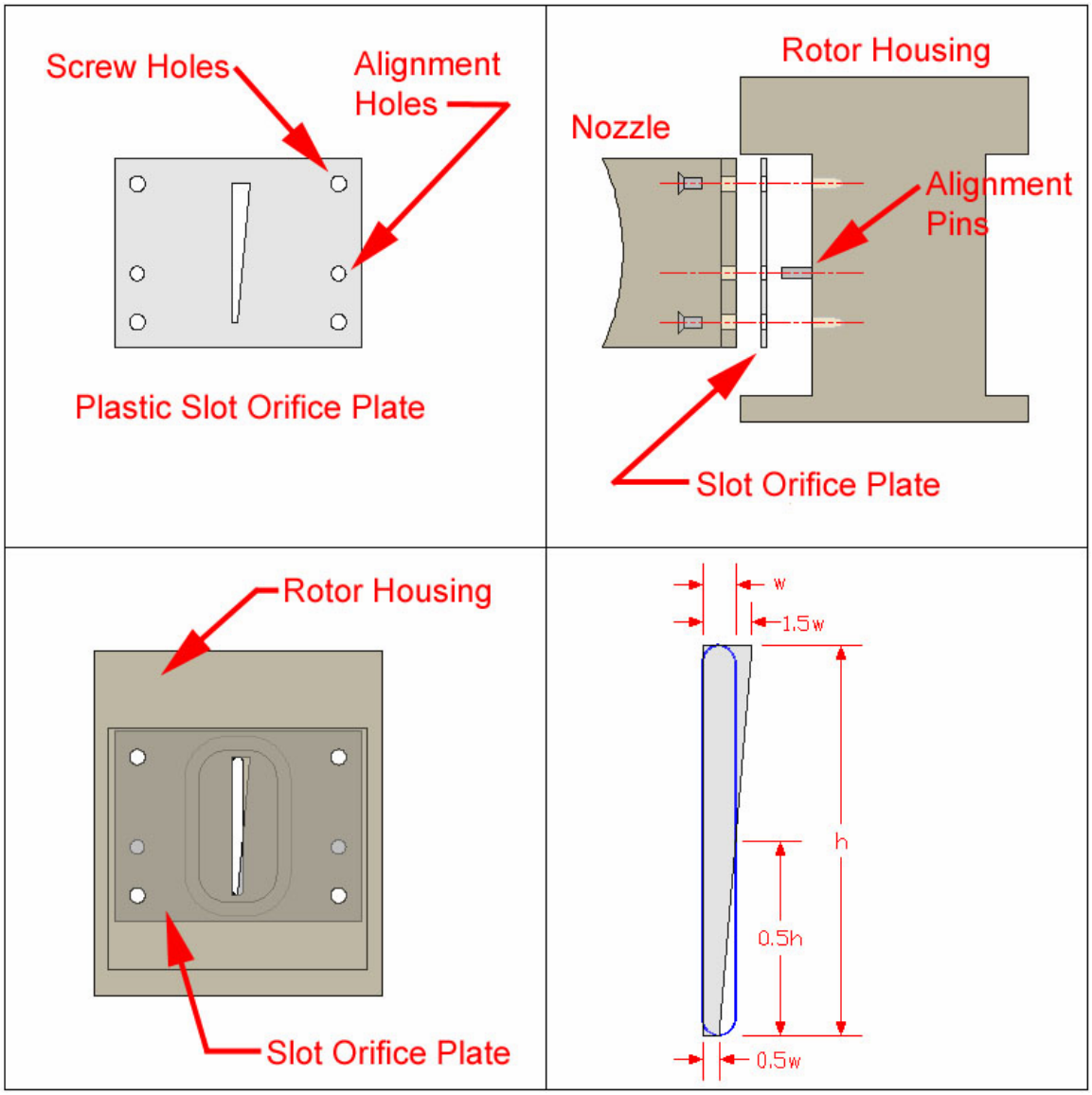

Figure 6.17: Diagram of Tapered Plastic Slot Orifice Plate

Actuator Control Hardware

The actuators were powered by two Maxon RE40 DC brushless 24-volt servomotors. These high power servomotors are capable of angular speed ranging from 0 to 8000 RPM and can change speeds very rapidly. Each motor was controlled by a Maxon ADS 50/10 servoamplifier, and required an additional choke because of low motor terminal inductance. Figure 6.18 shows the motor, servoamplifier, and encoder. Each

servoamplifier implemented closed loop speed control on its corresponding motor using the signals from a US Digital E2 optical encoder as feedback. The motor speed was ultimately set by sending a 0 to 10 Volt signal to the servoamplifiers from the PC. The angular speed of the motors was a linear function of control voltage.

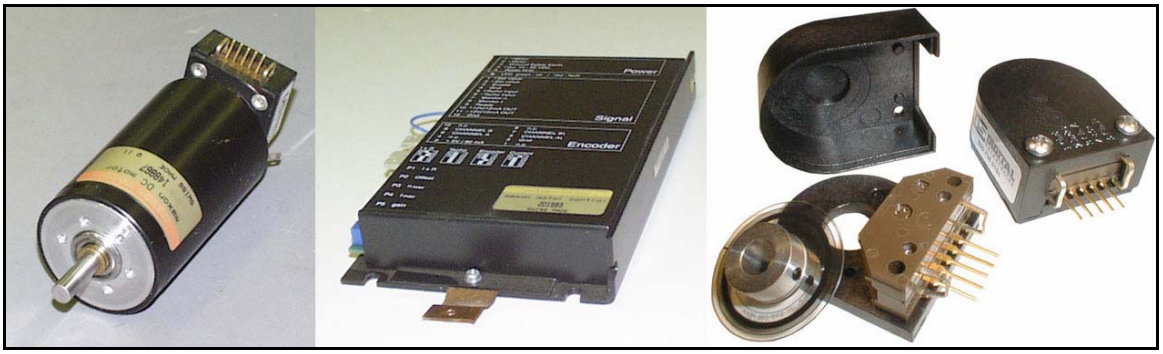

Figure 6.18: Pictures of Motor, Servo amplifier, and Encoder

The amplitude of the fluidic pulse is a function of the mass flow rate through the actuators or, alternatively, the static pressure at the actuator inlet. The ratio of mass flow rate through the actuators to the mass flow rate through the jet engine, expressed as a percentage (%MFR), was an important parameter in this study. Therefore it was important to measure and control the mass flow rate through the actuators. Mass flow rate was controlled using a Moore Model 77-3 electropneumatic transducer and two Moore Model 66-BA6 pneumatic amplifying relays in parallel. Figure 6.19 is a schematic of the mass flow control system and figure 6.20 is a picture. The PC sent an analog signal between 0 and 5 Volts to the electropneumatic transducer, which received its pneumatic input from a regulated air source. The output of the electropneumatic transducer was, in turn, hooked up to the input of the two pneumatic relays. The output pressure was proportional to the electrical signal, and served as a control signal for the

relays. The pneumatic relays are essentially pneumatic amplifiers. They are connected to a high pressure compressed air source, receive a pneumatic signal (from the transducer) and output a pressure proportionally higher than the signal pressure. The models used had a 1:6 input/output pressure ratio (gain). Two relays were used in parallel in order to obtain sufficient mass flow rates. In this way, it was possible to control the mass flow rate through the actuators with the PC.

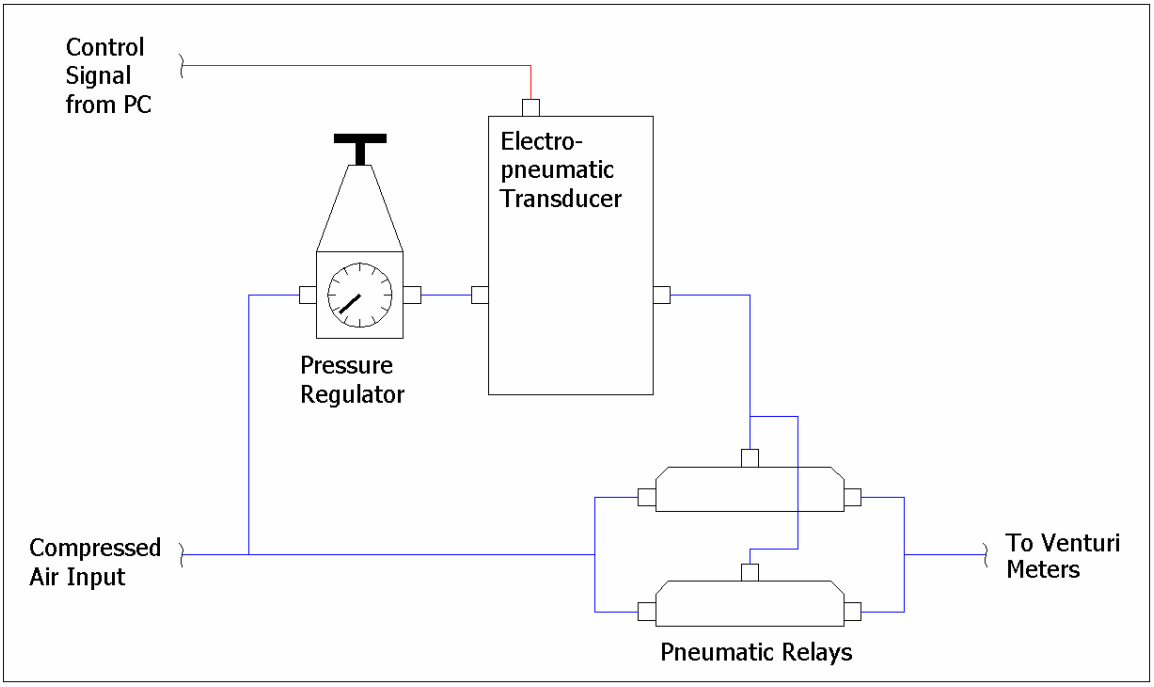

Figure 6.19: Schematic of the Actuator MFR Control System

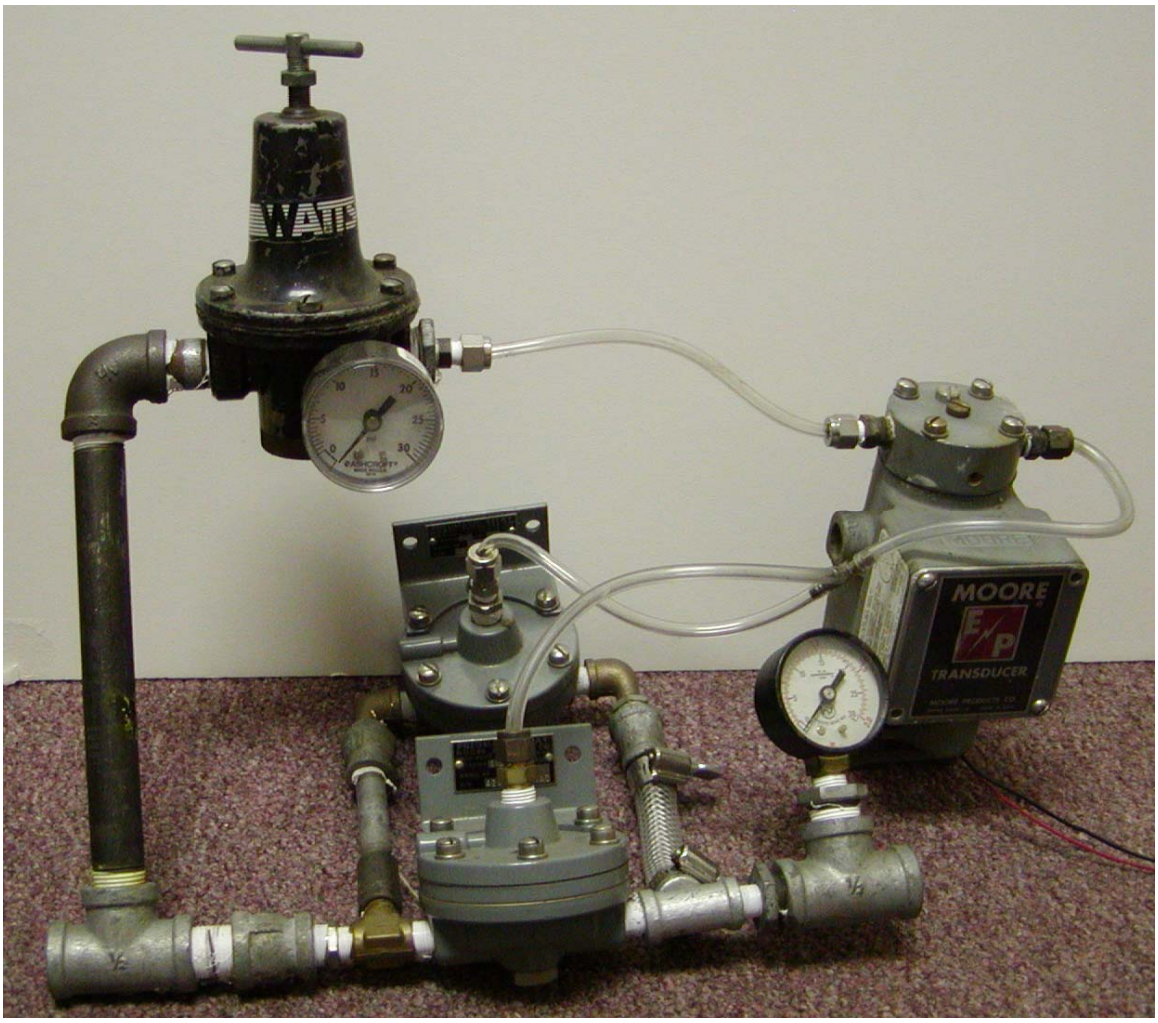

Figure 6.20: Picture of the Actuator MFR Control System

Actuator Measurement Hardware

Motor angular speed was measured with two US Digital model E2 optical encoders (see figure 6.18). The encoders were powered with 5 Volts from the servoamplifier, and have 2 quadrature TTL squarewave outputs and an index pulse. They have a resolution of 360 pulses per revolution. The outputs were connected to both the servoamplifier (for feedback control) and a counter/timer gate on the PC data acquisition card to measure the angular speed of the motors.

Mass flow rates through the two actuators were measured with two Flow-Dyne VSH1201-APM venturi flow meters. Figure 6.21 is a picture of one of the venturi meters. These venturis have an inner diameter of 0.5” and a throat diameter of 0.25”. The high pressure inlet port of each venturi was hooked up to a SenSym ASCX30DN pressure transducer. This is the same type of transducer (differential, amplified, temperature compensated, etc.) used to measure the dynamic pressure at the jet exit except it has a 0 to 30 PSID pressure range. The low pressure port on the throat of each venturi was hooked up to a SenSym ASCX15DN, 0 to 15 PSID pressure transducer.

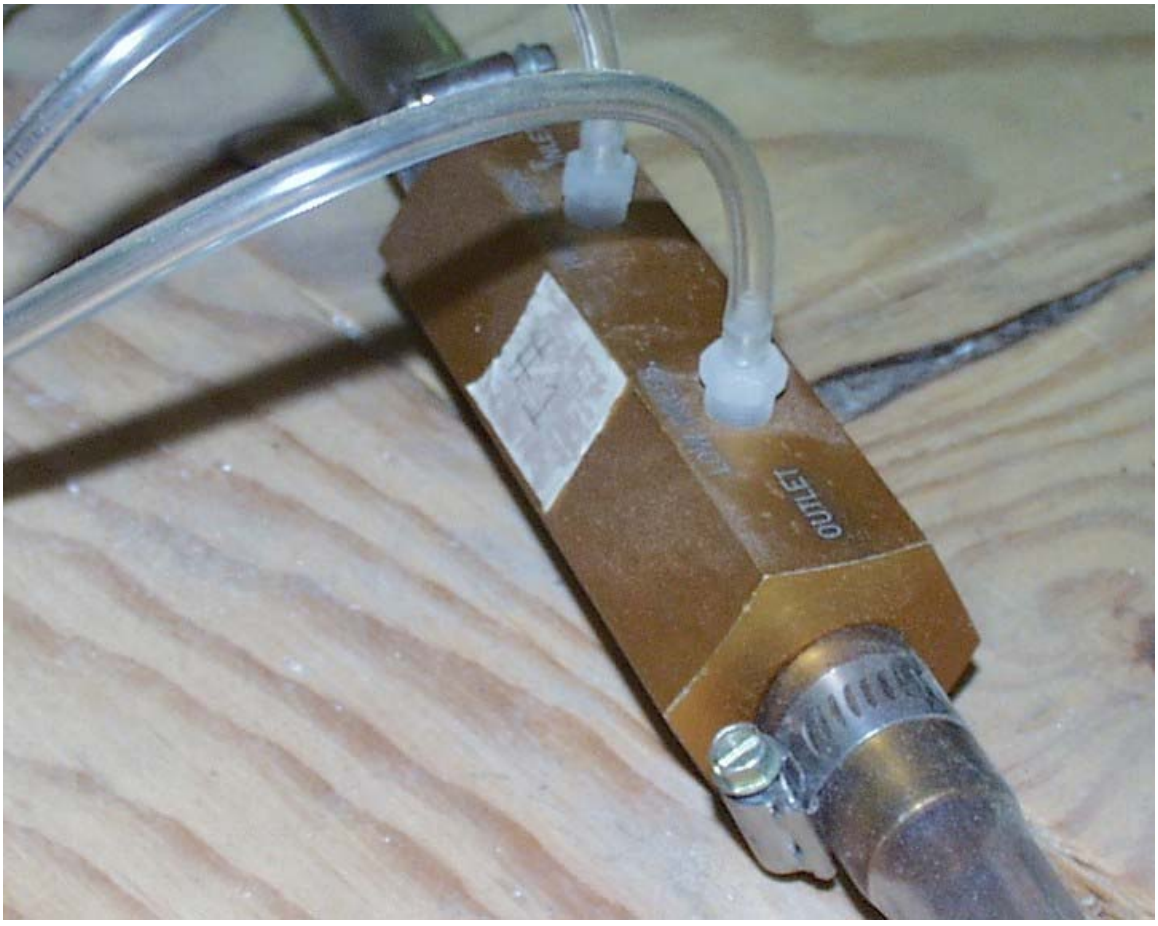

Figure 6.21: Picture of the FlowDyneVenturi Flowmeter

Data Acquisition and Control Hardware

Data acquisition and control was accomplished using two PCI plug in cards made by National Instruments. The first card is the PCI-MIO-16E-1 multipurpose input/output card. It has 8 differential (16 single ended) analog input channels and two ±10 volt analog output channels. The resolution for both analog input and analog output is 12 bits. It is capable of sampling at up to 1.25 million samples per second on a single input channel (two channels multiplexing can sample at half that speed, etc), and has built in multiplexing. It can output at up to 1 million samples per second on a single analog output channel. It also has an on board, software programmable, instrument amplifier that amplifies at 1, 2, 5, 10, 50, or 100. In addition, it has two 24-bit counter/timers that can operate at either 100 kHz or 20 MHz, and 8 digital Input/Output (I/O) channels. The second card is the 6711 analog output card. It has four 12-bit analog output channels that can output at up to 1 million samples per second on a single channel, a range of ±10 Volts, two 24-bit, 100 kHz or 20 MHz couter/timers, and 8 digital I/O channels.

All of the instruments and controllers were wired into a National Instruments SCB-68 shielded I/O connector box. This device facilitates wiring by providing screw terminals for easy connections. The terminal blocks are located in a shielded enclosure that helps reduce noise caused by electromagnetic induction. It also has an onboard temperature sensor for thermocouple cold-junction compensation.

Software

The operating system used on the PC was Microsoft Windows 2000. National Instruments LabView was used for data acquisition and instrument control. The data acquisition and control algorithms were written in “G”, the graphical programming language native to LabView. Post processing of data was performed with additional LabView algorithms, algorithms written in ANSI C, Microsoft Excel, Mathworks Matlab, and Amtec Tecplot.

CHAPTER 7

JET ENGINE - ANALYSIS RESULTS AND DISCUSSION

Chapter Overview

This chapter describes the results from mixing enhancement experiments performed on the small jet engine. There were two phases of experiments which took place a number of years apart. During the first phase single-sided actuation was implemented and mixing performance was primarily evaluated in terms of the dimensionless temperature T* defined as:

$$T^* = \frac{T_{Downstream} - T_{Ambient}}{T_{Exit} - T_{Ambient}} \tag{1}$$

The dimensionless pulsing frequency, or Strouhal number, was defined as the frequency times the outer diameter divided by the exit velocity:

$$St = \frac{fD_o}{U_{exit}} \tag{2}$$

Since the first phase of experiments was done before the small scale jet experiments, amplitude was initially defined in terms of the mass flow ratio of the actuators to jet, and was usually expressed as a percentage.

$$MFR = \frac{\dot{m}_{act}}{\dot{m}_{jet}} \tag{3}$$

After the small scale experiments were performed, amplitude was also defined in terms of the square root of the momentum ratio. In some cases both measures of amplitude are given.

$$SRMR = \sqrt{\frac{\left(\rho V^2 A\right)_{act}}{\left(\rho V^2 A\right)_{jet}}} \tag{4}$$

A computer program was written to control the jet and the actuators, and to acquire and log data. During a typical run with the jet many measurements were continuously made and logged to a file including: jet exit total pressure, jet exit temperature, ambient temperature, actuator mass flow rate, actuator frequency, and downstream temperature at a point in the flow field.

For frequency and amplitude sweeps, which were used to determine the optimal values, the majority of measurements were made on the centerline axis a distance of four outer diameters downstream. This location was outside of the potential core, or the equivalent for an annular jet, and well into the temperature decay region. The values of T* for the unforced jet at this location were in the range 0.45 – 0.5, depending on the Mach number. Other measurements were made in the flow field including velocity and temperature traverses across the jet for the pulsed and unpulsed cases.

During the second phase of testing, two phase locked actuators were used to pulse the jet and the phase between them was set to either 0° (axisymmetric) or 180° (antisymmetric). Total pressure was measured in the field allowing the mixing metric U/U_{exit} to be added alongside the T* metric. During this phase of testing frequency and amplitude sweeps were performed, but more emphasis was placed on cross traverses at various downstream locations to evaluate mixing enhancement. A couple of 1-sided pulsing cases were

repeated to verify consistency between the two phases of testing. Additionally, a number of characterization experiments were performed on both the jet engine and pulse fluidic actuators.

There was significant variability in the measurements, especially compared to the much cleaner small scale experiments. The best way to deal with this was to make many measurements and average over long periods of time. Some of the sources of variability were: the high level of turbulence in the flow, wear and tear of the engine components, and instabilities in the control system.

The basic layout for the rest of this chapter is as follows. First the results from actuator characterization are given. This is followed by characterization results for the jet engine. Next come the results and analysis for single sided pulsing experiments, followed by two sided pulsing with phase locked actuators. Last, there is a conclusions section.

Overall Objectives

There were two major objectives of the jet engine experiments. The first was to test the robustness of jet mixing enhancement via pulsed fluidic actuation on a ‘realistic’ system, in this case a miniature a jet engine. Realistic is simply meant to imply a technology that one would likely encounter in industry as opposed to the laboratory. The second major objective was to compare the results to the small scale and find common trends. In this way it could be determined whether the same phenomena were responsible for mixing enhancement compared to the ‘clean’ small scale jet.

Actuator Characterization

The rotary pulse fluidic actuators used to implement mixing enhancement on the jet engine were characterized in order to verify that they were operating in a consistent and effective manner. It also allowed assessment of design limitations.

Unsteady 2D Velocity Traverses

Planar 2D velocity traverses were performed on the rotary actuators near the nozzle exits. Velocity was measured using a total pressure probe connected to an unsteady Endevco pressure transducer. Figure 7.1 contains contour plots showing the normalized mean velocity profiles as well as pictures showing the coordinate axes used and important dimensions. Cartesian coordinates were used with the x-axis defined as the primary flow direction. Velocity contours were obtained for each actuator for the following cases: 0 Hz (blowing), 100 Hz, and 500 Hz. The amplitude was set to 0.01 lb_m/s measured by the venturi flowmeter. Measurements were taken in the plane indicated in the figure. The profiles obtained are wider than the nozzle orifice because the measurement plane was slightly downstream of the nozzle exit due to the nozzle's curved geometry. The distance from the exit varies with the curvature of the nozzle, and peaks at 0.178" at the z-direction midpoint (see dimensions in figure). This is almost two orifice widths downstream. So, as expected, entrainment has noticeably widened the pulse profiles.

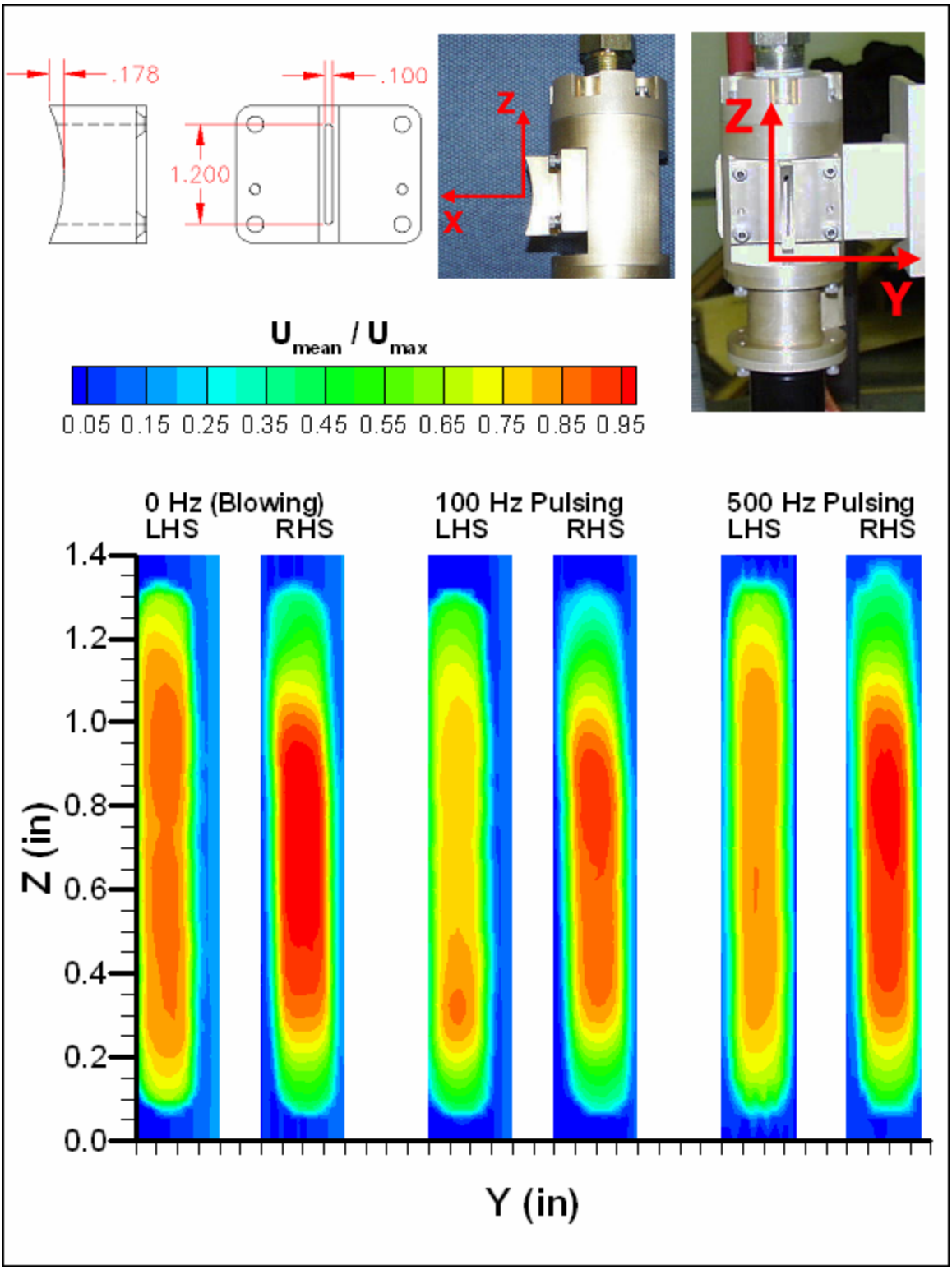

Figure 7.1: Mean Exit Velocity Profiles for LHS and RHS Rotary Actuators, A = 0.01 lb_m/s

Not obvious from the figure is the fact that there is a slight tendency for the flow to pile up on the bottom side of the actuator nozzle as it turns the corner. Table 7.1 summarizes the left to right and top to bottom symmetry of the pulses found by integrating the velocity on the respective sides for each nozzle and comparing. The table indicates, for example, that for the right hand side (RHS) actuator set to blowing the pulse is evenly balanced from left to right (50.3% – 49.7%), and slightly skewed from top to bottom (47.7% - 52.3%). All in all, symmetry of the velocity profile is quite good.

	Frequency (Hz)	% Top	% Bottom	% Left	% Right
RHS	0	47.7	52.3	50.3	49.7
	100	47.5	52.5	50.1	49.9
	500	48.7	51.3	49.2	50.8
LHS	0	49.9	50.1	49.9	50.1
	100	48.4	51.6	50.0	50.0
	500	50.3	49.7	50.1	49.9

Table 7.1: Actuator Pulse Symmetry

The velocities in figure 7.1 are all normalized by the same value, the maximum exit velocity for all six cases. It is clear that for the same mass flow rate, the contours for the LHS actuator are a little more dispersed than the RHS contours. Therefore, the peak velocity is lower for the LHS. On average, the peak velocity of the LHS actuator was about 87% of the peak velocity for the RHS actuator.

Unsteady Centerline Velocity Measurement

Hotwire measurements of the centerline velocity were made for the actuators at a single amplitude and the following frequencies: 0 Hz (blowing), 100 Hz, 200 Hz, 300 Hz, 400 Hz, 500 Hz, and 1000 Hz. The amplitude was set as follows. Actuator input pressure

was set to produce a mass flow rate of 0.01 lb_m/s for the blowing case. This input pressure then remained fixed as the actuator was run at the other frequencies. This was done to test the effect of varying the frequency on the pulse amplitude. Table 7.2 summarizes the results for the RHS actuator. As expected, the mass flow rate of the actuator is always lower when it is spinning (pulsing) than when it is stationary (blowing). This makes physical sense since the flow will be periodically blocked by the spinning drum. An analysis of the error in mass flow measurement can be found in Appendix C.

Frequency (Hz)	MFR (lbm/s)	Mean Centerline Velocity (m/s)
0	0.0101	69.37
100	0.0082	52.02
200	0.0077	55.94
300	0.0074	53.76
400	0.0080	58.34
500	0.0080	56.85
1000	0.0076	53.06

Table 7.2: Effect of Varying Frequency on MFR

Figure 7.2 shows examples of pulses obtained with the hotwire. Instantaneous pulses are compared to their phase averaged counterparts. The phase averaged pulses were computed as follows. First, a Fast Fourier Transform was performed on the data to accurately determine the peak frequency. This was then used to determine the cycle period and thus where to split up the data set to perform phase averaging. A high sampling rate (100 kHz) was used to minimize error, but some artificial smoothing occurred due to slight fluctuations about the calculated peak frequency. This smoothing is more pronounced at higher pulsing frequencies since the sampling rate was fixed.

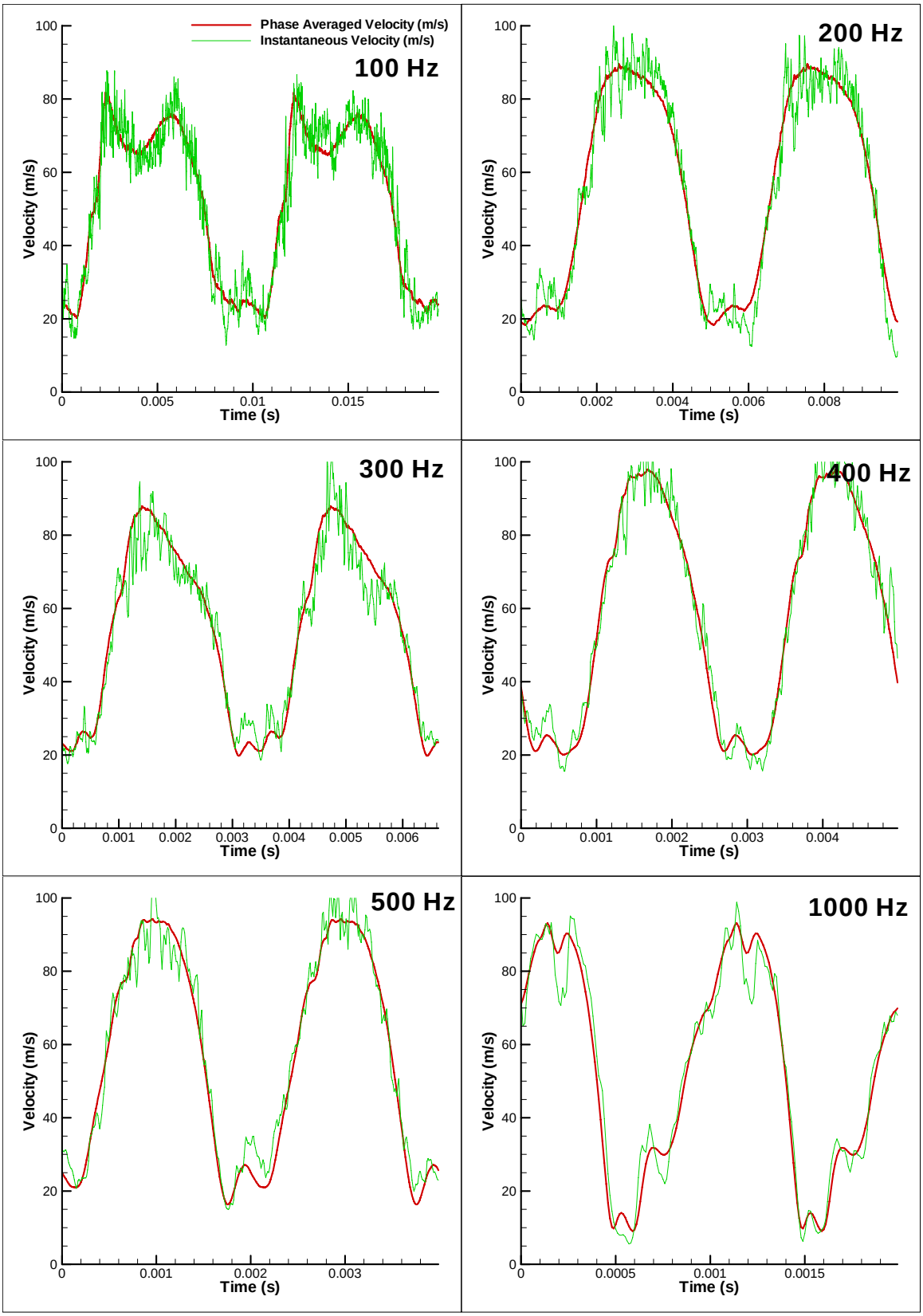

Figure7.2: Instantaneous and Phase Averaged Pulses Measured at the RHS Actuator Exit for the 100, 200, 300, 400, 500, and 1000 Hz cases, A = 0.008 lb_m/s

Figure 7.3 shows phase averaged waveforms at several frequencies for the RHS actuator and compares them to an ideal sine wave. A couple of things are worth pointing out which demonstrate the limitations of the actuator. First, there is a significant double hump at the top of the 100 Hz pulse indicating a resonance at another frequency. The second important observation is that none of the pulses go to zero. This is because the rotary actuator never completely seals. Even when the actuator is stopped and the slotted drum is turned to the 'blocking' position, there is still some air leaking out through the nozzle. This is a design trade off. The small gaps between components which allow slight air leaks also minimize friction and wear allowing the high pulsing frequencies needed to excite the jet. This offset in the pulse has a negative effect on mixing enhancement as shown by offset studies done on the small scale jet.

Jet Engine Characterization

Jet engine characterization involved several different velocity and temperature traverses of the unforced jet which are later used as a baseline to compare against forced jet cases where mixing enhancement is implemented. Velocity and temperature were measured with a combination pitot/thermocouple probe. Thus, only the streamwise component of velocity was measured. Figure 7.4 shows the coordinate system used for all of the traverses. Cartesian coordinates are used and x is always the primary flow direction.

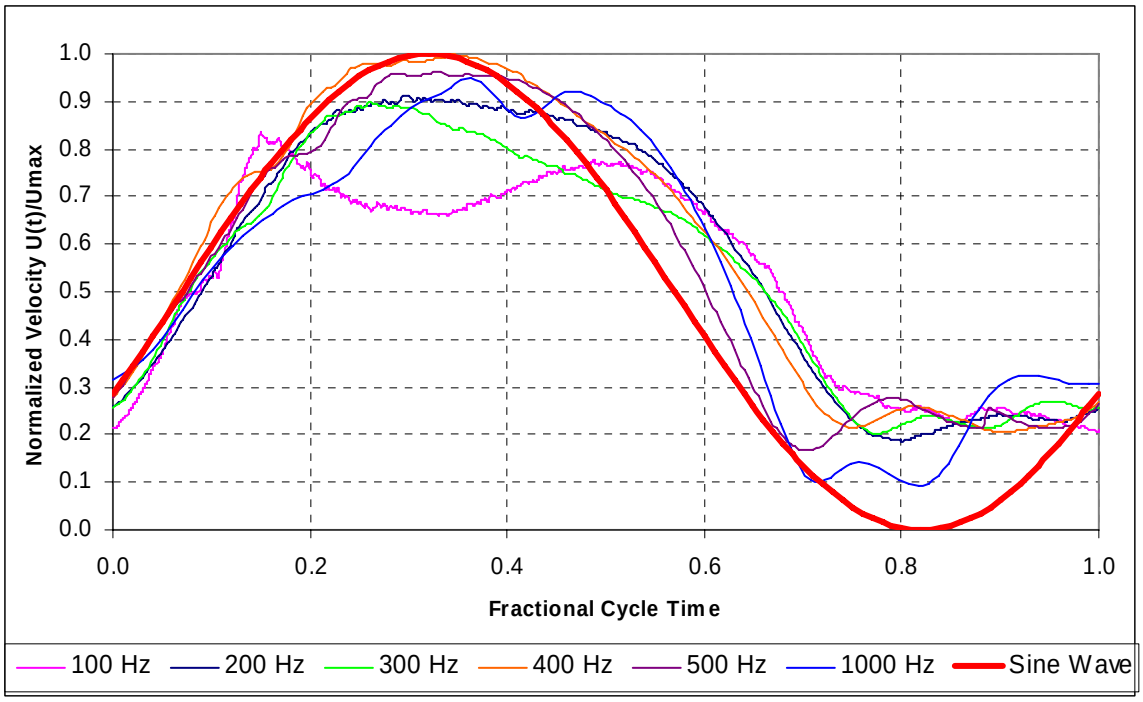

Figure 7.3: Comparison of the Normalized Phase Averaged Pulses to an Ideal Sine Wave Pulse

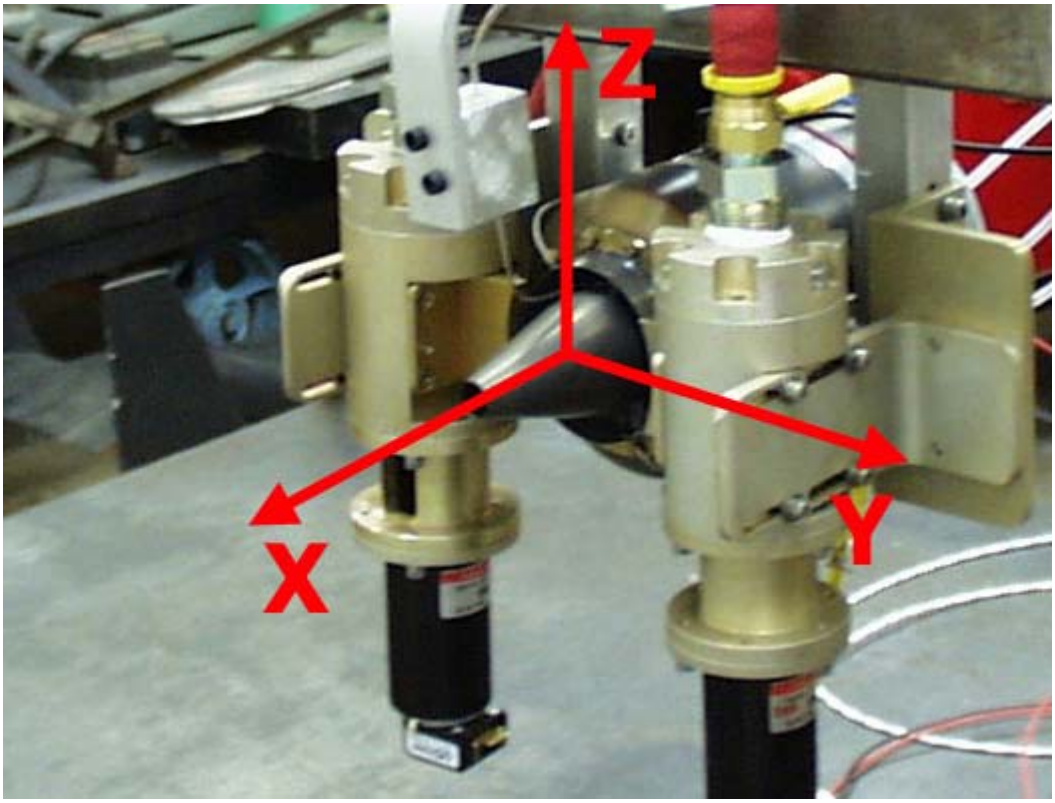

Figure 7.4: Picture Showing the Jet Coordinate Axes

Engine Consistency

It is particularly important to examine the statistics of the jet engine measurements because of their highly variable nature. Figures 7.5 and 7.6 are plots of the measurements from a data log taken during an example run with the jet engine. In this particular run, the Mach number was set to 0.18, the mass flow ratio was 5%, and the pulsing frequency and downstream measurement location were varied. There is clearly a lot of variation in the data, so sampling times needed to be long enough to get meaningful averages. On the other hand, sampling times were also limited because the engine burned fuel rather quickly. Thus a compromise had to be made. The data log consisted of online measurements (i.e. displayed in real time during the test) made every second. When a condition was set and the online measurements became somewhat 'stable', a longer measurement was made to obtain higher accuracy. These longer measurements were used to generate the plots found in this section. Typically, the longer temperature and velocity measurements were the average of sampling at kHz for a total of 10 seconds. However, longer sampling times were sometimes used when deemed necessary.

Figure 7.5: Sample Plot from Data Log for a Particular Run Showing the History of the Jet Mach number

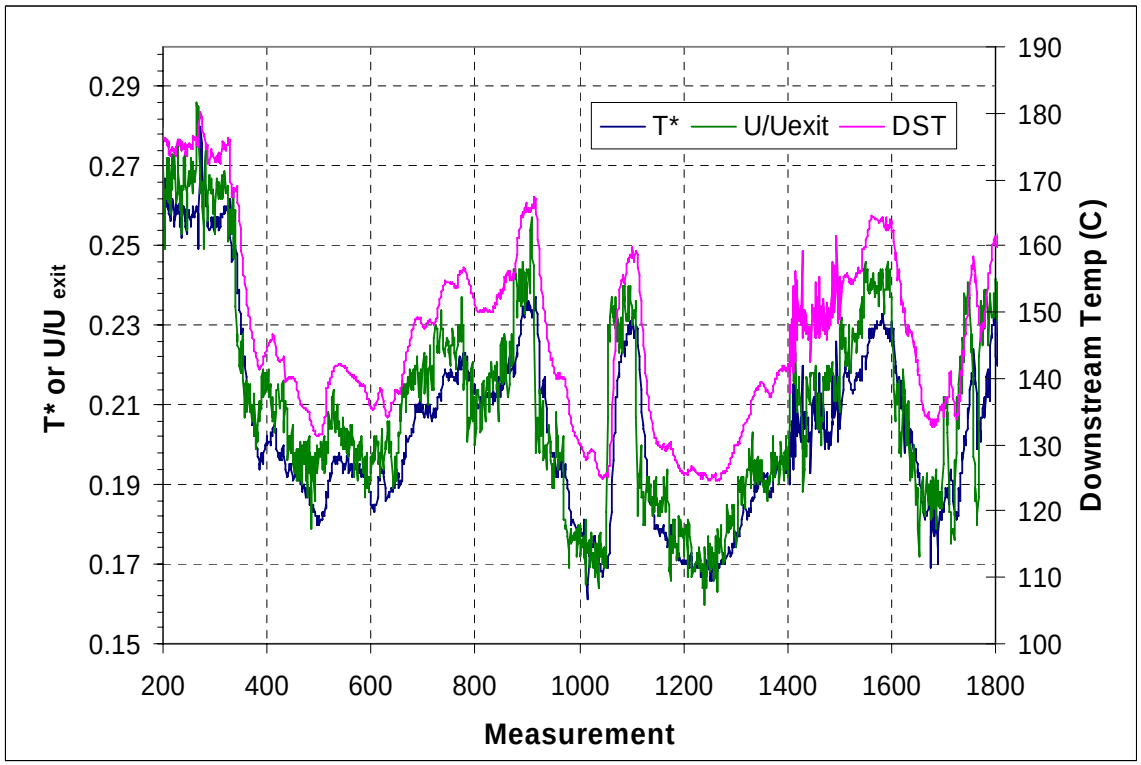

Figure 7.6: Sample Plot From Data Log For a Particular Run with the Jet Engine Showing the Variation of T*, U/Uexit, and Downstream Temperature

Velocity and Temperature Traverses

Centerline Temperature Decay

Figure 7.7 shows the centerline decay of T* for the unforced jet engine at three different mach numbers and compares it against the small scale velocity decay curve. The value for T* does not start at unity because measurement begins in the wake of the centerbody. Compared to the velocity decay for a clean axisymmetric jet, the curve breaks downward much sooner, and its slope is steeper.

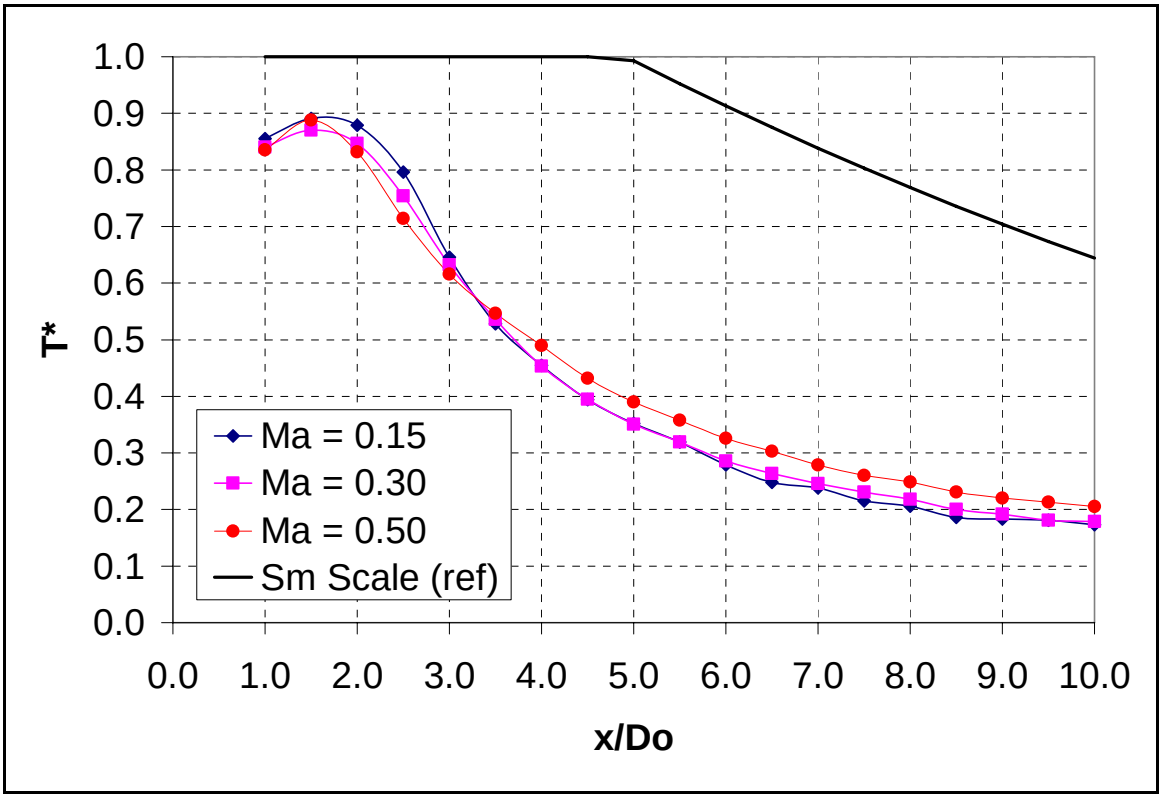

Figure 7.7: Jet Engine Temperature Decay Curves on the Centerline Axis

Velocity and Temperature Profiles

The profiles from a temperature and velocity traverse performed at the jet exit are shown in figure 7.8. The y coordinate axis, which begins at the centerbody and extends past the outer diameter of the jet, is scaled by the width of the annulus W. The temperature curve breaks downward before the velocity curve and extends out past the field of measurement. For all mixing enhancement experiments, the exit velocity and temperature were measured at the midpoint (y/W = 0.5) and the figure shows that this location gives a reasonable representation of average exit conditions. Note that measurements were not obtained in the boundary layer of the centerbody. Figure 7.9 shows velocity and temperature contours of the unforced jet out to just past three outer diameters downstream. Figure 7.10 shows velocity and temperature profiles of the unforced jet at $x/D_o = 4$ in the horizontal (y-axis) direction.

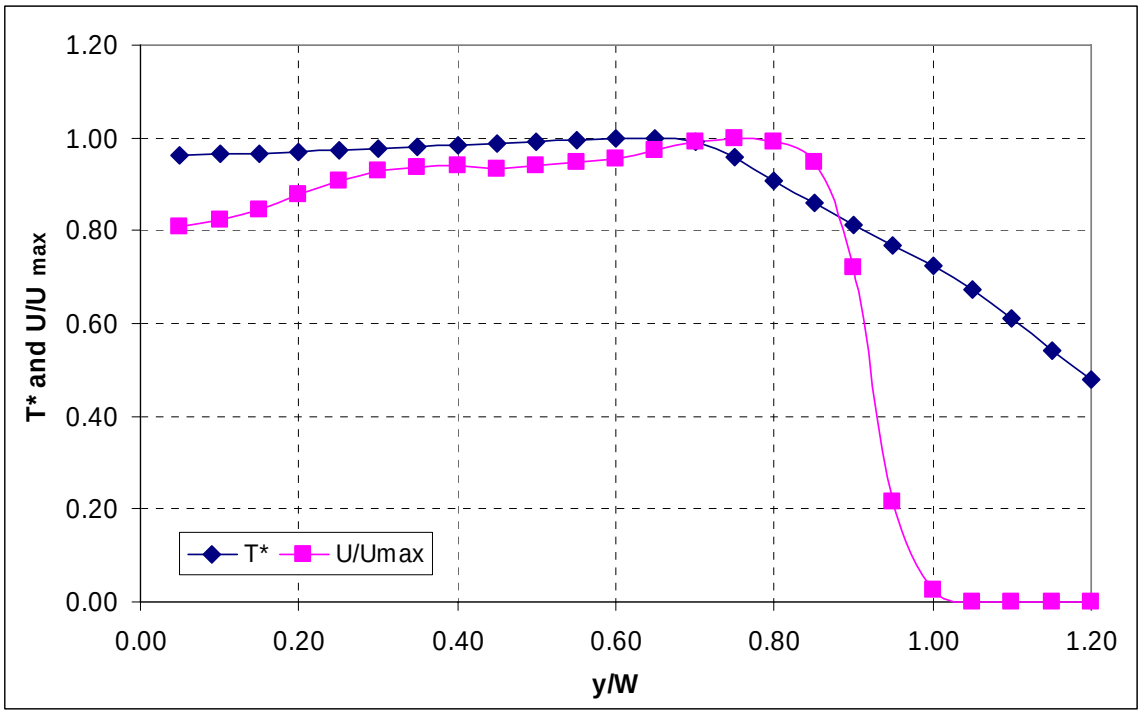

Figure 7.8: Normalized Jet Exit Velocity and Temperature Profiles

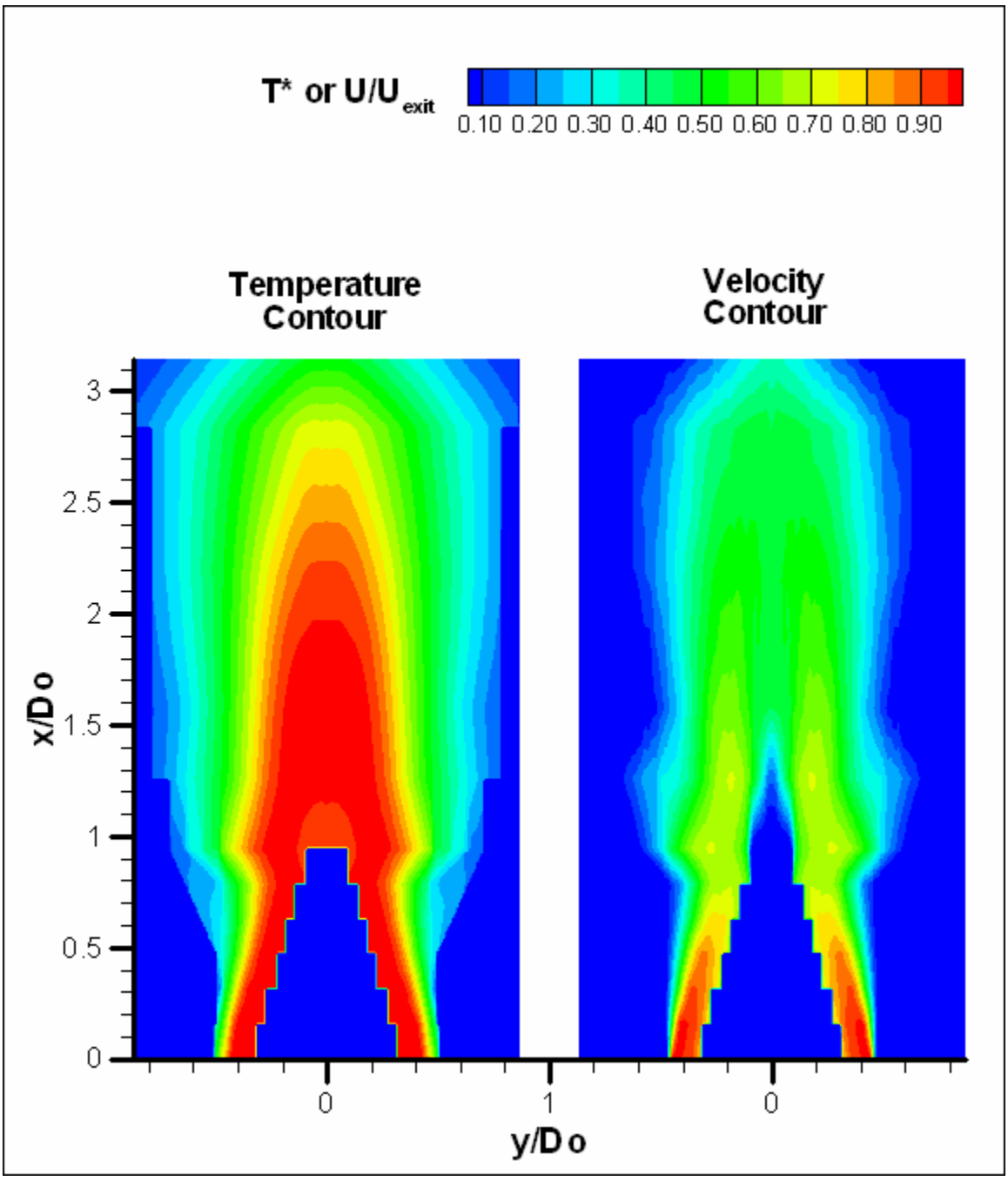

Figure 7.9: Normalized Temperature and Velocity Contours from the Unforced Jet Engine at Ma = 0.2

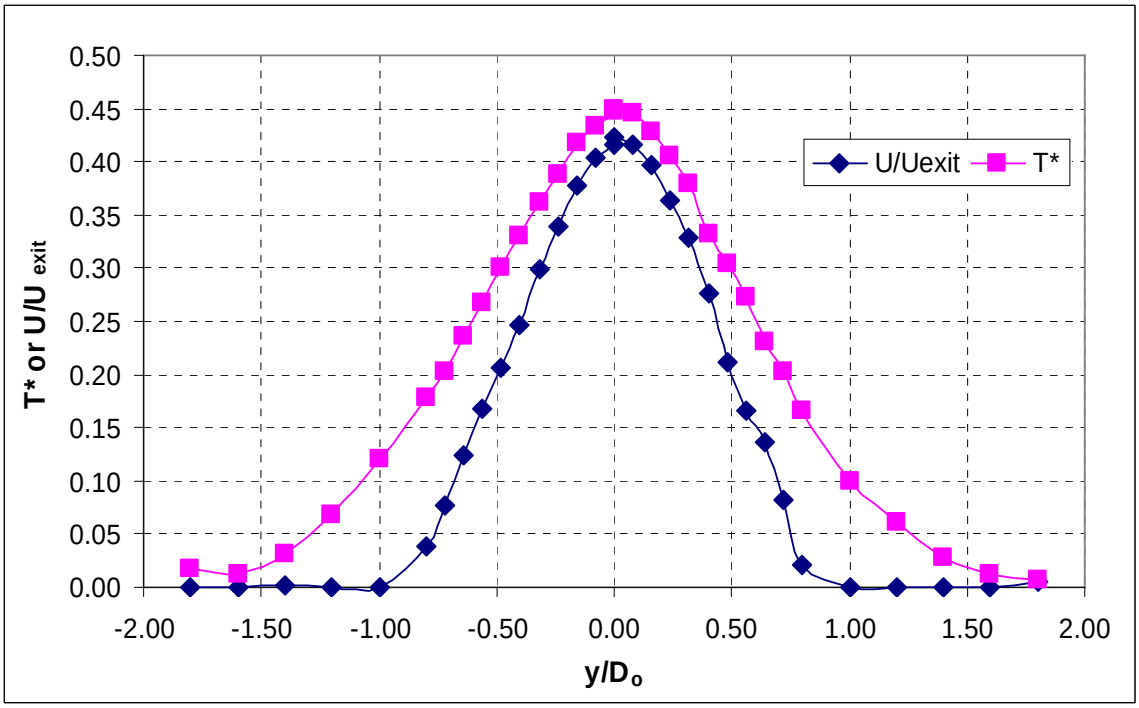

Figure 7.10: Normalized Velocity and Temperature Profiles from a y-axis Traverse of the Unforced Jet Engine, Ma = 0.17, x/Do = 4

Single-Sided Pulsing Results

Frequency Sweeps

Frequency sweeps were performed and the dimensionless temperature T* was measured on the centerline at $x/D_o = 4$. Figure 7.11 shows the resulting curves for four different mach numbers, which collapse quite well. It is worth noting that the Ma = 0.18 case was done a few years after the other three cases as a confirmation run during phase II of jet engine testing. The T* reduction is indicative of mixing enhancement in the same way as velocity reduction. For all of the Mach numbers shown, the value of T* decreases rapidly until it reaches an optimal Strouhal number, based on the outer diameter, of about 0.125. The value of T* then climbs rapidly out of the 'bucket' and begins to level off as it approaches the T* value for the unforced case. It is remarkable how similar the shape

of these curves are to small scale frequency sweep mixing curves using U* as the mixing metric. The values of T* for the unforced cases are also shown on the graph.

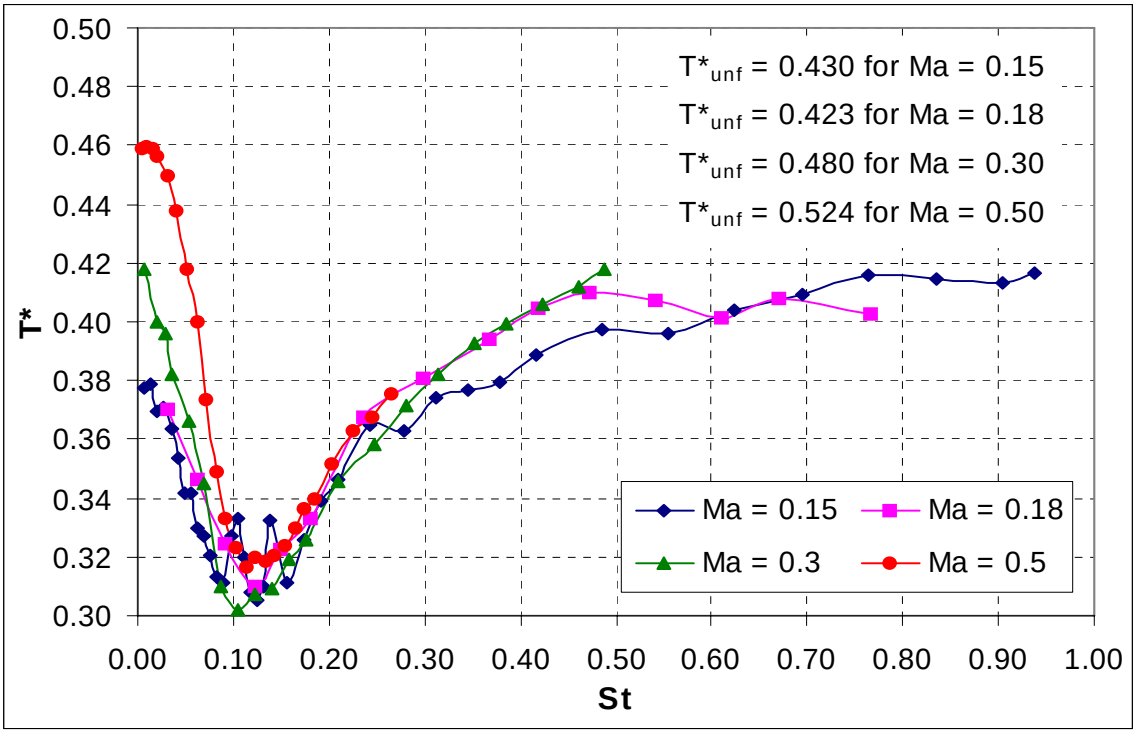

Figure 7.11: Frequency Sweeps for Single Sided Actuation, 5%MFR (SRMR = 0.126), Four Different Mach Numbers, x/Do = 4

Figure 7.12 shows the both T* and U/Uexit as mixing metrics for a frequency sweep on the jet engine at Mach 0.18. In this graph the values of the two mixing metrics follow each other fairly closely, and the optimal Strouhal bucket is slightly different, but close. There is clearly more waviness to the U/Uexit curve, but the overall shape is roughly the same as that for T*. It will be seen later that even when T* and U/Uexit are not always as close numerically as they are here, they are still correlated since the two curves have the same basic shape.

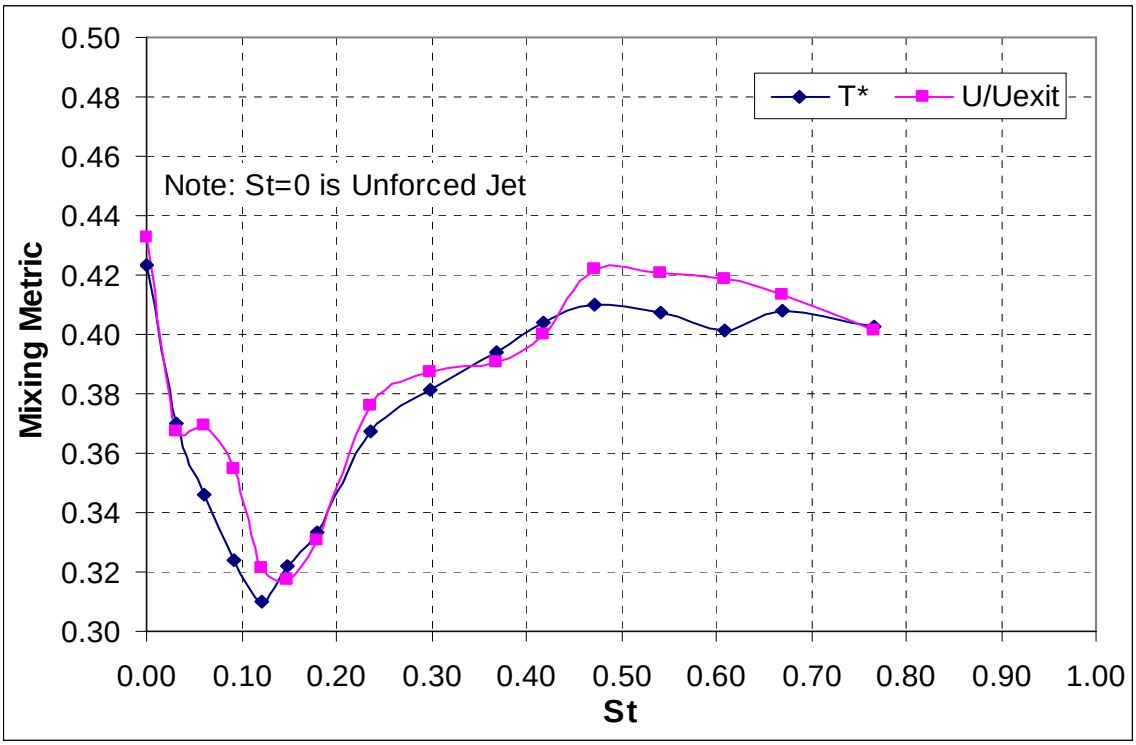

Figure 7.12: Frequency Sweeps for Single Sided Actuation, 5%MFR (SRMR = 0.126), Ma = 0.18, x/Do = 4, Comparison of T* and U/Uexit

Amplitude Sweeps

The actuator amplitude was varied from zero to ten percent mass flow ratio (%MFR) at two different Strouhal numbers (0.1 and 0.34) for a Mach 0.15 jet. Figure 7.13 shows the resulting curve fits to that data for the two frequencies tested. As the amplitude is increased from zero, the value of T* actually increases initially, before peaking just after 1% and then decreases rapidly with increasing amplitude. The effect of pulsing on the jet engine is to raise the exit temperature by introducing inertial obstacles at the exit which resist the flow. This raises the exit and downstream temperatures, and the net effect is an increase in T* until the mixing is sufficiently enhanced to overcome this effect. The curves do not show any hint of saturation, but this is because one sided pulsing vectors

the jet away from centerline resulting in false mixing enhancement measurements. Two sided results were different.

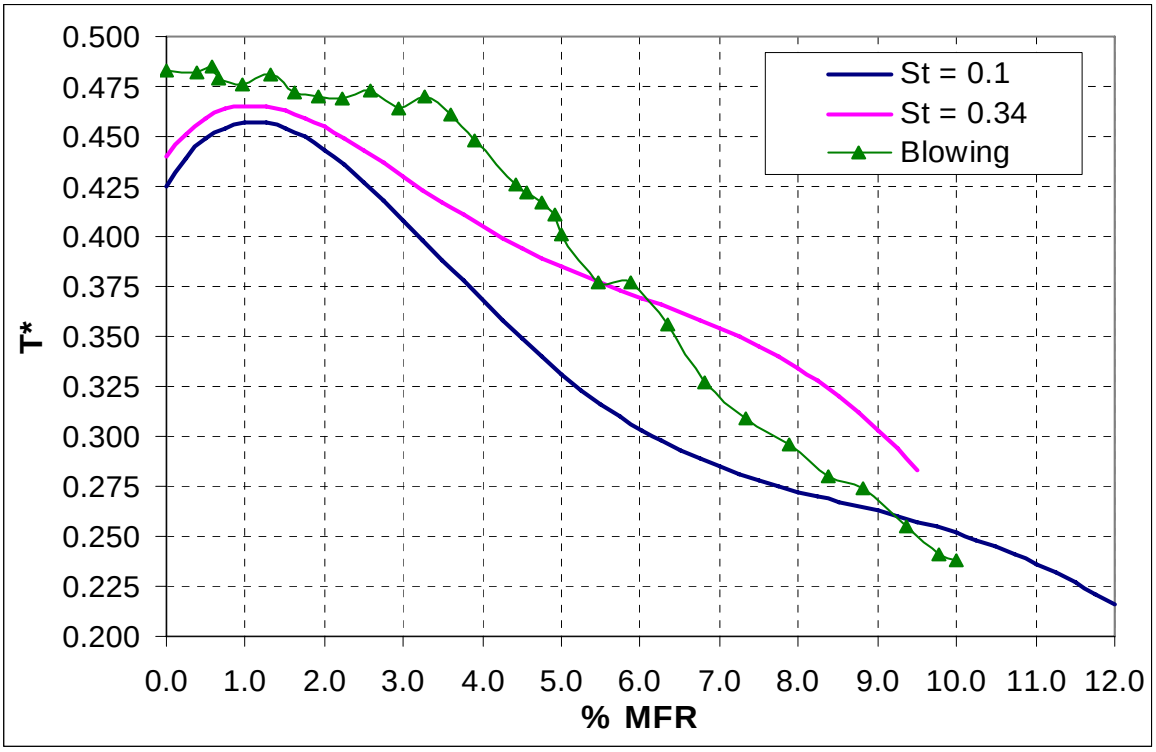

Figure 7.13: Amplitude Sweeps for Single Sided Actuation, Two Different Pulsing Frequencies and Blowing, Ma = 0.15, x/Do = 4

Two-Sided, Phase-Locked Pulsing Results

Confirmation of Phase Lock

Total pressure was measured simultaneously at both actuator nozzle exits using an unsteady pressure transducer to confirm whether mechanical phase locking was successful. Measurements made at multiple frequencies (100 Hz through 600 Hz) confirm successful implementation. Figures 7.14 through 7.17 show examples of total pressure waveforms obtained for two different frequencies for both the 0° and 180° phase pulsing cases.

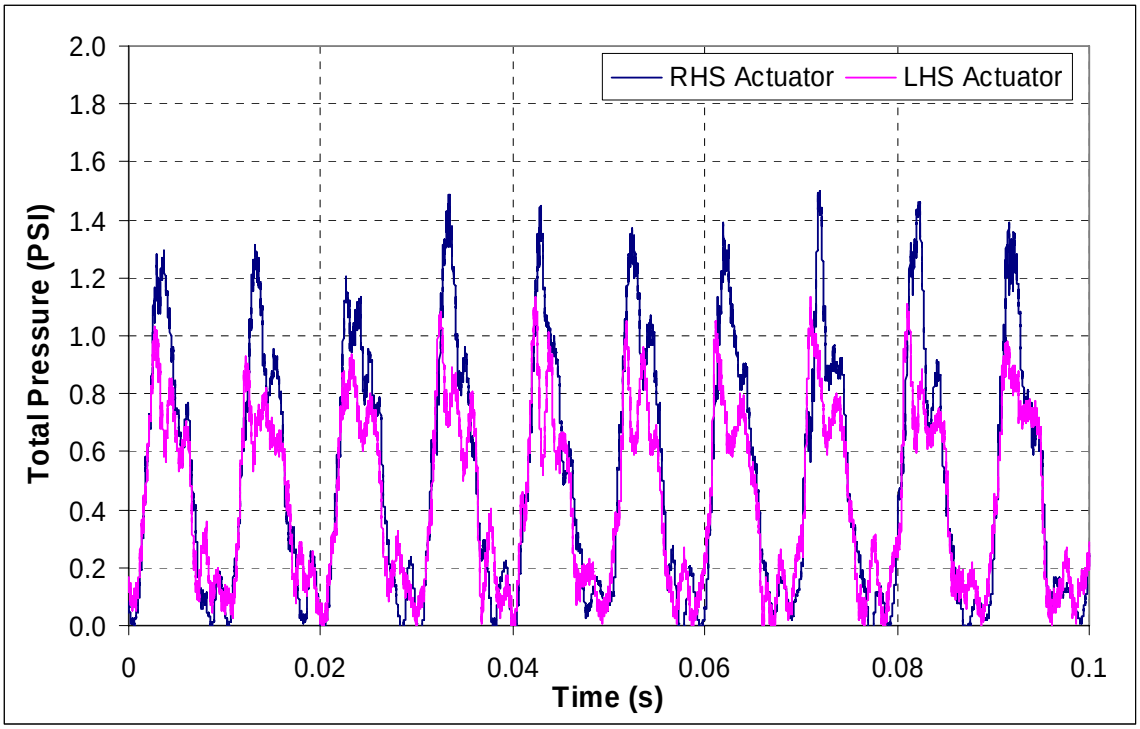

Figure 7.14: Confirmation of Phase Lock for Jet Engine Actuators, Total Pressure Measurements, 0° Phase, 100 Hz Pulsing

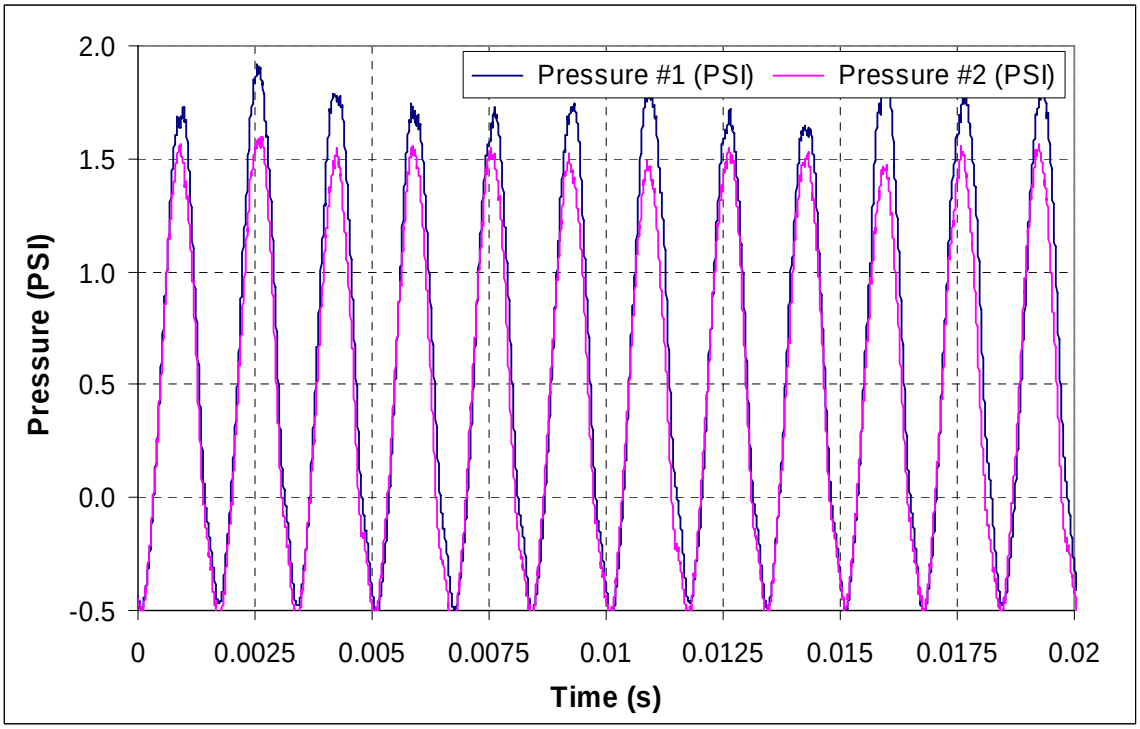

Figure 7.15: Confirmation of Phase Lock for Jet Engine Actuators, Total Pressure Measurements, 0° Phase, 600 Hz Pulsing

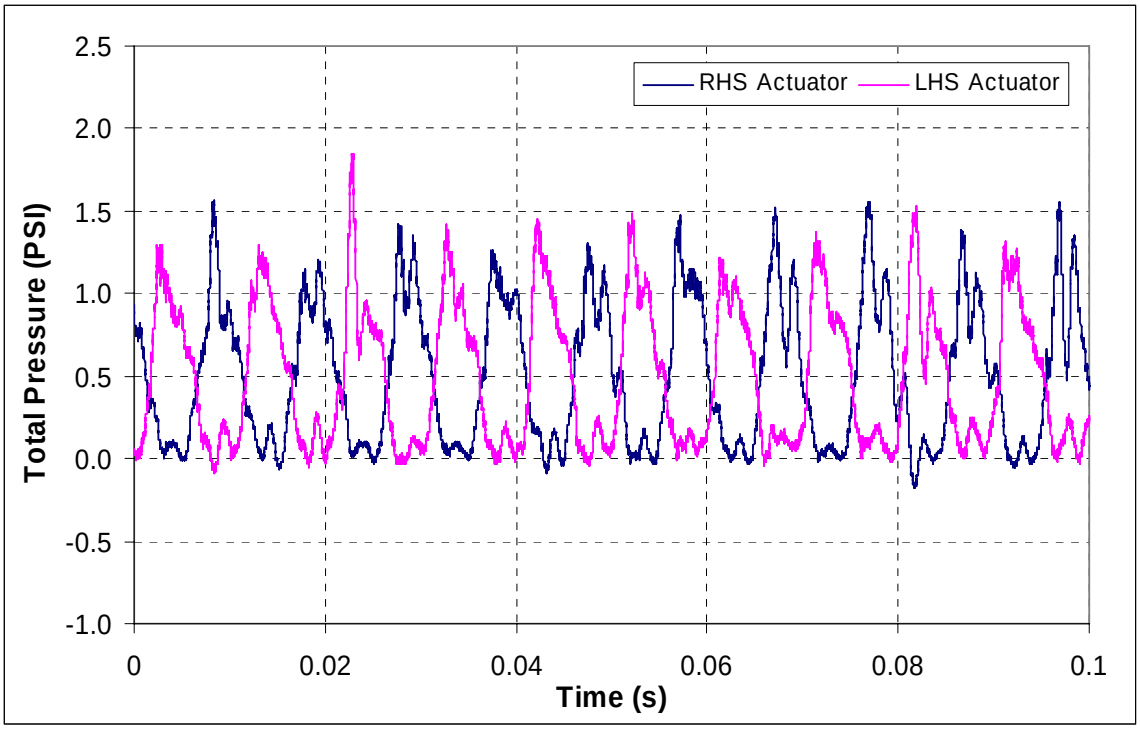

Figure 7.16: Confirmation of Phase Lock for Jet Engine Actuators, Total Pressure Measurements, 180° Phase, 100 Hz Pulsing

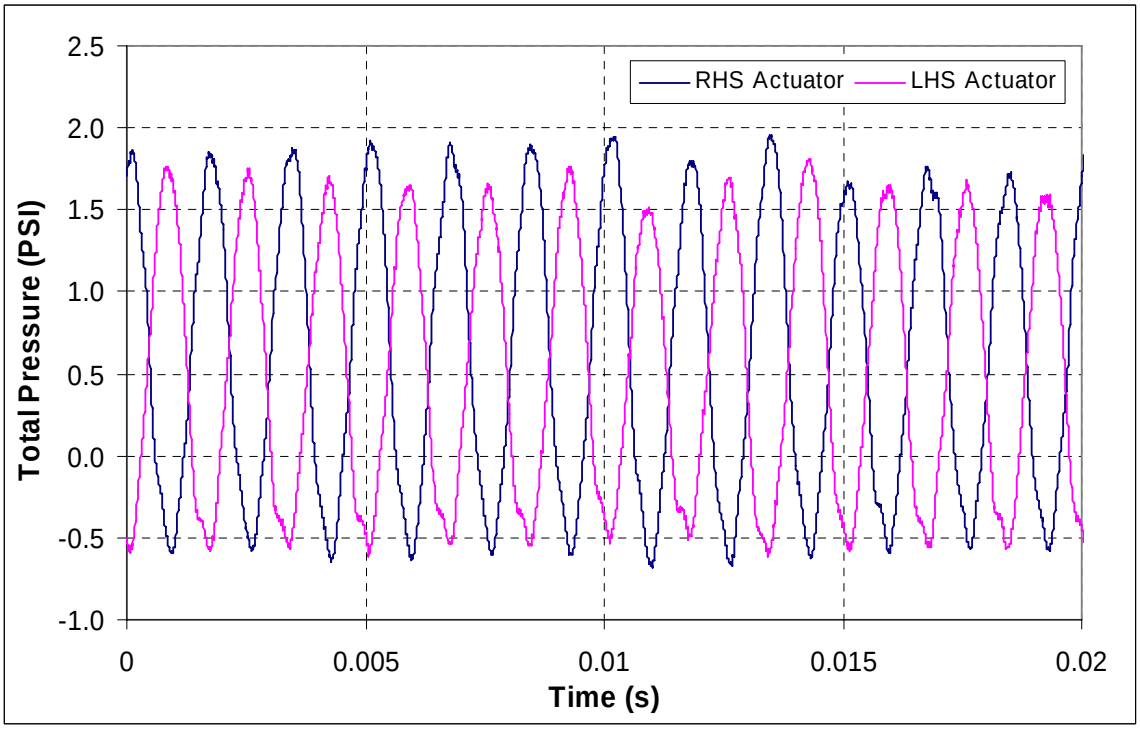

Figure 7.17: Confirmation of Phase Lock for Jet Engine Actuators, Total Pressure Measurements, 180° Phase, 600 Hz Pulsing

Comparison of 1 and 2-Sided Pulsing

Figure 7.18 compares amplitude sweeps for 1 and 2-sided (0° phase) pulsing performed under the same conditions. The T* curves match well, and the biggest difference between the two is that there appears to be less inertial blocking of the jet exit in the 2-sided case. Since %MFR refers to the total mass flow in the 2-sided case, the mass flow through each actuator is actually half that of the 1-sided case. Also included in the figure is the U/Uexit curve for the 2-sided case, which correlates well with the T* curve. Figure 7.19 compares frequency sweeps between the 1-sided and 2-sided pulsing cases. Note that the optimal Strouhal numbers are nearly identical. The figure suggests that single sided pulsing is more effective than two sided pulsing, but it is a little misleading. The lower T* is partly due to the fact that single sided forcing skews the profile away from the actuator. Measurement of T* on the shifted jet centerline reveals that the true minimum is near 0.35 instead of 0.3 as shown.

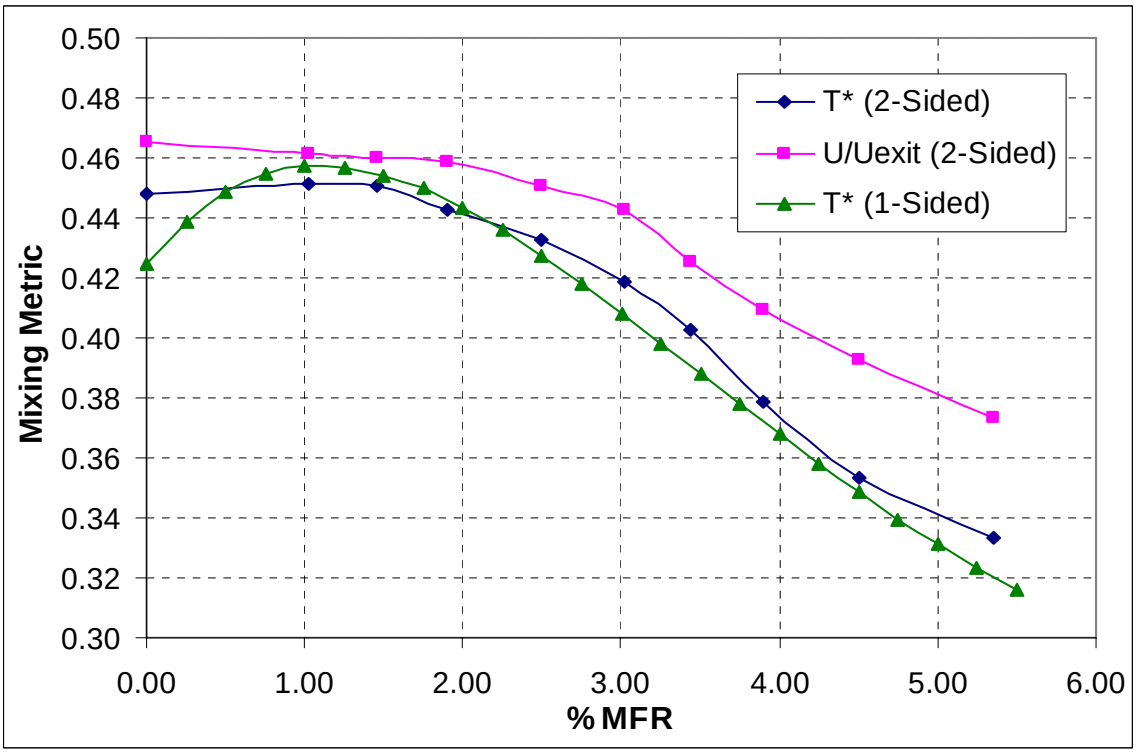

Figure 7.18: Amplitude Sweep, Comparison of 1 and 2-Sided Pulsing, Ma=0.16, St = 0.125, 0° Phase, x/Do=4

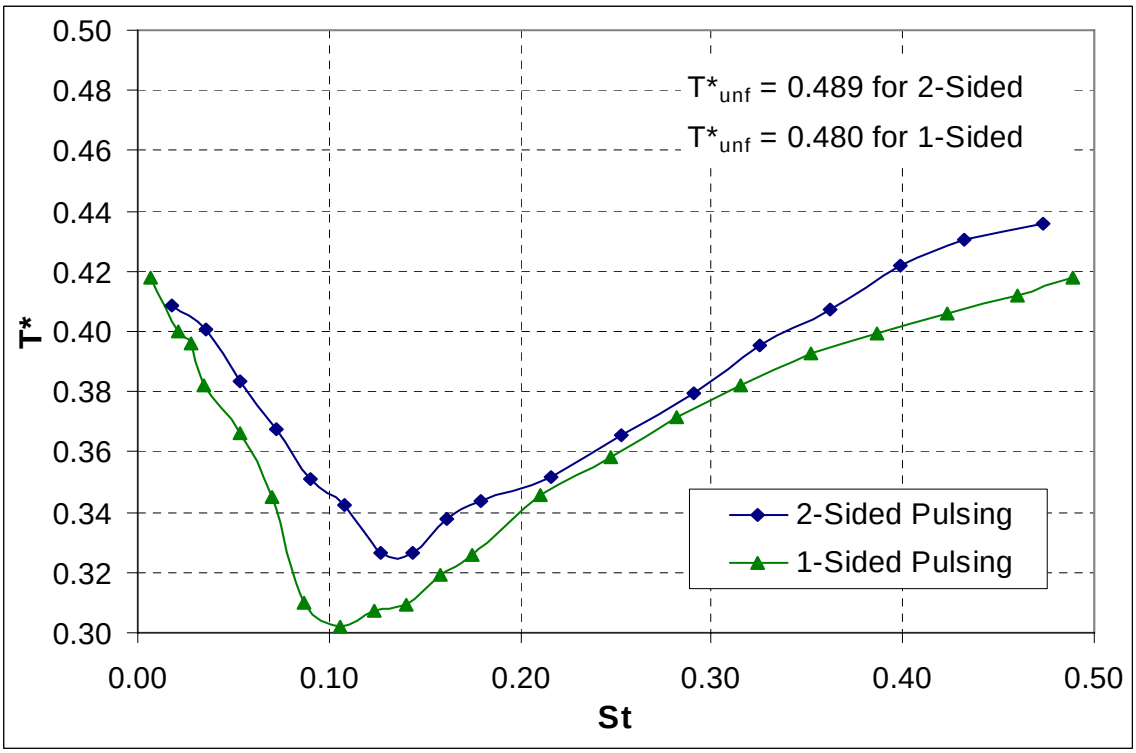

Figure 7.19: Frequency Sweeps, Comparison of 1 and 2 Sided Actuation, Ma=0.3, 5% MFR, 180° Phase, x/Do=4

Comparison of 0° and 180° Phase Pulsing

Frequency sweeps performed on the jet for both 0° and 180° 2-sided pulsing revealed that there was little, if any, difference between the two cases. Figure 7.20 shows one such frequency sweep at Mach 0.17. Other sweeps gave similar results. It appears possible that the 180° case may be slightly better than the 0° case, but it is not possible to say for certain. This result was unexpected because it differs from the small scale results where antisymmetric forcing resulted superior mixing compared to axisymmetric forcing. Most likely, the presence of the centerbody has the effect of isolating the two sides of the jet from one another. Thus, mixing enhancement is essentially independent of phase for all 2-sided runs.

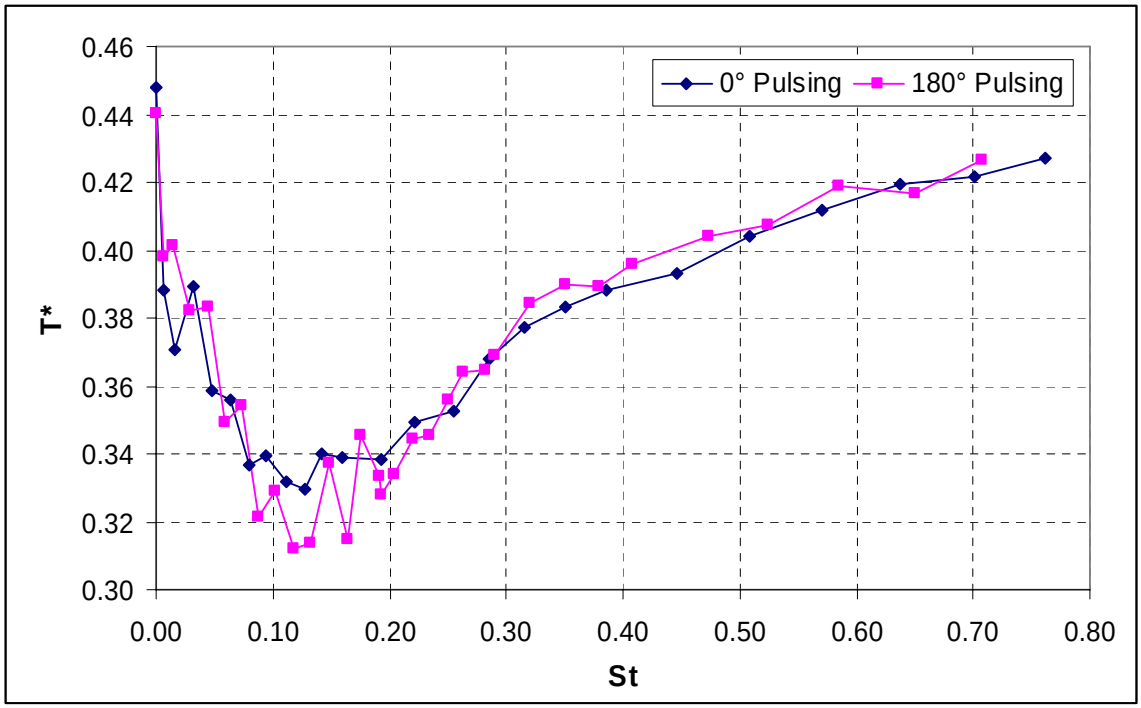

Figure 7.20: Strouhal Sweep, 2-Sided Pulsing, Ma=0.17, 5% MFR, x/Do=4, Comparison of 0° and 180° Phase

Traverse Results

Velocity and temperature traverses were performed in the y-direction at x/D_o = 4 to determine how the jet spread and compares to the natural jet. Measurements were made with a combination thermocouple pitot probe. Figures 7.21 and 7.22 show the traverse results for temperature and velocity respectively. Both the T* and U/Uexit metrics show the increased spread in the plane of forcing (the xy-plane). There are some slight differences between the data points for the axisymmetric and antisymmetric forcing modes, but it is not significant, especially considering the fact that the jet center was known to shift slightly at times.

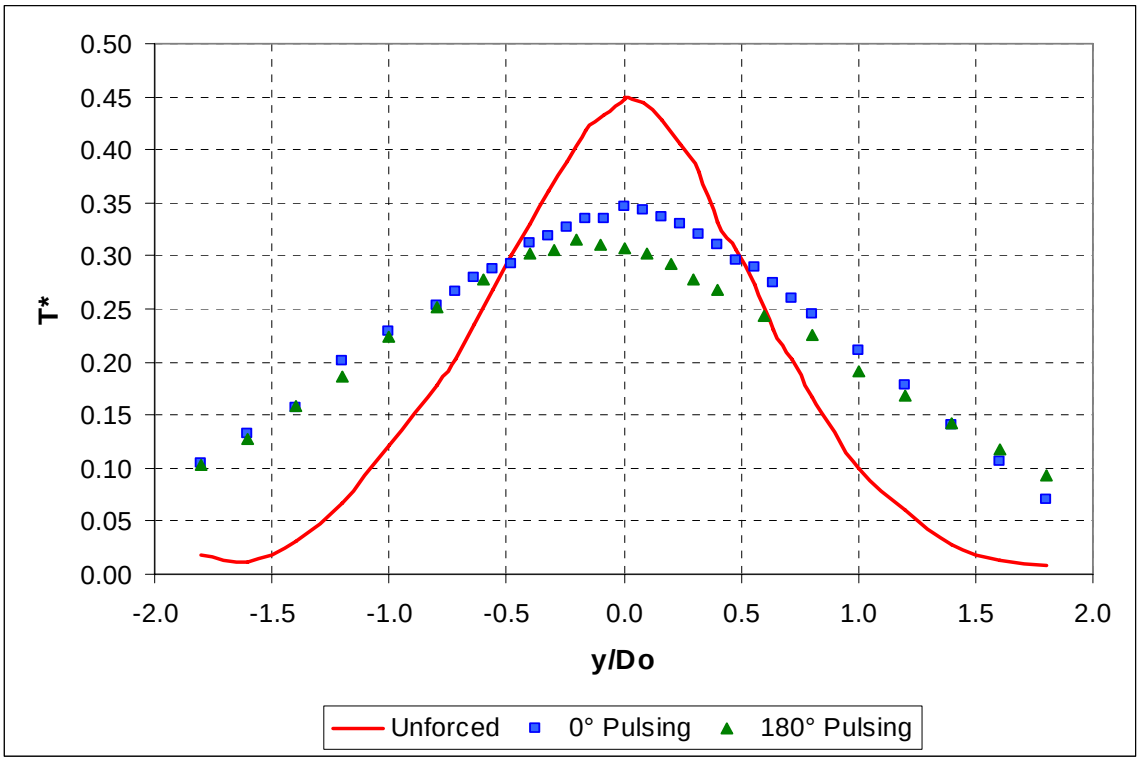

Figure 7.21: Y-axis Temperature Traverse of Jet Engine, Comparison of Unforced and Forced Jet, 2 Actuators, Ma=0.17, St=0.125, 5% MFR, x/Do=4

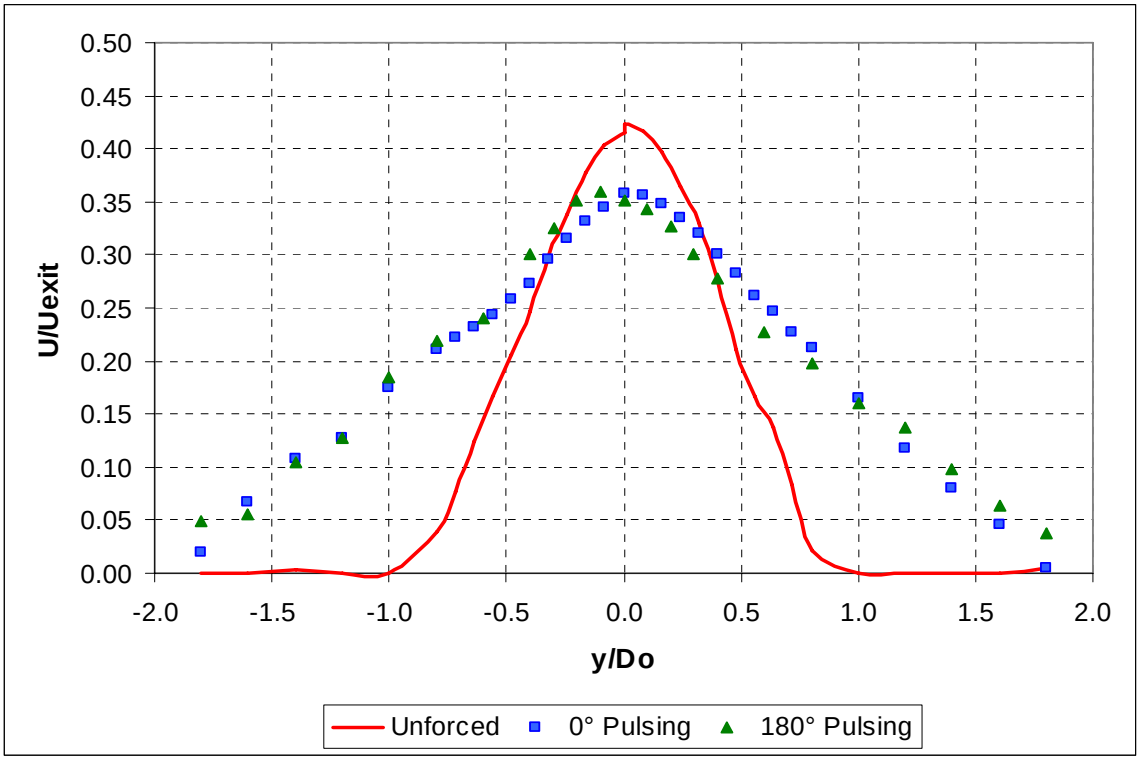

Figure 7.22: Y-axis Velocity Traverse of Jet Engine, Comparison of Unforced and Forced Jet, 2 Actuators, Ma=0.17, St=0.125, 5% MFR, x/Do=4

Simultaneous Frequency and Amplitude Sweeps

Simultaneous frequency and amplitude sweeps were performed on the engine like they were for the small scale jet. Figure 7.23 shows that the same shift downward in optimal Strouhal number that occurred for the small scale jet also occurred for the jet engine. As the pulsing amplitude was increased, the optimal 'bucket' moved to lower frequencies. Figure 7.24 shows that moving farther downstream results in a slightly reduced optimal Strouhal number as well. This too was discovered during the small scale experiments. The fact that the same trends found in the small scale jet are occurring for the jet engine indicates that the same phenomenon is likely responsible for mixing enhancement. Thus, one would expect the momentum ratio to be the key parameter for scaling the amplitude.

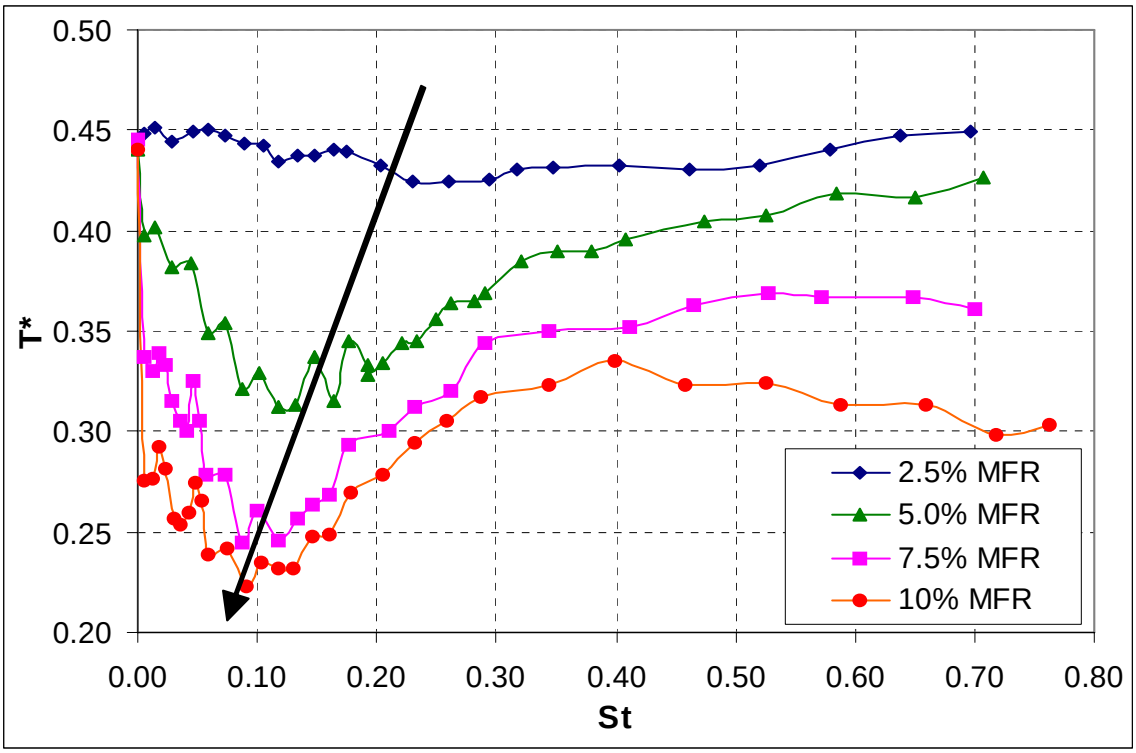

Figure 7.23: Frequency and Amplitude Sweeps, Ma=0.18, 2 Sided Actuation, 180° Phase, x/Do=4

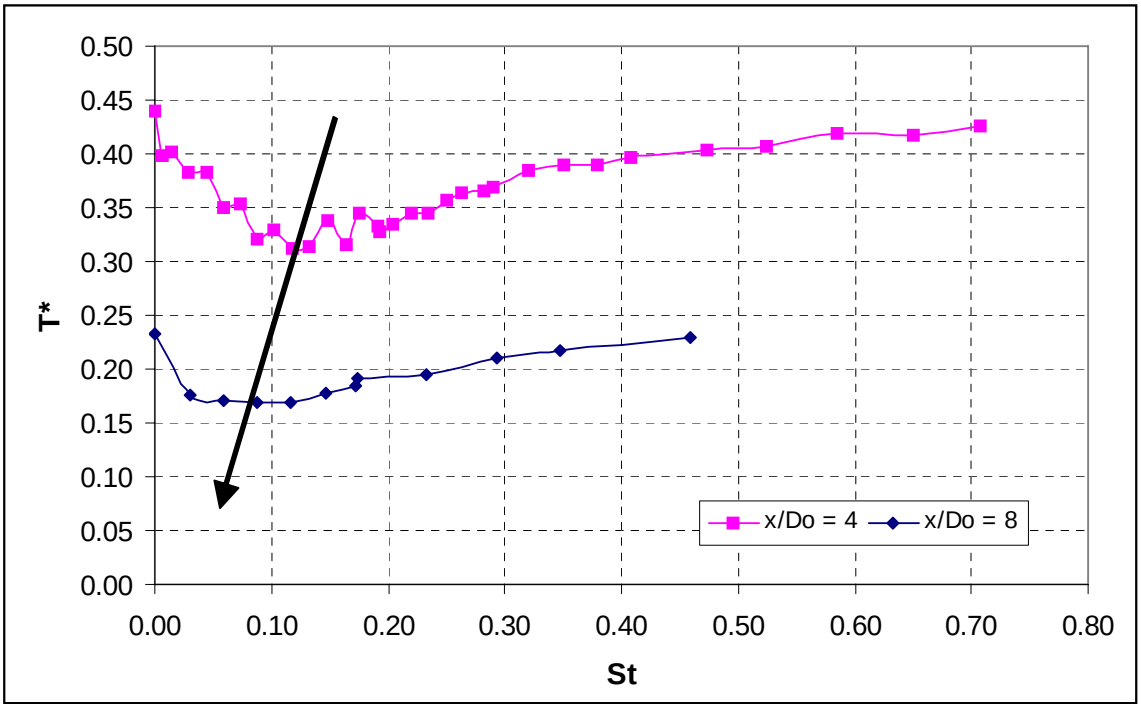

Figure 7.24: Frequency Sweeps at different x/Do, 2 Sided Actuation, Ma=0.18, 180° Phase, 5% MFR

Centerline Temperature Decay

The centerline temperature decay is compared for the forced and unforced cases in figure 7.25. Mixing enhancement has the effect of shifting the virtual origin of the jet about one and a half diameters upstream. Very large reductions in T* are seen to occur up to about $x/D_o = 4$.

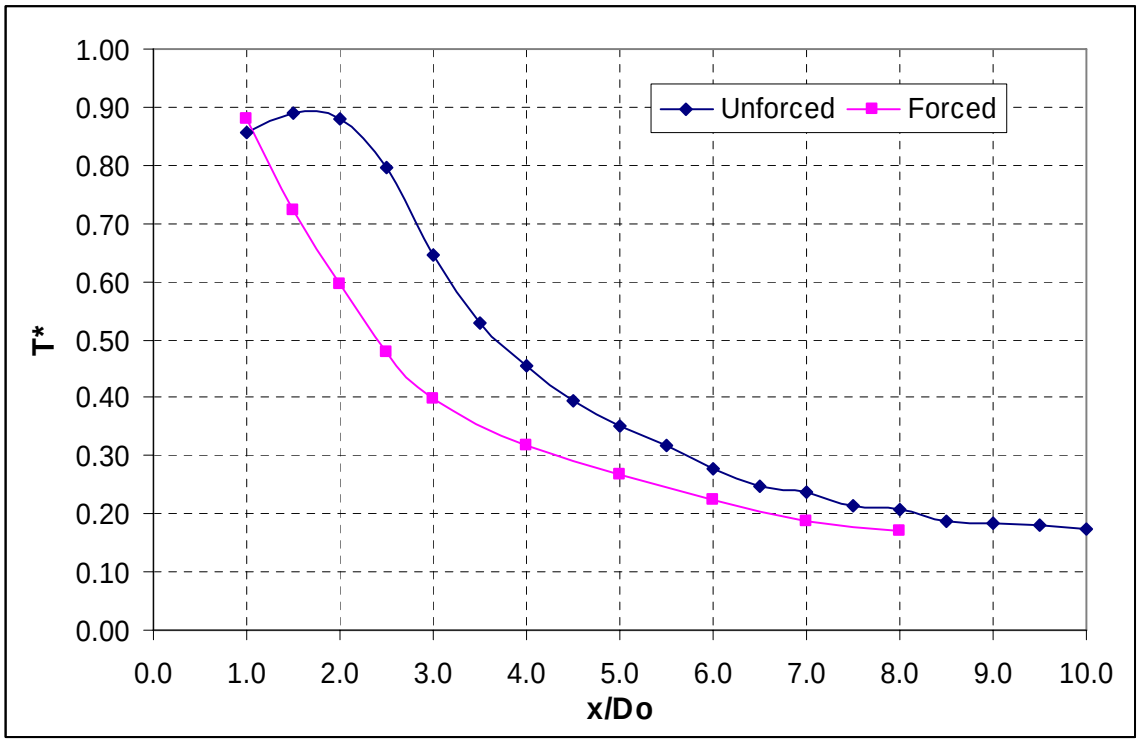

Figure 7.25: Centerline Temperature Traverses, Unforced vs. Forced, 2 Sided Actuation, Ma = 0.18, St = 0.12, 180° Phase, 5% MFR

Summary

The objectives stated at the beginning of the chapter were met. Pulse fluidic mixing enhancement was found to be effective for a realistic flow with high turbulence levels, annular flow, and swirl. Frequency and amplitude sweeps revealed that mixing saturates and the optimal frequency decreases with increasing amplitude, just as in the small scale.

The optimal Strouhal number, based on outer diameter, occurs at about St = 0.1. Two sided pulsing was more effective than one sided pulsing, but the pulsing phase didn't matter because of the centerbody. The mixing metrics T* and U/Uexit correlated well with each other.

CHAPTER 8

OPTIMIZATION OF MIXING ENHANCEMENT ON THE JET ENGINE VIA EVOLUTIONARY ALGORITHMS

Overall Description

In this work two types of optimization were performed on the jet engine using two different, but related, optimization methods. The two optimization methods are *evolution strategies* and *genetic algorithms*, and they belong to a class of algorithms from the discipline of soft computing known as evolutionary algorithms. An evolution strategy was used to optimize mixing enhancement on the small jet engine in real-time, whereas a genetic algorithm was used to optimize the parameters of a control algorithm which controlled the downstream plume temperature of a simulated jet with similar characteristics as the jet engine.

A program was written which utilized an evolution strategy for real-time optimization of mixing on the small jet engine. The algorithm determined in real-time the actuator frequency selected at each iteration based on minimizing the plume centerline temperature. This approach successfully determined an optimal actuator frequency that corresponds to the global minimum for the system without any *a priori* information about the flow or actuator characteristics. Additional results are presented that address robustness to noise and changes in plant conditions and convergence characteristics.

Another program, which employed a genetic algorithm, was written to optimize the gains of a PID algorithm used to *control* the downstream plume temperature of a *simulated* jet engine. The temperature response of the simulated jet was modeled after the real one using data taken from various runs at a single throttle setting and over a limited pulsing frequency range. The dynamic response of the measured plume temperature to frequency changes was modeled as a first order system with a time constant derived from the data. Fluctuating error was introduced as a random walk about an overall average, also derived from the data. This optimization problem had a three dimensional parameter space to search, making it much larger than the single variable parameter space searched by the evolution strategy. The genetic algorithm consistently converged on a set of PID parameters that significantly reduced the oscillations over the baseline case.

Classification of Evolution Strategies and Genetic Algorithms

Figure 8.1 is an illustration that shows where genetic algorithms and evolution strategies belong in the hierarchy of optimization algorithms. Both methods are part of a branch of optimization techniques known as stochastic methods, which differ from the more traditional gradient methods in their approach to optimization in that they do not assume any knowledge of the derivatives of the function being optimized. Stochastic methods generate random numbers and use them either directly or indirectly to produce ‘guess values’ for each iteration. The guess values are then evaluated based on a metric defined by the user which may actually be a combination of several different metrics. The algorithm is typically modeled after some natural phenomenon that involves random processes. Annealing and the theory of evolution are the two most popular. Stochastic

methods are less prone to getting trapped in local minima than gradient methods, but are also usually much slower.

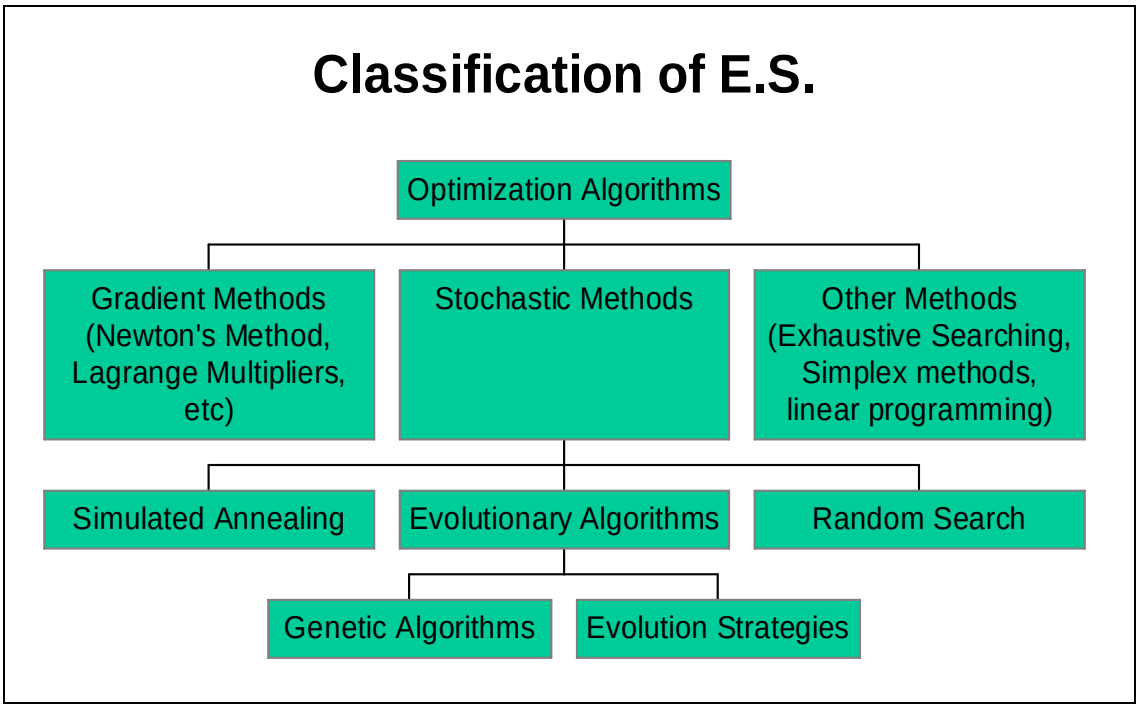

Figure 8.1: Classification of Genetic Algorithms and Evolution Strategies.

Evolutionary algorithms are a subset of stochastic methods, and include all algorithms that are modeled after the theory of evolution. Genetic algorithms and evolution strategies are the two most popular examples. Both evolution strategies and genetic algorithms use random numbers to seed the parameters to be optimized with initial guesses for the first iteration, or *generation*. The guesses are evaluated in terms of a *fitness function* that is either maximized or minimized. The algorithm proceeds to iterate in a way that is analogous to random natural selection. The best values from the previous generation are used to produce new values for the next generation, eventually converging on an optimal solution.

Scope of Application

Evolution Strategy Optimization

The current study considers the application of evolution strategies for optimization in real-time of a physical experiment. In this application, the variables that effect mixing include actuator number, placement, frequency, phasing, and amplitude. The number of actuators was fixed at either one or two, and the pulsing phase between the two was either 0° or 180°. Placement was also fixed; the actuators were located at the nozzle exit on opposing sides such that they pulsed in the horizontal plane (see setup figures in chapter 6). As previously shown in chapters 3 and 7, the optimal frequency depends on pulsing amplitude. These two variables could therefore not be varied simultaneously without moving the optimum. Additionally, it is trivial to consider the case where both frequency and amplitude are allowed to vary since mixing effectiveness increases monotonically with amplitude up to saturation. Thus optimization was performed on the pulsing frequency for fixed amplitude under the conditions described in the upcoming sections.

Genetic Algorithm Optimization

In order to accurately model the response of the jet engine to changing frequencies, the simulated jet throttle was fixed at Mach 0.15 and the pulsing amplitude was fixed at 5%MFR since a plurality of the data was obtained at these conditions. Additionally, the Strouhal number was limited to a range of 0 to 0.1 since this resulted in a temperature T* that spanned its entire range. The proportional, integral, and derivative gains were typically bounded from 0 to 10. Without all of these restrictions, the model would have

been prohibitively complicated. The overall goal was to make the plant model simple yet accurate enough to test the overall functionality of the algorithm and its ability to optimize the gains.

Description of the Algorithms

The Evolution Strategy

The specific approach followed in this work is similar to that implemented by Koumoutsakos, Freund, and Parekh in optimizing numerically modeled jet flows.[98] The objective of the current optimization algorithm was to select the pulsing frequency that maximizes jet mixing as indicated by plume downstream temperature T*. From iteration to iteration (or generation to generation) a new set of Strouhal numbers are created based on a random selection process, and the value of T* for each of them is compared against the values corresponding to a previous set. The Strouhal numbers that provide more desirable T* values survive and are the basis for selection of a new set of Strouhal values.

The specific search strategy employed was a simple 1 + 1 strategy in which only two function evaluations at a time are compared to determine the better parameter set. The initial evaluation of each set is referred to as the *parent* and the successive evaluation as the *child*. The algorithm for selection of the next parameter set for function evaluation is illustrated in Figure 8.2. The actuators were operated under computer control with the algorithm controlling in real time the pulsing frequency. Starting with a random initial guess for excitation frequency, the algorithm determines the next guess by random selection. The random distribution governing the “rolling of the dice” is a uniform

distribution of fixed width (referred to as the window width) centered about the previous guess. The function evaluation consists of measuring a short-time (1 to 2 seconds) average centerline temperature at a streamwise location 4 diameters downstream of the jet exit. Whichever frequency (parent or child) corresponds to a lower temperature is selected as the parent for the next iteration, or generation. Every ten iterations, the window width is either increased or decreased based on the 1/5-rule noted above. For some runs, there is also a 5% probability of *mutation* which means that 5% of the rolls are not limited to the current window size, but may fall anywhere in the entire search space. The code for the algorithm was written in the LabView graphical language G.

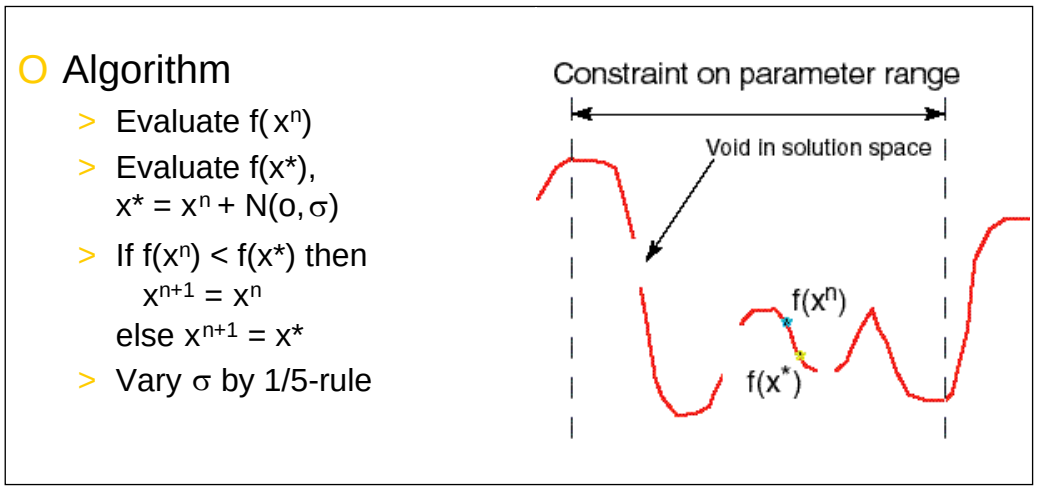

Figure 8.2: Selection Strategy for the Evolution Strategy.

The Simulated Jet and Genetic Algorithm

The Jet Simulation Model

The *ideal* temperature response was determined from a polynomial fit to the frequency sweep data of average T* vs. Strouhal number at Mach 0.15. This, however, doesn't account for dynamic response due to instantaneous frequency changes. From the

experimental data, it was found that the measured response of T* to a frequency change is essentially a first order response with a time constant of approximately 1 second. This is most likely due to the time needed for the thermocouple to reach thermal equilibrium with the flow. This *dynamic* response was included in the system model.

One final complication for the system model was the addition of random error. At any given frequency the temperature of the jet exhaust would fluctuate in a manner that was apparently random, so a similar random fluctuation was added to the model. The random error was modeled Monte Carlo style, meaning the error (assumed to be Gaussian distributed) was added directly to the dynamic temperature at each time step. The error was allowed to take a "random walk" about the expected dynamic temperature, but was bound to stay within 3 standard deviations (determined experimentally). The random walk was such that its mean and standard deviation about the dynamic temperature for a given length of time were the same as that determined experimentally. Thus, the dynamic temperature with error added to it is the *model* temperature. The difference between the ideal, dynamic, and model temperature is seen in figure 8.3 which is a plot of a step response simulated by changing the Strouhal number from 0.1 to 0.02.

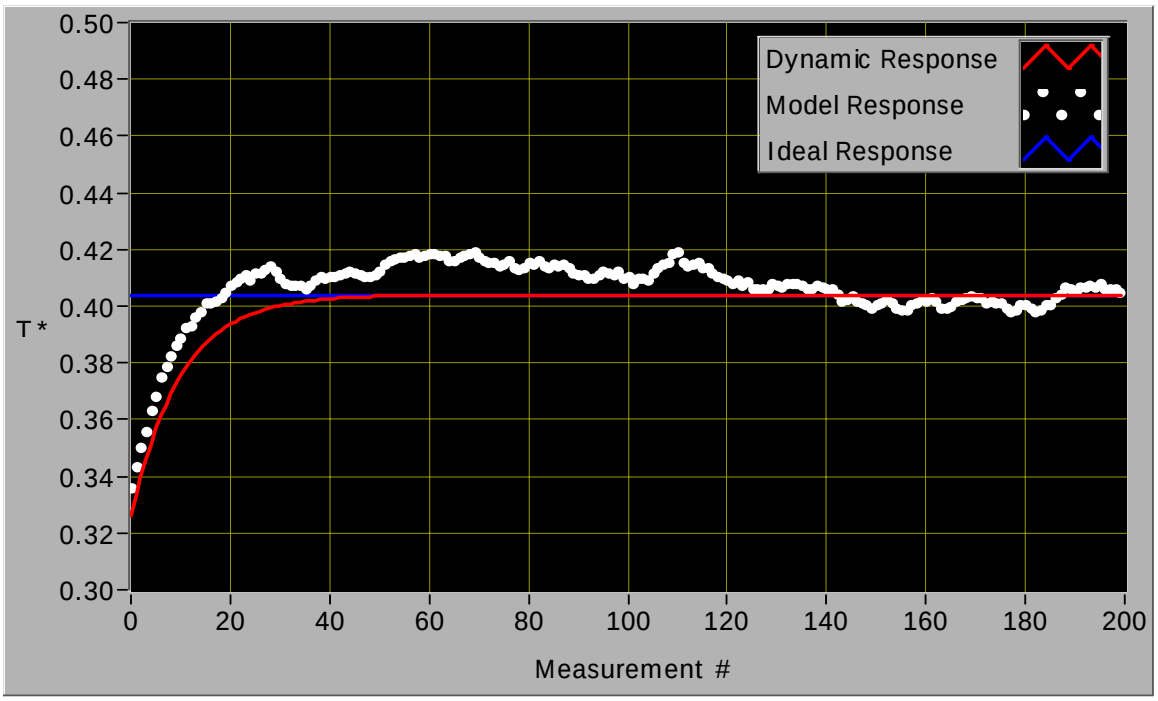

Figure 8.3: Simulated Ideal (Step), Dynamic, and Model Responses of T* to a Step Change in Strouhal Number.

The PID Controller

The time for a noticable change in temperature to begin due to a change in the Strouhal number was found experimentally to be between about 0.01 to 0.1 seconds. Therefore, 0.1 seconds was conservatively chosen as the control frequency and 0.01 seconds was selected as the measurement frequency (from the rule of thumb which says to use at least a 1/10 control to measurement frequency ratio). The algorithm keeps track of the dimensionless temperature error (the absolute value of desired minus actual) and adjusts the Strouhal number proportionally, with the integral, and with the derivative of this error to drive it down according to the PID gains selected. The integral and derivative terms were approximated using the trapezoidal rule and finite difference respectively.

The Genetic Algorithm

The algorithm selects an initial population of random numbers and evaluates their fitness in terms of the fitness function. In this case, the fitness function is the temperature error, and the goal is to minimize it. The population of numbers are then broken to pieces and recombined (like chromosomes during reproduction) for the next generation and the fitnesses are once again evaluated. As a simplified example, the two numbers 3.2 and 4.7 could be split and recombined to form the numbers 3.7 and 4.2. The process continues until the algorithm eventually converges on a set of optimal parameters. The major steps of the algorithm are as follows:

1) Set the error to zero.
2) Fill the PID array with the 1st generation of values.
3) Set the 1st PID parameters and evaluate the fitness function.
4) Wait the specified number of cycles to get the error.
5) Reset error to zero.
6) Set the 2nd PID parameters and evaluate the fitness function.
7) Loop to step 4 and repeat until all parameters are used and evaluated.
8) Sort values according to their fitness (low error = high fitness).
9) Keep some for the next generation.
10) Select parameters for "mating" according to their fitness.
11) Mate parameters (break up and recombine into new ones).
12) Refill PID array.
13) Loop to step 4 until "convergence" occurs or Genetic Algorithm is turned off.

All of the code for the simulation, control algorithm, and genetic algorithm was written in LabView G.

Results and Discussion

Evolution Strategy

A typical experimental result is shown in figure 8.4. The graphs show the history of variations in terms of specified excitation frequency and the corresponding measured temperature as a function of iteration number. In this run, the Mach number was 0.15 and pulsing amplitude was 5%MFR. The algorithm is able within a few iterations to get very close to the optimal value. As the optimization converges toward an optimal value, the width of the random distribution is automatically scaled down as is evident from the reduced variations in the child Strouhal numbers at the latter iterations. The expected convergence value of 0.12 is sometimes slightly different from the value to which the algorithm converged. This is because of: 1) the normal variability of the engine plume characteristics from run to run, and 2) measurement error which can slow convergence of the algorithm as is approaches the global minimum (see figure 8.5 for order of error on a typical curve). This illustrates the naturally adaptive nature of the technique.

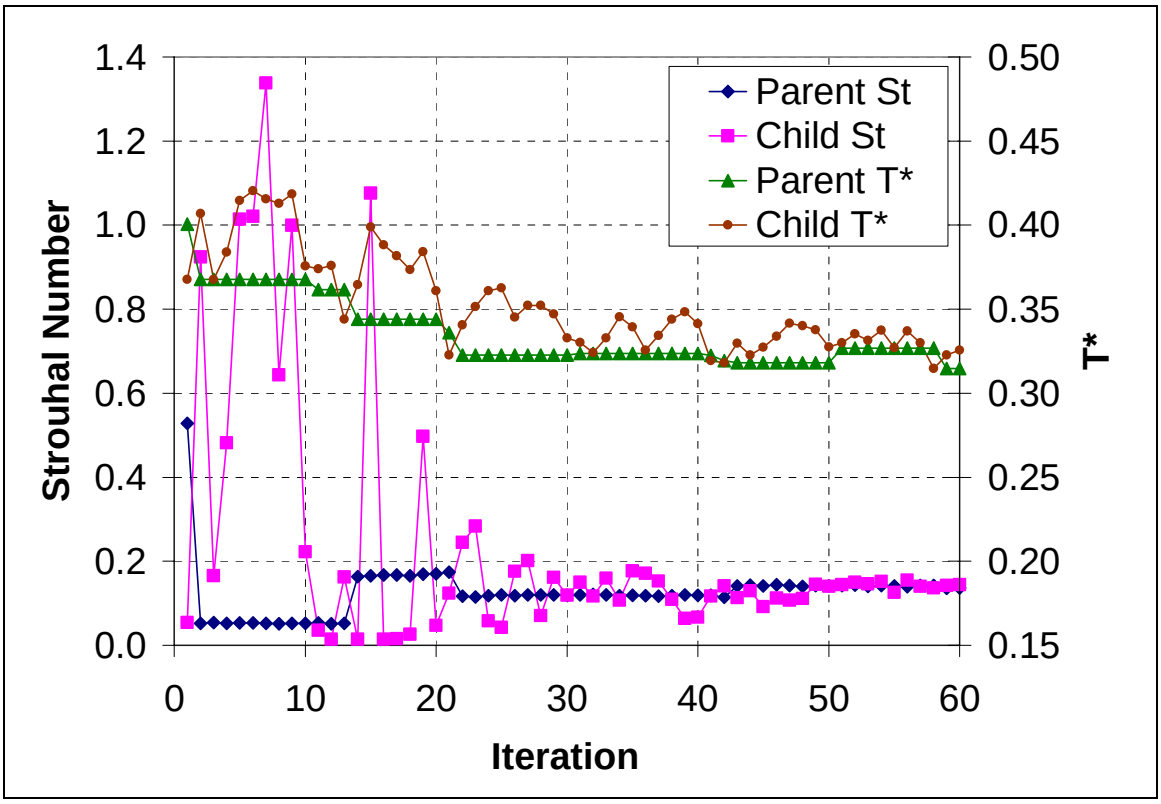

Figure 8.4: Example of the Evolution Strategy Converging to the Global Minimum. Ma=0.15, 5%MFR, Sampling Time= 1 s, No Mutation.

Three factors contributed to the jet characteristics differing significantly from those observed in generic jet flows from axisymmetric laboratory nozzles with top-hat exit velocity profiles. First, the presence of the centerbody results in a jet exhaust that decays much more rapidly than one would expect from simply scaling generic jet data based on the engine nozzle diameter. Second, being a hobby class engine, it is not designed to produce uniform non-swirling flow from the exit, and the engine speed control tolerance is only good to a few percent due to its susceptibility to electromagnetic interference. Third, in these flow control experiments, only one actuator is turned on. This provides information regarding the control authority of a single actuator as well as simulates failure of the second unit. While these factors are undesirable in a canonical flow

experiment, they are ideal for evaluating the general robustness of the optimization technique in the presence of realistic complexities and noise sources.

From a feedback control standpoint, one would like to be able to average over a short time when measuring the temperature sensor data to shorten the feedback loop time. This, however, results in significant uncertainty and variability in the information being fed back to the control loop (see figures 8.5 and 8.6). Consequently, a gradient search technique would be impractical to implement because of the difficulty of computing meaningful derivatives from the measured discrete data. In contrast, the genetic algorithms are able to handle this uncertainty with little difficulty.

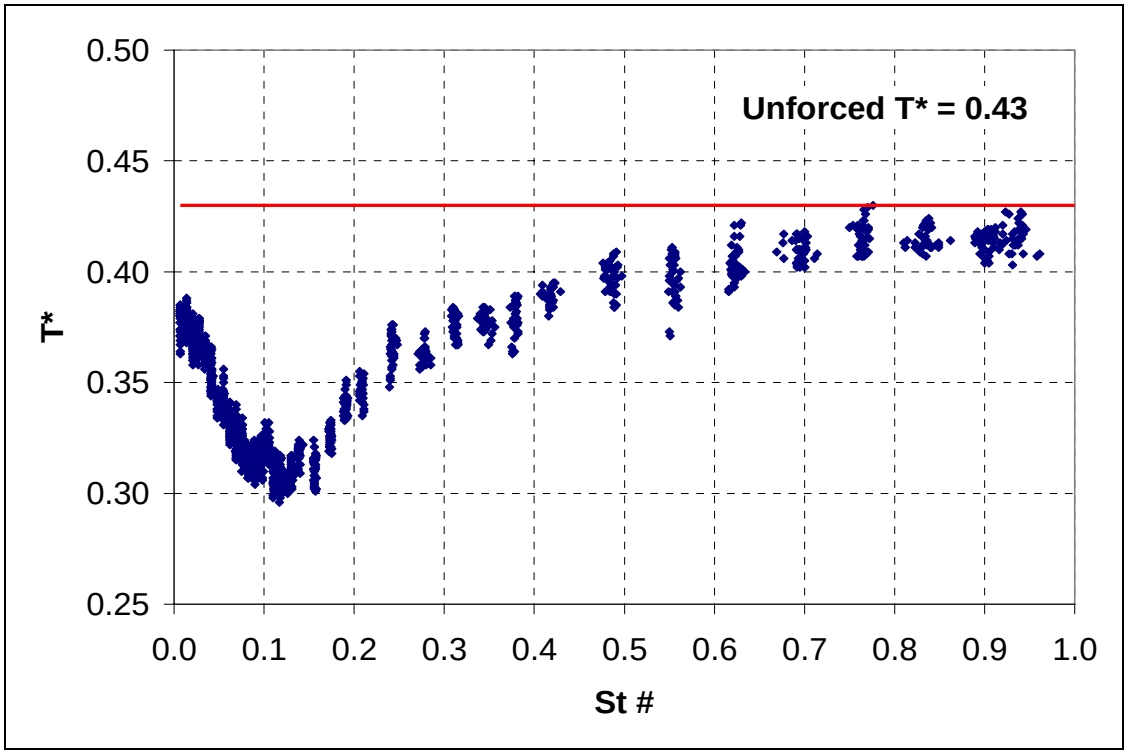

Figure 8.5: Data Scatter for a Frequency Sweep on the Jet Engine Measured at x/D=4, Ma=0.15, 5%MFR, Sampling Time = 1 s.

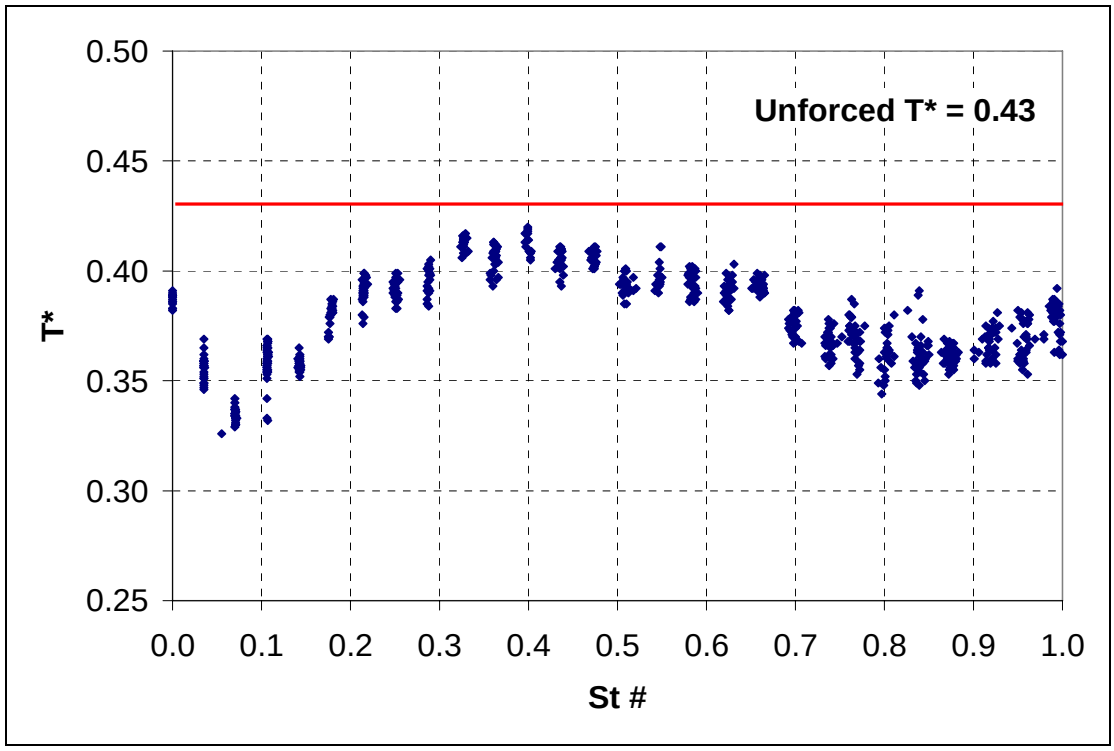

Figure 8.6: Data Scatter for a Frequency Sweep on the Jet Engine Measured at x/D=4, Ma=0.15, 5%MFR, Sampling Time = 1 s. Jet Mach Number Not Held Steady Under PID Control, Allowed to Vary with Actuator Motor Speed.

The result shown in figure 8.4 is an example of optimization on a simple solution space with a single global minimum and no local minimums. Figure 8.5 shows the solution space and the associated data scatter for a small increment frequency sweep. Because there were no local minima to get trapped in, the only challenges presented to the algorithm were the random error and dynamic response time for T* due to sudden frequency changes. Hence, more complicated scenarios were tested as well.

As explained in the experimental setup section, initial experiments with the jet engine demonstrated that the Mach number of the exhaust did not remain constant throughout a run, but was somewhat dependent on motor speed because of electromagnetic interference from the actuator motors. To remedy this problem the electronic control unit

that came with the jet engine was bypassed, and the engine was placed under computer control using a closed loop PID control algorithm to hold the Mach number steady. However, for most of the optimization experiments, this computer control of the jet engine was purposely *not* implemented in order to test the ability of the evolutionary algorithm to adapt to the added noise. The solution space changed as indicated in figure 8.6 where it is seen that there is now a local minimum in the vicinity of a Strouhal number of about 0.8 in addition to the usual global minimum at a Strouhal number of about 0.12.

Several different optimization experiments are presented in figures 8.7 through 8.10 for a pair of Mach numbers and varying initial guesses. Comparison of different experiments with identical initial guesses (figures 8.7 and 8.8) illustrates the variability of the convergence due to the inherent randomness in the process. The norm was for the algorithm to converge on a Strouhal number near the optimal value of 0.12. This illustrates the robust nature of the evolutionary algorithm to noise and uncertainty. Despite the addition of a local minimum and increased uncertainty in the measurement of the centerline temperature, the algorithm was still able to find the global minimum. Occasionally the algorithm oscillated about the local minimum for a while, but ultimately converged on the global optimum. Figure 8.9 provides a representative optimization experiment at a higher Mach number of 0.32. It is evident from the graph that mutation has been added to the algorithm.

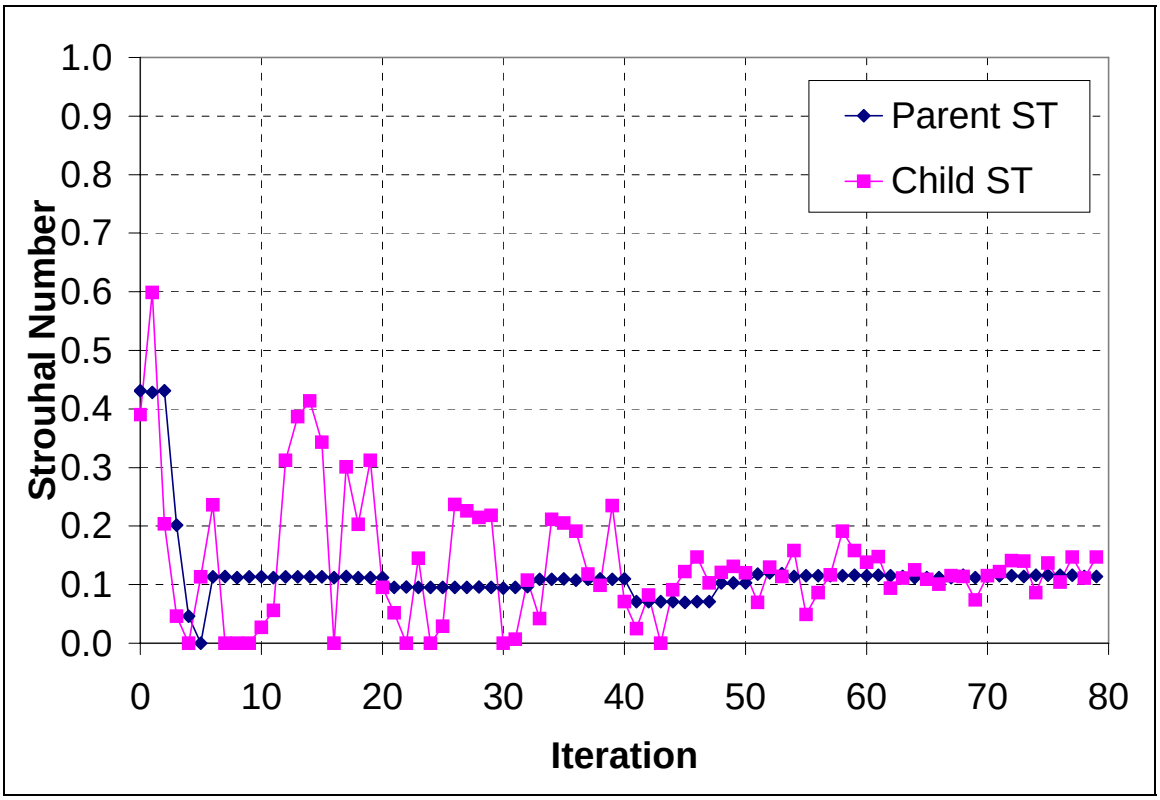

Figure 8.7: Example of Convergence to the Global Minimum, Mach Number Not Held Constant by Computer Control, Ma = 0.15, 5%MFR, Sampling Time = 2 s, No Mutation.

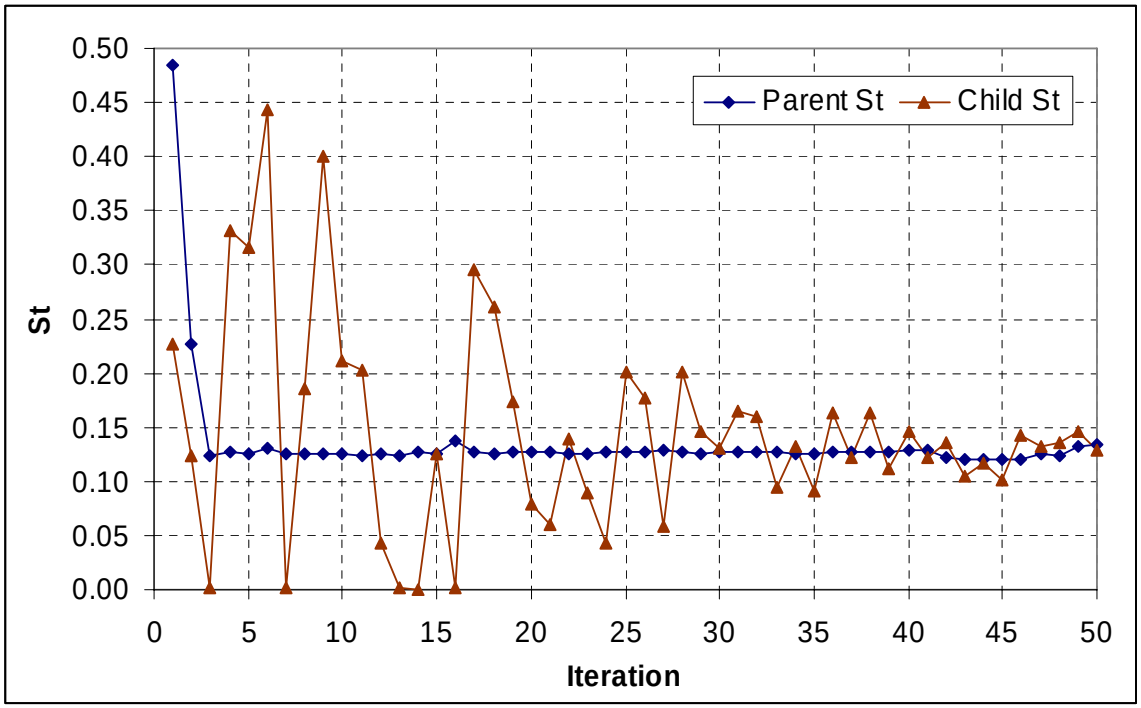

Figure 8.8: Another Example of Evolution Strategy Algorithm Convergence (Ma = 0.15, 5% MFR, 10 Generations/cycle)

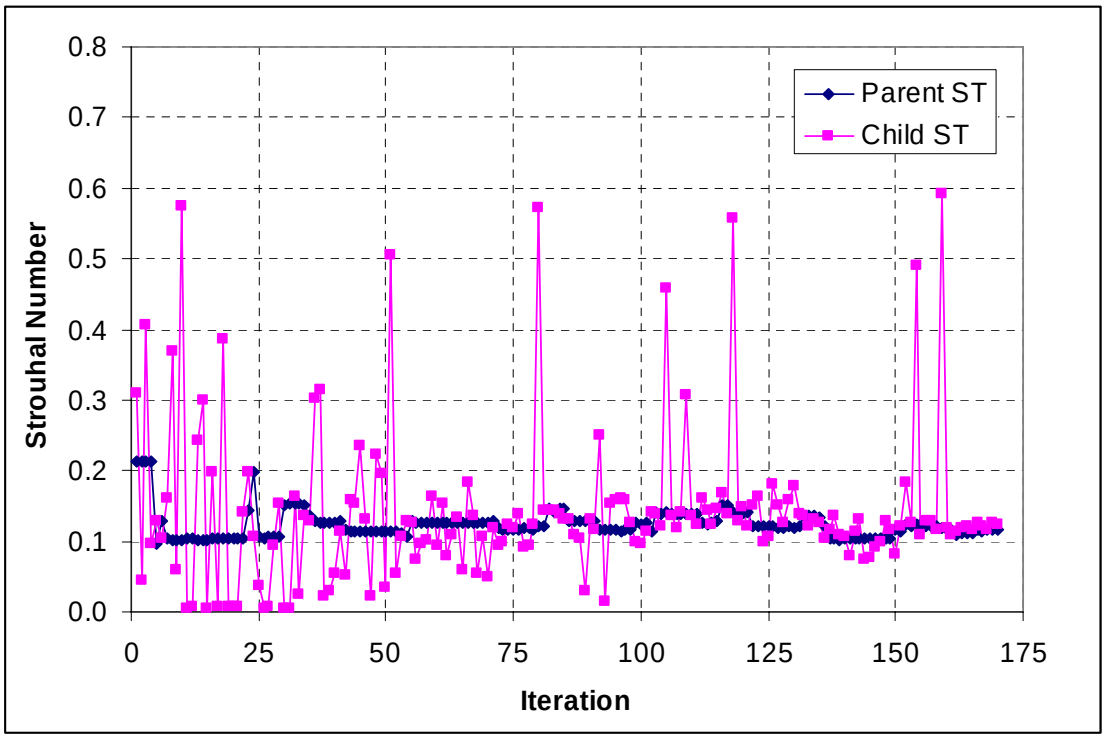

Figure 8.9: Convergence to the Global Minimum. Mach Number Not Held Constant by Computer Control. Ma=0.32, 5% MFR, Sampling Time=2 s, 10 Generations/Cycle, Mutation Added.

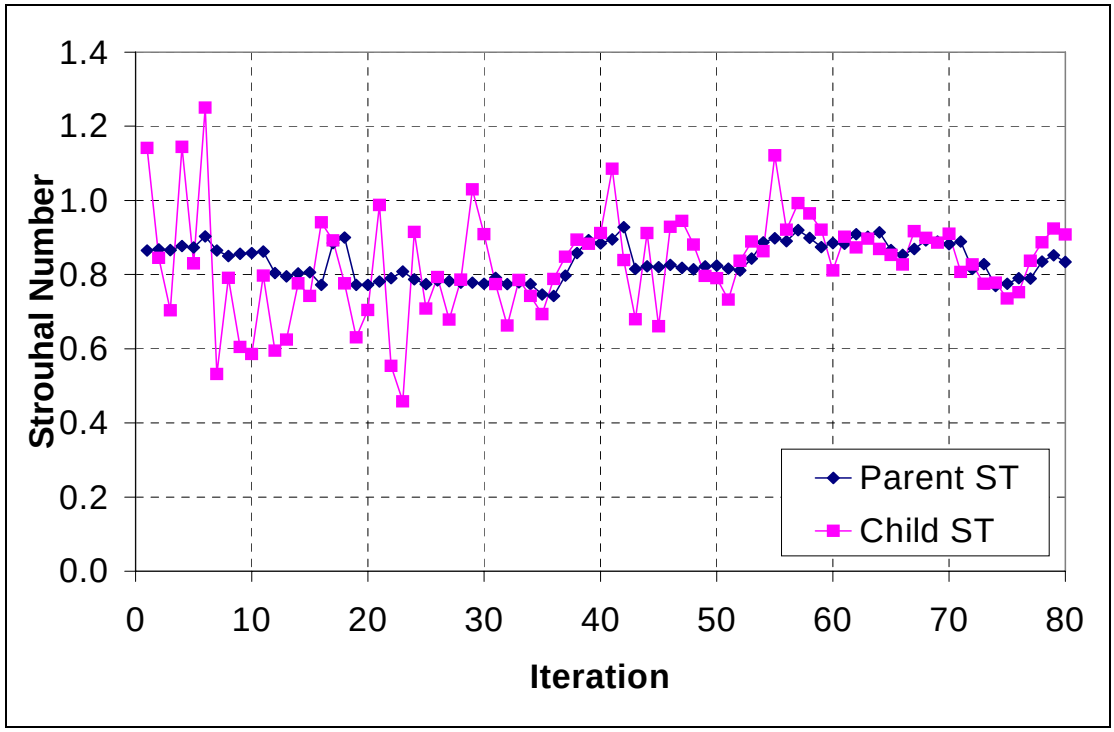

Figure 8.10: Example of Convergence to a Local Minimum. Mach Number Not Held Constant by Computer Control. Ma=0.15, 5% MFR, Sampling Time=2 s, No Mutation.

Without mutation, the algorithm is still considered an evolution strategy. Figure 8.10 shows a case without mutation and with an initial guess that happened to be a value near the local minimum. Under these conditions, the algorithm occasionally became trapped in the local minimum. Note that the 'convergence' is much less stable than the convergence to the global minimum above. With mutation, and given enough iterations, the algorithm would eventually find its way out of this trap. This reveals an important characteristic of evolutionary algorithms which is that although in principle they are relatively straightforward to code up, they often must be made more complex by adding things like mutation or restart to prevent them from getting trapped in local minima. Additionally, the program may need to be tailored somewhat to suit a particular application by setting appropriate bounds on the variables, applying the appropriate values for parameters, tweaking the rules, etc.

Convergence

In order to gain a better understanding of how quickly the evolutionary algorithm converges to the global minimum, ten independent runs were performed under the same conditions. Figure 8.11 shows the average convergence of the Strouhal number and T* for these ten runs. Figures 8.12 and 8.13 show all of the Strouhal and T* convergence data (respectively) for the runs with the average convergences superimposed on top (dark black lines). From these figures one gets an appreciation for how the convergence can vary from run to run.

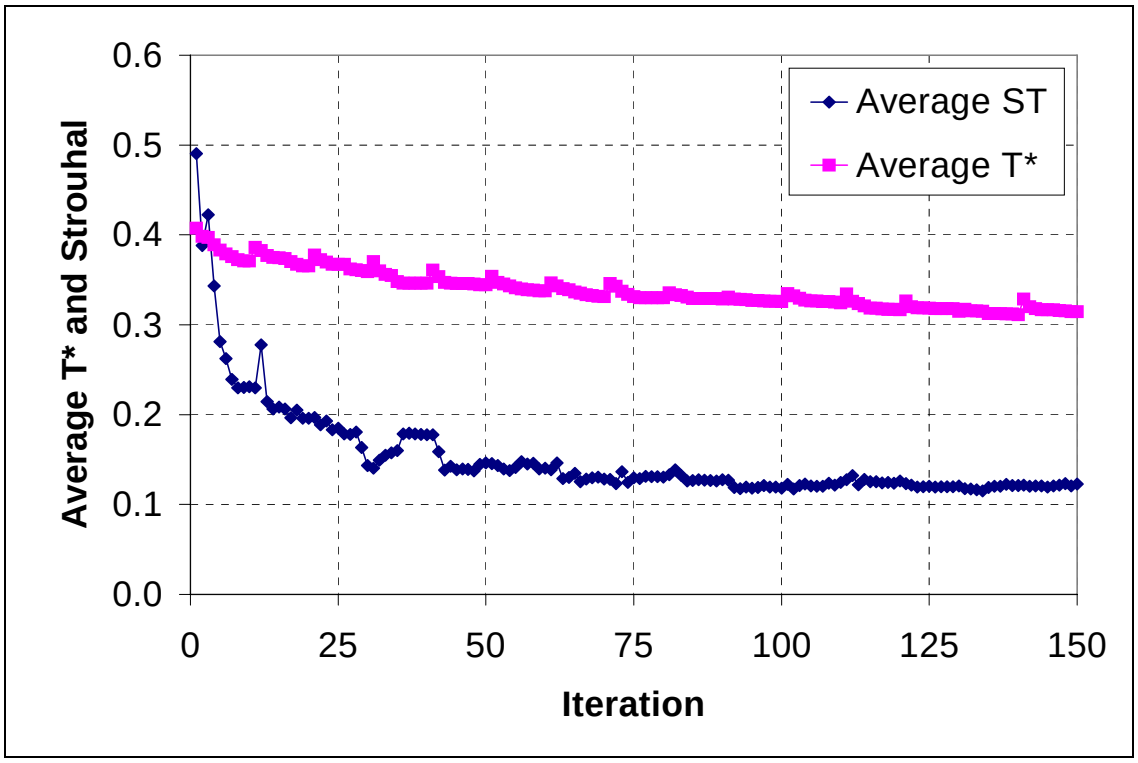

Figure 8.11: Average Parent T* and Strouhal Number for 10 runs. Ma=0.15, 5%MFR, Sampling Time=1 s.

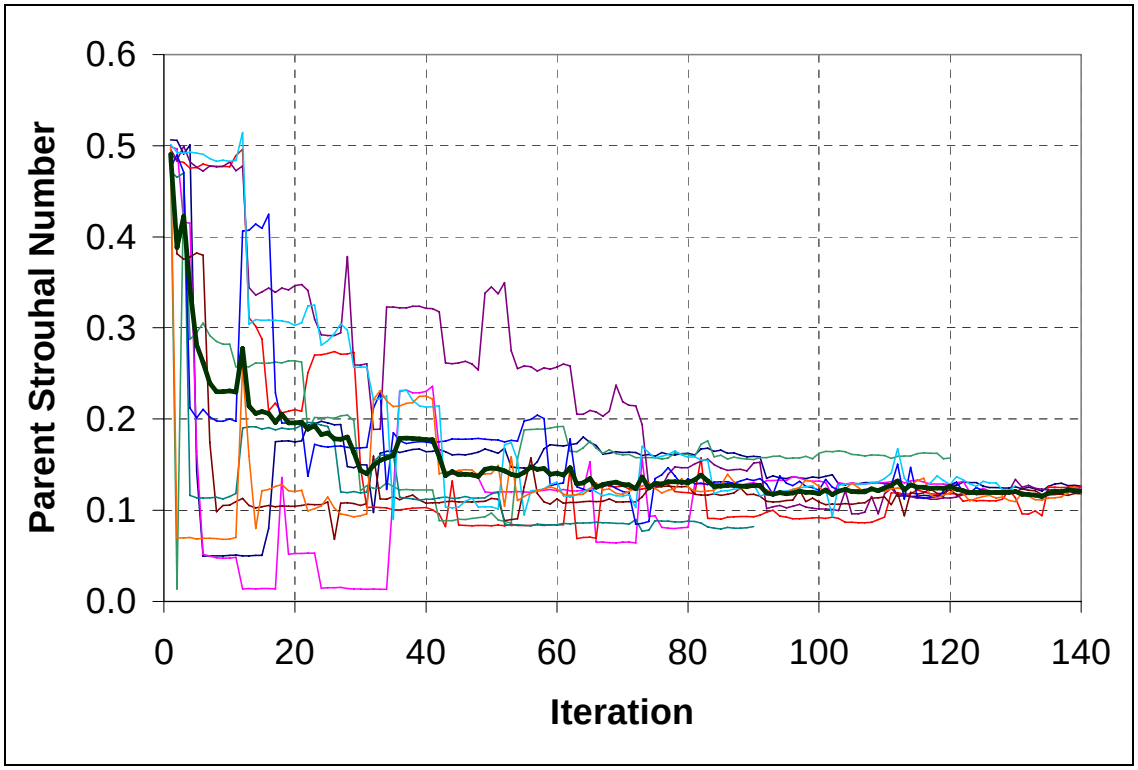

Figure 8.12: Strouhal Convergence Data for 10 runs. Ma=0.15, 5%MFR, Sampling Time=1 s. Bold Curve Represents Average.

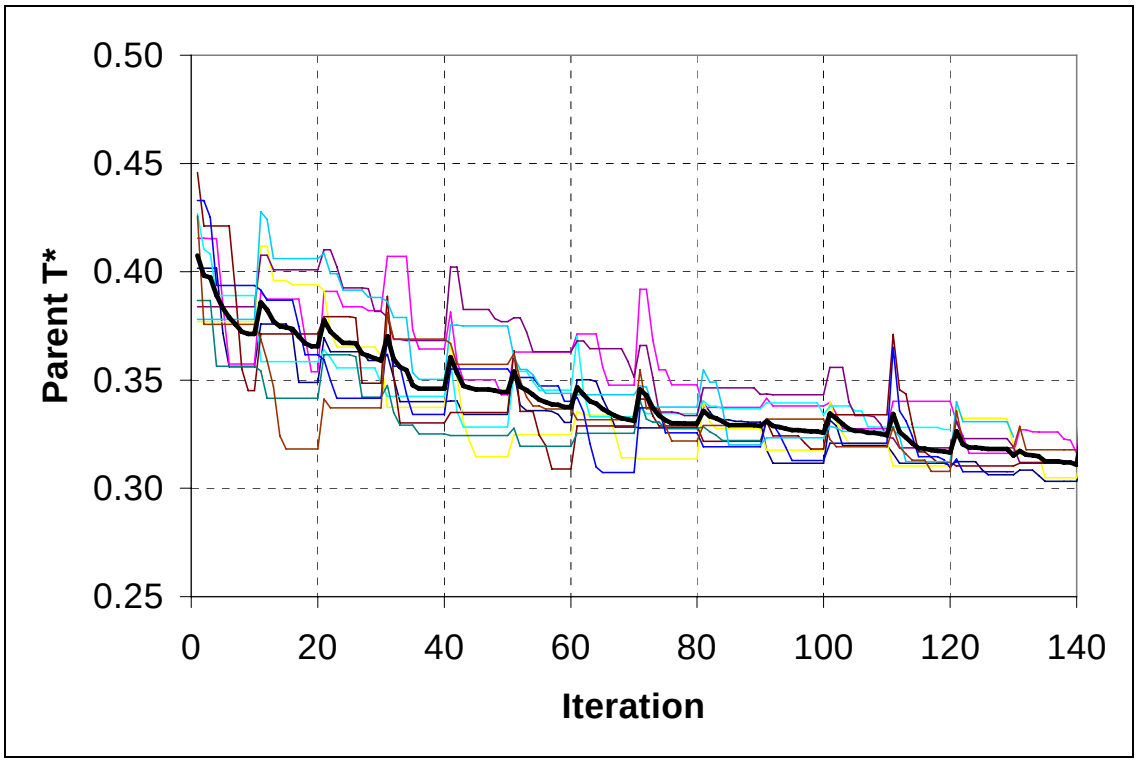

Figure 8.13: T* Convergence Data for 10 Runs. Ma=0.15, 5%MFR, Sampling Time=1 s. Bold Curve Represents Average.

Figure 8.14 shows how quickly the algorithm converges to the global minimum over the ten separate runs in a slightly different way. It counts the number of T*'s and Strouhal numbers within a specified range for iteration bins of size five. The count is then normalized so that all values within the range yields a fraction of one. For example, for the first bin (iterations 0 through 5), there are no T*'s within the specified T* range (0.3 to 0.33) and 6% of the Strouhal numbers are within the specified Strouhal range (0.1 to 0.14). Although the sizes of the ranges are somewhat arbitrary, their purpose is to represent a convergence to the known global minimum.

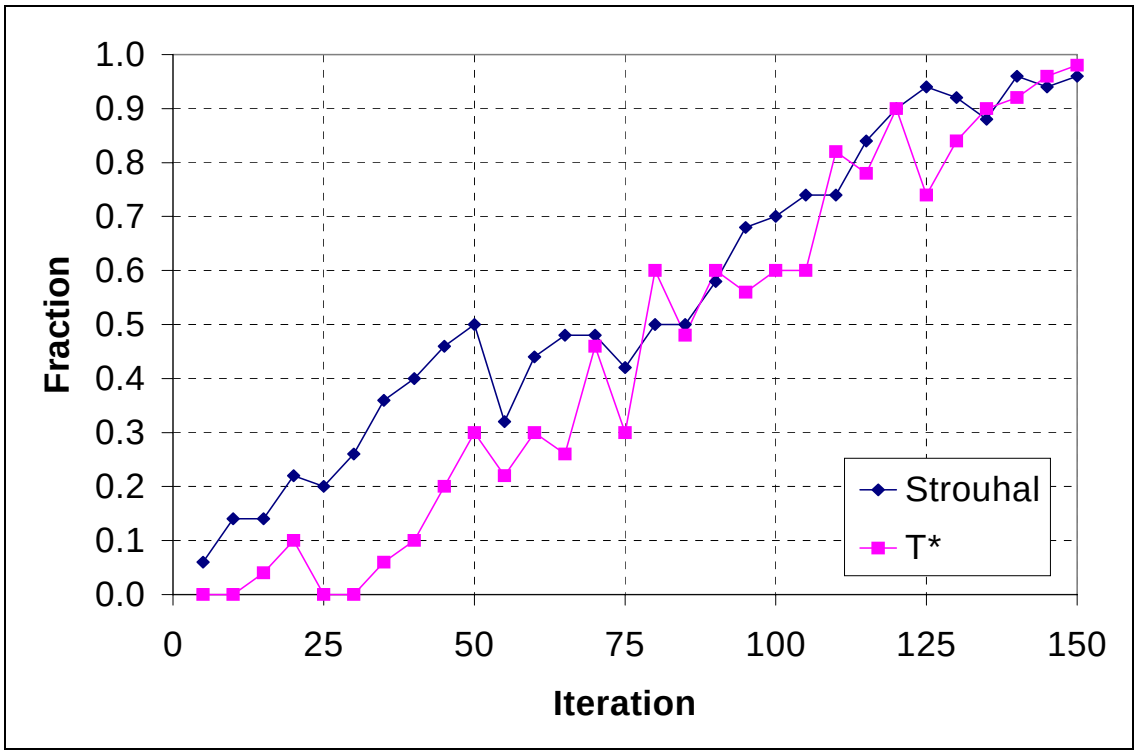

Figure 8.14: Fraction of Parent Strouhal Numbers Between 0.1 and 0.14 and T*'s Between 0.3 and 0.33 for Ten Separate Runs. Sampling Time=1 s.

Adaptation to System Changes

Additional runs were performed to test the ability of the evolutionary algorithm to adapt to changing throttle conditions during the run. No information about the engine speed nor even the fact that a change occurred was monitored by the algorithm, and thus it had no way to know that any change took place. The effect of changing the throttle was to slightly shift the optimal frequency (since the relative pulsing amplitude was thus varied) and to instantly change the dimensionless pulsing frequency (Strouhal number), which scales with the jet exit velocity. In these runs, the jet engine Mach number was not held constant under the computer controlled PID algorithm, allowing local minimums to be present. A representative result from these runs is figure 8.15. In this run, the algorithm is able to stay near the global minimum for two throttle increases, but then moves to the

local minimum after the throttle is decreased. If allowed to run longer, the algorithm would eventually find its way out of the local minimum and back to the global minimum. Thus, without any knowledge of the plant, the nature of the algorithm enables it inherently to adapt. Run lengths were limited by the fuel supply for the jet, and lasted anywhere from 5 to 30 minutes depending on the throttle setting.

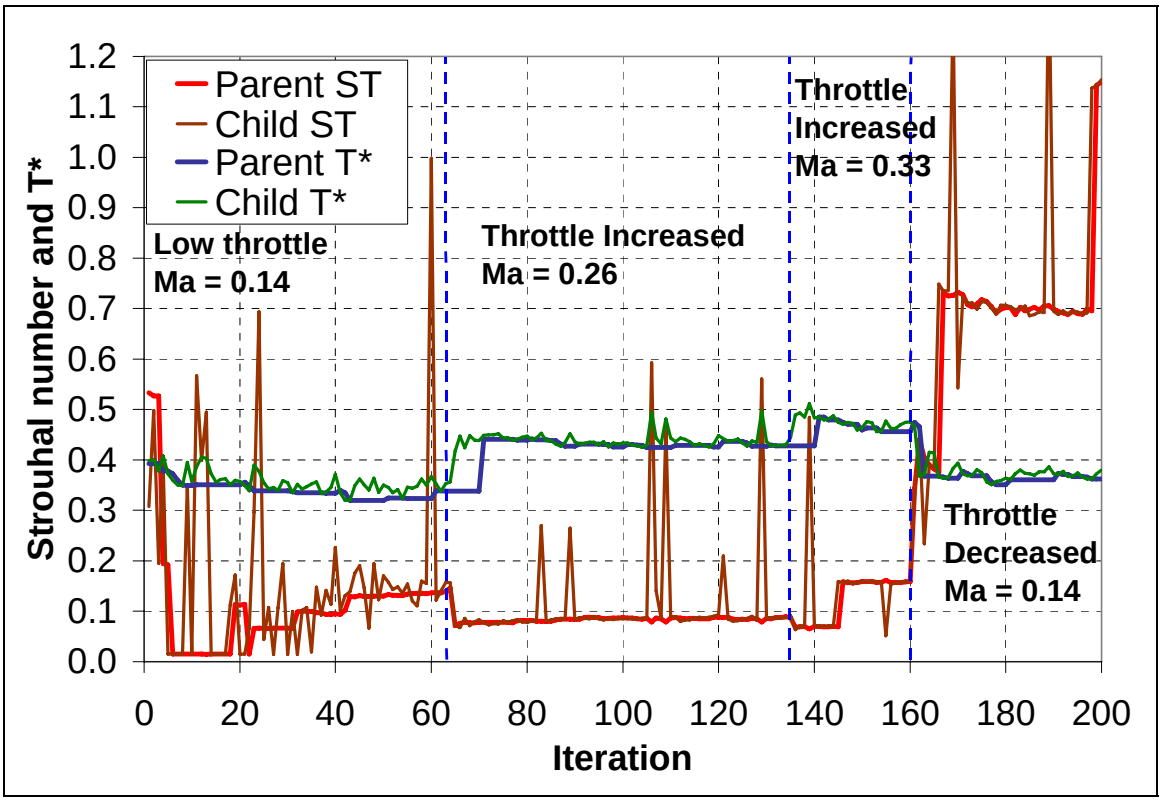

Figure 8.15: Convergence of the Evolution Strategy under Changing Throttle Conditions.

Genetic Algorithm

One way to evaluate how well the genetic algorithm was able to optimize the PID controller gains is to examine the dimensionless temperature signal for a given set of optimized gains. Since the objective of the controller is to hold T* at a desired value, large fluctuations about the desired T* are non-optimal and small fluctuations are

optimal. Figure 8.16 shows the resulting T* fluctuations (vs. time) for a proportional only controller with a gain of 10. Figure 8.17 shows how the addition of arbitrary integral and derivative gains affects the temperature signal. The oscillation frequency has increased, but the magnitude is about the same. If the integral gain is increased higher still, the oscillation magnitude increases. If it is decreased, the oscillation goes down slightly, but if it is decreased with a corresponding increase in D, the oscillation decreases significantly. But too much D or P will make the system unstable. Thus, the gains are interrelated, and the key to optimization is to test out various combinations. The genetic algorithm is well suited for this. It consistently converged to values of D in the neighborhood of 10, and much lower values of P and I. Figure 8.18 shows the temperature signal for P=1, I=0.2, and D=10.

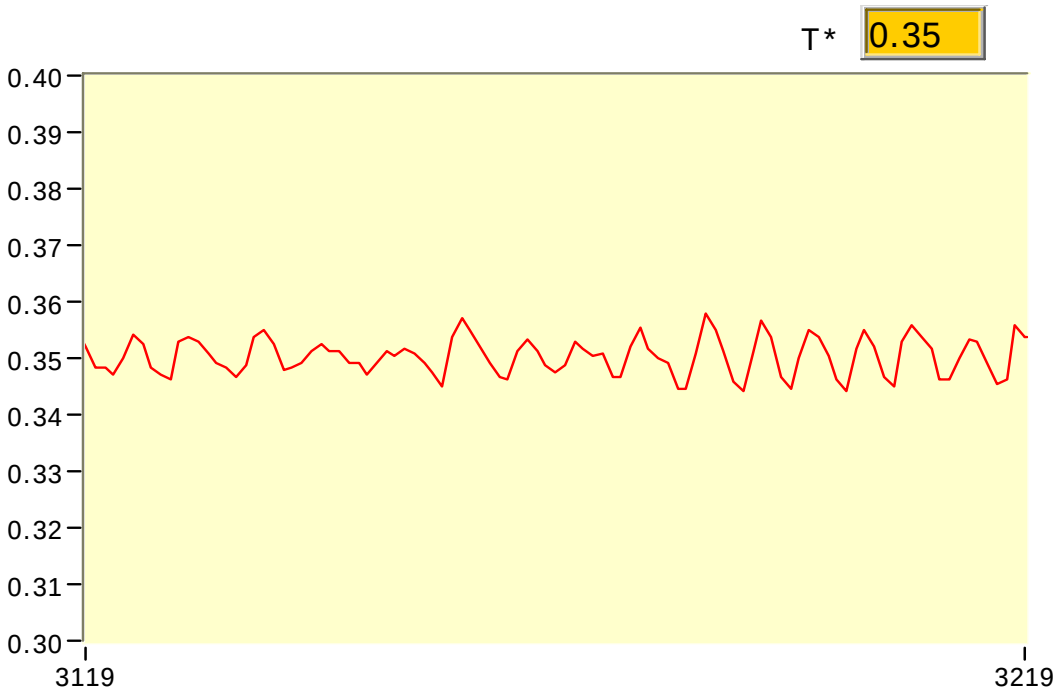

Figure 8.16: Oscillation of T* for a Proportional Controller (P=10, I=0, D=0), The x-axis is Arbitrary Time and the y-axis is T*

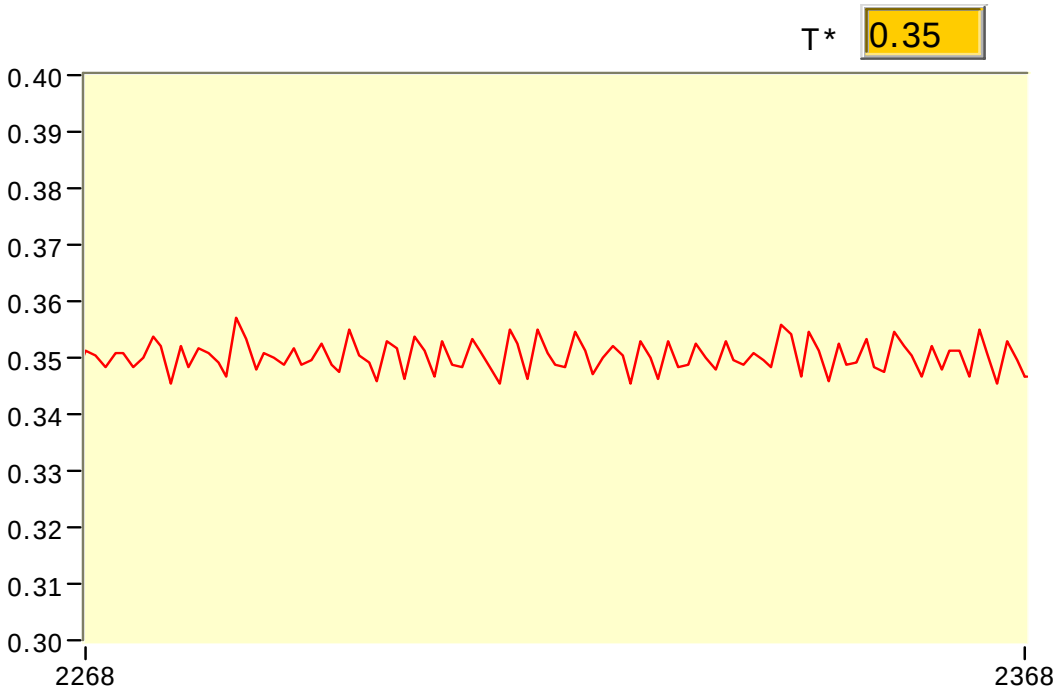

Figure 8.17: Oscillation of T* for P=I=D=10,
The x-axis is Arbitrary Time and the y-axis is T*

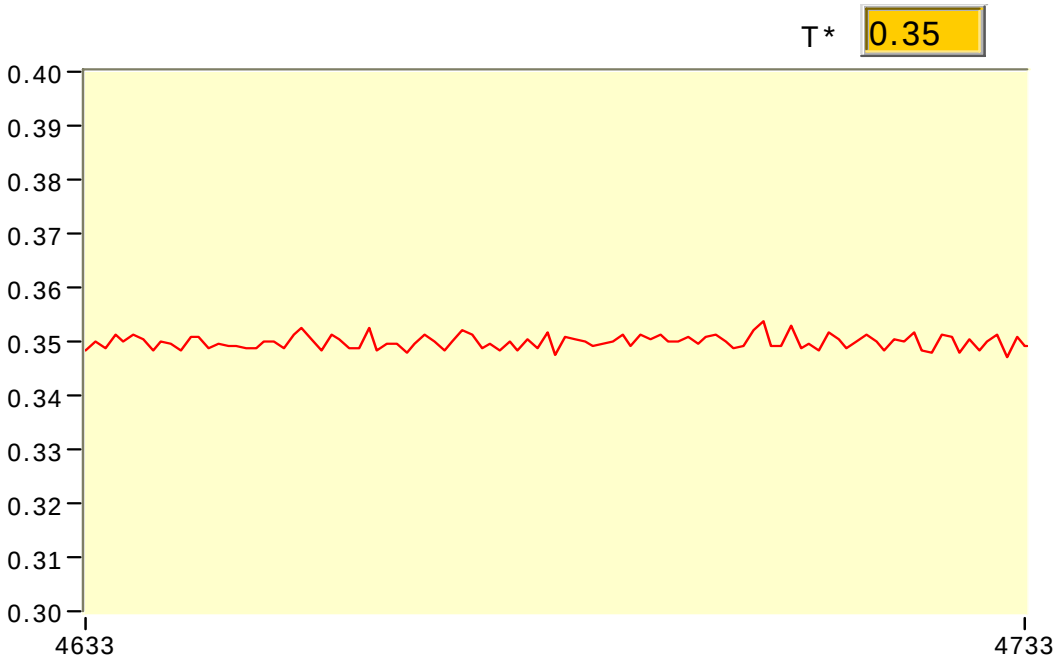

Figure 8.18: Oscillation of T* for a PID Controller with High D and Low P and I (P=1, I=0.2, D=10)

The algorithm did not converge to exactly the same numbers every time, but did converge to generally the same numbers. Ocassionally the algorithm got trapped in a noticably non-optimal case and required a restart. The P term seemed to have the most variation in convergence and it was discovered by adusting this parameter manually that it had no very little effect on the error for values up to about 3 or 4 when the I and D gains were as shown. Due to the presence of random error, it is unlikely that a single optimal set of PID gains exist but rather a neighborhood of values, as was found. This attests to the robustness of the algorithm, and it's ability to ultimately converge on a generally optimal solution.

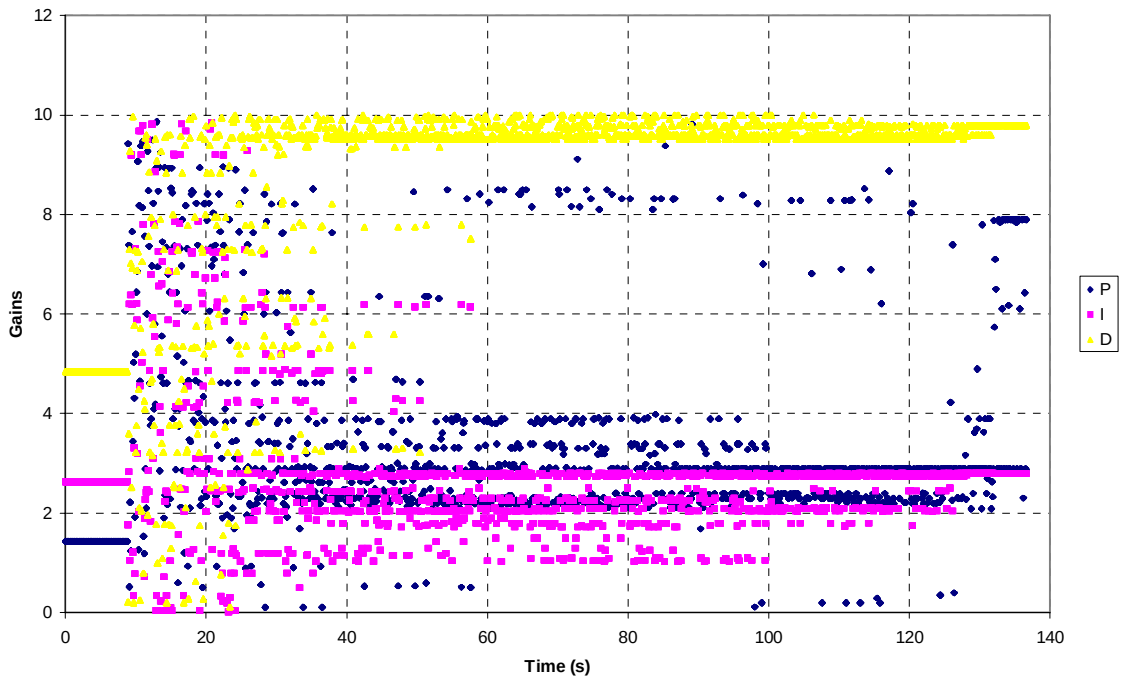

Figure 8.19: Example of Convergence of the PID Gains

Figure 8.19 is a graph showing an example convergence of the PID terms. Because the Genetic Algorithm is a stochastic method, this is only a representative convergence.

Each individual run had its own variances. There is initially a large spread in the values tested, and then a subsequent narrowing of the parameter values. Note that the algorithm continues to look for an optimal P value after it appears have converged. This is because the value of P (within the constraints used) has little effect on the control of the system when the I and D gains are optimized.

Summary

This chapter has presented an approach and successful implementation of evolution strategies for real-time optimization of jet mixing enhancement. The experimental apparatus consists of a small-scale jet turbine engine and pulsed-fluidic actuators with variable frequency and amplitude control. The results presented here focused on optimization of a single parameter, actuator frequency, but the approach is easily generalizable to the multi-parameter case. The utility of this approach is expected to be especially powerful in the complex, multi-parameter cases.

In the results presented here, the optimization technique is consistently able to select the forcing frequency that produces the global minimum in jet centerline temperature regardless of the engine operating speed with no prior knowledge of the characteristics of the jet or of the actuators. This optimization is possible even in the presence of large measurement uncertainty and engine speed unsteadiness. Additionally, this approach is able to adjust to changes in the state of the system, for example, abrupt changes in engine operating point. The approach routinely gets close to the optimal value within 10 iterations. However, since no independent metric, such as a desired T* range, is

specified, statistical convergence often takes over 50 iterations. This is the most generic case, where the algorithm objective is simply to find the global minimum in temperature.

In addition, a Genetic Algorithm was successfully used to tune the gains of a PID controller for a simulated jet engine with characteristics based on experimental data. The algorithm consistently converged to generally optimal values even though specific global optima didn't exist.

CHAPTER 9

CONCLUDING REMARKS

Overview

The overall objective of the current work was to help bring pulse fluidic mixing enhancement into use on realistic full scale turbulent flows, in particular for the purpose of cooling jet engine exhaust. In the present work, jet mixing enhancement by high amplitude pulse fluidic actuation was implemented and studied using three different experimental setups: a small scale clean laboratory jet, a small scale jet engine, and a simulated full scale core nozzle flow. The two major goals of the small scale experiments were to discover the key parameters relevant to pulse fluidic mixing enhancement and to gain a better understanding of the underlying fundamental mechanisms responsible for it. The goals of the experiments done with the jet engine and full scale jet were to verify the effectiveness of pulse fluidic jet mixing on more realistic flows and to compare the results with those of the small scale clean jet.

Pulse fluidic actuators were chosen for the current study since previous work has already established that they are an effective way to implement mixing enhancement for full scale realistic flows.[56, 137] They also have the advantage that they can easily be designed and built using widely available technologies. The fluidic pulses were delivered to the jet near the nozzle exit using high aspect ratio actuator nozzles in order to perturb a significant portion of the shear layer. Interchangeable actuator nozzles were used to deliver the fluidic pulse to the jet at the exit. The nozzle width was fixed such that

approximately 1/3 of the circumference of the jet was perturbed during an actuation cycle. The nozzle exit thickness was variable which allowed the momentum ratio of the actuator to main jet to be varied while keeping the mass flow rate constant.

Using high aspect ratio pulsed jets to excite the main jet flow results in spatially localized high amplitude disturbances of the jet's shear layer. This is in contrast with external acoustic excitation where a much lower amplitude acoustic wave interacts with the flow primarily at the nozzle lip through receptivity mechanisms. The result is an additional length scale, namely the actuator nozzle width, compared to the acoustically excited case. Nevertheless, many of the other actuation parameters are the same (e.g. frequency, amplitude, phase, etc). The fluidic pulses induce significantly larger perturbations in the jet than acoustic actuators resulting in nonlinear instability effects and a more complicated flow field. Therefore, the mechanisms of mixing enhancement which have been thoroughly studied for acoustically excited jets are not exactly the same as those studied here. Despite the differences, it is reasonable to expect some similarities between the two cases.

The pulse fluidic setup studied here also has several characteristics in common with two other systems that have been studied in detail: the jet in cross flow and tabbed nozzles. In a jet in crossflow a small jet penetrates the boundary layer and enters a larger flow of uniform velocity. For the current setup the actuator pulse is analogous to the jet and the main jet to the crossflow. The introduction of mass by fluidic pulses at the jet exit has been shown to have a similar effect on the local flow field as mechanical tabs protruding

into the flow.[13,14] It is thus also reasonable to expect that the current work may share some common traits with these two systems.

The following section summarizes the key results from each of the three experimental setups. It is followed by an overall discussion of the results where the fundamental mixing mechanisms are postulated. The final section describes the future work that needs to be done to answer questions brought up by the current work.

Summary of Results

Small Scale Setup

The small scale phase I experiments have shown that the following parameters affect mixing enhancement of a circular turbulent jet forced with fluidic pulses: frequency, amplitude, phase, configuration, offset, and duty cycle. The effects of each of these parameters are summarized in detail at the end of chapter 3. The key results are that the optimal frequency decreases with increasing forcing amplitude, mixing enhancement saturates for all frequencies (e.g. SRMR = 0.1 for St = 0.1), and mixing scales on the actuator to jet momentum ratio for a fixed slot width and varying slot thicknesses (in the streamwise direction).

The phase II experiments shed some light on the mechanisms of mixing enhancement. The most prominent features from the PIV pictures are the large scale vortical structures which form just downstream of the actuators. The vortices grow in size as they convect downstream and entrain large amounts of ambient fluid. The vortices appear to start off

at about the same size and strength for all frequencies at a constant amplitude, but it is unclear whether they initially grow at different rates. What is clear is that downstream the vortices for the lower frequency optimal cases remain coherent longer. This may be due to the larger spacing resulting in less interaction with neighboring vortices. The spacing of adjacent vortices is proportional to the jet exit velocity and inversely proportional to the pulsing frequency (for a constant duty cycle), hence the importance of Strouhal number based on jet diameter. PIV Images obtained for both jet-only and actuator-only seeding revealed that the vortices consist of swirling fluid from the jet, actuator, and ambient surroundings. This picture of mixing is contrasted with the case for the natural jet, where smaller scale structures form with much less coherence and regularity. For the excited case, the vortices clearly play a role in mixing enhancement, but are likely not the only mechanism.

Phased RMS calculations verify that the phase averaged values are good representatives of the instantaneous values. Phase averaged velocity measurements show that the large scale vortical structures are formed at the start of the pulse off cycle. Thus the rapid and complete turning off of the pulse is believed to be an important parameter relating to the formation of the vortices. This means the impulse of the fluidic pulse and the rate at which it rises and descends may be key parameters as well. The large scale vortices grow in size and move away from the jet in the radial direction as they travel downstream. The antisymetrically forced jet is clearly flapping in the near field, while the axisymmetrically forced jet is squeezed and released. Significant velocity reduction occurs for both cases by x/D = 5, but antisymmetric forcing is clearly superior.

PIV results show that higher frequency pulses ultimately penetrate less than lower frequency pulses. In the initial interaction region ($x/D < 0.25$), penetration saturated for all tested frequencies after only 8 milliseconds, meaning that all frequencies under 125 Hz are equivalent at this distance. But wider views show that lower frequencies, which have a larger pulse "on time", result in greater penetration further downstream. The additional flow present in lower frequencies helps the pulse to continue pushing its way into the center of the jet. Penetration is thus a function of both frequency and amplitude. Studies on pulsed jets in crossflow concluded that pulsing too close together (i.e. at high frequencies) results in less penetration because of the shorter "on time" and interaction of adjacent vortices.[50, 86]

Spectral Analysis, velocity profiles, and turbulence intensity profiles in the flow field at $x/D = 10$ show that the initial large scale structures no longer dominate the flow. There are no noticeable peaks in the spectra by 10D, suggesting that the oscillations that take place in the near field have essentially vanished. The velocity reduction mixing metric U* (defined as $U_{10D,forced}/U_{10D,unforced}$) is thus validated as a good indicator of mixing enhancement at that location.

The momentum ratio was confirmed as a key parameter during the phase II experiments. When two different actuator nozzles of the same width and different thicknesses were pulsed at different velocities but the same momentum, the result was an almost identical flow field from the interaction zone all the way down to 5D.

Measurements made in the 90°-rotated (xy) plane show that mixing is very three dimensional. The flapping (or squeezing for in phase pulsing) of the jet takes place only in the center as indicated by the velocity reduction there, while the outer edges show little if any effect from the pulsing. This indicates that the jet has bifurcated in a manner similar to jets with mechanical tabs mounted on the nozzle. Other researchers have shown that the primary mechanism of mixing enhancement for jets with tabs is the formation of streamwise counter rotating vortex pairs (CVPs).[4, 5, 13, 14, 15] These CVPs are believed to have formed under the current configuration as well.

Pulsing has the effect of increasing the thickness of the shear layer significantly compared to the natural jet and blowing cases. This was easy to see by comparing the velocity contours from the PIV data. Numerical calculation of the momentum thickness at various time increments were averaged together which verified that the time average momentum thickness for the forced case was almost double that of the natural jet case beyond x/D = 0.5.

Full Scale Setup

The full scale system exhibited very similar characteristics to the more controlled and cleaner small scale system. Some examples of this are:

1. The optimal Strouhal numbers were the same.
2. Saturation occurred at the same amplitude (SRMR).
3. The optimal Strouhal number decreased with increasing pulsing amplitude.

4. The mixing curves had the same shapes, though they were offset from each other.

The offset in the curves were caused by the higher initial turbulence level of the main jet, which was a consequence of the ejector/collector setup that was used. The high level of turbulence caused both the unforced and forced jet to decay more rapidly than the equivalent clean small scale jet.

Jet Engine

Pulse fluidic jet mixing was found to be effective on a realistic flow with high turbulence, an annular nozzle, and swirl. Similarities with the small scale jet include:

1. The optimal Strouhal numbers were similar, close to St = 0.1
2. The frequency sweep curves had similar shapes
3. Mixing saturated at similar amplitudes (for the 2-sided case)
4. The optimal Strouhal number decreased with increasing pulsing amplitude.

Two sided pulsing was more effective than one sided pulsing, but the pulsing phase (axisymmetric vs. flapping) didn't matter because of the centerbody. The mixing metrics T* and U/Uexit correlated well with each other.

Overall Discussion

It was not possible to point to a single phenomenon as the primary mixing enhancement mechanism. There are 3 different phenomena that affect pulse fluidic mixing enhancement to various degrees and determine the optimal pulsing parameters:

1) Instability of the jet's shear layer
2) Penetration depth and subsequent formation of a CVP
3) Alternate Vectoring of the Jet (for out of phase forcing only)

Instability

There is strong evidence for the importance of instability to pulse fluidic mixing enhancement. The most compelling evidence is the existence of an optimal frequency band (the "bucket") similar to that which occurs for acoustically excited jets. In the case of a low amplitude acoustically excited jet, the disturbance grows within the shear layer as the fluid travels downstream and amplifies such that a vortex forms. The vortex increases in size and eventually disappears as it gives way to turbulence. For pulse fluidic excitation a vortex is generated immediately downstream of the actuator at the start of the "off cycle". This vortex also grows in size and breaks down in a similar way. Additionally, at low forcing amplitudes the optimal frequency approaches that found by previous researchers using acoustic excitation (which ranges from St = 0.24 to 0.64). In the current work the optimal frequency for the lowest amplitude fluidic forcing was near St = 0.3 for both the axisymmetric and antisymmetric cases, which is near the most amplified frequency found by Crow and Champagne.[41] It is therefore speculated that stability theory is the dominant contributor to mixing enhancement at lower pulsing amplitudes (those significantly below saturation).

Although linear stability theory can not be applied to the current work to predict the initial growth rates of the instabilities generated by the nonlinear high amplitude

perturbations, it is reasonable to expect some of the same trends to persist. For example, stability theory predicts that axisymmetric forcing will result in a higher optimal frequency than antisymmetric forcing at the same amplitude (for realistic sized momentum thicknesses).[113] This was confirmed in the current work. Furthermore, it is known that near the jet exit the shear layer thickness affects the growth rate of the various frequency components present. For a jet entering a quiescent ambient environment, the most amplified frequency predicted by linear stability theory has been shown to be $St_\Theta \approx 0.016$.[72] Experiments have shown that the number is more like 0.012, which is reasonably close.[179] This Strouhal number is defined as the frequency times the momentum thickness divided by the velocity. Thus, the most amplified frequency is inversely proportional to the momentum thickness. The important point is that thickening the shear layer leads to faster growth of lower frequencies. One would therefore expect the thicker shear layer generated by the fluidic pulses to result in more amplification of lower frequencies and thus a lower optimal frequency. The data showed that pulsing has the effect of thickening the shear layer and that higher amplitude forcing results in more thickening. This is one possible explanation for why the optimal frequency decreases with increasing pulsing amplitude. Saturation may then be viewed as the point where the potential core is penetrated and no further thickening of the shear layer is possible. However, there is good evidence that other mechanisms may be involved as well.

Penetration

PIV measurements showed that lower frequency pulsing results in greater penetration downstream which is consistent with results found in the literature for pulsed jets in crossflow. Measurements in the xy-plane (rotated 90° from the actuation plane) for saturation level amplitudes show that the jet bifurcates which suggests that counter rotating vortex pairs similar to those generated by mechanical tabs are being generated. Additionally, contour plots of w-velocity show that the pulse picks up momentum as it travels through the center of the jet, also indicative of a CVP. It is important to note that the CVPs were not directly observed since no yz-plane PIV measurements were made, but simply that the orthogonal flow field is similar to those where they are known to be present. It is likely that as the pulsing amplitude is increased penetration depth and the formation of CVPs becomes a more important contributor to mixing and has the effect of pulling the optimal frequency down. This is another explanation for the downward shift in the optimal frequency with increasing amplitude. In this case, saturation (which for optimal frequencies occurs at SRMR ≈ 0.12) may correspond to the amplitude where the pulses penetrate the potential core and a larger CVP can not be formed. Higher pulsing frequencies also saturate, but at higher amplitudes since that is what is required to achieve the same depth of penetration.

An additional effect worthy of note at this point is the temporal limit on lowering the frequency. As an extreme case, imagine that lowering the frequency to 0.01 Hz results in the greatest amount of penetration. This would result in a pulse that initially penetrates deep into the jet and results in significant mixing enhancement for a short period of time.

However, since the cycle time is 100 seconds, the 50% duty cycle pulse will last for 50 seconds, meaning that most of the time blowing is being implemented. Over the entire cycle, the average mixing will be very close to that for blowing which is not nearly as good as that for pulsing. Studies on pulsed jets in crossflow have shown that pulsed jets penetrate significantly farther and mix significantly better than steady jets.[50, 70, 86]

Alternate Vectoring

Alternate vectoring of the jet is responsible for 'apparent' mixing enhancement close to the jet exit for saturation level amplitudes, and only for very high amplitudes (well above saturation) at x/D = 10. Apparent mixing simply means that a single velocity or temperature probe used to measure mixing will be fooled by a jet that is vectoring back and forth across it due to the fact that the off center measurements will bring the time average down. The vectoring of the jet near the exit, though not large, is clear from the PIV plots. Spectral measurements made throughout the flow field at x/D = 10 show that there is no longer any evidence of alternate vectoring for saturation level amplitudes. Thus the alternate vectoring of the jet has been "mixed out" by the time the jet reaches 10D and can not be seen to significantly bias the single point probe measurements at this location. The vectoring does contribute some to the spreading out of the jet because of the near field vectoring and subsequent downstream mixing, but the effect is not dominant as evidenced by the presence of the frequency bucket and likely presence of the CVP. Finally, it should be noted that the alternate vectoring only takes place in the center section of the jet as shown by the PIV measurements in the xy-plane.

Summary

The overall conclusion is that pulse fluidic actuation is an effective method for enhancing mixing in realistic turbulent flows with a wide variety of scales, initial conditions, and geometries. It has been shown that despite the differences in the configurations, certain key parameters determine the mixing effectiveness. Mixing was found to scale with the momentum ratio of the actuator pulse to the main jet. Pulsing in the antisymmetric mode at a Strouhal number between 0.1 and 0.15 with a SRMR of about 0.12 will generally result in significant mixing enhancement. A pulsing duty cycle of 30% to 50% is recommended, unless forcing at levels well below saturation. Additionally, one should go to great lengths to eliminate DC offset in the pulse. There is considerable flexibility in configuration and position of the actuators. High aspect ratio nozzles like those used in the current study are recommended.

Mixing enhancement is believed to be due to a combination of three different phenomena acting together: instability, penetration, and alternate vectoring. It is difficult to establish the exact effect of each, but some conclusions may be made. At low amplitudes stability almost certainly dominates since there is virtually no vectoring or penetration. At higher amplitudes (those approaching saturation) penetration becomes more important and has the effect of pulling the optimal frequency down since the lower frequencies result in greater penetration. Additionally, the thickening of the shear layer due to higher amplitude pulsing results in greater amplification of lower frequencies which also pulls down the optimal frequency. Saturation may be viewed in two ways. In terms of penetration, it is the point at which the pulse penetrates the potential core and thus no

more mixing due to increased penetration can occur since a larger CVP can not be produced. In terms of stability, it may also be viewed as the point at which the potential core is penetrated, but in this case the shear layer can not be further thickened. Saturation occurs at different levels for different frequencies, and may correspond to the point at which the same depth of penetration has occurred. Alternate vectoring plays a role in that it spatially separates a portion of the jet's central fluid so that the other mixing mechanisms can take effect on it resulting in a more spread out jet. For momentum ratios on the order of those studied (around 1%), this effect is small.

Future Work

The current work suggested that penetration results in the formation of a counter rotating vortex pair which contributes to mixing enhancement for saturation level amplitudes. Other researchers have conclusively shown the existence of the CVP for tabs and circular blowing jets, and provided evidence of them for circular pulsing jets, but no yz-plane measurements have been made for a high aspect ratio pulsing jet like those used in the current study. Thus, PIV or multidimensional hotwire measurements in the yz-plane for a configuration similar to the current one would conclusively answer the question as to whether the CVP exists. Detailed flow field measurements were made for several different frequencies at saturation level forcing, but there is little PIV or hotwire data to characterize the flow field for varying amplitudes, particularly at low amplitudes. The addition of this would help to determine whether different mixing mechanisms dominate at different amplitude levels as suggested in the current work. Finally, it would be

informative to vary other parameters such as the offset, duty cycle, and pulse waveform and examine the effect on the flow field with PIV.

APPENDIX A

ANNOTATED BIBLIOGRAPHY

Overview

This section contains the entire list of references used in the current study along with published abstracts for each. In most cases the abstract was written by the author. In cases where an author abstract was not available, a summary was written by the author of the current work.

Adrian, R. J. (1986). "Multi-point optical measurements of simultaneous vectors in unsteady flow-a review." International Journal of Heat and Fluid Flow **7**(2): 127-45.

Optical techniques for measuring large numbers of simultaneous velocity vectors in two- and three-dimensional regions of fluid flows are reviewed. These nonobtrusive methods provide spatial information of the type that is available from flow visualization with accuracy approaching that of single-point methods such as laser Doppler velocimetry and hot wire. The principle underlying each technique is the measurement of the imultaneous displacements of images of many marked fluid particles. Many methods are available. These include streak photography; marker image tracking methods using photography, cinematography, holography, and video recording; line tracking methods using hydrogen bubbles and photochromic tracers; and fluorescent particle tracing. Pulsed laser methods, specifically laser speckle velocimetry and particle image velocimetry, provide high spatial resolution and good accuracy

Adrian, R. J. (1989). Applications of particle image velocimetry. ASME Winter Annual Meeting, San Francisco, CA, ASME.

Particle image velocimetry (PIV) can be applied to a wide range of flow phenomena that are significant to engineering and science. Currently most of these applications remain in the research laboratory, but the potential exists for expansion into less ideal environments. This paper reviews some of the flows that have been studied by PIV.

Ahuja, K. K. (1993). Supersonic jet noise reduction by tabs and ejectors. 15th AIAA Aeroacoustics Conference. Long Beach, CA.

An experimental investigation is conducted of the effect of vortex-generating mechanical tabs, which protrude normally into the flow of a nozzle, on the mixing and noise emission characteristics of the jet at jet Mach numbers in the 0.8-1.4 range. Attention is given to the effect of two diametrically opposed tabs for three nozzle diameters. The test configurations are nozzle alone, nozzle and two tabs, nozzle and ejector, and nozzle with both tabs and ejector.

Ahuja, K. K. and W. H. Brown (1989). Shear flow control by mechanical tabs. 2nd AIAA Shear Flow Conference. Tempe, AZ.

This paper discusses results of an experimental study on jet-mixing enhancement of heated and unheataed, subsonic and underexpanded supersonic model jets by mechanical protuberances (tabs) located at the nozzle lip. It is shown that considerable mixing enhancement is obtained by these devices. Relative performance of two, three, and four tabs is also evaluated. It is found that the best overall effect is produced by two tabs located diametrically opposite to each other. Limited temperature measurements indicate considerable reduction in the plume temperature. Likewise, it is found that the screech noise associated with supersonic underexpanded jets can be reduced and in many cases completely eliminated.

AIAA (1999). Assessment of Experimental Uncertainty with Application to Wind Tunnel

Testing, AIAA.
The standard provides methodology for assessment of experimental uncertainty and a technique for evaluating wind tunnel error sources. The methodology is applied to a couple of sample cases. The document is a revision of the original which was based on a report of the NATO Advisory Group on Aerospace Research and Development (AGARD).

Amitay, M. and A. Glezer (1999). Aerodynamic Flow Control of a Thick Airfoil Using Synthetic Jet Actuators. 3rd ASME/JSME Joint Fluids Engineering Conference. San Francisco, CA, ASME.
The manipulation of global aerodynamic forces on bluff bodies using surface fluidic actuators based on synthetic jets technology is demonstrated in wind tunnel experiments using an unconventional thick airfoil. Synthetic jets are zero-mass-flux in nature and are synthesized from the working fluid in the flow system in which they are embedded. The interaction of the jets with a cross flow results in an apparent modification of the surface shape and is exploited for dynamic control of flow reattachment and separation over a thick airfoil. Without control, the airfoil stalls at $\alpha = 5°$. With control, fully attached flow can be achieved up to $\alpha = 17.5°$ and partial reattachment and recovery of lift can be achieved up to the maximum angle tested, $\alpha = 25°$. Both the location and the strength of the control input affect the extent of the reattached flow. Dramatic increase in lift and decrease in pressure drag are observed as a result of flow reattachment.

Amitay, M., A. Honohan, et al. (1997). Modification of the aerodynamic characteristics of bluff bodies using fluidic actuators. 28th AIAA Fluid Dynamics Conference. Snowmass Village, CO, AIAA.
The apparent aerodynamic shape (and thus lift and drag) of a 2D cylinder is modified in wind tunnel experiments using a spanwise pair of fluidic actuators based on synthetic jet technology. Because the jet actuators do not dispense new fluid into the flow (but allow for momentum transfer), their interaction with an embedding flow leads to the formation of closed recirculation regions and thus to an apparent modification of the flow boundary on scales that are one to two orders of magnitude larger than the characteristic length scale of the jets themselves. The cylinder can be rotated about its centerline so that the angle between the actuator jets and the direction of the free stream can be continuously varied. Smoke visualization experiments at low Reynolds numbers (4000) demonstrate that the closed recirculating flow regimes near the surface scale with the momentum coefficient and can displace local streamlines well outside the surface boundary layer. Azimuthal distributions of surface pressure measured at higher Reynolds numbers (75500) over a range of jet angles demonstrate that the jets effect a substantial concomitant increase in lift (up to $C_L = 0.55$) and a reduction in drag (up to 30 percent).

Amitay, M., V. Kibens, et al. (1999). The dynamics of flow reattachment over a thick airfoil controlled by synthetic jet actuators. AIAA, Aerospace Sciences Meeting and Exhibit, 37th. Reno, NV.

The manipulation of global aerodynamic forces on bluff bodies using surface fluidic actuators based on synthetic jets technology is demonstrated in wind tunnel experiments using an unconventional thick airfoil. Synthetic jets are zero-mass-flux in nature and are synthesized from the working fluid in the flow system in which they are embedded. The interaction of the jets with a cross flow results in an apparent modification of the surface shape and is exploited for dynamic control of flow reattachment and separation over a thick airfoil. Without control, the airfoil stalls at alpha = 5 deg. With control, fully attached flow can be achieved up to alpha = 17.5 deg and partial reattachment and recovery of lift can be achieved up to the maximum angle tested, alpha = 25 deg. Both the location and the strength of the control input affect the extent of the reattached flow. Dramatic increase in lift and decrease in pressure drag are observed as a result of flow reattachment.

Amitay, M., B. L. Smith, et al. (1998). Aerodynamic flow control using synthetic jet technology. 36th Aerospace Sciences Meeting & Exhibit. Reno, NV, AIAA.

The manipulation of global aerodynamic forces on bluff bodies using surface fluidic actuators based on synthetic jets technology is demonstrated in wind tunnel experiments using a 2D cylinder model. Because synthetic jets are zero-mass-flux and are synthesized from the working fluid in the flow system in which they are embedded, their interaction with a cross flow results in the formation of closed recirculation regions and in an apparent modification of the surface shape (and thus of surface pressure) with important consequences to flow separation. In the present experiments, the cylinder is instrumented with a pair of spanwise jet actuators and can be rotated about its centerline so that the angle between the jets and the direction of the free stream can be continuously varied. Azimuthal distributions of surface pressure measurements at Re_D up to 131,000 over a range of jet angles demonstrate that the jets effect a substantial increase in lift and a reduction in drag. Velocity measurements in the near wake show that as a result of the actuation, the cross stream extent of the wake, its velocity deficit, and all turbulent quantities are reduced. The response of the lift force and of the wake flow to a transient change in the control input are also investigated using pulsed amplitude modulation.

Behrouzi, P. and J. J. McGuirk (2004). Jet Mixing Enhancement Using Fluid Tabs. 2nd AIAA Flow Control Conference. Portland, Oregon, AIAA.

Techniques for increasing the rate of jet mixing in axisymmetric nozzle flows have been studied in the present work both experimentally and computationally. Near-field jet development from a “clean” axisymmetric nozzle is used as a datum against which to judge mixing effectiveness. A combination of water tunnel and high-speed airflow facilities are used to assess the near-field jet behavior experimentally. Classical solid tabs and “fluid” tabs (i.e. discrete radially discharging jets at nozzle exit) are examined. Both measurements and CFD calculations demonstrate that fluid tabs reproduce the same streamwise vortex formation process as solid tabs. For a tab jet flow rate of around 1% of the core nozzle flow, similar potential core length reductions and increased centre-line

velocity decay rates are observed in the near field. Since fluid tabs can be switched off when not needed, hence avoiding associated drag/thrust loss penalties, this technology is a promising technique worthy of further development.

Behrouzi, P. and J. J. McGuirk (2006). "Effect of tab parameters on near-field jet plume development." Journal of Propulsion and Power **22**(3): 576-85.

A full understanding of jet mixing behavior is essential in the aircraft design process, particularly when propulsion system integration issues are considered (for example, jet afterbody interactions, jet plume characterization, and jet noise reduction). The present work is motivated by an interest in unconventional jet exhaust nozzle design, specifically tabbed nozzles. The near-field mixing performance arising from a simple axisymmetric jet shear layer and three-dimensional perturbed jet shear layers created via a range of solid tab designs introduced at the nozzle exit plane has been studied under subsonic and supersonic operating conditions: the effects of velocity ratio, tab shape, tab number, and tab orientation angle are investigated. Flow visualization of the tab effects is accomplished via laser-induced fluorescence in low-speed flow and schlieren imaging under supersonic conditions. The mean and rms axial velocity as well as pitot pressure and total temperature profiles have been measured along the jet center-line and on orthogonal cruciform radial traverse lines downstream of the nozzle exit. The performance of the solid tab in causing bifurcation of the jet was found to follow the same trend under both subsonic and supersonic conditions, indicating that the dominant features of the streamwise vorticity introduced by the tabs are essentially independent of the Mach number. The experimental results revealed that the decay of the jet core velocity was only weakly dependent on velocity ratio (over the range studied here), tab orientation angle, and tab shape. The mixing of the jet was, however, a strong function of the tab projected area, tab width, and tab number. The optimum tab number was found to be 2

Behrouzi, P. and J. J. McGuirk (2006). Flow control of jet mixing using a pulsed fluid tab nozzle, San Francisco, CA, United States, American Institute of Aeronautics and Astronautics Inc., Reston, VA 20191, United States.

Flow control techniques for increasing the rate of jet mixing in axisymmetric nozzle flows have been investigated experimentally. The near-field jet development of a clean axisymmetric nozzle is used as a datum to judge increased mixing effectiveness. A combination of water tunnel and high-speed airflow facilities are used to assess the near-field jet behavior. Classical solid tab, fluid tab (i.e. discrete radially discharging control jets located close to the core jet nozzle exit), and pulsed fluid tab nozzles are compared. The effect of the fluid tab flow rate, pulse rate and pulse phase are studied. The measurements indicate that nozzles equipped with fluid tabs and pulsed fluid tabs generate a similar streamwise vortex formation process (and hence display increased mixing) as occurs in a solid-tabbed nozzle. The performance of pulsed fluid tabs is strongly influenced by the tab flow rate, pulse frequency and phase. In low speed tests the

mixing effectiveness with a pair of pulsed fluid tabs working 180 deg; out of phase was as good as a twin solid tab nozzle for a total control jet flow rate of only 0.5% of the core jet flow. In high speed testing similar benefits of fluid tab control jets over solid tab designs were observed, although evidence was obtained that the interaction mechanisms between the streamwise vortices which produce the increased mixing across the core jet shear layer may be subtly different under low speed and compressible conditions. Further study of pulsed fluid tabs is recommended, since they have attractive performance benefits over other rapid jet mixing control mechanisms (can be easily switched off when not needed), and offer attractive flexibility as the basis for an optimum active control mixing device.

Berkooz, G., P. Holmes, et al. (1993). "Proper orthogonal, decomposition in the analysis of turbulent flows." Annual Review of Fluid Mechanics **25**: 537.

Despite the fact the the governing laws are known, turbulent flows are still not understood. This is because the Navier Stokes equations are non-linear and all evidence indicates that turbulence involves the action of many degrees of freedom on spatial and temporal scales. Thus, to model turbulence with high accuracy would require an enormous number of dimensions. If one is willing to sacrifice some accuracy by reducing the number of degrees of freedom down to only those that are "most essential", one can model the essential characteristics of a turbulent flow. The first evidence that such a reduction in complexity might be possible for fully developed turbulent flows came with the discovery of coherent structures. The proper orthogonal decomposition provides a rational method for extracting these essential features. The POD is a procedure for extracting a basis for a modal decomposition from an ensemble of signals. It was introduced in the context of turbulence by Lumley in 1967. In other disciplines, POD is known as Karhunen-Loeve decomposition and Principle Components Analysis. POD is a linear procedure which results in certain limitations.

Berrebi, J., P. E. Martinsson, et al. (2004). "Ultrasonic flow metering errors due to pulsating flow." Flow Measurement and Instrumentation **15**(3): 179-85.

Transit-time ultrasonic flow meters present some advantages over other flow meters for district heating industries. They are both accurate and non-intrusive. It is well-known that ultrasonic flow meters are sensitive to installation effects. Installation effects could be static or dynamic. Among the possible dynamic installation effects is pulsating flow. The influence of pulsating flow on the prediction and the zero-crossing operations is investigated. Expressions are found for the prediction error and the zero-crossing error. The relative errors due to the prediction and the zero-crossing are plotted. The prediction error can reach dramatic values while the zero-crossing operation is hardly influenced by flow pulsations

Berrebi, J., J. van Deventer, et al. (2004). "Reducing the flow measurement error caused by pulsations in flows." Flow Measurement and Instrumentation **15**(5-6): 311-315.

Different types of errors are generated by pulsations in flows. Among these errors

is the sampling error due to a unadapted time-averaging of the flow rate. An improved model for pulsations in flows including harmonics is derived. The localization of the harmonics is performed by a detector. The period of the pulsations is estimated. It is then possible to reduce the sampling error by performing a correct averaging. The reduction of the sampling error is confirmed by simulations.

Bignell, N. (2000). "Using small sonic nozzles as secondary flow standards." Flow Measurement and Instrumentation **11**(4): 329-337.

When using sonic nozzles as secondary laboratory standards they must be calibrated. Standard methods of calculating discharge coefficient values are not useful with small nozzles of uncertain geometries. Calibration against primary standards is discussed. Alternatively, one nozzle can be directly compared with another by several techniques using ratios of pressure and temperature and sometimes flow. Several factors change the nozzle coefficient. Estimates of the changes due to pressure and humidity are given. Adiabatic cooling produces temperature changes that affect the nozzle coefficient by changing the throat area. Depending on the nozzle holder the inlet gas can also be cooled with an effect on the flow. Nozzles may be made by metal machining or by shrinking glass tubes. Sapphire cutting heads, which may be bought, can be used as sonic nozzles. An example of a promising but unsuitable form of nozzle having a square throat is given. The pressure dependence of these is discussed. The use of nozzles in arrays, for automatic operation as flow standards, is described.

Bignell, N. and Y. M. Choi (2002). "Thermal effects in small sonic nozzles." Flow Measurement and Instrumentation **13**(1-2): 17-22.

A study has been made of the effect of temperature on the coefficient used to characterise small sonic nozzles. Due to adiabatic cooling of the gas stream to -30 deg C in the throat, the body of the nozzle is also cooled. The temperature drop of several bodies during operation was measured. Using a gas flow standard that can operate in continuous mode, measurements were made of the change of the nozzle coefficient with temperature. The real gas correction factor, the discharge coefficient and the area of the throat are investigated to explain the observed change in the nozzle coefficient. Changes in these quantities are inadequate to explain the results. The maximum percentage changes likely to be experienced are estimated for a range of nozzle throat diameters

Bonnet, J. P., D. R. Cole, et al. (1994). "Stochastic estimation and proper orthogonal decomposition: complementary techniques for identifying structure." Experiments in Fluids **17**(5): 307-14.

The Proper Orthogonal Decomposition (POD) as introduced by Lumley (1967) and the Linear Stochastic Estimation (LSE) as introduced by Adrian (1975) are used to identify structure in the axisymmetric jet shear layer and the 2-D mixing layer. In this paper we will briefly discuss the application of each method, then focus on a novel technique which employs the strengths of each. This complementary technique consists of projecting the estimated velocity field

obtained from application of LSE onto the POD eigenfunctions to obtain estimated random coefficients. These estimated random coefficients are then used in conjunction with the POD eigenfunctions to reconstruct the estimated random velocity field. A qualitative comparison between the first POD mode representation of the estimated random velocity field and that obtained utilizing the original measured field indicates that the two are remarkably similar, in both flows. In order to quantitatively assess the technique, the root mean square (RMS) velocities are computed from the estimated and original velocity fields and comparisons made. In both flows the RMS velocities captured using the first POD mode of the estimated field are very close to those obtained from the first POD mode of the unestimated original fields

Brereton, G. J., W. C. Reynolds, et al. (1990). "Response of a turbulent boundary layer to sinusoidal free-stream unsteadiness." Journal of Fluid Mechanics **221**: 131-59.

Selected findings of a detailed experimental investigation are reported concerning the effects of forced free-stream unsteadiness on a turbulent boundary layer. The forced unsteadiness was sinusoidal and was superimposed locally on an otherwise-steady mainstream, beyond a turbulent boundary layer which had developed under constant-pressure conditions. Within the region over which free-stream unsteadiness was induced, the sinusoidal variation in pressure gradient was between extremes of zero and a positive value, with a positive average level. The local response of the boundary layer to these free-stream effects was studied through simultaneous measurements of the u- and v-components of the velocity field. Results are reported which allow comparison of the behavior of boundary layers under the same mean external conditions, but with different time dependence in their free-stream velocities. These time dependences correspond to: (i) steady flow, (ii) quasi-steadily varying flow, and (iii) unsteady flow at different frequencies of mainstream unsteadiness

Browand, F. K. and J. Laufer (1975). The role of large scale structures in the initial development of circular jets. Turbulence in liquids; Proceedings of the Fourth Biennial Symposium, Rolla, Mo., Science Press.

Experimental results are presented describing the flow field surrounding the potential core of a circular water jet in the Reynolds number region between 5000 and 15,000. This field is divided into three regions: (1) the shear layer instability zone; (2) the vortex interaction region; and (3) the zone of higher order instability mode and turbulence generation. It is shown that the origin of the large scale structures just downstream of the potential cone can be traced to the upstream vortices, but their statistical behavior (passage frequency, spatial coherence) seems to be independent of the initial shear layer instability.

Brown, G. B. (1932). "On Sensitive flames." Philosophical Magazine **13**: 161-195.

Description of tests of sensitive flames including six forms of high pressure jets and three low pressure jets. These were investigated as to the effect of frequency on their sensitivity, and the variation of the response with the amplitude of the sound. Experiments were also made on air jets containing smoke. For jet

diameters between 0.5 mm. and 0.5 cm. all streams show some sensitivity to sound. The position and construction of the tube supplying gas to the jet affect the sensitivity in so far as they influence the mode of outflow through the orifice. The frequencies producing maximum and minimum disturbance respectively are definite for a given gas, and do not vary with the kind of jet used. The range of frequency varies with the gas and the jet. With air it lies between 80 and 900, with unlit gas somewhat higher, and with ignited coal gas or hydrogen from 500 to 18,000.

Brown, G. L. and A. Roshko (1974). "On density effects and large structure in turbulent mixing layers." Journal of Fluid Mechanics **64**(pt.4): 775.

Plane turbulent mixing between two streams of different gases (especially nitrogen and helium) was studied in a novel apparatus. Spark shadow pictures showed that, for all ratios of densities in the two streams, the mixing layer is dominated by large coherent structures. High-speed movies showed that these convect at nearly constant speed, and increase their size and spacing discontinuously by amalgamation with neighboring ones. The pictures and measurements of density fluctuations suggest that turbulent mixing and entrainment is a process of entanglement on the scale of the large structures; some statistical properties of the latter are used to obtain an estimate of entrainment rates. Large changes of the density ratio across the mixing layer were found to have a relatively small effect on the spreading angle; it is concluded that the strong effects, which are observed when one stream is supersonic, are due to compressibility effects, not density effects, as has been generally supposed

Brown, W. H. and K. K. Ahuja (1989). Shear flow control of cold and heated rectangular jets by mechanical tabs. Volume 1: Results and discussion. Marietta, GA, Lockheed Aeronautical Systems Co.

The effects of mechanical protrusions on the jet mixing characteristics of rectangular nozzles for heated and unheated subsonic and supersonic jet plumes were studied. The characteristics of a rectangular nozzle of aspect ratio 4 without the mechanical protrusions were first investigated. Intrusive probes were used to make the flow measurements. Possible errors introduced by intrusive probes in making shear flow measurements were also examined. Several scaled sizes of mechanical tabs were then tested, configured around the perimeter of the rectangular jet. Both the number and the location of the tabs were varied. From this, the best configuration was selected. The conclusions derived were: (1) intrusive probes can produce significant errors in the measurements of the velocity of jets if they are large in diameter and penetrate beyond the jet center; (2) rectangular jets without tabs, compared to circular jets of the same exit area, provide faster jet mixing; and (3) further mixing enhancement is possible by using mechanical tabs.

Brown, W. H. and K. K. Ahuja (1989). Shear flow control of cold and heated rectangular jets by mechanical tabs. Volume 2: Tabulated data. Marietta, GA, Lockheed Aeronautical Systems Co.

The effects of mechanical protrusions on the jet mixing characteristics of rectangular nozzles for heated and unheated subsonic and supersonic jet plumes were studied. The characteristics of a rectangular nozzle of aspect ratio 4 without the mechanical protrusions were first investigated. Intrusive probes were used to make the flow measurements. Possible errors introduced by intrusive probes in making shear flow measurements were also examined. Several scaled sizes of mechanical tabs were then tested, configured around the perimeter of the rectangular jet. Both the number and the location of the tabs were varied. From this, the best configuration was selected. This volume contains tabulated data for each of the data runs cited in Volume 1. Baseline characteristics, mixing modifications (subsonic and supersonic, heated and unheated) and miscellaneous charts are included.

Bruun, H. H. (1995). Hot-wire anemometry : principles and signal analysis. Oxford ; New York, Oxford University Press.

A comprehensive book which provides a state-of-the-art survey on developments and use of HWA. A number of topics are covered including the response equations used for HWA signal interpretation and methods for data acquisition, processing, and presentation.

Caraballo, E., M. Samimy, et al. (2003). Low dimensional modeling of flow for closed-loop flow control. 41st Aerospace Sciences Meeting and Exhibit. Reno, NV, AIAA.

The focus of this work is on the use of detailed numerical simulation data to develop low dimensional models of a flow that can be used for the design of a control law for a feedback control-loop system. The subsonic flow over a shallow cavity was selected as the test bed. This research is an integral part of the closed-loop flow control group at the Collaborative Center of Control Science at The Ohio State University. Numerical simulations were carried out using different modeling options, and the preliminary results were compared with the experimental data. The simulation results showed that a quasi-3-D simulation, which solves the full 3-D Navier-Stokes equations but neglects the effects of the sidewalls, is a good compromise between providing sufficiently accurate data of the flow and quick turn around. The Proper Orthogonal Decomposition (POD) and Galerkin projection were used to obtain the spatial basis and the time evolution coefficient required for the low dimensional model. The results for the baseline case showed that four POD modes, using either a scalar or vector approach to determine norms, contain 96 percent of the energy and capture the essential dynamics of the flow. However, the system of ordinary differential equations for deriving the time coefficients for the reduced order model requires at least eight modes with the vector approach, but does not converge with the scalar approach.

Caraballo, E., M. Samimy, et al. (2001). Application of proper orthogonal decomposition to a high speed axisymmetric jet. 31st AIAA Fluid Dynamics Conference. Anaheim, CA, AIAA.

The work presented here is motivated by an ongoing research program on the use

of the Proper Orthogonal Decomposition (POD) method in conjunction with advanced optical measurements in high-speed flows. This paper presents results from the use of the snapshot POD method via its application to a spatio-temporal flow field generated from large eddy simulations (LES) of a high-speed jet. The LES data were obtained for an ideally expanded Mach 1.4 axisymmetric jet, for which flow fields from various cross sections of the jet were considered. Studies of the requirements of data set size for obtaining statistically converged POD eigenmodes were performed. Investigation of methods to obtain eigenmodes revealed that time uncorrelated planar data (e.g., from the use of optical techniques such as planar Doppler velocimetry) could be used for computing eigenmodes. The use of a few modes (namely, 12) was capable of producing a reasonable reconstruction of the spatio-temporal flow field. The POD modes and their temporal coefficients obtained at various streamwise locations suggest that the large-scale jet structures undergo a process of disorganization near the end of the potential core followed by reorganization farther downstream.

Carpinlioglu, M. O. and M. Y. Gundogdu (2001). "A critical review on pulsatile pipe flow studies directing towards future research topics." Flow Measurement and Instrumentation **12**(3): 163-74.

In spite of efforts concentrated since the early 1970s, the theory of pulsatile pipe flows supported by experimental investigations has not been completed yet, in comparison with the well-defined theory of steady pipe flows. Therefore it seems that there is much to be done in terms of experimental work in this flow field by the scientists of the 21st century. The study herein aims to present the state of art based on a critical and commentary analysis of an extended review on the manner covering the time period 1928-2000 to specify what is known together with the existing discrepancies, and what is unknown thereby offering fertile ground for further research particularly with flow measurements. Furthermore the information presented, related to the basics of pulsatile flow, presumably also helps the audience in flow measurement somehow due to the influence and therefore importance of flow pulsation itself on the sensitivity and accuracy of flow meters of any kind. The method of presentation is such that paying attention to the historical background, common terminology and basic equations describing the pulsatile flow field in all regimes are introduced to overcome the difficulty of handling a great variety of terms and even approaches in the available literature. Since laminar and transitional flows are considered as very different from a turbulent one, due to the nature of turbulent flow itself, the characteristics of laminar and transitional flow regimes are discussed later under suitable subject headings considering slightly compressible Newtonian fluid as the flow medium. Research topics which need further measurements are outlined, together with the experimental ranges of dominant flow parameters to aid those who intend to search in the field

Carpinlioglu, M. O. and M. Y. Gundogdu (2001). "Presentation of a test system in terms of generated pulsatile flow characteristics." Flow Measurement and Instrumentation **12**(3): 181-190.

A complete test system associative with the measurement and data acquisition components was designed and constructed for an experimental investigation on pulsatile pipe flows. The basics of the test system and conducted experiments directed towards the determination of pulsatile flow characteristics at the measurement site in passage from laminar to turbulent regime are presented in this paper. Pulsatile flow was produced by superimposing a purely sinusoidal oscillation on steady axial flow in a rigid circular cross-sectional pipe. The flow nature at the measurement site was determined via cross-sectional velocity and wall pressure gradient measurements in the range of time-averaged Reynolds number; 1800 < Re < 60,000. The covered ranges for the dominant oscillation parameters; dimensionless frequency parameter root ω prime and the oscillation velocity amplitude ratio; A_1 were 5 < sqrt(ω') < 28 and 0.0035 < A_1< 0.7113 respectively. The so-called flow reversal observed for the cases with sqrt(ω') = 7 and sqrt(ω') = 12.5 was represented in terms of correlations between Re>, oscillating Reynolds number; Re_{os} and A_1 to describe the flow behavior in the critical stage prior to the flow reversal.

Chen, Y., S. Liang, et al. (1999). Enhanced Mixing in a Simulated Combustor Using Synthetic Jet Actuators. 37th AIAA Aerospace Sciences Meeting and Exhibit. Reno, NV, AIAA.

Mixing in a turbine engine combustor significantly influences fuel efficiency, performance and lifetime of the engine, and pollutant emissions such as NO_X. Thus, various passive and active control techniques have been used to control and improve mixing processes in the combustor. The present paper demonstrates the use of a novel active control technology, synthetic jets, to enhance mixing in a facility simulating the dilution zone in a typical gas turbine combustor. Synthetic jets are jets synthesized from the surrounding fluid using zero-mass-flux actuators. They can improve momentum transfer without requiring the introduction of additional fluid. Dilution zone conditions were simulated by using two streams of hot and cold temperatures. Mixing between the streams was determined by measuring temperature distributions downstream of synthetic jets. This could be enhanced to differing degrees by varying the degree of actuation, i.e. mean velocity, of synthetic jets. However, there appears an upper limit in the actuation of synthetic jets beyond which the improvement in mixing is marginal. Velocity measurements suggest that the wake structure from the bluff body formed by interactions between synthetic jets and crossflow is responsible for improved mixing. Thus, the present investigation shows that synthetic jet technology may be ideal for improving dilution zone mixing in a turbine engine combustor without using additional cold dilution air.

Chenault, C. F., J. D. III, et al. (2000). Active core exhaust (ACE) control for reduction of thermal loading. Fluids 2000 Conference and Exhibit. Denver, CO.

Pulsed jet blowing for mixing enhancement in a hot jet is examined using numerical simulation. Numerical simulations have been completed for a sub-scale turbojet engine, a full scale ground demonstration case, and a High-Bypass Ratio Engine (HBRE). These simulations have shown that pulsed jet blowing can

significantly reduce jet plume potential core lengths at static and forward flight conditions. The numerical scheme utilizes large timestep implicit integration for efficiency, and a second order physical space algorithm for robustness. The pulsed jet disturbance is calculated directly and a turbulence model is employed to represent the cascade to smaller length scales. Experimental data corresponding to the numerical simulations are also presented and indicate similar benefits from pulsed jet mixing.

Christiansen, T. and P. Bradshaw (1981). "Effect of Turbulence on Pressure Probes." Journal of Physics E: Scientific Instruments **14**: 992-997.

The effect of turbulence on static pressure probes of different designs is examined. The conclusion is that when using any device in an intensely turbulent flow where the reading varies nonlinearly with yaw angle, great care should be taken. The authors recommend that the disc static probe and yaw meters not be used in such flows. Standard pitot probes can be used, but the error will increase with increasing turbulence intensity.

Citriniti, J. (1997). "Azimuthal mode interaction in an unforced, high Reynolds-number axisymmetric shear layer."

The dynamics of large scale azimuthally coherent structures obtained in a high Reynolds-number axisymmetric mixing layer are presented. The structure dynamics is obtained by application of the Proper Orthogonal Decomposition (POD) to an ensemble of realizations of the streamwise velocity field obtained at 138 simultaneous positions, 3 diameters downstream of the nozzle exit. The velocity field is measured at all 138 positions simultaneously, making it possible to obtain the instantaneous coefficients of the POD modes as well as extract the large scale structure. Pictures showing the dynamics of the structure interaction in the mixing layer demonstrate the importance of the mode 0, 3, 4, 5 and 6 azimuthal structures in both the entrainment and advection of fluid in the layer. The azimuthal structure does not appear to be a single structure but rather is made up of pairs of counter rotating streamwise vortices and are very similar to the ribs seen in simulations of the axisymmetric layer and in plane mixing layers. It is hypothesized that recent success in mixing enhancement by multiple-mode excitation is due to the increased energy placed in these modes.

Cohen, J. and I. Wygnanski (1987). "The evolution of instabilities in the axisymmetric jet. I. The linear growth of disturbances near the nozzle." Journal of Fluid Mechanics **176**: 191-219.

The modal distributions of coherent structures evolving near the nozzle of a circular jet are considered. The effects produced on the instability modes by transverse curvature, flow divergence, inhomogeneous inflow conditions, and the detailed shape of the mean velocity profile, are investigated both theoretically and experimentally. Linear stability analysis applied to a thin shear layer surrounding a large-diameter jet (i.e. a jet whose diameter is large in comparison with a typical width of the shear layer) indicates that many azimuthal modes are equally unstable. An increase in the relative thickness of the shear layer limits the number

of unstable modes, and only one helical mode remains unstable at the end of the potential core. The linear model used as a transfer function is capable of predicting the spectral distribution of the velocity perturbations in a jet. This provides a rational explanation for the stepwise behavior of the predominant frequency resulting from a continuous increase in the jet velocity

Cohen, J. and I. Wygnanski (1987). "The evolution of instabilities in the axisymmetric jet. II. The flow resulting from the interaction between two waves." Journal of Fluid Mechanics **176**: 221-35.

For part I see ibid., vol.176, p.191 (1987). Leading nonlinear interactions generated by waves externally superimposed on an axisymmetric jet are considered theoretically, and the results verified experimentally. The mean flow in the jet loses its axial symmetry whenever the jet is excited simultaneously by two different azimuthal modes of the same frequency. Subharmonic resonance occurs in this flow whenever the conditions warrant such an occurrence, generating azimuthal modes which may not have been present otherwise in this flow. Some of these resonance conditions are explored

Crow, S. C. and F. H. Champagne (1971). "Orderly structure in jet turbulence." Journal of Fluid Mechanics **48**(pt.3): 547-91.

Past evidence suggests that a large-scale orderly pattern may exist in the noise producing region of a jet. Using several methods to visualize the flow of round subsonic jets, the authors watched the evolution of orderly flow with advancing Reynolds number. As the Reynolds number increases from order 10^2 to 10^3, the instability of the jet evolves from a sinusoid to a helix, and finally to a train of axisymmetric waves. At a Reynolds number of around 10^4, the boundary layer of the jet is thin and two kinds of axisymmetric structure can be discerned: surface ripples on the jet column, thoroughly studied by previous workers, and a more tenuous train of large-scale vortex puffs. The surface ripples scale on the boundary-layer thickness and shorten as the Reynolds number increases toward 10^5. The structure of the puffs, by contrast, remains much the same: they form at an average Strouhal number of about 0.3 based on frequency, exit speed and diameter

Cruz-Maya, J. A., F. Snchez-Silva, et al. (2006). "A new correlation to determine the discharge coefficient of a critical Venturi nozzle with turbulent boundary layer." Flow Measurement and Instrumentation **17**(5): 258-66.

A toroidal Venturi nozzle, operating mainly at critical conditions and shaped according to the recommendation of the ISO Standard 9300, was selected for the present study. The focus of this paper is to provide a new theoretical and numerical correlation for the calculus of the discharge coefficient on turbulent boundary layer conditions for gases at Pr=0.7. This study was performed to investigate the effects of the viscous stresses in the boundary layer, dimensionless wall temperature in the throat nozzle, and the flow field curvature at the nucleus of the nozzle on the discharge coefficient. The determination of this coefficient was based on the turbulent boundary layer theory and a numerical simulation for a

two-dimensional flow. The numerical simulation of the flow was carried out by means of the commercial CFD code. The correlation obtained was validated by means of a direct comparison between the experimental correlations of the discharge coefficient of ISO-9300 and the correlations obtained by the Korea Research Institute of Standards and Science (KRISS) with turbulent boundary layer. This validation was performed for throat Reynolds numbers from 1.4 to $2.6x10^6$. The agreement of the theoretical and measured discharge coefficients by these correlations was better than 0.2%.

Dahm, W. J. A. and P. E. Dimotakis (1985). Measurements of Entrainment and Mixing in Turbulent Jets, Reno, NV, USA, AIAA, New York, NY, USA.

An experimental investigation of entrainment and mixing in the self-similar far field of an axisymmetric free turbulent jet in water is presented. Length and time scales for the flame length fluctuations of reacting jets are shown to be approximately equal to the local characteristic large scale length and time of the flow. It is also shown that instantaneous radial profiles of concentration across the jet do not resemble the mean concentration profile, indicating that the mean profile is a poor representation of the mixed fluid states within the jet.

Davis, M. R. (1982). "Variable Control of Jet Decay." **20**(5): 606.

The influence of blowing radially inward with a pair of control jets toward the centerline of and close to the exit from a circular main nozzle is investigated. Two regimes of control-jet influence exist, corresponding to conditions where the control jets are swept away in the turbulent mixing layer of the main jet or where they penetrate the central smooth-core flow. In the first regime, local velocity reductions in the main jet of up to 30% can be achieved with control-jet mass flows of 0.5% of that in the main-jet nozzle without severely distorting the main jet from its circular cross section. In the second regime, the main jet is strongly distorted from a circular cross section and local velocities in the main jet are less sensitive to control-jet velocity. The main-nozzle mass flow is influenced significantly in the second regime only when the control jets are very close to the main-nozzle lip.

Davis, S. A. and A. Glezer (2000). The Manipulation of Large- and Small-Scales in Coaxial Jets using Synthetic Jet Actuators. 38th AIAA Aerospace Sciences Meeting and Exhibit, Reno, NV, AIAA.

The modification and control of large- and small-scale motions and mixing processes in the shear layers of coaxial round jets are investigated using an azimuthal array of co-flowing synthetic jet actuators placed around the edge and in the exit plane of the outer primary jet. The effect of flow manipulation on the structure of the merging coaxial primary jets is investigated using two component hot-wire anemometry, and the mixing of a passive scalar is studied using planar laser-induced fluorescence (PLIF) of acetone-seeded in the annular flow. Both the velocity field of the primary jet and mixing processes are studied at three velocity ratios (inner to outer flow) Ui/U = 0.35, 0.65, and 1.4. High frequency forcing leads to increases in the radial extent of the jet and turbulent intensity in the near-

field ($x/D_o < 1$), vortical structures within the inner shear layer, and increased turbulent dissipation downstream. Amplitude modulation of the excitation waveform (f_m = 60 Hz) results in the formation of large-scale vortical structures and significant mixing enhancement.

Davitian, J., S. Megerian, et al. (2006). Control of Transverse Jet Shear Layer Instabilities. 42nd AIAA/ASME/SAE/ASEE Joint Propulsion Conference & Exhibit. Los Angeles, CA, AIAA.

This paper describes experimental results pertaining to the nature and control of shear layer instabilities associated with the single jet in crossflow or transverse jet, a flowfield widely used in propulsive devices. These studies suggest that the character of the jet's nearfield shear layer instability can be significantly different for the transverse jet as compared with the free jet. For transverse jets, the instabilities can be initiated much closer to the jet orifice, for either flush or elevated jet injection, and are much stronger, with earlier development of subharmonic and higher harmonic modes. For the case of flush injection, the nature of the transverse jet instability also differs significantly for lower values of the jet-to-crossflow velocity ratio R (below 3.5) as compared to jets at higher R; in the case of flush injection, there is a rapid initiation of strong, distinct modes that are not affected by external sinusoidal forcing. No such behavior at low R values is observed for the elevated jet. These findings help to explain differences observed in strongly forced transverse jet behavior and suggest strategies for the application of jet forcing in the control of its mixing and penetration.

Demayo, T. N., M. Y. Leong, et al. (2003). "Assessing jet-induced spatial mixing in a rich, reacting crossflow." Journal of Propulsion and Power **19**(1): 14-21.

In many advanced low NO_x gas turbine combustion techniques, such as rich-burn-quick-mix, lean-burn (RQL), jet mixing in a reacting, hot, fuel-rich crossflow plays an important role in minimizing all pollutant emissions and maximizing combustion efficiency. Assessing the degree of mixing and predicting jet penetration is critical to the optimization of the jet injection design strategy. Different passive scalar quantities, including carbon, oxygen, and helium, are compared to quantify mixing in an atmospheric RQL combustion rig under reacting conditions. The results show that the O_2 based jet mixture fraction underpredicts the C-based mixture fraction due to jet dilution and combustion, whereas the He tracer overpredicts it possibly due to differences in density and diffusivity. The He method also exhibits significant scatter in the mixture fraction data that can most likely be attributed to differences in gas density and turbulent diffusivity. The jet mixture fraction data were used to evaluate planar spatial unmixedness, which showed good agreement for all three scalars. This investigation suggests that, with further technique refinement, either O_2 or a He tracer could be used instead of C to determine the extent of reaction and mixing in an RQL combustor.

Dimotakis, P. E. (2005). "Turbulent mixing." Annual Review of Fluid Mechanics **37**: 329-356.

The ability of turbulent flows to effectively mix entrained fluids to a molecular scale is a vital part of the dynamics of such flows, with wide-ranging consequences in nature and engineering. It is a considerable experimental, theoretical, modeling, and computational challenge to capture and represent turbulent mixing which, for high Reynolds number (Re) flows, occurs across a spectrum of scales of considerable span. This consideration alone places high-Re mixing phenomena beyond the reach of direct simulation, especially in high Schmidt number fluids, such as water, in which species diffusion scales are one and a half orders of magnitude smaller than the smallest flow scales. The discussion below attempts to provide an overview of turbulent mixing; the attendant experimental, theoretical, and computational challenges; and suggests possible future directions for progress in this important field.

Durbin, P. A. and B. A. P. Reif (2001). Statistical theory and modeling for turbulent flows. Chichester ; New York, Wiley.

The turbulence problem is not a problem of physical law. That is known (the Navier-Stokes equations). Rather, it is a problem of how to describe a turbulent flow, which is highly complex. There are two major characteristics of turbulent flows: the ability to stir a fluid (mixing) and the ability to dissipate kinetic energy. Dissipation takes place via an energy cascade. A turbulent flow has eddies on many scales. The larger eddies feed the smaller ones, and so on. The energy originally starts out as orderly motion. Small perturbations develop and grow (production and transport of turbulence). These phenomena are not well understood, and thus the term "eddy" is purposefully unclear. Turbulence phenomena can be described statistically in terms of mean quantities. Statistical modeling of turbulence attempts to solve the governing equations for average properties without calculating the random instantaneous field properties. This results in a closure problem where there are more unknowns than governing equations. Closure models provide the extra equations to solve the system, but they are not necessarily accurate. The book describes how turbulence is modeled statistically.

Eroglu, A. and R. E. Breidenthal (2001). "Structure, penetration, and mixing of pulsed jets in crossflow." AIAA Journal **39**(3): 417-423.

Effects of periodic disturbances on the structure and mixing of a transverse jet have been investigated through chemically reactive laser-induced fluorescence experiments in a water model. Flow visualization experiments with a steady round jet in crossflow revealed a distinct vortex loop merging pattern among the vortices that make up the curved shear layer around the jet. As the vortex loops are stretched and distorted, certain parts of the neighboring loops with the opposite or the same sign of vorticity merge, resulting in cancellation or intensification of the vorticity in the corresponding regions of the jet. When the flow rate of this jet was periodically modulated by a square wave, however, distinct vortex rings were created whose spacing and strength were dictated by the pulsing frequency for a given jet and crossflow combination. At low pulsing rates, these rings penetrated into the crossflow significantly deeper than the steady jet. An optimum pulsing

frequency was found at which closely spaced vortex rings were observed, which penetrated as discrete vortices into the crossflow in the near field. Strong interactions among neighboring rings were observed farther downstream. Experiments with high Reynolds number jets revealed up to a 70% increase in jet penetration, whereas the flame length of the jet was reduced by 50% at this optimum pulsing frequency.

Faivre, V. and T. Poinsot (2002). Experimental and numerical investigations of jet control for combustion applications, Montreal, Que., United States, American Society of Mechanical Engineers, New York, NY 10016-5990, United States.

The purpose of the present study is to quantify experimentally the effects of forcing on the aerodynamic field in a model configuration: a non reactive jet of air. Such configurations are found in many combustion systems and constitute basic elements for many active control strategies. In the present work, jet control is achieved by adding either steady or pulsated swirl to the main jet through the actuators system. Results show that one of the strongest effects of the actuator is to enhance the mixing of the jet with the ambient fluid. This effect can be noted even if the flow rate in the actuator is low. A second aspect of research for this actuator is to use it in an unsteady regime to use smaller flow rates and minimize the control cost.

Farokhi, S., R. Taghavi, et al. (1992). "Modern developments in shear flow control with swirl." AIAA Journal **30**(6): 1482.

Excitability of a turbulent swirling round jet is explored both qualitatively and quantitatively in the subsonic regime. Plane-wave acoustic excitation as the forcing mechanism caused periodic coherent vortical structures to appear in the shear layer, very close to the nozzle lip. Spectra of the hot-wire measurements along the jet axis reveal the growth of the fundamental wave and no amplification of a subharmonic. Vortex pairing as a mechanism for jet spread in the near field is hence ruled out for turbulent swirling jets. At large forcing amplitudes, a 10% reduction of the mean centerline velocity at nine nozzle diameters, and a corresponding increase in the shear-layer momentum thickness, are measured. It is remarkable to achieve this level of mixing enhancement in a rotating jet by a axisymmetric excitation, while the jet's `preferred' mode is of helical nature corresponding to Taylor-Gortler instability waves

Fiedler, H. E. (1988). "Coherent structures in turbulent flows." Progress in Aerospace Sciences **25**(3): 231.

Coherent structures have received a lot of attention in recent decades and the hope was that an alternative to the usual statistical description of turbulence would arise. After the initial period of enthusiasm followed a period of criticism and scrutiny. The debate is over the uniqueness, the ubiquity, and the importance of coherent structures. Although a great number of turbulent flow configurations-essentially all of `classical' flows-have to some extent been investigated and scrutinized for their content of structural organization, many questions remain open and the dispute is by no means settled. This review is restricted to trying to

summarize a few of the more important results and issues without trying to settle this argument. At the same time some open questions are discussed.

Fiedler, H. E. and H. H. Fernholz (1990). "On management and control of turbulent shear flows." Progress in Aerospace Sciences **27**(4): 305.

Concepts of turbulent flow control have become of growing importance during the last few years, following increased interest in the detailed structural scenario of turbulence—in particular our improved understanding of coherent structures on the one hand (the prerequisite), and a need for improvement of technological processes on the other (the goal). These considerations have mainly been followed by engineers and physicists concerned with problems in aerodynamics. It is our aim to draw the attention of a wider group of engineers to turbulent flow control in order to speed up the transfer of knowledge from aerodynamics to applications in other fields of engineering. In this paper an attempt is made to compile a major body of the available knowledge on flow control in separated and wall bounded turbulent flows. After a brief introduction of the basics of control theory (Section 2) and of the major flow structures and their stability characteristics (Section 3) free and wall bounded turbulent shear flows are discussed (Sections 4 and 5). This discussion summarizes the main relationships between structure and flow behavior and shows possibilities of influencing properties of these flows such as increasing mixing or avoiding separation.

Fincham, A. M. and G. R. Spedding (1997). "Low cost, high resolution DPIV for measurement of turbulent fluid flow." Experiments in Fluids **23**(6): 449-62.

An optimized cross-correlation based imaging velocimetry system is described and its performance is evaluated in numerical and physical experiments. Given a discrete image array pair, the flow seeding and image processing parameters are optimized to maximize displacement accuracy, regardless of the computational cost; collectively these techniques are known as correlation imaging velocimetry (CIV). Order of magnitude improvements over standard DPIV methods can readily be obtained, allowing high resolution measurements to be made with low cost standard resolution cameras. Fundamental limits on the measurable range of length, velocity and vorticity scales are identified, and related to those encountered in homogeneous, 3D turbulence. The current restrictions apply to all imaging velocimetry measurements; some paths for future research that are likely to be profitable are identified, together with some that are not. Extensive use of CIV in this and other laboratories has allowed direct verification of these optimization principals

Freund, J. B. and P. Moin (2000). "Jet mixing enhancement by high-amplitude fluidic actuation." AIAA Journal **38**(10): 1863.

Recent experiments have shown that properly designed high-amplitude, low mass flux pulsed slot jets blowing normal to a jet's shear layer near the nozzle can significantly alter the jet's development. In contrast to commonly used low-amplitude forcing, this strong excitation appears to overwhelm the turbulence, having nearly the same effect at high and low Reynolds numbers. It can,

therefore, be studied in detail by direct numerical simulation. Direct numerical simulations of Mach 0.9, Reynolds number $3.6x10^3$ jets exhausting into quiescent fluid are conducted. Physically realistic slot jet actuators are included in the simulation by adding localized body-force terms to the governing equations. Three cases are considered in detail: a baseline unforced case and two cases that are forced with flapping modes at Strouhal numbers 0.2 and 0.4. (St = 0.4 was found to be the most amplified frequency in the unforced case.) Forcing at either frequency causes the jet to expand rapidly in the plane parallel with the actuators and to contract in the plane perpendicular to the actuators, as observed experimentally. It is found that the jet responds closer to the nozzle when forced at St = 0.4, but forcing at St = 0.2 is more effective at spreading the jet farther downstream. Several different measures of mixing (scalar dissipation, volume integrals of jet fluid mixture fraction, and point measurements of mixture fraction) are considered, and it is shown that by most, but not all, measures forcing at St = 0.2 is the more effective of the two at mixing.

Funk, R., K. K. Ahuja, et al. (2004). Jet mixing enhancement, Manchester, United Kingdom, American Institute of Aeronautics and Astronautics Inc., Reston, VA 20191, United States.

The application of a combustion-driven, pulsed fluidic actuator to jet mixing enhancement is described. An array of 14 combustion actuators was distributed around a 2.4" diameter nozzle. A sequential actuation scheme is described to achieve higher actuation frequencies. Fluidic and acoustic measurements were performed on the actuated jet. The jets were tested at speeds up to Mach 1. Enhanced mixing was shown at speeds up to Mach 0.55. Acoustic measurements showed increased jet noise at these low subsonic speeds.

Garcia-Villalba, M., J. Frohlich, et al. (2006). "Identification and analysis of coherent structures in the near field of a turbulent unconfined annular swirling jet using large eddy simulation." Physics of Fluids **18**(5): 055103.

Large eddy simulations of incompressible turbulent flow in an unconfined annular swirling jet at Reynolds number 81500 are reported, based on the outer radius of the jet. The results are in excellent agreement with experimental data for mean flow, turbulent statistics, and power spectral densities of velocity fluctuations. Two dominant families of large-scale coherent structures are identified in the flow. Both are orthogonal to the mean three-dimensional streamlines, which suggests that they are formed as the result of a Kelvin-Helmholtz instability. Instantaneous vortex structures as well as different types of spectra and two-point correlations are presented to further elucidate the properties of the flow.

Gaster, M., E. Kit, et al. (1985). "Large-scale structures in a forced turbulent mixing layer." Journal of Fluid Mechanics **150**: 23.

The large-scale structures that occur in a forced turbulent mixing layer at moderately high Reynolds numbers have been modeled by linear inviscid stability theory incorporating first-order corrections for slow spatial variations of the mean flow. The perturbation stream function for a spatially growing time-periodic

traveling wave has been numerically evaluated for the measured linearly diverging mean flow. In an accompanying experiment periodic oscillations were imposed on the turbulent mixing layer by the motion of a small flap at the trailing edge of the splitter plate that separated the two uniform streams of different velocity. The results of the numerical computations are compared with experimental measurements. When the comparison between experimental data and the computational model was made on a purely local basis, agreement in both the amplitude and phase distribution across the mixing layer was excellent. Comparisons on a global scale revealed, not unexpectedly, less good accuracy in predicting the overall amplification

Ginevsky, A. S., Y. V. Vlasov, et al. (2004). Acoustic control of turbulent jets. Berlin ; New York, Springer.

Results of experimental research on aerodynamic and acoustic control of subsonic turbulent jets by acoustic excitation are presented. It was demonstrated that these control methods not only can intensify mixing (by acoustic irradiation at low frequency), but also notably ease it (at high-frequency irradiation). This research monograph presents the updated results of the authors supplemented by other investigations conducted in USA, Germany and Great Britain. The methods for the numerical simulation of subsonic turbulent jets under acoustic excitation are described in detail, and examples are reviewed of practical applications, including reduction of turbojet engine noise and acoustic control of self-sustained oscillations in wind tunnels.

Glauser, M., E. Eaton, et al. (1999). Low-dimensional descriptions of turbulent flows - Experiment and modeling. 30th AIAA Fluid Dynamics Conference. Norfolk, VA, AIAA.

We present applications of the Proper Orthogonal Decomposition (POD) and Linear Stochastic Estimation (LSE), the physics based low dimensional approaches that we have been using over the past several years, to both the axisymmetric jet and the axisymmetric sudden expansion. For the high Reynolds number incompressible axisymmetric jet, we demonstrate, from both low dimensional models and experimental low dimensional descriptions, that the dynamics can be described with relatively low dimensional information (1 POD mode and 5 or 6 azimuthal modes). We also show recent experimental low dimensional results that suggest that the compressible jet (Mach numbers of 0.3 and 0.6) exhibit a similar low dimensional character. For the axisymmetric sudden expansion, we use an LSE based low dimensional approach to demonstrate the large-scale unsteadiness of the reattachment region. We conclude with recent experimental results, which show how this large-scale unsteadiness leads to a very low dimensional character for this flow. Specifically, we find from the POD based experimental low dimensional description that the m = 1 azimuthal mode dominates throughout the flow field which has exciting implications for active flow control applications in such separated flows.

Glezer, A. and M. Amitay (2002). "Synthetic jets." Annual Review of Fluid Mechanics **34**: 503-529.

The evolution of a synthetic (zero-net mass flux) jet and the flow mechanisms of its interaction with a cross flow are reviewed. An isolated synthetic jet is produced by the interactions of a train of vortices that are typically formed by alternating momentary ejection and suction of fluid across an orifice such that the net mass flux is zero. A unique feature of these jets is that they are formed entirely from the working fluid of the flow system in which they are deployed and, thus, can transfer linear momentum to the flow system without net mass injection across the flow boundary. Synthetic jets can be produced over a broad range of length and timescale, and their unique attributes make them attractive fluidic actuators for a number of flow control applications. The interaction of synthetic jets with an external cross flow over the surface in which they are mounted can displace the local streamlines and induce an apparent or virtual change in the shape of the surface, thereby effecting flow changes on length scales that are one to two orders of magnitude larger than the characteristic scale of the jets. This control approach emphasizes an actuation frequency that is high enough so that the interaction domain between the actuator and the cross flow is virtually invariant on the global timescale of the flow, and therefore, global effects such as changes in aerodynamics forces are effectively decoupled from the operating frequency of the actuators.

Glezer, A., Z. Kadioglu, et al. (1989). "Development of an extended proper orthogonal decomposition and its application to a time periodically forced plane mixing layer." Physics of Fluids A. **Vol 1**: 1363-1373.

Two extensions of the classical proper-orthogonal-decomposition (POD) methodology exposited by Lumley (1967 and 1981) for turbulent flows are presented. First, the extended POD (EPOD) can deal with flows lacking statistical stationarity by summing the velocity correlations of an ensemble of time series. Second, the EPOD can deal with flows having one or more length scales exceeding the spatial range over which simultaneous measurements can be made. Both new capabilities have been exercised by applying the EPOD to the streamwise velocity component measured by a cross- stream hot-wire rake in an anharmonically forced turbulent plane mixing layer that is not statistically stationary and is statistically homogeneous in only one direction. It is discovered that as few as three one- dimensional modes are capable of capturing as much as 78 percent of the 'action' in data from 10 wires.

Grinstein, F. F. (1999). Coherent structure dynamics and transition to turbulence in rectangular jet systems. 30th AIAA Fluid Dynamics Conference. Norfolk, VA, AIAA.

An overview of recent investigations of low aspect-ratio rectangular jets based on numerical simulations is presented. Our understanding of the effects of initial conditions on axis-switching phenomena is reviewed, with special focus on the underlying dynamics and topology of coherent vortical structures, including: vortex ring self-deformation, vortex ring bifurcation, the role of braid vortices, aspect ratio (AR) effects, and the transition to turbulence from laminar initial jet conditions. Modeling issues relevant to the numerical simulation of free jets are addressed, and the jet model is discussed in this context. Qualitatively different

vortex interaction geometries characterizing the near flow field of low-AR rectangular jets are demonstrated, involving: i) self-deforming and bifurcating (AR=4) vortex rings; interacting ring and rib (braid) vortices -- including, ii) single ribs aligned with comer regions (AR>2), and iii) rib pairs (hairpins) aligned with the comers (AR=1); iv) elongated "worm" vortices in the turbulent jet regime. The near field entrainment properties of low-AR rectangular jets are largely determined by the characteristic coupling between ring and braid vortices.

Guo-Hui, H., D. J. Sun, et al. (2001). "A numerical study of dynamics of a temporally evolving swirling jet." Physics of Fluids **13**(4): 951.

Direct numerical simulation (DNS) of a swirling jet near the outlet of a nozzle with axisymmetric and non-axisymmetric disturbances is performed to investigate the dynamic characteristics of the flow. The early (linear) stage of the jet evolution agrees well with the predictions of linear stability theory. In the nonlinear stage, the axisymmetric DNS shows that the interaction between the primary vortex ring and the streamwise columnar vortex creates a secondary vortex structure with opposite azimuthal vorticity near the columnar vortex. Then a vortex pair consisting of the primary and secondary vortices forms and travels radially away from the symmetry axis, causing a rapid increase of the thickness of mixing layer. The non-axisymmetric DNS shows that the streamwise vortex layer developed in the early stage of evolution due to azimuthal instability breakdowns into small eddies under the joint stretch of the axial and azimuthal shear. The results reveal several mechanisms of mixing enhancement by swirl, i.e., the radial motion of vortex ring pairs, the rapid growth of streamwise vorticity, and the creation of three-dimensional small eddies. They are all favorable for fluid entrainment in swirling jets

Hammad, K. J. and A. Shekarriz (1998). Turbulence in confined axisymmetric jets of Newtonian and non-Newtonian fluids, Washington, DC, USA, ASME, Fairfield, NJ, USA.

In this study, we have investigated the effect of Reynolds number and confinement geometry on turbulence within axisymmetric jets of Newtonian and Pseudoplastic non-Newtonian liquids. A mechanistic analytical model based on turbulent kinetic energy budget for a submerged jet within an enclosure is developed. The closed form solution shows that while turbulent kinetic energy along the centerline of the jet does not depend on Reynolds number it varies as a function of the confinement aspect ratio. Using laser Doppler velocimetry, we have experimentally verified these results for two different fluids: Newtonian and pseudoplastic. Measurements include mean and fluctuating components of the axial velocity for 10 less than or equal x/D less than or equal 100 and 2,000 less than or equal Re_D less than or equal 100,000. Our results show turbulence within the enclosure, measured along the jet centerline, to be independent of Reynolds number beyond a critical Reynolds number of 10,000. Further, repeated measurements in the Newtonian jet reveal that centerline turbulent kinetic energy is higher than previous measurements for a free jet. However, we have found that turbulence in the particular Non-Newtonian jet studied is no different than that

within a Newtonian free jet. These results are consistent with the analytical findings as discussed throughout this paper.

Haupt, R. L. and S. E. Haupt (1998). Practical genetic algorithms. New York, Wiley.
This book deals with the fundamentals of genetic algorithms and their applications in a variety of different areas of engineering and science. The use of genetic algorithms (GAs) to solve large and often complex computational problems has given rise to many new applications in a variety of disciplines. This introductory text takes the reader through the new and rapidly expanding field of genetic algorithms step by step, from a discussion of numerical optimization, to a survey of current extensions to genetic algorithms and applications. Theory is linked to practical application in a variety of disciplines through the presentation of numerous examples.

Hermanson, J. C., A. Wahba, et al. (1998). "Duty-cycle effects on penetration of fully modulated, turbulent jets in crossflow." AIAA Journal **36**(10): 1935-7.
Presents a systematic study of the effects of fully modulated pulsing on the penetration, entrainment, and mixing characteristics of transverse jets in a crossflow. Of particular interest are the specific effects of the pulsing parameters, especially the duty cycle, i.e., the jet-on fraction for each cycle. Research performed in pulsed transverse jets to date has generally been performed by varying the frequency, and therefore the injection time, for a fixed value of the duty cycle (0.5). Controlling the duty cycle as an independent parameter allows the separate specification of the injection time and frequency, with implications for both the structure of jet puffs and the nature of their interaction. The paper describes the initial results of this study using pulsed, nonreacting transverse jets to determine jet penetration for several values of injection time and duty cycle

Hilgers, A. and B. J. Boersma (2001). "Optimization of turbulent jet mixing." Fluid Dynamics Research **29**(6): 345.
We introduce an approach for controlling jet mixing that combines direct numerical simulation of an incompressible jet flow with stochastic optimization procedures. The jet is excited with helical and combined helical and axial actuations at the orifice. An objective function that measures the spreading of the jet evaluates the performance of the actuation parameters. The optimization procedure searches for the best actuation by automatically varying the parameters and calculating their objective function value. Solutions that lead to a pronounced spreading of the jet are found within reasonable time, although the evaluation of the objective function, the DNS of the jet, is expensive. For a jet flow at low Reynolds number the performance of different search algorithms (simulated annealing and evolution strategies) is evaluated. We compare various objective functions based on radial velocity and the concentration of a passive scalar, including functions that penalize actuation with high amplitudes. We find that a combined axial and helical actuation is much more efficient with respect to jet mixing than a helical actuation alone.

Ho, C. M. and P. Huerre (1984). Perturbed free shear layers. Annual review of fluid mechanics. Vol.16, Annual Reviews**:** 365.

Reviews free shear layers of the kind that are formed by the merging of two streams initially separated by a thin surface. Intensive mixing occurs in the velocity-gradient region between the two free streams, and such layers are often referred to as mixing layers

Ho, C.-M. and L.-S. Huang (1982). "Subharmonics and Vortex Merging in Mixing Layers." Journal of Fluid Mechanics **119**: 443-473.

The spreading rate of a mixing layer can be greatly manipulated at a very low forcing level if the mixing layer is perturbed near a subharmonic of the most-amplified frequency. This technique causes several vortices to merge simultaneously in a "collective interaction" and results in a large increase in the spreading rate.

Holdeman, J. D. (1993). "Mixing of multiple jets with a confined subsonic crossflow." Progress in Energy and Combustion Science **19**(1): 31-70.

This paper summarizes experimental and computational results on the mixing of single, double, and opposed rows of jets with an isothermal or variable temperature mainstream in a confined subsonic crossflow. The studies from which these results came were performed to investigate flow and geometric variations typical of the complex three-dimensional flowfield in the dilution zone of combustion chambers in gas turbine engines. The principal observations from the experiments were that the momentum-flux ratio was the most significant flow variable, and that temperature distributions were similar, independent of orifice diameter, when the orifice spacing and the square-root of the momentum-flux ratio were inversely proportional. The experiments and empirical model for the mixing of a single row of jets from round holes were extended to include several variations typical of gas turbine combustors, namely variable temperature mainstream, flow area convergence, noncircular orifices, and double and opposed rows of jets, both inline and staggered. All except the last of these were appropriately modeled with superposition or patches to the basic empirical model. Combinations of flow and geometry that gave optimum mixing were identified from the experimental and computational results. Based on the results of calculations made with a three-dimensional numerical model, the empirical model was further extended to model the effects of curvature and convergence. The principal conclusions from this study were that the orifice spacing and momentum-flux relationships were the same as observed previously in a straight duct, but the jet structure was significantly different for jets injected from the inner wall of a turn than for those injected from the outer wall. Also, curvature in the axial direction caused a drift of the jet trajectories toward the inner wall, but the mixing in a turning and converging channel did not seem to be inhibited by the convergence, independent of whether the contraction was radial or circumferential. The calculated jet penetration and mixing in an annulus were similar to those in a rectangular duct when the orifice spacing was specified at the radius dividing the annulus into equal areas.

Holdeman, J. D., D. S. Liscinsky, et al. (1999). "Mixing of multiple jets with a confined subsonic crossflow: Part II - opposed rows of orifices in rectangular ducts." Journal of Engineering for Gas Turbines and Power, Transactions of the ASME **121**(3): 551-562.

This paper summarizes experimental and computational results on the mixing of opposed rows of jets with a confined subsonic crossflow in rectangular ducts. The studies from which these results were excerpted investigated flow and geometric variations typical of the complex three-dimensional flowfield in the combustion chambers in gas turbine engines. The principal observation was that the momentum-flux ratio, J, and the orifice spacing, S/H, were the most significant flow and geometric variables. Jet penetration was critical, and penetration decreased as either momentum-flux ratio or orifice spacing decreased. It also appeared that jet penetration remained similar with variations in orifice size, shape, spacing, and momentum-flux ratio when the orifice spacing was inversely proportional to the square-root of the momentum-flux ratio. It was also seen that planar averages must be considered in context with the distributions. Note also that the mass-flow ratios and the orifices investigated were often very large (jet-to-mainstream mass-flow ratio > 1 and the ratio of orifices-area-to-mainstream-cross-sectional-area up to 0.5, respectively), and the axial planes of interest were often just downstream of the orifice trailing edge. Three-dimensional flow was a key part of efficient mixing and was observed for all configurations.

Huang, H. T., H. E. Fiedler, et al. (1993). "Limitation and improvement of PIV. I. Limitation of conventional techniques due to deformation of particle image patterns." Experiments in Fluids **15**(3): 168-74.

The deformation of particle image patterns by strong velocity gradients and out-of-pattern motions is a major source of error for the PIV (Particle Image Velocimetry) technique. This deformation is investigated and its effect on conventional PIV techniques is quantified for 2D flows. Simulations and comparisons with independent experiments verify the results

Hui, L. (1998). "Identification of coherent structure in turbulent shear flow with wavelet correlation analysis." Transactions of the ASME. Journal of Fluids Engineering **120**(4): 778-85.

In order to identify coherent structure of turbulent shear flow, a new combination of familiar techniques of signal processing, called wavelet correlation analysis, is developed based on the wavelet transform. The wavelet correlation analysis provides the unique capability for decomposing the correlation of arbitrary signals over a two-dimensional time delay-period plane. By analyzing two superposition functions implicating several pure frequencies, the correlation of periodic oscillations at several frequencies can well be separated and observed clearly. Coherent structures in the intermediate region of a plane turbulent jet are investigated using the wavelet correlation method. It is shown that the wavelet correlation analysis can extract the most essential scales governing features of eddy motions. The coherent structure information and apparent flapping behaviors are clearly revealed over a two-dimensional time-period plane

Humphreys, W. M., Jr. (1994). Probabilistic Extraction of Vectors in PIV Hampton, NASA Langley Research Center**:** 10.

Probabilistic technique for extraction of velocity vectors in particle-image velocimetry (PIV) implemented with much less computation. Double-exposure photograph of particles in flow illuminated by sheet of light provides data on velocity field of flow. Photograph converted into video image then digitized and processed by computer into velocity-field data. Velocity vectors in interrogation region chosen from magnitude and angle histograms constructed from centroid map of region.

Hussain, A. K. M. F. and A. R. Clark (1981). "On the coherent structure of the axisymmetric mixing layer: a flow-visualization study." Journal of Fluid Mechanics **104**: 263.

In an effort to resolve some controversies regarding the turbulent mixing layer structure the near field of a large air jet has been investigated for the jet exit speed of 30 m s/sup -1/. The smoke-laden axisymmetric mixing layer has been illuminated by a thin sheet of laser light in an azimuthal plane passing through the jet axis. High-speed visualization films of the mixing layer in the region of its self-preservation (of which a few picture sequences depicting space-time evolutions of the structure of the layer are presented) reveal that most of the time the mixing layer is in a state of disorganization, consisting of relatively smaller scale, random and diffuse turbulent motions; only occasionally are organized distinct large-scale coherent structures formed

Hussain, A. K. M. F. and K. B. M. Q. Zaman (1980). "Vortex pairing in a circular jet under controlled excitation. II. Coherent structure dynamics." Journal of Fluid Mechanics **101**(pt.3): 493.

For part I see ibid., vol.101, p.449-91 (1980). The coherent structure dynamics in the near field of a circular jet has been experimentally explored by inducing `stable' vortex pairing through controlled excitation (see pt.I) and applying phase-averaging techniques. Hot-wire measurements were made in a 7.62 cm air jet with laminar exit boundary layer at the Reynolds number $Re_D = 3.2x10^4$, excited at the Strouhal number St_D=0.85. The coherent structure Reynolds stress is found to be much larger than the background turbulent Reynolds stress for 0<x/D< 3, but these two are comparable near the end of the jet potential core. The zone average of the coherent structure Reynolds stress over the cross-section of the merging vortex pair is much larger than that over a single vortical structure either before or after the completion of pairing

Ibrahim, I. M., S. Murugappan, et al. (2005). Penetration, mixing and turbulent structures of circular and non-circular jets in cross flow, Reno, NV, United States, American Institute of Aeronautics and Astronautics Inc., Reston, VA 20191, United States.

Particle Image Velocimetry (PIV) was used to investigate penetration, mixing and turbulent structures of a jet injected perpendicularly into a free stream through several circular and non-circular shaped orifices. The two controlling parameters

were the geometry of the jet exit and the blowing ratio. Both the shape and orientation of the nozzle was found to have a prominent effect on the jet spread and penetration. Compared to the baseline circular nozzle, the slot major highest penetration where as the triangle flat penetrates the least. Each nozzle has a distinctive region of reverse flow which affects its entrainment and mixing in the cross stream. The jet trajectory was scaled using r, rd, r^2d parameters in an attempt to collapse the jet trajectory with existing data from PIV, Hot wire, PLIF and numerical computation. All the three scaling laws showed a large spread. A fourth scaling law which includes the initial condition of the jet was found to provide a better collapse.

Ibrahim, M. K., R. Kunimura, et al. (2002). "Mixing enhancement of compressible jets by using unsteady microjets as actuators." AIAA Journal **40**(4): 681.

Lateral steady/unsteady injection of an array of microjets, which are placed along the circumference of the nozzle exit of a primary jet at equal intervals of azimuthal angle, was studied experimentally to clarify the characteristics of mixing and noise of compressible primary jets. Two modes of the microjets were investigated: axisymmetric and antisymmetric injections. Fully expanded and underexpanded primary jets issued from a convergent nozzle are considered in the present study. The unsteady microjets were injected at a Strouhal number Sr of 0.16, based on the nozzle exit diameter and the velocity at the nozzle exit, for two cases of total mass injection: 4 and 6% of primary jet mass flow rate. Results of the mean flowfield showed that the antisymmetric injection has a higher spreading rate than the steady and unsteady axisymmetric injections in terms of centerline velocity decay. Those results were confirmed from linear stability analysis, which showed that antisymmetric modes for natural disturbances are more unstable in the downstream region than the corresponding axisymmetric modes. Moreover, reduction in the radiated noise was observed in steady axisymmetric injection. Thus, these results suggest that unsteady microjets have the potential for future use as a device for shear flow control

Ishibashi, M. and M. Takamoto (2000). "Methods to calibrate a critical nozzle and flowmeter using reference critical nozzles." Flow Measurement and Instrumentation **11**(4): 293-303.

Methods to calibrate a critical nozzle and a flowmeter against reference critical nozzles are developed to replace the time-consuming conventional procedures. The discharge coefficient of a critical nozzle at a low Reynolds number was measured in a series connection with a reference nozzle in the upstream position, and its Reynolds number dependence was obtained by changing the reference nozzle. The dependence of similar critical nozzles with negligible machining error measured at low pressures using the series connections and at atmospheric pressure using a constant volume tank system coincide within ±0.04%. The same configuration was employed to measure the stability of the choking flow rate, which revealed premature unchoking phenomenon. The discharge coefficient of a critical nozzle under a reference condition was measured by a combination of three series connections with two reference critical nozzles at the upstream

positions. Reynolds number dependence of a critical nozzle was measured using a combination of three series connections with four reference critical nozzles. These two methods require only one pressure gauge whose sensitivity is constant in a narrow range. An air flowmeter was calibrated at various volumetric flow rates against only one critical nozzle by controlling the upstream pressure of the nozzle.

Jin, T. and F. Hussain (1989). "Organized motions in a fully developed turbulent axisymmetric jet." Journal of Fluid Mechanics **203**: 425-48.

An experiment has been conducted to study the occurrence, configuration and dynamics of large-scale coherent vortical motions in the fully developed region of a turbulent axisymmetric jet. The key idea is to use vorticity signals from a spatial grid to detect and sample large-scale vortical structures and then use the (smoothed) vorticity peaks of spatial vorticity patterns to align and ensemble average successive realizations to determine structure configuration and dynamics. Measurements were made in an air jet at Re_D=69,000 by employing a radial rake of seven x-wires to obtain the azimuthal vorticity map. Two additional conditioning probes were placed ±90º away from the rake to determine the three-dimensional phase and hence the structure configuration. Structures with axisymmetric, helical and double helical configurations have been educed. Among them, the helical structures are far more dominant than the others, and the jet dynamics are thus discussed in terms of these helical structures. Helical structures move radially outward as they advect downstream. This radial movement, in conjunction with simultaneous local ejection of turbulent fluid and subsequent entrainment of the ejected fluid with ambient fluid, appears to be a major means of jet spreading. The shear strain rate is strong on the downstream side of the structure, causing intense small-scale turbulence production and mixing there

Johansson, P. B. V. (2006). Analysis of large data sets using proper orthogonal decomposition, San Francisco, CA, United States, American Institute of Aeronautics and Astronautics Inc., Reston, VA 20191, United States.

In this paper, the attention is directed towards application of Proper Orthogonal Decomposition (POD), with special focus on analysis of large data sets. Using modern tools it is common that simulations or measurements of flows result in very large amounts of data. Today, the principal difficulty is to be able to manage the large data set to post-process it and thereby compute the quantities of interest. To study the dynamics of the large scale structures it is common to apply POD. Here, analysis of three flow cases are presented. The common denominator among the flows is that the amount of data to process is vast. The three cases investigated are: direct numerical simulation (DNS) of stably stratified shear flow, DNS of a channel, and large eddy simulation (LES) of a compressible boundary layer.

Johari, H., M. Pacheco-Tougas, et al. (1999). "Penetration and mixing of fully modulated turbulent jets in crossflow." AIAA Journal **37**(7): 842-850.

Fully modulated, incompressible, turbulent transverse jets were studied

experimentally in a water tunnel over a range of pulsing frequencies and duty cycles and at two jet-to-crossflow velocity ratios. The jet flow was completely modulated by operating an in-line solenoid valve resulting in the shutoff of jet supply during a portion of the cycle. The planar laser-induced fluorescence technique was used to determine the penetration, dilution, and structural features of the pulsed jets. The molecular mixing rate was quantified using a chemical reaction between the jet and crossflow fluids. Short injection times resulted in creation of vortex ring structures, whereas long injection times produced axially elongated turbulent puffs, similar to a segment of a steady jet. The latter case resulted in only modest enhancement of the jet penetration depth and dilution. Pulsed jets dominated by vortex rings had penetration depths significantly greater than a steady jet with the same velocity ratio, up to a factor of 5 at 50 jet diameters downstream of the exit. For short injection times, duty cycle had a significant effect on the behavior of pulsed jets. Increasing the duty cycle for a fixed injection time reduced the jet penetration. The dilution and mixing of pulsed jets with short injection time was also improved over the steady jet for duty cycles as high as 0.5. The greatest increase in the mixing rate was approximately 50% for well-separated pulses with short injection times.

Jørgensen, F. E. (2005). How to Measure Turbulence with Hot-Wire Anemometers - A Practical Guide, Dantec Dynamics.

This guide gives the technical details for setting up and running a hot-wire experiment, focusing on practical aspects. Included is information on selecting equipment, planning the experiment, configuration of the equipment, velocity calibration, and data reduction. There is also information on estimating measurement uncertainty and basic principles of hotwire anemometry.

Kassab, S. Z. (1990). "Pitot tube as a calibration device for turbulence measurement." Review of Scientific Instruments **61**(6): 1757-9.

The author demonstrates that one can correct hot-wire turbulence measurements simply by using a Pitot tube to obtain the mean velocity distribution in fully developed, turbulent pipe flow. The basic idea is simply a combination of two independent derivations given in the late sixties. A test case is given to prove the idea

Kastner, J., J. Hileman, et al. (2004). Exploring high-speed axisymmetric jet noise control using Hartmann tube fluidic actuators, Reno, NV, United States, American Institute of Aeronautics and Astronautics Inc., Reston, United States.

This work is part of an ongoing effort to better understand the influence of frequency and amplitude when controlling high Reynolds number, high-speed jets using a Hartmann Tube Fluidic Actuator (HTFA). In addition to HTFA forcing, a steady mass injector (SMI) with the same mass flow rate as the HTFA was used. Forcing was applied with two actuators separated by 180deg; and four actuators separated by 90° in the azimuthal direction. The jet under study was axisymmetric with Mach numbers between 0.6 and 0.98 and Reynolds number between 5.7 x 10^5 and 7.6 x 10^5. To understand the influence of forcing on far-field noise,

acoustic measurements were acquired at 30° and 60° with reference to the jet axis. With two actuators, the jet noise increased when the actuators operated at a frequency between St_D = 0.2 - 0.5. Forcing with two or four actuators at higher Strouhal numbers (St > 0.75) or with steady mass injection slightly reduced the peak broadband jet noise and increased the high frequency noise. The slight reduction was only observed when the total mass injection was greater than 1%. The actuators (SMI or HTFA) had their largest impact when they were injected at an angle between 45° and 60° with respect to the jet axis.

Kibens, V., J. D. III, et al. (1999). Active flow control technology transition - The Boeing ACE program. AIAA Fluid Dynamics Conference, 30th. Norfolk, VA, AIAA.

A process is detailed whereby laboratory observations of the effect of external excitation on the mixing characteristics of a jet plume are developed into an active flow control (AFC) mixing enhancement system. Installed and tested on a full-scale JT8D engine, the Active Core Exhaust Control (ACE) system continues to be developed toward implementation on a Heavy Lift Transport (HLT). The requisite intermediate stages in the technology development process are described. Test results from a full-scale engine mounted on a test stand are compared with laboratory data from scale model tests and numerical simulations of AFC-enhanced plume mixing.

King, G. F., J. C. Dutton, et al. (1999). "Instantaneous, quantitative measurements of molecular mixing in the axisymmetric jet near field." Physics of Fluids **11**(2): 403.

Results from a dual-tracer planar laser-induced fluorescence (PLIF) technique for making instantaneous, quantitative measurements of molecularly mixed fluid fraction are presented for an axisymmetric jet in a slow co-flow. The two-camera, two-laser technique uses PLIF of nitric oxide seeded in a nitrogen jet to mark the unmixed jet fluid fraction, while PLIF of acetone seeded into the low velocity air co-flow marks the total co-flow fluid fraction. By combining data from these two simultaneous images, quantitative measurements of molecularly mixed jet fluid fraction can be made on a pixel-by-pixel basis, while simultaneously allowing visualizations of large-structure behavior and regions of subresolution stirring. Instantaneous images of molecularly mixed jet fluid fraction and jet fluid mixing efficiency, probability density functions (PDFs) of mixed jet fluid fraction, and associated statistics are presented for Re_{jet} = 51000, 5000, 10,000, 50,000, and 100,000. For fully turbulent conditions (Re_{jet}>30,000), stirring at subresolution scales is detected primarily on the jet side of the mixing layer. This creates a hybrid PDF behavior (stationary on the jet side of the mixing layer, marching on the co-flow side) that is not shown by passive scalar methods at equivalent image resolution.

Klopfenstein, R., Jr. (1998). "Air velocity and flow measurement using a Pitot tube." ISA Transactions **37**(4): 257-263.

The accurate measurement of both air velocity and volumetric airflow can be accomplished using a Pitot tube, a differential pressure transducer, and a computer system which includes the necessary hardware and software to convert

the raw transducer signals into the proper engineering units. The incorporation of sensors to measure the air temperature, barometric pressure, and relative humidity can further increase the accuracy of the velocity and flow measurements. The Pitot tube measures air velocity directly by means of a pressure transducer which generates an electrical signal which is proportional to the difference between the pressure generated by the total pressure and the still air (static pressure). The volumetric flow is then calculated by measuring the average velocity of an air stream passing through a passage of a known diameter. When measuring volumetric flow, the 'passage of a known diameter' must be designed to reduce air turbulence as the air mass flows over the Pitot tube. Also, the placement of the Pitot tube in the passage will influence how accurately the measured flow tracks the actual flow through the passage. Calibrating the measurement system in a wind tunnel can further increase the accuracy of the velocity and the flow measurements. This objective of this paper is to provide the field engineer with single, concise source of information on flow measurement using a Pitot tube.

Ko, N. W. M. (1980). "Annular Jets of Small Inner Diameter." Journal of Sound and Vibration **68**(3): 468-472.

Coherent structures within the initial region of an annular jet have been previously investigated. From the pressure measurements jet vortices were found in the outer mixing region of the conical annular jet. For the basic annular jet, however, besides the jet vortices, wake vortices also were found behind the interface at the nozzle exit. Due to the inner diameter and the Mach number used in the previous studies, the Strouhal number of the wake vortices was very near that of the most preferred mode of the jet. This resulted in the excitation of the outer mixing region by the disturbances associated with the wake vortices and the formation of the additional train of wake excited vortices in that region. The more recent study of the basic annular jet of Ko was aimed at flow visualization of these different trains of vortices. The inner diameter of the annular jet was chosen so that excitation of the outer mixing region by the disturbances associated with the inner wake vortices occurred. The schlieren photographs showed, besides the jet vortices, the additional strong wake excited vortices in the outer mixing region. Further, both the jet and wake excited vortices seemed to be affected by the wake vortices and were generated alternately. The present investigation was aimed at understanding more fully these different trains of vortices when the inner diameter was small. In other words, the Strouhal number of the wake vortices generated behind the interface was deliberately chosen to be much different from that of the most preferred mode of the jet.

Ko, N. W. M. and K. M. Lam (1984). "Further Measurements in the Initial Region of an Annular Jet." Journal of Sound and Vibration **92**(3): 333-348.

The results of spectral and correlation measurements relevant to coherent structures in the initial region of a basic annular jet associated with the jet vortices and the wake induced vortices are discussed showing evidence that for the wake induced vortices the first mode constituent (m equals 1) is more dominant in the region where their pressure intensity is high. Further downstream the first mode

constituent becomes only slightly higher than that of the axisymmetric (m equals 0) mode. For the jet vortices during their generation and formation near the nozzle exit the first mode constituent is slightly more dominant than the axisymmetric constituent. Further downstream the axisymmetric constituent becomes more dominant.

Ko, N. W. M., K. K. Lau, et al. (1998). "Dynamics of interaction modes in excited annular jets." Experimental Thermal and Fluid Science **17**(4): 319-338.

Evolution of coherent structures and their interaction dynamics are educed in the near field of an acoustically excited basic annular jet using conditional sampling technique based on a multiple triggering criterion to detect the two dominating modes of structure pattern. Acoustic excitation is applied with an aim to better organize the phase alignment of initial rolling and pairing process in the outer shear layer. Negligible modification of the time-averaged flow field results from the excitation. The educed coherent vorticities show that the two modes of evolution are due to the corresponding two modes of shedding pattern of the wake structures from the centerbody, namely the mode one wake and the mode zero wake. In both modes, the shear-layer mode jet vortex rings in the outer layer are perturbed by the shedding of wake structures in the inner region and interaction involving primary merging of three successive jet vortex rings or their partial circumferential sections is found. This results in the formation of wake-induced structures of the corresponding mode pattern, which possesses concentration of coherent vorticity and fluid circulation over a large spatial extent at $1 < x/D < 2$. Secondary interactions, such as vortex tearing, are also observed.

Kolovandin, B. A., V. A. Sosinovich, et al. (1978). "To the theory of the mechanism of mixing in turbulent flows with coherent structures." Letters in Heat and Mass Transfer **5**(5): 253.

A system of linear equations has been obtained which governs the fields of velocity and of the scalar passive impurity in a turbulent incompressible liquid flow. This system is considered as a simple model characterizing the large-scale coherent structures which have been found experimentally in many turbulent flows. The means to account for these structures when describing the mechanism of mixing are discussed

Koumoutsakos, P., Freund, J., Parekh, D. (1998). Evolution strategies for parameter optimization in jet flow control. Proceedings of the Center for Turbulence Research Summer Program, Stanford, CA

We present results from the application of evolution strategies for parameter optimization in direct numerical simulations and vortex models of controlled jet flows. It is shown that evolution strategies are a portable, highly parallel method that can complement our physical intuition in the parameter optimization of such flows.

Koumoutsakos, P., J. Freund, et al. (2001). "Evolution strategies for automatic optimization of jet mixing." AIAA Journal **39**(5): 967.

Evolution strategies (ES) are introduced for the optimization of active control parameters for enhancing jet mixing. It is shown that the evolution algorithms can identify, in an automated fashion, nor only previously known effective actuations but also find good but previously unidentified parameters. In the study, simulations of model jets are used to demonstrate the feasibility of the methods. ES are robust, highly parallel, and portable algorithms that may be most useful in an experimental setting at realistic Reynolds numbers. Simulations of inviscid incompressible flows using vortex models, as well as direct numerical simulations (DNS) of very low-Reynolds-number compressible flows, are used to evaluate different forcing parameters. Our objective is twofold: 1) explore the possibility of ES to find previously identified modes of efficient operation and 2) discover previously unknown effective actuations. Practical engineering concerns will dictate the choice of actuator parameters and relevant cost functions

Kuhlman, J. M. (1987). "Variation of entrainment in annular jets." AIAA Journal **25**(3): 373.

Mean velocity distributions for axisymmetric circular and annular jets entering a stagnant ambient have been obtained, from which centerline velocity decay and jet width growth data have been extracted. In all instances, linear width growth and inverse centerline velocity decay laws are observed in the far field. The annular jet results in enhanced near-field mixing, as indicated by a consistent inward shift of the virtual origin. Also, far-field centerline velocity decay and jet width growth occur more quickly for the annular jet than for the circular jet. This is true even when the data are rescaled using characteristic length and velocity scales formed from the integrated initial jet mass flux and momentum flux. More importantly, far-field entrainment rates for some annular jet configurations are increased by more than 40% relative to the circular jet entrainment rate. It is believed that this is the result of enhancement of the near-field wake vortex train in the lee of the centerbody used to create the annular jet

Kyung-Am, P., K. Jae-Hyung, et al. (2006). "Computational/experimental study of a variable critical nozzle flow." Flow Measurement and Instrumentation **17**(2): 81-6.

Recently, critical nozzles have been extensively utilized to measure the mass flow rate in a variety of industrial applications. For the measurement of the mass flow rates in a wide range of operation conditions, the critical nozzle is required to be designed with different diameters. The objective of the present study is to investigate the effectiveness of a variable critical nozzle. A rod with a small diameter is inserted into the critical nozzle to change the effective cross-sectional area of the critical nozzle. Experimental work is performed to measure the mass flow rate of the critical nozzle with rod. Computational work is carried out using the two-dimensional, axisymmetric, compressible Navier-Stokes equations which are discretized using a fully implicit finite volume method. The diameter of the rod is varied to obtain different mass flow rates through the variable critical nozzle. Computational results predict well the measured mass flow rates. The boundary layer displacement and momentum thickness at the throat of the critical nozzle are given as a function of Reynolds number. The discharge coefficient of

the critical nozzle is given as an empirical equation.

Lardeau, S., E. Collin, et al. (2003). "Analysis of a jet-mixing layer interaction." International Journal of Heat and Fluid Flow **24**(4): 520.

The improvement of mixing in free-shear flows via external jets has been proven efficient in subsonic and supersonic flows as well. However, the hyper-mixing process is not well known. The present study deals with an experimental and a numerical approach of the interaction of an external control jet with a turbulent mixing layer. The main conclusion is that an intermittent penetration of the control jet occurs both in supersonic and subsonic configurations. Moreover, all results tend to show that the control jet flapping frequency and the spacing between the structures involved downstream of the interaction are respectively very close to the frequency and wavelength of the Kelvin-Helmholtz structures at the impact location. Two hypotheses are provided in order to explain the mechanism of the interaction. The first one is based upon the interaction with the passage of Kelvin-Helmholtz structures in the mixing layer, the other deals with an intrinsic instability of such a flow configuration.

Lau, J. C., M. J. Fisher, et al. (1972). "The intrinsic structure of turbulent jets." Journal of Sound and Vibration **22**(4): 379.

The object of this paper is to present some experimental results relating to the part of the jet where a potential core exists. The measurements have been made, in the main, in the nonturbulent regions of the jet (viz. the potential core and the entrainment region), and they suggest that underlying the normally-accepted picture of a random process in the mixing region of the jet there exists a relatively periodic and deterministic flow structure. A simple model of jet structure, purporting to explain the particular phase relationships between the fluctuating pressure and the components of the fluctuating velocity obtained here, is postulated. This model appears to be well substantiated and found to be applicable even to conditions in the mixing region, provided allowance is made for non-linear effects to take place in the mixing region. A special study was made of the use of standard microphones for measuring pressure fluctuations in regions of significant mean flow, and it was found that, to a first-order approximation, this method was justified

Lee, K. and J. T. C. Liu (1998). "Mixing enhancement in high-speed turbulent shear layers using excited coherent modes." AIAA Journal **36**(11): 2027.

For noise reduction purposes, it is often desirable to promote rapid mixing close to the jet exhaust. Excited high-frequency coherent wave modes for mixing enhancement in the initial region of high-speed jet exhaust were studied theoretically. The jet in this region is modeled as a two-dimensional mixing layer. Integral kinetic energy equations for the mean flow and the control modes are derived from the compressible Navier-Stokes equations, with the flow quantities split into mean, coherent wave modes and fine-grained turbulence. Turbulence effects are characterized by an eddy viscosity; the coherent modes are explicitly characterized by their nonlinear amplitudes and the shape functions of the

eigenmodes of a local linear stability theory according to the developing shear layer. The initial region considered is two dimensional where the initial boundary layer is assumed to be thin relative to the jet size. The upstream velocity and temperature wake, due to wall boundary layers, are accommodated in the mean flow shape assumptions. Two significant nonequilibrium effects associated with the initial control region are: 1) the embedded wake evolves into a similar mixing region downstream and 2) the interaction between excited control modes and the mean flow is strongly dependent on initial conditions. It is found that excitation of high-frequency modes could give rise to enhanced spreading of the mixing layer in the initial wake mixing-layer region; the effects of varying the relative initial two stream shear-layer thickness and temperature ratios are also studied.

Lefebvre, A. H. (1998). Gas Turbine Combustion. Philadelphia, PA, Taylor & Francis. pp. 111 - 118

In this section the results of a number of studies on jets in crossflow are summarized. This is covered in order to give the reader information on proper design of the dilution zone where colder air is mixed with hot combustion products to achieve an outlet temperature distribution that is acceptable to the turbine. The conclusion is that the penetration depth of the jet is a function of the square root of the momentum flux ratio. The effects of various configurations on mixing are also examined.

Lepicovsky, J. (1989). Role of nozzle-exit boundary-layer velocity gradient in mixing enhancement of free jets, San Diego, CA, USA, Publ by American Soc of Mechanical Engineers (ASME), New York, NY, USA.

An analysis of experimental data indicates that shearing motion in the nozzle-exit boundary layer (the velocity gradient across the nozzle-exit boundary layer) plays a decisive role in the jet mixing and spreading rates. It appears that jets with high nozzle-exit boundary-layer velocity gradient attain high mixing rates which cannot be further improved by acoustic excitation or vice versa. Based on this conclusion, a novel approach is proposed to further enhance the free-jet mixing and spreading rates by increasing the nozzle-exit boundary-layer velocity gradient. This can be achieved by suitable modification (suction) of the nozzle-exit boundary layer.

Li, H. (1998). "Wavelet statistical analysis of the near field flow structure in a turbulent jet." Transactions of the Japan Society for Aeronautical and Space Sciences **41**(133): 132-139.

In the present paper, the definitions of the wavelet-based statistical quantities on turbulence analysis were first developed to study the characteristics of statistics in frequency space. Then, the wavelet statistical quantities were used to analyze eddy motions and the structure of the energy transfer over a two-dimensional frequency-physics plane in a plane jet. In the shear layer, behaviors of Reynolds stress reversals were easily detected at several frequencies for $x/b_0 = 2$, 6 and 10. This phenomenon indicated that fluctuation energy is transferred from high frequency component to low frequency component. The frequency of wavelet

Reynolds stress reversal decreases toward downstream and the interaction between positive and negative production in frequency space leads to the formation of the coherent structures.

Lumley, J. L. (1967). The structure of inhomogeneous turbulent flows. Atmospheric Turbulence and Wave Propagation. NAUKA, MOSCOW**:** 166-178.

Physical definition of large eddy leads to application of proper orthogonal decomposition to turbulent velocity fields

Mankbadi, R. R. (1985). "The mechanism of mixing enhancement and suppression in a circular jet under excitation conditions." Physics of Fluids **28**(7): 2062.

The present work is a numerical study of the shear layer's growth in a turbulent round jet under forced axisymmetric periodic disturbances. The forced oscillation is found to either enhance or reduce the momentum thickness along the jet depending on the forcing Strouhal number St, where St is defined as fd/U_e. Here f is the frequency in Hertz, d is the nozzle exit diameter, and U_e is the jet exit velocity. At low Strouhal numbers ($St<0.5$), no subharmonic of the forced fundamental is amplified. The momentum thickness is found to increase monotonically with the forcing level, and the effect is pronounced for forcing levels higher than 0.5% of the jet exit velocity. At forcing Strouhal numbers in the range of 0.6-1.0, the first subharmonic of the fundamental is amplified. The increase in the momentum thickness caused by forcing at this Strouhal number range is proportional to the forcing level and is pronounced at low forcing levels in the range of 0.01%-1% of the jet exit velocity. If the forcing Strouhal number is close to the `shear layer instability mode', $St_\Theta \approx 0.015$, several subharmonics are generated and the forcing is found to result in a reduction in the momentum thickness along the jet

Mathieu, J. C., G (1981). Structure and development of turbulent jets Fluid dynamics of jets with applications to V/STOL / North Atlantic Treaty Organization, Advisory Group for Aerospace Research and Development, Lisbon, Portugal.

The behavior and the modeling of turbulent jet flow are surveyed. The essential ideas are discussed in connection with industrial and aeronautical applications. After an introduction of the quasi-equilibrium state related to the length and time scales, the coherent structures and spreading processes are analyzed. Specific topics considered are the intermittency in the axial region, the characteristics of the production centers of the turbulent kinetic energy, the round and plane jet, the acoustic properties with their interactions with the turbulent structure, the initial conditions, and the phenomena in the stagnation region of an impinging jet. A general review of modeling methods precedes examination of computations carried out in physical space and of the large eddy simulation approach.

McKeon, B. J., J. Li, et al. (2003). "Pitot probe corrections in fully developed turbulent pipe flow." Measurement Science & Technology **14**(8): 1449-58.

Mean flow measurements taken in fully developed turbulent pipe flow over a wide Reynolds number range are used to evaluate current methods of correcting

Pitot probe data. Based on this evaluation, a new form for the displacement correction is proposed which appears to be more accurate over a wider range of conditions than those currently available. The difficulty of obtaining the true near-wall velocity profile near the wall is explored

Michalke, A. (1984). "Survey on Jet Instability Theory." Progress in Aerospace Sciences **21**(3): 159.

Theoretical results concerning the instability of axisymmetric jets are reviewed. For inviscid parallel jet flow the various parameters affecting jet instability such as shear layer thickness, Mach number, temperature ratio, and external flow velocity are discussed. Furthermore, viscous and nonlinear effects are considered. Finally, the influences of flow divergence and of nozzle-jet interaction are discussed.

Milano, M. and P. Koumoutsakos (2002). "A clustering genetic algorithm for cylinder drag optimization." Journal of Computational Physics **175**(1): 79.

A real coded genetic algorithm is implemented for the optimization of actuator parameters for cylinder drag minimization. We consider two types of idealized actuators that are allowed either to move steadily and tangentially to the cylinder surface ("belts") or to steadily blow/suck with a zero net mass constraint. The genetic algorithm we implement has the property of identifying minima basins, rather than single optimum points. The knowledge of the shape of the minimum basin enables further insights into the system properties and provides a sensitivity analysis in a fully automated way. The drag minimization problem is formulated as an optimal regulation problem. By means of the clustering property of the present genetic algorithm, a set of solutions producing drag reduction of up to 50% is identified. A comparison between the two types of actuators, based on the clustering property of the algorithm, indicates that blowing/suction actuation parameters are associated with larger tolerances when compared to optimal parameters for the belt actuators. The possibility of using a few strategically placed actuators to obtain a significant drag reduction is explored using the clustering diagnostics of this method. The optimal belt-actuator parameters obtained by optimizing the two-dimensional case is employed in three-dimensional simulations, by extending the actuators across the span of the cylinder surface. The three-dimensional controlled flow exhibits a strong two-dimensional character near the cylinder surface, resulting in significant drag reduction.

Monkewitz, P. A. (1988). "Subharmonic resonance, pairing and shredding in the mixing layer." Journal of Fluid Mechanics **188**: 223.

An instability-wave analysis is presented to describe the spatial evolution of a fundamental mode and its subharmonic on an inviscid parallel mixing layer. It incorporates explicitly the weakly nonlinear interaction between the two modes. The computational finding that the development of the subharmonic, leading eventually to pairing or shredding, crucially depends on its phase relation with the fundamental is fully confirmed. Furthermore it is shown that a critical

fundamental amplitude has to be reached before the (spatial) subharmonic becomes phase locked with the fundamental and exhibits a modified growth rate. Then the analysis is exploited to explain the occurrence of amplitude modulations in `natural' mixing layers and to estimate the width of the subharmonic spectral peaks

Monkewitz, P. A. and P. Huerre (1982). "Influence of the velocity ratio on the spatial instability of mixing layers." Physics of Fluids **25**(7): 1137.

The linear spatial instability of the tanh and Blasius mixing layers is studied for different values of the ratio between the difference and the sum of the velocities of the two co-flowing streams. The growth rate, phase velocity, and perturbation velocity distributions are determined numerically and the results are compared with expansions for small shear or low frequency. It is found that the maximum growth rate is approximately proportional to the velocity ratio. This is shown to be consistent with the observed variation of shear layer spreading rate with velocity ratio and with a recent model of flight effects on jet mixing noise

Morris, P. J. (1976). "The spatial viscous instability of axisymmetric jets." Journal of Fluid Mechanics **77**(pt.3): 511.

The stability of three axisymmetric jet profiles is reviewed. These profiles represent the development of an incompressible jet from a nearly top-hat profile to a fully developed jet profile. The disturbance equations for arbitrary mode number in a region of zero shear, which provide the boundary conditions for the numerical solution, are solved analytically through use of the disturbance vorticity equations. Numerical solutions for the spatial stability for the axisymmetric (n=0) disturbance and the asymmetric n=1 disturbance are presented. Previously published calculations of least stable modes are shown to be incorrectly interpreted and their actual mode types are given. The critical Reynolds number is found to increase as the profile varies from a top-hat to a fully developed jet form

Muller, S., M. Milano, et al. (1999). Application of machine learning algorithms to flow modeling and optimization. Center for Turbulence Research Annual Research Briefs.

The authors develop flow modeling and optimization techniques using biologically inspired algorithms such as neural networks and evolution strategies. The results presented encompass a wide variety of problems such as drag minimization, neural net modeling of the near wall structures, enhanced jet mixing, and parameter optimization in turbine blade film cooling. The evolutionary optimization algorithms have been applied to a number of optimization problems with sufficient success.

Müller, S. D., J. H. Walther, et al. (2001). "Evolution Strategies for Film Cooling Optimization." AIAA Journal 2001 **39**(3): 537-539.

Optimization algorithm and parameters were used in automated design cycle of turbine blade film cooling to reduce coolant mass flow and achievement of homogeneous surface temperature. The external aerodynamic and thermal conditions for a two-dimensional blade geometry were considered to compute the

heat transfer coefficient and temperature in the boundary layer. The results depicted the efficiency of evolutionary algorithm to present a robust, automated optimization tool for the optimization of engineering devices using gradient-based methods.

Murakami, E. and D. Papamoschou (2001). Experiments on Mixing Enhancement in Dual-Stream Jets. 39th AIAA Aerospace Sciences Meeting and Exhibit. Reno, NV, AIAA.

Flow exiting a convergent-divergent nozzle operated at off-design conditions exhibits an instability that causes mixing enhancement in the flow itself and can destabilize an adjacent flow. The latter property enables mixing enhancement of an arbitrary jet via parallel injection of a secondary gas flow. In this study we extend the method of mixing enhancement using secondary parallel injection (MESPI) to high-aspect ratio rectangular (2D) jets and obtain data on flow structure and scalar mixing for both 2D and axisymmetric jets. The turbulent structure is visualized using spark schlieren photography and planar laser induced fluorescence (PLIF). The rate of mixing is described by centerline velocity distributions, obtained by pitot surveys, and concentration measurements, obtained by time-averaged PLIF. The MESPI jet is compared to a reference jet with equal mass flow rate and equal momentum flux. The mixing diagnostics show that MESPI halves the length of the potential core in both round and 2D jets. A short distance past the potential core, mixing enhancement causes a reduction in centerline Mach number of 30% in round jets and 20% in 2D jets. The corresponding reduction in the peak molar concentration of a scalar injected in the primary flow is 65% in round jets and around 40% in 2D jets.

Nakamura, H., I. Asano, et al. (2005). "Analysis of pulsating flow measurement of engine exhaust by a Pitot tube flowmeter." International Journal of Engine Research **6**(1): 85-93.

The Pitot tube flowmetering technique has been used to measure pulsating flow from a vehicle engine exhaust. In general, flowmetering techniques that utilize differential pressure measurements based on Bernoulli's theory are likely to show erroneous readings when measuring an average flowrate of pulsating flow. The primary reason for this is the non-linear relationship between the differential pressure and the flowrate; i.e. the flowrate is proportional to the square root of the differential pressure. Therefore, an average of the differential pressure does not give an average of pulsating flow. In this study fast response pressure transducers have been used to measure the pulsating pressure. Then the pulsating differential pressure is converted to the flowrate while keeping the pulsation unaveraged. An average flowrate is then calculated in the flowrate domain in order to maintain linearity before and after averaging. The peak amplitude of a pulsation measured here was about 1800 L/min at an average flowrate of 70 L/min when the engine ran at idle speed. This measurement has been confirmed by measuring the pulsation with a gas analyser. The results show a large amount of back and forth gas movement in the exhaust tube. This magnitude of pulsation can cause as much as five times higher erroneous results with the pressure domain averaging when compared to a flowrate domain averaging

Nakazono, Y. (1996). Flow Structure of Annular Jets and Effect of Acoustic Excitation on Their Mixing. 34th Aerospace Sciences Meeting and Exhibit. Reno, NV, AIAA.

The effect of inner-to-outer nozzle diameter ratio on the flow structure of the wake and jet vortex speed were studied by using a flow visualization method and a conditional sampling techinque. As a result, the convection velocity of the wake vortex is faster than that of jet vortex. When the inner-to-outer nozzle diameter ratio is small, the wake has a helical mode. But, for large inner-to-outer diameter ratio, this mode changes, and a large energetic wake vortex is generated periodically and moves downstream. Next, the effects of sound waves on their mixing were studied. Sound waves related to the shear layer were mainly selected. The mean velocity, the fluctuation velocity, and its spectra, were measured, and the jet flow was investigated by using Schlieren photography and a smoke-wire method.

Naughton, J. W., L. N. Cattafesta, III, et al. (1997). "An experimental study of compressible turbulent mixing enhancement in swirling jets." Journal of Fluid Mechanics **330**: 271.

Compressible jets with various amounts of swirl and compressibility are investigated experimentally. The mixing layer growth rate is obtained from time-averaged images of the mixing layer using the planar laser scattering (PLS) technique, and the swirl is quantified with laser Doppler velocimetry and intrusive probes. The results conclusively demonstrate that the addition of swirl to the jet increases entrainment by up to 60% compared to a corresponding non-swirling case. Instantaneous PLS images reveal modified turbulent structure in the mixing layer of the swirling jet. In particular, analysis of these images indicates that both the spatial extent cases. A parameter beta that correlates the observed growth rate. This parameter is derived assuming that the streamwise mixing layer by the addition of small amounts of swirl mixing that increases the growth rate. When the available growth rate data for swirling jets are plotted against this parameter, they collapse to a single curve with increased enhancement for higher values of beta. This result implies that the degree of enhancement actually increases with compressibility, although the dimensional growth rates for the present compressible swirling jet cases are still less than those of their incompressible counterparts

Nedungadi, A., T. J. Barber, et al. (2001). The Effects of Pulsed Blowing on Jet Mixing and Noise Generation. 39th Aerospace Sciences Meeting and Exhibit. Reno, NV, AIAA.

Active control concepts are numerically studied by introducing localized disturbances, produced by an azimuthal array of small synthetic jets placed close to the nozzle exit face. These actuators are simulated as unsteady boundary conditions, providing a normal component of velocity into the primary jet flow. Independent control of each actuator allows for different frequency, amplitude, and modal distribution of the periodic input. Through use of a RANS-acoustic analogy methodology, assessments of the enhanced mixing and noise reduction characteristics are made. This work builds on earlier efforts which demonstrated

that enhanced mixing could be achieved when actuators were driven at ¥2 the jet preferred frequency using an m = ±l excitation pattern. The current effort considers a larger range of frequency, amplitude and modal excitations.

Nickels, T. B. and I. Marusic (2001). "On the different contributions of coherent structures to the spectra of a turbulent round jet and a turbulent boundary layer." Journal of Fluid Mechanics **448**(448): 367-385.

This paper examines and compares spectral measurements from a turbulent round jet and a turbulent boundary layer. The conjecture that is examined is that both flows consist of coherent structures immersed in a background of isotropic turbulence. In the case of the jet, a single size of coherent structure is considered, whereas in the boundary layer there are a range of sizes of geometrically similar structures. The conjecture is examined by comparing experimental measurements of spectra for the two flows with the spectra calculated using models based on simple vortex structures. The universality of the small scales is considered by comparing high-wavenumber experimental spectra. It is shown that these simple structural models give a good account of the turbulent flows.

Papadopoulos, G. and W. M. Pitts (1998). "Scaling the near-field centerline mixing behavior of axisymmetric turbulent jets." AIAA Journal **36**(9): 1635-42.

Detailed measurements of the centerline mixing behavior in the near field of variable-density jets were performed. Real-time measurements of jet fluid concentration for a propane jet and a methane jet issuing into still air were made utilizing Rayleigh light scattering. The initial conditions were those of fully developed pipe flow, and testing was done for flow rates yielding Reynolds numbers in the range of $3.3x10^3$ - $2.3x10^4$, based on the average discharge velocity, exit diameter, and initial fluid properties. Centerline decay characteristics in the near field exhibited a downstream shift with increasing Reynolds number, which was attributed to the initial velocity distribution at the jet exit. Investigation of the mean and turbulent characteristics of the initial velocity distribution yielded a proposed near-field scale variable that effectively captured this dependence on Reynolds number. Collapse of the near-field centerline velocity and concentration distributions was achieved using the proposed scaling

Papadopoulos, G. and W. M. Pitts (1999). "Generic centerline velocity decay curve for initially turbulent axisymmetric jets." Journal of Fluids Engineering, Transactions of the ASME **121**(1): 80-85.

Recently the authors introduced a length scale which effectively collapsed the near field centerline development of velocity and mass fraction for variable density axisymmetric jets whose initial conditions correspond to those of fully developed turbulent pipe flow. The new length scale incorporated the initial mass, momentum, and turbulence intensity per unit area to capture the Reynolds number dependence of near field development for the velocity and scalar distributions observed in low Reynolds number turbulent jets. The present paper extends the analysis for a constant density jet to the intermediate and self-similar far fields

further downstream using a dynamic length scale based on the local centerline turbulence intensity. The normalized mean velocity distributions of an air jet collapse over the entire flow distance investigated when the axial distance is normalized by the proposed length scale, thus scaling the virtual origin shift and effectively incorporating the Reynolds number dependence.

Parekh, D. E. (1988). Bifurcating Jets at High Reynolds Numbers. Mechanical Engineering, Stanford. **Ph. D.**

This work focuses on the use of dual-mode acoustic forcing to alter the structure of round turbulent jets. Properly combined axial and helical excitation can cause a round jet to split into two distinct jets. This Y-shaped jet is known as a "bifurcating jet", and exhibits spreading angles as high as 80°. A vortex filament code was written which simulated the large scale features of the bifurcating jet. The simulation showed that inviscid vortex interactions cause the dramatic changes in jet development and that the spreading angle increases with axial Strouhal number. The major conclusions are that dual mode (axial and helical) acoustic excitation can produce bifurcated jets at high Reynolds numbers and that the jet spreading angle increases with both excitation amplitudes. Furthermore, the excitation level needed to create the bifurcation increases with Reynolds number, but the corresponding excitation Strouhal number is invariant.

Parekh, D. E., V. Kibens, et al. (1996). Innovative Jet Flow Control - Mixing Enhancement Experiments. 34th Aerospace Sciences Meeting and Exhibit. Reno, NV, AIAA.

This work uses a technique for injecting high-frequency and high-intensity signals into subsonic and supersonic shear layers for the purpose of jet mixing enhancement. Based on previous work in low-speed flows, a family of novel piezoelectric excitation devices was developed for the active control of shear layers. The effects of these devices on high-aspect-ratio rectangular jets were investigated for subsonic and supersonic jet Mach numbers up to M = 1.1. Additionally, mixing enhancement by a family of pulsed fluidic actuators is demonstrated and characterized in subsonic axisymmetric jets. Measurements included schlieren visualization, near- and far-field acoustic surveys, and evaluation of mixing effectiveness using pressure-probe surveys.

Park, K. A., Y. M. Choi, et al. (2001). "The evaluation of critical pressure ratios of sonic nozzles at low Reynolds numbers." Flow Measurement and Instrumentation **12**(1): 37-41.

A sonic nozzle is presently used as a reference flow-meter in the area of gas flow-rate measurement. The critical pressure ratio of the sonic nozzle is an important factor in maintaining its operating condition. ISO 9300 suggested that the critical ratio of a sonic nozzle should be a function of area ratio. In this study, 13 nozzles designed according to ISO 9300, with diffuser half angles of 2º-8º and throat diameters of 0.28 to 4.48 mm were tested. The testing result for the angles of 2º-6º are similar to that of ISO 9300. But the critical ratio for the nozzle of 8° decreases by 5.5% in comparison with ISO 9300. However, ISO 9300 does not predict the critical pressure ratio at Reynolds numbers lower than 10^5. To express

the critical pressure ratio of sonic nozzles at low Reynolds numbers, it is found that the critical pressure ratio should be related as a function of Reynolds number rather than area ratio, as used by ISO 9300. A correlated relation of critical pressure ratios and low Reynolds numbers for small sonic nozzles is suggested in this investigation, with an uncertainty of ±3.2% at 95% confidence level.

Paschereit, C. O., E. Gutmark, et al. (1999). "Coherent structures in swirling flows and their role in acoustic combustion control." Physics of Fluids **11**(9): 2667-2678.

Interaction between flow instabilities and acoustic resonant modes and their effect on heat release were investigated and controlled in an experimental low-emission swirl stabilized combustor. Acoustic boundary conditions of the combustor were modified to excite combustion instability at various axisymmetric and helical unstable modes in a fully premixed combustion. Closed loop active control system was employed to suppress the thermoacoustic pressure oscillations and to reduce NO_x emissions. Effective suppression of the pressure oscillations and the concomitant reduction of NO_x emissions were associated with a reduced coherence of the flow structures which excited the thermoacoustic instability.

Raman, G. (1997). "Using controlled unsteady fluid mass addition to enhance jet mixing." AIAA Journal **35**(4): 647.

A rectangular jet was excited by controlled unsteady fluid mass addition using two miniature fluidic jets placed on either side of its narrow dimension. The subharmonic of the primary's preferred jet column frequency [$St_{De} = fDe/U_j = 0.15$] was forced in the antisymmetric mode because such forcing persists for longer downstream distances than the fundamental. Details of the phase-averaged flowfield, velocity gradient terms, velocity spectra, and the mean and fluctuating flowfields were documented. The fluidically excited mode grew and persisted in the flow beyond the potential core region. Unsteady fluid mass addition of 12% (4% momentum addition) per fluidic jet resulted in a 35% reduction of the potential core length and about a 60% increase in the normalized mass flux (percentages are with reference to the primary unforced jet). On the basis of the results, it appears that fluidic devices have the potential for use in shear flow control applications

Raman, G., M. Hailye, et al. (1993). "Flip-flop jet nozzle extended to supersonic flows." AIAA Journal **31**(6): 1028.

An experiment studying a fluidically oscillated rectangular jet flow was conducted. The Mach number was varied over a range from low subsonic to supersonic. Unsteady velocity and pressure measurements were made using hot wires, piezoresistive pressure transducers, and pitot probes. In addition, smoke flow visualization using high-speed photography was used to document the oscillation of the jet. For the subsonic flip-flop jet, it was found that the apparent time-mean widening of the jet was not accompanied by an increase in the mass flux. Fluidically oscillated jets up to a Mach number of about 0.5 have been reported before, but to the authors' knowledge there is no information on fluidically oscillated supersonic jets. It was found that it is possible to extend the

operation of these devices to supersonic flows. The streamwise velocity perturbation levels produced by this device were much higher than the perturbation levels that could be produced using conventional excitation sources such as acoustic drivers. In view of this ability to produce high amplitudes, the potential for using a small-scale fluidically oscillated jet as an unsteady excitation source for the control of shear flows in full-scale practical applications seems promising

Raman, G., A. Mills, et al. (2004). "Development of powered resonance-tube actuators for aircraft flow control applications." Journal of Aircraft **41**(6): 1306-1314.

The present paper addresses both active-flow-control actuator technology development and the demonstration of the effectiveness of actuators that could be easily integrated into practical aircraft applications. The actuator used is an adaptation of the Hartmann oscillator. Demonstration experiments that illustrate the effectiveness of this actuator include cavity tone suppression at transonic speeds and the reduction of jet-impingement tones. The actuator concept is based on a high-speed jet aimed at the mouth of a cylindrical tube closed at the other end. The result is a high-amplitude self-sustaining fluctuating field accompanied by an intense narrowband tone, all in the region between the supply jet and the resonance tube. Using unsteady pressure sensors and flow visualization, we explored the effect of varying actuator parameters such as the spacing between the power jet and the resonance tube, supply pressure, resonance-tube depth, diameter, shape, and lateral spacing. By varying the depth of the tube, the frequency could be varied from about 1.6 kHz to over 10 kHz and amplitudes as high as 156 dB (microphone location dependent) were obtained in the vicinity of actuation. To integrate this concept into practical aircraft applications, two generations of a more complex version of this device known as the powered resonance-tube bank (PRTB) were developed and demonstrated. Results indicate that by using high-frequency excitation at 5-kHz suppression levels in excess of 20 dB were consistently obtained over a range of operating conditions in both cavity and impingement flow situations. Based on our results, we have grounds to believe that a properly designed PRTB has significant advantages over conventional actuators such as acoustic, piezo, and oscillatory microstructures.

Raman, G. and E. J. Rice (1991). "Axisymmetric jet forced by fundamental and subharmonic tones." AIAA Journal **29**(7): 1114.

A circular jet was excited simultaneously by two harmonically related tones. The results of this excitation on jet behavior are reported for three pairs of Strouhal numbers [$St(D) = fD/U_j = 0.2$ and 0.4, 0.3 and 0.6, 0.4 and 0.8]. For each case, the initial phase difference between the two tones was varied in steps of 45 deg for one full cycle, and the amplitude of the fundamental and subharmonic tones was varied independently over the range of 0.1-7.0% of the jet exit velocity. Several results of this study agreed with other published findings, such as a critical amplitude of the fundamental being required for subharmonic augmentation and the initial phase difference being critical in determining whether the subharmonic is augmented or suppressed. In addition, the detailed documentation of several

aspects of this phenomenon, measured in the same experimental facility in a controlled manner, brought out two important points that had eluded previous researchers. First, at high levels of the fundamental and subharmonic forcing amplitudes, the subharmonic augmentation is independent of the initial phase difference. Second, two-frequency excitation is indeed more effective than single-frequency excitation in jet mixing enhancement. Higher spreading rates seem to go along with higher subharmonic levels.

Raman, G., E. J. Rice, et al. (1991). An experimental study of natural and forced modes in an axisymmetric jet, Case Western Reserve Univ. **Ph. D.**

The experiment consisted of two parts. The first part was an effort to study naturally occurring instability modes in the axisymmetric shear layer of a high Reynolds number turbulent jet. Untripped (transitional) and tripped (turbulent) nozzle exit conditions, both with 0.1 percent core turbulence, were studied. For the turbulent nozzle exit boundary layer case, the core turbulence was varied systematically from 0.1 to 5 percent of the jet exit velocity. The region up to the end of the potential core was dominated by the axisymmetric mode. The azimuthal modes grew rapidly but dominated only downstream of the potential core region. For the jet excited by natural disturbances, the energy content of the higher order modes (m is less than 1) was significantly lower than that of the axisymmetric and m = +/-1 modes. The initial boundary layer had a profound effect on the natural jet evolution and its excitability. The shorter potential core allowed the jet in the transitional case to support helical disturbances closer the nozzle exit than the turbulent case. The natural jet evolution was found to remain unaffected for varying initial core turbulence over the range of 0.15 to 5 percent of the jet velocity. Target modes for efficient excitation of the jet were determined from the results of the naturally occurring jet instability mode experiments. The second part of this work describes an effort to control the axisymmetric shear layer by artificially exciting target modes. Under optimum conditions, two-frequency excitation is indeed more effective than single frequency plane wave excitation as far as jet mixing is concerned. At high amplitudes of fundamental and subharmonic forcing, the subharmonic augmentation and the axial location of the peak were independent of the initial phase difference. Two-frequency excitation also has its limitations, since axisymmetric waves are damped beyond the potential core. Higher spreading rates are obtained when multi-modal forcing is applied.

Ramaprian, B. R. and S. W. Tu (1983). "Fully Developed Periodic Turbulent Pipe Flow. Part 2. The Detailed Structure of the Flow." Journal of Fluid Mechanics **137**: 59-81.

Experimental data reported in Part 1 of this paper are examined in greater detail to understand the effect of imposed oscillation on the flow structure, at moderate to large oscillation frequencies. Data on phase and amplitude and energy spectrum are used to study the effect of the imposed oscillation on the turbulence structure at these interactive frequencies of oscillation. Additional experiments which were performed to study the effect of oscillation frequency on the flow structure are also reported. Based on the present observations as well as on the data from other

sources, it is inferred that turbulent shear flows respond very differently from laminar shear flows to imposed unsteadiness. A turbulent Stokes number relevant for characterizing the unsteady turbulent shear flows is identified and used to classify such flows.

Reynolds, W. C., D. E. Parekh, et al. (2003). "Bifurcating and blooming jets." Annual Review of Fluid Mechanics **35**: 295.

It is classically assumed that the far field of a round turbulent jet discharging into quiescent fluid has a unique behavior characterized only by its momentum flux. However, there is now considerable evidence that different discharge conditions at the jet nozzle exit can give rise to very different far-field flows. Perhaps the most striking examples of these are the bifurcating and blooming jets produced by appropriate combinations of controlled axial and circumferential excitations at the nozzle exit. With the right excitations, a jet can be made to divide into two separate jets (bifurcating jet), each of which carries half the axial momentum and spreads in a manner similar to a single jet. Trifurcating jets can also be produced. Other excitations can produce blooming jets, in which the jet explodes into a shower of vortex rings, producing a far-field flow that is quite unlike a normal unexcited jet. Bifurcating and blooming jets exhibit much greater mixing than normal jets, suggesting possible applications in flow control. This article summarizes our work on bifurcating and blooming jets, which began with our discovery of them in the early 1980s and continued through the mid-1990s. One of us (D.E.P.) continued exploration of flow control using excited jets, first at the McDonnell Douglas Corporation, and more recently at the Georgia Institute of Technology. The key to flow control is the manipulation of the large vortical structures in the near field of the jet. Ultimately this work, and that of others, led to full-scale testing of jet engine exhaust mixing control. There it was shown that the jet temperature downstream of the engine can be very significantly reduced by application of well-designed and easily implemented excitation at the engine discharge, thereby solving problems encountered during ground operations. Related jet control work by other investigators is included in this review.

Ritchie, B. D. (2006). Quantitative Acetone Plif Measurements Of Jet Mixing With Synthetic Jet Actuators. Aerospace Engineering. Atlanta, GA, Georgia Institute of Technology. **Ph. D**.

Fuel-air mixing enhancement in axisymmetric jets using an array of synthetic jet actuators around the perimeter of the flows (primarily parallel to the flow axis) was investigated using planar laser-induced fluorescence of acetone. Both a single jet and coaxial jets were tested, including different velocity ratios for the coaxial jets. The actuators generated small-scale structures in the outer (and inner, for the coaxial jets) mixing layers. These structures significantly enhanced the mixing in the near field ($x/D < 1$) of the jets, which would be useful for correcting an off-design condition in a combustor. The amplitude modulation generated large-scale structures that became apparent farther downstream ($x/D > 1$). The impulse at the start of the duty cycle was responsible for creating the structures. The large structures contained broad regions of uniformly mixed fluid,

and also entrained fluid significantly. In addition, highly asymmetric forcing geometries displayed the power of the actuators to control the spatial distribution of jet fluid. This spatial control is important for the correction of hot spots in the pattern factor.

Rossi, M., Ed. (2000). Lecture Notes in Physics: Of Vortices and Vortical Layers - An Overview. Vortex Structure and Dynamics, Springer.

A theoretical overview of local flow models such as hyperbolic point flows or localized vorticity structures is presented. Vortex layers and tubes are particularly emphasized. Various exact Navier-Stokes or Euler solutions are introduced to analyze generic features of vorticity dynamics: vorticity gradients, vorticity stretching, interplay between axial and azimuthal vorticity, effect of a large scale strain rate or the existence of a helical symmetry. The linear stability of some of these basic flows is considered.

Samet, M. M. and R. A. Petersen (1988). "Effects of excitation level on the stability of an axisymmetric mixing layer." Physics of Fluids **31**(11): 3246-3252.

The effect of various levels of excitation on the stability and development of an axisymmetric mixing layer was studied experimentally. The flow was excited axisymmetrically by a single speaker placed at the base of the plenum chamber. Measurements of mean and phase-averaged velocity profiles were made using an array of hot-wire probes. The measured profiles were compared to eigenfunctions calculated from linear, viscous stability theory. It is shown that the theoretical predictions, based on measured profiles of mean velocity, compare very well with the phase-averaged measurements, even when the local disturbance reaches levels as high as 24% of the jet speed. The cumulative effect of excitation on the mean flow is examined as a function of local Strouhal number as well as excitation level.

Sanger, J. L. and P. A. Dellenback (1998). "Heat Transfer in Counterswirled Coaxial Jet Mixing." Journal of Propulsion and Power **14**(3): 384-391.

Convective heat transfer data are presented for the mixing of two counterswirled coaxial jets confined by a constant-diameter tube. The inner jet Reynolds number was $3x10^4$, its swirl number was 1, and its diameter was approximately twice the annular gap dimension. Annular jet swirl numbers varied from 0 to 1.2. Annular flow rates were characterized by a ratio of annular-to-inner jet axial momentum (denoted by MFR), which was varied from 0 to 8.2. Plots of local Nusselt numbers show minimums and maximums corresponding to the separation and reattachment points associated with wall-bounded recirculation cells. Local heat transfer coefficients were found to be a strong function of streamwise position and annular swirl number at low values of MFR, yet at high values of MFR, there is minimal streamwise variation in heat transfer coefficient as the mean flow largely dictates heat transfer rates. The product of MFR and annular swirl number is shown to be a key parameter in describing heat transfer enhancement downstream of wall-bounded recirculation cells. Several quantitative results should be useful to gas turbine combustor design efforts.

Smith, B. L. and A. Glezer (1997). Vectoring and small-scale motions effected in free shear flows using synthetic jet actuators. 35th Aerospace Sciences Meeting and Exhibit. Reno, NV, AIAA.

Novel fluidic actuators based on synthetic jet technology are used to effect thrust vectoring and manipulate small-scale motions in conventional air jets. Synthetic jets operate without net mass injection (and thus are comprised entirely of entrained fluid), have finite streamwise momentum, and are synthesized by the time-harmonic formation of a train of two-dimensional vortices at the edge of a sharp orifice. In the present experiments, millimeter-scale high aspect ratio actuator jets are placed along the long sides and near the exit plane of a primary rectangular jet scaling one to two orders of magnitude larger. The primary jet can be vectored either towards or away from the actuator jets at angles exceeding 30 deg (and 80 deg when pairs of actuator jets are operated in concert). The actuation frequency is at least an order of magnitude higher than the unstable frequency of the primary jet and thus results in direct excitation of small scale motions and enhanced turbulent dissipation.

Smith, B. L., M. A. Trautman, et al. (1999). Controlled interactions of adjacent synthetic jets. AIAA, Aerospace Sciences Meeting and Exhibit, 37th. Reno, NV.

The formation, evolution and interactions of coflowing pairs of plane synthetic jets that are mounted in a flat plate such that they are parallel along the long dimension of their orifices is investigated, using particle image velocimetry (PIV). Each of these zero net mass flux jets are synthesized by a train of vortices that are formed at the edge of the jet orifice and are driven by the motion of a diaphragm mounted on the wall of a sealed cavity under the orifice plate. The strong entrainment of ambient fluid that is induced near the flow orifice by the jet formation is exploited for dynamic vectoring of adjacent jets by varying the relative phase of their driving waveforms. The direction of the ensuing merged jet is affected by the pressure field near the exit plane and by the interaction of the adjacent vortex pairs.

Smith, D. R., M. Amitay, et al. (1998). Modification of lifting body aerodynamics using synthetic jet actuators. AIAA, Aerospace Sciences Meeting & Exhibit, 36th. Reno, NV, AIAA.

The control of separated flow on an unconventional airfoil using synthetic jet actuators was investigated experimentally. A symmetric airfoil based on the aft portion of a NACA four-digit series airfoil with a cylindrical leading edge was used in the experiment. The tests were conducted at Re(c) of 3×10^5. For alpha not less than 5 deg, the flow separated from the airfoil surface. Applying synthetic jet control near the leading edge, upstream of the separation point, reattached the separated flow for angle of attack up to 18 deg. The effect of control location and amplitude was investigated for different angles of attack. Hot wire measurements in the near-wake of the airfoil revealed a transient passing of vortices associated with the transition from separated to reattached flow on the airfoil.

Smith, S. H. and M. G. Mungal (1998). "Mixing, structure and scaling of the jet in crossflow." Journal of Fluid Mechanics **357**: 83.

The mixing of the round jet normal to a uniform crossflow is studied for a range of jet-to-crossflow velocity ratios, r, from 5 to 25. Planar laser-induced fluorescence (PLIF) of acetone vapor seeded into the jet is used to acquire quantitative two-dimensional images of the scalar concentration field. Emphasis is placed on r=10 and r=20 and a few select images are acquired up to r=200. The Reynolds number based on the jet exit diameter, d, and the exit velocity varies from 8400 to 41500. Images are acquired for conditions in which the product rd is held constant, requiring decreasing d for increasing r. Results from this experimental study concern structural events of the vortex interaction region, and mixing and mean centerline concentration decay in the near and far fields. The results cover all three regions of the transverse jet, and suggest that the jet scales with three length scales: d, rd and r/sup 2/d. Events within the vortex interaction region display d-scaling, including the crossflow boundary layer separation and roll-up. Over the range of velocity ratios studied, the vortex interaction region shows r-dependent variations in the flow field, including the emergence of jet fluid in the wake structures for r>10 and a slower development of the counter-rotating vortex pair (CVP) in higher-r jets. The trajectory and physical dimension of the jet in both the near and far field display rd-scaling. The near field is characterized by a centerline concentration decay along the centerline coordinate s of $s^{-1.3}$, different from the decay rate (s^{-1}) of the free jet. When normalized by rd, the decay of each velocity-ratio jet branches away from the s/sup -1.3/ decay, approaching a decay of $s^{-2/3}$, a rate predicted by modeling efforts. The branch points represent a transition in the flow field from enhanced mixing to reduced mixing compared to the free jet. When normalized by r^2d, the branch points occur at a uniform jet position, $s/r^2d=0.3$, which is viewed to be the division between the near and far fields. Self-similarity is not seen in the near field, but may be present in the far field. The view of the branch points as a place of transition in the flow is supported by the probability density function (p.d.f.) of concentration along the upper edge of the jet. Before the branch points, the p.d.f.s. are non-marching in character, and after the branch points, they are tilted in character. Instantaneously, the CVP is asymmetric in shape and concentration. End views reveal extensive motion of the CVP and plan views show this motion can occur in both axisymmetric and sinusoidal motion. Ensemble-averaged images show the jet concentration is asymmetric about the centerline plane

Smith, T. D., A. B. Cain, et al. (2001). "Numerical simulation of enhanced mixing in jet plumes using pulsed blowing." Journal of Aircraft **38**(3): 458-463.

Pulsed jet blowing for mixing enhancement in a hot jet is examined using numerical simulation. Numerical simulations have been completed for a subscale turbojet engine, a full-scale ground demonstration case, and a high-bypass-ratio engine. These simulations have shown that pulsed jet blowing can significantly reduce jet plume potential core lengths at static and forward flight conditions. The numerical scheme uses large time-step implicit integration for efficiency and a second-order physical space algorithm for robustness. The pulsed jet disturbance

is calculated directly, and a turbulence model is employed to represent the cascade to smaller length scales. Experimental data corresponding to the numerical simulations are also presented and indicate similar benefits from pulsed jet mixing.

Smith, T. R., J. Moehlis, et al. (2005). "Low-dimensional modelling of turbulence using the proper orthogonal decomposition: A tutorial." Nonlinear Dynamics **41**(1-3): 275-307.

The proper orthogonal decomposition identifies basis functions or modes which optimally capture the average energy content from numerical or experimental data. By projecting the Navier-Stokes equations onto these modes and truncating, one can obtain low-dimensional ordinary differential equation models for fluid flows. In this paper we present a tutorial on the construction of such models. In addition to providing a general overview of the procedure, we describe two different ways to numerically calculate the modes, show how symmetry considerations can be exploited to simplify and understand them, comment on how parameter variations are captured naturally in such models, and describe a generalization of the procedure involving projection onto uncoupled modes that allow streamwise and cross-stream components to evolve independently. We illustrate for the example of plane Couette flow in a minimal flow unit - a domain whose spanwise and streamwise extent is just sufficient to maintain turbulence.

Stone, J. R. and D. J. McKinzie, Jr. (1984). Acoustic Excitation - A Promising New Means Of Controlling Shear Layers**:** 32.

Techniques have long been sought for the controlled modification of turbulent shear layers, such as in jets, wakes, boundary layers, and separated flows. Relatively recently published results of laboratory experiments have established that coherent structures exist within turbulent flows. These results indicate that even apparently chaotic flow fields can contain deterministic, nonrandom elements. Even more recently published results show that deliberate acoustic excitation of these coherent structures has a significant effect on the mixing characteristics of shear. A research effort was therefore initiated to develop both an understanding of the interaction mechanisms and the ability to use it to favorably modify various shear layers. Acoustic excitation circumvents the need for pumping significant flow rates, as required by suction or blowing. Control of flows by intentional excitation of natural flow instabilities involves new and largely unexplored phenomena and offers considerable potential for improving component performance. Nonintrusive techniques for flow field control may permit much more efficient, flexible propulsion systems and aircraft designs, including means of stall avoidance and recovery. The techniques developed may also find application in many other areas where mixing is important, such as reactors, continuous lasers, rocket engines, and fluidic devices.

Su, L. K. and M. G. Mungal (2004). "Simultaneous measurements of scalar and velocity field evolution in turbulent crossflowing jets." Journal of Fluid Mechanics **513**: 1-45.

Simultaneous planar laser-induced fluorescence (PLIF) and particle image velocimetry (PIV) yield measurements of two-dimensional jet fluid concentration

and velocity fields in turbulent crossflowing jets. The jet-to-crossflow velocity ratio is r = 5.7 and the jet exit Reynolds number is approximately 5000. The measurements are focused on the developing region of the flow. Two flow configurations are studied, one in which the jet nozzle is flush with the tunnel wall and the other where the nozzle protrudes into the uniform region of the tunnel flow. The jet nozzle in both cases is a simple pipe. The averaged scalar and velocity fields show a strong similarity in growth rates and centerline decay rates between the two nozzle configurations when using the centerline downstream coordinate s. This suggests that the flow geometry is less important than, for example, jet exit conditions in determining the initial flow development. The velocity fields show indications of jet-like scaling in the near field, and a possible approach to wake-like scaling in the far field. These canonical scalings are less evident in the scalar fields. Results are presented for the averaged scalar variance, $\langle C'^2 \rangle$, the scalar flux components, $\langle u'_i C' \rangle$, the turbulent normal stresses, u'^2; and v'^2, and the turbulent shear stress, u'v'. We also discuss the resolution issues bearing on the determination of small-scale fluctuations

Su, L. K. and M. G. Mungal (2005). Mixing in crossflowing jets: Turbulence quantities, Reno, NV, United States, American Institute of Aeronautics and Astronautics Inc., Reston, VA 20191, United States.

Simultaneous planar laser-induced fluorescence (PLIF) and particle image velocimetry (PIV) yield measurements of two-dimensional jet fluid concentration and velocity fields, both the mean and fluctuating terms, in turbulent crossflowing jets. The jet-to-crossflow velocity ratio is r = 5.7 and the jet exit Reynolds number is approximately 5000. The measurements concern the developing region of the flow. Two flow configurations are studied, one in which the jet nozzle is flush with the tunnel wall and the other where the nozzle protrudes into the uniform region of the tunnel flow. The jet nozzle in both cases is a simple pipe. Previous work focused on the averaged scalar and velocity fields. Here, we discuss the resolution issues bearing on the determination of small scale fluctuations, and present results for the averaged scalar variance, $\langle C'^2 \rangle$, the scalar flux components, $\langle u'_i C' \rangle$, the turbulent normal stresses, $\langle u'^2 \rangle$ and $\langle v'^2 \rangle$, and the turbulent shear stress, $\langle u'v' \rangle$. These results should prove particularly useful for assessment of crossflowing jet simulation efforts. The range of length scales spanned by the measurements also makes possible direct assessment of models and model assumptions used for scalar transport and mixing in large-eddy simulation (LES). Sample results demonstrate the use of the present data in these LES model assessments.

Tamburello, D. A. and M. Amitay (2006). Manipulation of an axisymmetric jet using a single perpendicular control jet, San Francisco, CA, United States, American Institute of Aeronautics and Astronautics Inc., Reston, VA 20191, United States.

The mechanisms associated with the interaction of an axisymmetric free jet (Re_{Ue} = 6,600 and 26,500) and a single continuous control jet (perpendicular to the main jet) on mixing, spreading, and direction were examined experimentally. The flow field was measured using PIV in two planes, along and across the control jet's line

of action. The interaction of the main jet with the control jet was investigated for different momentum coefficients, upstream locations of the control jet (i.e., within the main jet nozzle), and Reynolds numbers. When the control jet is located near the main jet exit plane ($t_c/d_e = 0.4$), the main jet is vectored away from the control jet, while, with the control jet located farther upstream from the main jet exit ($t_c/d_e = 1.15$), the main jet is drawn back toward the control jet. A plausible mechanism for this behavior is provided in the paper, where it is speculated that when the control is applied farther upstream (i.e., into the nozzle) the flow is drawn back toward the control jet due to a virtual modification of the nozzle shape. Furthermore, the direction of the main jet can also be controlled by the momentum coefficient of the control jet at a fixed t_c/d_e. The data suggest that there are two competing mechanisms that affect the main jet vectoring: (1) the momentum from the control jet that pushed the main jet away from the control jet, and (2) the nozzle shape modification that causes the flow to vector towards the control jet side. Finally, the effectiveness of the control jet in altering the main jet flow was found to be more pronounced when the interaction occurs at lower Reynolds numbers.

Taylor, B. N. and C. E. Kuyatt (1994). Guidelines for Evaluating and Expressing the Uncertainty of NIST Measurement Results, NIST**:** 24.

This technical note serves as a guide on how to express measurement uncertainty. It is based on the approach developed by the International Committee for Weights and Measures.

Tu, S. W. and B. R. Ramaprian (1983). "Fully Developed Periodic Turbulent Pipe Flow. Part 1. Main Experimental Results And Comparison With Predictions." Journal of Fluid Mechanics **137**: 31-58.

Experimental data on instantaneous velocity and wall shear stress were obtained at a mean Reynolds number of 50,000 in a fully developed turbulent pipe flow in which the volumetric flow rate was varied sinusoidally with time around the mean. Two oscillation frequencies at significant levels of flow modulation were studied in detail. The present paper contains the main experimental results and comparisons of these results with the results of a numerical calculation procedure which employs a well-known quasi-steady turbulence closure model. The experimental data are used to study the manner in which the time-mean, the ensemble-averaged and the random flow properties are influenced by flow oscillation at moderate to high frequencies. In addition, the data are also used to bring out the capability and limitations of quasi-steady turbulence modeling in the prediction of unsteady shear flows.

Utami, T., R. F. Blackwelder, et al. (1991). "A cross-correlation technique for velocity field extraction from particulate visualization." Experiments in Fluids **V10**(4): 213-223.

A rapid time series of photographs of the horizontal cross-sections of several y + locations were taken of a turbulent open-channel water flow with Re d = 3,900. A pair of photographic images were obtained with a time difference of 1.3 v/u tau 2 at each y + locations. The pictures were digitized into 8 bit data with a spatial

resolution of 2.5 viscous scales. Instead of identifying discrete particles, a variable interval spatial correlation technique was used to extract the velocity components. With this technique, two-dimensional spatial cross-correlations of the illumination intensities were taken between a pair of picture images. The correlations were taken over small areas and the peak of the correlation coefficients were used to obtain the convection velocity yielding the u and w components of velocity. Some statistical properties were calculated and are shown to be comparable with previous data. Spatial correlations of the velocity components revealed some unique characteristics related to the structure of turbulence.

Van Rensburg, P. J. S., I.S. Van Wyk, J.D. (1998). Adaptive PID control using a genetic algorithm. Second International Conference on Knowledge-Based Intelligent Electronic Systems, Adelaide, SA, Australia, IEEE.

Plant parameters change mostly due to ageing of the plant or changes in the load. This means that PID constants are no longer optimal and need to be updated. The paper describes how a genetic algorithm could be used to update PID constants so that optimal control could be maintained.

Viets, H. (1975). "Flip-flop jet nozzle." AIAA Journal **13**(10): 1375.

A nozzle development program was undertaken to produce a time-dependent flow at the nozzle exit. The oscillatory character of the flow was achieved without the use of moving parts by incorporating a fluidic feedback loop into the nozzle design. The nozzle thrust efficiencies approached 90% and the half-width spreading rates attained exceeded that of the slot nozzle by a factor of more than three

von Glahn, U., J. Goodykoontz, et al. (1986). Velocity And Temperature Decay Characteristics Of Inverted-Profile Jets, Reno, NV, USA, AIAA, New York, NY, USA.

In order to design efficient, lightweight flap systems for future engine under-the-wing STOL aircraft, the velocity and temperature decay rate of the jet plume must be increased relative to that for single-stream nozzles in order to provide local flap loads and structural temperatures within acceptable limits. The jet plume decay rate of dual flow engines can be increased by resorting to inverted-profile velocity and temperature nozzle concepts. In the present paper, the peak axial decay characteristics of model-scale, two-stream inverted-profile nozzle flows are empirically correlated. Also discussed are the radial and spreading characteristics of inverted-profile nozzle flows.

von Glahn, U. H. (1983). "Correlation Of Flight Effects On Centerline Velocity Decay For Cold-Flow Acoustically Excited Jets." NASA Technical Memorandum: 16.

Acoustic excitation can influence the large-scale shear layer structure of jet flow, thereby causing the jet centerline velocity to decay more rapidly. This phenomenon has numerous practical applications, such as the reduction of jet/flap impingement velocity in order to reduce flap structural loads for under-the-wing STOL aircraft concepts. In the present paper, cold-flow centerline velocity decay data obtained with acoustic excitation of the jet exhaust flow are correlated with

and without flight effects. Initially, static data are correlated in terms of a new acoustic parameter involving the threshold sound level needed to initiate acoustic excitation of the jet plume. It is shown that for a given flight speed, the same acoustic excitation parameter as that developed for the static condition is valid. Finally, an aerodynamic flight effects parameter is included to correlate the static and flight centerline velocity decay data with and without acoustic excitation.

von Glahn, U. H. (1984). On Some Flow Characteristics Of Conventional And Excited Jets. Aerospace Sci. Meeting, Reno, NV, USA, AIAA, New York, NY, USA.

Improved correlations of jet centerline velocity and static temperature decay data for convergent nozzles are developed. From these empirical correlations, a relationship was devised by which the static temperature decay for a nonisothermal jet plume can be determined from cold-flow jet centerline velocity decay data or prediction. This relationship is shown to apply as well to jet plumes for various nozzle shapes. It is assumed, by analogy, that this relationship also applies to acoustically excited jet plumes. Jet plume spreading with and without excitation is discussed. Finally, the radial velocity and temperature profiles for conventional and enhanced mixing jet flows are shown and their implication for excited flows is discussed.

von Glahn, U. H. (1987). Two-Dimensional Nozzle Plume Characteristics**:** 21.

Future high performance aircraft will likely feature asymmetric or two-dimensional nozzles with or without ejectors. In order to design two-dimensional nozzle/ejector systems of minimum size and weight, the plume decay and spreading characteristics of basic two-dimensional nozzles must first be established. The present work deals with the experimental analyses of these plume characteristics and includes the effects of nozzle aspect ratio and flow conditions (jet Mach number and temperature) on the plume decay and spreading of two-dimensional nozzles. Correlations including these variables are developed in a manner similar to those previously developed successfully for conic and dual-flow plumes.

von Lavante, E., A. Zachcial, et al. (2000). "Numerical and experimental investigation of unsteady effects in critical Venturi nozzles." Flow Measurement and Instrumentation **11**(4): 257-264.

A Venturi nozzle, operating mainly at critical conditions, and shaped according to the recommendation of the ISO Standard 9300, was selected for the present study. The flow in the nozzle was investigated numerically for a range of Reynolds numbers and backpressures. The results for one Reynolds number were validated experimentally, making a direct comparison between the numerical and experimental data possible. In the numerical part, the unsteady compressible viscous flow was simulated by Navier-Stokes solver ACHIEVE, developed by the authors. The experimental work employed flow visualization and accurate pressure measurements to analyze the flow. Significant unsteady phenomena were discovered, leading in some cases to a decrease in the average flow rate and fluctuating discharge coefficient C_D.

Watanabe, S. and M. G. Mungal (1999). Velocity field measurements of mixing-enhanced compressible shear layers 37th Aerospace Sciences Meeting and Exhibit. Reno, NV, AIAA.

Two-dimensional velocity fields of mixing enhanced compressible, planar shear layers are measured via PIV at convective Mach numbers, M_c, of 0.63 and 0.25 in order to investigate the mechanism of mixing enhancement by sub-boundary layer triangular disturbances. Instantaneous side- and plan-views are obtained, and turbulence quantities are derived from the data through an ensemble averaging. A schlieren investigation is also conducted to show global effects of the enhancement technique on the shear layer growth rate. The results show that at M_c= 0.63, streamwise velocity profile across the shear layer has double inflection points, while it has periodical inflection points in spanwise direction. A pair of counter-rotating streamwise vortices due to the disturbances are also observed. It is found that the enhanced case shows higher turbulent intensity and Reynolds at M_c = 0.63, suggesting mixing enhancement effects through a large momentum transportation. The schlieren results reveal the present mixing enhancement technique increases shear layer growth rate by 45% at M_c = 0.63 although it does not show a distinguishable growth rate increase in a far-field at M_c = 0.25.

Weitao, B., S. Yasuhiko, et al. (2003). "Time-resolved proper orthogonal decomposition of the near-field flow of a round jet measured by dynamic particle image velocimetry." Measurement Science & Technology **14**(8): 1-5.

In this study time-resolved proper orthogonal decomposition (POD) is proposed for the new technique of dynamic (digital) particle image velocimetry (DPIV), and applied to study the coherent structures at the near field of a round jet flow. Time-resolved POD is computed in the radial direction, the axial direction and the temporal domain, in which the turbulence can be easily measured by DPIV. As a result, large-scale vortical structures and their spatial and temporal evolution at the round jet mixing layer are uncovered

Wickersham, P. and D. Parekh (2001). Real-Time Optimization of Jet Mixing via Evolution Strategies. ASME Fluids Engineering Division Summer Meeting New Orleans, Louisiana, ASME.

This paper presents initial findings in the application of evolution strategies for real-time optimization of jet mixing enhancement. The experimental apparatus consists of a small-scale jet turbine and pulsed fluidic actuators operated under computer control. An optimization algorithm determines in real time the actuator frequency selected at each iteration based on minimizing the plume centerline temperature. This approach successfully determined an optimal actuator frequency that corresponds to the global minimum for the system without any a priori information about the flow or actuator characteristics. Additional results are presented that address robustness to noise and changes in plant conditions and convergence characteristics.

Willert, C. E. and M. Gharib (1991). "Digital particle image velocimetry." Experiments

in Fluids **V10**(4): 181-193.

Digital particle image velocimetry (DPIV) is the digital counterpart of conventional laser speckle velocimetry (LSV) and particle image velocimetry (PIV) techniques. In this novel, two-dimensional technique, digitally recorded video images are analyzed computationally, removing both the photographic and opto-mechanical processing steps inherent to PIV and LSV. The directional ambiguity generally associated with PIV and LSV is resolved by implementing local spatial cross-correlations between two sequential single-exposed particle images. The images are recorded at video rate (30 Hz or slower) which currently limits the application of the technique to low speed flows until digital, high resolution video systems with higher framing rates become more economically feasible. Sequential imaging makes it possible to study unsteady phenomena like the temporal evolution of a vortex ring described in this paper. The spatial velocity measurements are compared with data obtained by direct measurement of the separation of individual particle pairs. Recovered velocity data are used to compute the spatial and temporal vorticity distribution and the circulation of the vortex ring.

Wiltse, J. M. and A. Glezer (1993). "Manipulation of free shear flows using piezoelectric actuators." Journal of Fluid Mechanics **249**: 261.

An air jet emanating from a square conduit having an equivalent diameter of 4.34 cm and a centerline velocity of 4 m/s is forced using four resonantly driven piezoelectric actuators placed along the sides of the square exit. Excitation is effected via amplitude modulation of the resonant carrier waveform. The flow is normally receptive to time-harmonic excitation at the modulating frequency but not at the resonant frequency of the actuators. When the excitation amplitude is high enough, the excitation waveform is demodulated by a nonlinear process that is connected with the formation and coalescence of nominally spanwise vortices in the forced segments of the jet shear layer. As a result, the modulating and carrier wave trains undergo spatial amplification and attenuation, respectively, downstream of the exit plane. Strong instabilities of the jet column are excited when the jet is forced at phase relationships between actuators that correspond (to lowest order) to the azimuthal modes m = 0, ±1, ±2, and -1 of an axisymmetric flow. The streamwise velocity component is measured phase locked to the modulating signal in planes normal to the mean flow. Resonantly driving the actuators with different carrier amplitudes results in a distorted mean flow having a featureless spectrum that can be tailored to provide favorable conditions for the introduction and propagation of desirable low-frequency disturbances

Wiltse, J. M. and A. Glezer (1998). "Direct excitation of small-scale motions in free shear flows." Physics of Fluids **10**(8): 2026.

The conventional approach to small-scale mixing enhancement in free shear flows by the manipulation of global flow instabilities and the ensuing large-scale vortical structures depends on the classical cascading mechanism to transfer the control influence to the scales at which molecular mixing takes place. Thus the manipulation of mixing at the smallest scales is indirect and only weakly coupled

to the control input. The present work focuses on direct excitation of the small scales within the dissipation range of a free shear flow. This approach is demonstrated in a shear layer segment of an air jet emanating from a square conduit. The flow is forced at a frequency that is approximately an order of magnitude lower than the passage frequency of eddies at the Kolmogorov scale using cantilevered piezoelectric actuators. Cross-stream distributions of the streamwise velocity component are measured at a number of streamwise stations downstream of the actuator using hot wire anemometry. Direct small scale excitation results in enhanced energy transfer from the large to the small scales and in a substantial increase in the dissipation and in the decay rate of turbulent kinetic energy

Winant, C. D. and F. K. Browand (1974). "Vortex pairing: the mechanism of turbulent mixing-layer growth at moderate Reynolds number." Journal of Fluid Mechanics **63**(pt.2): 237.

A mixing layer is formed by bringing two streams of water, moving at different velocities, together in a lucite-walled channel. The Reynolds number, based on the velocity difference and the thickness of the shear layer, varies from about 45, where the shear layer originates, to about 850 at a distance of 50 cm. Dye is injected between the two streams just before they are brought together, marking the vorticity-carrying fluid. Unstable waves grow, and fluid is observed to roll up into discrete two-dimensional vortical structures. These turbulent vortices interact by rolling around each other, and a single vortical structure, with approximately twice the spacing of the former vortices, is formed. This pairing process is observed to occur repeatedly, controlling the growth of the mixing layer

Wygnanski, I. and R. A. Petersen (1985). Coherent Motion in Excited Free Shear Flows. AIAA Shear Flow Control Conference. Boulder, CO, AIAA.

Coherent structures in classical turbulent shear flows are viewed as manifestations of the Rayleigh instability. All of these flows (jets, wakes, and mixing layers) can therefore be treated theoretically in the same manner. A predictive model for highly excited flow is outlined and some of its implications are discussed. Prevailing concepts like "vortex pairing" in the mixing layer or "preferred mode" in the core of the jet are viewed as heuristic alternate descriptions of the observed phenomena.

Yuan, C. C. L., M. Krstic, et al. (2004). "Active control of jet mixing." IEE Proceedings-Control Theory and Applications **151**(6): 763-72.

A control law to improve jet flow mixing is presented. The control law employs a pair of actuators at the jet nozzle exit that act on the shear layers near the corners by blowing and subtracting fluid in an anti-symmetric fashion and a sensor downstream or at the nozzle exit with a time delay that measures the pressure difference across the nozzle diameter. A 2-D jet flow is numerically simulated along with massless/mass particles and a passive scalar. The mixing enhancement produced by these controllers is demonstrated visually by snapshots of the vorticity, streaklines, particle distribution and scalar field. Probability function for

the particles and the scalar field are constructed, which serve as an index of mixing quality and the effectiveness of the controllers. This closed-loop control law successfully alters the jet flow and improves the mixing of particles with mass and passive scalar

Zaman, K. B. M. Q. and A. K. M. F. Hussain (1980). "Vortex pairing in a circular jet under controlled excitation. I. General jet response." Journal of Fluid Mechanics **101**(pt.3): 449.

Hot-wire and flow-visualization studies have been carried out in three air jets subjected to pure-tone acoustic excitation, and the instability, vortex roll-up and transition as well as jet response to the controlled excitation have been investigated. The centre-line fluctuation intensity can be enhanced by inducing stable vortex pairing to a level much higher than even that at the `preferred mode', but can also be suppressed below the unexcited level under certain conditions of excitation. The conditions most favorable to vortex pairing were determined as a function of the excitation Strouhal number, the Reynolds number (Re_D), and the initial shear-layer state, i.e. laminar or turbulent. It is shown that the rolled up vortex rings undergo pairing under two distinct conditions of excitation: the shear layer mode and the jet column mode

APPENDIX B

ACTUATOR MECHANICAL DRAWINGS

Overview

The actuators used on the small scale jet and the small jet engine were designed and built by GTRI. Each small scale actuator consisted of a fast acting solenoid valve, a pipe adapter, a diffuser, and a nozzle. The two actuators for the jet engine were rotary type actuators driven by DC servomotors. The mechanical drawings used to construct and assemble both types of actuators are given in this appendix. The following table lists the drawings in the order they appear.

Small Scale Actuators		Jet Engine Actuators	
DWG #	**Drawing Name**	**DWG #**	**Drawing Name**
1	Large Actuator Diffuser	1	Slotted Rotor
2	Large Actuator Diffuser Cover Plate	2	Rotor Housing
3	Large Actuator Nozzles	3	Housing to Motor Coupling
4	Small Actuator Diffuser	4	Coupling Adaptor
5	Small Actuator Diffuser Cover Plate	5	Motor Adaptor
6	Small Actuator Nozzles	6	Air Feed Plate
7	Diffuser to Pipe Adapter	7	Nozzle
8	Actuator Test Stand Assembly	8	Center Body
9	Actuator Test Stand Mounting Ring	9	Center Body Shims
10	Actuator Test Stand Bottom Plate	10	Fixed Actuator Mounting Bracket
11	Actuator Test Stand Ring Support	11	Sliding Actuator Mounting Bracket
		12	Actuator Assembly
		13	Actuator Mounting

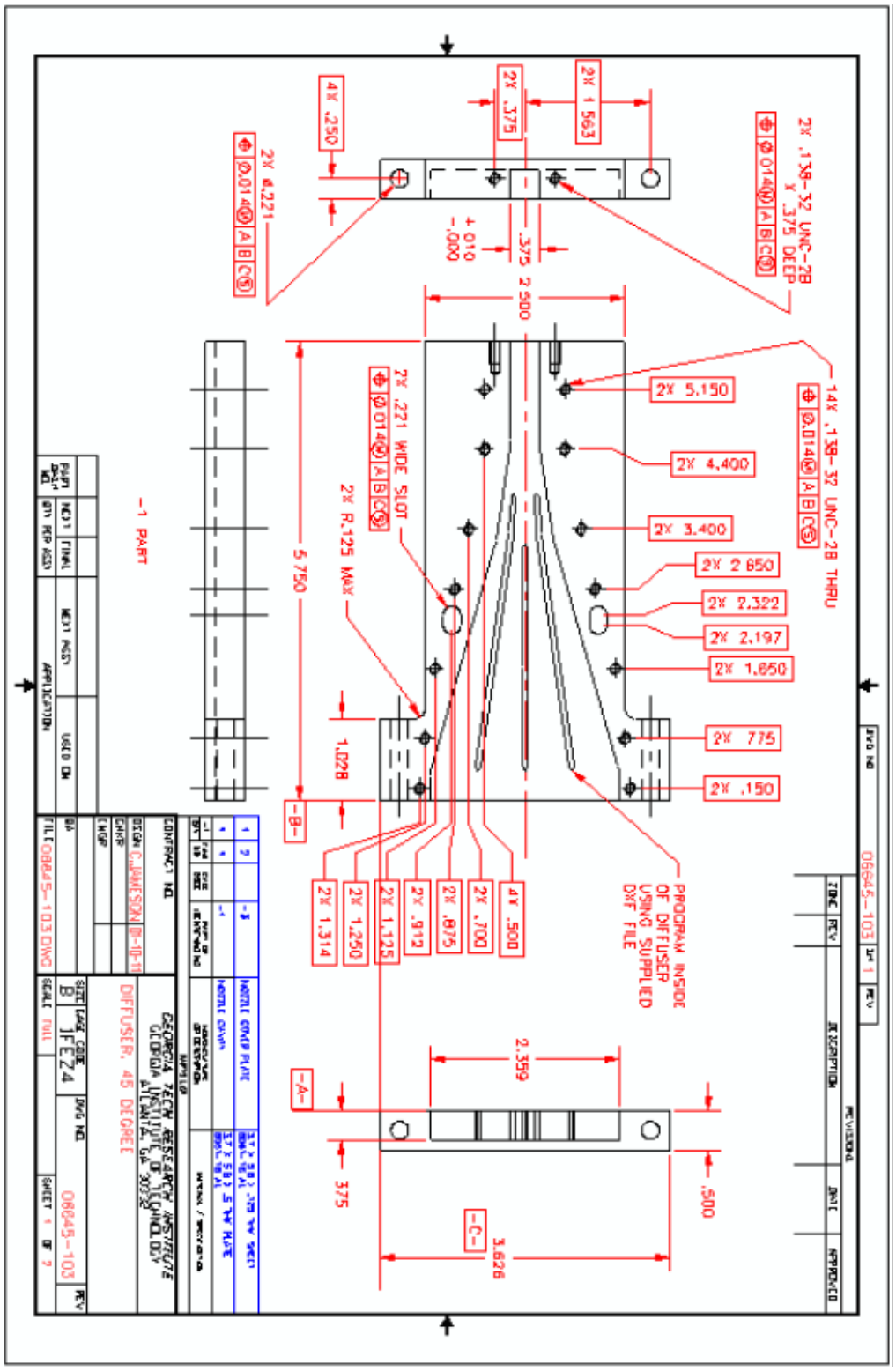

Figure A.1: Small Scale Jet, Large Actuator Diffuser

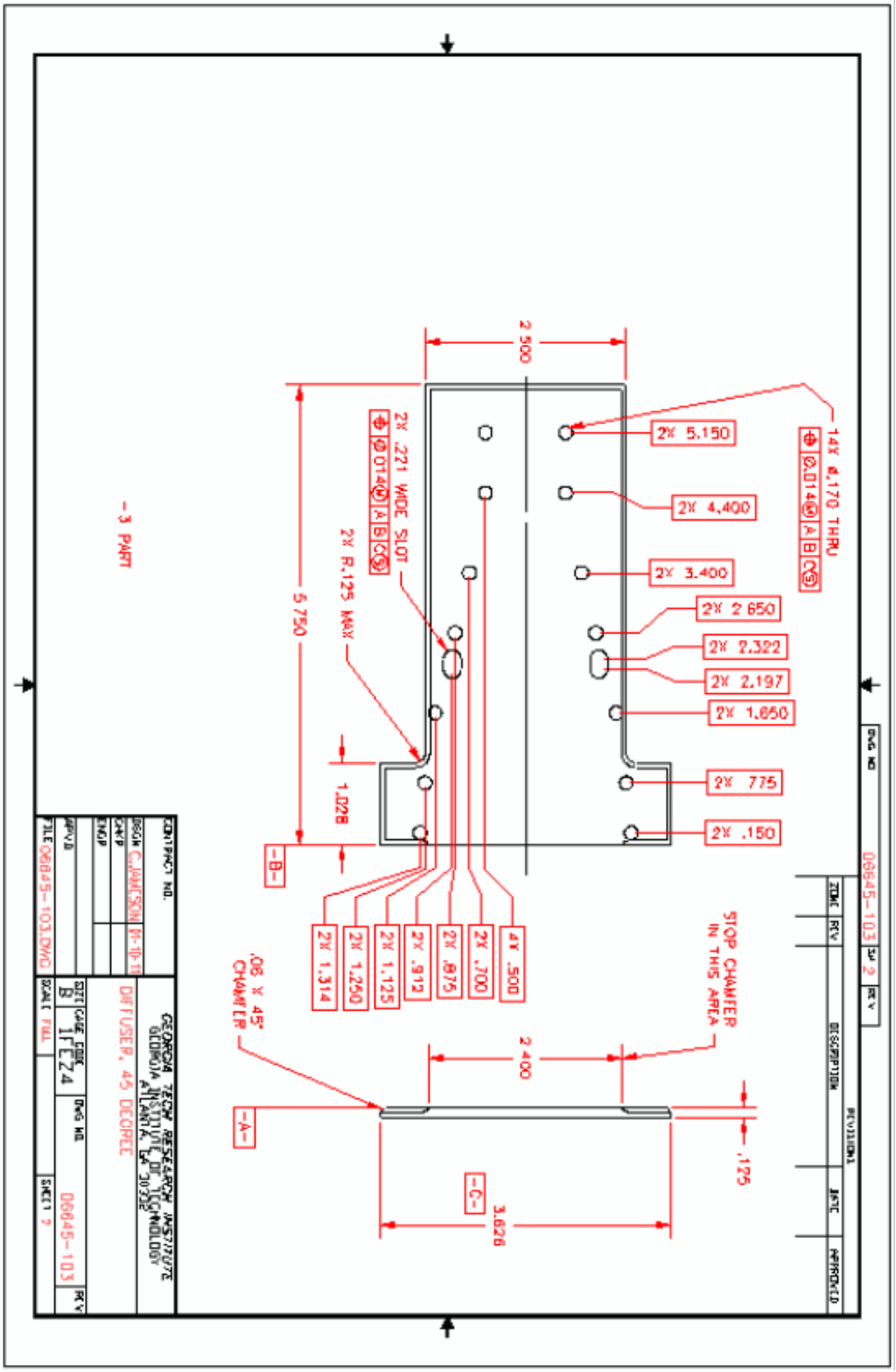

Figure A.2: Small Scale Jet, Large Actuator Diffuser Cover Plate

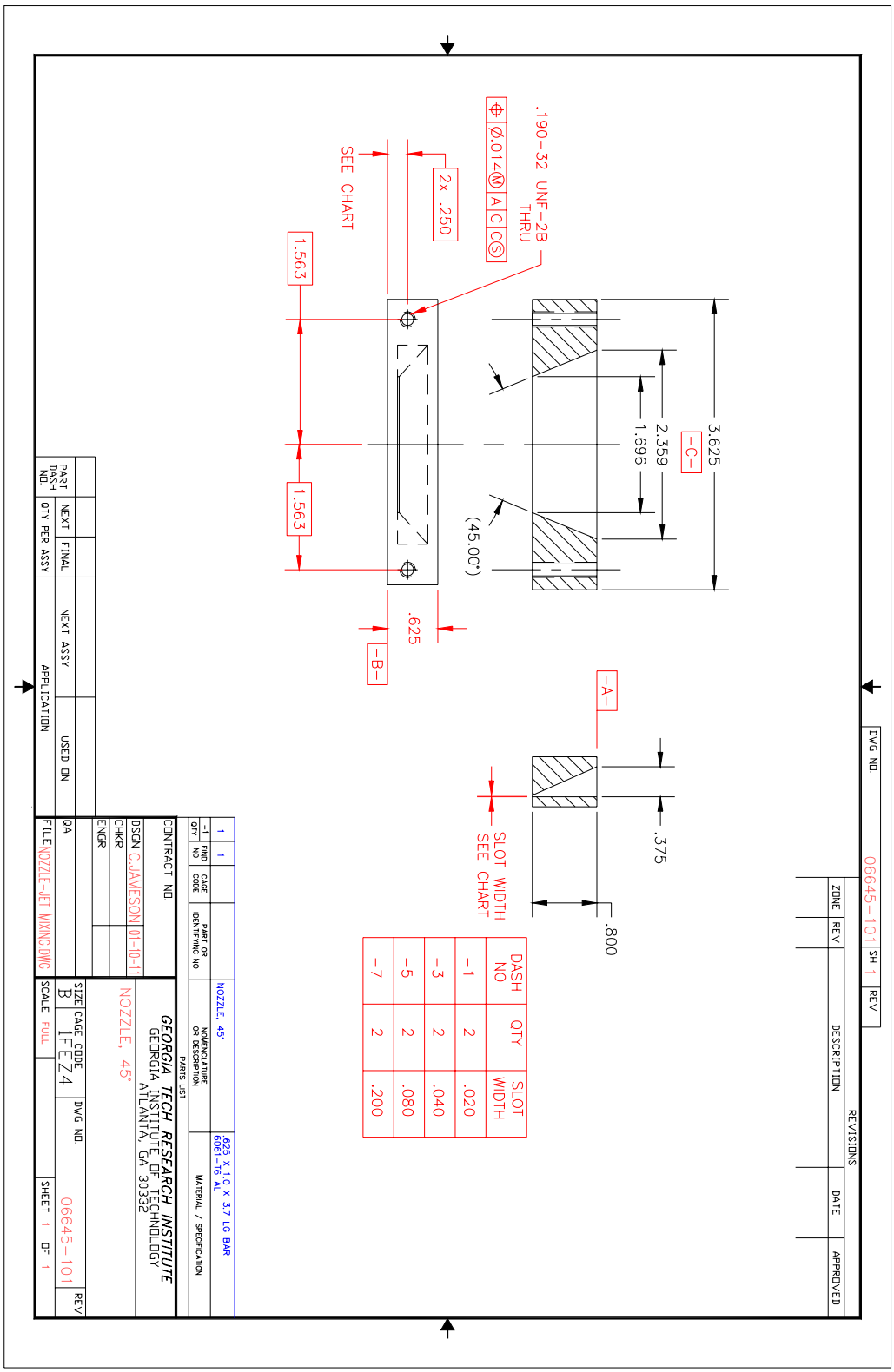

Figure A.3: Small Scale Jet, Large Actuator Nozzles

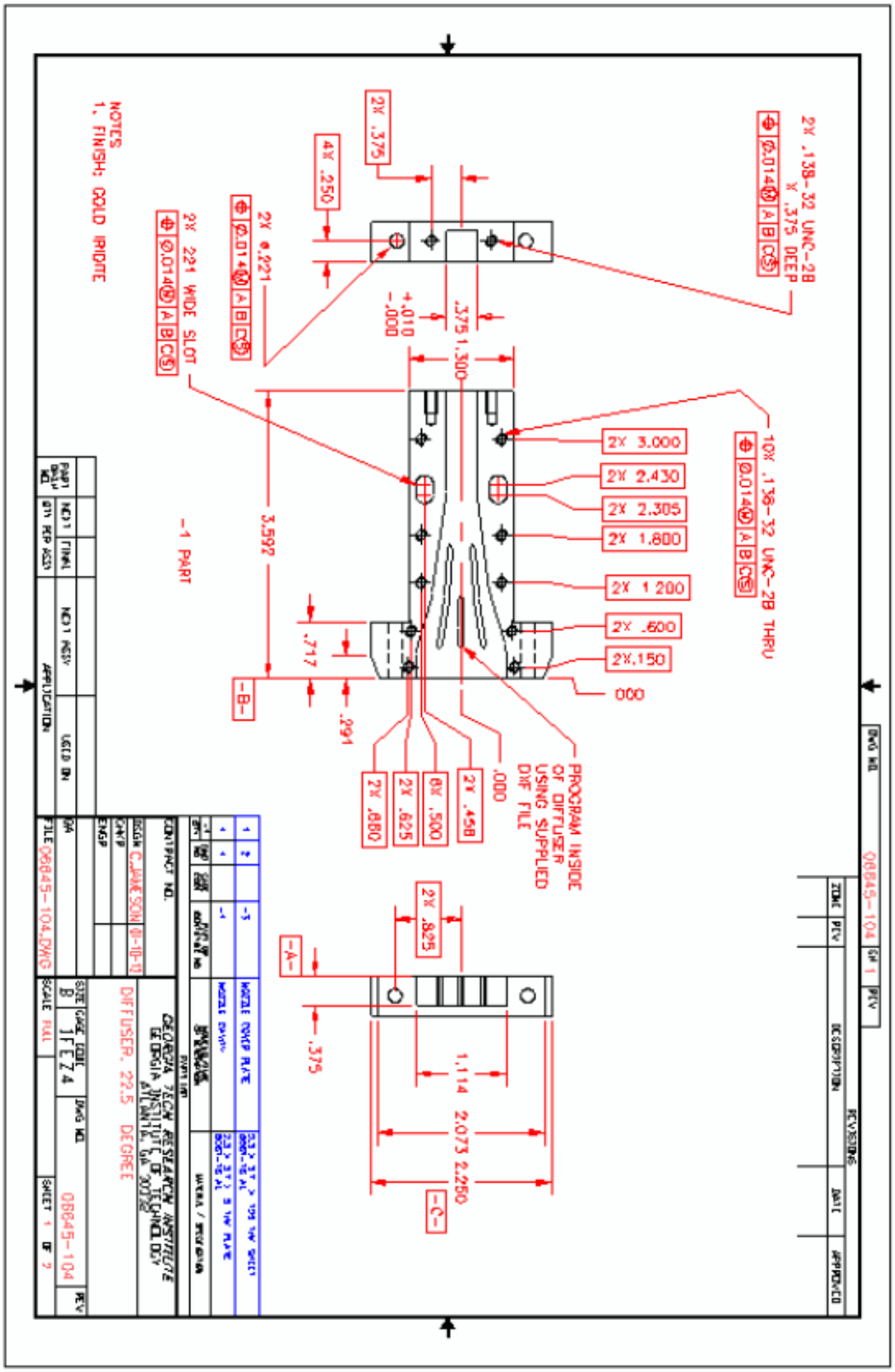

Figure A.4: Small Scale Jet, Small Actuator Diffuser

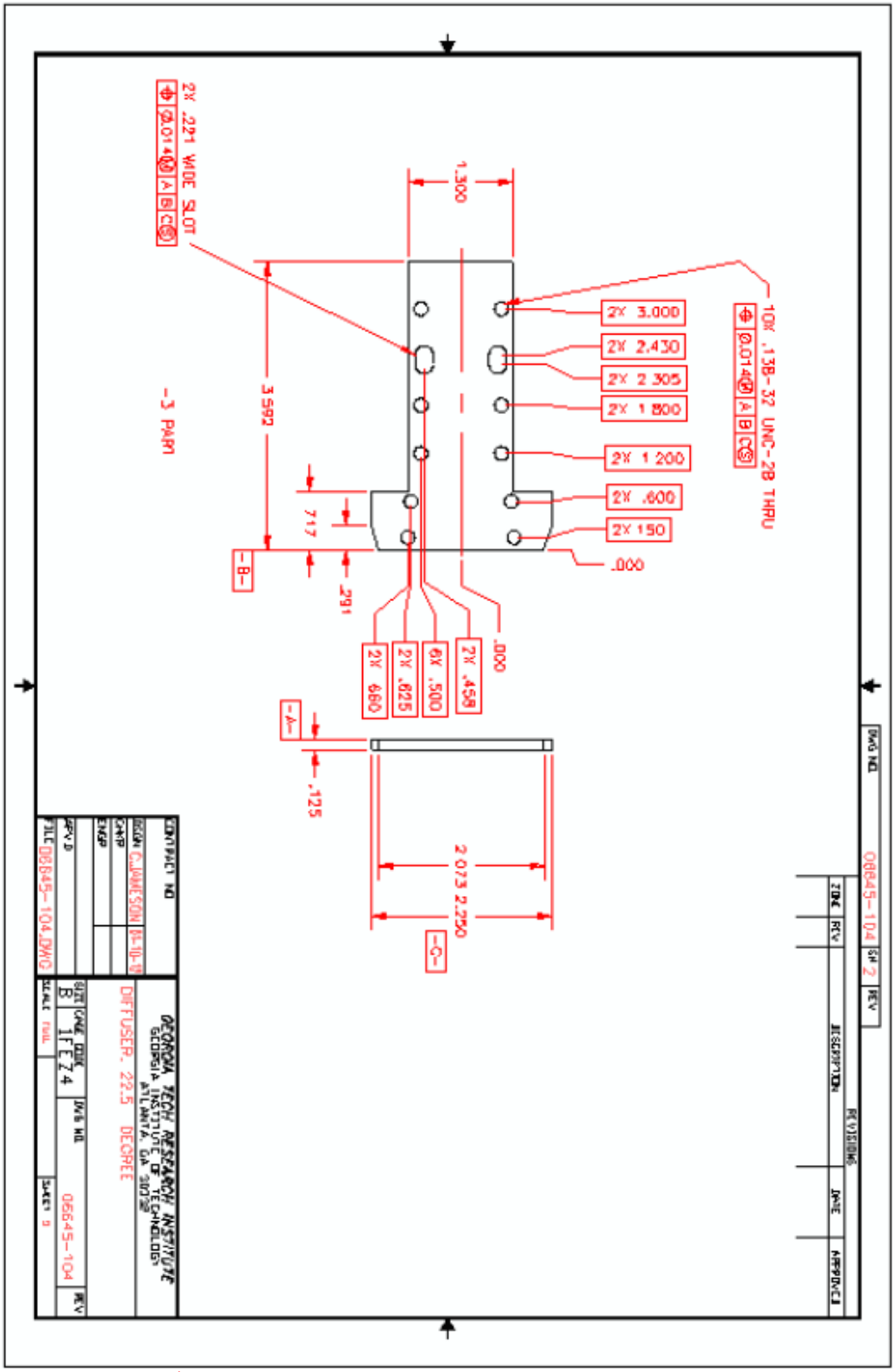

Figure A.5: Small Scale Jet, Small Actuator Diffuser Cover Plate

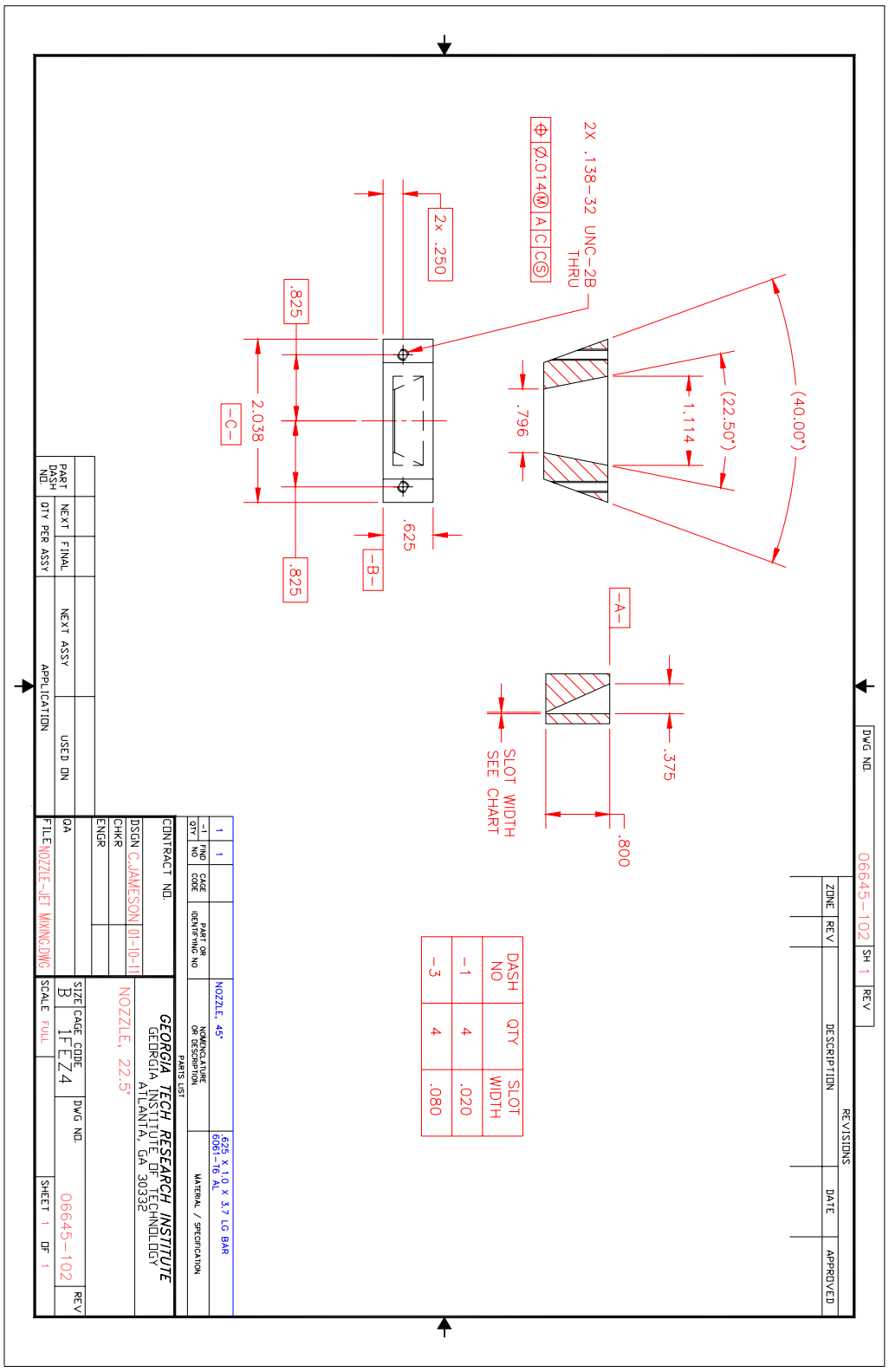

Figure A.6: Small Scale Jet, Small Actuator Nozzles

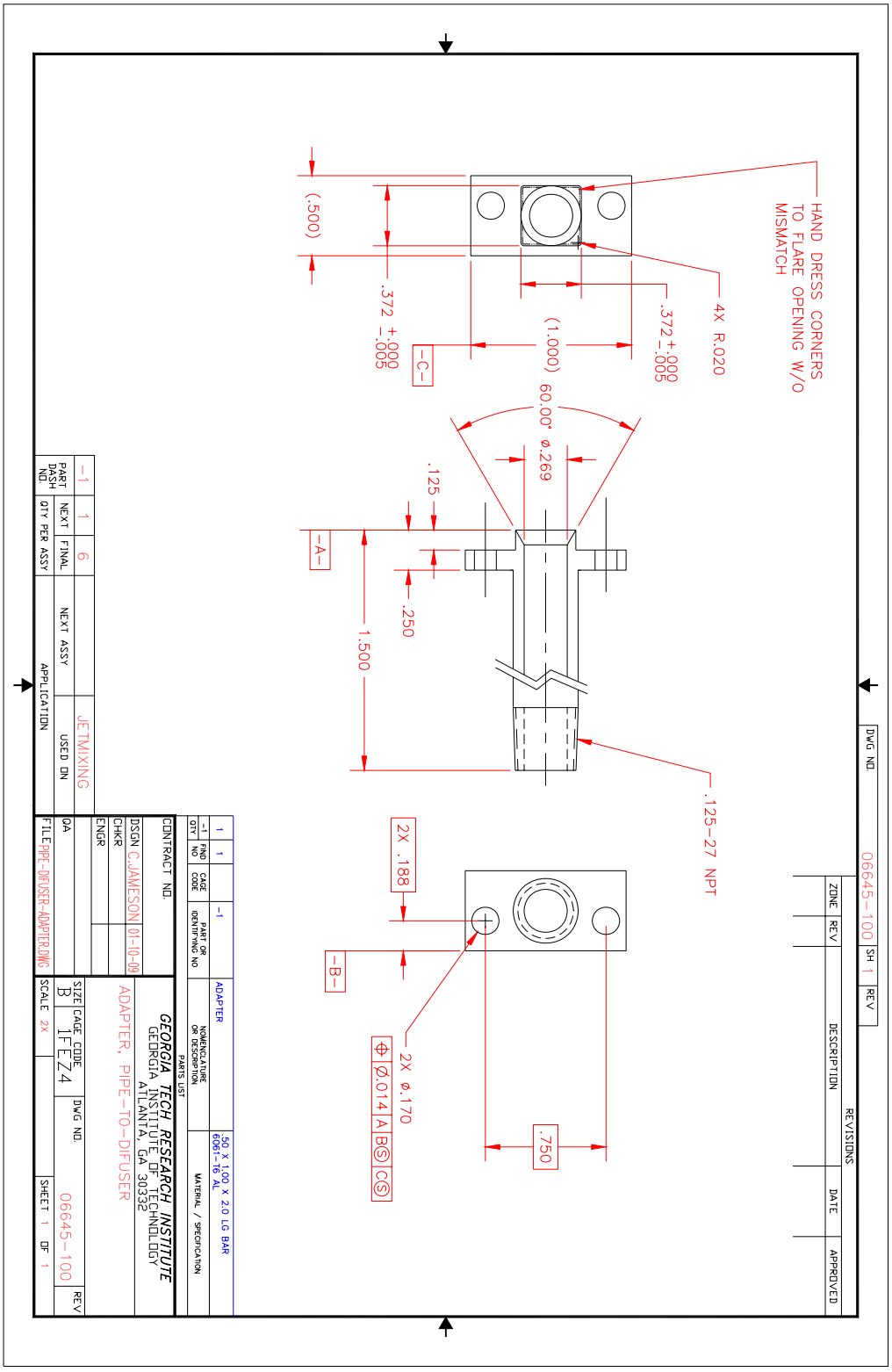

Figure A.7: Small Scale Jet, Diffuser to Pipe Adapter

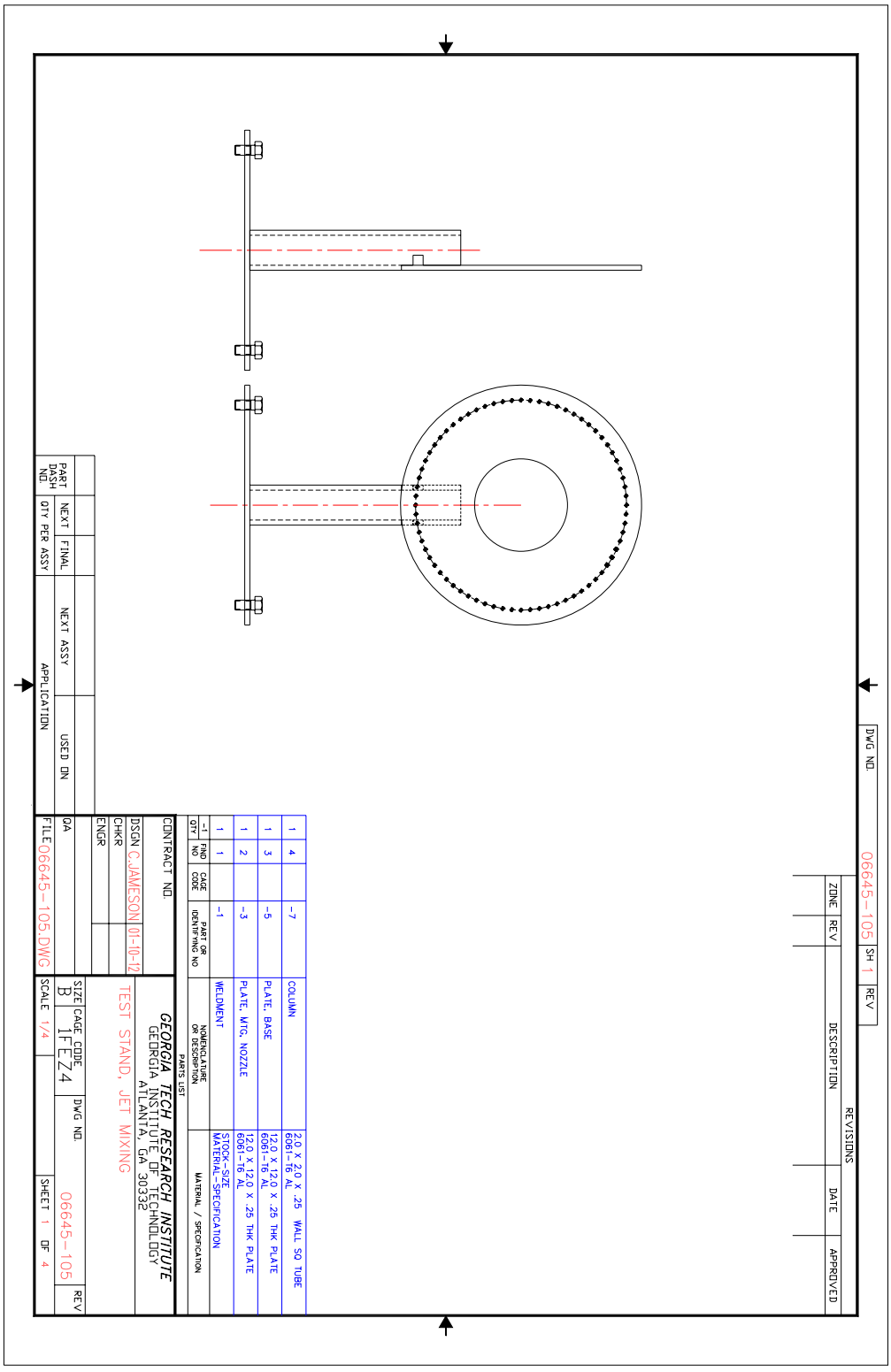

Figure A.8: Small Scale Jet, Actuator Test Stand Assembly

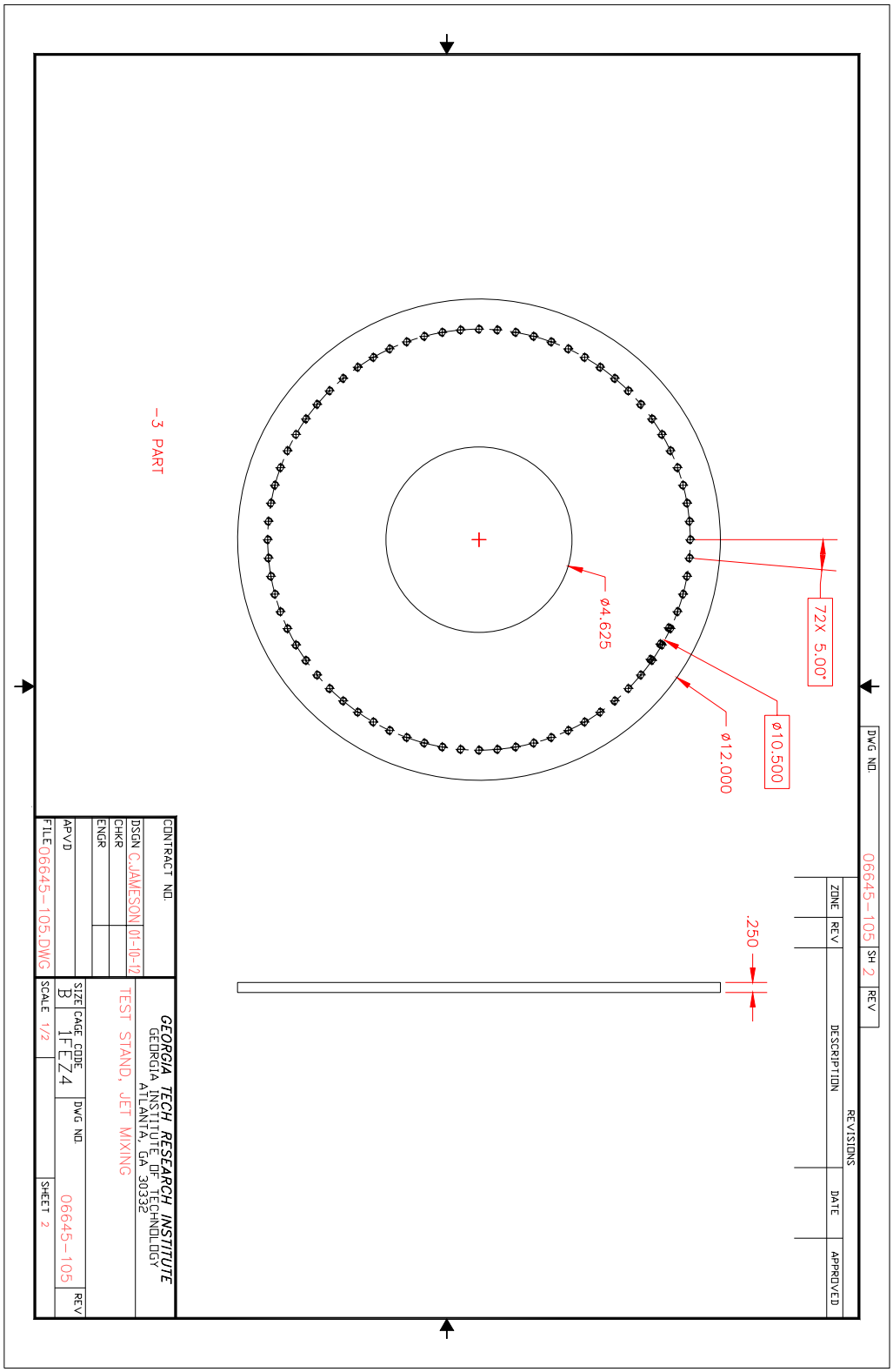

Figure A.9: Small Scale Jet, Actuator Test Stand Mounting Ring

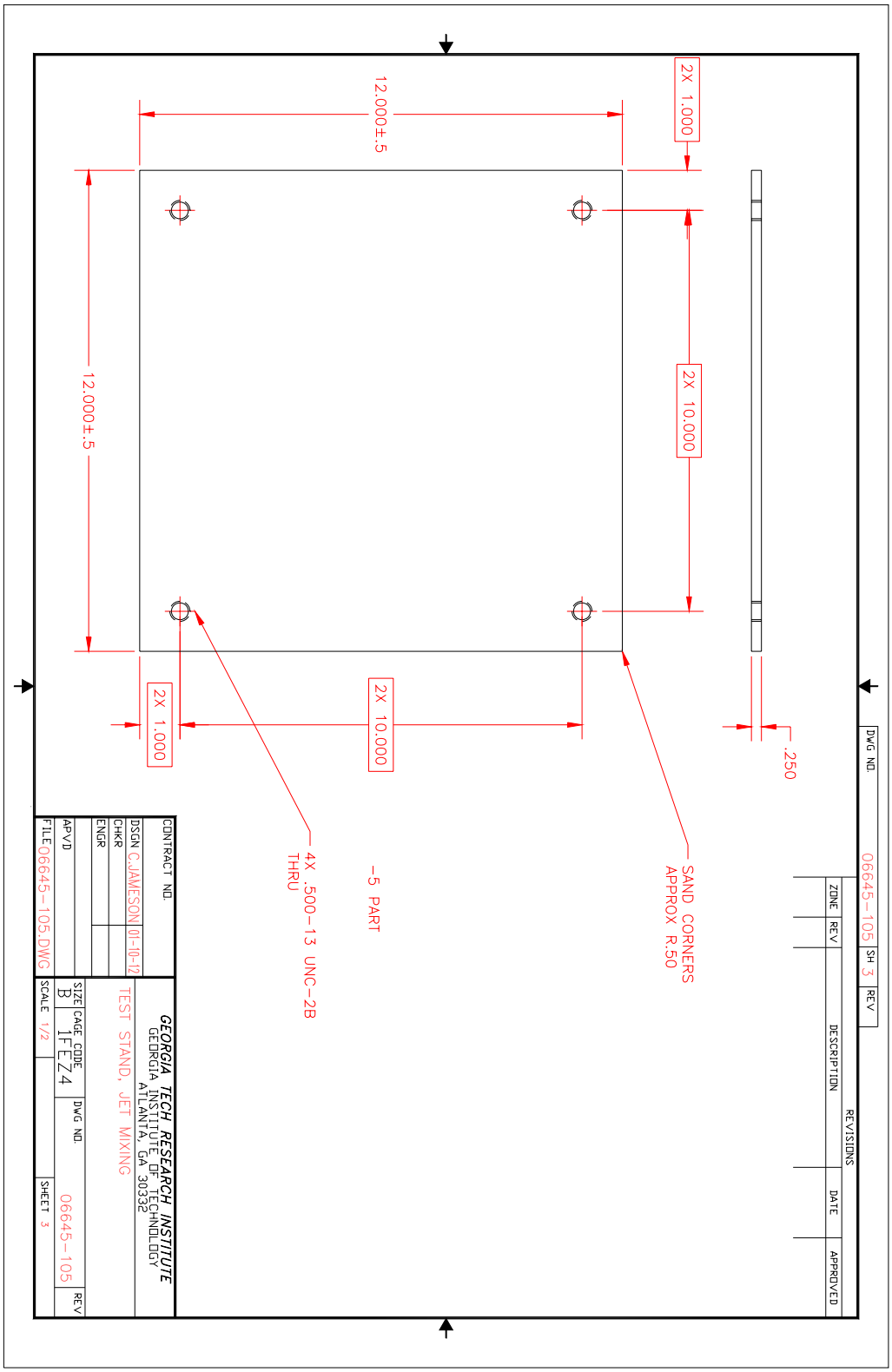

Figure A.10: Small Scale Jet, Actuator Test Stand Bottom Plate

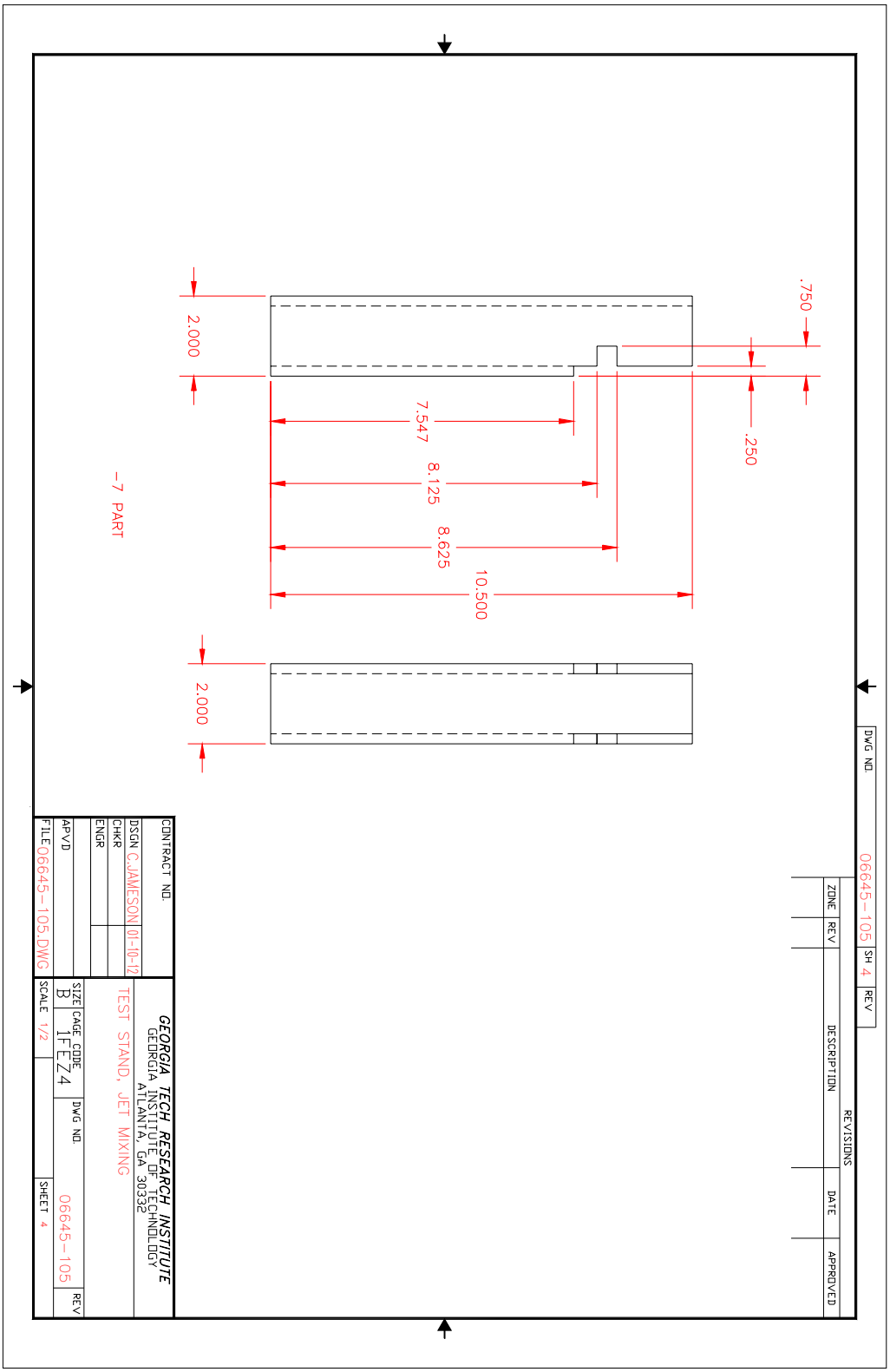

Figure A.11: Small Scale Jet, Actuator Test Stand Ring Support

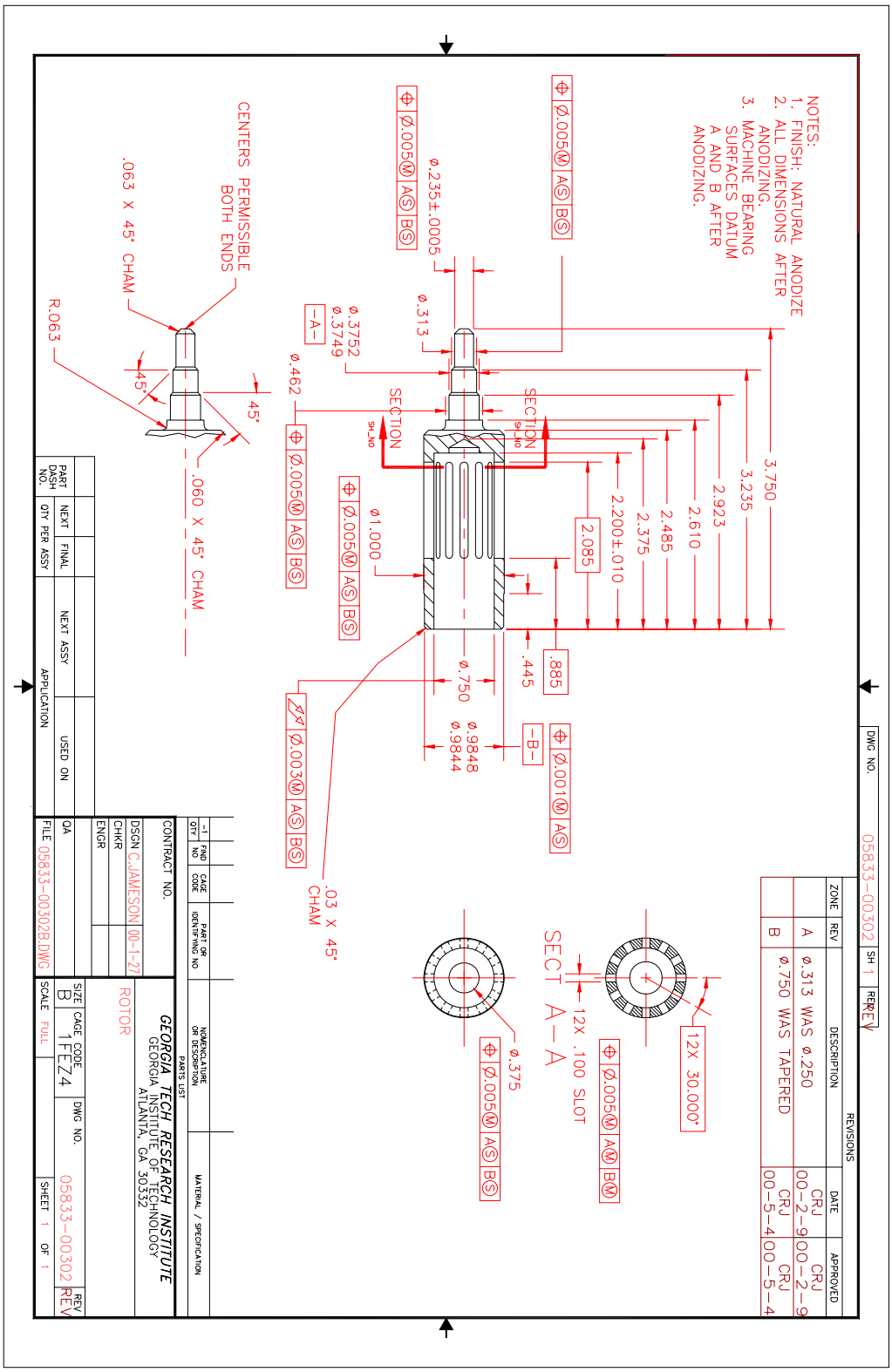

Figure A.12: Jet Engine, Slotted Rotor

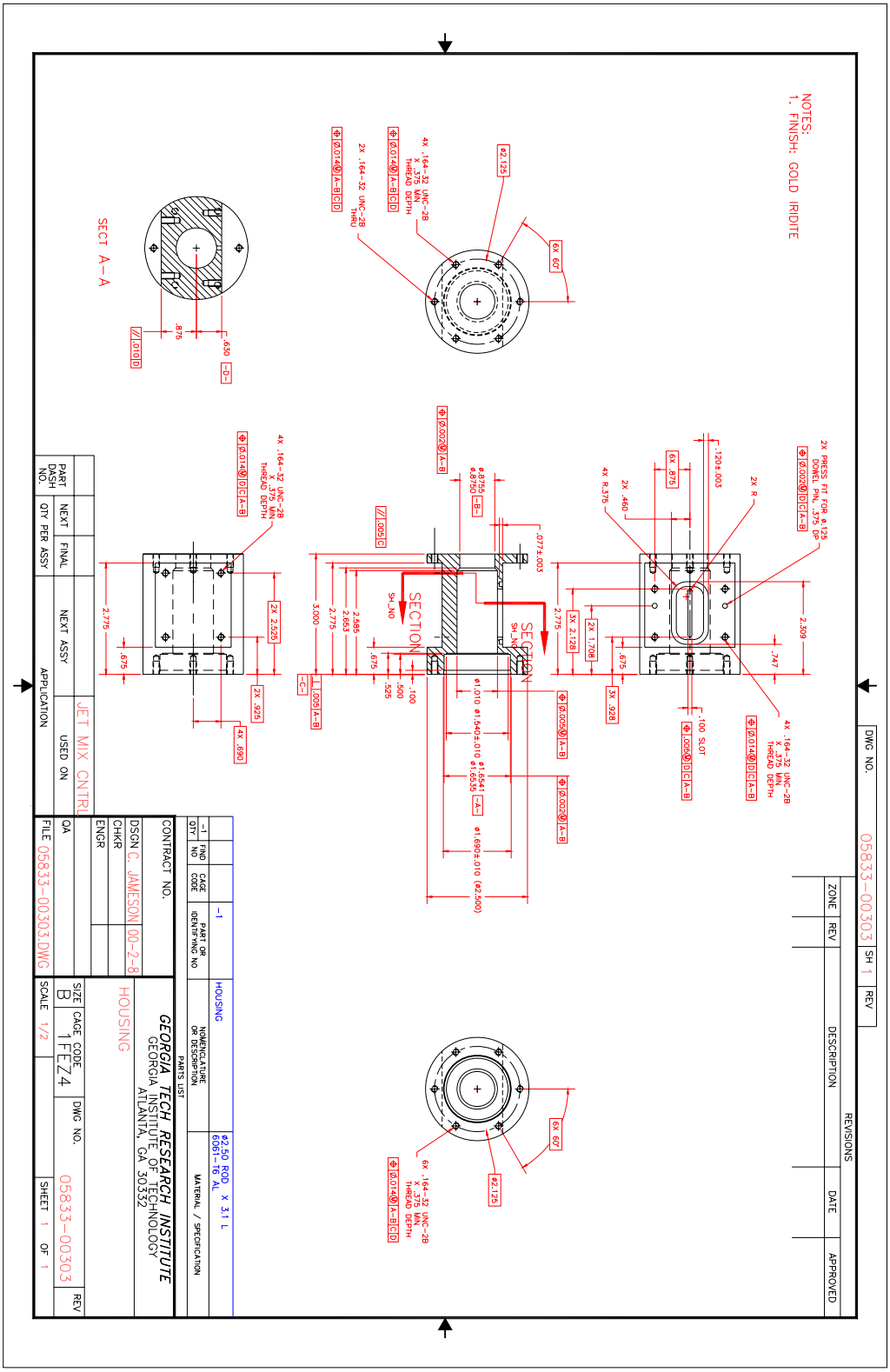

Figure A.13: Jet Engine, Rotor Housing

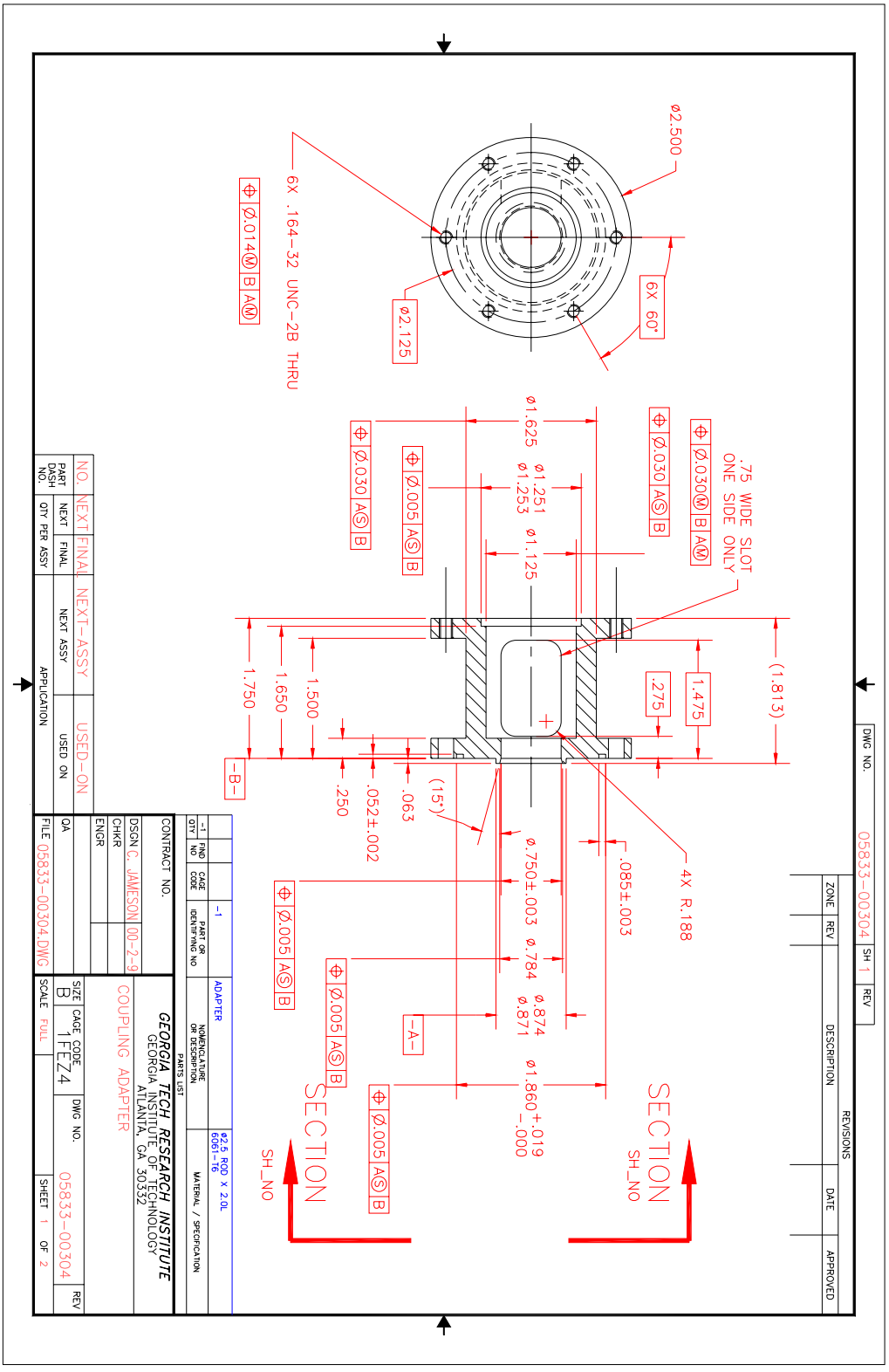

Figure A.14: Jet Engine, Housing to Motor Coupling

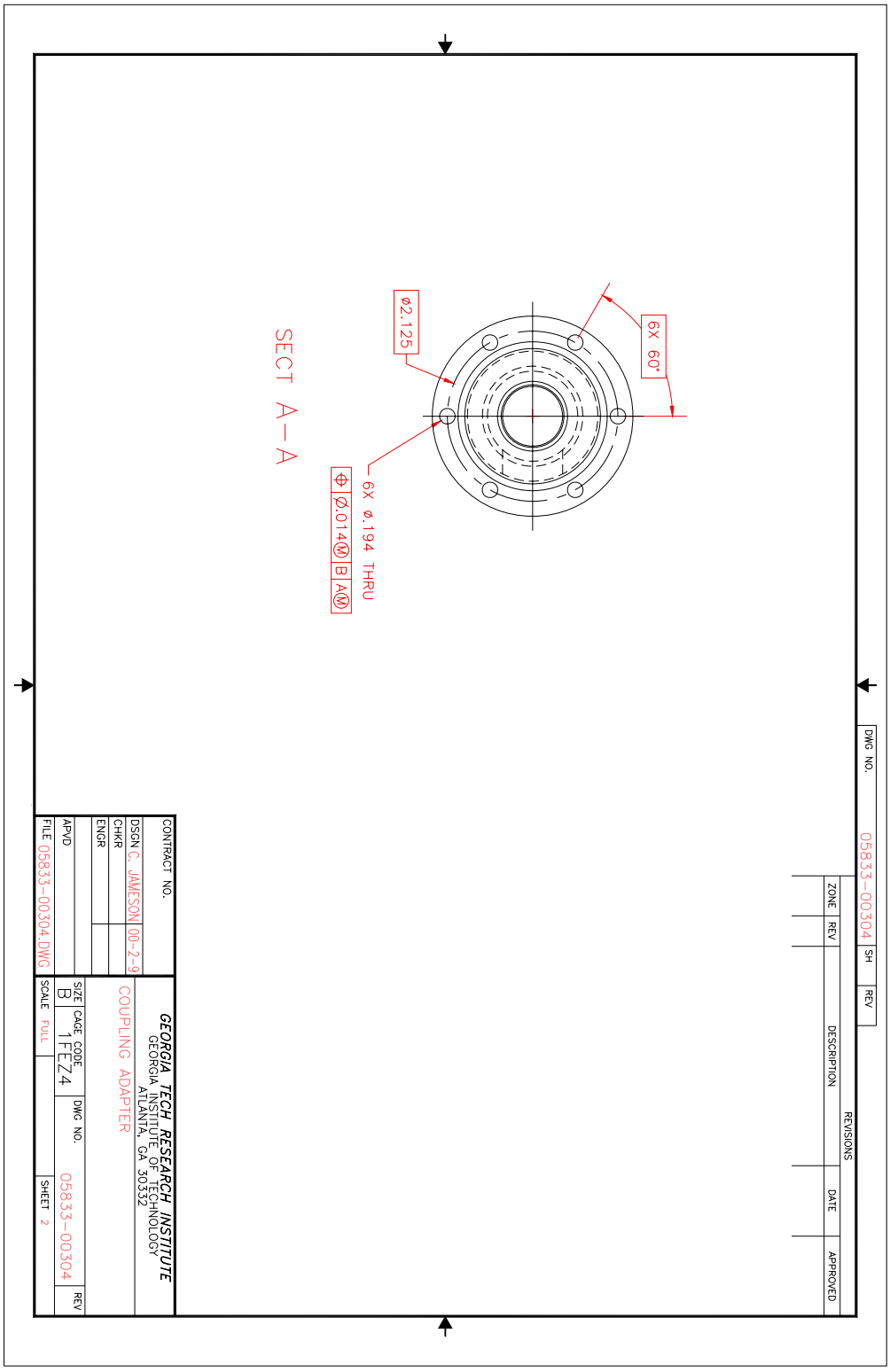

Figure A.15: Jet Engine, Coupling Adapter

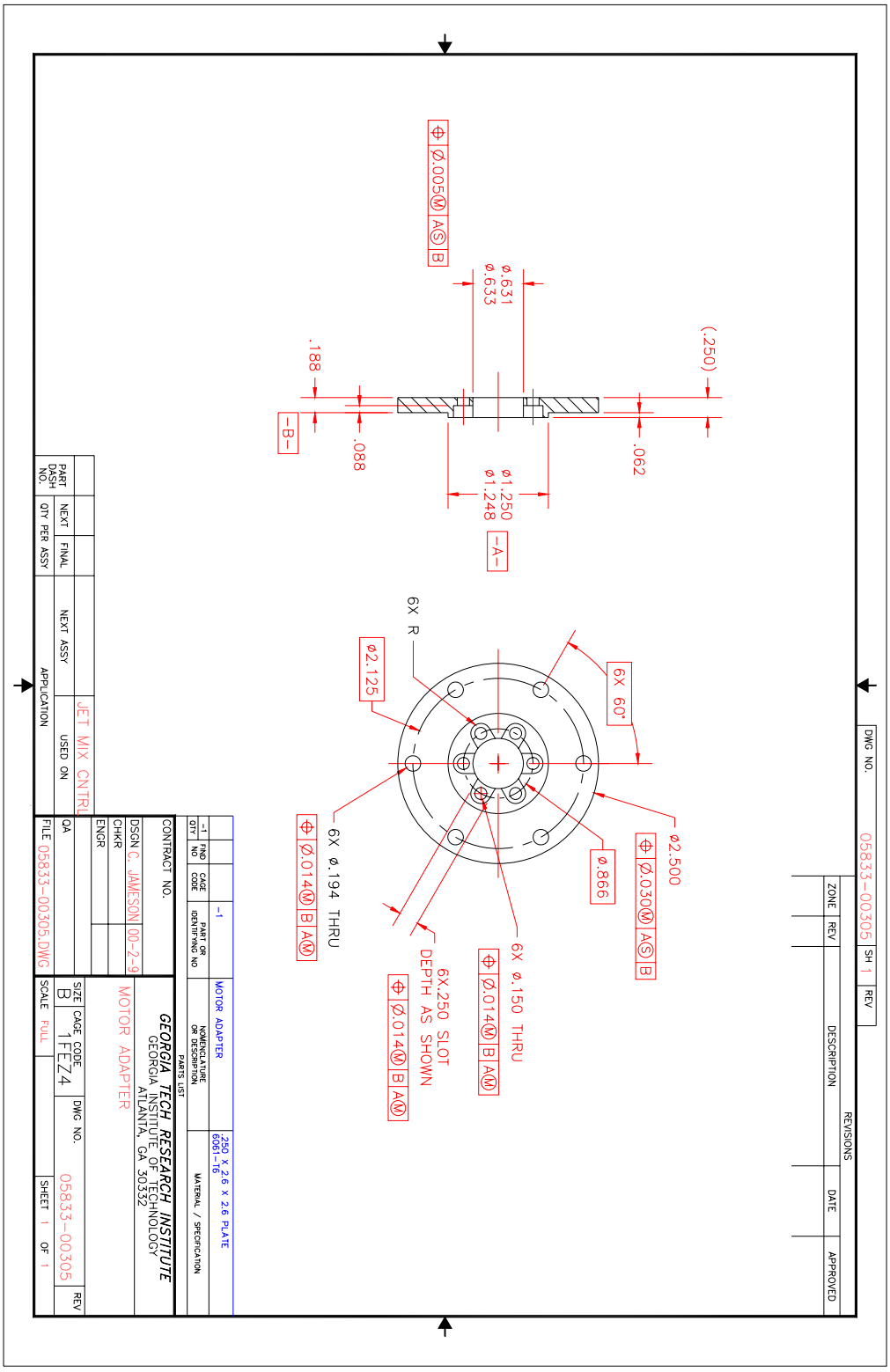

Figure A.16: Jet Engine, Motor Adapter

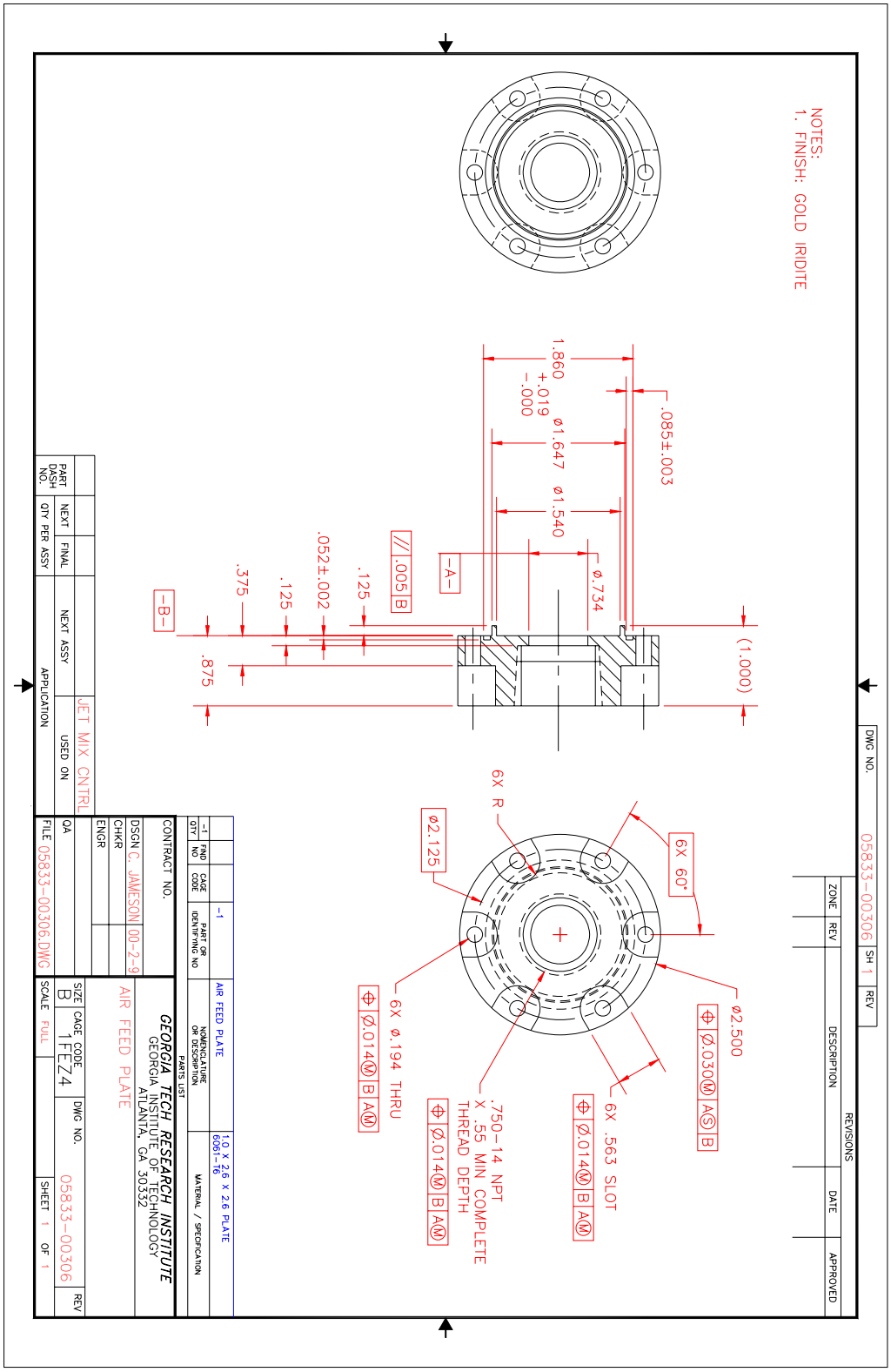

Figure A.17: Jet Engine, Air Feed Plate

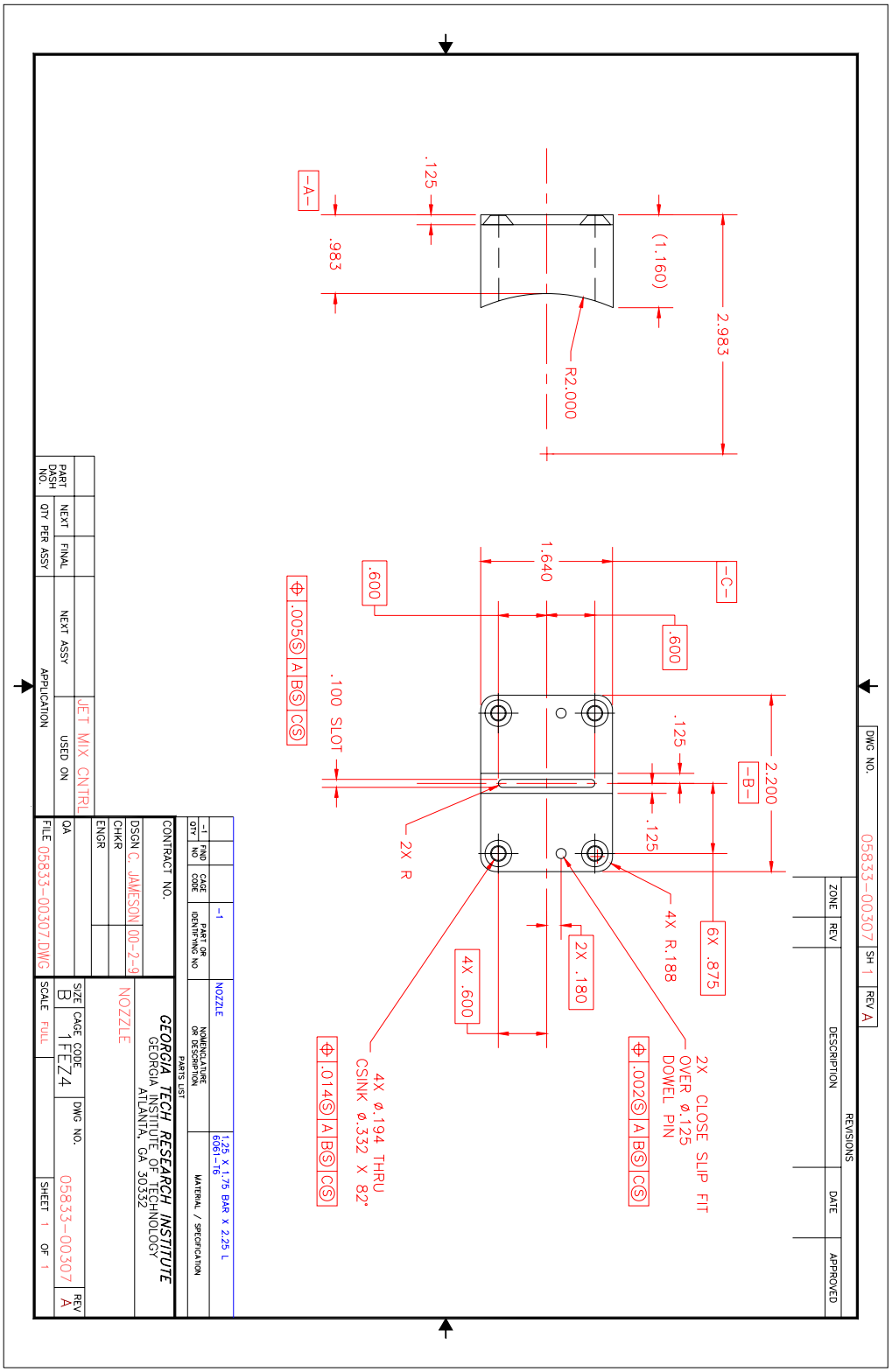

Figure A.18: Jet Engine, Actuator Nozzle

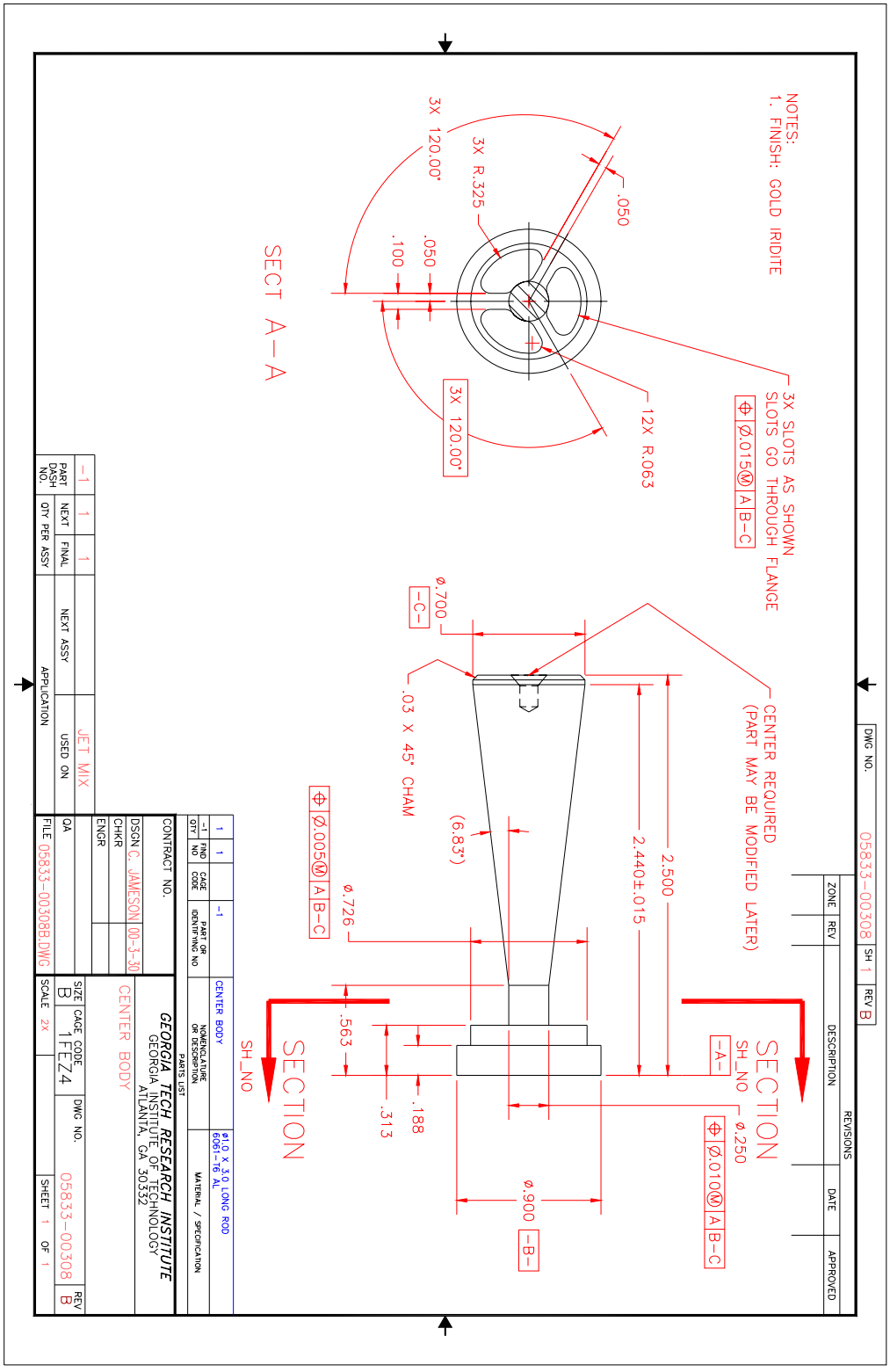

Figure A.19: Jet Engine, Actuator Center Body

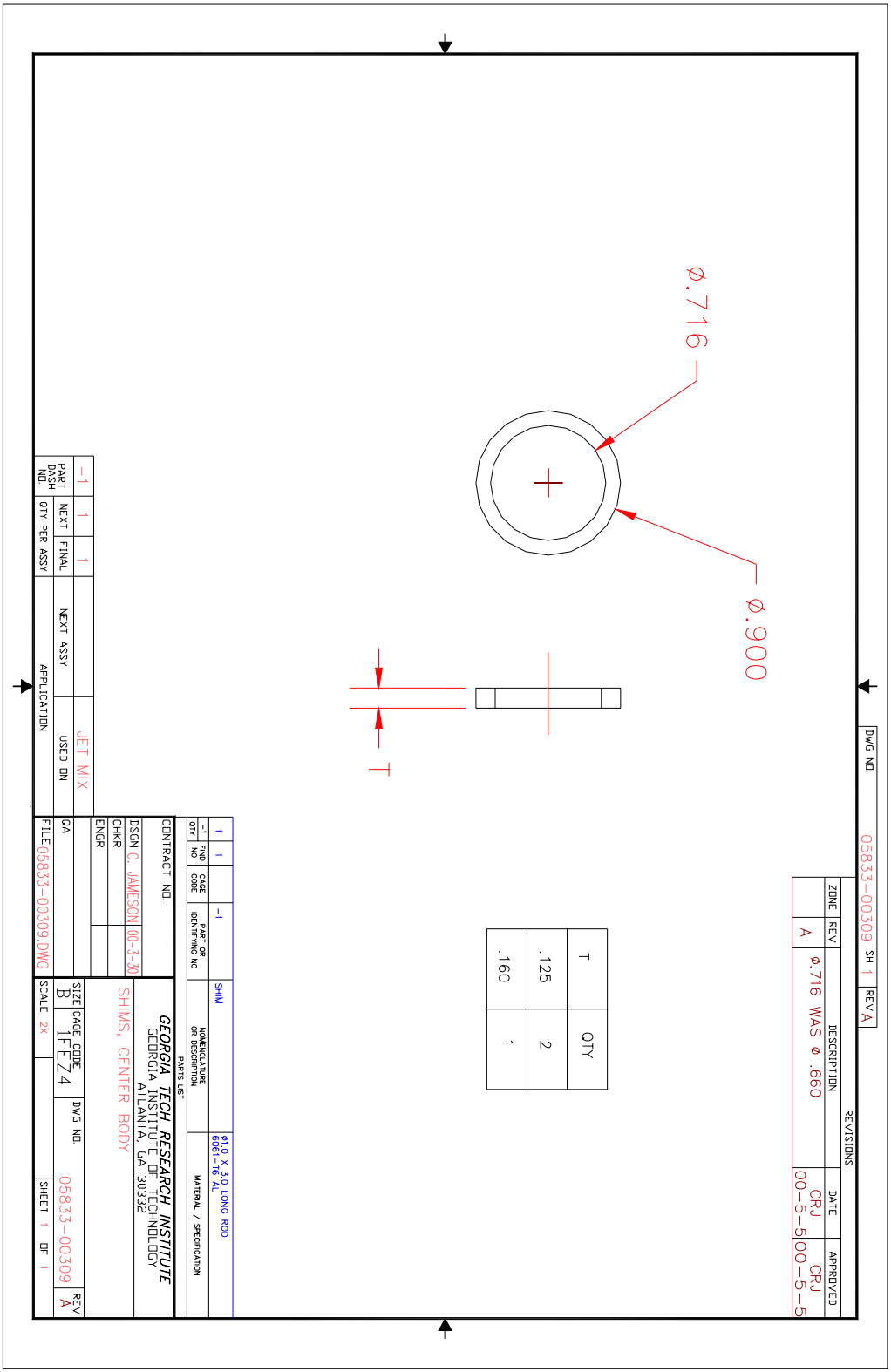

Figure A.20: Jet Engine, Center Body Shims

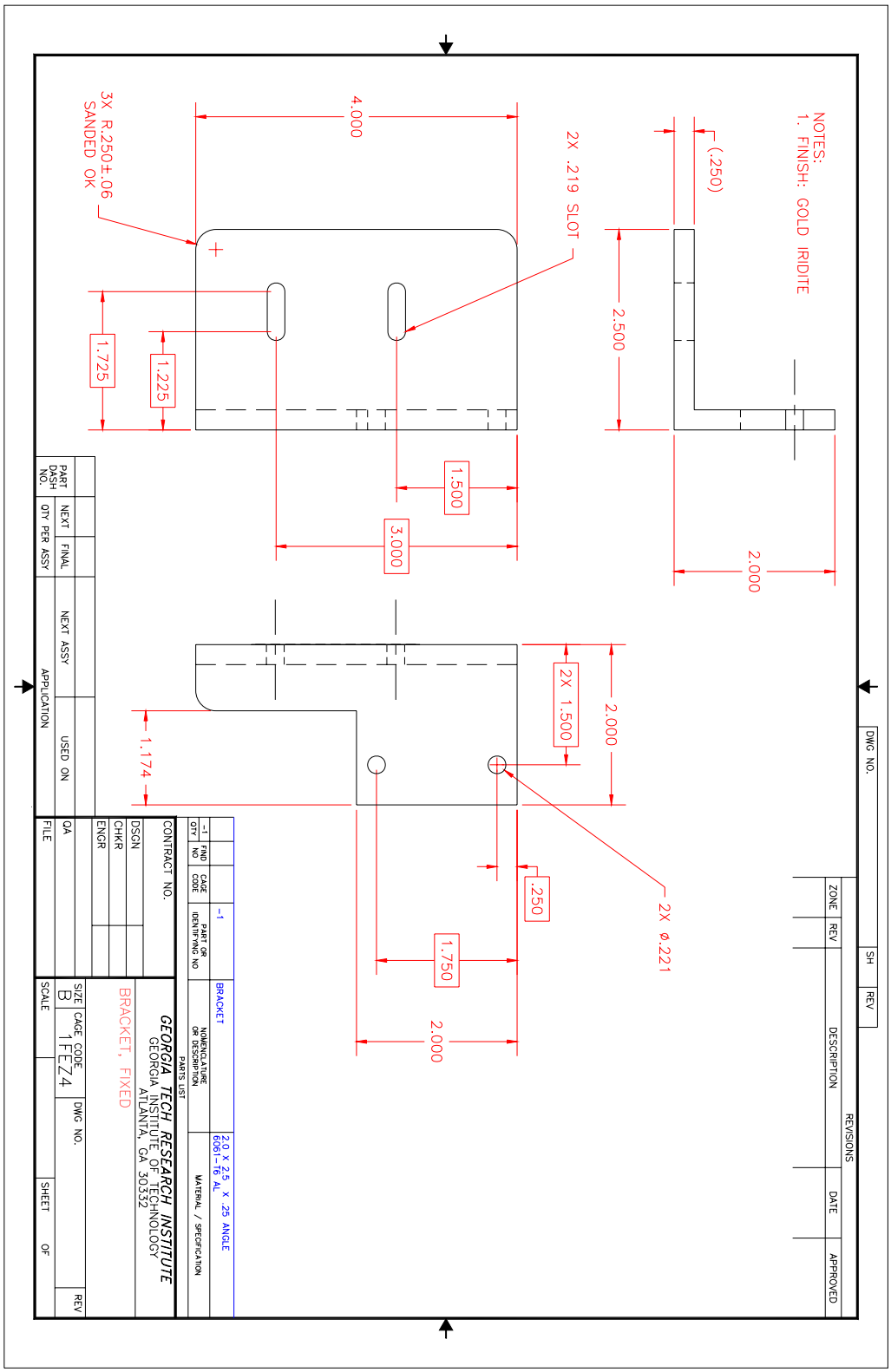

Figure A.21: Jet Engine, Fixed Actuator Mounting Bracket

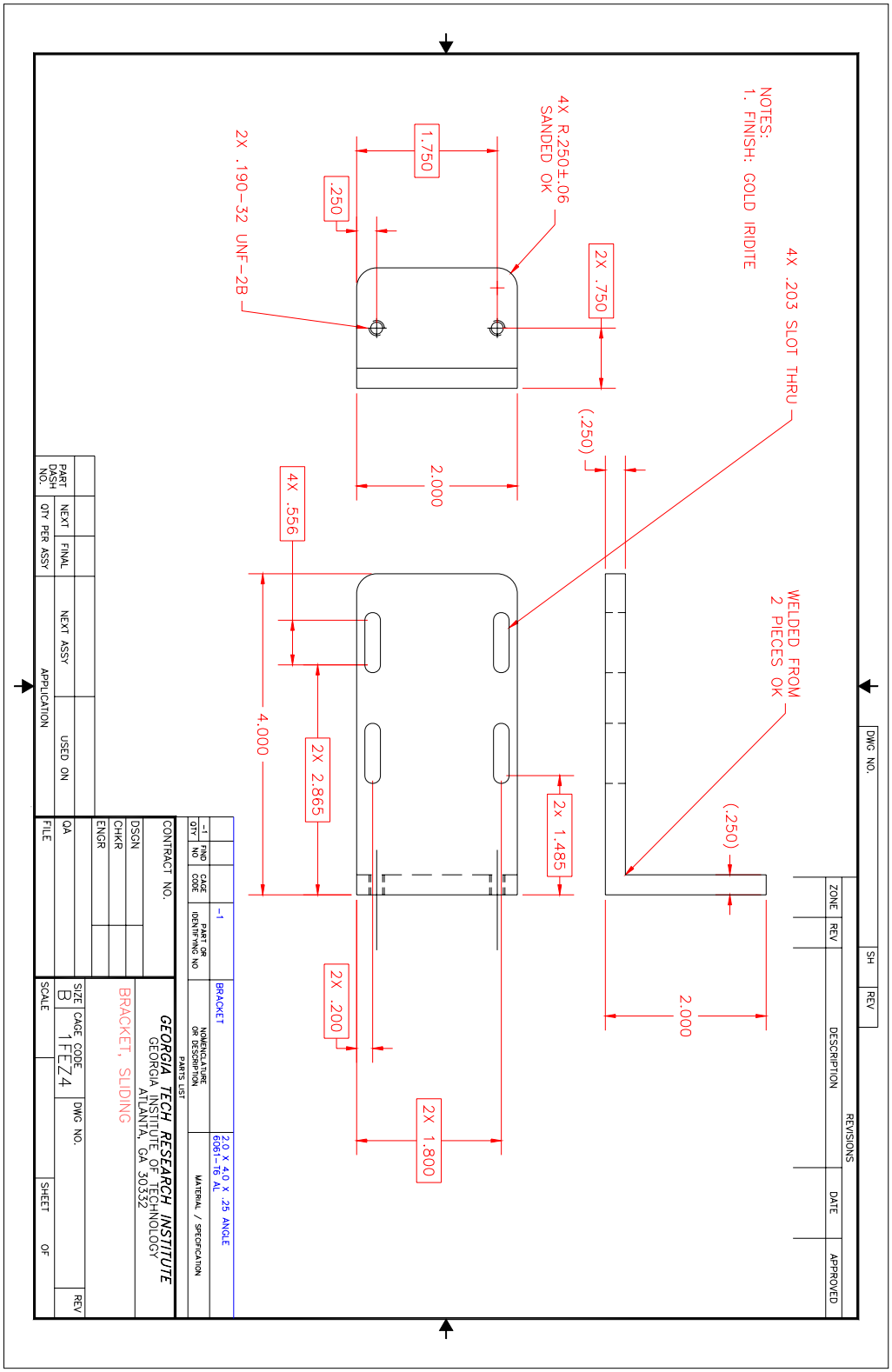

Figure A.22: Jet Engine, Sliding Actuator Mounting Bracket

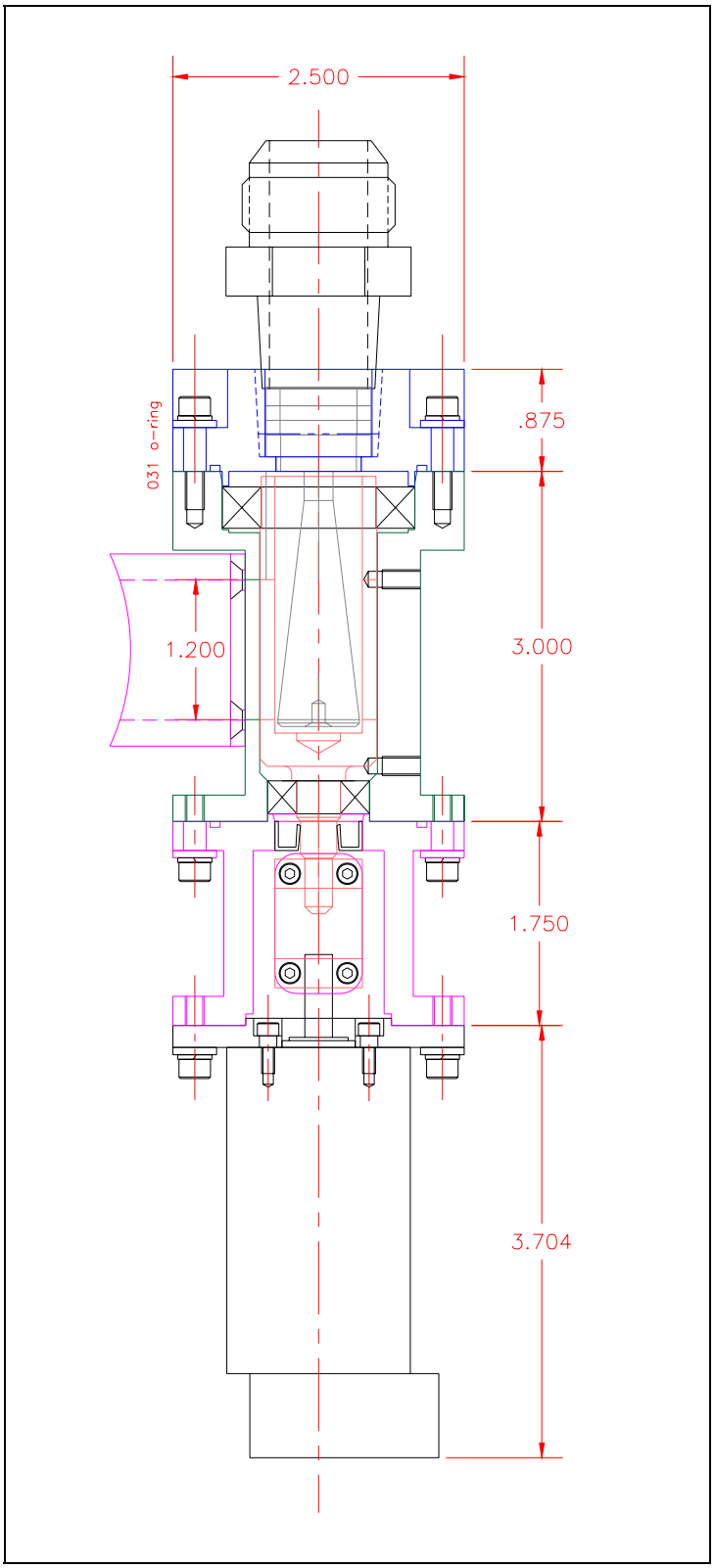

Figure A.23: Jet Engine, Actuator Assembly

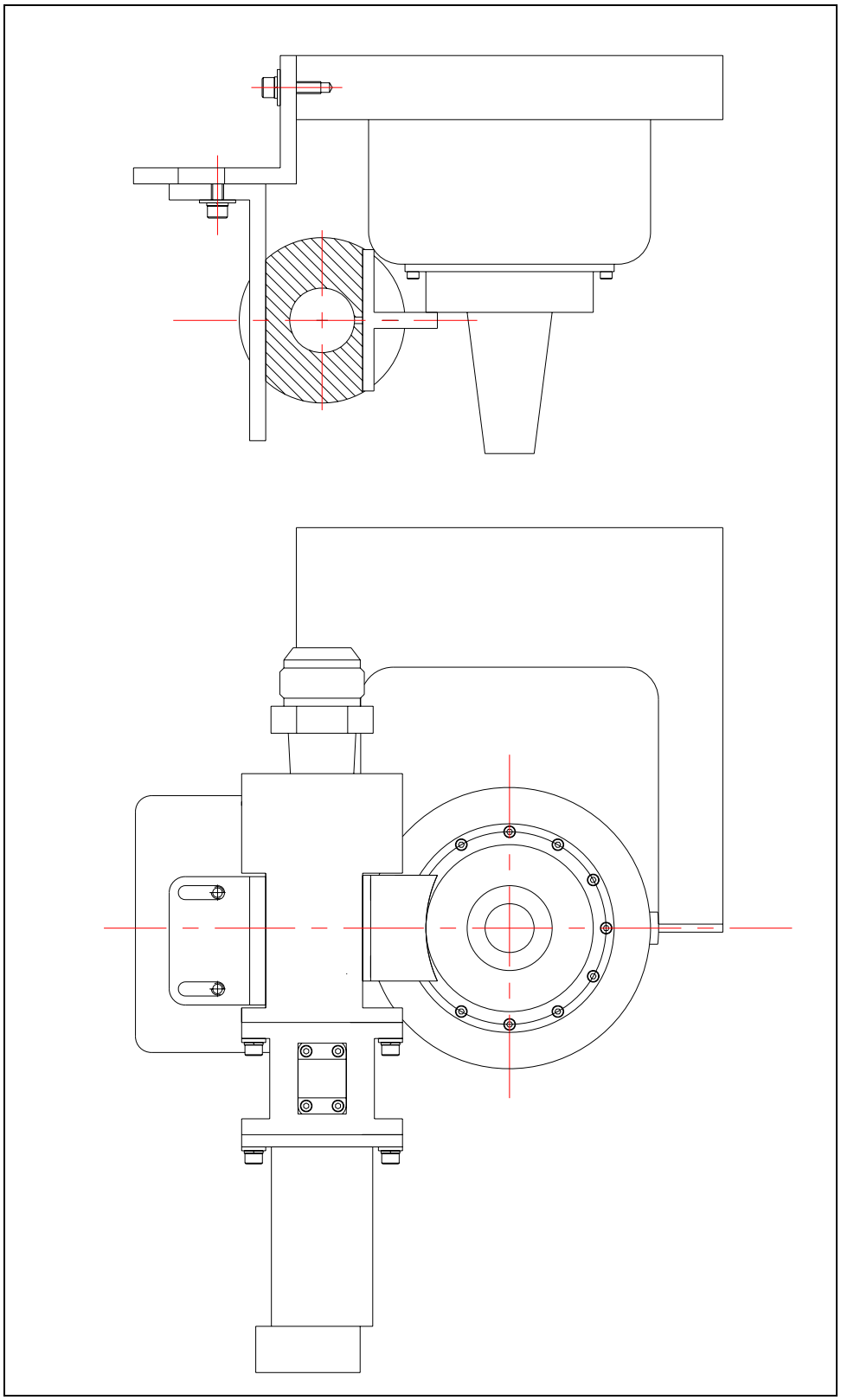

Figure A.23: Jet Engine, Actuator Mounting

APPENDIX C

MASS FLOW RATE VALIDATION

Overview

The collapse of mixing on momentum ratio was a key discovery made during the small scale experiments. Thereafter momentum ratio was used as the primary indicator of actuator amplitude. During the experiments, momentum ratio was not directly measured but calculated with knowledge of the mass flow rate and the thermodynamic properties of the air leaving the jet and actuators (i.e. the temperature and static pressure). The thermodynamic properties were measured with the usual probes, and the mass flow rate was measured with a venturi flow meter. However a standard assumption in the use of a venturi is that the flow is steady, and in this case the flow through the venturi was pulsatile. In some cases the flow was only slightly pulsatile (e.g. out-of-phase pulsing on the small scale jet). In other cases pulsation was more significant. It was therefore necessary to quantify the amount of pressure fluctuation in the venturis during actuation and to make alternate independent mass flow measurements in order to validate the mass flow measurements made during the various jet mixing experiments.

Two different methods of independent validation were used. The first method involved measuring mass flow rate with the venturi while simultaneously measuring velocity at the actuator nozzle exits with a velocity probe (typically a hot wire anemometer). The mass flow rate from each actuator was then calculated from the unsteady velocity data and the results were compared with the venturi measurements. The second independent

validation method made use of a critical flow venturi nozzle in series with the original venturi. Critical flow devices are insensitive to downstream fluctuations as long as they remain choked. Mass flow measurements were made simultaneously with both the venturi and the critical flow nozzle for a wide range of frequencies and amplitudes and compared.

This appendix contains 5 major sections: General Approach, Small Scale, Full Scale, Jet Engine, and a Summary. The General Approach section provides important background information and describes the validation methods and mathematical calculations used in this appendix. The next three sections provide the details relevant to validation experiments performed on each type of jet actuator. The last section summarizes the overall findings.

General Approach for Mass Flow Rate Validation

Venturi Meters in Pulsatile Flow

Venturi meters are affected by pulsatile flow for the following reasons: [11]

1. Pulsatile flow has a different velocity profile than fully developed steady flow.
2. The pressure transducers may not be able to follow the fluctuations.
3. Resonance of some component in the system may occur at the pulsing frequency.
4. The equation relating differential pressure to flow is non-linear.

An important parameter for analyzing pulsatile flow in differential pressure devices is the so called pressure fluctuation ratio, calculated as the value of the RMS fluctuation (i.e.

the standard deviation) of the differential pressure across the venturi divided by the mean. When this value is smaller than 0.5 the main cause of error is number 4, commonly referred to as square root error.[11] Figure C.1 is a graphic that shows how this error comes about. If the measured differential pressure is averaged and then converted to flow rate, it is not equal to the average flow rate because the flow rate is a function of the square root of the differential pressure. Square root error can be eliminated by using a fast response unsteady transducers and by performing the conversion to flow rate (or at least the square root) on the acquired voltages before averaging. Using an unsteady transducer also helps with numbers 2 and 3 if short pressure leads are used.

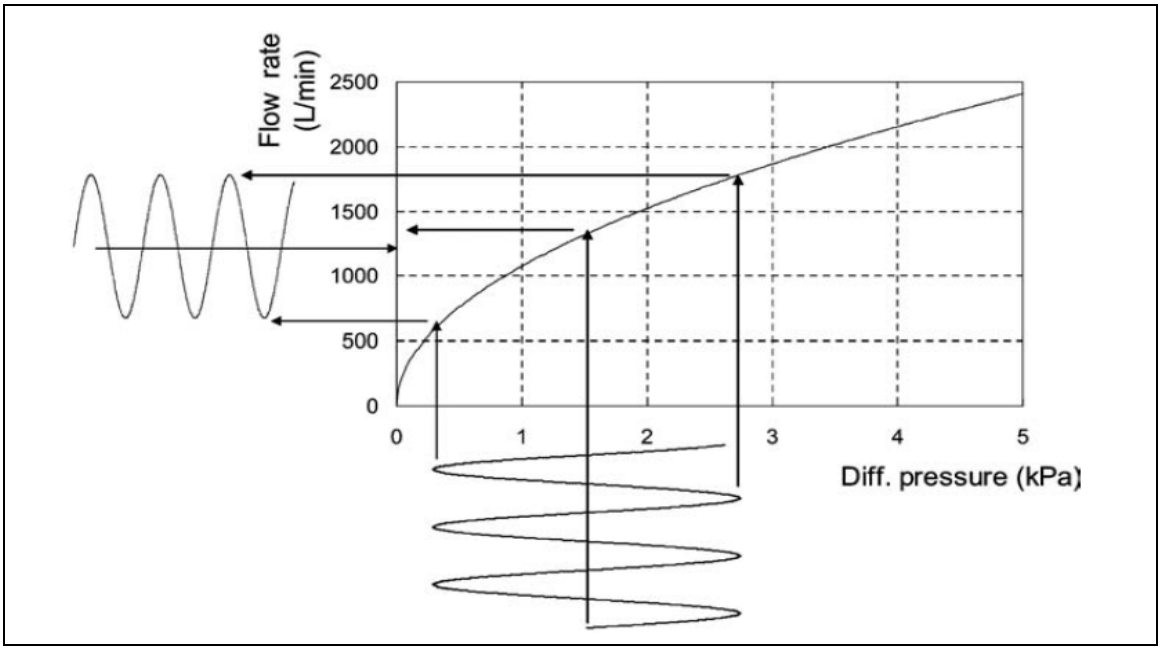

Figure C.1: Graphic Showing the Origin of Square Root Error

Validation Method I: Choked/Critical Flow

For validation experiments on the jet engine actuator a 0.08" venturi flow meter was used as a critical flow device. The venturi choked at mass flow rates above 0.002 lb_m/s. The

0.08” venturi was added upstream of the original 0.25” venturi which used steady transducers and long pressure connections to measure mass flow for the jet engine actuators. Fast response unsteady transducers were used on the critical flow venturi to characterize pulsation. Figure C.2 is a plot of the correlation of the two venturis under steady flow. The correlation is good, but the slope is not quite equal to one. Figure C.3 is a plot showing the percent difference between the venturis as a function of mass flow measured by the 0.25” venturi. The plot assumes that the 0.08” venturi is the standard, so positive differences signify that the 0.25” venturi is measuring higher than the 0.08” venturi by the percent indicated. The difference initially varies from about 2.5% to 5%, but thereafter the difference is constant at about 4%. The initial unsteadiness is mainly due to transducer inaccuracies/nonlinearities at the low end of their ranges. The constant offset of 4% is due to calibration inaccuracy.

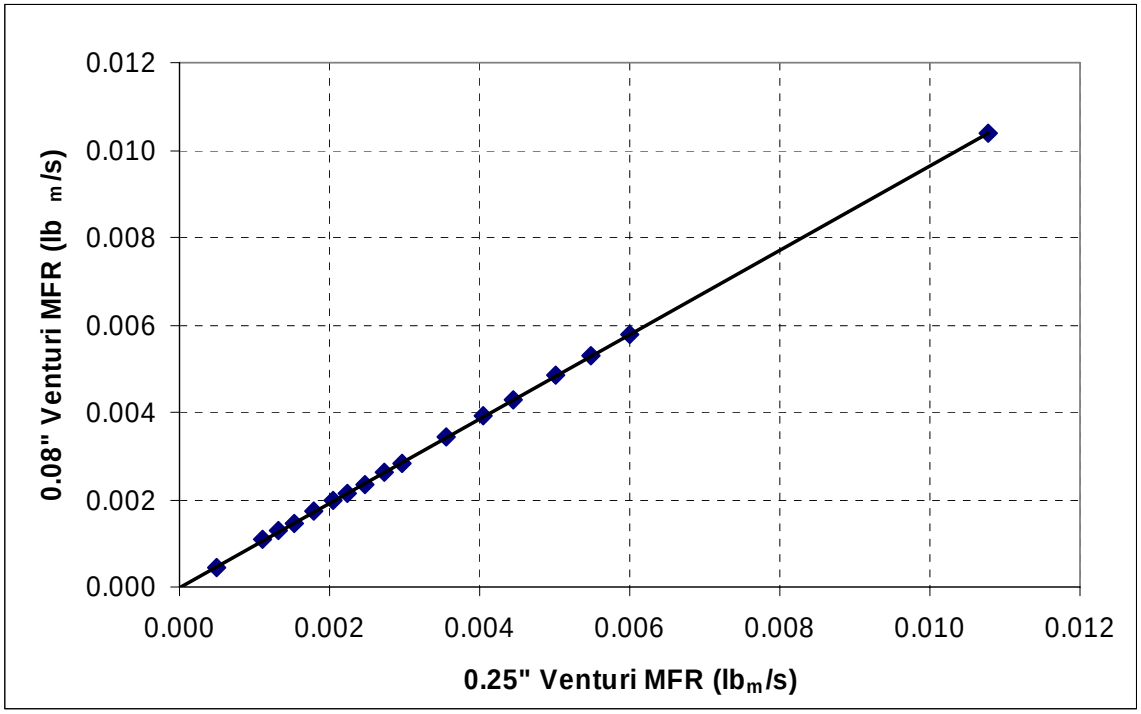

Figure C.2: Correlation of the 0.08” and 0.25” Venturis Under Steady Flow

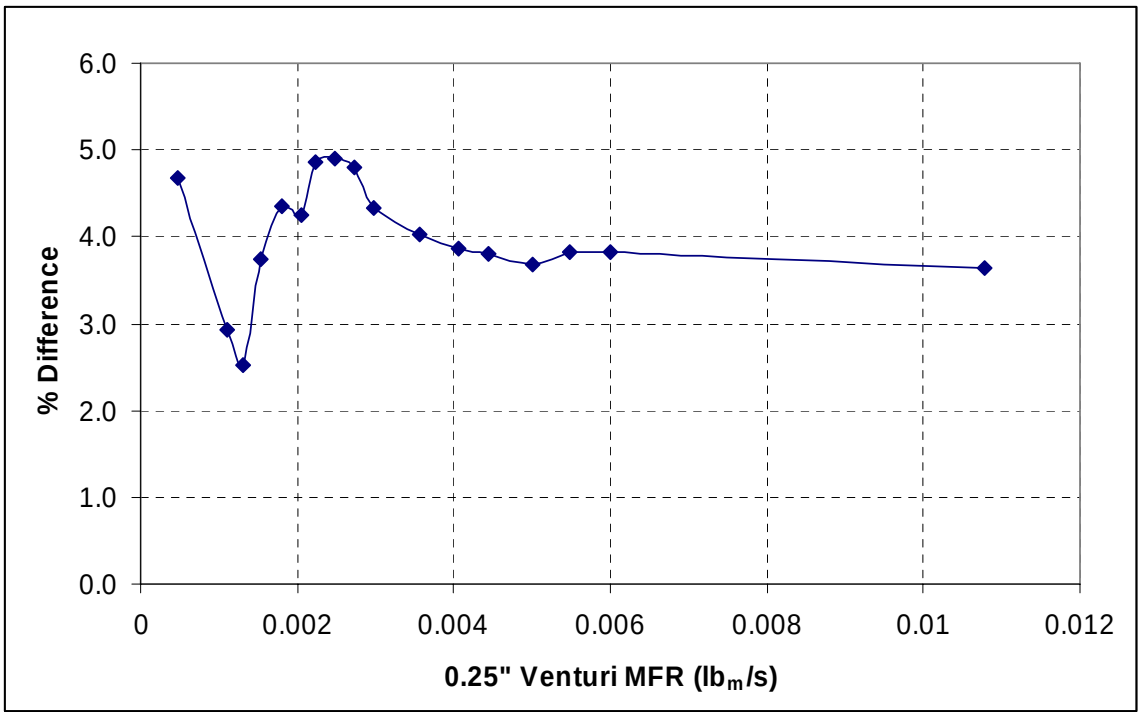

Figure C.3: Difference Between the 0.25" (Standard) and 0.08" (Choked) Venturis Under Steady Flow

Validation Method II: Actuator Exit Velocity

The second method for validating mass flow rate was to compare venturi measurements against mass flow rate calculations made from knowledge of the actuator velocity pulses at different frequencies and amplitudes. This was done using the following equation:

$$\dot{m}_{calc} = C_d \rho \overline{U}_{CL} A \tag{1}$$

Where:

C_d = the discharge coefficient of the actuator, calculated from velocity traverses

ρ = the density of air, calculated from the thermodynamic properties

U_{CL} = the average actuator exit centerline velocity, measured with a hotwire or total pressure probe

A = the geometric exit area of the actuator nozzle

Flow rates were summed for all actuators during a complete cycle to give the total mass flow rate. The discharge coefficient was assumed to be constant over all frequencies and amplitudes. Though not completely true, this is a decent first order approximation. The thermodynamic properties used to calculate the air density were temperature and static pressure (assumed to be ambient).

Small Scale

The small scale setup was described in detail in Chapter 2. The key features here are that a 0.08" venturi equipped with fast response unsteady transducers mounted directly on the venturi was used to measure mass flow rate. It should be noted that this is the same venturi that was used as a critical flow meter to validate mass flow measurements made with a 0.25" venturi for the jet engine actuators. However it was *not* run as a critical flow meter for the small scale actuator mass flow measurements. This is because it was not possible to choke the flow for the small scale actuators since the solenoid orifices, located downstream of the venturi, were too small.

Pressure Fluctuation Characteristics

2-Actuators, 0.08" Nozzles, 180° Phase

Characterization experiments reveal that pressure fluctuations through the 0.08" venturi were not large for out of phase pulsing. This is shown in figure C.4 which gives pressure fluctuation ratio (ΔPrms/ΔPmean) curves for amplitude sweeps at 10, 20, 40 and 80 Hz

pulsing. The fluctuation ratio is higher for low mass flow rates and levels off at about 0.1 as the amplitude increases past 0.001 lb_m/s. For a 10 m/s jet, this corresponds to a mass flow ratio of 0.45% (the momentum ratio will depend on the actuator nozzle used). Most of the small scale experiments used mass flow rates well above this value. At all times the pressure fluctuation ratio is below the target of 0.5.

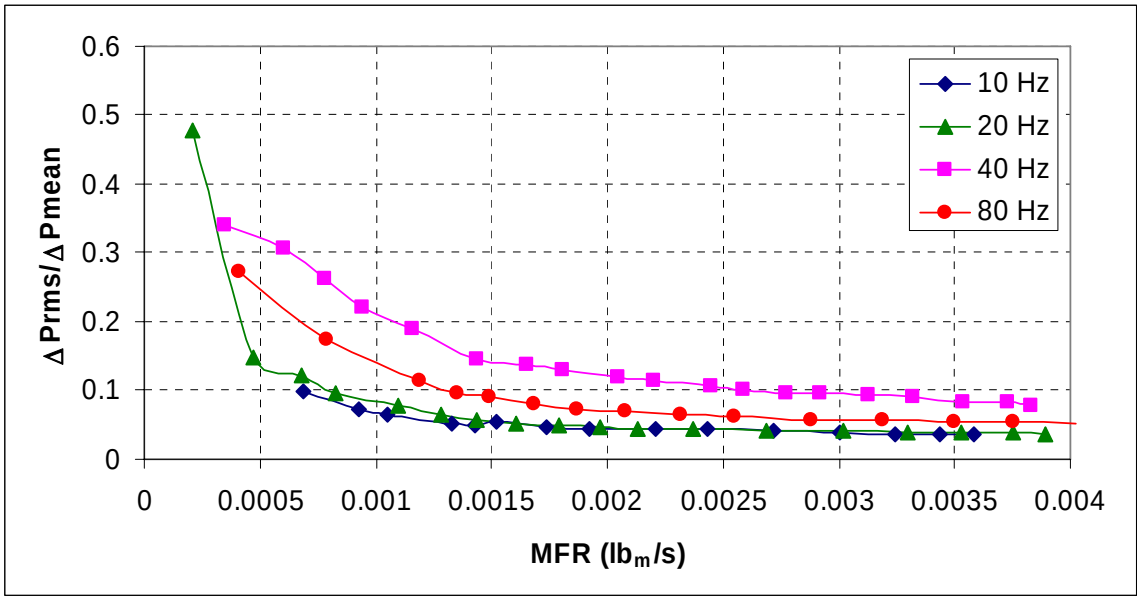

Figure C.4: Differential Pressure Fluctuation Ratio for 0.08" Venturi, 2-Actuators, 180° Pulsing, Amplitude Sweeps, Small Scale Actuators w/ 0.08" Nozzles

Figure C.5 shows the fluctuation ratio for frequency sweeps at three different amplitudes. There is clearly a resonance around 45 Hz which causes the curves to spike, but overall the values are quite good. Even with the effect of the resonance, the fluctuation ratio stays below the target value of 0.5. Square root error was eliminated since unsteady transducers were used and acquired voltage was converted directly to flow rate before averaging. The only error left was measurement bias error and the effect of the slightly

pulsatile flow on the velocity profile of the air moving through the venturi throat. The level of this error is unknown, but it's estimated to be on the order of a few percent.[22]

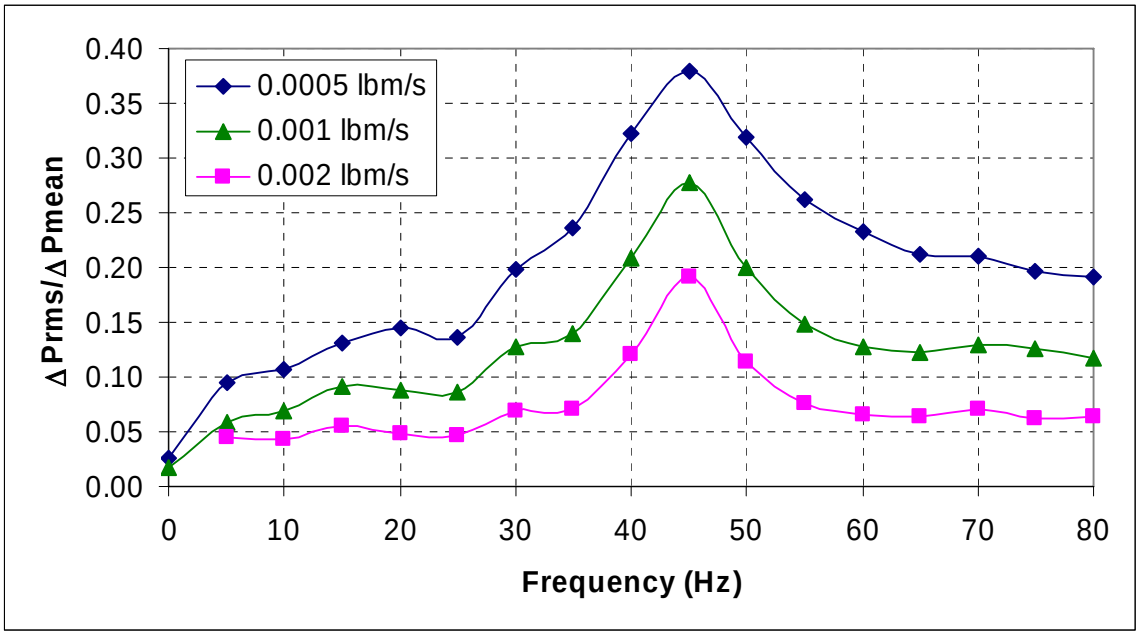

Figure C.5: Differential Pressure Fluctuation Ratio for 0.08" Venturi, 2-Actuators, 180° Pulsing, Frequency Sweeps, Small Scale Actuators w/ 0.08" Nozzles

2-Actuators, 0.08" Nozzles, 0° Phase

Figure C.6 shows the pressure fluctuation ratio curves for in-phase pulsing. The ratios are more than double what they were for the out of phase pulsing case, but most values still fall below the 0.5 target. Not unexpectedly, the curve for the frequency nearest the resonance (40 Hz) is noticeably higher. There is more variation in the in-phase curves than the out-of-phase curves, but they are surprisingly similar at low frequencies (10 and 20 Hz) as seen in figure C.7. Low fluctuation levels were expected for the out-of-phase case because flow was always going through one of the two actuators, just switching paths. Fluctuation levels for the in-phase case, however, are surprisingly low considering

that the actuators shut off the flow completely for half of each cycle. This suggests that there is enough capacitance (i.e. volume) in the system to absorb/supply pressure when the valves open/close.

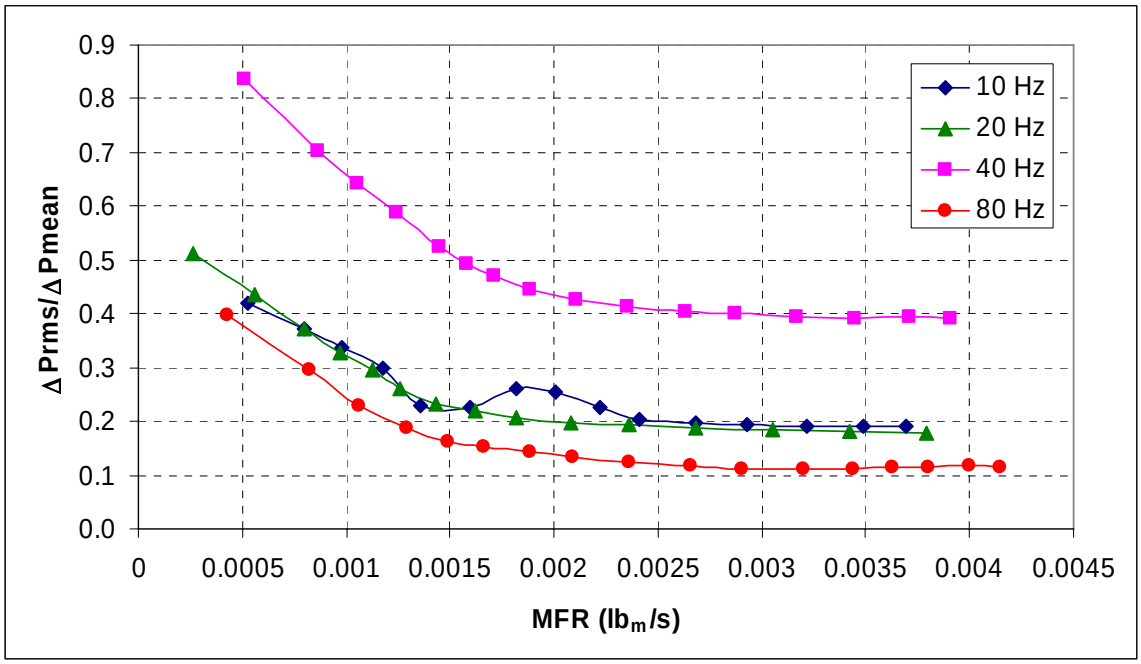

Figure C.6: Pressure Fluctuation Ratio for 0.08" Venturi, 2-Actuators, 0º Pulsing, Amplitude Sweeps, Small Scale Actuators w/ 0.08" Nozzles

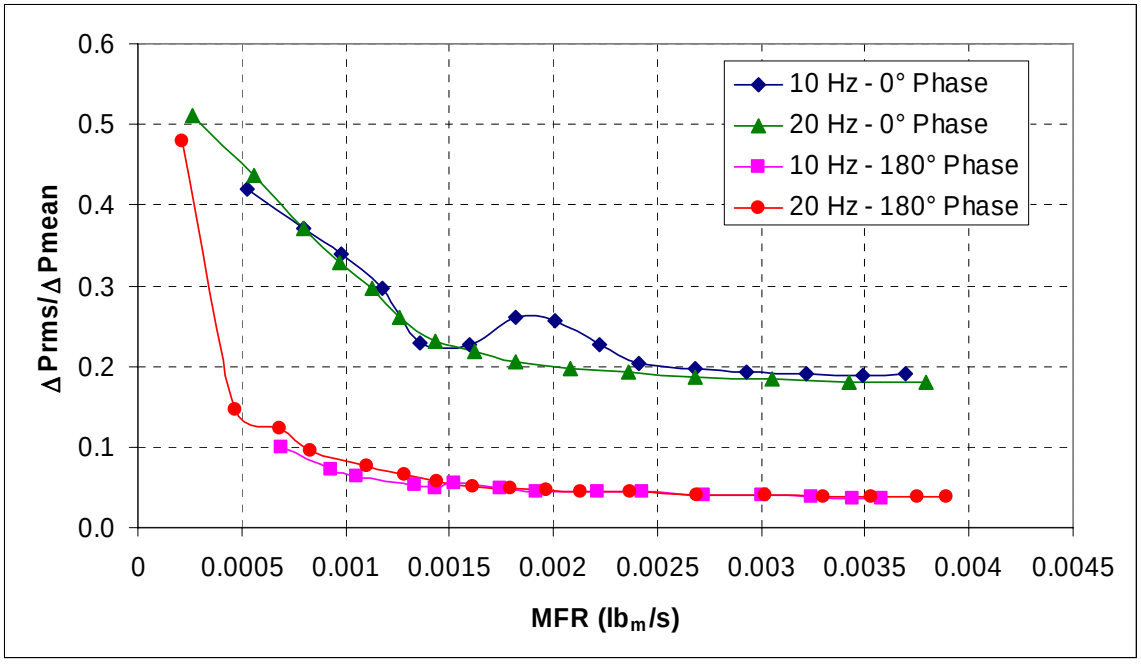

Figure C.7: Comparison of Pressure Fluctuation Ratio for 0.08" Venturi, 0º vs. 180º Pulsing, 2-Actuators, Amplitude Sweeps, Small Scale Actuators w/ 0.08" Nozzles

Other Nozzle Sizes

The pressure fluctuation characteristics for other actuator nozzle sizes should be comparable to those obtained for the 0.08" nozzles. The smallest flow area in the actuator is the solenoid orifice. This area is of the same order as the venturi throat and an order of magnitude smaller than the exit area of the smallest actuator nozzle (0.02"). While changing to a smaller actuator nozzle results in additional resistance to the flow, it is small compared to that already present in the solenoid. Therefore the effect on differential pressure fluctuation in the venturi throat would be minimal.

Validation Against Velocity Pulses

Independent validation of the mass flow rate was performed by comparing mass flow measured with the venturi against mass flow calculated from measurements made at the

actuator centerline exit with a hotwire using the equation and methods previously described. In chapter 2, it was reported that the discharge coefficient for two actuators with 0.08" nozzles was 0.86, obtained from numerical integration of velocity traverses for blowing at the equivalent of 1% MFR. This value was assumed to remain constant and the mass flow rate was calculated for different frequencies and amplitudes. The calculated flow rate was taken as the standard and compared with the flow rate measured with the venturi.

Figure C.8 shows the results for frequency sweeps at a single amplitude (equivalent to 1% MFR for a 10 m/s jet) for both in-phase and out-of-phase pulsing. Two things stand out in the figure. The first is the large spike for the in-phase (0^o) case near the resonant frequency. The second is the drop in the curves above 50 Hz. Since the mass flow rate measured by the venturi is constant, the spike at the resonant frequency signifies a decrease in the average centerline exit velocity. On the other hand, the small dips at high frequencies signify that the average centerline exit velocity for the actuator increases. This increase is due to the larger offset and duty cycle for the higher frequency pulses.

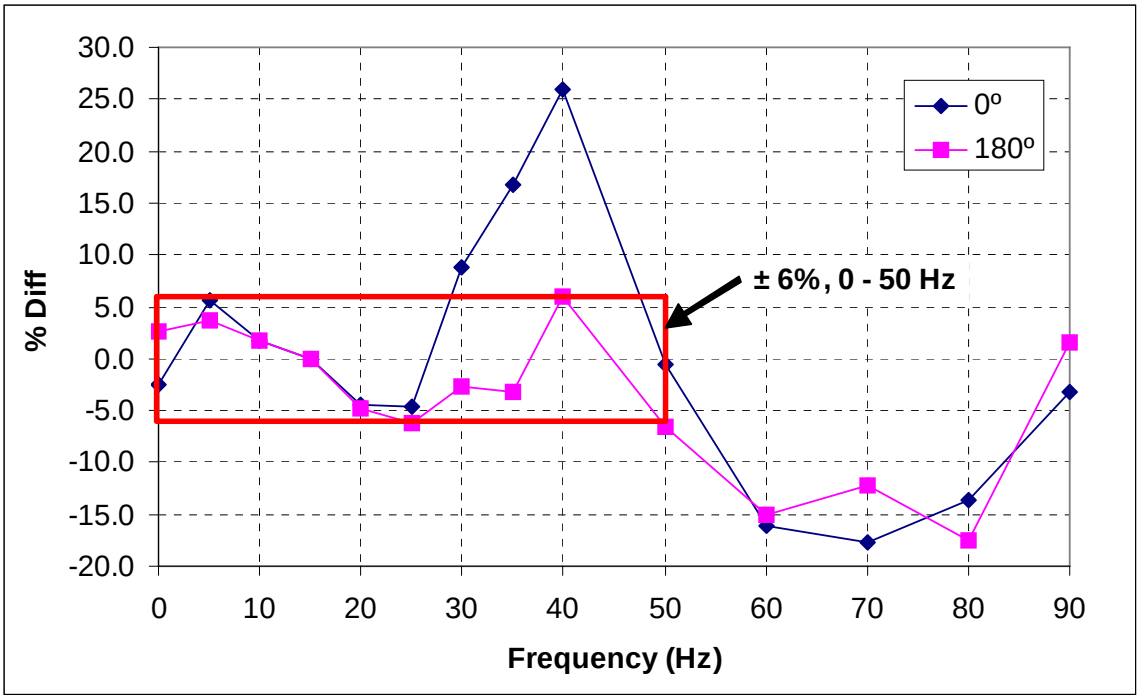

Figure C.8: Mass Flow Measurement Error Using Actuator Centerline Hot Wire Measurements and Cd = 0.86 as the Standard, 2-Actuators, Frequency Sweeps, 0.0027 lb_m/s (1% MFR for a 10 m/s Jet)

The curves for in-phase and out-of-phase pulsing follow each other closely except near the resonant frequency. Both curves actually spike near the resonant frequency of 45 Hz, but for the in-phase case it is much more pronounced. The spikes correlate well with increases in the pressure fluctuation ratio seen in figures C.5 and C.6. The two curves jump up again at 90 Hz, a harmonic of the 45 Hz resonance. The most reliable jet mixing results are in the 0 – 50 Hz range because the pulse quality is better and more consistent in that range. Additionally, out-of-phase pulsing is of greater interest since it results in more mixing enhancement than in-phase pulsing. Therefore, a large majority of the experiments were done using out-of-phase pulsing. The red box in figure C.8 indicates that the percent difference for out-of-phase pulsing from 0 - 50 Hz was ±6%. It should

also be noted that for 10 Hz and 15 Hz, the optimal frequencies for in-phase and out-of-phase pulsing with a 10 m/s jet, the percent difference is on the order of 1%.

This method of mass flow validation has a number of limitations but does confirm that the mass flow measurements are at least in the ballpark. The assumption that C_d is a constant is erroneous. The time averaged velocity profile depends on both the time averaged Reynolds number (i.e. velocity) and the pulsing frequency. It also depends on additional parameters such as duty cycle, offset, and pulse shape (square wave, sinusoid, etc.), which are themselves functions of frequency. Venturi measurement is therefore expected to be the more accurate of the two methods used when the fluctuation ratio is low, which was usually the case except for pulsing in-phase near the resonant frequency.

Correlation of Mass Flow Rate with Velocity

The momentum ratio of the actuator pulses to the jet was the amplitude metric of primary importance. It was therefore important to know how accurately it could be determined from the mass flow rate measured with the venturi. For frequencies below 50 Hz, the average wave top velocity measured at the center of the actuator nozzle exit was a good representative of the pulse velocity since the waveform was close to that of a square wave with very little offset. The wave top was calculated from centerline pulse measurements made with the hotwire. The mass flow rate measured with the venturi correlated well with the wave top velocity. This is seen in figure C.9 which shows the correlation for a 10 Hz out-of-phase pulse. Also included in the figure is the correlation with the mean centerline velocity. Linear regression of the data results in trend lines with very high

correlation coefficients (above 0.998 for both cases). The results shown are typical for frequencies up to 50 Hz for both in-phase and out-of-phase pulsing.

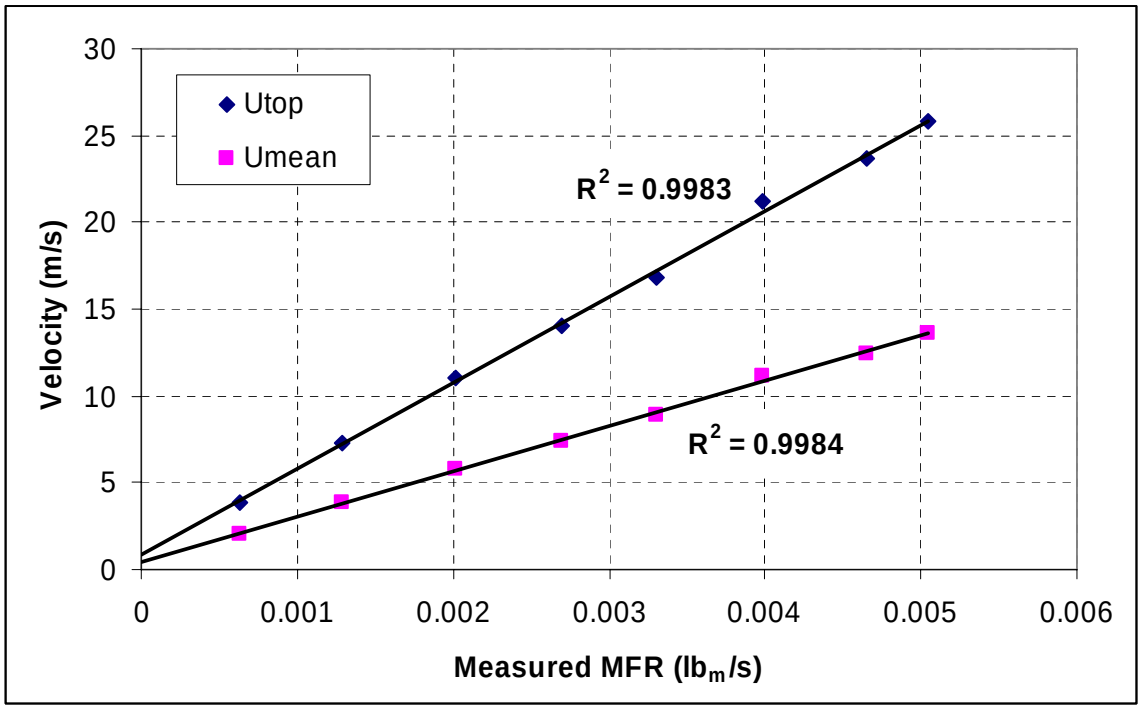

Figure C.9: Correlation of Venturi Measured Mass Flow with Cycle Mean and Wave Top Velocities Measured with the Hotwire, 10 Hz, 180° Phase Pulsing

Figure C.10 shows the correlation of measured mass flow with mean centerline velocity for both in-phase and out-of-phase pulsing at several different frequencies (including the 0 Hz blowing case). There is some spread in the data points between frequencies, but for any particular frequency the correlation is very good. The data for 0 Hz (blowing) and 10 Hz in-phase pulsing are indistinguishable from each other, whereas the data for 10 Hz out-of-phase pulsing are slightly shifted. Not unexpectedly, the data for the in-phase case nearest the resonant frequency (40 Hz) are shifted significantly away from the other

cases. The linear correlation of this data, however, is still good indicating that even though there is venturi measurement error present it is consistent.

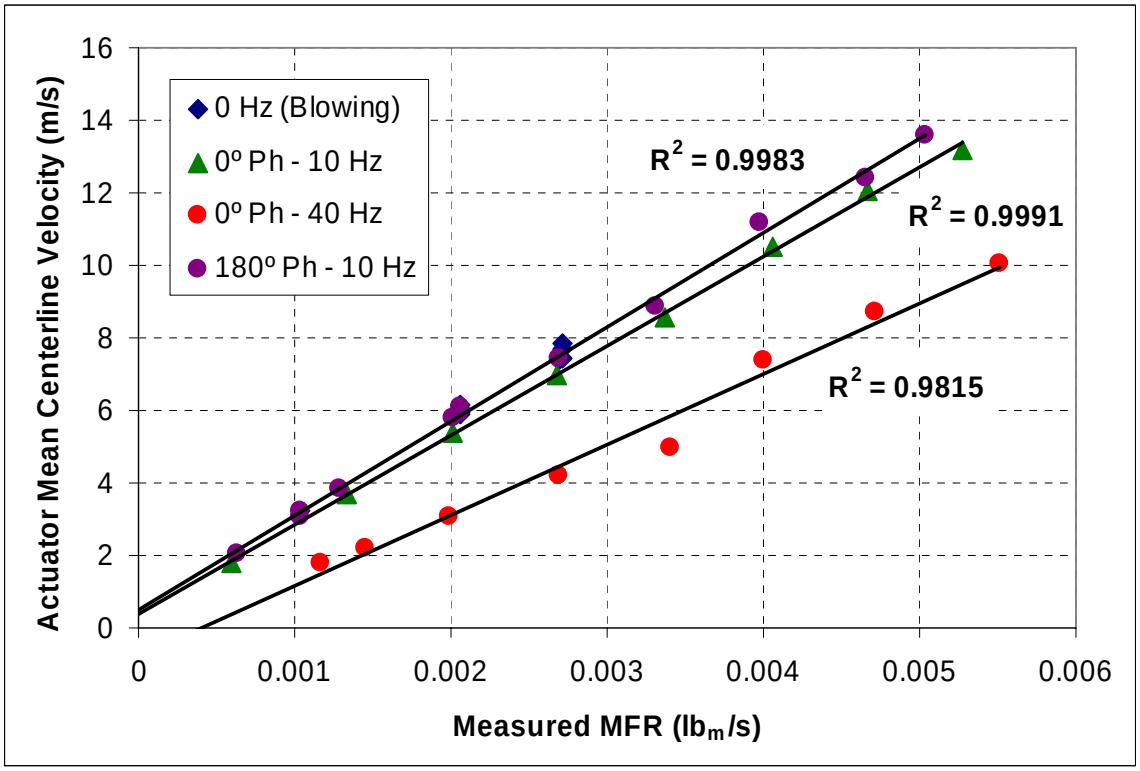

Figure C.10: Correlation of Venturi Measured Mass Flow with Actuator Mean Centerline Velocity for Multiple Frequencies and Phases

The key result from all of this is that mass flow rate measured with the venturi is a very good indicator of wave top velocity and therefore momentum ratio. There is some variation in the data between frequencies, but it is not large except near the 45 Hz resonance for in-phase pulsing. In this case the measured mass flow still correlates well with wave top velocity despite the offset in the data. Out-of-phase pulsing at all frequencies below 50 Hz results in accurate measurements of momentum ratio. This validates the momentum ratio collapse curves of chapter 3. Figure C.11 shows the resulting pulse waveforms obtained when the actuator amplitude is doubled. Here the

pulsing frequency is 5 Hz and the nominal amplitudes are 0.5% and 1.0% MFR for a 10 m/s jet. The wave top for the 1.0% MFR case is almost exactly two times that of the 0.5% MFR case. The correlation is even better than it appears in the figure if the measured mass flow values are used instead of the nominal ones. The ratio of the measured mass flow rates 1.912 compared to the ratio of the wave top velocities which is 1.896.

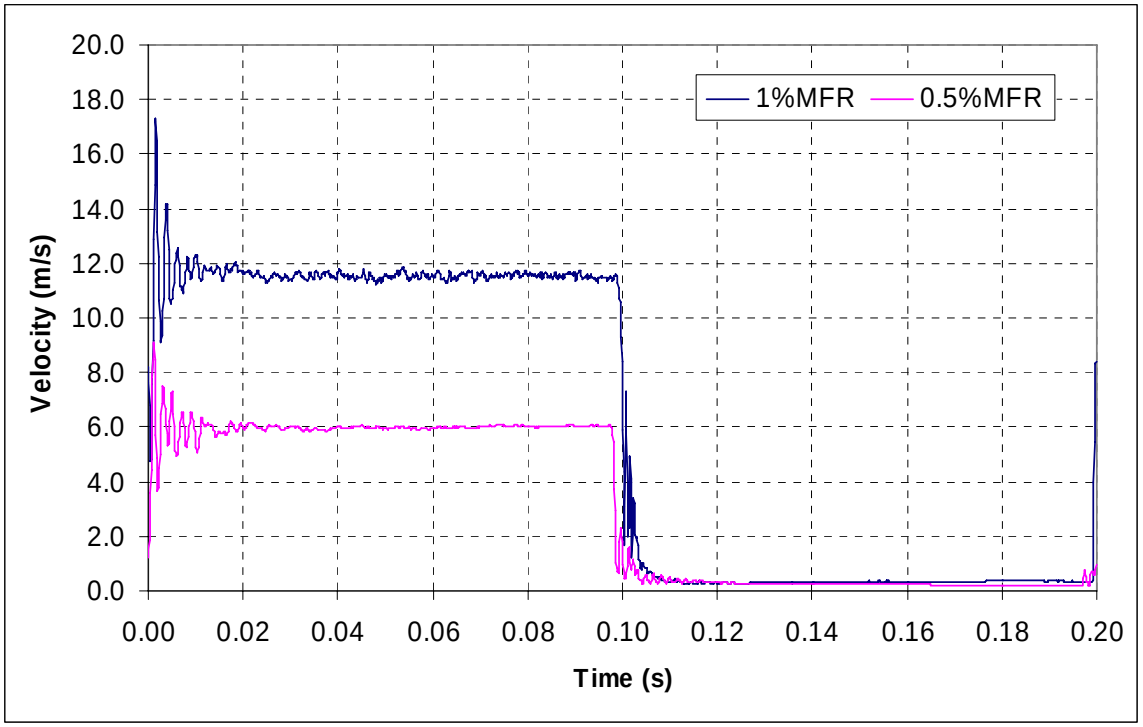

Figure C.11: Example of 5 Hz Pulse Waveforms Scaling with Mass Flow Rate, Nominal Values for Amplitude

Full Scale

The full scale jet actuators were bi-stable fluidic oscillators which pulsed only in the antisymmetric mode. The pulse quality was good for all frequencies tested. Mass flow rate for the full scale jet was measured with a 1" venturi and steady flow, high pressure

transducers with ¼" diameter by 10' long pressure lines. A detailed description of the setup can be found in chapter 4.

Validation Against Velocity Pulses

Actuator mass flow rate measurements for the full scale jet were validated against slot exit velocities measured with permanently mounted total pressure probes as described in chapter 4. Total pressure was converted to velocity and the mass flow rate was calculated using equation (1). The average C_d for the actuator slots was 0.716. For purposes of comparison, the calculated mass flow rate was assumed to be the standard, and the percent difference between the measurements made with the venturi and the standard was calculated. Frequency sweeps were performed and the resulting percent difference vs. frequency curves for cold and 250ºF flow are shown in figure C.12. Almost all of the error is negative, indicating that the venturi measurements are slightly lower than those calculated from velocity for pulsatile flow. This may be partly due to transducer calibration error, but it can't be the only reason since the error varies with frequency. The error range is very good (+1% to -4%) indicating that this method of mass flow rate validation was well suited for the full scale jet.

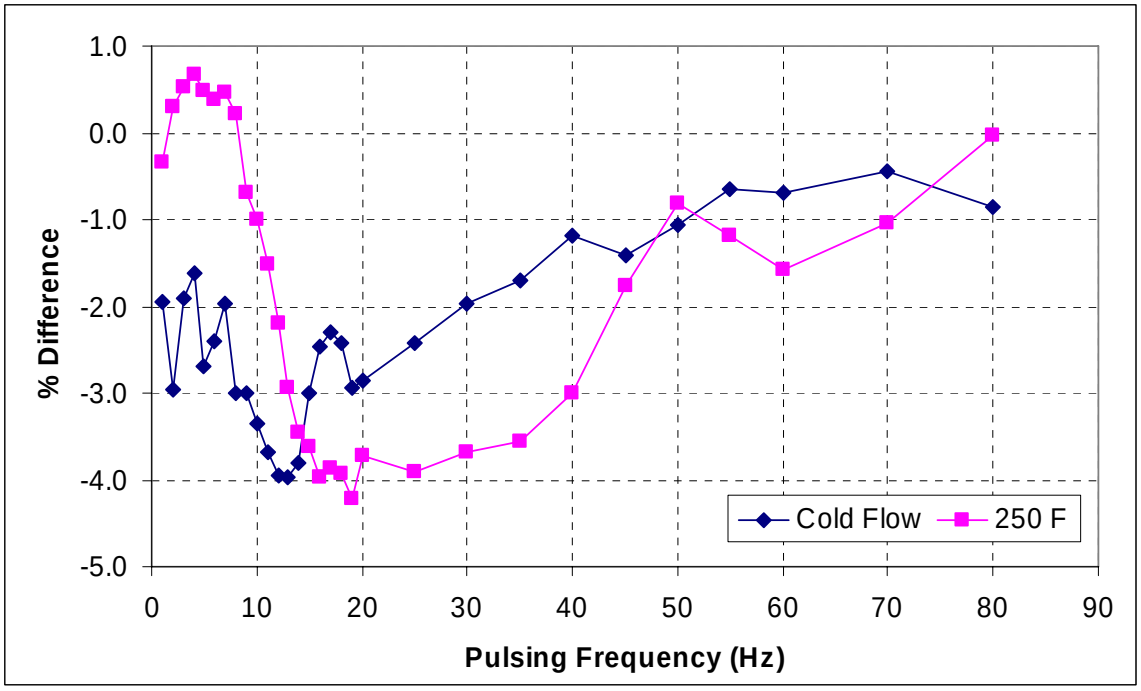

Figure C.12: Difference between Mass Flow Rate Measured with Venturi and Calculated from Slot Exit Velocities for Full Scale Jet Actuators, 1.3% MFR (0.57 lb_m/s) for Cold Flow, 1.41% MFR (0.617 lb_m/s) for 250ºF Flow

Figure C.13 shows the correlation of the venturi mass flow measurements with the average actuator slot exit velocities for an amplitude sweep on a 6 Hz pulse. Also included for reference is the data for the frequency sweep. The correlation coefficient for the regression on the amplitude sweep data is very close to one. The correlation with wave tops (not shown) is equally good. There is little spread in the frequency data signifying that the effect of frequency on measured mass flow rate is minimal for these actuators. Mass flow measurement is therefore a very good indicator of momentum ratio.

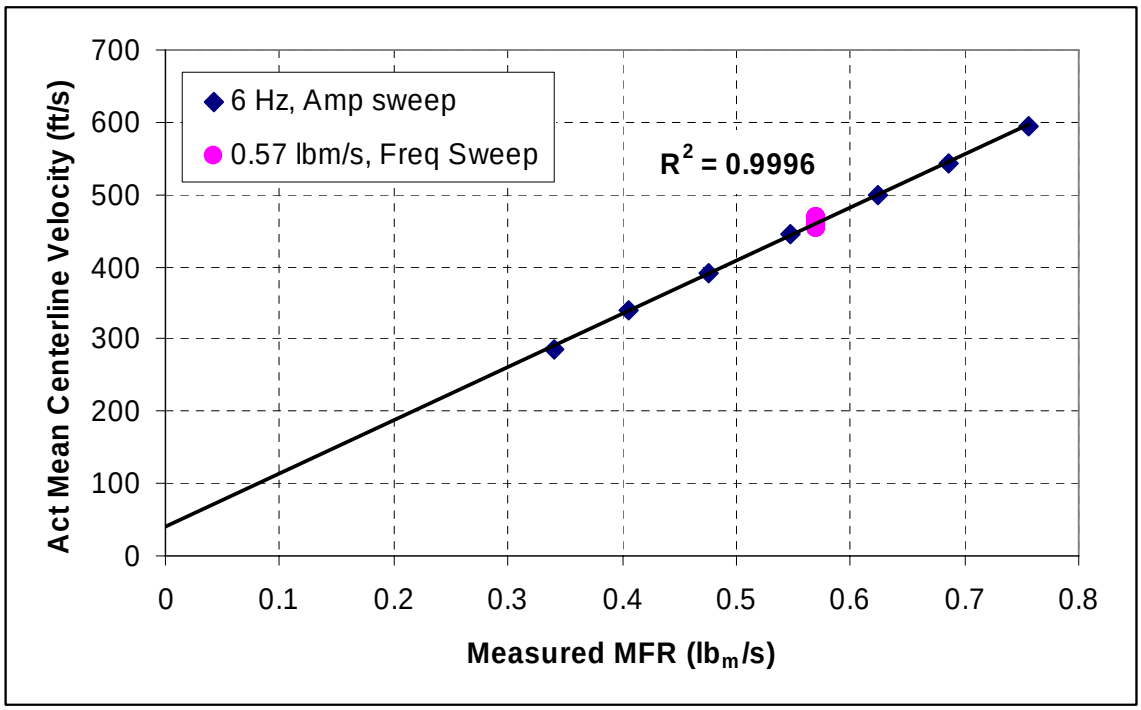

Figure C.13: Correlation of Venturi Measured Mass Flow with Actuator Mean Centerline Velocity, Full Scale Jet Actuators

It is not known which measurement method of determining mass flow rate (venturi or total pressure) was more accurate. Assuming the venturi fluctuations weren't too large, which is reasonable considering actuation was limited to the antisymmetric mode and there was plenty of capacitance (volume) in the system, it is logical to conclude that the venturi measurement was probably more accurate. This cannot be confirmed, however, since the setup was dismantled after the experiments concluded.

Jet Engine

The mass flow rate for each of the jet engine rotary actuators was measured independently with a 0.25" venturi hooked up to steady flow Sensym pressure transducers. Pressure lines from the venturi to the transducers were ¼" in diameter and about 4' long. The actuators were validated in two different ways: against a critical flow

venturi nozzle, and against actuator centerline velocity pulses. To perform the validation experiments, the actuators were mounted on a table using the same equipment (transducers, motor drives, pressure hoses, tubing, etc.) used during the jet mixing experiments.

Validation Against a Choked Venturi

A 0.08" venturi with unsteady transducers was hooked up in series with one of the 0.25" venturis originally used to measure mass flow. The 0.08" venturi was run in the critical flow regime (choked) and measurements were made simultaneously with the 0.25" venturi and compared against each other. This contrasts with the small scale actuator validation experiments, during which the 0.08" venturi would not choke because of the small solenoid orifices. The larger flow rate through this actuator allowed the 0.08" venturi to choke. Figure C.14 shows the correlation between the two venturis for steady flow and two different pulsing frequencies. A linear fit to the data (not shown) results in a correlation coefficient that is close to one within 4 decimals for all three cases: steady, 10 Hz, and 100 Hz. Choking of the venturi occurred around 0.002 lb_m/s and thereafter there was a constant difference between the two venturi measurements of about 4%. The largest contributor to this difference was most likely error in the transducer sensitivities since the transducers were run using factory defaults and were not recalibrated with a manometer prior to this testing. The transducers for both venturis were several years old and it is likely that they drifted slightly from factory calibration values.

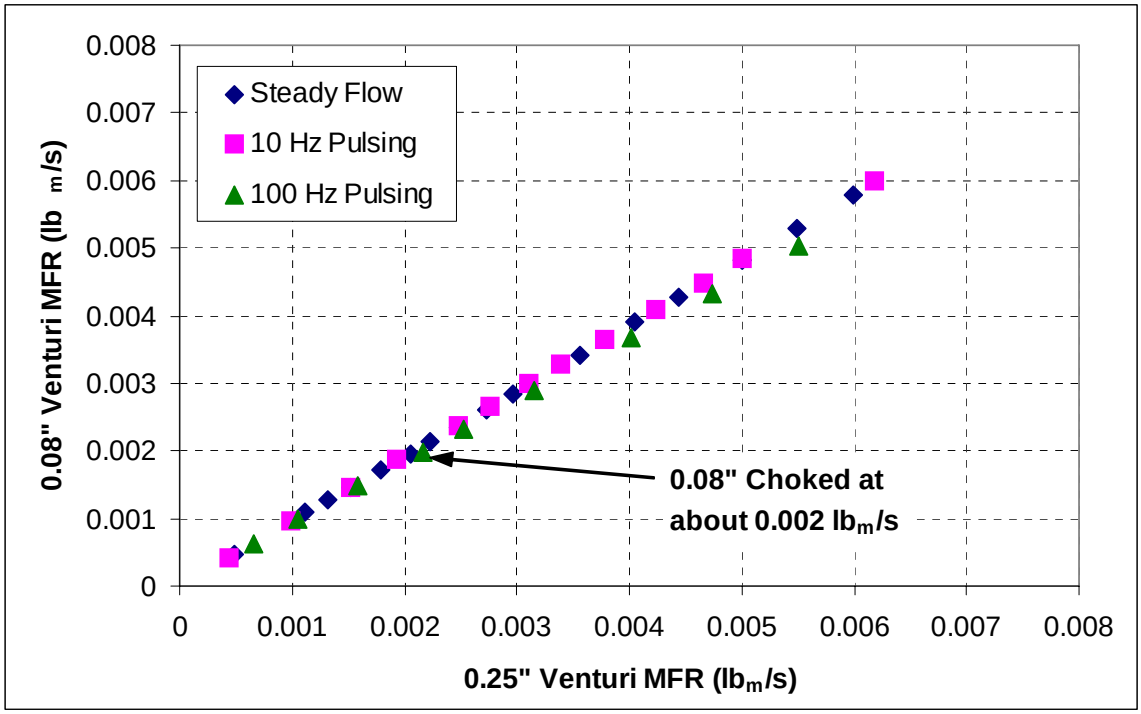

Figure C.14: Correlation of the 0.08" and 0.25" Venturis for Steady Blowing and Two Different Pulsing Frequencies

Figure C.15 shows the percent difference between the two venturis assuming the 0.08" is chosen as the standard. The error clearly depends on frequency, but is flat in the choked region (after 0.002 lb_m/s) for all frequencies. Thus it was necessary to perform a frequency sweep, which is shown in figure C.16. The red line in the figure represents the average difference of 4% between the two venturi measurements. Deviation of the curve from this line represents measurement error by the 0.25" venturi due to frequency effects. Any other error is bias error and is unknown since there is no way to tell which of the two venturi measurements is more correct for steady.

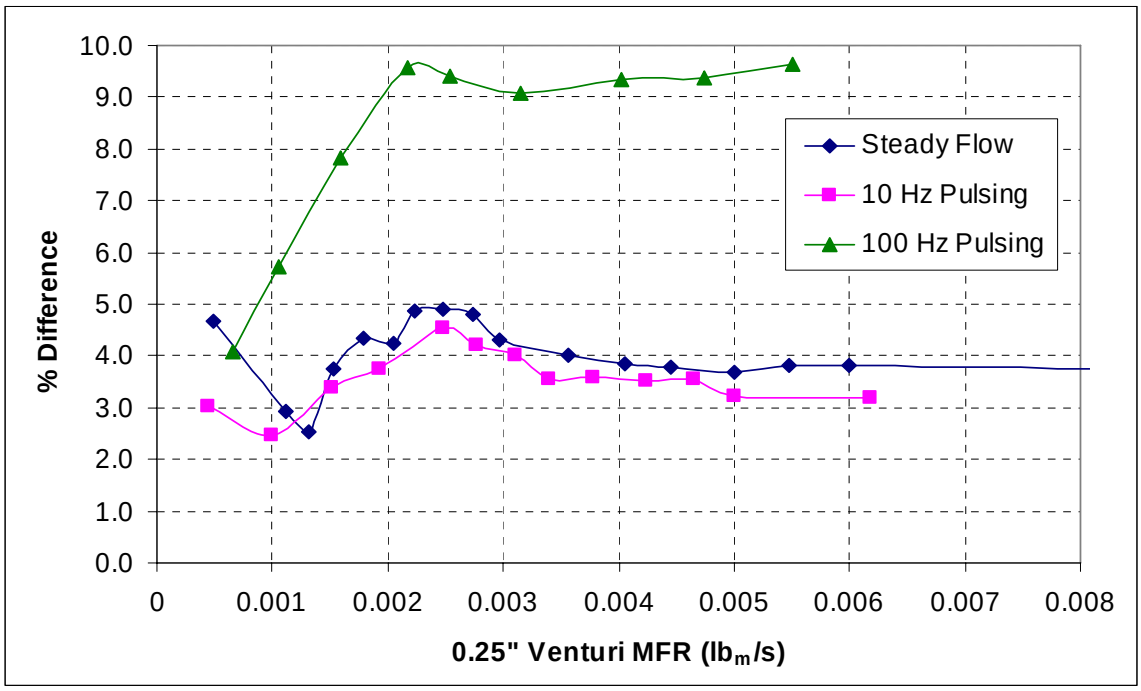

Figure C.15: Percent Difference between 0.08" and 0.25" Venturi Measurements using the 0.08" as the Standard

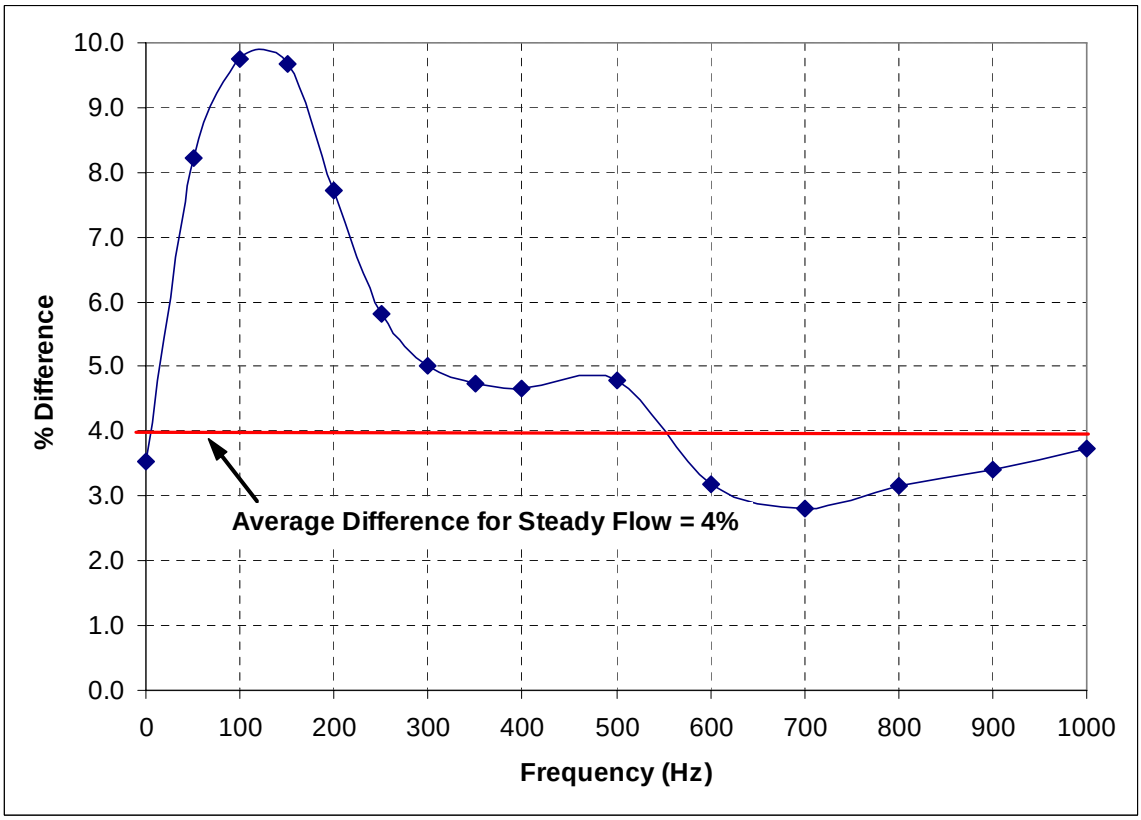

Figure C.16: Percent Difference between 0.08" and 0.25" Venturi Measurements, Frequency Sweep at a Single Amplitude (0.005 lb_m/s)

The error also depends on amplitude, so the next step was to sweep both frequency and amplitude. Figures C.17 and C.18 show the pressure fluctuation ratios for both venturis measured during the amplitude and frequency sweeps. The curves in figure C.17 for the 0.25" venturi have many points above the target fluctuation ratio of 0.5, especially in the 100 – 400 Hz range. The fluctuations depend on both frequency and amplitude and tend to decrease with increasing amplitude meaning higher mass flow rate measurements should be more accurate. On the other hand, the fluctuation values in figure C.18 for the choked venturi are extremely low (less than 0.01) indicating that there is virtually no pressure fluctuation. Therefore, this venturi has no fluctuation error associated with it.

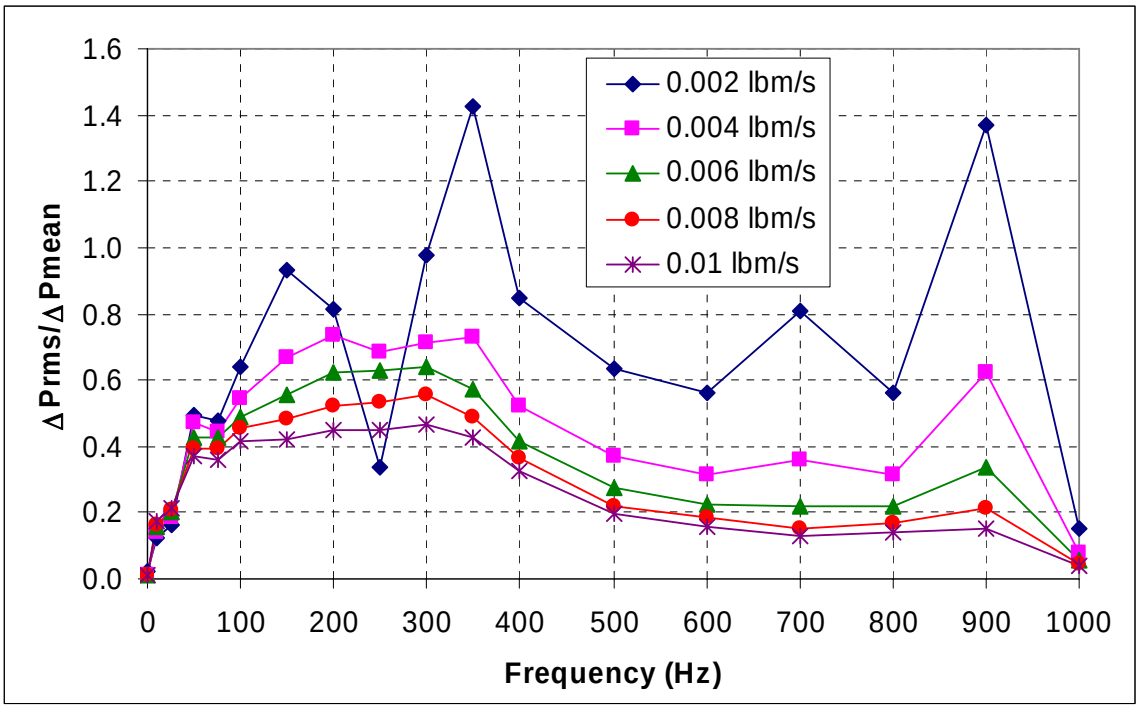

Figure C.17: Differential Pressure Fluctuation Ratios for the 0.25" Venturi, Jet Engine Actuator, Frequency and Amplitude Sweeps

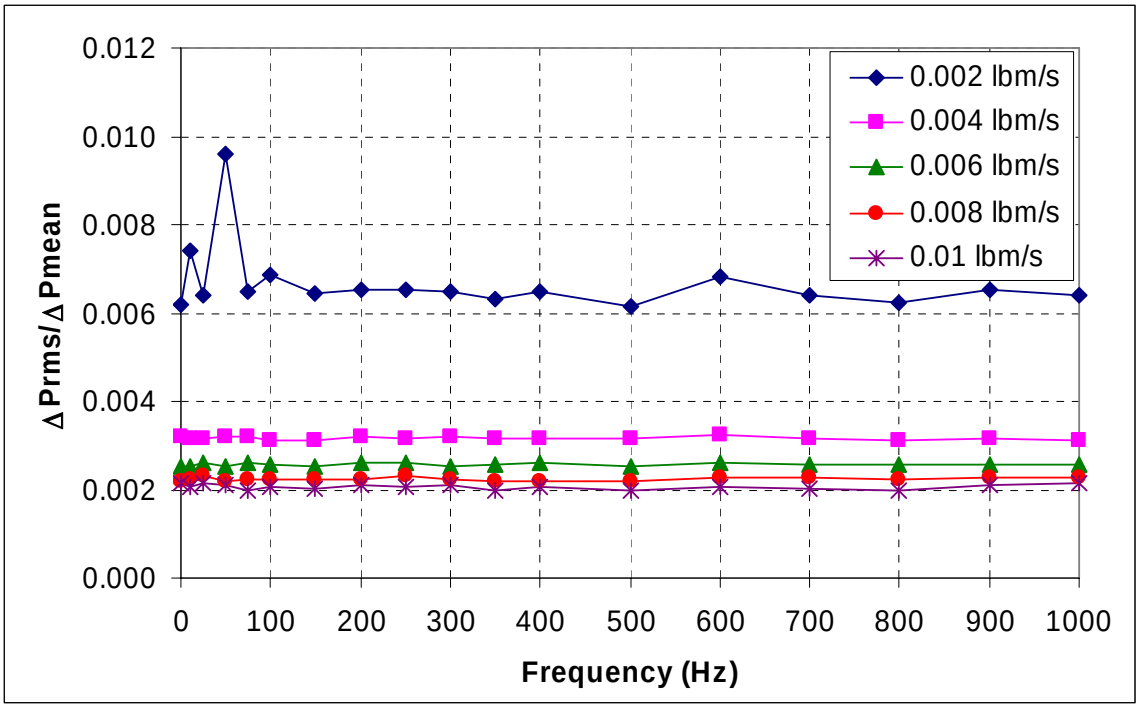

Figure C.18: Differential Pressure Fluctuation Ratios for 0.08" (Choked) Venturi, Jet Engine Actuator, Frequency and Amplitude Sweeps

Figure C.19 shows the percent error in the venturi measurement due to pulsation while sweeping both the frequency and the amplitude. In this case the 4% difference between the two venturis has been subtracted out. The curves in figure C.19 encompass a majority of the tests performed on the jet engine. They could therefore be used, via interpolation, to correct for pulsation error if desired. The overall range of mass flow rate error due to pulsation is from about -3% to +7% for the frequencies and amplitudes tested. Since all transducers were calibrated prior to the jet mixing experiments, transducer sensitivity error is expected to be low for mass flow measurements made during the jet mixing experiments.

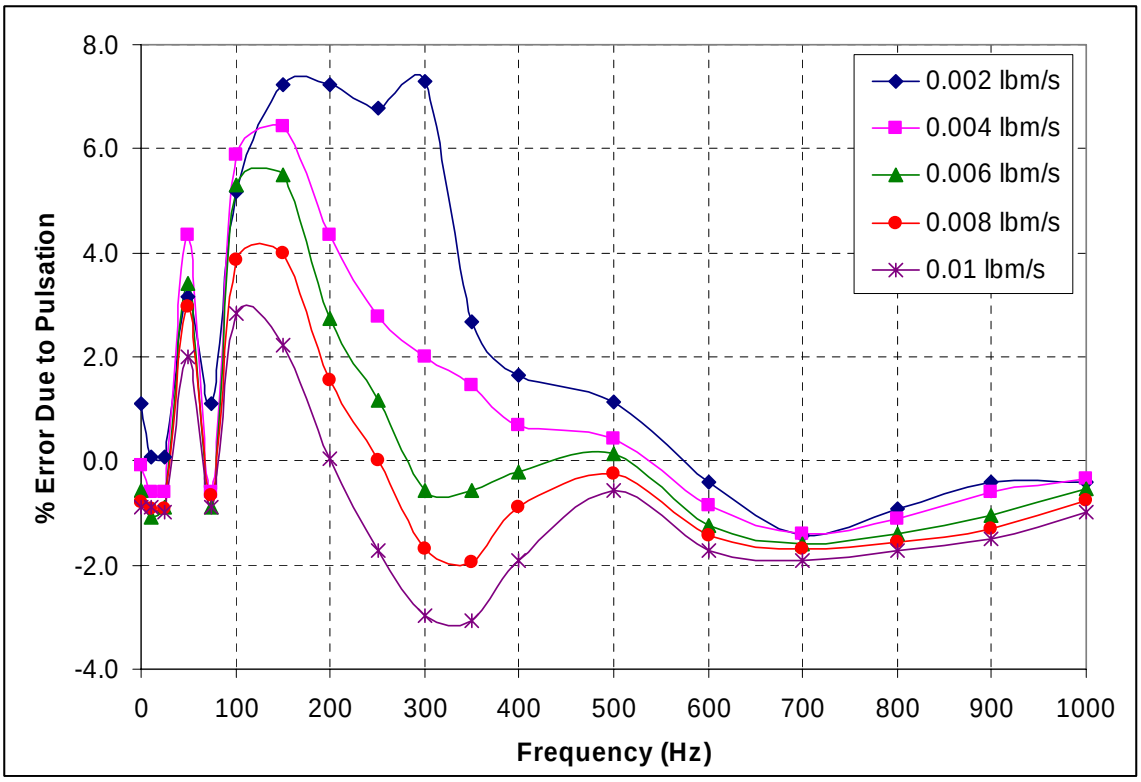

Figure C.19: Percent Error in Measurement Due to Pulsation of the Jet Engine Actuator Using a 0.25" Venturi and Steady Flow Sensym Transducers at Multiple Frequencies and Amplitudes

Validation Against Centerline Velocity Pulses

As in the cases for the small scale and full scale jet actuators, mass flow measurement for the jet engine actuators were initially validated using the actuator average centerline velocity. This was done before the critical flow nozzle was implemented. In this case a 7500 in^3 plenum was added upstream of the rotary actuator and downstream of the venturi to dampen the pulsation at the venturi. Differential pressure fluctuation ratio in the venturi was reduced to below 0.1. The mass flow rate was set, frequency was swept, and the actuator centerline exit velocity was measured with a hotwire. The velocity measurements were correlated with the mass flow measurements, and results are shown in figure C.20 for exit velocity normalized by the 0 Hz (steady blowing) case for each

mass flow rate. The spread of points is slightly better than ±10% over all frequencies and amplitudes.

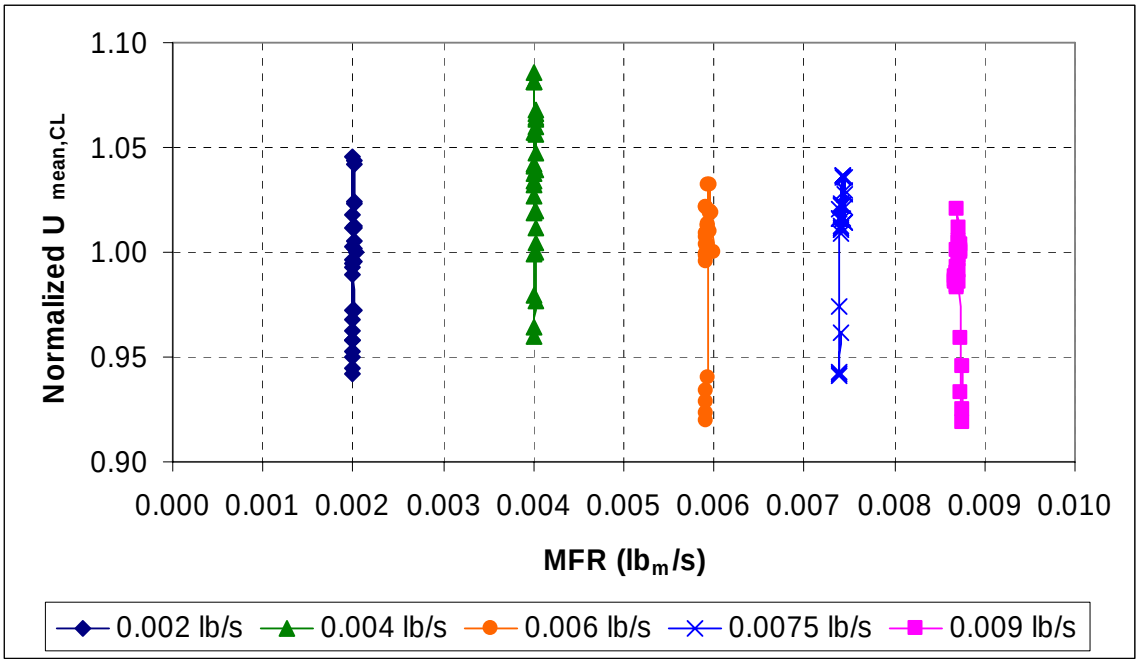

Figure C.20: The Span of Normalized Average Actuator Centerline Exit Velocities, Frequency and Amplitude Sweeps, Velocities are Normalized by the Steady Flow Case

Figure C.21 shows the response of the mean centerline velocity to frequency for different amplitudes. There is somewhat of a pattern, but it is not completely clear. All amplitudes show initial oscillations at frequencies up to about 300 to 400 Hz (corresponding to the upshoot in figure C.19 curves), followed by a settling, a slight decline, and then a slight rise approaching 1000 Hz. A correlation between pulsation error and mean centerline velocity resulted in random scatter.

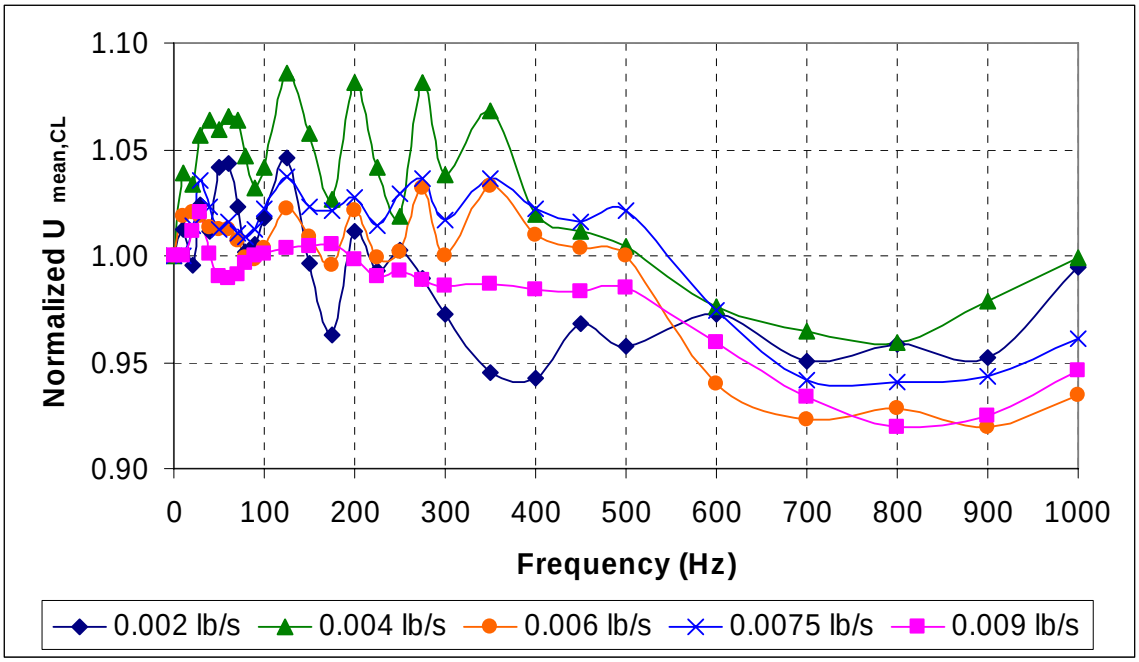

Figure C.21: Normalized Average Actuator Centerline Exit Velocity as a Function of Pulsing Frequency

Correlation of measured MFR to pulse centerline velocity was performed as well and the results were similar to those obtained on the small scale jet actuators. As in the small scale case, amplitude sweeps at many different frequencies resulted in correlations that were good for individual frequencies, but with some variation between frequencies. Most of the results were clustered together near the steady blowing line. Pulsing near 100 Hz showing the most deviation (i.e. it was the least accurate), as originally seen in figure C.14. Since the pulse waveforms were not square and both frequency and amplitude had noticeable affects on the wave shape, no correlation was done against the wave tops since they were difficult to define. The momentum ratio was simply though of as the cycle average mass flow rate squeezed into half of the cycle. This was somewhat restrictive since the waves were sinusoidal and offset was not insignificant. It should suffice,

however, as a first order approximation since the mass flow rate should roughly correlate with momentum.

Summary

Despite the pulsatile conditions, measuring mass flow rate with a venturi was found to be accurate for the small scale, full scale, and jet engine actuators. The only exception occurred with the small scale actuators near a system resonance frequency when in-phase pulsing was implemented. Additionally, it was found that measured mass flow correlated very well with wave top velocity and thus was a good indicator of momentum for square wave pulses in the small scale and full scale actuators.

REFERENCES

1. Adrian, R.J., *Multi-point optical measurements of simultaneous vectors in unsteady flow-a review*. International Journal of Heat and Fluid Flow, 1986. **7**(2): p. 127-45.

2. Adrian, R.J. *Applications of particle image velocimetry*. in *ASME Winter Annual Meeting*. 1989. San Francisco, CA: ASME.

3. Adrian, R.J., *Particle-Imaging Techniques for Experimental Fluid Mechanics*. Annual Review of Fluid Mechanics, 1991. **23**: p. 261-304.

4. Ahuja, K.K., *Supersonic jet noise reduction by tabs and ejectors*, in *15th AIAA Aeroacoustics Conference*. 1993: Long Beach, CA.

5. Ahuja, K.K. and W.H. Brown, *Shear flow control by mechanical tabs*, in *2nd AIAA Shear Flow Conference*. 1989: Tempe, AZ.

6. AIAA, *Assessment of Experimental Uncertainty with Application to Wind Tunnel Testing*. S-071A-1999. 1999: AIAA. 84.

7. Amitay, M. and A. Glezer, *Aerodynamic Flow Control of a Thick Airfoil Using Synthetic Jet Actuators*, in *3rd ASME/JSME Joint Fluids Engineering Conference*. 1999, ASME: San Francisco, CA.

8. Amitay, M., et al., *Modification of the aerodynamic characteristics of bluff bodies using fluidic actuators*, in *28th AIAA Fluid Dynamics Conference*. 1997, AIAA: Snowmass Village, CO.

9. Amitay, M., et al., *The dynamics of flow reattachment over a thick airfoil controlled by synthetic jet actuators*, in *AIAA, Aerospace Sciences Meeting and Exhibit, 37th*. 1999: Reno, NV.

10. Amitay, M., B.L. Smith, and A. Glezer, *Aerodynamic flow control using synthetic jet technology*, in *36th Aerospace Sciences Meeting & Exhibit*. 1998, AIAA: Reno, NV.

11. Baker, R.C., *Flow measurement handbook : industrial designs, operating principles, performance, and applications*. 2000, Cambridge, U.K. ; New York: Cambridge University Press. xxxv, 524 p.

12. Baker, R.C., *Introductory guide to flow measurement*. 2004, New York: ASME Press. xx, 161 p.

13. Behrouzi, P. and J.J. McGuirk, *Jet Mixing Enhancement Using Fluid Tabs*, in *2nd AIAA Flow Control Conference*. 2004, AIAA: Portland, Oregon.

14. Behrouzi, P. and J.J. McGuirk. *Flow control of jet mixing using a pulsed fluid tab nozzle*. 2006. San Francisco, CA, United States: American Institute of Aeronautics and Astronautics Inc., Reston, VA 20191, United States.

15. Behrouzi, P. and J.J. McGuirk, *Effect of tab parameters on near-field jet plume development.* Journal of Propulsion and Power, 2006. **22**(3): p. 576-85.

16. Berkooz, G., P. Holmes, and J.L. Lumley, *Proper orthogonal, decomposition in the analysis of turbulent flows.* Annual Review of Fluid Mechanics, 1993. **25**: p. 537.

17. Berrebi, J., et al., *Ultrasonic flow metering errors due to pulsating flow*. Flow Measurement and Instrumentation, 2004. **15**(3): p. 179-85.

18. Berrebi, J., J. van Deventer, and J. Delsing, *Reducing the flow measurement error caused by pulsations in flows.* Flow Measurement and Instrumentation, 2004. **15**(5-6): p. 311-315.

19. Bignell, N., *Using small sonic nozzles as secondary flow standards.* Flow Measurement and Instrumentation, 2000. **11**(4): p. 329-337.

20. Bignell, N. and Y.M. Choi, *Thermal effects in small sonic nozzles.* Flow Measurement and Instrumentation, 2002. **13**(1-2): p. 17-22.

21. Bonnet, J.P., et al., *Stochastic estimation and proper orthogonal decomposition: complementary techniques for identifying structure.* Experiments in Fluids, 1994. **17**(5): p. 307-14.

22. Brereton, G.J., W.C. Reynolds, and R. Jayaraman, *Response of a turbulent boundary layer to sinusoidal free-stream unsteadiness.* Journal of Fluid Mechanics, 1990. **221**: p. 131-59.

23. Browand, F.K. and J. Laufer. *The role of large scale structures in the initial development of circular jets*. in *Turbulence in liquids; Proceedings of the Fourth Biennial Symposium*. 1975. Rolla, Mo.: Science Press.

24. Brown, G.B., *On Sensitive flames.* Philosophical Magazine, 1932. **13**: p. 161-195.

25. Brown, G.B., *Sensitive Flames.* Science Progress in the Twentieth Century, 1932. **26**: p. 672-677.

26. Brown, G.L. and A. Roshko, *On density effects and large structure in turbulent mixing layers.* Journal of Fluid Mechanics, 1974. **64**(pt.4): p. 775.

27. Brown, W.H. and K.K. Ahuja, *Shear flow control of cold and heated rectangular jets by mechanical tabs. Volume 1: Results and discussion*. 1989, Lockheed Aeronautical Systems Co.: Marietta, GA.

28. Brown, W.H. and K.K. Ahuja, *Shear flow control of cold and heated rectangular jets by mechanical tabs. Volume 2: Tabulated data*. 1989, Lockheed Aeronautical Systems Co.: Marietta, GA.

29. Bruun, H.H., *Hot-wire anemometry : principles and signal analysis*. 1995, Oxford ; New York: Oxford University Press. xxiii, 507 p.

30. Caraballo, E., M. Samimy, and J. DeBonis, *Low dimensional modeling of flow for closed-loop flow control*, in *41st Aerospace Sciences Meeting and Exhibit*. 2003, AIAA: Reno, NV.

31. Caraballo, E., et al., *Application of proper orthogonal decomposition to a high speed axisymmetric jet*, in *31st AIAA Fluid Dynamics Conference*. 2001, AIAA: Anaheim, CA.

32. Carpinlioglu, M.O. and M.Y. Gundogdu, *Presentation of a test system in terms of generated pulsatile flow characteristics.* Flow Measurement and Instrumentation, 2001. **12**(3): p. 181-190.

33. Carpinlioglu, M.O. and M.Y. Gundogdu, *A critical review on pulsatile pipe flow studies directing towards future research topics.* Flow Measurement and Instrumentation, 2001. **12**(3): p. 163-74.

34. Chen, Y., et al., *Enhanced Mixing in a Simulated Combustor Using Synthetic Jet Actuators*, in *37th AIAA Aerospace Sciences Meeting and Exhibit*. 1999, AIAA: Reno, NV.

35. Chenault, C.F., et al., *Active core exhaust (ACE) control for reduction of thermal loading*, in *Fluids 2000 Conference and Exhibit*. 2000: Denver, CO.

36. Christiansen, T. and P. Bradshaw, *Effect of Turbulence on Pressure Probes.* Journal of Physics E: Scientific Instruments, 1981. **14**: p. 992-997.

37. Citriniti, J., *Azimuthal mode interaction in an unforced, high Reynolds-number axisymmetric shear layer*. 1997.

38. Cohen, J. and I. Wygnanski, *The evolution of instabilities in the axisymmetric jet. I. The linear growth of disturbances near the nozzle.* Journal of Fluid Mechanics, 1987. **176**: p. 191-219.

39. Cohen, J. and I. Wygnanski, *The evolution of instabilities in the axisymmetric jet. II. The flow resulting from the interaction between two waves.* Journal of Fluid Mechanics, 1987. **176**: p. 221-35.

40. Coley, D.A., *An introduction to genetic algorithms for scientists and engineers*. 1999, Singapore ; River Edge, NJ: World Scientific.

41. Crow, S.C. and F.H. Champagne, *Orderly structure in jet turbulence.* Journal of Fluid Mechanics, 1971. **48**(pt.3): p. 547-91.

42. Cruz-Maya, J.A., F. Snchez-Silva, and P. Quinto-Diez, *A new correlation to determine the discharge coefficient of a critical Venturi nozzle with turbulent boundary layer.* Flow Measurement and Instrumentation, 2006. **17**(5): p. 258-66.

43. Dahm, W.J.A. and P.E. Dimotakis. *Measurements of Entrainment and Mixing in Turbulent Jets*. 1985. Reno, NV, USA: AIAA, New York, NY, USA.

44. Davis, M.R., *Variable Control of Jet Decay.* 1982. **20**(5): p. 606.

45. Davis, S.A. and A. Glezer. *The Manipulation of Large- and Small-Scales in Coaxial Jets using Synthetic Jet Actuators*. in *38th AIAA Aerospace Sciences Meeting and Exhibit*. 2000. Reno, NV: AIAA.

46. Davitian, J., et al., *Control of Transverse Jet Shear Layer Instabilities*, in *42nd AIAA/ASME/SAE/ASEE Joint Propulsion Conference & Exhibit*. 2006, AIAA: Los Angeles, CA.

47. Demayo, T.N., et al., *Assessing jet-induced spatial mixing in a rich, reacting crossflow.* Journal of Propulsion and Power, 2003. **19**(1): p. 14-21.

48. Dimotakis, P.E., *Turbulent mixing.* Annual Review of Fluid Mechanics, 2005. **37**: p. 329-356.

49. Durbin, P.A. and B.A.P. Reif, *Statistical theory and modeling for turbulent flows*. 2001, Chichester ; New York: Wiley. xiii, 285 p.

50. Eroglu, A. and R.E. Breidenthal, *Structure, penetration, and mixing of pulsed jets in crossflow.* AIAA Journal, 2001. **39**(3): p. 417-423.

51. Faivre, V. and T. Poinsot. *Experimental and numerical investigations of jet control for combustion applications*. 2002. Montreal, Que., United States: American Society of Mechanical Engineers, New York, NY 10016-5990, United States.

52. Farokhi, S., R. Taghavi, and E.J. Rice, *Modern developments in shear flow control with swirl.* AIAA Journal, 1992. **30**(6): p. 1482.

53. Fiedler, H.E., *Coherent structures in turbulent flows.* Progress in Aerospace Sciences, 1988. **25**(3): p. 231.

54. Fiedler, H.E. and H.H. Fernholz, *On management and control of turbulent shear flows.* Progress in Aerospace Sciences, 1990. **27**(4): p. 305.

55. Fincham, A.M. and G.R. Spedding, *Low cost, high resolution DPIV for measurement of turbulent fluid flow.* Experiments in Fluids, 1997. **23**(6): p. 449-62.

56. Freund, J.B. and P. Moin, *Jet mixing enhancement by high-amplitude fluidic actuation.* AIAA Journal, 2000. **38**(10): p. 1863.

57. Funk, R., et al. *Jet mixing enhancement*. 2004. Manchester, United Kingdom: American Institute of Aeronautics and Astronautics Inc., Reston, VA 20191, United States.

58. Garcia-Villalba, M., J. Frohlich, and W. Rodi, *Identification and analysis of coherent structures in the near field of a turbulent unconfined annular swirling jet using large eddy simulation.* Physics of Fluids, 2006. **18**(5): p. 055103.

59. Gaster, M., E. Kit, and I. Wygnanski, *Large-scale structures in a forced turbulent mixing layer.* Journal of Fluid Mechanics, 1985. **150**: p. 23.

60. Ginevsky, A.S., Y.V. Vlasov, and R.K. Karavosov, *Acoustic control of turbulent jets*. 2004, Berlin ; New York: Springer. xiii, 232 p.

61. Glauser, M., et al., *Low-dimensional descriptions of turbulent flows - Experiment and modeling*, in *30th AIAA Fluid Dynamics Conference*. 1999, AIAA: Norfolk, VA.

62. Glezer, A. and M. Amitay, *Synthetic jets.* Annual Review of Fluid Mechanics, 2002. **34**: p. 503-529.

63. Glezer, A., Z. Kadioglu, and A. Pearlstein, *Development of an extended proper orthogonal decomposition and its application to a time periodically forced plane mixing layer.* Physics of Fluids A., 1989. **Vol 1**: p. 1363-1373.

64. Green, S.I., *Fluid vortices*. Fluid mechanics and its applications ; v. 30. 1995, Dordrecht ; Boston: Kluwer Academic Publishers. xxxii, 878 p.

65. Grinstein, F.F., *Coherent structure dynamics and transition to turbulence in rectangular jet systems*, in *30th AIAA Fluid Dynamics Conference*. 1999, AIAA: Norfolk, VA.

66. Guo-Hui, H., D.J. Sun, and Y. Xie-Yuan, *A numerical study of dynamics of a temporally evolving swirling jet.* Physics of Fluids, 2001. **13**(4): p. 951.

67. Gyr, A., W. Kinzelbach, and A. Tsinober, *Fundamental problematic issues in turbulence*. Trends in mathematics. 1999, Basel ; Boston: Birkhèauser. viii, 480 p.

68. Hammad, K.J. and A. Shekarriz. *Turbulence in confined axisymmetric jets of Newtonian and non-Newtonian fluids*. 1998. Washington, DC, USA: ASME, Fairfield, NJ, USA.

69. Haupt, R.L. and S.E. Haupt, *Practical genetic algorithms*. 1998, New York: Wiley. xiv, 177 p.

70. Hermanson, J.C., A. Wahba, and H. Johari, *Duty-cycle effects on penetration of fully modulated, turbulent jets in crossflow*. AIAA Journal, 1998. **36**(10): p. 1935-7.

71. Hilgers, A. and B.J. Boersma, *Optimization of turbulent jet mixing.* Fluid Dynamics Research, 2001. **29**(6): p. 345.

72. Ho, C.M. and P. Huerre, *Perturbed free shear layers*, in *Annual review of fluid mechanics. Vol.16*. 1984, Annual Reviews. p. 365.

73. Ho, C.-M. and L.-S. Huang, *Subharmonics and Vortex Merging in Mixing Layers.* Journal of Fluid Mechanics, 1982. **119**: p. 443-473.

74. Holdeman, J.D., *Mixing of multiple jets with a confined subsonic crossflow.* Progress in Energy and Combustion Science, 1993. **19**(1): p. 31-70.

75. Holdeman, J.D., D.S. Liscinsky, and D.B. Bain, *Mixing of multiple jets with a confined subsonic crossflow: Part II - opposed rows of orifices in rectangular ducts.* Journal of Engineering for Gas Turbines and Power, Transactions of the ASME, 1999. **121**(3): p. 551-562.

76. Huang, H.T., H.E. Fiedler, and J.J. Wang, *Limitation and improvement of PIV. I. Limitation of conventional techniques due to deformation of particle image patterns.* Experiments in Fluids, 1993. **15**(3): p. 168-74.

77. Hui, L., *Identification of coherent structure in turbulent shear flow with wavelet correlation analysis.* Transactions of the ASME. Journal of Fluids Engineering, 1998. **120**(4): p. 778-85.

78. Humphreys, W.M., Jr. , *Probabilistic Extraction Of Vectors In PIV* 1994, NASA Langley Research Center: Hampton. p. 10.

79. Hussain, A.K.M.F. and A.R. Clark, *On the coherent structure of the axisymmetric mixing layer: a flow-visualization study.* Journal of Fluid Mechanics, 1981. **104**: p. 263.

80. Hussain, A.K.M.F. and K.B.M.Q. Zaman, *Vortex pairing in a circular jet under controlled excitation. II. Coherent structure dynamics.* Journal of Fluid Mechanics, 1980. **101**(pt.3): p. 493.

81. Ibrahim, I.M., S. Murugappan, and E.J. Gutmark. *Penetration, mixing and turbulent structures of circular and non-circular jets in cross flow*. 2005. Reno, NV, United States: American Institute of Aeronautics and Astronautics Inc., Reston, VA 20191, United States.

82. Ibrahim, M.K., R. Kunimura, and Y. Nakamura, *Mixing enhancement of compressible jets by using unsteady microjets as actuators.* AIAA Journal, 2002. **40**(4): p. 681.

83. Ishibashi, M. and M. Takamoto, *Methods to calibrate a critical nozzle and flowmeter using reference critical nozzles.* Flow Measurement and Instrumentation, 2000. **11**(4): p. 293-303.

84. Jin, T. and F. Hussain, *Organized motions in a fully developed turbulent axisymmetric jet.* Journal of Fluid Mechanics, 1989. **203**: p. 425-48.

85. Johansson, P.B.V. *Analysis of large data sets using proper orthogonal decomposition*. 2006. San Francisco, CA, United States: American Institute of Aeronautics and Astronautics Inc., Reston, VA 20191, United States.

86. Johari, H., M. Pacheco-Tougas, and J.C. Hermanson, *Penetration and mixing of fully modulated turbulent jets in crossflow.* AIAA Journal, 1999. **37**(7): p. 842-850.

87. Jones, F.E., *Techniques and topics in flow measurement*. 1995, Boca Raton: CRC Press. 163 p.

88. Jørgensen, F.E., *How to Measure Turbulence with Hot-Wire Anemometers - A Practical Guide*. 2005, Dantec Dynamics.

89. Kassab, S.Z., *Pitot tube as a calibration device for turbulence measurement.* Review of Scientific Instruments, 1990. **61**(6): p. 1757-9.

90. Kastner, J., J. Hileman, and M. Samimy. *Exploring high-speed axisymmetric jet noise control using Hartmann tube fluidic actuators*. 2004. Reno, NV, United States: American Institute of Aeronautics and Astronautics Inc., Reston, United States.

91. Kibens, V., et al., *Active flow control technology transition - The Boeing ACE program*, in *AIAA Fluid Dynamics Conference, 30th*. 1999, AIAA: Norfolk, VA.

92. King, G.F., J.C. Dutton, and R.P. Lucht, *Instantaneous, quantitative measurements of molecular mixing in the axisymmetric jet near field.* Physics of Fluids, 1999. **11**(2): p. 403.

93. Klopfenstein, R., Jr., *Air velocity and flow measurement using a Pitot tube.* ISA Transactions, 1998. **37**(4): p. 257-263.

94. Ko, N.W.M., *Annular Jets of Small Inner Diameter.* Journal of Sound and Vibration, 1980. **68**(3): p. 468-472.

95. Ko, N.W.M. and K.M. Lam, *Further Measurements in the Initial Region of an Annular Jet.* Journal of Sound and Vibration, 1984. **92**(3): p. 333-348.

96. Ko, N.W.M., K.K. Lau, and K.M. Lam, *Dynamics of interaction modes in excited annular jets.* Experimental Thermal and Fluid Science, 1998. **17**(4): p. 319-338.

97. Kolovandin, B.A., V.A. Sosinovich, and S.V. Kravar, *To the theory of the mechanism of mixing in turbulent flows with coherent structures.* Letters in Heat and Mass Transfer, 1978. **5**(5): p. 253.

98. Koumoutsakos, P., Freund, J., Parekh, D. *Evolution strategies for parameter optimization in jet flow control*. in *Proceedings of the Center for Turbulence Research Summer Program*. 1998. Stanford, CA

99. Koumoutsakos, P., J. Freund, and D. Parekh, *Evolution strategies for automatic optimization of jet mixing.* AIAA Journal, 2001. **39**(5): p. 967.

100. Kuhlman, J.M., *Variation of entrainment in annular jets.* AIAA Journal, 1987. **25**(3): p. 373.

101. Kyung-Am, P., K. Jae-Hyung, and K. Heuy-Dong, *Computational/experimental study of a variable critical nozzle flow.* Flow Measurement and Instrumentation, 2006. **17**(2): p. 81-6.

102. Lardeau, S., et al., *Analysis of a jet-mixing layer interaction.* International Journal of Heat and Fluid Flow, 2003. **24**(4): p. 520.

103. Lau, J.C., M.J. Fisher, and H.V. Fuchs, *The intrinsic structure of turbulent jets.* Journal of Sound and Vibration, 1972. **22**(4): p. 379.

104. Lee, K. and J.T.C. Liu, *Mixing enhancement in high-speed turbulent shear layers using excited coherent modes.* AIAA Journal, 1998. **36**(11): p. 2027.

105. Lefebvre, A.H., *Gas Turbine Combustion*. 2nd ed. 1998, Philadelphia, PA: Taylor & Francis. pp. 111-118.

106. Lepicovsky, J. *Role of nozzle-exit boundary-layer velocity gradient in mixing enhancement of free jets*. 1989. San Diego, CA, USA: Publ by American Soc of Mechanical Engineers (ASME), New York, NY, USA.

107. Li, H., *Wavelet statistical analysis of the near field flow structure in a turbulent jet.* Transactions of the Japan Society for Aeronautical and Space Sciences, 1998. **41**(133): p. 132-139.

108. Lumley, J.L., *The structure of inhomogeneous turbulent flows*, in *Atmospheric Turbulence and Wave Propagation*. 1967: NAUKA, MOSCOW. p. 166-178.

109. Mankbadi, R.R., *The mechanism of mixing enhancement and suppression in a circular jet under excitation conditions.* Physics of Fluids, 1985. **28**(7): p. 2062.

110. Mathieu, J. and J. Scott, *An introduction to turbulent flow*. 2000, Cambridge ; New York: Cambridge University Press. ix, 374 p.

111. Mathieu, J.C., G. *Structure and development of turbulent jets* in *Fluid dynamics of jets with applications to V/STOL / North Atlantic Treaty Organization, Advisory Group for Aerospace Research and Development*. 1981. Lisbon, Portugal.

112. McKeon, B.J., et al., *Pitot probe corrections in fully developed turbulent pipe flow.* Measurement Science & Technology, 2003. **14**(8): p. 1449-58.

113. Michalke, A., *Survey on Jet Instability Theory.* Progress in Aerospace Sciences, 1984. **21**(3): p. 159.

114. Milano, M. and P. Koumoutsakos, *A clustering genetic algorithm for cylinder drag optimization.* Journal of Computational Physics, 2002. **175**(1): p. 79.

115. Miller, R.W., *Flow measurement engineering handbook.* 3rd ed. 1996, New York: McGraw-Hill.

116. Monkewitz, P.A., *Subharmonic resonance, pairing and shredding in the mixing layer.* Journal of Fluid Mechanics, 1988. **188**: p. 223.

117. Monkewitz, P.A. and P. Huerre, *Influence of the velocity ratio on the spatial instability of mixing layers.* Physics of Fluids, 1982. **25**(7): p. 1137.

118. Morris, P.J., *The spatial viscous instability of axisymmetric jets.* Journal of Fluid Mechanics, 1976. **77**(pt.3): p. 511.

119. Muller, S., M. Milano, and P. Koumoutsakos. *Application of machine learning algorithms to flow modeling and optimization*. in *Center for Turbulence Research Annual Research Briefs*. 1999.

120. Müller, S.D., J.H. Walther, and P.D. Koumoutsakos, *Evolution Strategies for Film Cooling Optimization.* AIAA Journal 2001, 2001. **39**(3): p. 537-539.

121. Murakami, E. and D. Papamoschou, *Experiments on Mixing Enhancement in Dual-Stream Jets*, in *39th AIAA Aerospace Sciences Meeting and Exhibit*. 2001, AIAA: Reno, NV.

122. Nakamura, H., et al., *Analysis of pulsating flow measurement of engine exhaust by a Pitot tube flowmeter.* International Journal of Engine Research, 2005. **6**(1): p. 85-93.

123. Nakazono, Y., *Flow Structure of Annular Jets and Effect of Acoustic Excitation on Their Mixing*, in *34th Aerospace Sciences Meeting and Exhibit*. 1996, AIAA: Reno, NV.

124. Naughton, J.W., L.N. Cattafesta, III, and G.S. Settles, *An experimental study of compressible turbulent mixing enhancement in swirling jets.* Journal of Fluid Mechanics, 1997. **330**: p. 271.

125. Nedungadi, A., et al., *The Effects of Pulsed Blowing on Jet Mixing and Noise Generation*, in *39th Aerospace Sciences Meeting and Exhibit*. 2001, AIAA: Reno, NV.

126. Nickels, T.B. and I. Marusic, *On the different contributions of coherent structures to the spectra of a turbulent round jet and a turbulent boundary layer.* Journal of Fluid Mechanics, 2001. **448**(448): p. 367-385.

127. Ower, E. and R.C. Pankhurst, *The measurement of air flow*. 5th ed. 1977, Oxford ; New York: Pergamon Press. xi, 362 p.

128. Panton, R.L., *Incompressible flow*. 2nd ed. 1996, New York: Wiley. xvii, 837 p.

129. Papadopoulos, G. and W.M. Pitts, *Scaling the near-field centerline mixing behavior of axisymmetric turbulent jets.* AIAA Journal, 1998. **36**(9): p. 1635-42.

130. Papadopoulos, G. and W.M. Pitts, *Generic centerline velocity decay curve for initially turbulent axisymmetric jets.* Journal of Fluids Engineering, Transactions of the ASME, 1999. **121**(1): p. 80-85.

131. Parekh, D.E., *Bifurcating Jets at High Reynolds Numbers*, in *Mechanical Engineering*. 1988, Stanford.

132. Parekh, D.E., et al., *Innovative Jet Flow Control - Mixing Enhancement Experiments*, in *34th Aerospace Sciences Meeting and Exhibit*. 1996, AIAA: Reno, NV.

133. Park, K.A., et al., *The evaluation of critical pressure ratios of sonic nozzles at low Reynolds numbers.* Flow Measurement and Instrumentation, 2001. **12**(1): p. 37-41.

134. Paschereit, C.O., E. Gutmark, and W. Weisenstein, *Coherent structures in swirling flows and their role in acoustic combustion control.* Physics of Fluids, 1999. **11**(9): p. 2667-2678.

135. Pope, S.B., *Turbulent flows*. Repr. with corrections. ed. 2003, Cambridge ; New York: Cambridge University Press. xxxiv, 771 p.

136. Raffel, M., C.E. Willert, and J. Kompenhans, *Particle image velocimetry : a practical guide*. 1998, Berlin ; New York: Springer. xvi, 253 p.

137. Raman, G., *Using controlled unsteady fluid mass addition to enhance jet mixing.* AIAA Journal, 1997. **35**(4): p. 647.

138. Raman, G., M. Hailye, and E.J. Rice, *Flip-flop jet nozzle extended to supersonic flows.* AIAA Journal, 1993. **31**(6): p. 1028.

139. Raman, G., A. Mills, and V. Kibens, *Development of powered resonance-tube actuators for aircraft flow control applications.* Journal of Aircraft, 2004. **41**(6): p. 1306-1314.

140. Raman, G. and E.J. Rice, *Axisymmetric jet forced by fundamental and subharmonic tones.* AIAA Journal, 1991. **29**(7): p. 1114.

141. Raman, G., E.J. Rice, and E. Reshotko, *An experimental study of natural and forced modes in an axisymmetric jet*. 1991, Case Western Reserve Univ.

142. Ramaprian, B.R. and S.W. Tu, *Fully Developed Periodic Turbulent Pipe Flow. Part 2. The Detailed Structure of the Flow.* Journal of Fluid Mechanics, 1983. **137**: p. 59-81.

143. Reynolds, W.C., et al., *Bifurcating and blooming jets.* Annual Review of Fluid Mechanics, 2003. **35**: p. 295.

144. Ritchie, B.D., *Quantitative Acetone Plif Measurements Of Jet Mixing With Synthetic Jet Actuators*, in *Aerospace Engineering*. 2006, Georgia Institute of Technology: Atlanta, GA.

145. Rossi, M., ed. *Lecture Notes in Physics: Of Vortices and Vortical Layers - An Overview*. Vortex Structure and Dynamics. Vol. 555. 2000, Springer. 40-123.

146. Samet, M.M. and R.A. Petersen, *Effects of excitation level on the stability of an axisymmetric mixing layer.* Physics of Fluids, 1988. **31**(11): p. 3246-3252.

147. Sanger, J.L. and P.A. Dellenback, *Heat Transfer in Counterswirled Coaxial Jet Mixing.* Journal of Propulsion and Power, 1998. **14**(3): p. 384-391.

148. Smith, B.L. and A. Glezer, *Vectoring and small-scale motions effected in free shear flows using synthetic jet actuators*, in *35th Aerospace Sciences Meeting and Exhibit*. 1997, AIAA: Reno, NV.

149. Smith, B.L., M.A. Trautman, and A. Glezer, *Controlled interactions of adjacent synthetic jets*, in *AIAA, Aerospace Sciences Meeting and Exhibit, 37th*. 1999: Reno, NV.

150. Smith, D.R., et al., *Modification of lifting body aerodynamics using synthetic jet actuators*, in *AIAA, Aerospace Sciences Meeting & Exhibit, 36th*. 1998, AIAA: Reno, NV.

151. Smith, S.H. and M.G. Mungal, *Mixing, structure and scaling of the jet in crossflow.* Journal of Fluid Mechanics, 1998. **357**: p. 83.

152. Smith, T.D., A.B. Cain, and C.F. Chenault, *Numerical simulation of enhanced mixing in jet plumes using pulsed blowing.* Journal of Aircraft, 2001. **38**(3): p. 458-463.

153. Smith, T.R., J. Moehlis, and P. Holmes, *Low-dimensional modelling of turbulence using the proper orthogonal decomposition: A tutorial.* Nonlinear Dynamics, 2005. **41**(1-3): p. 275-307.

154. Stanislas, M., J. Westerweel, and J. Kompenhans, *Particle image velocimetry : recent improvements : proceedings of the EUROPIV 2 Workshop held in Zaragoza, Spain, March 31-April 1, 2003*. 2004, Berlin ; New York: Springer.

155. Stone, J.R. and D.J. McKinzie, Jr., *Acoustic Excitation - A Promising New Means Of Controlling Shear Layers*. 1984. p. 32.

156. Su, L.K. and M.G. Mungal, *Simultaneous measurements of scalar and velocity field evolution in turbulent crossflowing jets.* Journal of Fluid Mechanics, 2004. **513**: p. 1-45.

157. Su, L.K. and M.G. Mungal. *Mixing in crossflowing jets: Turbulence quantities*. 2005. Reno, NV, United States: American Institute of Aeronautics and Astronautics Inc., Reston, VA 20191, United States.

158. Tamburello, D.A. and M. Amitay. *Manipulation of an axisymmetric jet using a single perpendicular control jet*. 2006. San Francisco, CA, United States: American Institute of Aeronautics and Astronautics Inc., Reston, VA 20191, United States.

159. Taylor, B.N. and C.E. Kuyatt, *Guidelines for Evaluating and Expressing the Uncertainty of NIST Measurement Results*. 1994, NIST. p. 24.

160. Tennekes, H. and J.L. Lumley, *A first course in turbulence*. 1972, Cambridge, Mass.,: MIT Press. xii, 300 p.

161. Tu, S.W. and B.R. Ramaprian, *Fully Developed Periodic Turbulent Pipe Flow. Part 1. Main Experimental Results And Comparison With Predictions.* Journal of Fluid Mechanics, 1983. **137**: p. 31-58.

162. Utami, T., R.F. Blackwelder, and T. Ueno, *A cross-correlation technique for velocity field extraction from particulate visualization.* Experiments in Fluids, 1991. **V10**(4): p. 213-223.

163. Van Rensburg, P.J.S., I.S. Van Wyk, J.D. *Adaptive PID control using a genetic algorithm*. in *Second International Conference on Knowledge-Based Intelligent Electronic Systems*. 1998. Adelaide, SA, Australia: IEEE.

164. Viets, H., *Flip-flop jet nozzle.* AIAA Journal, 1975. **13**(10): p. 1375.

165. von Glahn, U., J. Goodykoontz, and C. Wasserbauer. *Velocity And Temperature Decay Characteristics Of Inverted-Profile Jets*. 1986. Reno, NV, USA: AIAA, New York, NY, USA.

166. von Glahn, U.H., *Correlation Of Flight Effects On Centerline Velocity Decay For Cold-Flow Acoustically Excited Jets.* NASA Technical Memorandum, 1983: p. 16.

167. von Glahn, U.H. *On Some Flow Characteristics Of Conventional And Excited Jets*. in *Aerospace Sci. Meeting*. 1984. Reno, NV, USA: AIAA, New York, NY, USA.

168. von Glahn, U.H., *Two-Dimensional Nozzle Plume Characteristics*. 1987. p. 21.

169. von Lavante, E., et al., *Numerical and experimental investigation of unsteady effects in critical Venturi nozzles.* Flow Measurement and Instrumentation, 2000. **11**(4): p. 257-264.

170. Watanabe, S. and M.G. Mungal, *Velocity field measurements of mixing-enhanced compressible shear layers* in *37th Aerospace Sciences Meeting and Exhibit*. 1999, AIAA: Reno, NV.

171. Weitao, B., et al., *Time-resolved proper orthogonal decomposition of the near-field flow of a round jet measured by dynamic particle image velocimetry.* Measurement Science & Technology, 2003. **14**(8): p. 1-5.

172. Wickersham, P. and D. Parekh. *Real-Time Optimization of Jet Mixing via Evolution Strategies*. in *ASME Fluids Engineering Division Summer Meeting* 2001. New Orleans, Louisiana: ASME.

173. Willert, C.E. and M. Gharib, *Digital particle image velocimetry.* Experiments in Fluids, 1991. **V10**(4): p. 181-193.

174. Wiltse, J.M. and A. Glezer, *Manipulation of free shear flows using piezoelectric actuators.* Journal of Fluid Mechanics, 1993. **249**: p. 261.

175. Wiltse, J.M. and A. Glezer, *Direct excitation of small-scale motions in free shear flows.* Physics of Fluids, 1998. **10**(8): p. 2026.

176. Winant, C.D. and F.K. Browand, *Vortex pairing: the mechanism of turbulent mixing-layer growth at moderate Reynolds number.* Journal of Fluid Mechanics, 1974. **63**(pt.2): p. 237.

177. Wygnanski, I. and R.A. Petersen, *Coherent Motion in Excited Free Shear Flows,* in *AIAA Shear Flow Control Conference*. 1985, AIAA: Boulder, CO.

178. Yuan, C.C.L., M. Krstic, and T.R. Bewley, *Active control of jet mixing.* IEE Proceedings-Control Theory and Applications, 2004. **151**(6): p. 763-72.

179. Zaman, K.B.M.Q. and A.K.M.F. Hussain, *Vortex pairing in a circular jet under controlled excitation. I. General jet response.* Journal of Fluid Mechanics, 1980. **101**(pt.3): p. 449.